UQAC
Université du Québec
à Chicoutimi

THESIS PRESENTED TO THE

UNIVERSITY OF QUEBEC AT CHICOUTIMI

IN PARTIAL FULFILLMENT OF THE

REQUIREMENT FOR THE DEGREE OF

DOCTOR OF PHILOSOPHY IN ENGINEERING

BY

MOHAMED HASSAN A. ABDELAZIZ

MICROSTRUCTURAL AND MECHANICAL CHARACTERIZATION OF TRANSITION ELEMENTS-CONTAINING Al-Si-Cu-Mg ALLOYS FOR ELEVATED-TEMPERATURE APPLICATIONS

QUÉBEC, CANADA

UQAC
Université du Québec
à Chicoutimi

THÈSE PRÉSENTÉE À

L'UNIVERSITÉ DU QUÉBEC À CHICOUTIMI

COMME EXIGENCE PARTIELLE

DU DOCTORAT EN INGÉNIERIE

PAR

MOHAMED HASSAN A. ABDELAZIZ

CARACTÉRISATION MICROSTRUCTURALE ET MÉCANIQUE DES ALLIAGES Al-Si-Cu-Mg CONTENANT DES ÉLÉMENTS DE TRANSITION POUR DES APPLICATIONS À TEMPÉRATURE ÉLEVÉE

QUÉBEC, CANADA

Dedicated to my parents, my wife Aya,

and my daughter Laura

RÉSUMÉ

L’objectif principal de cette étude est de comprendre et d’améliorer les performances mécaniques des alliages 354 Al-Si-Cu-Mg à température ambiante et à température élevée avec ajout de zirconium (Zr) comme élément d’alliage de base et l’ajout subséquent de nickel (Ni) et DE manganèse (Mn) pour valider l’utilité de ces alliages dans l’industrie automobile. Les motifs de ces ajouts sont de développer une microstructure thermiquement stable, capable de résister au grossissement provoqué par une exposition prolongée à des températures élevées et donc de préserver des propriétés mécaniques acceptables lorsqu'il est utilisé dans des applications à haute température.

L’analyse des données obtenue par différentiel scanning calorimétrique (DSC) et par l’identification des phases démontre que les alliages de type 354 développe une microstructure complexe à l’état brut de coulée qui contient des phases communes incluant: α-Al, silice eutectique, aluminure de cuivre (Al_2Cu) avec différente morphologies, phases riche en Mg comme le siliciure de magnésium (Mg_2Si), phase-Q ($Al_5Cu_2Mg_8Si_6$) et des phases intermétalliques à base de Fe incluant β-Al_5FeSi, α-Al15(Fe, Mn)$_3Si_2$, and π-$Al_8FeMg_3Si_6$.

En ce qui concerne les précipités de renforcement, les études microscope électronique transmission (MET) confirment que les alliages étudiés ont été renforcés principalement par les précipités θ-Al_2Cu et S-Al_2CuMg et leurs précurseurs, en plus d'un effet de renforcement secondaire par des précipités en Al_x(Zr, Ti) Si qui s'est formé après l'addition de Zr. Les données montrent que l'alliage de base (M1S), qui est un alliage sans Ni, comprend des fractions plus élevées de précipités de θ-Al_2Cu que l'alliage contenant 4% de Ni (M4S).

Les additions de Ni et Mn en différentes quantités et combinaisons (alliages M2S à M5S) ont augmenté la fraction volumique des composés intermétalliques par rapport à l'alliage de base (M1S) (2,5% pour l'alliage M1S et 12,21% pour l'alliage M4S). Ils ont des effets indiscutables sur les propriétés mécaniques. Les ajouts proposés ont amélioré les performances mécaniques des alliages, à savoir les propriétés de traction à température ambiante et élevée, les valeurs de dureté et les propriétés d'impact. Pour les alliages contenant du Mn, les performances mécaniques améliorées ont été attribuées à la formation de particules de boue sous la forme de α-Al_{15} (Fe, Mn)$_3Si_2$ à côté de la phase α de type script qui pourrait résister aux propagations de fissures; tandis que la précipitation de phases portant Ni dans les alliages contenant du Ni (tels que: Al_9FeNi, Al_3CuNi et Al_3Ni) était considérée comme gênant la propagation des fissures et améliorant ainsi les propriétés mécaniques.

La présence d'entailles asymétriques s'avérait plus délétère que les propriétés symétriques des propriétés de traction obtenues à température ambiante et à 250°C, même si la surface réduite était la même en raison de l'état complexe des contraintes qui se développent à la racine de l'entaille. Les effets de diverses additions chimiques sur les

propriétés de traction des barres crantées obtenues à température ambiante et à 250°C se sont révélés faibles comparés à leurs effets évidents sur les propriétés en traction des barres lisses (non entaillées). À la température ambiante, les valeurs de résistance à la traction (NTS) étaient inférieures aux valeurs de résistance à la traction obtenues pour les barres lisses (non entaillées) correspondantes attribuées à la ductilité limitée des alliages coulés Al-Si-Cu-Mg (type 354). Le ramollissement qui a eu lieu lors des essais de traction à 250°C a rendu les alliages quelque peu ductiles, en particulier les alliages M1S à M3S. Par conséquent, les barres de traction crantées avec des trous asymétriques de ces alliages présentaient des valeurs élevées de NTS par rapport à la résistance à la traction des barres non tordues soumises à des conditions de traitement similaires, à l'exception de la condition T5 de l'alliage M2S.

La variation de la technique d'exposition thermique de statique à dynamique, a eu un effet subtil sur les données de traction et de dureté obtenues à température ambiante; ainsi, la technique d'exposition statique (stabilisation) pourrait être utilisée pour simuler le comportement du matériau employé dans une application d'exposition thermique dynamique (comme dans les composants du moteur). Le grossissement des précipités de renforcement après l'exposition prolongée à 250°C a eu un effet délétère sur les propriétés de traction et les valeurs de dureté. Une réduction notable des valeurs de résistance, en particulier la limite élastique, et une augmentation remarquable des valeurs de ductilité ont été observées en association avec une stabilisation à 250°C. Cependant, la cinétique de précipitation des précipités s'est détériorée avec le temps en raison de l'augmentation continue de la distance entre les précipités avec l'augmentation du temps d'exposition et donc une sérieuse détérioration des performances mécaniques associée à une exposition à 250°C pendant les 100 premières heures. Cependant, une exposition thermique supplémentaire jusqu'à 200 heures n'a pas entraîné de réduction supplémentaire des valeurs de résistance et de dureté.

Les valeurs de résistance mécanique: limite élastique (LE) et limite ultime (LU) obtenues à température ambiante pour les conditions stabilisées T5 étaient comparables à celles des conditions stabilisées T6, et elles étaient plus élevées dans le cas d'essais de traction à température élevée des conditions stabilisées. En ce qui concerne les valeurs de dureté, les alliages traités au T5 ont présenté des valeurs de dureté supérieures à celles des alliages traités au T6 après application du traitement de stabilisation; tandis que les alliages traités au T6 ont montré de meilleures valeurs de dureté que les alliages traités au T5 sans appliquer le traitement de stabilisation.

De manière intéressante, les résultats montrent que l'addition de 0,75% en poids de Mn était compétitive à l'addition de 2 et 4% en poids de Ni par rapport aux valeurs de résistance à température élevée et ambiante, respectivement; de plus, l'alliage contenant du Mn (alliage M3S) présentait des valeurs de ductilité améliorées à la température ambiante et à 250°C par rapport à celles des matériaux contenant du Ni. L'étude de fractographie a révélé le rôle avantageux des particules de boue dans l'amélioration des performances des alliages contenant du Mn en résistant à la propagation des fissures qui ont été développées dans de nombreuses phases intermétalliques. Cette constatation est considérée comme

économiquement significative en raison du prix plus bas du manganèse comparativement à celui du nickel.

La modification thermique des particules de silicium s'est révélée plus efficace avec des alliages modifiés au Sr plutôt qu'avec des homologues sans Sr. L'évolution des particules de silicium au cours des traitements en solution prolongée a suivi les mêmes tendances et séquences pour les alliages non modifiés de type 354 et 356 ainsi que pour les alliages de type 354 et 356 modifiés par Sr à différentes vitesses d'évolution. Le grossissement des particules de Si eutectique a été obtenu grâce à la coalescence des particules et aux mécanismes de mûrissement d'Ostwald; les deux mécanismes étaient actifs en même temps; Cependant, ils ont fonctionné de manière indépendante et additive. Les piqûres qui peuvent exister dans les particules de silicium peuvent être comprises comme l'impression (impression ou empreinte) laissée derrière la agglomération et la diffusion de petites particules avec / dans une (des) plus grande (s) particule (s).

Pour les résultats des essais de traction obtenus à température ambiante, le traitement thermique en solution a amélioré les valeurs LU et de ductilité des alliages modifiés et non modifiés au Sr au cours des 100 premières heures du traitement, suivi de la réduction des valeurs de ces propriétés par le résultat du changement morphologique des particules de Si. De plus, les valeurs LE ont resté presque inchangées. Les changements morphologiques des particules de Si ont eu un effet vraiment limité sur les propriétés de traction à haute température et cet effet limité s’est étonnamment étendue aux valeurs de la ductilité.

ABSTRACT

The main objective of this study was to understand how to enhance the mechanical performance of 354-type Al-Si-Cu-Mg cast alloys at both ambient and elevated temperatures through the addition of zirconium (Zr) as a base alloying element and subsequent additions of nickel (Ni) and manganese (Mn), to validate the use of such alloys in automotive engine applications. The motive behind these additions was to develop thermally stable microstructures capable of resisting coarsening instigated by prolonged exposure at elevated temperatures and hence preserve acceptable mechanical properties of these alloys when employed in high-temperature applications.

Examination of the data obtained from differential scanning calorimetric (DSC) and phase identification analyses shows that 354-type alloys developed complex as-cast microstructures containing the commonly existing phases, including α-Al, eutectic silicon, copper aluminide (Al_2Cu) with different morphologies, Mg-rich phases such as magnesium silicide (Mg_2Si), Q-phase ($Al_5Cu_2Mg_8Si_6$), and Fe-based intermetallic phases including β-Al_5FeSi, α-$Al_{15}(Fe, Mn)_3Si_2$, and π-$Al_8FeMg_3Si_6$. The addition of transition elements Zr, Ni, and Mn produced other phases such as $(Al,Si)_3(Ti,Zr)$, $(Al,Si)_3Zr$, Al_9FeNi, Al_3Ni, Al_3CuNi, $Al_9FeSi_3Ni_4Zr$, and α-$Al_{15}(Fe,Mn)_3Si_2$. Nickel proved to have a retarding effect on the kinetics of precipitation of the α-Al network and the eutectic Al-Si structure. Also, the presence of Ni consumed a considerable amount of Cu to form Al-Cu-Ni particles instead of Al_2Cu particles. Comparison between DSC thermograms obtained for as-cast and as-quenched alloys revealed that solution treatment at 495°C for 5 hours was sufficient to dissolve a large amount of Al_2Cu particles in the α-Al matrix, which is mandatory for a successful aging treatment.

With respect to the strengthening precipitates, transmission electron microscopy (TEM) investigations confirmed that the investigated alloys were strengthened primarily by θ-Al_2Cu and S-Al_2CuMg precipitates and their precursors, in addition to a secondary strengthening effect by precipitates in the form of $Al_x(Zr,Ti)Si$ which formed following the addition of Zr. The data showed that the base alloy M1S, which is a Ni-free alloy, comprised higher fractions of θ-Al_2Cu precipitates than the 4 wt.% Ni-containing alloy M4S.

Additions of Ni and Mn in different amounts and combinations increased the volume fraction of intermetallic compounds in the resulting alloys M2S through M5S, compared to the base alloy (cf. 12.21% for M4S with 2.5% for M1S), producing a significant effect on the mechanical performance. The proposed additions enhanced the mechanical performance of the alloys, namely, the ambient- and elevated-temperature tensile properties, hardness values, and impact properties. For the Mn-containing alloys, the improvement in properties was attributed to the formation of sludge particles in the form of blocky α-$Al_{15}(Fe,Mn)_3Si_2$ alongside the script-like α-iron phase which resisted crack propagation. The precipitation of Ni-bearing phases such as Al_9FeNi, Al_3CuNi, and Al_3Ni

in the Ni-containing alloys hindered the propagation of cracks and thus improved the mechanical properties.

The presence of asymmetric notches in the tensile test bars proved more deleterious than symmetric notches to the tensile properties obtained at ambient temperature and at 250°C, even if the reduced area was the same, owing to the complex state of stresses that develop at the notch root. The effects of various chemical additions on the tensile properties at ambient and high temperature were feeble in the case of notched bars compared to their obvious effects on the tensile properties of smooth (unnotched) bars. At ambient temperature, notch tensile strength (NTS) values were lower than the tensile strength values obtained for the corresponding smooth (unnotched) bars, attributed to the limited ductility of the Al-Si-Cu-Mg (354-type) cast alloys. The softening that took place during tensile testing at 250°C rendered the alloys some ductility, in particular, the M1S, M2S and M3S alloys. Consequently, the notched tensile bars with asymmetric holes for these alloys exhibited high NTS values compared to the tensile strength of unnotched bars subjected to similar treatment conditions, except for the M2S alloy in the T5-treated condition.

Varying the thermal exposure technique from static into dynamic had little effect on the tensile and hardness data obtained at room temperature. This permitted using the static exposure (stabilization) technique to simulate the behavior of the material under dynamic thermal exposure conditions as in the case of engine components. Coarsening of the strengthening precipitates following prolonged exposure at 250°C had a deleterious effect on the tensile properties and hardness values. Noticeable reduction in the strength values, particularly the yield strength, and a remarkable increase in the ductility values were observed. The coarsening kinetics of the precipitates decayed with time, due to the continuously increased distance between the precipitates with increase in the exposure time, causing the observed deterioration in the mechanical performance after stabilization at 250°C up to the first 100 hours. However, further thermal exposure up to 200 hours did not result in further reduction in the strength and hardness values.

The strength values (UTS and YS) obtained at room temperature for the stabilized T5-treated conditions were comparable to those of the stabilized T6-treated conditions, and higher in the case of elevated-temperature tensile testing of the stabilized conditions. With respect to the hardness values, T5-treated alloys exhibited higher hardness values than T6-treated alloys after applying the stabilization treatment. Without stabilization, however, the T6-treated alloys showed better hardness values than T5-treated ones.

Interestingly, the results showed that the addition of 0.75 wt.% Mn was competitive with the addition of 2 and 4 wt.% Ni with respect to the elevated-temperature and ambient temperature strength values, respectively. In addition, the Mn-containing alloy M3S exhibited improved ductility values at ambient temperature and at 250°C, compared to the Ni-containing alloys. Examination of the fracture surface of tested samples revealed the advantageous role of sludge particles in enhancing the performance of Mn-containing alloys through their resistance to the propagation of cracks that developed in many intermetallic phases. This finding is considered to be economically significant in view of the lower price of manganese compared to that of nickel.

Thermal modification of silicon particles proved to be more effective in the Sr-modified alloys rather than their Sr-free counterparts. The evolution of silicon particles during extended solution treatments followed the same trends and sequences for non-modified and Sr-modified 354- and 356-type alloys, at different evolution rates. The coarsening of eutectic Si particles occurred through particle coalescence and Ostwald ripening mechanisms. While both mechanisms were active at the same time, however, they operated independently and additively. The pinholes observed in the silicon particles derive from the impression or imprint left behind from the agglomeration of small particles with, and their diffusion into, larger particles.

With respect to the tensile test data obtained at room temperature, solution heat treatment improved the UTS and ductility values of both Sr-modified and non-modified alloys in the first 100 hours of the treatment followed by reduction in the values as a result of the morphological changes in the Si particles; however, YS values remained almost unchanged. Morphological changes in the Si particles had a very limited effect on the high temperature tensile properties and, surprisingly, this limited effect extended to the ductility values as well.

ACKNOWLEDGEMENTS

By the grace of Almighty Allah, I have been endowed the enthusiasm and strength to complete this work.

My feelings of gratitude are indebted to my advisor Prof. Fawzy Hosny Samuel for his guidance, support, providing me with every opportunity, and believing in me in all aspects of my study since the very beginning to the final stages. His advices and guidance throughout this work have been of immeasurable help; not only in academic work, but also in developing my life experiences.

A most heartfelt appreciation and gratefulness are due to Prof. Agnes-Marie Samuel, research professor at Université du Québec à Chicoutimi (Canada), for her continuous guidance, valuable assistance, and mentoring during the entire duration of the study, in addition to editing the thesis. Thank you for being a role model in morals as well as kindness and gentleness.

Also, I would like to express my gratitude to Dr. Emad Elgallad for his invaluable comments, fruitful discussions, and help in all aspects of scanning microscopy. My appreciation is extended to Dr. Mohamed Ibrahim for his technical assistance during the course of the study.

Financial support received from General Motors Powertrain Group (USA), Natural Sciences and Engineering Research Council of Canada (NSERC), and Corporativo Nemak (Mexico) is gratefully acknowledged.

Thanks are also due to Mr. Samuel Dessureault, technician of TAMLA group at UQAC, for his tremendous efforts in castings and sample preparation, as well as to Dr. David Liu, McGill University, for assisting in carrying out FESEM and TEM investigations.

Lastly but most importantly, I wish to express my heartfelt and deep gratitude to my parents, my wife, my daughter, and my sisters and dear brother for their guidance, moral support, encouragement, understanding and infinite love. I could never ever pay them back all their efforts, love, and all what they have done for me. Without their love none of this achievement would have been possible.

To all of them, thank you so much …

Mohamed H. Abdelaziz

PUBLICATIONS

Journal Papers

1. M.H. Abdelaziz, E.M. Elgallad, H.W. Doty, S. Valtierra, F.H. Samuel, "Melting and Solidification Characteristics of Zr-, Ni-, and Mn-containing 354-type Al-Si-Cu-Mg cast alloys", submitted to Journal of Materials Characterization, manuscript ID: MATERIALSCHAR_2018_698.

2. L. Alyaldin, M.H. Abdelaziz, A.M. Samuel, H.W. Doty, S. Valtierra, F.H. Samuel, "Effect of transition metals addition on the microstructure, incipient melting and tensile properties of 354-based alloys", submitted to Journal of Advances in Materials Science and Engineering, manuscript ID: 8307907.

3. Alyaldin, L., M. H. Abdelaziz, A. M. Samuel, H. W. Doty, S. Valtierra, and F. H. Samuel. "Effects of Alloying Elements and Testing Temperature on the Q-Index of Al–Si Based Alloys." *International Journal of Metalcasting* (2018): 1-14.

4. Alyaldin, Loay, M. H. Abdelaziz, Agnes M. Samuel, Herbert W. Doty, Salvador Valtierra, and Fawzy H. Samuel. "Effect of Ni and Mn Additions on the Ambient and High-Temperature Performance of Zr-Containing Al–Si–Cu–Mg-Based Alloys: Role of Precipitation Hardening." *International Journal of Metalcasting* (2018): 1-14.

5. Elsharkawi, E. A., M. H. Abdelaziz, H. W. Doty, S. Valtierra, and F. H. Samuel. "Effect of β-Al 5 FeSi and π-Al 8 Mg 3 FeSi 6 Phases on the Impact Toughness and Fractography of Al–Si–Mg-Based Alloys." *International Journal of Metalcasting* 12, no. 1 (2018): 148-163.

6. M. H. Abdelaziz, M. Paradis, A. M. Samuel, H. W. Doty, and F. H. Samuel, "Effect of Aluminum Addition on the Microstructure, Tensile Properties, and Fractography of Cast Mg-Based Alloys." *Advances in Materials Science and Engineering, vol. 2017,* Article ID 7408641, 10 pages, 2017. doi:10.1155/2017/7408641.

7. Paradis, M., M. H. Abdelaziz, A. M. Samuel, H. W. Doty, and F. H. Samuel. "Effect of Mold Type on the Microstructure and Tensile Properties of A356 Alloy." *International Journal of Metalcasting* 11, no. 3 (2017): 523-535.

8. Paradis, M., M. H. Abdelaziz, H. W. Doty, and F. H. Samuel. "On the Mechanical Properties of Lost Foam Cast A356 Automotive Components: Effects of Melt Treatment and Solidification Conditions." *International Journal of Metalcasting*11, no. 3 (2017): 494-505.

Book Chapter

9. Ibrahim, Mohamed F., Mohamed H. Abdelaziz, Herbert W. Doty, Salvador Valtierra, and Fawzy H. Samuel. "Effect of Microalloying Elements on the Heat Treatment Response and Tensile Properties of Al-Si-Mg Alloys." In *Solidification*. InTech, 2018.

Manuscripts under Preparation

10. M.H. Abdelaziz, E.M. Elgallad, H.W. Doty, S. Valtierra, F.H. Samuel, "Precipitation strengthening in transition elements-containing 354-based alloys"

11. M.H. Abdelaziz, H.W. Doty, S. Valtierra, F.H. Samuel, "Mechanical performance of Zr-containing 354-type Al-Si-Cu-Mg cast alloy: Part I- Role of additions and heat treatment"

12. M.H. Abdelaziz, H.W. Doty, S. Valtierra, F.H. Samuel, "Mechanical performance of Zr-containing 354-type Al-Si-Cu-Mg cast alloy: Part II- Role of geometrical discontinuities"

13. M.H. Abdelaziz, A.M. Samuel, H.W. Doty, S. Valtierra, F.H. Samuel, "Effect of static versus dynamic thermal exposure on the mechanical performance of transition metals-containing Al-Si-Cu-Mg cast alloy"

14. M.H. Abdelaziz, A.M. Samuel, H.W. Doty, S. Valtierra, F.H. Samuel, "Mechanical behavior of transition metals-containing Al-Si-Cu-Mg cast alloy subjected to prolonged thermal exposure"

15. M.H. Abdelaziz, M.F. Ibrahim, H.W. Doty, S. Valtierra, F.H. Samuel, "Evolution of eutectic silicon particles during extended solution treatment: PartI: Metallographic study"

16. M.H. Abdelaziz, A.M. Samuel, H.W. Doty, S. Valtierra, F.H. Samuel, "Evolution of eutectic silicon particles during extended solution treatment: PartII: Quantitative study"

17. M.H. Abdelaziz, H.W. Doty, S. Valtierra, F.H. Samuel, "Effect of extended solution treatment on the mechanical performance of Zr-containing 354-type alloys and 356-type alloys"

TABLE OF CONTENTS

LIST OF FIGURES

LIST OF TABLES

Chapter 2

Chapter 3

Chapter 4

Chapter 5

CHAPTER 1

INTRODUCTION AND OBJECTIVES

CHAPTER 1

INTRODUCTION AND OBJECTIVES

1.1 SYNOPSIS AND PROBLEM STATEMENT

The subject of transportation economics has acquired great public awareness as a result of fluctuating oil prices and its politics. The vehicles in both automotive and aerospace industries are main energy consumers in the daily life. Therefore any reduction, even little, in energy consumption in the transportation sector will have a remarkable impact on the world's total energy expenditure. Alongside the economic aspects, environmental concerns are being raised regarding the harmful emissions created by the transportation sector and their critical effect on climate change and global warming.[1-5] Thus, enormous efforts are being implemented towards minimizing these harmful emissions by reducing the fuel consumed by the transportation sector; one approach of doing so is reducing the weight of automotive and aerospace vehicles.

Heat-treatable aluminium alloys play an important role in lowering vehicle weight and promoting fuel economy in the automotive industry because of their lightweight and improved properties such as outstanding response to plastic deformation and casting processes, good corrosion resistance, and high strength/weight ratio. The Ducker Worldwide Company conducted a survey on the amount of aluminum alloys used in North

American automotive vehicles; the results showed that aluminum usage has increased from about 37 kg in 1974 to 155 kg in 2012 and it is projected to reach 250 kg by 2025.[6]

On the technological side, some concerns regarding the use of aluminum alloys in the automotive sector have been raised regarding the reliability of aluminum engine components when employed in modern engines with higher specific powers which produce increased combustion pressure and temperature as shown in Figure 1.1.[7, 8, 9] The replacement of iron-based alloys in engine components by others made of lighter aluminum alloys should not impair the performance of the vehicles; so that all efforts towards enhancing the properties of aluminum alloys to meet service requirements will be beneficial towards reducing emissions and developing greener societies.

Figure 1.2 shows the increasing trend of replacing the commonly used heavy alloys (mainly iron-based alloys) by lighter alloys such as aluminum and magnesium alloys. The expectations reveal that by the year 2035 the share of light alloys will increase to approach 40% while the usage of heavy alloys will be remarkably decreased.[10]

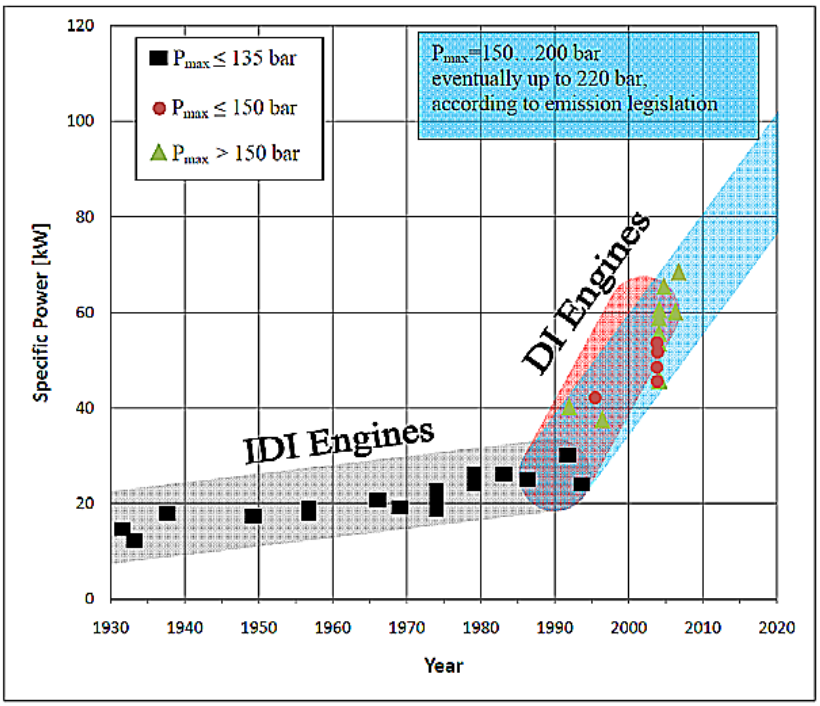

Figure 1.1 Development of specific performance and ignition pressure of passenger car.[8]

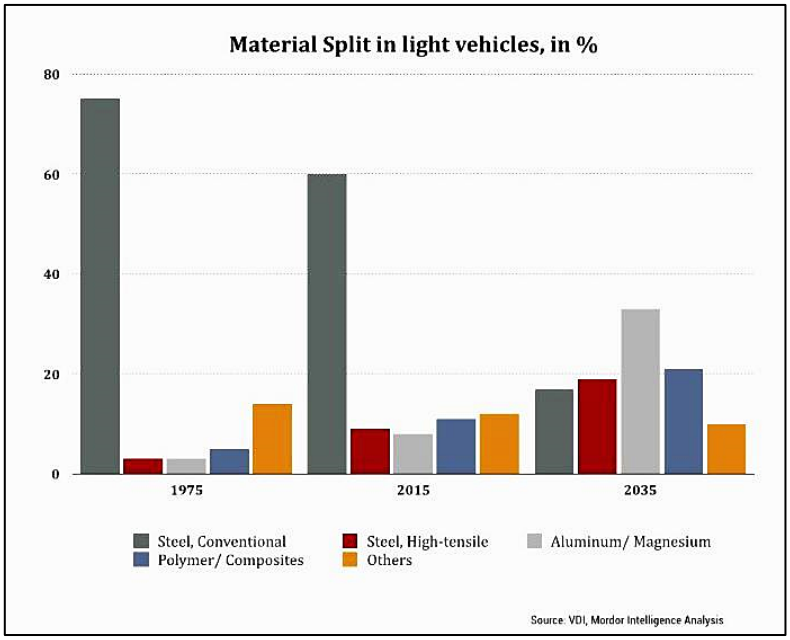

Figure 1.2 The growing percentage of light alloys use in automotive vehicles.[10]

It is well known that the performance of heat-treatable aluminum alloys deteriorates seriously when subjected to elevated temperatures, especially when this temperature exceeds the aging temperature (for T6-heat treated alloys), as a result of alloy softening; this deterioration in the mechanical properties is mainly dependent on both the exposure temperature and duration.

Recently several studies[11-18] have been undertaken in an attempt to overcome the problems encountered when utilizing aluminum alloys in high temperature applications. The hypothesis, which these studies were based on, is to form more stable intermetallic compounds and precipitates which are coarsening resistant at elevated temperatures, because alloy softening due to the coarsening of the precipitates is considered as the main cause of loss in mechanical properties. The common approach that has been followed in these studies was to use minor additions of transition elements such as Zr, Sc, Ni, Ti, V, and Mn to cast aluminum alloys to form more stable intermetallic compounds, mainly Al_3M type trialuminides where M is a transition element that should enhance the ambient- and elevated-temperature mechanical properties of the alloys. Many studies[11, 12, 15, 17, 18] showed promising results; however, still more work needs to be done in order to have a thorough understanding of this area of research. The current study is expected to provide in-depth understanding and knowledge in this respect, with an emphasis on the effects of extended exposure to elevated temperatures during solutionizing, and stabilization at 250°C treatments on the mechanical properties of the alloys under investigation. Furthermore, the presence of fine details (holes and grooves) in the geometry of the final products, which are intended to be made out of the alloys under study, will also be taken into account.

The 354-type alloy lies within the category of Al-Si-Cu-Mg system. This alloy was selected for study because it is being extensively used in the automotive industry due to its superior mechanical properties following the application of appropriate heat treatments. The potential applications of this alloy in the automotive industry are engine cooling fans, timing gears, crankcases, and rocker arms.[11, 19, 20]

1.2 RESEARCH OBJECTIVES

The main objective of this study is to understand and to enhance the mechanical performance of 354-type Al-Si-Cu-Mg cast alloys at both ambient and elevated temperatures through the addition of zirconium (Zr) as a base alloying element and subsequent additions of nickel (Ni) and manganese (Mn) so as to validate the use of such alloys in automotive engine applications.

A promising approach for achieving this main objective would be to address the following specific objectives:

1- Understanding the effect of transition element (Zr, Ni, and Mn) additions to 354-type alloys, traditional heat treatments, and the presence of geometrical discontinuities on their mechanical performance by:

a. Applying the traditional heat treatments (T5 and T6) to the as-cast tensile bars;

b. Characterizing the microstructural features of the investigated alloys using optical and advanced microscopy techniques in order to have a comprehensive insight of the phases and intermetallic compounds that exist in the alloy structure;

c. Exploring the tensile properties at both ambient and elevated temperatures, the hardness values, and impact properties of the investigated alloys; and

d. Correlating the mechanical properties to the microstructural features of the corresponding alloy/condition to determine the strengthening/softening mechanisms responsible for the observed properties.

e. Comparing the effect of asymmetric vs. symmetric notches on the ambient-temperature tensile properties;

f. Quantifying the detrimental effect of asymmetric notches on the tensile properties at ambient and elevated temperatures;

2- **Understanding the effect of prolonged thermal exposure (stabilization) at elevated temperatures on the mechanical properties of the alloys studied by**:

a. Exposing the T5- and T6-treated tensile bars to prolonged high-temperature thermal exposure (stabilization). For T6-treated bars both static and dynamic stabilization techniques will be applied;

b. Examining the evolution of the strengthening precipitates following prolonged thermal exposure;

c. Exploring the tensile properties at both ambient and elevated temperatures, and the hardness values of the investigated alloys; and

d. Correlating the mechanical properties to the state of the strengthening precipitates in the corresponding alloy/condition in order to be able to define the softening mechanisms that may exist.

3- **Understanding the role of the extended solution treatments on the mechanical properties of the studied alloys by:**

   a. Exploring the morphological changes in the eutectic silicon particles associated with increase in the solution treatment time up to 400h by quantifying the characteristics of the eutectic silicon particles at different durations of solution heat treatment; and

   b. Determining the dependency of the mechanical properties (tensile properties at ambient and elevated temperatures) on the characteristics of eutectic silicon particles.

1.3 RESEARCH OUTLINE

In order to address the aforementioned objectives, the results of this study are presented in eight chapters, as follows:

Chapter 1 defines the research problem and motivation for undertaking this study, stating the main aim of the study and the specific objectives to be followed to achieve the main aim of the present study.

Chapter 2 states the background of aluminum silicon cast alloys, the related metallurgical factors and practices that may influence the alloy performance, and the concept of quality indices. An up-to-date survey of the literature is presented in this chapter, describing the recent findings and advances related to the main metallurgical and geometrical parameters considered in the current study.

Chapter 3 provides details of the methodology and experimental procedures that were carried out in this research work, namely, the alloys under investigation, the melting and casting procedures, heat treatments, machining of the notches, and the mechanical testing, metallographic and microstructural characterization techniques employed.

Chapter 4 presents the full characterization of microstructures of the alloys under investigation obtained at low cooling rate of 0.35 °C s^{-1} including: DSC analysis data, description of melting and solidification sequences, the existing phases and intermetallic compounds, and characterization of the strengthening precipitates.

Chapter 5 presents the microstructure characterization of test bars obtained at a high cooling rate of 7 °C s^{-1} including the effect of the solution treatment on the intermetallic compounds and eutectic silicon particles; followed by, the effect of alloying elements and heat treatments on the room- and elevated-temperature tensile properties of smooth and notched bars of the alloys, and discusses the results in terms of alloy quality using the concept of quality index and quality charts. At the end of this chapter, hardness and impact properties are presented and interpreted.

Chapter 6 presents the effect of prolonged thermal exposure at elevated temperature on the room- and elevated-temperature mechanical properties of the alloys studied again using the quality index concept and quality charts to analyze the results. A comparison between the effects of static and dynamic thermal exposure on the ambient-temperature tensile properties and hardness values is also included in this chapter. This chapter also includes a section on fractography, wherein the

effect of stabilization at elevated temperature for prolonged durations is discussed and analyzed.

Chapter 7 reports on the extended solution-heat treatment and the associated morphological changes that may take place in the eutectic silicon particles and the consequent effect on the room- and elevated-temperature tensile properties of the alloys. This chapter comprises two parts:

- Part I: Evolution of eutectic silicon particles during extended solution-heat treatments,
- Part II: Effect of the morphological changes of eutectic silicon particles on the tensile properties.

Chapter 8 summarizes the salient conclusions derived from this study. Suggestions and recommendations for the future work are provided at the end of the chapter.

CHAPTER 2

SURVEY OF THE LITERATURE

CHAPTER 2

SURVEY OF THE LITERATURE

2.1 INTRODUCTION

"What do you think of a metal as white as silver, as unalterable as gold, as easily melted as copper, as tough as iron, which is malleable, ductile, and with the singular quality of being lighter than glass? Such a metal does exist and that in considerable quantities on the surface of the globe." Thus wrote Charles Dickens, in 1857, about the newly discovered metal "Aluminum" and its prospective applications. Despite the exaggeration in describing the properties of aluminum with respect to other metals, Dickens's forecast came true, however, by the value which aluminum gained in industries in future years.[21]

Aluminum alloys are distinguished by their unique combination of light weight (one third that of iron), good corrosion resistance, high strength-to-weight ratio, manufacturing feasibility, and their relatively low cost compared to other materials. Moreover, aluminum is preferred to other light metals, such as magnesium and beryllium, owing to its minor processing problems and cost-wise as well. These advantages have pushed to increase the use of aluminum alloys in many industries,[8] particularly in the automotive and aerospace sectors. Today, aluminum alloys are being used commonly in manufacturing cylinder heads, engine blocks, pistons, intake manifolds, and many other automotive components.[22, 23]

Basically, cast aluminum alloys are classified into different families or series based on the primary alloying element(s). The Aluminum Association and other standards organizations[24, 25] classify cast Al-alloys into the following eight series shown in Table 2.1.

Table 2.1 Classification of cast Al-alloys

Series	Main alloying element/s
1xx	99% Pure Al alloys
2xx	Al-Cu alloys
3xx	Al-Si alloys with additions of Mg or Cu or both
4xx	Al-Si alloys
5xx	Al-Mg alloys
7xx	Al-Zn alloys with additions of Mg, Cu, Cr, Mn or combinations
8xx	Al-Sn alloys

Minor variations in the original chemical composition (i.e. at impurity level) are represented by a capital letter in front of the alloy number (e.g., 356 and A356, or 319 and B319). Cast alloys from 3xx and 4xx families are widely used in important applications because of their improved mechanical, corrosion, and casting characteristics.

2.2 ALUMINUM-SILICON CAST ALLOYS

Hardenable cast Aluminum-Silicon (Al-Si) alloys are most commonly used in foundries because of their superior casting characteristics, good wear resistance, low thermal expansion, high heat and electrical conductivity, relatively high strength-to-weight ratio, and high hardness. Hence, recently Al-Si cast alloys are finding their way in manufacturing engine components instead of heavy alloys which were previously used. The objective of replacing the heavy alloys by lighter ones is to reduce vehicle weight in an attempt to minimize both fuel consumption and, consequently, harmful emissions (CO_2)

without impairing the performance of the vehicle.[11, 26] Al-Si castings can be used in automotive engine components partially or entirely, such as engine blocks, pistons, cylinder heads, intake manifolds, rocker arms, brake systems, pump components, and many other components. Besides the economic and environmental advantages of utilizing Al-Si alloys in automotive components, another valuable advantage related to the safety of passengers is that aluminum has the ability to absorb impact energy with twice the capability of steel with the same weight in the case of accidents.[27-30]

Pure aluminum melts at 660°C, while pure silicon melts at 1414°C. The phase diagram of Al-Si alloys is a binary eutectic system with a eutectic composition and temperature of 12.2% Si, and 577°C, respectively. The silicon content in commercial cast Al-Si alloys ranges from 5 to 23%.[29, 31, 32] Al-Si alloys are classified into three categories according to the Si content [27] as described in Figure 2.1; the respective microstructures are shown in Figure 2.2. Accordingly, Al-Si cast alloys are classified as:

1- Hypoeutectic alloys, in which the silicon content ranges from 5 to 10%

2- Eutectic alloys, in which the silicon content lies between 11 and 14%

3- Hypereutectic alloys, in which the silicon content ranges between 14-25%.

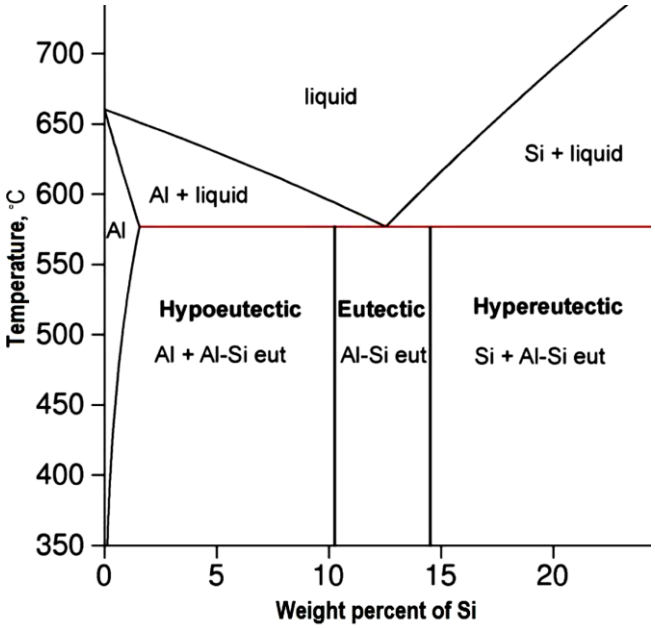

Figure 2.1 Aluminum-rich portion of the Al-Si phase diagram.[33]

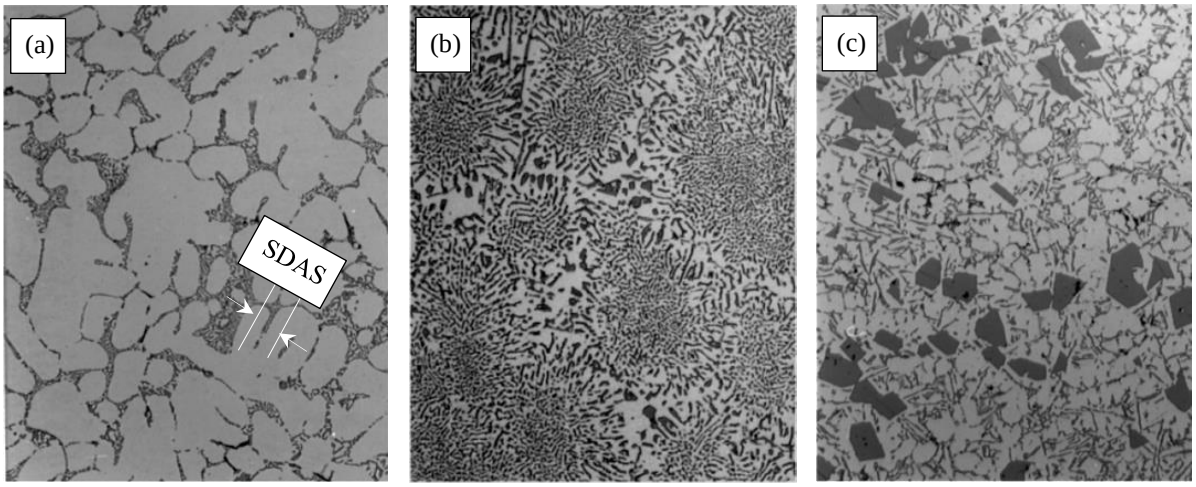

Figure 2.2 Cast Al-Si alloys (a) Microstructure of hypoeutectic Al-Si alloy 150X. (b) Microstructure of eutectic Al-Si alloy 400X. (c) Microstructure of hypereutectic Al-Si alloy 150X.[27]

The typical microstructure of hypoeutectic Al-Si alloys consists mainly of the primary α-Al phase and the Al-Si eutectic structure. Solidification starts at the mold walls with the formation of aluminum crystals with lower Si content than the surrounding liquid due to the reduced solubility of Si in Al as the temperature is lowered. The segregated Si at

the interface between Al solid-crystals and the liquid will lead to a decrease in the solidification temperature in this region. If the solidifying Al crystals find a low-silicon medium which is thermodynamically favourable to solidification, the crystals will continue solidifying as dendrites. These protuberances keep growing rapidly, which justify the tree-like shape (or dendrites) of Al crystals instead of an equiaxed or needle-like shape. Figure 2.3 displays a schematic representation of the dendrite structure commonly found in Al-Si alloys. The dendritic structure is characterized using two parameters, the primary dendrite arm spacing (PDAS) and the secondary dendrite arm spacing (SDAS), respectively, as shown in Figure 2.3. Their values may vary from 10 to 150 μm, depending on the cooling rate during the solidification process.[25-27, 34]

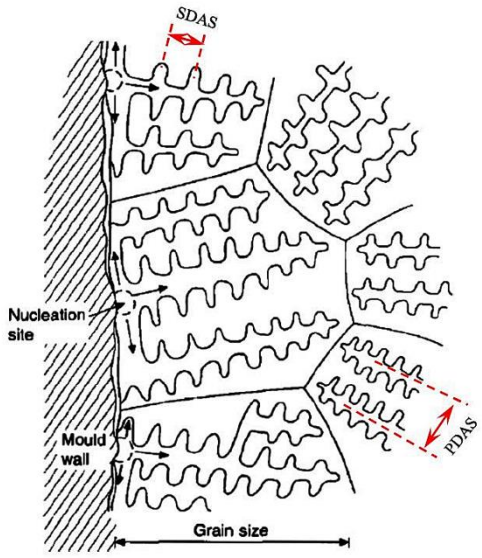

Figure 2.3 Schematic representation of a dendrite.[25, 35]

The remaining liquid between the dendrite arms is rich in silicon, and with the progress of solidification, the eutectic structure will form. During solidification of the remaining liquid in the inter-dendritic regions, platelets of almost pure Al precipitate and

the rejected Si will be drained forming almost pure Si platelets as well, which will constitute the lamellar eutectic structure; the eutectic growth sequence is schematically represented in Figure 2.4.

The current research study will concentrate on investigating the mechanical performance of hypoeutectic Al-Si-Cu-Mg or 354-type alloys following the addition of certain transition elements, namely, zirconium (Zr), nickel (Ni), and manganese (Mn); however, in one part of the study, Al-Si-Mg or 356-type alloys will be investigated for the sake of comparison with the 354-type alloys. Thus, the following pages will elaborate on the chemical composition, mechanical properties, and the industrial importance of these two alloy systems and alloy types.

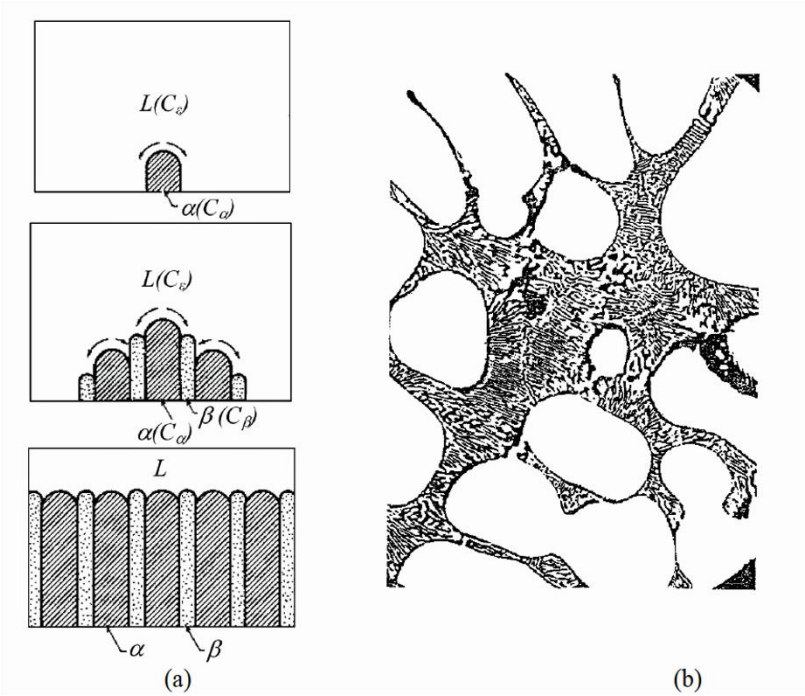

Figure 2.4 (a) Growth of a lamellar eutectic, and (b) lamellar eutectic schematic representation.[25]

2.2.1 354 (Al-Si-Cu-Mg) ALLOY SYSTEM

Among the category of Al-Si alloys, there are three major alloy systems in the 3xxx series, i.e., Al-Si-Mg, Al-Si-Cu and Al-Si-Cu-Mg systems. The 354 alloy belongs to the Al-Si-Cu-Mg system, along with the well-known B319 alloy. In our research group, while alloy 354 has been successively investigated in the context of improving its mechanical properties and performance, yet this alloy system still requires further research work.[11, 12, 36] Permanent mold-cast 354-type alloys display superior mechanical properties after the application of appropriate heat treatment procedures. The anticipated improvement in the mechanical properties is owed to the presence of both copper (Cu) and magnesium (Mg) as hardening elements.[24, 36-38] Table 2.2 shows the chemical composition limits of the 354-type alloy.[19, 20, 39, 40] In this alloy system, iron is considered as an impurity and thus Mn is added to neutralize the effect of iron-based intermetallics, such as the β-Al_5FeSi platelet phase, through the formation of less detrimental intermetallics with more compact morphologies.

The 354 alloy has a high silicon content which improves the alloy castability and reduces shrinkage; however, the presence of Cu negatively affects the corrosion resistance and hot-tearing tendency of the alloy. On the other hand, the addition of Cu noticeably enhances the yield strength (YS) and the ultimate tensile strength (UTS) of the 354 alloy through the formation of intermetallic phases with Al in two probable forms, block-like Al_2Cu or eutectic $Al+Al_2Cu$. Moreover, the presence of Mg enhances the strain hardenability as well as the strength by forming Mg_2Si precipitates.[24, 41] The room

temperature tensile properties of 354 alloy in the T6-treated condition are listed in Table 2.3.[11, 12, 39, 40]

Owing to the previously mentioned characteristics, the 354 alloy is considered as an optimum candidate for the manufacture of multiple parts and components in the automotive and aerospace industries, including engine cooling fans, crankcases, high speed rotating parts, structural aerospace components, timing gears, rocker arms, and many others.[11, 19, 20]

2.2.2 356 (Al-Si-Mg) ALLOY SYSTEM

The Al-Si-Mg system represents another alloy system in the 3xxx series, of which 356 alloy is a typical example. Both sand and permanent mold castings are prepared from 356 alloys. This alloy possesses excellent castability, reduced solidification shrinkage, and high resistance to hot-tearing. Permanent mold castings of 356 alloy are usually heat treated according to the T6 temper. The hardening element in this category of alloys is magnesium (Mg), where the hardening is achieved by the formation of Mg_2Si strengthening precipitates.[11, 39, 40]

The chemical composition limits of the 356 alloy are presented in Table 2.2.[39, 40] By increasing the Mg content (within the limits listed in Table 2.2), the strength increases and the ductility decreases, and the corrosion resistance is improved. The presence of iron in this alloy is considered as an impurity originating from the extraction and processing of the alloy; the iron forms harmful intermetallics which severely reduce the ductility of the alloy with a noticeable effect on the strength. Thus, in premium quality alloys which are used in aerospace parts, the iron level is kept at a minimum.[20, 39, 42, 43] The room temperature tensile

properties of a permanent-mold casting of 356 alloy in the T6-treated condition are listed in Table 2.3.[11, 12, 39, 40]

The outstanding properties allow the 356 alloy to be widely used in the transportation sector. A sample of the potential applications of this alloy includes aircraft pump parts, automotive transmission cases, water-cooled cylinder blocks, and many others.[39]

Table 2.2 Chemical composition limits of 354 and 356 type alloys[19, 20, 39, 40]

Alloy	Elements (wt.%)								
	Si	Cu	Mg	Fe	Mn	Zn	Ti	Others	Al
354	8.6-9.5	1.6-2	0.4-0.6	0.2 max	0.1 max	0.1 max	0.2 max	0.15	Bal.
356	6.5-7.5	0.25	0.2-0.45	0.6	0.35	0.35	0.25	0.15	Bal.

Table 2.3 Room temperature tensile properties of permanent mold cast 354 and 356 alloys in the T6 condition[11, 12, 39, 40]

Alloy Condition	Room Temperature Tensile Properties		
	Ultimate Tensile Strength (MPa)	Tensile Yield Strength (MPa)	Ductility (%)
354-T6	296	227	2
356-T6	262	185	5

The properties of Al-Si cast alloys may vary widely according to multiple metallurgical parameters which can be introduced or applied to the alloys, starting from the early stages of processing and ending by the continuous variations that take place during the service life of the cast alloy component. Exposing cast aluminum alloys to elevated temperatures for long periods of time during service will lead to the softening of these

alloys and hence deterioration in their mechanical properties during service. The different factors that may influence the mechanical behavior of cast aluminum alloys is schematically represented in Figure 2.5. The parameters which will be addressed specifically in this study are highlighted in green.

The remainder of this chapter will elaborate on the background and provide an up-to-date review of the literature on the metallurgical and geometrical parameters involved in the present study, divided into sections that will cover (i) metallurgical aspects including effects of alloying elements, melt treatment, heat treatment, strengthening mechanisms in Al-alloys, addition of transition elements, and prolonged thermal exposure at elevated temperature; (ii) the concept of quality index where, due to variation in the mechanical properties, the quality index values of the alloys studied will vary. Two concepts of quality indices will be discussed: those of Cáceres and Drouzy, where the former will be used for analyzing the ambient-temperature tensile test results, while Drouzy's concept will be used for elevated-temperature tensile properties; and (iii) the effect of geometrical discontinuities (notches) on the mechanical properties.

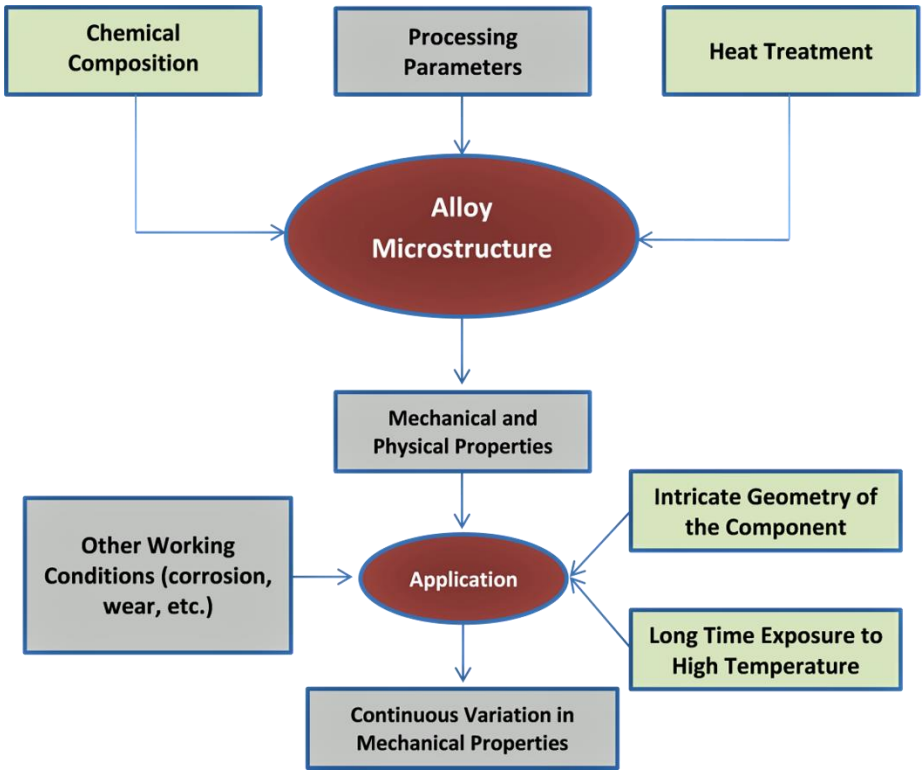

Figure 2.5 Schematic representation of factors affecting alloy performance.

2.3 METALLURGICAL ASPECTS

The mechanical performance of Al-Si alloys is mainly dependent on the manufacturing process and subsequently on the microstructure of the alloys under investigation. The microstructure is highly affected by (i) *alloy preparation* including the processing technique, alloying elements and melt treatment, and (ii) *post-casting treatments* such as heat treatment including the traditional treatments and thermal exposure during service life.[8] These aspects are discussed in the following subsections.

2.3.1 PROCESSING TECHNIQUE

The quality of Al-Si alloys is highly dependent on the casting technique, as the latter determines the cooling rate and subsequently the alloy microstructure, leading to either enhancement or deterioration in the mechanical properties. Higher cooling rates usually account for improved mechanical properties, which is the case in permanent mold die casting. The improvement in properties is attributed mainly to lower secondary dendrite arm spacing (SDAS) values achieved with the fast cooling rates associated with permanent mold casting, as opposed to the situation in sand casting. Moreover, it has been proved that the lower the SDAS, the better the mechanical performance of the component.[25] The relation between SDAS and the solidification time (t_s) is governed by the following empirical equation:

$$\text{SDAS}\ (\mu\text{m}) = \text{K}.\,t_s^{\frac{1}{n}} \qquad \textbf{(2.1)}$$

where: K and n are constants.

2.3.1.1 TRADITIONAL ALLOYING ELEMENTS

The properties of aluminum alloys can be further altered by the addition of alloying elements. In what follows, the roles and functions of major as well as some minor alloying elements commonly added to Al-Si alloys will be briefly considered.

2.3.1.1.1 EFFECT OF COPPER AND MAGNESIUM

The addition of copper and magnesium to Al-Si alloys aims at improving both the strength and hardness of the alloy. These elements are commonly known as strengthening elements, due to their immediate positive effect on the alloy strength and hardness upon

addition, which can then be further enhanced and/or optimized through the application of adequate heat treatment procedures.[11, 36, 44]

Copper is considered as an effective hardening element which improves alloy strength and hardness[45-47] at both room and elevated temperatures; these improvements are attributable to the formation of copper intermetallic phases. These copper intermetallic phases may appear in the form of (i) eutectic-like Al-Al_2Cu, (ii) block-like Al_2Cu, and (iii) blocky Q-$Al_5Mg_8Cu_2Si_6$.

Samuel *et al.*[48] proposed the precipitation mechanism of Al_2Cu phase as follows. At the start of solidification, the dendritic network of α-Al is formed associated with the segregation of both Cu and Si in the liquid ahead of the solidification front. Upon reaching the eutectic temperature, the silicon particles precipitate eventually, resulting in areas with higher Cu concentrations which subsequently solidify as copper intermetallic phases.

Lemon and Howle[37] investigated the effect of Cu content on the ambient temperature tensile properties of Al-9%Si-0.5%Mg alloy after being heat treated according to T6 and T62 procedures. The results of their study are shown in Figure 2.6, where the straight lines are connecting the values obtained from T6 and T62 tempers. The authors found that the optimum compromise between the strength, ductility and the overall quality of the alloy is achieved when the copper content varies between 1.6 and 2 wt%. Based on the data shown in Figure 2.6, Sigworth[49] observed that a copper content up to 1.8 wt% has a beneficial effect on the quality index of Al-9%Si-0.5%Mg cast alloys; the author credited this enhancement to the significant increase in alloy strength associated with a slight decrease in the ductility.

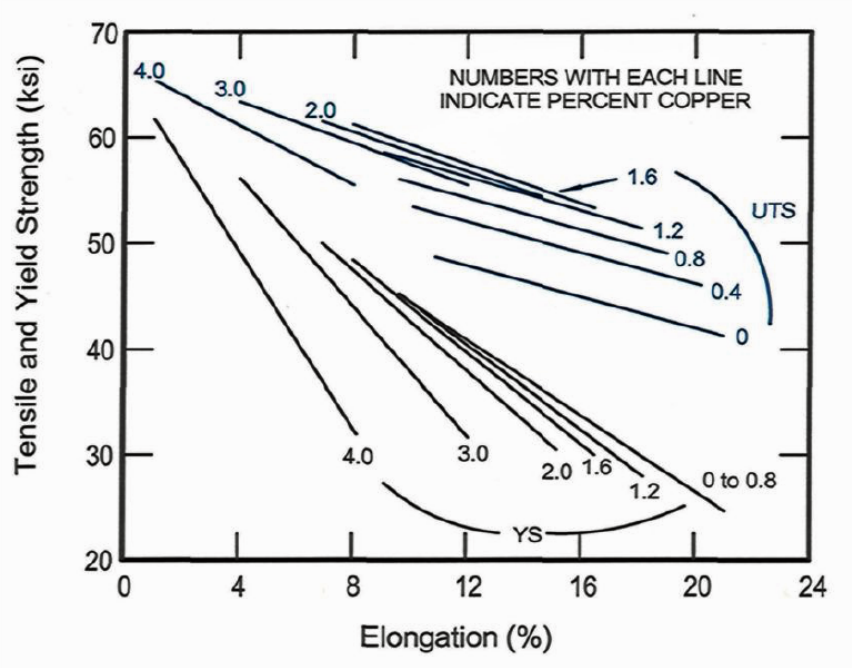

Figure 2.6 Ambient temperature tensile properties of Al-9%Si-0.5%Mg cast alloy with different Cu contents and subjected to T6 and T62 tempers.[37]

The addition of magnesium to Al-Si alloys enhances the yield and ultimate strength as well as the impact toughness of alloys; however the presence of magnesium significantly reduces the ductility of this category of alloys.[11, 36, 44] The presence of Mg leads to the segregation of Cu in areas away from the silicon-rich regions during solidification. This practice results in the formation of the block-like Al_2Cu as well as the Q-$Al_5Mg_8Cu_2Si_6$ intermetallic phase. The Q-$Al_5Mg_8Cu_2Si_6$ phase may form out of the block-like Al_2Cu phase along its edges, during the last stage of solidification.

The presence of Cu in Al-alloys leads to the formation of Al_2Cu during solidification; this phase can exist either in blocky form or as finely dispersed particles within the interdendritic regions. If the cooling rate is high and if Al_5FeSi platelets exist in the microstructure, the fine Al_2Cu phase will form, accordingly. The fine Al_2Cu phase dissolves easily within two hours of solution treatment. On the other hand, the block-like

Al_2Cu phase is not that easy to dissolve under the same conditions (see Figure 2.7).[50] Practically the same situation occurs in the case of Mg addition, the phase Mg_2Si is the non-equilibrium phase responsible for strengthening age-hardenable Al-Si-Mg alloys. In the absence of Cu, high Fe and Mg contents lead to the formation of π-$FeMg_3Si_6Al_8$ phase which is difficult to dissolve during the solution treatment process.[51, 52]

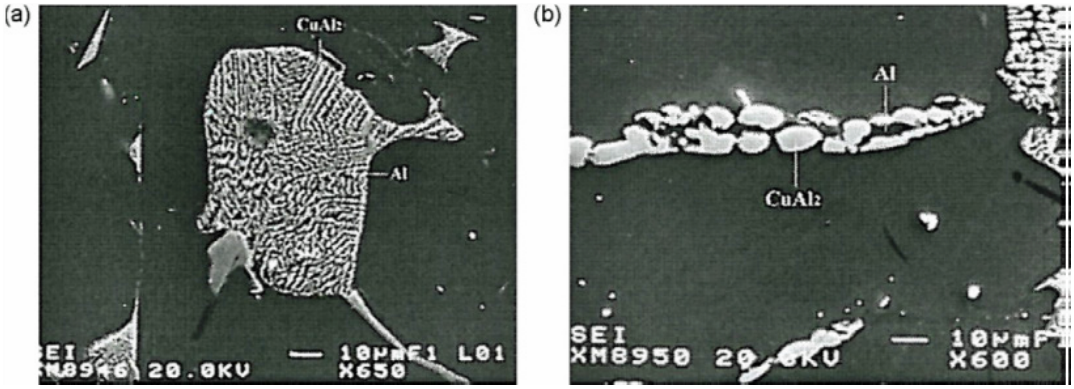

Figure 2.7 Cu-rich phases in as-cast 319 alloy: (a) Eutectic Al_2Cu and (b) blocky Al_2Cu.[50]

This segregation behavior of Cu may lead to incipient melting during solution treatment which will apparently reduce the alloy strength; yet if it is possible to avoid the segregation of Cu, it is possible to combine the strengthening effect of Cu by forming Al_2Cu precipitates besides the strengthening effect of Mg by the formation of Mg_2Si precipitates which will lead to a very high level of strengthening. [53, 54]

Dunn and Dickert[43] studied the influence of adding up to 0.55% Mg on the mechanical properties of A380 and 383 cast alloys. The authors found that the ultimate tensile strength, yield strength and hardness values improved in the presence of Mg. However it was also clear that increasing the Mg content led to reduction in the ductility of the alloys, and acceptable ductility values were attained with max 0.35% Mg content.[43] Mg

addition was also found to have a negative effect on Si modification using Sr, as it resulted in changing the Si morphology from a well-modified to a partially-modified one. This reduction in modification level was attributed to the formation of a complex $Mg_2SrAl_4Si_3$ intermetallic phase, which probably formed prior to the eutectic reaction.[42]

Magnesium content may also affect the Fe-containing intermetallic phases. Narayanan *et al.*[55] found that increasing the level of Mg in Al-Si alloys will lead to reduction in the eutectic temperature; this will cause difficulty in the formation of the α-Fe phase in alloys with high Mg content even if the melt is superheated to 900°C. The same effect was reported by Awano and Shimizu.[56] The authors found that it is difficult to force the β-Al_5FeSi phase formation temperature to occur below the eutectic temperature in high-Mg alloys employing melt super-heating to a very high temperature or using a high cooling rate or even employing both together. In contrast, Samuel *et al.*[57] found that the addition of Mg to 319 type alloys transformed a large proportion of the β-Al_5FeSi needles into the π-$Al_8Mg_3FeSi_6$ compacted Chinese-script phase.

Cáceres *et al.*[58] studied the influence of the content of Cu and other elements, such as Mg, Si, Fe and Mn, as well as that of the cooling rate on the mechanical properties and quality index of T6-tempered Al-Si-Cu-Mg casting alloys. The authors concluded that the overall effect of Cu and Mg is to lower the quality index values of the alloys, as may be seen in the quality chart shown in Figure 2.8. The loss in the quality in this case is directly related to the decreased ductility as a result of the cracking of second phase particles occurring in the strengthened alloys. It was also observed that the degree to which the quality index is affected by the addition of copper depends not only on the Cu content itself

but also on the presence of other elements such as Mg, Si, and Fe, as may be seen from Figure 2.8.

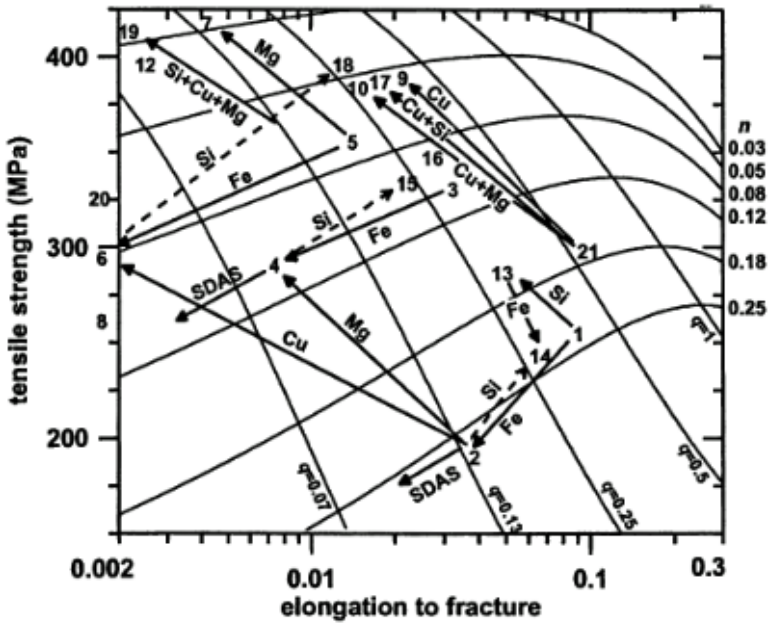

Figure 2.8 Quality chart illustrating the influence of the content of Cu and other elements (Mg, Si, Fe, and Mn) and cooling rate, as indicated by arrows, on the strength and quality index of Al-Si-Cu-Mg alloys. The numbers 1 through 21 located in the chart represent various alloy compositions.[58]

2.3.1.1.2 EFFECT OF IRON AND MANGANESE

The presence of iron as an impurity in aluminum castings is a common matter. Iron appears in combination with other elements as intermetallic phases. There are frequently appearing phases such as α-$Al_{15}(Fe,Mn)_3Si_2$ and β-Al_5FeSi, while the less common phases are δ-Al_4FeSi_2 and π-$Al_8Mg_3FeSi_6$. One can distinguish between the α-phase and the β-phase on the microstructural scale by their morphology (as shown in Figure 2.9); the α-phase appears in the form of Chinese script particles and the β-phase has a needle-like or platelet structure.[59]

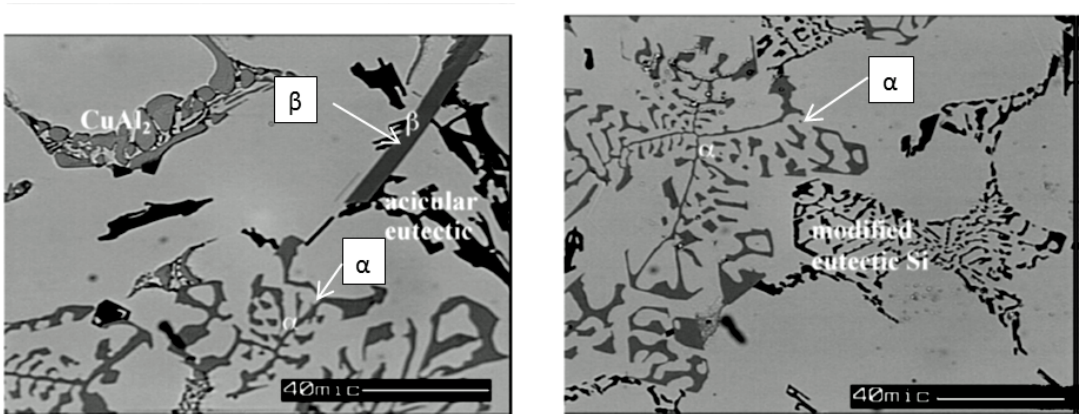

Figure 2.9 Optical micrographs obtained from an as-cast 319 alloy showing the morphology of β-Fe and α-Fe intermetallic phases.[59]

The effects of Fe-content on the mechanical properties and quality index of Al-Si casting alloys have been discussed in several studies which report similar results about the deleterious effect of iron on the mechanical properties.[49, 60-65] G. Sigworth[64] reported that as the Fe content in 356 alloys is increased, a continuous reduction in the ductility is observed, whether the alloys are modified or non-modified, as displayed in Figure 2.10.

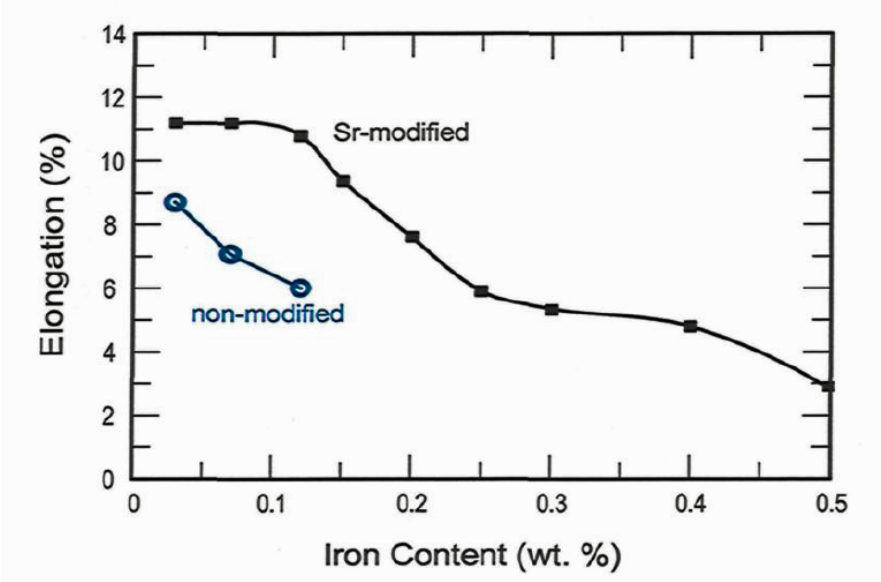

Figure 2.10 Influence of Fe-level on the ductility of modified and unmodified 356-T6 alloys.[64]

It was reported that in Al-Si alloys if the iron content increases from 0.5 to 1.2%, the mechanical properties, particularly the ductility, will be significantly reduced due to the formation of the brittle β-Al_5FeSi phase.[66] According to Bonsack,[67] due to the presence of the β-phase in Al-Si alloys, whenever the iron content is higher than 0.5%, alloys will show an increase in strength, and a reduced ductility; however if the iron content exceeds 0.8%, the ductility will decrease dramatically. In Al-Si-Cu alloys, it was also observed that as the iron content increases the ductility will decrease, specifically, when the iron content exceeds 0.9%.[68]

There is a debate in the literature regarding the iron content at which the β-iron phase appears. It is commonly known that when the iron content exceeds 1%, the β-phase will appear.[68] However, Backerud *et al.*[69] stated that, in 356 alloys, the β-phase can exist at an iron content of 0.48%. A recent study states that the relation between the presence of the β-phase and iron content is mainly dependent on the cooling rate. The β-phase is favored at low cooling rates (0.1 °C/s); while it is inhibited at high cooling rates (10 °C/s), and with very high cooling rates (20 °C/s) the β-phase is strongly favored.[55]

The addition of manganese (Mn) to Fe-containing aluminum alloys is a practice commonly used to neutralize the negative effects of Fe. Manganese can modify the morphology and the type of Fe-intermetallic phases which usually exist in aluminum cast alloys.[70, 71 66] Mondolfo[71] stated that Mn is considered as the most effective neutralizing additive for iron correction, compared to other elements such as chromium (Cr), molybdenum (Mo), and nickel (Ni).

The addition of Mn will promote the formation of the less harmful α-iron AlFeMnSi phase with Chinese script-like morphology; which will, in turn, improve the overall mechanical properties of Al-alloys.[20, 67 72] Figure 2.11 shows a simplified Al-Si-Fe system phase diagrams at constant manganese levels, it is clear that by increasing the Mn content, the α-AlFeMnSi phase region expands accordingly. This means that the crystallization of the α-AlFeMnSi phase will be achievable even at higher Fe content.[69] The morphology and chemical composition of both α-$Al_{15}(Fe,Mn)_3Si_2$ and α-Al_8Fe_2Si are similar to a large extent except that the first phase contains some amounts of Mn. The α-AlFeMnSi phase can also dissolve a good amount of Ni, Cr, and Cu if they exist as alloying elements. This dissolution will replace part of the iron and, thus, the overall chemical composition of the phase remains almost unchanged.

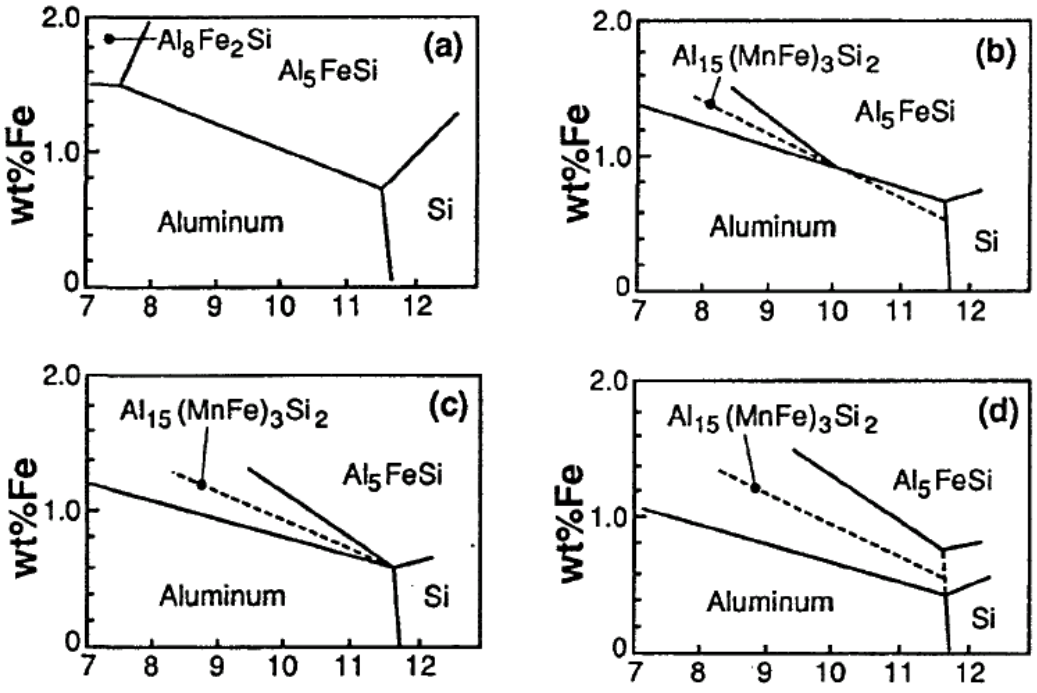

Figure 2.11 Simplified phase diagrams of the Al-Fe-Si system at constant Mn levels of (a) 0%, (b) 0.1%, (c) 0.2%, and (d) 0.3%.[69]

The Mn:Fe ratio plays an important role in neutralizing the effect of iron; the ANSI/ASTM specification[20] states that the Mn content should not be less than half of the iron content when the iron content exceeds 0.45%. Colwell and Kissling[73] reported that when the Mn content equals half of the iron, Mn starts breaking down the needle-like β-AlFeSi phase so that the mechanical properties as well as the castability of the alloys will improve. Mascré[74] developed the formula shown in Equation 2.2 to calculate the Mn content to achieve best neutralization effect in both sand and permanent-mold Al-13% Si cast alloy having upto 1.2% Fe and 1.3% Mn.

$$Mn\% = 2(Fe\% - 0.5) \quad \textbf{(2.2)}$$

Komiyama *et al.*[75] pointed out that the Mn content has a strong effect on the alloy tensile strength when the iron content is higher than 1%. However, when the Mn:Fe ratio exceeds a certain limit, the Mn addition in this case will have a harmful effect on the mechanical strength. Narayanan *et al.*[55] stated that at low cooling rates and in the presence of Mn, the iron intermetallics changed to the α-phase with script-type morphology, whereas at high cooling rates, both the α- and β-iron phases formed.

When a higher ratio of Mn: Fe is used, and in the presence of Cr, sludge will form instead of the favorable α-iron script phase. The sludge is a modified α-phase, α-$Al_{15}(Fe,Mn,Cr)_3Si_2$, with a star-like morphology. These sludge particles are detrimental to the mechanical properties because of their extreme hardness. In order to control the formation of these particles, the sludge factor can be calculated. The sludge factor (S.F.) is related to the weight percentages of Fe, Mn and Cr in the alloy according to the formula:[76]

$$\text{Sludge Factor (S.F.)} = 1 \times \text{wt\% Fe} + 2 \times \text{wt\% Mn} + 3 \times \text{wt\% Cr} \quad \textbf{(2.3)}$$

The sludge factor is also dependent on the casting temperature. If the casting temperature is 650°C or higher, the critical sludge factor beyond which the hard particles will form is 1.8; however if the casting temperature is lower than 650°C, the critical sludge factor value will be 1.4.

Nam and Lee,[77] Lee *et al.*,[78] and Park and Nam[79] reported that the addition of 0.5 wt% or higher levels of Mn to Al alloys will enhance the strength values (UTS and YS) significantly without affecting the ductility. The same trend was also observed by Garza-Elizondo[11] with the addition of 0.75 wt% Mn to Al-Si-Cu-Mg alloys. The increased amount of Mn in Al-Si-Cu-Mg alloys resulted in the transformation of the β-phase needles into α-phase in script-like form and as large polygonal particles. These large particles were similar in morphology to the previously reported sludge particles, however, without Cr. Thus it was concluded by Garza-Elizondo[11] that the presence of these large particles, termed as sludge, is not necessarily harmful to the mechanical properties as is commonly reported in the literature; the same conclusion was also reported earlier by Samuel *et al.*[80]

2.3.1.2 MELT TREATMENT

The main objective of carrying out the melt treatment process is to improve the quality of the Al castings and thus enhance their mechanical properties. Essentially, the melt treatment consists of three main practices: (i) Eutectic silicon modification, (ii) Grain refining, and (iii) Melt degassing.

2.3.1.2.1 EUTECTIC-SILICON MODIFICATION

Modifying the coarse acicular (plate-like) eutectic silicon morphology in hypoeutectic Al-Si alloys is of great importance in relation to the strength and ductility of this category of alloys. The modification is usually carried out as a melt treatment process where the addition of chemical elements such as strontium (Sr), sodium (Na), calcium (Ca), or antimony (Sb) to the molten Al-Si alloy substantially changes or 'modifies' the growth characteristics of the eutectic Si phase, which leads to a more refined, fibrous morphology and consequently improves the strength and ductility. The modification process can also be accomplished by applying a high cooling rate during solidification. Figure 2.12 displays different morphologies of the eutectic silicon as they appear in microstructures typical of (a) unmodified, (b) Sr-modified, and (c) Sb-modified Al-Si alloys.[52, 81, 82]

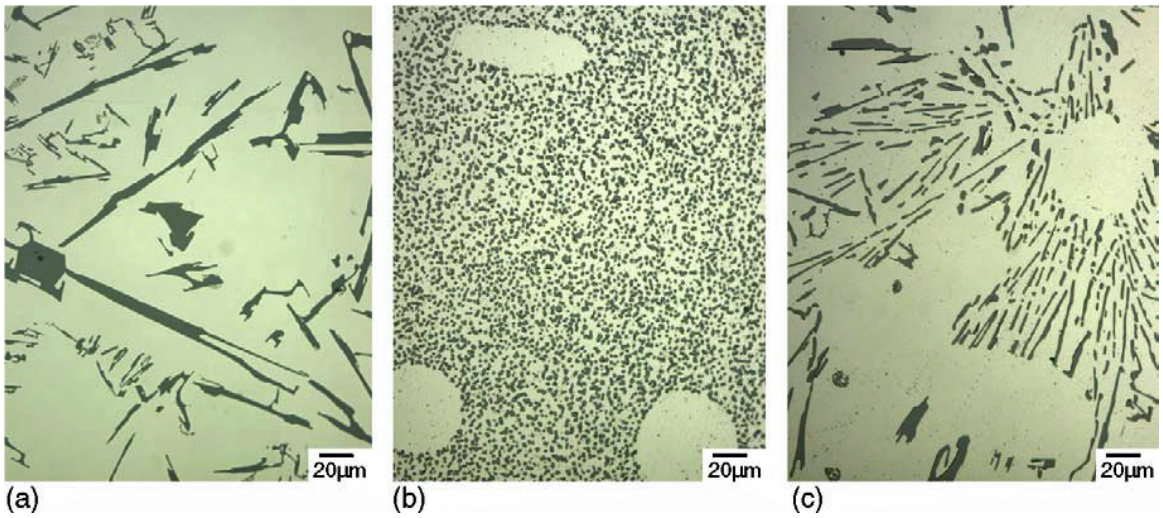

Figure 2.12 Silicon morphologies in (a) unmodified, (b) Sr-modified (300 ppm Sr) and (c) Sb-modified (2400 ppm Sb) hypoeutectic aluminum–silicon alloys.[81]

Strontium is considered an effective commercial modifying element. Addition of Sr to Al-Si alloys transforms the morphology of the eutectic Si from a coarse lamellar or acicular structure to a fine fibrous form. This transformation positively influences the

mechanical properties of Al-Si alloys. It is a common practice to add Sr to the melt in the form of an Al-Sr master alloy. The addition of Sr is usually done in the order of 100-200 ppm (0.01- 0.02 wt%).[8, 27, 50]

According to Hetke and Gundlach,[83] the amount of Sr or Na required to achieve a complete modification of the eutectic Si morphology is dependent on the cooling rate. Higher cooling rates require lower amounts of Sr or Na to achieve complete modification and vice versa. The simultaneous addition of both Sr and Na is allowed because the two elements are mutually compatible.[25]

2.3.1.2.2 GRAIN REFINEMENT

Grain refining is another melt treatment process commonly applied to Al-Si alloys to refine the grain size and thereby enhance the microstructure. Grain refiners act to hinder the formation of columnar grains and promote the formation of equiaxed grains. Titanium (Ti) is added as a refining element to Al-Si alloys in order to reduce the α-Al grain size. This practice improves the overall mechanical properties leading to isotropic behavior rather than anisotropic one. In order to achieve effective grain refining, the lattice coherency of the grain refiner must match perfectly with the lattice coherency of the Al matrix.[52]

2.3.1.2.3 MELT DEGASSING

The need for high quality aluminum castings necessitates cleaning (degassing) the melt from undesirable inclusions and impurities, which may be in the form of dissolved hydrogen or other gases, and solid particles such as oxides, carbides, and intermetallic

compounds. Their presence limits the fluidity of the melt and, consequently, the mechanical properties of the castings. Therefore melt degassing is commonly used in aluminum casting processes. The most common technique for degassing is to inject an inert gas (in most cases dry argon) into the aluminum melt through a rotating impeller. Figure 2.13 shows a schematic drawing of the rotary degassing process. The mechanism of hydrogen removal is by diffusion across the gas/liquid interface, whereas the solid inclusions and become attached to the inert gas bubbles that rise to the surface of the melt as dross. The dross layer is then carefully skimmed from the surface of the melt, thus removing the inclusions and impurities.[84-86]

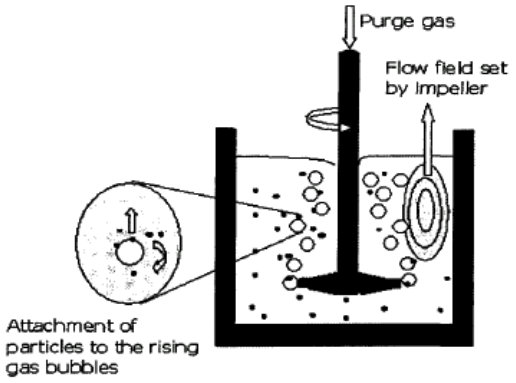

Figure 2.13 Schematic representation of the melt degassing process using a rotating impeller.[86]

2.3.2 HEAT TREATMENT

Heat treatments are a series of controlled heating and cooling procedures employed to alter the mechanical properties of heat-treatable alloys. An appropriate heat treatment provides the means to enhance the as-cast mechanical properties of such alloys to suit the application requirements of components cast from these alloys. The improvement in properties is achieved by modifying the microstructure of the alloy by optimizing the

parameters of temperature, time, and heating and cooling rates used in the heat treatment process.

In order to achieve beneficial results with high repeatability and reliability, and consequently high quality products capable of competing in the market.[87] These considerations include:

- High control of the time-temperature profile,
- Tight uniformity of temperature,
- Compliance with the industrial standards and specifications,
- Low production cost,
- Environmental issues.

Aluminum alloys are very versatile owing to their suitability to be used in many heat treatments; depending on the alloy chemical composition and the required mechanical properties.[38] Table 2.4 lists the common standardized heat treatments used for aluminum alloys.[38, 52]

Table 2.4 Designations and Practices of common Al heat treatment[52]

Treatment	Solutionizing	Quenching	Aging
T4	Yes	Yes	Room Temperature only
T5	No	No	Elevated Temperature
T6	Yes	Yes	Elevated Temperature (Increased strength)
T7	Yes	Yes	Elevated Temperature (Dimensional stability)

The main idea of the heat treatment in Al-alloys is to precipitate secondary hard phase in the matrix during changes in temperature due to the variation in solubility of the alloying elements with temperature. The T6 and T7 heat treatments are commonly used for

Al-Si alloys in industry. They comprise solution treatment at high temperature followed by rapid cooling to ambient temperature (quenching), and finally either natural aging at room temperature or artificial aging at higher temperatures. The enhancement in the properties of alloys following such treatments is accredited to two main factors related to the alloy microstructure: the first is the formation of non-equilibrium precipitates during the aging treatment; and the second is related to the changes in the eutectic Si particle characteristics which occur during the solution treatment.[52, 87, 88]

The strengthening mechanism of heat-treatable Al alloys is known as precipitation hardening or age hardening, originating from the nomenclature of age-hardenable Al alloys. This mechanism is mainly based on the concept of the level of solid solubility of an alloying element (solute) in the matrix (solvent) depending on the temperature, i.e. at a high temperature the solid solubility increases and vice versa. The strengthening is achieved by heating the alloy to a temperature slightly below the eutectic isotherm or to a single phase region for a sufficient period of time during which the solute atoms dissolve completely in the matrix owing to the increased solid solubility between the solute and solvent at high temperatures. This step is commonly known as solution treatment or solutionizing, following which the alloy is rapidly cooled (quenched) to room temperature using a proper cooling medium in order to form a supersaturated solid solution at ambient temperature. The final stage in this process is the aging treatment, during which the fine precipitates start to form. Aging is commonly attained by heating to elevated temperatures in order to accelerate the formation of the precipitates. The alloy response to age-hardening is primarily dependent on the fraction, size, distribution, and coherency of the precipitates

formed with the matrix. Figure 2.14 presents schematically the heat treatment steps followed in carrying out the T6 heat treatment.[52, 88-90]

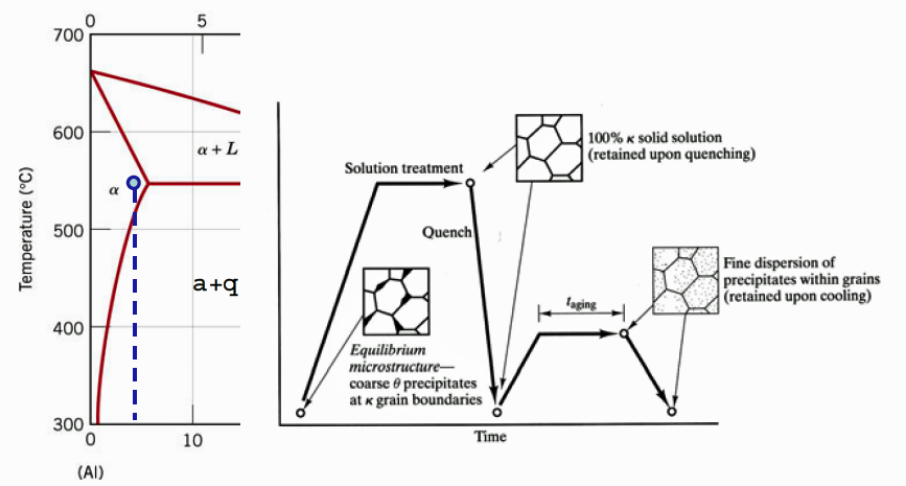

Figure 2.14 Illustration of precipitation hardening treatment.[91]

The presence of Cu and Mg improves the age-hardening tendency of Al-alloys. Cáceres *et al.*[58] studied the effects of Si, Cu, Mg, Fe, and Mn besides the solidification rate on the mechanical properties of Al-Si-Cu-Mg alloys. The authors found that the increase in strength and decrease in ductility observed was related to the increased Cu and Mg content; whereas increasing the Fe content had a detrimental effect on both strength and ductility. They also reported that the content of Cu and Mg defines the alloy response to age-hardening depending on the volume fraction of the copper-rich and magnesium-rich intermetallic phases obtained.[52, 58]

The three stages of the T6 and/or T7 heat treatment processes are reviewed in the following subsections.

2.3.2.1 SOLUTION HEAT TREATMENT

The primary objective of solution heat treatment is to obtain a supersaturated solid solution at elevated temperatures. A homogeneous supersaturated solid solution (SSSS) will form at high temperature by dissolving the existing phases in the as-cast structure, such as β-Mg_2Si, θ-Al_2Cu, Q-$Al_5Cu_2Mg_8Si_6$, π-$Al_9FeMg_3Si_5$ and β-Al_5FeSi phases. The SSSS is considered as the reservoir of the strengthening precipitates. The β-Mg_2Si and θ-Al_2Cu phases can be easily dissolved when the optimum solutionizing temperature and time are used, whereas the π-$Al_9FeMg_3Si_5$ phase, for example, if present, is harder to dissolve because of the limited diffusivity of Fe in Al.[88, 92, 93] The solution treatment temperature is determined according to the alloy composition and solid solubility limit; however it must be lower than the melting point of the phases that exist in the as-cast structure to avoid incipient melting of these phases.[87, 94]

Many researchers have reported controversial conclusions related to the solution treatment temperatures of certain alloys. Solution treatment at temperature of 495°C or lower is preferred to avoid incipient melting of the copper-rich phase, which would lead to overall deterioration in the mechanical properties; however this range of temperatures will not be sufficient to either maximize the dissolution of copper-rich phase or to modify the eutectic silicon morphology.[52, 95, 96] Ouellet *et al.*[97] employed a solution temperature of 500°C instead of 505°C for an Al-Si-Cu-Mg alloy containing low Mg content (0.5 wt.%) in order to avoid the fusion of low melting point phases, while Wang *et al.*[98] used a solution treatment temperature of up to 520°C for a similar alloy and reported improvement in mechanical properties without noticeable localized melting.

With the aim of avoiding incipient melting of Cu-rich phase in Al-Si-Cu-Mg alloys, the solutionizing temperature of this category of alloys should be lowered if the Cu content is increased. For example, Wang *et al.*[99] reported that alloys containing around 2% Cu should be solution treated at about 500°C which, to a large extent, match the conclusions of Ouellet *et al.*[97]

Thus, selecting the conservative temperature of 495°C for solution treating Al-Si-Cu-Mg alloys is preferable, in order to avoid incipient melting as far as possible.[52, 100, 101] The solutionizing time is decided on as a compromise between the mechanical properties required, alloy quality, and economic efficiency. The solution treatment time must be sufficient to ensure a uniformly homogeneous structure, and it is dependent on the chemical composition of the alloy, solutionizing temperature, structural coarsening, and the casting method.[87, 88, 102, 103] For alloys containing high Cu content, the complete dissolution of Al_2Cu is not achievable; nevertheless, the solution treatment time must be carefully chosen to allow maximum dissolution of this phase, bearing in mind at the same time the cost of long solution treatments and the possible deterioration in mechanical properties owing to the formation of secondary porosity and coarsening of the microstructural constituents.[52, 92, 96]

2.3.2.2 QUENCHING

Quenching (rapid cooling) is done after the completion of the solution treatment, and it is primarily responsible for (a) retaining the supersaturated solid solution at ambient temperature by preserving the SSSS structure, or blocking the solute atoms in their positions which were achieved at the high temperature during solution treatment, (b)

obtaining as many vacancies as possible within the lattice structure to act as potential sites for the precipitates which will form during the artificial aging stage.[87] This practice is followed in order to avoid precipitation of the hardening phase during cooling; as such precipitation would be harder to control than in the case of an aging treatment. The presence of the SSSS at the ambient temperature means that the concentration of the solute atoms exceeds the equilibrium concentration at this temperature, which is not a stable state for the solute atoms.[88]

The cooling rate during quenching would depend on the initial temperature of the solution-treated alloy/part being quenched, the final required microstructure and mechanical properties, and the alloy chemical composition (Figure 2.15).[38] If the cooling rate is fast enough to avoid the formation of precipitates during cooling, a final structure of finely distributed solute atoms in the matrix will be achieved.

In Al alloys, the cooling rate should be high enough to avoid precipitation during cooling within the temperature range of 450°C to 200°C as, within this range, the precipitates form rapidly as a result of the high level of supersaturation as well as a high diffusion rate. At higher temperatures, lower levels of supersaturation will be obtained and if the alloy temperature is lower than this range, the diffusion rate will be slow.[104]

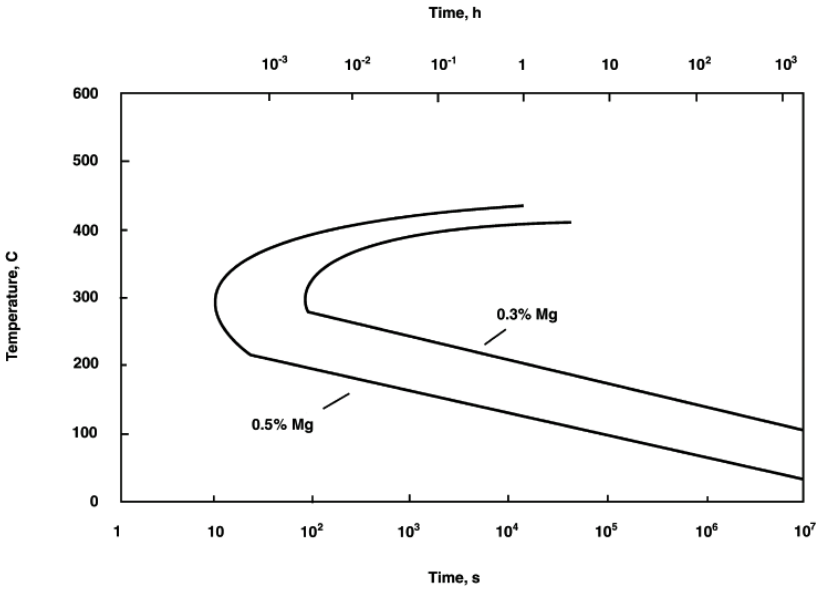

Figure 2.15 Minimum time to avoid precipitation during quenching of Al alloys depending on the Mg content (in wt.%).[38]

An optimum quenching rate should be selected in order to avoid or limit the formation of precipitates during quenching, and to minimize part distortion after quenching if the rate was slow.[52]

Some of the mechanical properties can be correlated to the quenching rate, based on *quenching sensitivity* of the alloy. As per its definition, quenching sensitivity is a measure of the susceptibility of an alloy to form non-hardening precipitates during quenching. It has been reported in different studies that cast Al alloys have a quenching sensitivity higher than that of wrought Al alloys, since they contain higher percentages of alloying elements than do wrought alloys.[88, 100, 104]

In Al alloys, quenching mediums include water, brine solution, and polymer solution. Despite the fact that water is frequently used as the quenching medium for Al alloys, Mohamed and Samuel[52] reported that water quenching can lead to distortion,

cracking, and residual stresses. However, water quenching at temperatures between 60 and 70°C may positively affect the properties of cast Al alloys.

2.3.2.3 AGING TREATMENT

The phenomenon of precipitation strengthening was discovered in the early 20th century by Ardel.[105] He found that the hardness of Al alloys containing Cu and Mg increased at room temperature with time, so that the phenomenon came to be defined later on as age hardening.

An aging treatment or aging involves the development of coherent strengthening precipitates within the matrix, which are subsequently required to be sheared through the movement of dislocations. Temperature and time play a major role in determining the mechanical properties obtained following the aging treatment. Generally, aging results in enhancing the tensile strength, reducing residual stresses, and stabilization of the microstructure. The precipitates formed can occur either at room temperature - termed "natural aging" or at higher temperatures - termed "artificial aging". Temperatures within the range of 90-260°C may be used for Al alloys to accelerate the precipitation process.[52]

In many Al alloys, the equilibrium precipitates are not formed at the beginning of the aging treatment, but through a sequence of different forms of precipitates which occur successively during the treatment.[106] The solute atoms, which exist in the supersaturated solid solution (SSSS) obtained after solution treatment and quenching, start to form clusters of atoms known as Guinier-Preston (GP) zones. These GP zones, consisting of ordered groups of solute atoms, are coherent with the lattice structure and dispersed in the matrix.

These groups of atoms usually have sizes different than those of the lattice structure of the Al matrix; therefore distortion occurs in the lattice structure, producing coherency-strain fields, leading to a strengthening effect. These GP zones are metastable and they will dissolve in the presence of a more stable phase. Following dissolution of the GP zones as the aging treatment progresses, metastable coherent or semi-coherent precipitates start to form. These precipitates continue to grow by diffusion of atoms from the SSSS, which results in the alloy achieving its maximum or peak strength/properties. As aging continues further, the metastable coherent precipitates become totally incoherent. In this condition, the opposition of the precipitates to dislocation movement is reduced, leading to the consequent reduction in mechanical properties.[88, 106] The time needed for this sequence to be completed depends on the thermal history of the alloy, its chemical composition, and the artificial aging temperature employed.

In Al-Si-Cu alloys, the main strengthening precipitates are those of the θ-Al_2Cu phase;[52, 88, 107] these precipitates are formed in the following sequence:

$$\alpha_{sss} \rightarrow \text{GP zones} \rightarrow \theta'' \rightarrow \theta' \rightarrow \theta\ (Al_2Cu)$$

The sequence starts by clustering of Cu atoms which are formed from decomposition of the supersaturated solid solution. At room temperature, these clusters appear homogeneously, forming GP zones. These GP zones exist as thin disks with a diameter of approximately 3-5 nm. By increasing the time at the same temperature, the GP zones increase in number; the size, however, remains almost constant. Increasing the aging temperature to above 100°C, the GP zones start to dissolve and form particles of θ'' precipitates. The θ'' fine particles nucleate uniformly and coherently with the matrix lattice

structure. Due to the high degree of coherency, extensive coherency-strain fields are developed, leading to increase in the peak strength of the alloy. In other words, the formation of θ'' precipitates lead to distortion in the lattice structure in, and around, the vicinity of themselves; these distortions will impede the dislocation movements during plastic deformation, leading to strengthening and hardening effects.[52, 90, 107] As aging continues, θ'' will dissolve forming θ' phase which is plate-like in shape. As precipitates of θ' grow, they lose coherency with the matrix, leading to reduction in the lattice distortion and consequently a decrease in strength values is observed. Further aging will cause the formation of equilibrium θ-Al_2Cu particles. These equilibrium precipitates are totally incoherent with the matrix, relatively large in size, and have a coarse distribution in the matrix; all these parameters lead to further reduction in the strength. The stages in the precipitate formation sequence are illustrated clearly in the schematic diagrams shown in Figure 2.16 and Figure 2.17.

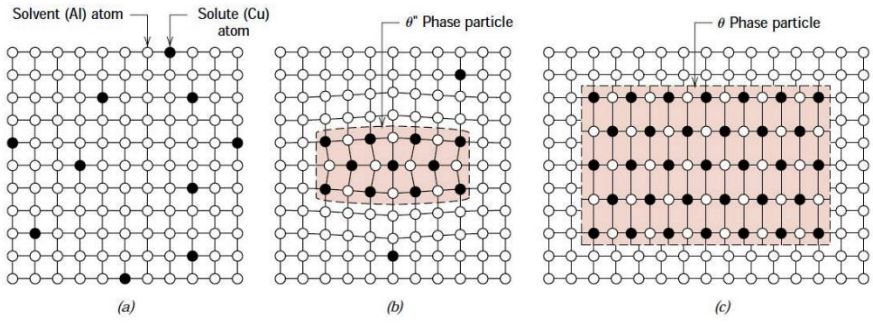

Figure 2.16 Schematic representations for the stages of forming the equilibrium precipitate (θ). (a) Supersaturated α solid solution. (b) Transition θ'' precipitates. (c) Equilibrium θ phase, within the α-matrix. Actual phase particle sizes are much larger than shown.[91]

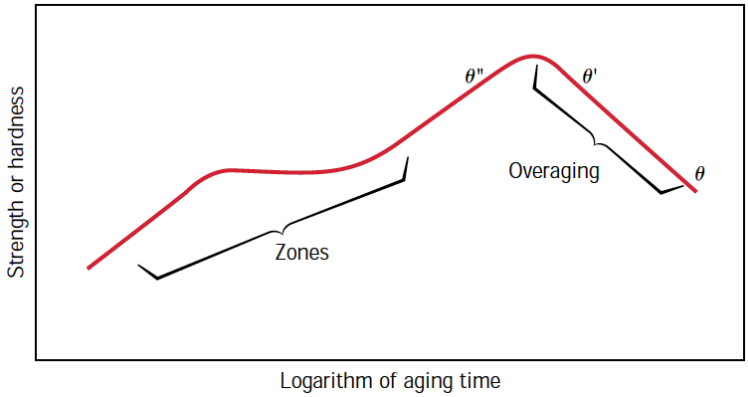

Figure 2.17 Schematic diagram showing strength and hardness as a function of the logarithm of aging time at constant temperature during the aging treatment.[91]

The main strengthening precipitate in Al-Si-Mg alloys is the β-Mg_2Si phase and the sequence of the formation of precipitates occurs as follows:

1- Formation of GP zones (10 nm long, needle-shaped),
2- Intermediate homogeneous precipitates of β''-Mg_2Si,
3- Intermediate heterogeneous precipitates of β'-Mg_2Si,
4- Equilibrium precipitates β-Mg_2Si (rod or plate-shaped).

In the quaternary Al-Si-Cu-Mg alloy system, multiple precipitates may form based on the level of alloying elements in the alloy (e.g. Mg/Si, Cu/Mg, Cu and Si contents), and the aging time and aging temperature. The precipitation of a quaternary Q-phase and its precursors during the aging treatment of Al-Si-Cu-Mg alloy was reported by many authors.[108-111] The composition of the Q-phase is $Al_4Mg_8Cu_2Si_6$ and it can coexist with the Al_2Cu, Mg_2Si, and Si phases depending on the levels of Cu, Mg, and Si as mentioned above.[110, 112-114] The mechanism for formation of the Q-phase was suggested as follows:[115, 116] the Cu atoms dissolve in the β'' phase which can then evolve to become either a stable β-phase or the Q-phase, depending on the chemical composition of the alloy and if the precipitate forms in a metastable or stable state.

The precipitation sequences of Al_2Cu and Mg_2Si precipitates have been mentioned in the preceding paragraphs. The precipitation sequence that leads to the formation of the stable Q-phase in Al-Si-Cu-Mg alloys is as follows:

$$QP \rightarrow QC \rightarrow Q' \rightarrow Q$$

Table 2.5 lists the crystal structure and morphology of the Q-phase and its precursors which were reported to precipitate during the aging treatment of Al-Si-Cu-Mg alloys.

Table 2.5 Characteristics of Q-phase and its precursors formed during aging treatment of Al-Si-Cu-Mg alloys[54, 55, 57]

Precipitated Phase	Unit Cell	Morphology
QP	Hexagonal a = 3.93Å, c = 4.05Å	Rods
QC	Hexagonal a = 6.7Å,c = 4.05Å	Rods
Q'	Hexagonal	Laths
Q	Hexagonal a=10.4Å, c = 4.05Å	Rods

2.4 ROLE OF SOLUTION TREATMENT IN MICROSTRUCTURE EVOLUTION

A series of interactive metallurgical processes take place during heat treatments to alter the microstructure of aluminum alloys. Solution heat treatment consummates three roles: i) the dissolution of soluble phases and intermetallic compounds, ii) homogenization of the as-cast structure, and iii) morphological changes in the eutectic silicon particles. The quenching process is intended to form a supersaturated solid solution at room temperature,

however some precipitations are expected at slower cooling rates. During the artificial aging treatment, the supersaturated solid solution starts to decompose at elevated temperatures and the precipitation of fine dispersoids takes place. In the following subsections, each process during solution treatment will be discussed separately.

2.4.1 DISSOLUTION OF SOLUBLE INTERMETALLIC COMPOUNDS

As a rule, the dissolution process needs heat to accelerate the reaction. Optimum solution treatment parameters (e.g. temperature and time) should be used in order to efficiently dissolve the alloying elements to make them available for precipitation hardening. The dissolution process is a diffusion-controlled process of the phases in the matrix; thus the presence of multiple phases will complicate the diffusion process due to the overlapping of the diffusion fields.

Recently, numerical models have been developed in order to describe the dissolution kinetics of the existing phases.[117, 118] Complete dissolution of the Mg_2Si phase in Al-Si-Mg alloys following 15 min of solutionizing at 540°C was predicted using a model developed by Rometsch *et al.*[119] Later on this valuable finding was experimentally confirmed for A356 alloy by Zhang *et al.*[120] Furthermore, Rometsch *et al.*[121] developed another numerical model to predict the co-dissolution of the Mg_2Si and π-$Al_8Si_6Mg_3Fe$ phase in A356 alloy, where the authors reported complete dissolution of Mg_2Si phase within 4 minutes at 540°C, whereas most of the π-$Al_8Si_6Mg_3Fe$ particles dissolved within 30 minutes at the same temperature, and complete dissolution was achieved after 12 hours. Such models give good predictions about the optimum range of solution temperatures and times, and while they should be validated experimentally, however, such models save the

time, money, and effort that would be expended in carrying out experimental trials to arrive at the optimum conditions.

2.4.2 HOMOGENIZATION OF THE AS-CAST STRUCTURE

Due to the dendritic solidification of Al alloys, solute atoms segregate in the eutectic areas within the dendrites in a manner that is detrimental to the mechanical properties. It is known that the kinetics of homogenization are controlled primarily by the dendrite arm spacing of the as-cast structure, the level of the solute segregation within the dendrites, and the diffusion coefficient of the solute element in the matrix.[122] An homogenization process would minimize the segregation effect; however, sufficient time would be needed to ensure the results. The time selected would be based on both the solution treatment temperature and the characteristics of the dendritic structure.[24, 38, 52]

2.4.3 MORPHOLOGICAL CHANGES OF EUTECTIC SILICON

The amount and morphology of eutectic silicon particles have a significant effect on the mechanical properties of Al-Si alloys. In the as-cast microstructure, the eutectic silicon has a coarse lamellar or acicular structure which is detrimental to the mechanical properties. By modifying the acicular morphology into spheroidal form the mechanical properties are improved, in particular the ductility. Prior to heat treatment, primary modification can be accomplished chemically by the addition of Sr which changes or ‘modifies’ the acicular morphology to a fine, fibrous form. Later, solution treatment helps in spherodizing the eutectic silicon in either non-modified or modified alloys.[87] The change in the eutectic Si morphology occurs in two stages: (i) dissolution or fragmentation of the eutectic Si branches after necking, and (ii) granulation or spheroidization of the fragmented branches

as their average size decreases, allowing eventual spheroidization. Many authors[123-125] have stated that fragmentation of acicular silicon is facilitated by a previous Sr treatment, so that the resulting fibrous eutectic silicon would be spheroidized in a shorter time; this behaviour was attributed to the larger interfacial area of the fibrous structure and driving force for morphological change.[126-128] On the other hand, non-modified structures will take longer time to be spheroidized. Figure 2.18 shows the sequence of spheroidization of the eutectic silicon particles in both non-modified and modified Al-Si alloys.[52, 87, 128-132]

The processes of spheroidization and coarsening of eutectic silicon particles results mainly from the reduction in the surface energy associated with the interface between the silicon particles and the Al-matrix.[122, 133] At elevated temperatures, the size and frequency of surface perturbations increase at the interface, leading to the formation of near-spherical Si particles due to the breakdown of the eutectic silicon particles. Subsequently, these near-spherical particles tend to coarsen to further reduce the interfacial area; the coarsening occurs by the dissolution of the smaller Si particles into the larger (more stable) particles following the Ostwald ripening mechanism.

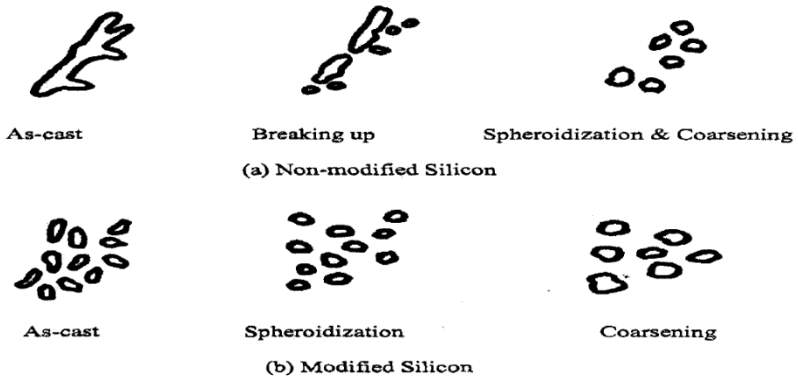

Figure 2.18 Schematic diagram showing change of eutectic Si particles morphology during solution heat treatment: (a) non-modified and (b) modified Al-Si cast alloys.[132]

Ogris *et al.*[134] studied the fragmentation of eutectic silicon rods into spheres in Al-Si-Mg alloy by considering the model shown in Figure 2.19, where the cylindrical rod in the top half of the model is representing the interconnected modified silicon particles. The authors concluded that the fragmentation time for eutectic silicon rods during solution treatment is highly dependent on the initial rod radius, and the solutionizing temperature.

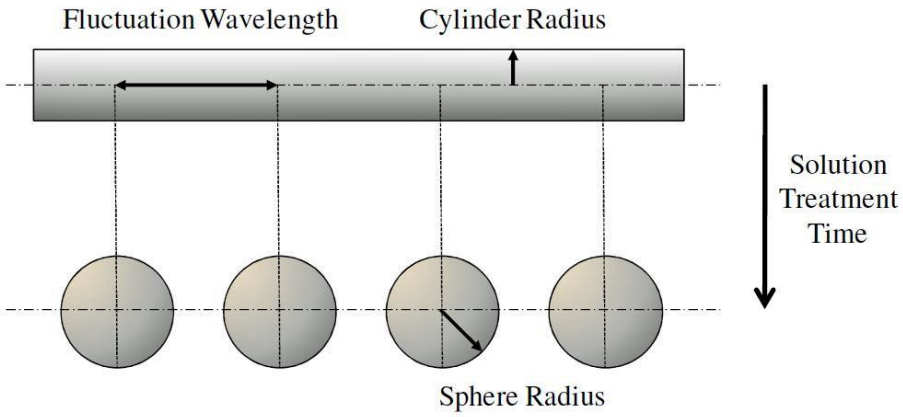

Figure 2.19 Schematic illustrating a rod-shaped eutectic particle that fragments into a series of spherical particles.[134]

The coarsening rate of Sr-modified eutectic silicon particles in Al-Si-Mg alloys was previously studied by Parker, and Rhines and Aballe.[123, 124] The coarsening rate can be calculated using Equation 2.4 following diffusion-controlled growth model,[135, 136] also known as the LSW model after Lifschitz, Slyozov and Wagner.

$$r^3 - r_o^3 = \frac{8}{9}\frac{DC_0\gamma V^2}{R_{gas}T}t \qquad \textbf{(2.4)}$$

where T and t are the temperature and time, r is the final equivalent radius of a spherical particle (m), r_o is the initial equivalent radius of a spherical particle at t=0, R_{gas} is the gas

constant, V is the molar volume, C_0 is the equilibrium concentration of structures in the matrix, γ is the surface energy of the particle, and D is the diffusion coefficient.

In non-modified Al-Si-Mg alloys, the coarsening rate of eutectic silicon was found to follow the LSW model after an initial time delay during which the fragmentation of the silicon plates takes place.[125, 126]

Therefore it will be of importance to investigate the fragmentation and coarsening processes of eutectic silicon particles in the Al-Si-Cu-Mg alloys used in the present study, in modified and non-modified conditions, and following the addition of transition elements.

2.5 STRENGTHENING MECHANISMS IN AL ALLOYS

Selective strengthening mechanisms that act in age hardenable Al-Si alloys will be addressed briefly in this section. The two mechanisms which will be discussed are second phase particle strengthening and precipitation strengthening. These mechanisms are relevant to such alloys as this category of alloys can produce strengthening precipitates following heat treatment, and they also contain eutectic silicon particles which will act as strengthening particles similar to the case of metal matrix composites. However, strengthening due to mechanical working or due to solid-solution is not included in the scope of this part of the review.

2.5.1 SECOND PHASE PARTICLE STRENGTHENING

Al-Si cast alloys may be categorized as two-phase alloys because they have hard silicon particles dispersed within the soft aluminum matrix. The distribution of these Si particles embedded in the aluminum metal matrix would provide an overall strengthening

effect similar to that of the reinforcement particles employed in metal matrix composites (MMCs).[137] Typically, these hard Si particles, which act as reinforcing particles, exist in volume fractions varying between 5 and 20%, and their equivalent spherical diameters may be in the range of 10-30 μm, although recently, a larger size range of 5-250 μm has been employed. In hypoeutectic Al-Si cast alloys, the silicon percent is up to a volume fraction of 12%, and the size of the silicon particles is usually around 5-10 μm in equivalent diameter except for the coarsened silicon particles that may exist following prolonged solution treatment.

Based on the aforementioned, the strengthening effect due to the presence of silicon particles in aluminum alloys can be explained in the same manner analogous to that used for composite materials. The applied load is transferred from the ductile aluminum matrix to the brittle silicon particles through the development of shear stress at the Al/Si interface. The load transfer process can be modelled by a number of approaches including the shear lag model, the Eshelby model, and finite element models based on continuum mechanics. In general, if the second phase particles, i.e. eutectic silicon, are strongly bonded to the Al matrix, and both constituents (Si particles and Al matrix) behave elastically, an equation based on the rule of mixtures can be easily used to calculate the overall strength:

$$\sigma_{tot} = V_{f,p}.\sigma_p + \left(1 - V_{f,p}\right).\sigma_m \qquad \textbf{(2.5)}$$

where $V_{f,p}$ is the volume fraction of the strengthening particles (Si particles), and σ_{tot}, σ_p and σ_m are the total strength of the material, the particle strength and the matrix strength respectively.[138] If the material is allowed to deform plastically, Equation 2.5 is modified as:

$$\sigma_{tot} = V_{f,p}.\sigma_p + \left(1 - V_{f,p}\right).\sigma'_m \quad \textbf{(2.6)}$$

where: σ'_m is the stress acting on the matrix at the particle fracture strain.[138]

2.5.2 PRECIPITATION STRENGTHENING

Fundamentally, the strengthening effect in age-hardenable alloys is achieved by hindering the motion of dislocations. This may be achieved by either the strain field around GP zones or around the precipitates, arising from their coherency with the matrix (distortion in the lattice structure), or the presence of the precipitates themselves. To pass the precipitates and continue their movement, dislocations will be compulsorily required to cut through the precipitates or form a loop around them to continue their motion, both of which will require much energy and therefore increase the alloy strength.

As Figure 2.20 shows, dislocations can pass the precipitates in two different ways, by shearing the precipitate, termed as the Friedel effect or by forming a loop around it and then moving on, termed the Orowan looping mechanism. The Friedel effect (shearing mechanism) represented in Figure 2.20(a) is attainable in the early stages of aging when the precipitates are small and coherent or semi-coherent with the matrix. In this case, the strengthening effect comes from one or more of the following mechanisms: (i) coherency strengthening, (ii) modulus strengthening, (iii) chemical strengthening, (iv) atomic order strengthening, and (v) stacking fault strengthening; details of these mechanism may be found elsewhere. [139] As the aging treatment continues, the precipitates grow to become incoherent with the matrix, thus the dislocation will bow between precipitates and form loops in order to continue its movement; strengthening in this case arises from the bowing

of the dislocation and the opposing tension of the dislocation line to this action and the formation of dislocation loops according to the Orowan mechanism as shown in Figure 2.20(b).[52, 88, 139]

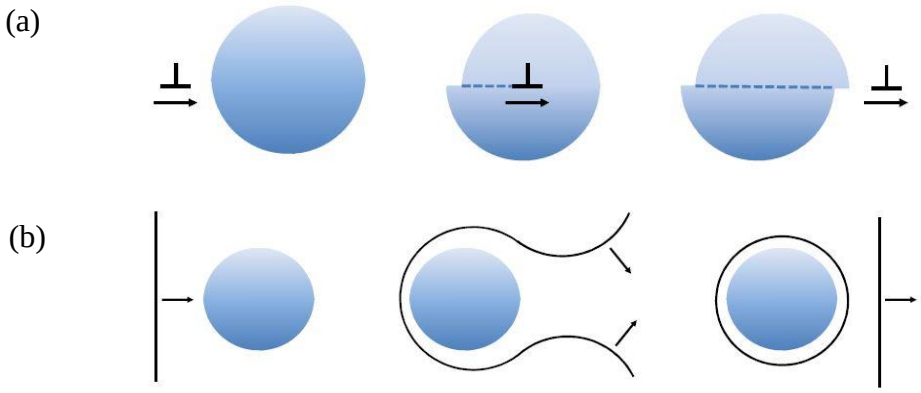

Figure 2.20 Schematic representation of dislocation movement according to: (a) Friedel effect and (b) Orowan-looping mechanism.[88, 139]

The strength of the precipitates increases with increasing size of the precipitates till the precipitate size reaches a critical value at which the Friedel effect (i.e. particle shearing) is still active. However, with further aging and increase in the size of precipitates, it will become more difficult to cut through the precipitates so that the Orowan mechanism will be favored over the latter, and the dislocations will pass the precipitates by forming loops around them and continue moving on. Subsequent reduction in strength values will be experienced with further aging or precipitate growth. The occurrence of these two processes in relation to the precipitate size and strength is displayed in Figure 2.21.

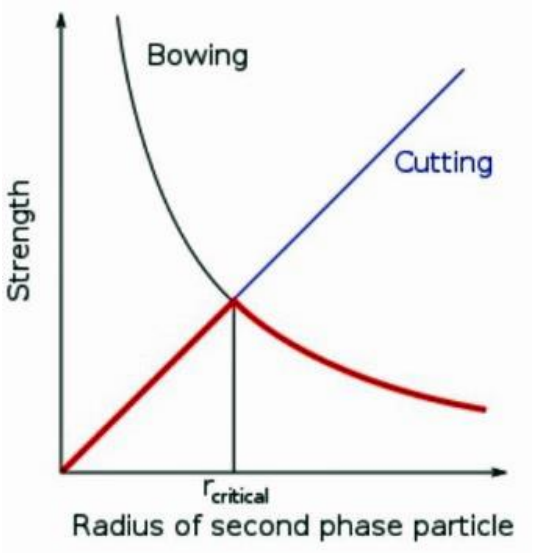

Figure 2.21 Relationship between precipitate radius and strength of the particles to resist shearing or bypassing by dislocations.[14]

In more detail, when a moving dislocation is hindered by a precipitate, a balance of forces will develop due to the precipitate/dislocation interaction, as shown schematically in Figure 2.22. The force balance that develops between the moving dislocation and the precipitates can be described using the following equation:[140]

$$F = 2\Gamma \sin\left(\frac{\theta_C}{2}\right) = 2\Gamma \cos\left(\frac{\Psi_C}{2}\right) \quad \textbf{(2.7)}$$

where F represents the precipitate resistance force, Γ indicates the line tension of the moving dislocation, and Ψc is the critical dislocation bowing angle. It is apparent that as the precipitate size decreases, the angle (θc) increases whereas Ψc decreases, resulting in higher resistance force (F) as well as line tension of the moving dislocation (T), reflecting the presence of strong obstacles or precipitates.

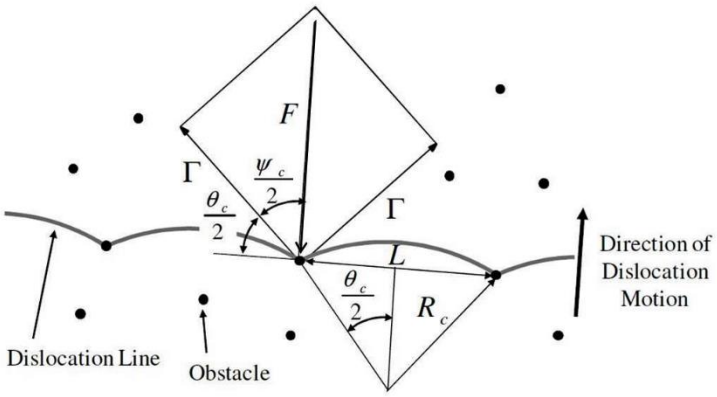

Figure 2.22 The balance of forces between a moving dislocation and a precipitate resisting its motion.[139, 140]

In this type of interaction, there will be two possibilities based on the nature of the precipitates. In the case of hard precipitates, the particle will not deform which will lead to a resistance force (F) higher than the line tension (2Γ), so that the dislocation will bypass the precipitate either by cross-slip or by Orowan looping as was shown in Figure 2.20(b). In the case of soft precipitates, the particles will be sheared by the moving dislocation as the line tension (2Γ) will be greater that the resisting force (F), so that the Friedel effect shown in Figure 2.20(a) will come into play. It should be noted that hard precipitates provide a greater strengthening effect than the soft ones; however, the strengthening effect of hard precipitates is generally a function of their volume fraction and size: the strengthening effect increases as the volume fraction increases and as the precipitates size decreases. These factors can alternatively be expressed in terms of the inter-particle spacing between the precipitates. Orowan has expressed the relation between the yield strength of an alloy and the inter-particle spacing between hard precipitates by the formula:[140, 141]

$$\Delta\tau_y = Gb/L \qquad \textbf{(2.8)}$$

where $\Delta\tau_y$ is the increase in the yield strength due to the resistance to dislocation motion by the hard particles, G is the shear modulus of the matrix, b is the dislocation Burger's vector, and L is the inter-particle spacing. Thus, by decreasing the inter-particle spacing, i.e. by increasing the volume fraction of the precipitates and by decreasing their size, the increase in the yield strength as given by Equation 2.8 will be higher.

The following section will discuss the use of transition element additions for tailoring Al alloys to improve their elevated-temperature mechanical properties, which is the main objective of the present study.[8, 25, 27] Firstly, the selection criteria of suitable additions (i.e. elements) will be discussed followed by the effect of Zr and Ni additions.

2.6 TAILORING AL ALLOYS FOR ELEVATED-TEMPERATURE APPLICATIONS USING TRANSITION ELEMENT ADDITIONS

As mentioned earlier, the particular characteristics of aluminum alloys allow them to be used extensively in the automotive industry. However, continuous advancements in automotive technology have resulted in higher combustion temperatures and pressures, so that aluminum alloys generally start losing their mechanical properties rapidly when employed at temperatures higher than 200°C for longer times.

Many studies[11, 12, 14, 17, 142, 143] have been carried out in the past decade on how to maintain the mechanical properties of aluminum alloys at service temperatures that exceed 200°C. Among these, the addition of small amounts of transition metals was found to be a promising approach to maintain the mechanical properties of aluminum alloys at temperatures of up to 300°C.

The following subsections will address the criteria for selecting suitable transition elements, and the effects of zirconium and nickel additions on the mechanical properties at elevated temperatures, since these two elements, in addition to manganese, appear to be promising additions in this respect. In a previous study carried out in the same research group,[11] it was determined that the addition of Zr is important for maintaining the mechanical properties at elevated temperatures through the formation of Zr-trialuminides. Based on these findings, Zr addition was considered as an essential addition when forming the base or reference alloy (Al-Si-Cu-Mg-Zr) in this study. As the addition of other transition elements was shown to be beneficial from the point of view of enhancing the precipitation strengthening of trialuminides,[144-146] Ni and Mn were also added to the Zr-containing Al-Si-Cu-Mg in this study in an attempt to enhance the room- and elevated-temperature mechanical properties of such alloys used in automotive engine components.

2.6.1 SELECTION CRITERIA OF TRANSITION ELEMENTS

Knipling *et al.*[147] have introduced four criteria which have to be satisfied in the selection process of alloying elements in order to obtain castable, precipitation-strengthened aluminum alloys with both high stability and strength at elevated temperatures. These criteria state that the alloying element must:

i. produce a suitable strengthening phase (precipitates);
ii. have a low solid-solubility in aluminum at the aging temperatures involved;
iii. have a low diffusivity in aluminum; and
iv. preserve the alloy capability to be conventionally solidified.

As mentioned previously, the strengthening effect is increased with increase in the volume fraction of the precipitates and decrease in their size (Orowan theory). In order to satisfy criterion (i), due to the intrinsically low volume fraction of precipitates in aluminum-based alloys, the size of the dispersed phase must be in the range of 10nm or less and maintain this small size throughout thermal exposure (i.e., the precipitates resist coarsening) during service life. The authors[147] investigated the formation of trialuminide compounds (Al_3M) in Al-based alloys, where the trialuminides exhibited a cubic $L1_2$ crystal structure. These compounds are chemically and structurally analogous to Ni_3Al compounds in Ni-based alloys. Al_3M trialuminide compounds have attractive characteristics that include low density (they are nominally 75% Al on an atomic basis), high specific strength, good thermal stability (they have generally very high melting points), and excellent oxidation resistance (again, mostly due to the high Al content). Besides the chemical composition of the trialuminide precipitates, it is desirable that these precipitates have the cubic $L1_2$ structure in order to form a coherent interface with the Al matrix due to the similarity in crystal structure, with a low lattice parameter mismatch between the matrix and the precipitates. The existence of a coherent interface, in turn, maximizes the strengthening effectiveness of the dispersed phase. Furthermore, coherency minimizes the surface energy per unit area of the hetero-phase interface, conferring stability at elevated temperatures through the reduction in the precipitate coarsening driving force.

In order to maximize the strengthening effect, it is important to increase the volume fraction of the precipitates and to prevent their dissolution. This target can be achieved by using alloying elements that have a large maximum solubility, so that when the alloy is solutionized it is easy to obtain an alloy with a single α-Al phase prior to precipitation

hardening. On the other hand, a low equilibrium solid solubility at the anticipated service temperature is vital to obstruct diffusion-controlled coarsening and prevent the dissolution of the dispersed phase.

The third criterion states the necessity of limited diffusivity of the solutes in the Al-matrix, which will also help in preventing the precipitates from coarsening, so that the precipitates will continue to act as barriers to dislocation movement at elevated temperatures.

The last criterion or requirement of the alloy to be conventionally solidified is relevant when considering cost-effectiveness at the industrial production level. It is important to have a solid-liquid partition coefficient (k_o) close to unity in order to minimize solute segregation and allow conventional solidification. In eutectic systems, the first solid to form is the solute-poor α-Al; whereas for peritectic systems the first solid to form is the solute-rich primary phase (Al_3M). Accordingly, in the peritectic system, there is a strong tendency to lose a considerable amount of the solute in order to form the primary phase besides the significant increase in the melting temperature. In order to minimize these harmful effects, a shallow Al_3M liquidus boundary is desirable in the peritectic system, for decreasing the casting temperature and suppressing the precipitation of the Al_3M primary phase during solidification.

Having defined and discussed the selection criteria, it is important now to find the elements which satisfy these criteria. Referring to criterion (i), there are a number of elements that can form trialuminides (Al_3M); however the highly symmetric $L1_2$ cubic structure and the related tetragonal $D0_{22}$ and $D0_{23}$ structures are commonly attainable

through the addition of transition and rare earth elements. The $L1_2$, $D0_{22}$, and $D0_{23}$ structures are schematically illustrated in Figure 2.23. The low-symmetry tetragonal structures ($D0_{22}$ and $D0_{23}$) result in a very brittle precipitates; however the $L1_2$ structured trialuminides are very desirable as they are commensurate with the Al matrix. There are thirty-one elements that can form trialuminides when added to aluminum; however only six elements – Sc, Er, Tm, Yb, Lu, U and Np can form thermodynamically stable trialuminide precipitates with an $L1_2$ structure. The cost of these six elements is relatively high for them to be used on an industrial scale. On the other hand, the addition of elements from Group IV such as Ti, Zr, and Hf will form metastable $L1_2$ structures with a very slight degree of metastability; that means that hundreds of hours at elevated temperatures are required before these trialuminides attain the equilibrium tetragonal structure.

As mentioned above, there are multiple elements that can form stable or slightly metastable $L1_2$-structured trialuminides in equilibrium with the α-Al solid solution. These elements comprise the first transition element in Group III which is scandium (Sc), the three elements of Group IV - Ti, Zr, and Hf, and the four lanthanide elements Er, Tm, Yb, and Lu. Among these elements Sc and Zr are the best for multiple reasons; however, the high cost of Sc restricts its use, and the only preferable element left to consider is Zr.

Based on the above arguments, Zr was added to the 354 alloy used in this study to form the base or reference alloy, and other elements (Ni and Mn) were subsequently added individually or in combination to study their mutual effect with Zr on the mechanical properties of 354 alloy at room and elevated temperatures. The reported effects of these

alloying elements on the room- and elevated-temperature mechanical properties of Al alloys are reviewed hereafter.

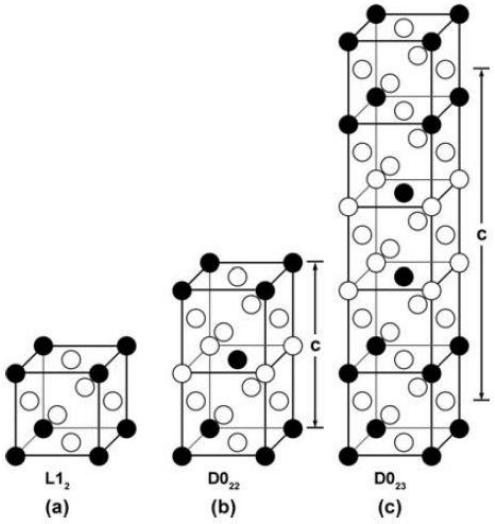

Figure 2.23 The possible trialuminide structures (a) $L1_2$, (b) $D0_{22}$, and (c) $D0_{23}$.[147]

2.6.2 ZIRCONIUM

Zirconium is a transition element that is commonly used in a wide range of aluminum alloys to control the microstructure and hence influence the mechanical properties.[24 86 148 149] Zirconium is widely employed due to its reasonable price which also facilitates its use on an industrial scale, in contrast to other expensive transition elements such as Sc. Zirconium is commonly added to Al alloys in order to regulate the grain structure and inhibit recrystallization during heat treatment processes; these effects result from the presence of fine coherent dispersoids which obstruct dislocations motion.[142] As mentioned earlier, in order to enhance the elevated temperature mechanical properties of aluminum alloys, it is necessary to have a microstructure containing thermally stable and coarsening-resistant precipitates/particles. These precipitates resist coarsening by lowering

the interface energy with the matrix, and if their diffusivity and solubility in the matrix are minimal.[147 150]

Zirconium has one of the lowest diffusion rates in aluminum in comparison to other transition elements.[151] Addition of Zr in the range of 0.1 to 0.3 wt.% to aluminium-based alloys leads to the formation of fine metastable $L1_2$-structured Al_3Zr precipitates which have a very low lattice parameter mismatch with the Al matrix.[86 152, 153] These Al_3Zr precipitates are noticeably stable and resist coarsening during heating, as the addition of Zr satisfies the four criteria proposed by Knipling *et al.*[147] As a result, these precipitates effectively inhibit recovery and recrystallization during heat treatment through their resistance to dislocation motion, so that their presence increases the strength and hardness of the associated alloys.[154 155]

The Al-rich portion of the Al-Zr phase diagram is shown in Figure 2.24. The phase diagram shows a peritectic point at about 660°C. As mentioned previously, in the context of peritectic systems, the Al_3Zr trialuminide phase is the first solid to form during solidification when the Zr content exceeds 0.1 wt.%. As can be seen from the phase diagram (Figure 2.24), the maximum equilibrium solubility of Zr in Al at the peritectic isotherm is 0.083 at.% (i.e. ~ 0.3 wt.%).[15, 147, 156] Moreover, it is apparent that precipitation of the dispersoids is thermodynamically possible if the Zr content exceeds 0.08 at.% at a temperature of 500°C. Precipitation will thus occur at the dendrite cores with Zr concentrations of more than 0.15 at.% and will continue until the concentration is reduced to 0.08 at.%, which is the minimum required limit for precipitation at or near 500°C.

Thus in order to increase the volume fraction of Al_3Zr precipitates and based on the phase diagram of Al-Zr, the concentration of Zr in the alloys investigated in this study was kept at around 0.3 wt.%.

The effectiveness of Al_3Zr precipitates is dependent on their size, spacing, and distribution in the matrix. These precipitates are heterogeneously distributed in the matrix, resulting from the dendritic micro-segregation of the Zr atoms during the solidification process. The uneven distribution of the precipitates results in the formation of interdendritic precipitate-free zones; these zones degrade the mechanical properties at both ambient and elevated temperatures.[17]

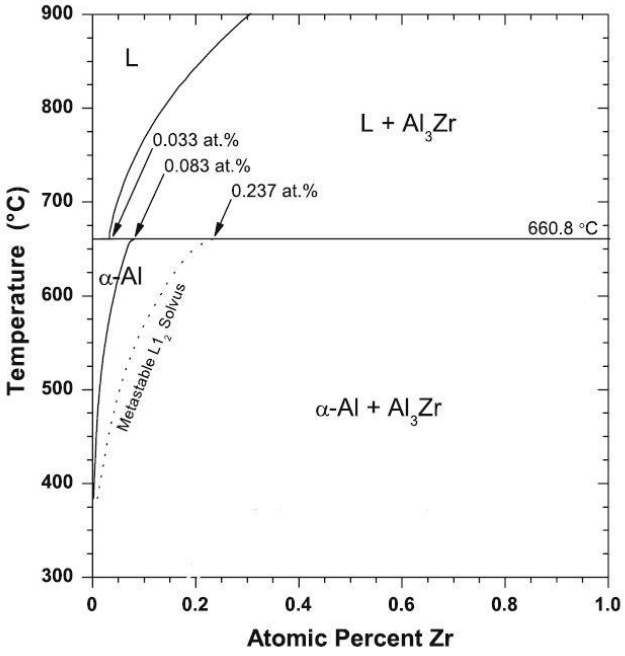

Figure 2.24 Equilibrium Al-rich Al-Zr binary phase diagram.[156]

Knipling *et al.*[157] studied two binary Al-Zr alloys namely Al-0.1 at.% Zr (corresponding to an Al-0.34 wt.% Zr alloy), and an Al-0.2 at.% Zr (corresponding to an Al-0.67 wt.% Zr alloy). These alloys exhibited precipitate-rich and precipitate-free regions as seen in Figure 2.25. At the centre of the dendrites where the solute is supersaturated, small Al_3Zr precipitates exist (<R> = 6.7 ± 1.7 nm), with the metastable cubic $L1_2$ structure coherent with α-Al, and homogeneously distributed in high number densities. In positions away from the dendrite centres, where the supersaturation decreases, the precipitates showed larger sizes, with smaller number density. Moreover, insufficient solute in the interdendritic regions affected homogeneous nucleation, so that these areas appeared mostly as precipitate-free regions. However, small (R <10 nm) spheroidal $L1_2$ precipitates within the dendritic cells constituted the most prevalent precipitate morphology in the examined Al-Zr alloys.[157] Obviously, it is the small, coherent, high number density Al_3Zr ($L1_2$) precipitates within the dendrites that are responsible for the marked precipitation hardening response.[156, 157]

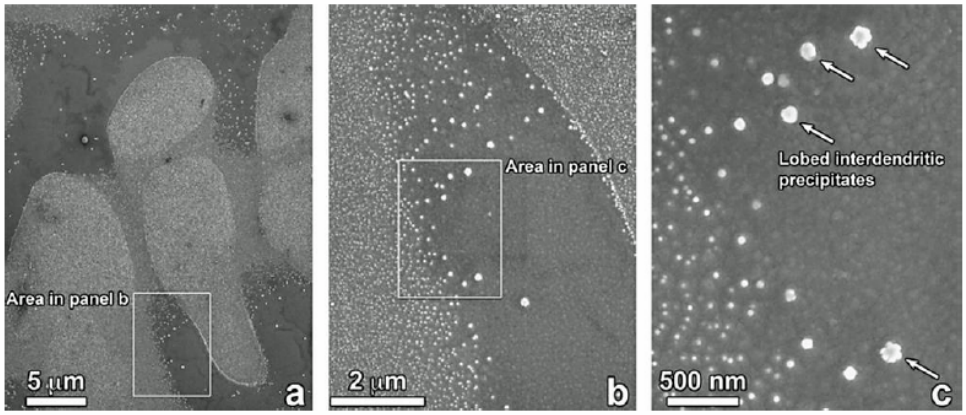

Figure 2.25 SEM micrographs of Al3Zr ($L1_2$) precipitates in Al-0.2Zr at.% aged at 425°C for 400h, showing an inhomogeneous distribution of Al_3Zr precipitates within the dendrites.[157]

Sepehrband *et al.*[150] and Mahmudi *et al.*[151] reported that the hardness of 319 cast alloys was enhanced with a minor addition of Zr in both as-solutionized and aged conditions provided that the alloy was solutionized for sufficiently long times. This enhancement in hardness was attributed to the formation of Al_3Zr precipitates; moreover, the enhancement in hardness was associated with a remarkable increase in wear resistance. It was also found that the alloy continued to exhibit the same peak hardness attained after aging, a clear evidence of the resistance of these precipitates to coarsening.[150, 151]

Yin *et al.*[143] studied the influence of adding both 0.1%Zr and 0.2%Sc to Al-5%Mg alloy. The authors found that the strength exceptionally increased by 150 MPa and the ductility remained almost unchanged at high values. These enhancements were attributed to multiple effects such as: grain-refinement strengthening, the formation of strengthening precipitates $Al_3(Zr, Sc)$, and substructure strengthening.

Jia *et al.*[158] and Forbored *et al.*[159] reported that the Al_3Zr metastable coherent precipitates strengthen the Al alloy through a pinning effect that prevents movement of the dislocations. These tiny precipitates also pinned the grain boundaries, thus slowing down recrystallization. The authors also reported that Al_3Zr precipitates are stable and resist coarsening at elevated temperatures due to their limited solubility and diffusivity in the Al-matrix.

2.6.3 NICKEL

Nickel is also among the transition elements, the Ni-based super-alloys are used only for important high temperature applications due to their high cost. Ni-based super-alloys can maintain strength of 150MPa at service temperature of 0.75Tm, where Tm is the absolute melting temperature of the alloy.[17] Aluminum is added to nickel to form a solid solution; due to the larger atomic diameter of aluminum, there will be a lattice expansion associated with its addition to Ni, which will produce the hardening effect in Ni-based alloys. Aluminum addition leads to the formation of γ' (Ni_3Al) intermetallic phase which provides a remarkable strengthening effect to the Ni-based alloys. This phase has a face-centered cubic (fcc) structure similar to the γ-matrix. Moreover, the Ni_3Al phase has a very slight mismatch in lattice constant of about 1% with the matrix; so that it will be coherently dispersed in the matrix, resulting in more effective strengthening.[20] It is expected that by increasing the volume fraction of the Ni_3Al precipitates, the ambient and elevated temperature strengths will increase as well.

Similar to the outstanding behaviour of Ni-based alloys at high homologous temperature owing to the existence of the Ni_3Al phase, researchers anticipated that a similar trend in behaviour–could be achieved in Al-based alloys by developing the Al_3Ni phase which is analogous to the Ni_3Al (γ') phase. It was expected that, with the existence of Al_3Ni phase in Al-based alloys, these alloys could behave satisfactorily at high temperatures, possibly up to 400°C, provided the Al_3Ni phase would be thermodynamically stable at the intended service temperature.[17] The strengthening effect of nickel addition to

wrought aluminum alloys has already been reported, and the mutual addition of Ni and Cu is often used to enhance the high temperature performance of Al-based alloys.[160]

The maximum solid solubility of Ni in aluminum at room temperature is 0.04 wt.%; if the nickel content is increased further, it will appear in the form of insoluble intermetallic compounds resulting from its interaction with iron and copper. As the nickel content increases up to 2 wt.% in aluminum alloys, the strength increases and the ductility decreases. Nickel is added usually to Al-Cu and Al-Si alloys in order to enhance both hardness and strength of these alloys at elevated temperatures.[161] The binary Al-Ni phase diagram is shown in Figure 2.26.

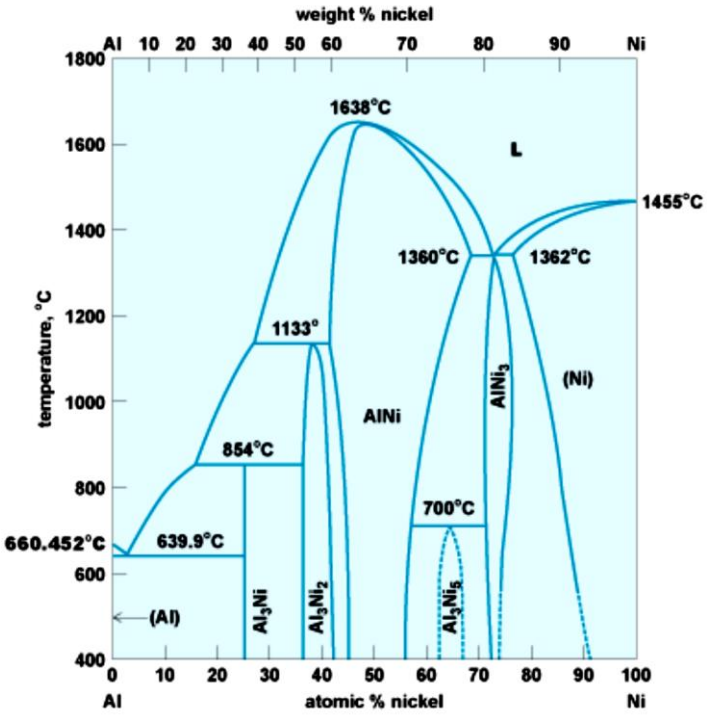

Figure 2.26 Binary Al-Ni phase diagram.[31]

Srinivasan *et al.*[142] and Sepehrband *et al.*[150] studied the influence of Ni content on the mechanical behaviour of Al-Si alloys. The results showed that up to 2% Ni content, there is no noticeable enhancement in the mechanical properties. Nickel exists in aluminum-based alloys as an acicular dispersion of Al_3Ni; the amount of this phase increases with increasing nickel content. In order to increase the strengthening effect, the Al_3Ni phase should either be finer, or have a much higher volume fraction, or satisfy the two conditions simultaneously. However, continuously increasing the nickel content in Al-based alloys in order to attain higher strength and hardness is not practical, since this will increase the cost of the alloy. Therefore, it becomes very important to achieve an optimal nickel content in aluminum alloys so that the mechanical properties at ambient and elevated temperatures can be enhanced without excessively increasing the cost.[31]

Asghar *et al.*[16] stated that addition of Ni in the range of 0.6-1.9 wt.% has a slight advantageous effect on the elevated-temperature strength of cast aluminum alloys. Moreover, the addition of 1.2 wt.% Ni with 0.7 wt.% Fe to Al-Si alloy formed ~ 8 vol.% of both Ni and Fe aluminides.[162] It was reported that Ni and Fe aluminides have a higher strength and elastic modulus than that of α-Al, especially at elevated temperatures.[163]

Hernandez-Sandoval[12] carried out a detailed study on improving the elevated-temperature performance of the A354 alloy through additions of Ni and/or Zr. The results showed that there is no significant difference in the UTS and YS values of heat-treated alloys at different testing temperatures. The same finding was reported for A356 alloy with additions of 600ppm Ni and 1000ppm V.[164] Hernandez-Sandoval[12]observed, however, that at 300°C testing temperature, there is a slight enhancement in the strength values (UTS and

YS) associated with the addition of Ni and Zr in the heat-treated condition compared to the base alloy. Furthermore the combined addition of 0.2 wt.% Ni and 0.2 wt.% Zr showed an improvement in UTS in the as-cast condition compared to the base alloy; the author attributed this observation to the formation of Ni- and Zr-rich intermetallic compounds that would obstruct further development of cracks.[12, 165]

The present study was planned as the next step in a line of studies aimed at exploring the development of Al-Si-Cu-Mg alloys for high temperature applications. In this sense, it is considered a continuation of the work done by Garza-Elizondo[11] from the same research group. While Garza-Elizondo[11] studied the effect of similar additions as those used in the present study including Zr, Ni and Mn, however, he characterized these alloys solely at ambient temperature with the objective of exploring their tensile properties and optimizing the heat treatment process. He concluded that the combined additions of Zr+ Ni, Zr+ Mn, or Zr+ Ni+ Mn resulted in improved ambient-temperature tensile properties.

The effect of Mn addition to cast aluminum alloys was described previously in section 2.3.1.1.2 and therefore is not discussed here. The following sections will discuss the effect of melt treatment on the microstructure and mechanical properties of Al alloys.

2.7 THERMAL EXPOSURE

Elevated-temperature exposure of Al alloys with or without applied stress may result in certain changes in the alloy microstructure, such as nucleation and growth of new phases, formation of subgrains, variation in dislocation density and distribution, and initiation, growth, and coalescence of microcracks.[166] Besides the aforementioned microstructural changes, the phenomenon of precipitate coarsening associated with the development of precipitate free zones is considered as being the dominant factor responsible for degrading the alloy strength. It was shown that overaging together with the presence of applied stresses will accelerate the coarsening rate,[167] these parameters representing the real service conditions in automotive engines.

With the increasing use of Al-Si cast alloys in the automotive industry, especially in key engine components, it is expected that these alloys will be exposed to high temperatures for a long time during their service life. Such prolonged exposure to elevated temperatures will definitely introduce changes in the microstructure which, in turn, will affect the mechanical properties of the alloys used. Alloy A356 which is widely used in the peak-aged condition (T6 heat-treated) for engine components was found to have some limitations when the components were used for long times at high temperatures (~200°C and higher). These limitations were related to the rapid coarsening of the precipitates which resulted in reducing the alloy strength.[168, 169]

In recent times, Al-Si-Cu-Mg type alloys are being increasingly employed in automotive engine applications as a suitable solution for the limitations imposed by the use of A356/A357 alloys at elevated temperatures over long periods of time. In this context,

research efforts are being continually made for improving the high-temperature performance of Al-Si-Cu-Mg alloys by introducing elements which may form more stable precipitates and intermetallic compounds that will resist coarsening when being exposed to high temperatures.[165, 169]

Several of these research studies have focused on investigating the effect of prolonged high-temperature exposure on the mechanical properties of Al-Si cast alloys. The major findings in this area are summarized below.

Ceschini *et al.*[169] compared the capabilities of T6-treated A356 and C355 alloys after being exposed to high temperature (210°C) for 41 hours. The results showed the superiority of C355 alloy (containing Cu) over the A356 alloy (Cu-free) in the tensile properties in the overaged condition. However, the variation in the tensile properties of the two alloys in the T6 condition was not that high.

Feng *et al.*[170] investigated the microstructure evolution and the mechanical properties of Al-Si-Cu-Mg-Ni alloy following to its exposure to 350°C for times of up to 1000 h. The results showed that in the first 100 h, the ultimate tensile strength at both room and elevated temperature decreased remarkably, as well as the Brinell hardness. After the first 100 h stabilization time and up to 1000 h, the deterioration in the mechanical properties was not significant. The authors also found that the eutectic silicon particles grew continuously with the increase in exposure time as well as the amount of Q phase.

Jabra *et al.*[171] examined six aluminum alloys which were exposed to different high temperatures (80°, 230°, and 290°C) for different holding times (0.1, 0.5, 2, 10, 100, and 1000 h). They found that the strength of the alloys deteriorated considerably with higher temperatures and longer exposure times, vice-versa their ductility.

In a TEM study, Kai *et al.*[172] found that the strength of 7050 Al alloy was reduced when the alloy was exposed to elevated temperature for longer periods; the amount of reduction in strength is proportional to the temperature. The thermal exposure was done at different temperatures (100°, 125°, and 150°C) for 500 h. The authors explained this reduction in strength as a result of the coarsening behavior of both GP zones and η' precipitates, and also due to the increasing width of the precipitate free zones (PFZ).

2.8 CONCEPT OF QUALITY INDICES AND CHARTS

The concept of the quality of aluminum casting alloys was introduced to simplify the presentation of the tensile properties of cast Al alloys so as to better understand the influence of the metallurgical variables involved on these properties. Optimum alloy quality is achieved by a suitable compromise between multiple factors, such as alloy chemical composition, solidification rate, heat treatment, and microstructural constituents, which lead to the best combination between the alloy performance and cost efficiency. The concept of the quality index (Q) was originally developed in 1980 by Drouzy *et al.*,[60] followed by further improvements proposed by researchers such as Cáceres[61] and others.[173-176] Quality charts constructed from Q values and the tensile properties of specific alloys are useful in selecting the optimum conditions which will provide superior tensile properties and optimum quality.

2.8.1 QUALITY INDEX (Q) PROPOSED BY DROUZY *ET AL.*

Drouzy *et al.*[60] proposed a new concept that of the quality index (Q), to express the performance of cast Al-Si-Mg alloys, where they related the quality index of these alloys to their mechanical properties, namely, the ultimate tensile strength and percentage elongation to fracture. The quality index was empirically developed using the following equation:

$$Q = S_{UTS} + d\log(e_f) \quad \textbf{(2.9)}$$

where Q is the quality index (MPa); S_{UTS} refers to the ultimate tensile strength (MPa), e_f refers to the percentage elongation to fracture, and d is a material constant equal to 150 MPa for Al-7Si-Mg alloys.

For the same alloys, the probable yield strength ($S_{p(ys)}$) was identified by the following formula:

$$S_{p(ys)} = aS_{UTS} - b\log(e_f) + \mathrm{C} \quad \textbf{(2.10)}$$

where coefficients a, b, and c were quantified as 1, 60 MPa, and -13 MPa respectively, for Al-7Si-Mg alloy.

Figure 2.27 presents the quality chart proposed by Drouzy *et al.*[60] In this chart, the lines labeled “Q” are defined as *iso-Q* lines that are generated using Equation 2.9; whereas the lines labeled “YS” are named as *iso-YS* lines, and they represent the probable yield strength values calculated using Equation 2.10.

As mentioned earlier, quality charts are mainly used to facilitate the process of evaluating, selecting, and possibly predicting the best metallurgical conditions that may be applied to cast Al-alloys to achieve the optimum compromise between the mechanical properties and quality of the alloy of interest. The quality index value (Q) is intrinsically related to the quality of the castings which is susceptible to improvement through adequate control of impurity elements, casting defects, modification, solution heat treatment and solidification conditions. The probable yield strength (YS) depends mainly on the presence of hardening elements such as Mg and Cu, and also on the age-hardening conditions applied to the castings.[60, 61, 82]

The proper selection of the metallurgical parameters may increase both the quality index values as well as the probable yield strength in the directions specified in Figure 2.27. The quality chart proposed by Drouzy *et al.*[60] is very useful in giving sufficient information for each point located on the chart. As is clear from Figure 2.27, each point on the chart defines the ultimate tensile strength (S_{UTS}), percentage elongation to fracture (e_f), probable yield strength (YS), and the quality index value (Q) at that location.

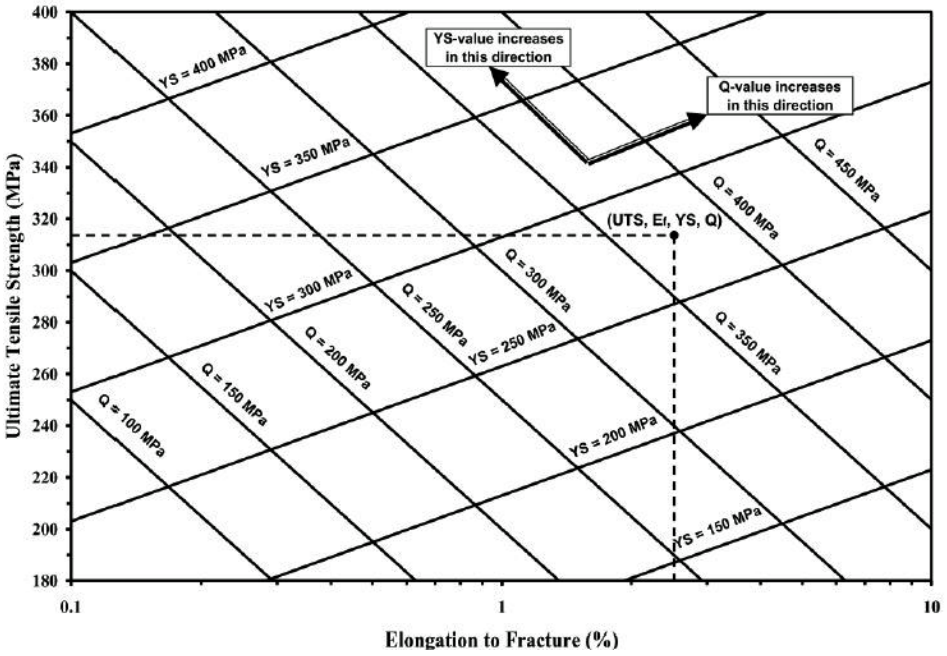

Figure 2.27 Example of the quality chart proposed by Drouzy *et al.*[60] with iso-Q and iso-YS lines generated using Equations 2.9 and 2.10.

It was reported that for Al-Si-Mg alloys with a definite Mg content, when plotting the ultimate tensile strength of samples subjected to different aging conditions against the percentage elongation to fracture (i.e., as in the quality chart proposed by Drouzy *et al.*[60]), the experimental points tend to follow a single iso-Q line (i.e. the quality index value remains unchanged with varying aging conditions); this finding has been reported in the case of underaged and for moderately over-aged material.[60, 177, 178]

Although the concept of the quality index was originally developed for Al-7Si-Mg alloys, it has occasionally been applied to other alloy systems as well.[62, 178-181]

However, upon applying this concept to the Al-Cu-Mg-Ag alloy system,[182] it was observed that the experimental points did not follow a linear behavior as reported for the Al-Si-Mg alloys but displayed a curvilinear contour instead, as shown in Figure 2.28 for

alloy 201. Moreover, the parameters previously defined in Equations 2.9 and 2.10 showed numerical values that varied according to the aging condition.

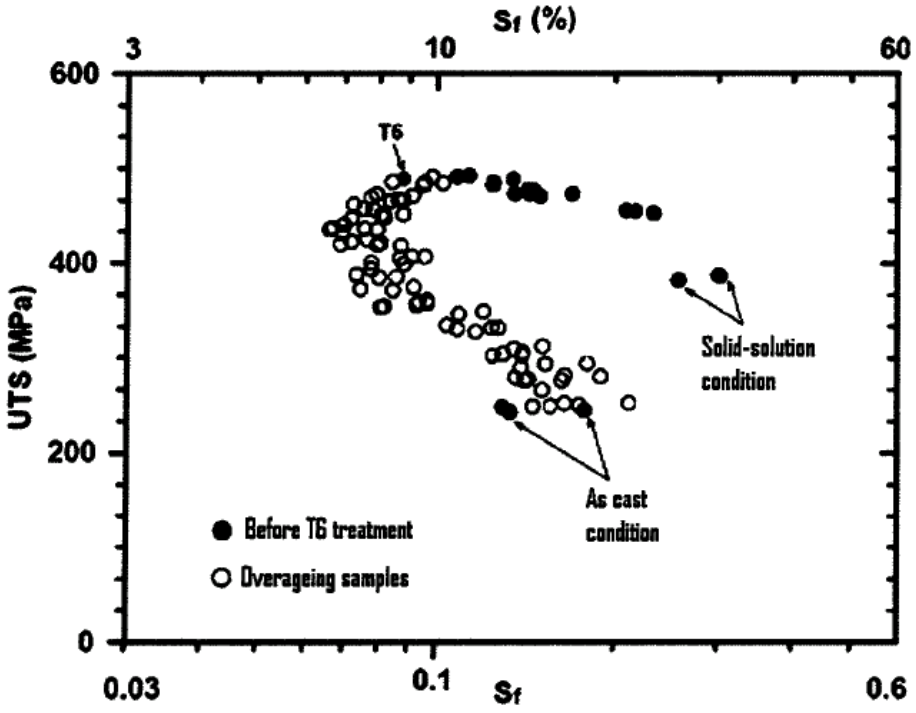

Figure 2.28 Effects of overaging in tensile properties of a 201 alloy.[180]

The curvilinear contour may also appear in the quality charts proposed by Drouzy *et al.* due to variation in the aging conditions,[179, 183] and is mainly observed in Cu-containing Al alloys, which entails the fact that in order to broaden the quality index concept to include systems other than the Al-Si-Mg cast alloys, it will be important to determine the behavior of the strength-ductility relationship as the material undergoes the aging process. Cáceres[62] developed an experimental model that provided a simple physical meaning to the quality index of an alloy.

2.8.2 QUALITY INDEX (Q_C) PROPOSED BY CÁCERES

Following the empirically developed concept of quality index proposed by Drouzy *et al.*[60, 61] Cáceres developed a theoretical model which was capable of describing the physical significance of the quality index.[61, 183, 184] He developed his model on the assumption that the material undergoes a plastic deformation that may be described by the Holloman equation:

$$\sigma = K\varepsilon^n \quad \textbf{(2.11)}$$

where σ is the true stress (MPa), ε is the true plastic strain, n is the strain-hardening exponent, and K is the strength coefficient (MPa).

The strain-hardening exponent (*n)* can be correlated to the strain-hardening rate through the fact that n can be defined as the slope of the plastic deformation line represented on a log-log scale, as shown in Figure 2.29.

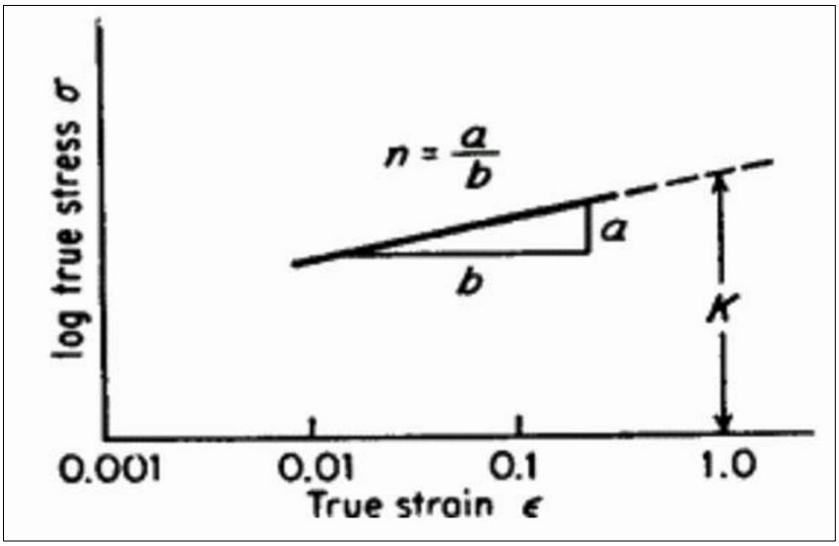

Figure 2.29 A log-log plot of true stress versus true strain for calculating n and K values in Equation 2.11.[185, 186]

$$n = \frac{d(\log\sigma)}{dlog(\varepsilon)} = \frac{d(\ln\sigma)}{d(\ln\varepsilon)} = \frac{\varepsilon}{\sigma} \times \frac{d\sigma}{d\varepsilon} \quad \text{simplified to } \frac{d\sigma}{d\varepsilon} = n\frac{\sigma}{\varepsilon} \qquad \textbf{(2.12)}$$

The tensile samples may exhibit necking during tensile testing depending on their ductility. The necking occurs at the point of stress instability when the true stress value equals the rate of strain-hardening, as described schematically in Figure 2.30. In this case, Equation 2.12 would give

$$\text{At necking, as } \frac{d\sigma}{d\varepsilon} = \sigma, \text{ by substituting into Eq. 2.12, } n = \varepsilon_u \qquad \textbf{(2.13)}$$

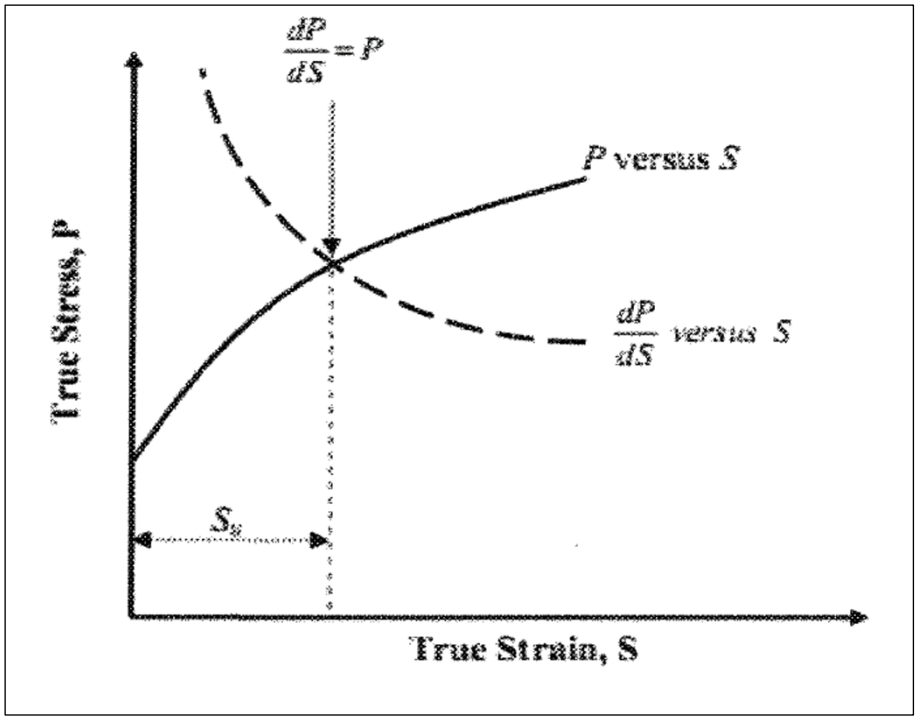

Figure 2.30 Determining the beginning of necking based on the true-stress/true-strain curve during tensile testing.[185, 186]

This means that the necking will start when the strain-hardening exponent is equal to the true uniform plastic strain. In other words, the true uniform plastic strain represents the critical strain at which the necking starts.[185, 186] Thus samples which exhibit necking will have maximum quality index values, when $\varepsilon_f = \varepsilon_u = n$ (i.e. $\varepsilon_f/n = 1$); where ε_f is the strain at fracture, and ε_u is the critical strain at the start of necking. However, lower values of quality index may be attained when $\varepsilon_f < \varepsilon_u$ or $\varepsilon_f < n$.

Cáceres proposed the term relative quality index (q) based on the assumption that necking will start when $e_u = \varepsilon_u = n$, where e_u represents the engineering strain at the onset of necking; this assumption is based on the fact that Cáceres neglected the engineering elastic strain which makes sense in the case of cast alloys with limited ductility. Thus, based on the aforementioned assumptions,

i. The maximum relative quality index value can be obtained when $e_f/n \approx 1$

ii. The minimum relative quality index value can be obtained when $e_f \approx 0$, which means that the sample fractured at the yield point.

The relative quality index values between these maximum and minimum values may be represented by iso-lines describing the ratio between the percent engineering strain to fracture, e_f, and the critical engineering strain, e_u (or strain hardening exponent as they are equal at necking). So that the relative quality index proposed by Cáceres may be expressed in the form:[62, 63, 178, 183, 184, 187-191]

$$q = \frac{e_f}{e_u} \cong \frac{e_f}{n} \quad \textbf{(2)}$$

Recalling that Cáceres assumed that the true strain is equal to the engineering strain, i.e. $e = \varepsilon$, and by recalling the relationships between true stress and strain and engineering stress and strain where true stress is equal to $\sigma = S(1+e)$ and the true strain is equal to $\varepsilon = \ln(1+e)$ (S and e being the engineering stress and strain, respectively), we can substitute these expressions into Equation 2.11 to arrive at the following expression for S:

$$S = K[\ln(1+e)]^n \, exp^{-\ln(1+e)} \cong Ke^n \, exp^{-e} \quad \textbf{(2.15)}$$

By substituting the strain-hardening (n) from Equation 2.14 into Equation 2.15, the relative quality index can be expressed in terms of engineering stress and strain as follows:

$$S = K \, e^{\frac{e}{q}} \, exp^{-e} \quad \textbf{(2.16)}$$

Equations 2.15 and 2.16 are used to generate the iso-flow lines and iso-q lines, respectively, in the quality chart proposed by Cáceres as shown in Figure 2.31. At the upper right corner of the chart, there is the maximum iso-q line which represents the maximum quality achievable, while the other iso-q lines represent lower quality values.

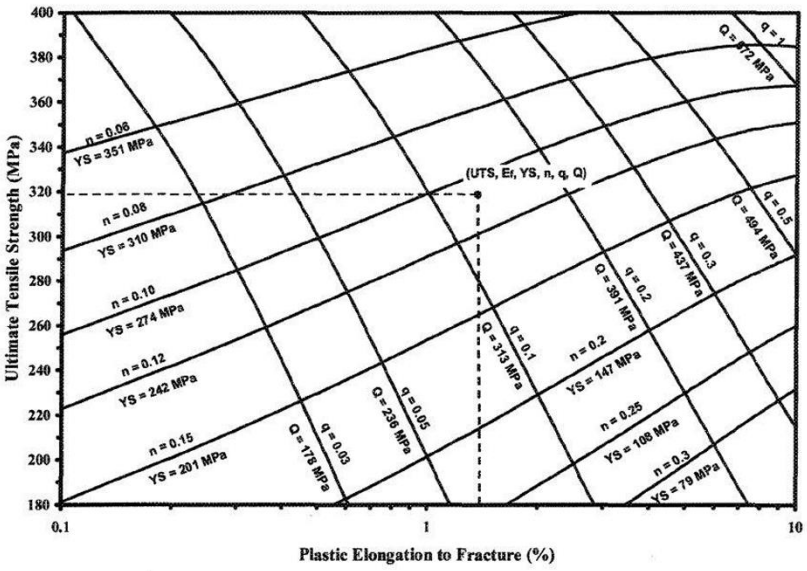

Figure 2.31 Example of the quality chart proposed by Cáceres illustrating iso-flow and iso-q lines generated using Equations 2.15 and 2.16, respectively, with K= 511 MPa.[173]

Though Equation 2.16 is used to generate the iso-q lines, it does not calculate the Q-values proposed by Drouzy *et al.* in Equation 2.9. Moreover, by consulting Figure 2.32 which is a combination of both the Drouzy *et al.* and Cáceres quality charts, it can be observed that the iso-q lines are quasi-parallel to the empirical iso-Q lines. This relative relationship between iso-q lines and iso-Q lines has a physical meaning for the values of the quality index: it means that it is possible to describe the Q-value in terms of the relative quality index or relative ductility.[62, 178, 183, 184, 188] The same observation may be noted for the iso-YS and iso-flow lines which are virtually parallel, indicating that it is possible to represent the iso-YS lines using the iso-flow lines.

Based on the aforementioned observations regarding the iso-Q and iso-q lines which are generated using Equations 2.9 and 2.16, respectively, it can be easily concluded that the slope of the iso-q lines is roughly equivalent to the parameter d which is the slope of the iso-Q lines generated using Equation 2.9. Thus in order to correlate the parameter d in Equation 2.9 to K and q, we differentiate Equation 2.16 with respect to the engineering strain at q = 1, taking into account the semi-log scale in Figure 2.32. This leads to the following equation:

$$d = -\frac{d(S)}{d(e)} \cong 0.4K \ \ at\ (q = 1) \qquad \textbf{(2.17)}$$

By combining Equations 2.9, 2.14, 2.15 and 2.17, the quality index Q can be calculated using the relative quality index (q), strain-hardening exponent (n), and the strength coefficient (K) through the following equation:

$$Q_c = K[(qn)^n\ exp^{-qn} + 0.4\log(100qn)] \qquad \textbf{(2.18)}$$

Equation 2.18 calculates the Q-values corresponding to each relative quality index value q, such that each iso-q line represents two values (Q and q) which identify the material quality as shown in Figure 2.31.

In order to calculate the quality index from the tensile test results knowing only the value of K, we may combine Equations 2.9 and 2.16 considering that Equation 2.16 is a valid equation for any value of q; this will yield the following equation:[192]

$$\mathrm{Q_c} = \mathrm{S_{UTS}} + 0.4\mathrm{K}\log(\mathrm{e_f}) \qquad \textbf{(2.19)}$$

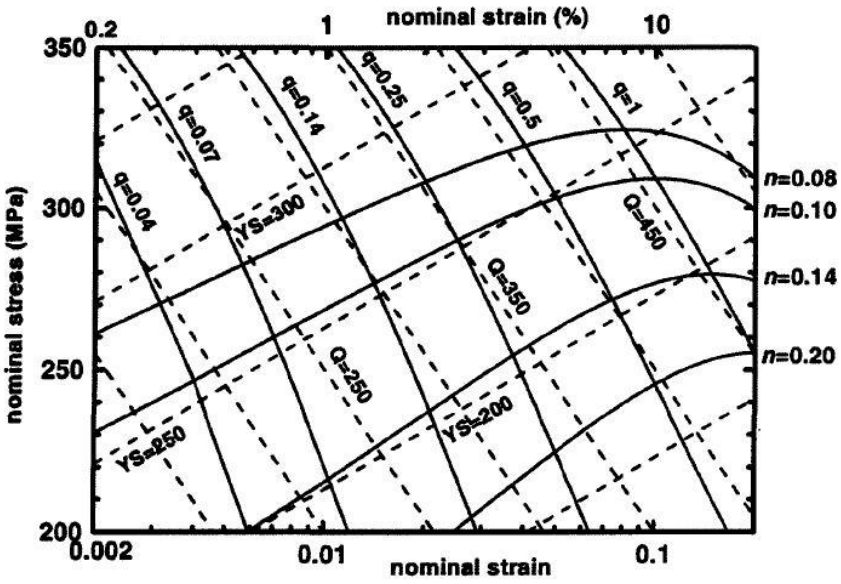

Figure 2.32 Two models of quality charts for the A356 alloy; the dashed lines are iso-Q and iso-YS lines calculated from Equations 2.9 and 2.10, respectively. The solid lines are iso-flow lines and iso-q lines calculated using Equations 2.15 and 2.16, respectively, with K = 430 MPa.[62, 178, 183, 184, 188]

The quality chart proposed by Cáceres (Figure 2.31) shows many significant properties for each experimental point located in the chart; namely, the ultimate tensile strength (UTS), the plastic elongation to fracture (e_f), the probable yield strength (YS), the relative quality index value (q), and the quality index value (Q_c). Moreover, the theoretical model developed by Cáceres enables us to design and develop a quality chart for any alloy (regardless its chemical composition), and use this chart to compare different alloys in one single plot, such that it becomes possible to define the variations in the mechanical properties which would result from variations in the chemical composition, microstructure, and heat treatment conditions.[36, 58, 180]

Thus, the concept of quality index and quality charts is a vital tool for evaluating the quality of cast aluminum alloys based on the mechanical properties of these alloys. Besides using quality charts to select the optimum alloy/conditions vis-à-vis the application, quality charts also show the precise path to be followed in order to improve the quality of the material.[11] The use of this concept for supporting material selection was reported in several studies.[36, 60-63, 173-175, 180, 183, 184, 188-190, 193-197]

2.9 GEOMETRICAL DISCONTINUITIES (NOTCHES)

Typically any discontinuity in a component's shape or even nonuniformity in a material structure is referred to by the term "notch".[198] Notches may be alternatively referred to as "stress raisers"; due to their effect of developing high localized stresses that may results in crack initiation and subsequently premature failure; the presence of notches may also lead to reduction in the load-carrying capacity of the material and to its sudden failure. Generally, notches may be categorized into three types as follows:

i- *Metallurgical notches* that may exist on the microscopic scale due to metallurgical defects such as presence of inclusions, blowholes, quenching cracks, etc.

ii- *Mechanical notches* represented by geometrical discontinuities that may exist in the geometry of the component; this category of notches is commonly produced using machining processes; notches of this type may include holes, threads, grooves, keyways, etc.

iii- Se*rvice notches* which may be formed during the service life in response to the working environment; some examples are chemical or corrosion pits, fretting indentation, etc.

Typically, the design of automotive engine components is intricate and comprises many details including geometrical discontinuities in the form of shoulders, keyways, oil holes, passages for cooling fluids, etc. These geometrical details are commonly described as type (ii) or mechanical notches; it is important to mention that the term "notch" is more conveniently used for mechanical notches.[199] The mechanical loading of components with notches is totally different than the loading of smooth counterparts, so that studying the influence of notches on the mechanical performance and fracture behavior of aluminum cast alloys is a good approach to truly characterize alloys intended for manufacturing automotive engine components.

2.9.1 EFFECT OF NOTCHES

In mechanical structures, studying the effect of notches on the mechanical and fracture behavior is very valuable because the notches are considered the common positions at which most failures occurs.[200-202] The presence of notches limits the load-carrying capacity of the material due to the reduced cross-section area at the notch location. When a notched component is loaded, localized stress and strain concentrations are developed at the notch area.[199] The stresses at the root of the notches are noticeably increased exceeding the yield limit of the material even if a relatively low nominal stress was applied. The localized increase in the stress values at the root of the notches can be quantified using the term "theoretical stress concentration factor (K_t)", which is defined as the ratio between the peak

stress in a notched sample at the notch root to that attained in a corresponding unnotched sample. The peak stress in notched samples can be calculated mathematically, photoelastically, by X-ray measurements, or using finite-element methods; while the peak stresses in unnotched samples are determined from the experimental tensile test results.[198, 199, 203-205]

The tensile testing of notched cylindrical samples, in most cases, develops a triaxial state of tensile stresses which lead to reduced ductility.[206, 207] To simply describe how the triaxiality is being developed in a sample under testing, consider the notched cylindrical bar in Figure 2.33. Under tensile loading, the small volume of the highly stressed material near the notch root tends to deform plastically at a lower load than the material in the regions away from the notch due to the stress concentration effect. The bulk of the less stressed material away from the notch tip inhibits this plastic flow of the highly stressed material; so that the radial distortion or Poisson's effect which accompanies the axial strain is restricted, and a state of triaxial tensile stress is developed. This restriction to plastic flow in the triaxial state of stress contributes to reduced fracture ductility in notched specimens under tensile testing. There are other factors, however, that may affect the degree of triaxiality in the notch region such as the notch depth and notch root radius.

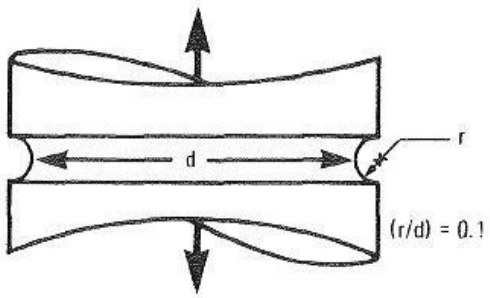

Figure 2.33 Cylindrical Notched bar.[206]

The tendency for the reduction in ductility in case of triaxial state of stress is commonly known as "notch sensitivity".[185, 206, 208] The condition of the material is examined to determine if it is notch sensitive (notch weakened) or not through the calculation of its notch sensitivity ratio (NSR). The notch sensitivity ratio is the ratio between the ultimate tensile strength in a notched sample at the notch root and the ultimate strength of an identical smooth sample. The ultimate tensile strength in a notched sample is calculated by dividing the ultimate load achieved during tensile testing by the cross-section area of the sample at the notch (reduced area). If the NSR is less than unity, the material is defined as notch sensitive (notch weakened); however if the NSR is greater than unity, the material is defined as notch strengthened. Generally, as the ductility increases, the tendency of the material to be notch strengthened increases as well, and vice-versa.

CHAPTER 3

METHODOLOGY AND EXPERIMENTAL PROCEDURES

CHAPTER 3

METHODOLOGY AND EXPERIMENTAL PROCEDURES

3.1 INTRODUCTION

This chapter outlines and discusses the methodology and experimental procedures followed in this research in order to achieve the overall objectives of the study. The undertaken experimental work was planned along three axes, each axis representing a certain work phase. Each work phase focused on a specific aspect, so that finally, an overall picture of the whole study could emerge.

Phase I concentrated on the effects of alloying elements, traditional heat treatments, and presence of notches and their geometry on the mechanical performance of the Zr-containing 354-type alloy at ambient and elevated temperatures. Phase II focused on the idea of exposing the already heat-treated materials (T5 and T6) to prolonged thermal exposure at elevated temperature for times up to 200 hours, followed by tensile testing at ambient and elevated temperatures and hardness testing in order to investigate the effect of Zr, Ni and Mn additions on preserving the mechanical performance following the prolonged thermal exposure at elevated temperature. Phase III aimed at investigating the eutectic silicon morphological changes concomitant to the extended solution treatments and their effect on the ambient- and elevated-temperature mechanical properties of the 354

alloys. Being a well-known alloy, the 356 Al-Si-Mg type alloy - in Sr-modified and non-modified forms – was also used in this work phase for comparison purposes.

The experimental procedures described in this chapter cover a list of the alloys investigated; their melting and casting procedures; the applied heat treatment processes involved in each work phase; machining of notches in the specimens used in Phase I; the mechanical testing techniques and equipment used for room and elevated tensile testing, hardness measurements and impact testing; and the various microstructural characterization and phase identification techniques used in this study, namely DSC analysis, optical microscopy (OM), scanning electron microscopy (SEM), field-emission scanning electron microscopy (FESEM) and associated EDS and WDS techniques, and transmission electron microscopy (TEM). All the experimental data was carefully collected using data acquisition systems connected to each of these instruments.

3.2 MATERIALS AND ALLOYS

The base alloy used in this work is 354-type alloy with ~0.3 wt.% Zr (coded M1S). This alloy was selected based on its improved room- and high-temperature tensile properties as reported in previous studies conducted by the same research group.[11, 13] Nickel (Ni) and manganese (Mn) were added to this base alloy in different weight percentages and combinations in order to explore the effect of the combined addition of Zr + Ni, Zr + Mn, and Zr + Ni+ Mn on the room- and elevated- temperature mechanical performance of the 354 alloy.

The following series of Sr-modified alloys, developed from the base 354 alloy, was also investigated in the current study, where the suffix "S" at the end of the alloy code refers to strontium modification:

1- Alloy M1S (Alloy 354 + 0.02 wt.% Sr + 0.3 wt.% Zr);
2- Alloy M2S (Alloy M1S + 2 wt.% Ni);
3- Alloy M3S (Alloy M1S + 0.75 wt.% Mn;
4- Alloy M4S (Alloy M1S + 4 wt.% Ni);
5- Alloy M5S (Alloy M1S + 2 wt.% Ni + 0.75 wt.% Mn).

The non-modified base alloy, Alloy M1, was investigated together with its Sr-modified counterpart, Alloy M1S, in Phase III of the study, related to the extended solution treatments. In addition, the Sr-modified and non-modified 356 (Al-Si-Mg) alloys were also included in this part of the work. Following the same coding system, the alloys investigated in Phase III were as follows:

1- Alloy M1 (Alloy 354 + 0.3 wt.% Zr);
2- Alloy M6 (Alloy 356);
3- Alloy M6S (Alloy 356 + 0.02wt.% Sr).

Table 3.1 lists the chemical composition and codes of the various alloys as obtained from the samplings for chemical analysis taken from the corresponding melts prepared for this study.

The 354 alloy was received in the form of 12.5-kg ingots. The same melting, alloying, and casting procedures were followed for all alloys prepared in this study, as described in the next section. Two cooling rates were employed in the present study using the casting techniques which are described in sections 3.3.1 and 3.3.2. The castings

obtained under slow cooling rate (0.35 °C s^{-1}) conditions were used for differential scanning calorimetry (DSC) analysis, phase identification purposes, and TEM investigations, while those obtained at high cooling rate (7 °C s^{-1}) were used for preparing the samples for the tensile, hardness, and impact testing.

Table 3.1 Chemical composition of the alloys investigated in this study

Chemical Analysis (wt.%)											
Alloy description		**Elements**									
Type	**Code**	**Si**	**Cu**	**Mg**	**Fe**	**Ti**	**Zr**	**Ni**	**Mn**	**Sr**	**Al**
354	M1	8.6	1.8	0.60	0.12	0.19	0.3	<0.1	0.01	--	Bal.
	M1S	8.5	1.76	0.50	0.1	0.2	0.32	<0.1	0.01	0.02	Bal.
	M2S	8.4	1.7	0.60	0.14	0.21	0.33	1.9	0.01	0.02	Bal.
	M3S	8.6	1.8	0.50	0.11	0.25	0.33	< 0.1	0.74	0.02	Bal.
	M4S	8.6	1.8	0.67	0.18	0.22	0.29	4	0.01	0.02	Bal.
	M5S	8.6	1.8	0.60	0.15	0.25	0.29	1.9	0.77	0.02	Bal.
356	M6	7.19	0.12	0.32	0.12	0.12	--	--	--	--	Bal.
	M6S	7.2	0.12	0.32	0.12	0.12	--	--	--	0.02	Bal.

3.3 MELTING AND CASTING

The as-received 354 alloy ingots were cut, dried, and melted in a 70-Kg capacity SiC crucible using an electric resistance furnace, as shown in Figure 3.1(a). The melt was kept at a temperature of 800 ± 5 °C. This melt superheating was carried out in order to assure the complete melting of all Zr- and Ni-containing compounds from master alloys. The various alloying additions were made using the necessary elements either in pure form or as master alloys. Silicon (Si), copper (Cu), and magnesium (Mg) were added in the form

of pure elements, whereas the other alloying elements were added in the form of master alloys.

The environmental parameters in the foundry during casting were as follows: humidity level was about 23%, and temperature of surroundings was about 22°C. The Sr-modified alloy series was obtained by adding ~ 200ppm Sr using Al-10 wt.% Sr master alloy, whereas, the grain refinement was accomplished through the addition of Al-5 wt.% Ti-1 wt.% B master alloy in the form of rods in order to achieve a level of ~0.2 wt.% Ti in the final alloys. The iron and manganese additions were carried out using Al-25 wt.% Fe and Al-25 wt.% Mn master alloys to achieve the required levels of 0.12 wt.% and 0.75 wt.%, respectively. Additions of Zr and Ni were carried out using Al-15 wt.% Zr and Al-20 wt.% Ni master alloys to achieve levels of 0.3 wt.% Zr, and 2 and 4 wt.% Ni, respectively. Three samplings for chemical analysis were also taken at different times during the casting process in order to ensure the homogeneity of the chemical composition; these samplings were taken at the start, the middle, and the end of the casting process. The chemical analysis was carried out using a Spectrolab-JrCCD Spark Analyzer. The average chemical compositions (three burns per alloy sample) are reported in Table 3.1.

3.3.1 HIGH COOLING RATE CASTING

In the high cooling rate casting, the 354 alloy ingots were cut, dried, and melted in a 70-Kg capacity SiC crucible using an electric resistance furnace, as shown in Figure 3.1(a). The melt was kept at a temperature of 800 ± 5 °C. The addition of master alloys was carried out instantly before starting the degassing process in order to ensure homogeneous mixing of additives during degassing. The degassing process was carried out using a rotary

graphite impeller that rotates at ~120 rpm for 15-20 min, the graphite impeller is shown in Figure 3.1(b); pure dry argon was pumped inside the melt through the rotating impeller at a constant rate of 20m^3/h. After degassing, the melt was carefully skimmed to remove the oxide layers from the melt surface. The melt was then poured into the preheated permanent mold of interest. Each permanent mold employed was preheated at 450°C in order to remove all traces of moisture from the mold.

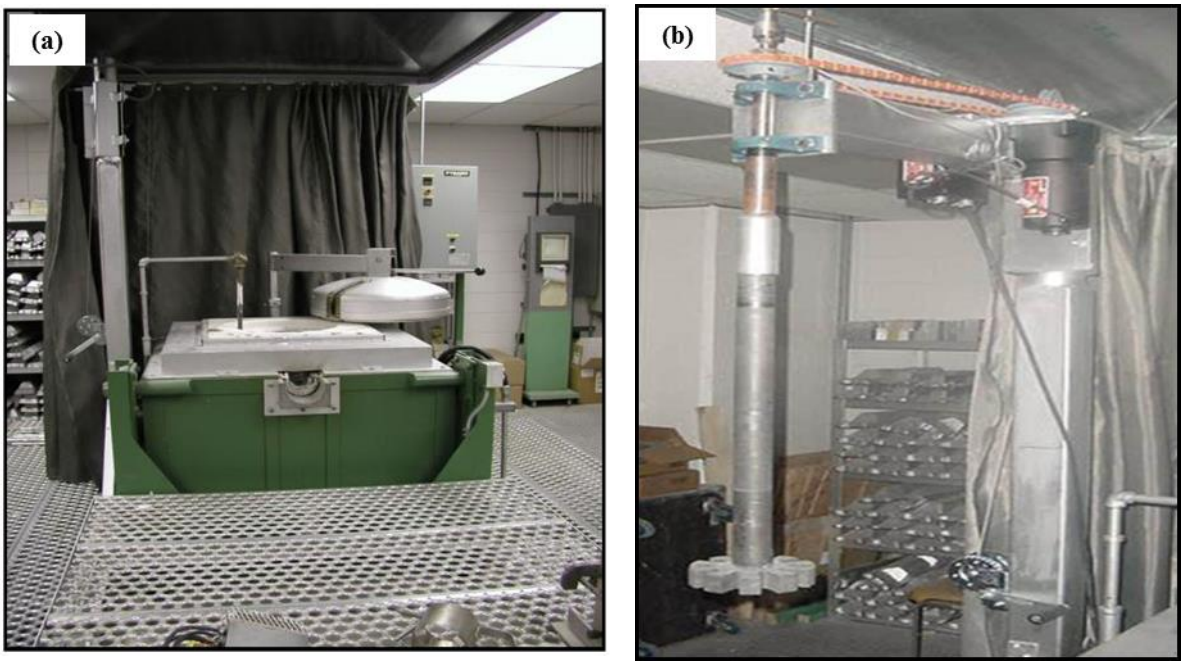

Figure 3.1 (a) Electrical resistance furnace, and (b) Graphite impeller used in degassing process.

An ASTM B-108 type permanent mold was used to prepare castings from which the standard tensile test bars were obtained. Each casting produced two tensile test bars as shown in Figure 3.2. The detailed geometry and dimensions of the standard tensile test bars are given in Figure 3.3.

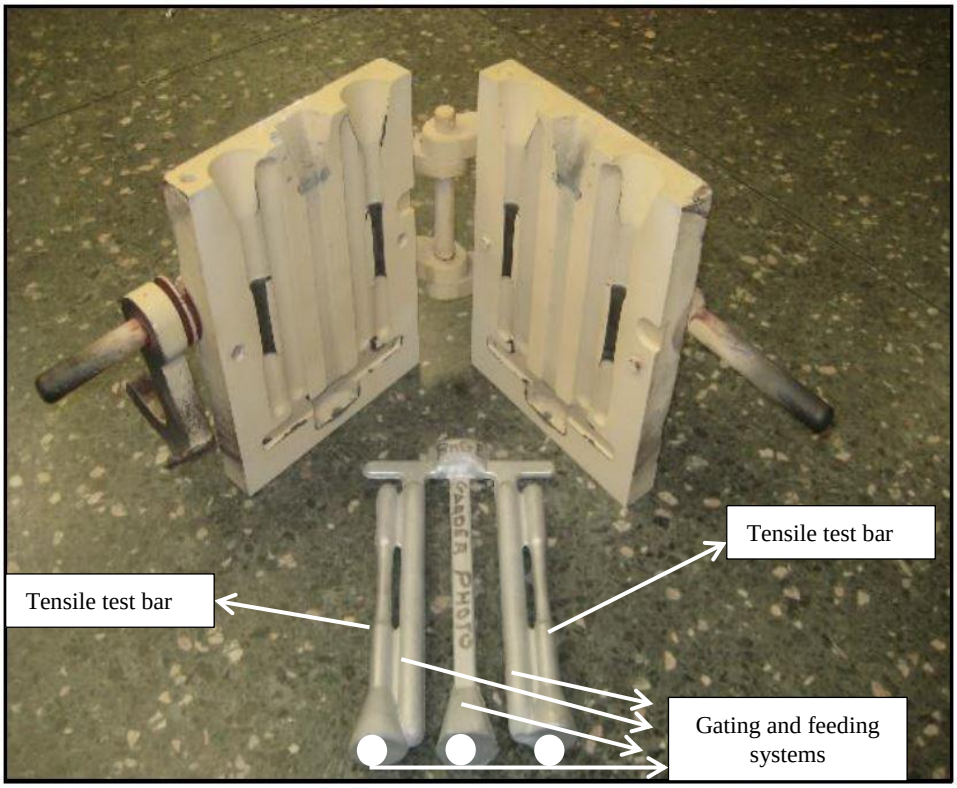

Figure 3.2 ASTM B-108 permanent mold and casting.

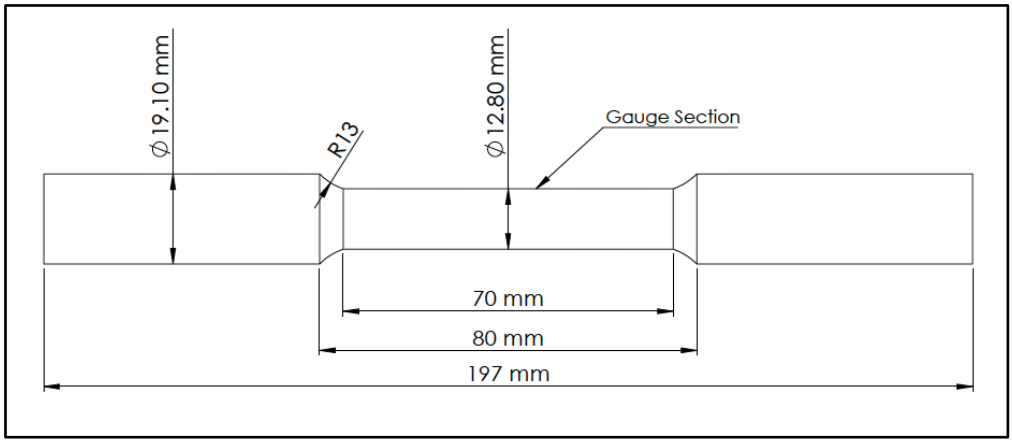

Figure 3.3 Geometry of the standard tensile test bar obtained from ASTM B-108 permanent mold.

For preparing unnotched impact test bars, a star-like mold, Figure 3.4(a), was used to produce the casting shown in Figure 3.4(b) according to the ASTM E23 standard. One such casting can provide ten impact test bars. The impact test bars were cut from the star-like casting and subsequently machined to remove irregularities and to achieve the final

testing geometry of the test bars. The test bars have a square cross-sectional area of 10x10 mm^2 and a length of 55 mm as shown in Figure 3.4(c).

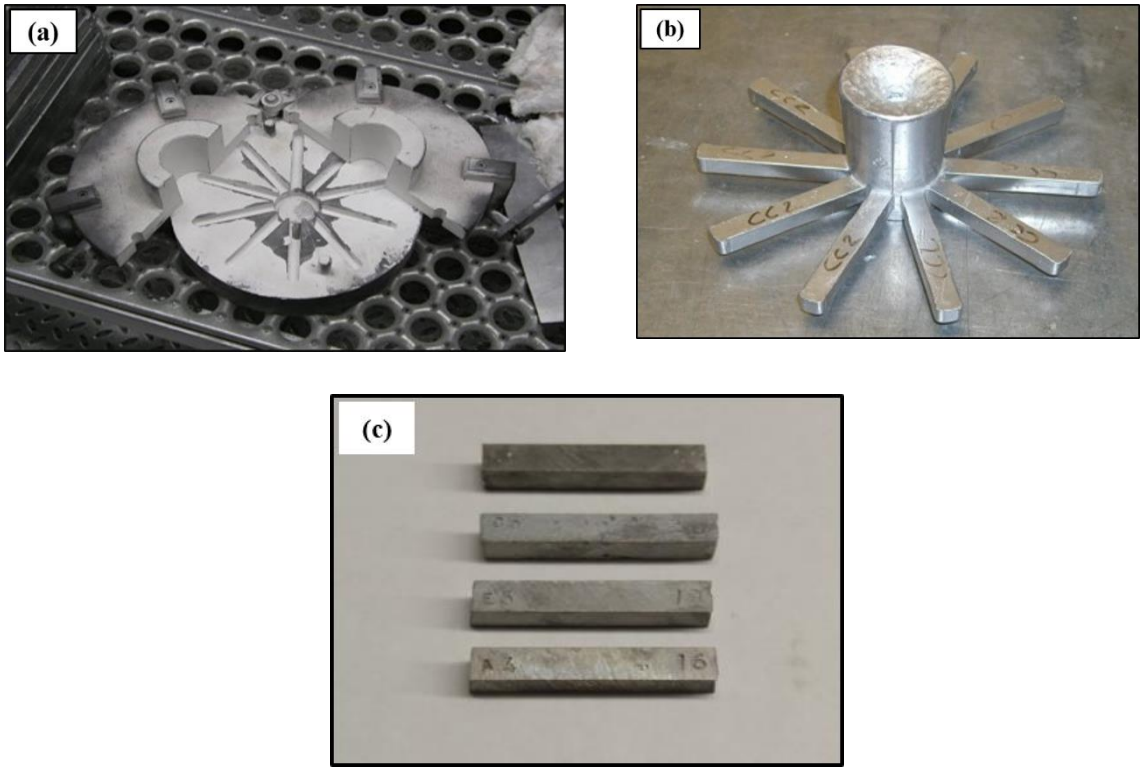

Figure 3.4 (a) Star-like mold, (b) Geometry of the star-like mold casting, and (c) Impact test bars.

For the hardness test bars, the L-shaped mold shown in Figure 3.5(a) was used to produce an L-shaped casting as shown in Figure 3.5(b). After cutting off the feeding head, each casting was cut as shown in Figure 3.5(c) along the blue planes to produce three rectangular bars which were subsequently machined to the final geometry of the hardness test bars. The hardness test bars are rectangular in cross section with dimensions of 35x30x80 mm, as shown in Figure 3.5(d).

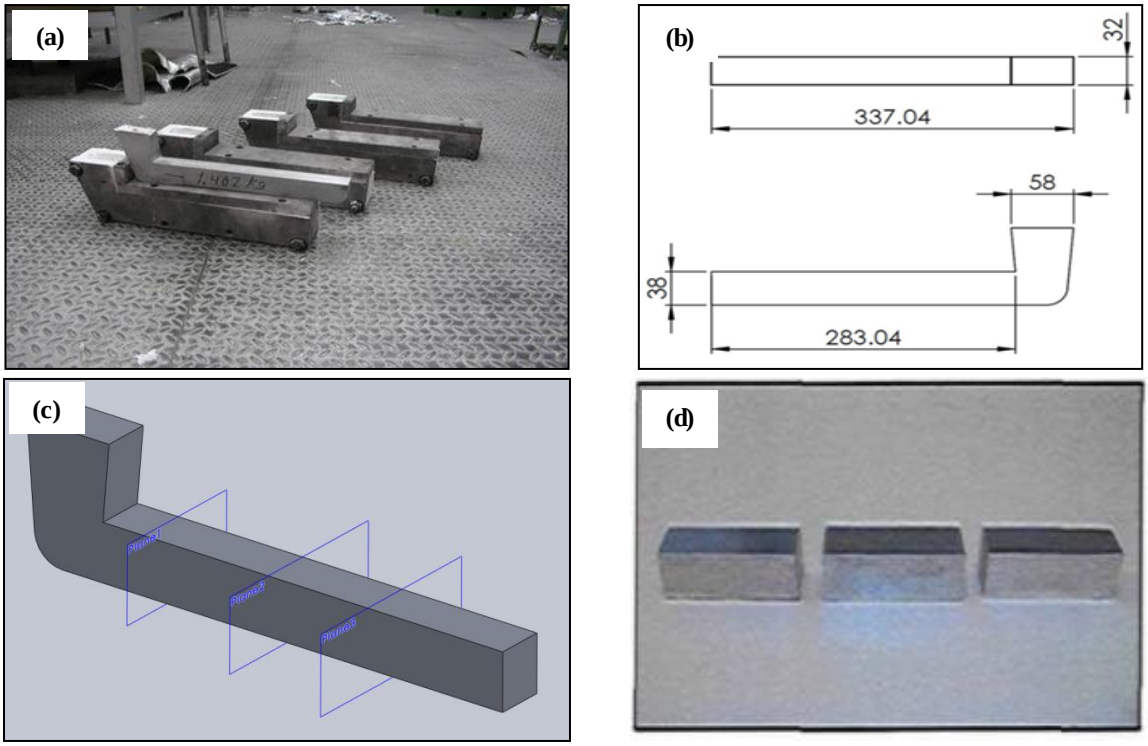

Figure 3.5 L-Shape castings: (a) L-shape mold, (b) Geometry of the L-shape casting, (c) Cutting sequence of L-shaped casting to produce smaller rectangular bars, and (d) Hardness test bars.

3.3.2 SLOW COOLING RATE CASTING

For DSC analysis, phase identification purposes, and TEM investigations, samples from the alloys M1S through M5S were cast at a lower cooling rate (0.35 °C s^{-1}) than that used in producing the tensile, impact, and hardness test bars (7 °C s^{-1}). The slow cooling rate was used in order to allow sufficient time for the phases formed during solidification to grow which would facilitate their identification process as well as produce more pronounced reactions during the DSC analysis.

Following the same procedures for the preparation of the 354 alloy melts and alloying additions as before, the melting process in this case, however, was carried out using a smaller electrical resistance furnace with a cylindrical graphite crucible of 2-Kg capacity. The melting temperature was also maintained at 800°C. The molten metal was

poured into an 800 grams capacity graphite mold preheated to 650°C to obtain near equilibrium solidification conditions (0.35 °C s^{-1}). The arrangement used for producing the slow cooling rate castings is shown in Figure 3.6.

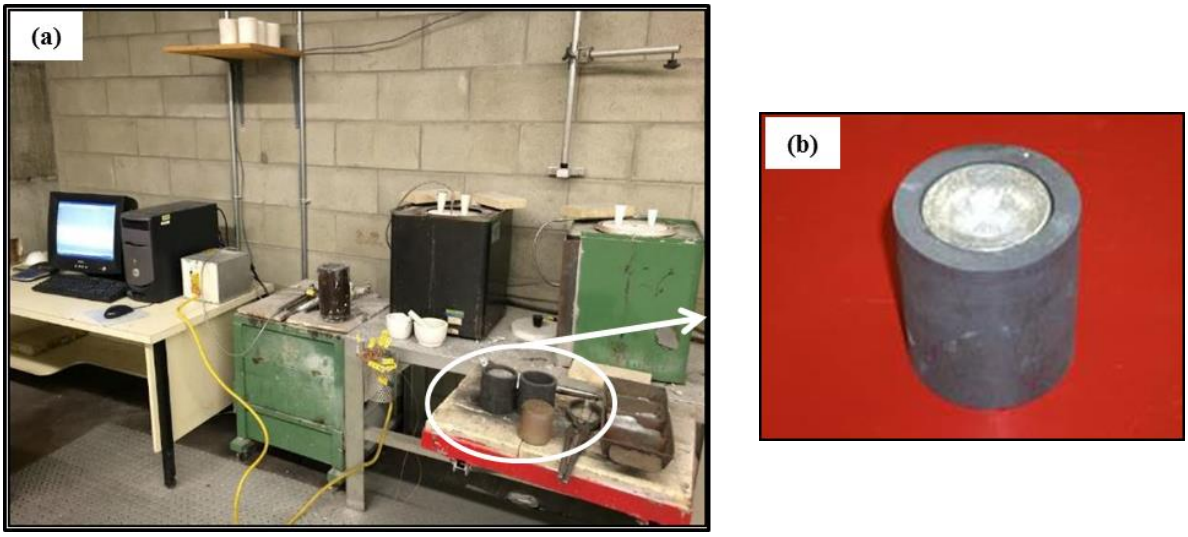

Figure 3.6 Slow cooling rate casting set-up: (a) Electrical resistance furnace, and (b) Cylindrical graphite mold used for casting.

3.4 HEAT TREATMENT

Following casting and prior to heat treatment, the test bars of each alloy were divided into bundles of 5 bars each. The bars in each bundle were assembled together using a steel wire in order to facilitate their handling in the heat treatment process. For the alloys investigated in Phases I, and II (i.e. M1S through M5S), tensile test bars of the five alloys were heat treated following the T5 and T6 temper procedures. For the T5-temper, the test bars were artificially aged only. For the T6-temper procedure the test bars were solution-heat treated, quenched in warm water, and then artificially aged. The heat treatment procedures and parameters for the alloys used in Phases I, and II are listed in Table 3.2. The same treatments and parameters were used for both ambient and elevated tensile testing.

Table 3.2 Heat treatment procedures and parameters applied to alloys investigated in Phases I, and II

Heat treatment procedures and parameters			
Heat treatment	**Solution treatment**	**Quenching**	**Aging**
SHT*	495°C for 5 h	Warm water (60°C)	NA
T5 temper	NA	NA	180°C for 8 h
T6 temper	495°C for 5 h	Warm water (60°C)	180°C for 8 h

*SHT: Solution heat treatment

The alloys M1S through M5S - used in the work of Phase II (prolonged elevated-temperature thermal exposure), were heat treated according to T5 and T6 procedures using the same parameters listed in Table 3.2. However, following these traditional heat treatments, the test bars were subjected to prolonged exposure (stabilization) at elevated temperature for 100 h and 200 h, before being tested.

In addition, in Phase II, three alloys (M1S through M3S) were selected to further explore the effect of stabilization on their ambient temperature mechanical performance. These alloys were selected based on the following: (i) the base alloy M1S was selected as the reference alloy, (ii) alloys M2S and M3S were selected based on their observed improved performance, and (iii) the economic costs involved were also taken into consideration. Thus alloy M4S (containing 4 wt.% Ni) was not included due to the high cost of Ni.

A more detailed investigation of the effects of the stabilization process included tensile and hardness testing after stabilization at shorter intervals of time (5, 10, 25, 50, 100, and 200 h) and employing two different techniques of stabilization, namely, static and dynamic stabilizations, which are described below in detail.

a) Static stabilization

The test bars of alloys M1S, M2S, and M3S (Table 3.1) in the T6-condition were placed in the heat treatment furnace for times of 5, 10, 25, 50, 100, and 200 h. The test bars were exposed continuously to a temperature of 250°C for the required times without interruption and then removed from the furnace to cool down naturally under atmospheric conditions, as shown schematically in Figure 3.7(a); the stabilized samples were then pulled to fracture at room temperature.

b) Dynamic stabilization

In this case, the test bars of alloys M1S, M2S, and M3S (Table 3.1) in the T6-condition were stabilized in an interrupted manner for the same times used as in the static stabilization (i.e. 10, 25, 50, 100, and 200 h). In this practice, all bars were placed inside the heat treatment furnace at 250°C. After 5 h at 250°C, the bars were removed from the furnace to cool down naturally to room temperature (25°C) within a period of two hours, then placed again in the furnace at 250°C for 30 minutes to heat the bars back followed by another 5 h at 250°C, covering a duration of 10 h at 250°C in two intervals of 5 h each; after that all bars were extracted from the furnace to cool down (25°C) within 2 h. At this stage, the bars to be tested after undergoing 10 h of dynamic stabilization process were pulled to fracture. The remaining bars were placed again in the furnace for the next heating cycle, and so forth; the heating intervals, however, were varied and not limited to 5 h each. The dynamic stabilization treatment described above is illustrated schematically in Figure 3.7(b).

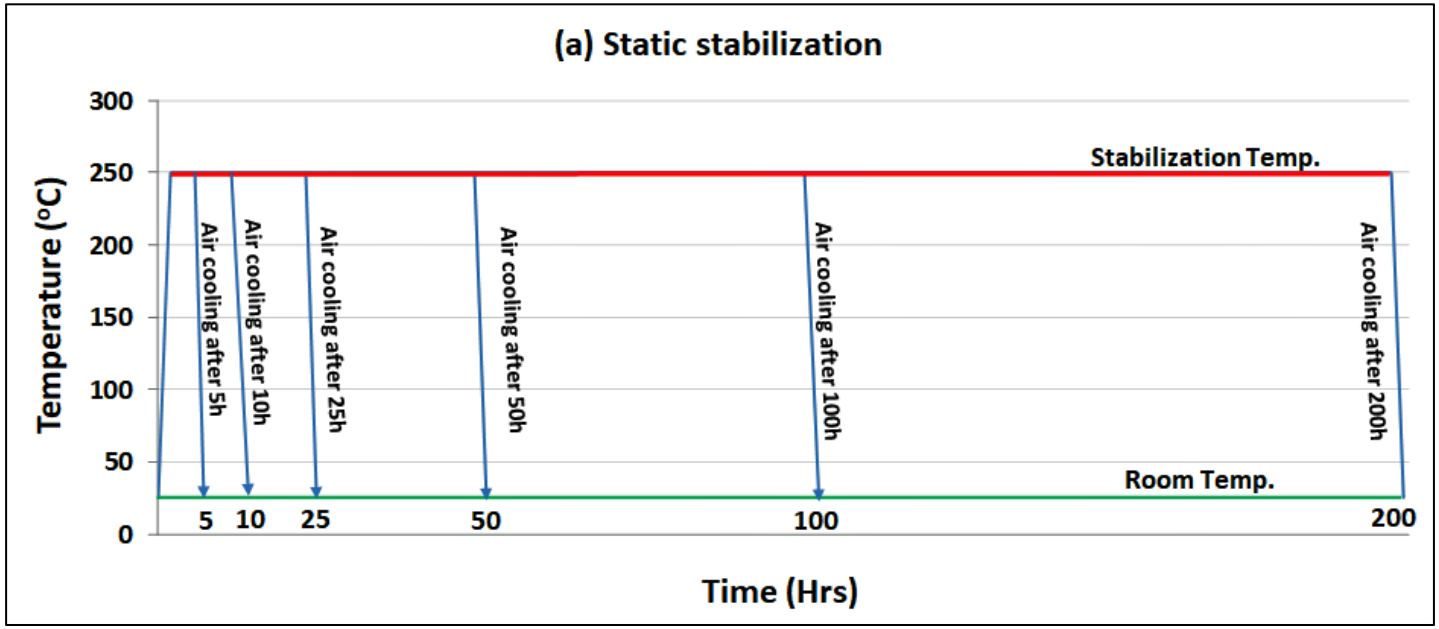

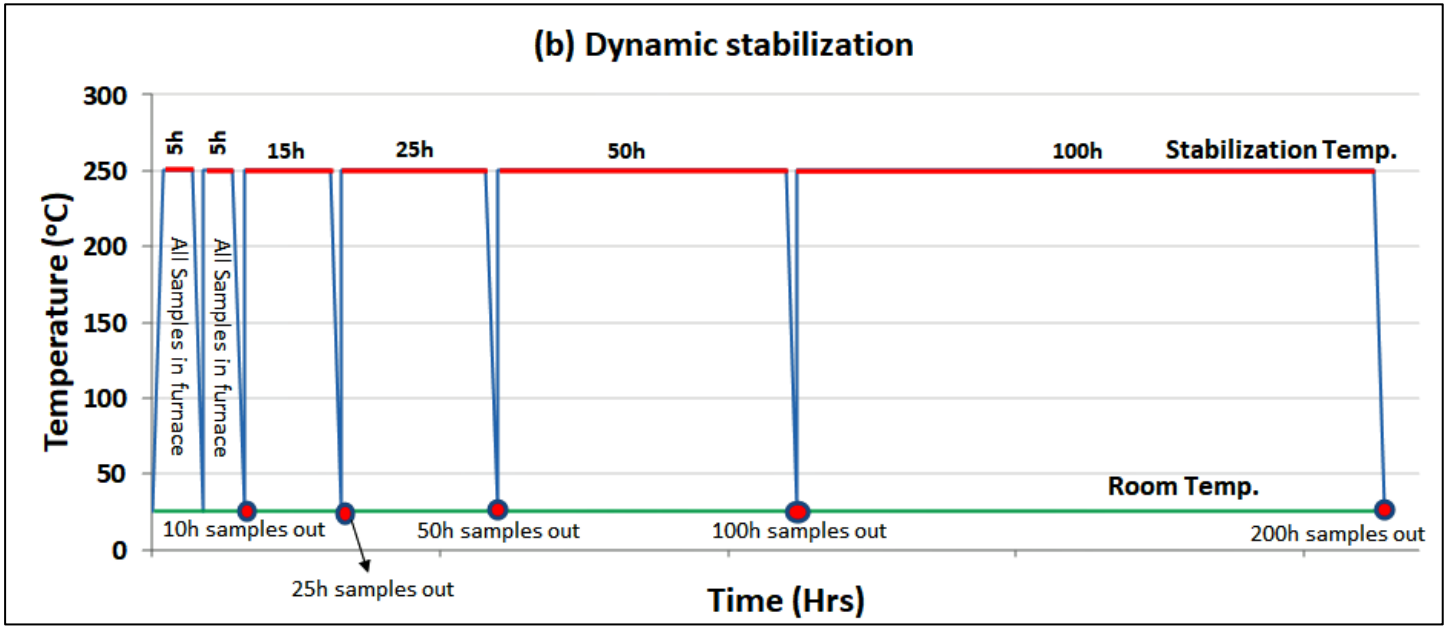

Figure 3.7 Schematic illustration describing the activity of thermal exposure: (a) Static stabilization and (b) Dynamic stabilization.

Table 3.3 summarizes the alloys used and the corresponding stabilization practices applied to these alloys during thermal exposure at elevated temperature.

Table 3.3: Stabilization parameters applied to alloys used in Phase II

Thermal exposure at 250°C												
Alloy codes	**Stabilization time and technique**											
	5 h		**10 h**		**25 h**		**50 h**		**100 h**		**200 h**	
	Static	**Dynamic**	**Static**	**Dynamic**	**Static**	**Dynamic**	**Static**	**Dynamic**	**Static**	**Dynamic**	**Static**	**Dynamic**
M1S	√	√	√	√	√	√	√	√	√	√	√	√
M2S	√	√	√	√	√	√	√	√	√	√	√	√
M3S	√	√	√	√	√	√	√	√	√	√	√	√
M4S	NA	NA	NA	NA	NA	NA	NA	NA	√	NA	√	NA
M5S	NA	NA	NA	NA	NA	NA	NA	NA	√	NA	√	NA

For the work Phase III, related to extended solution treatments, alloys M1, M1S, M6, and M6S were investigated following solutionizing treatment, i.e. T4 treatment. For each alloy, five solutionizing times were selected. For the 356-type alloys (M6 and M6S), however, a higher solutionizing temperature was selected compared to that used in case of alloys M1 and M1S, and longer solution times were employed, as well. The justification for the selection of solutionizing parameters was to decide if there is a maximum level of silicon coarsening for each temperature and time. Table 3.4 lists the different solutionizing times corresponding to each alloy used in this part of the study.

Table 3.4 Heat treatment parameters used for the alloys investigated in Phase III (extended solution treatment)

Alloy type	Alloys	Condition	Solution Treatment		Quenching	Aging
			Temperature	Time (h)		
354	**M1 and M1S**	T4	510°C	8, 25, 50, 100, 200	Warm water (60°C)	NA
356	**M6 and M6S**	T4	550°C	8, 50, 100, 200, 400	Warm water (60°C)	NA

The heat treatment was carried out using a Lindberg Blue M electric furnace (Figure 3.8). It is important to mention that the time elapse between removal of the test-bar bundles from the furnace and quenching was at most ~5 seconds.

Figure 3.8 Lindberg Blue M electric furnace used for heat treatment.

3.5 MACHINING OF NOTCHES

The main idea of introducing geometrical discontinuities is to imitate the geometry of automotive engine components which contain a lot of details that result in stress concentration and premature fracture. Most of the tensile properties of cast aluminum alloys reported in the literature represent the data obtained from smooth (unnotched) tensile bars. When these alloys are employed in an actual component, however, the mechanical properties will be affected due to the presence of the fine details constituting the cast piece. With this point in mind, four different notch geometries were employed in the current study: two hole-type geometries and two types of V-notches (symmetric and asymmetric for each).

The notches were machined using a CNC milling machine followed by grinding and polishing of the notch surfaces. All notch geometries were selected with the intention of having the same reduced area of ~105 mm^2 (the minimum area in the tensile bar) instead of ~127 mm^2 corresponding to smooth bars. The asymmetric notches were selected to facilitate the fracture because in this case there would be various critical locations to initiate cracks, whereas the symmetric notches were used for comparison purposes. Moreover, all notches were introduced to cylindrical tensile bars in order to unify the geometry of the tensile specimens so that the specimen geometry is not considered as a variable parameter.

The V-notched specimens are shown in Figure 3.9(a) and Figure 3.9(c), and the details of the symmetric and asymmetric notches are provided in Figure 3.9(b) and Figure 3.9(d); the notch root radius is maintained at a value of 0.4 mm for the asymmetric

and symmetric notches. Specimens with symmetric and asymmetric holes and the details of their geometries are shown in Figure 3.9(e) and Figure 3.9(f).

(a)

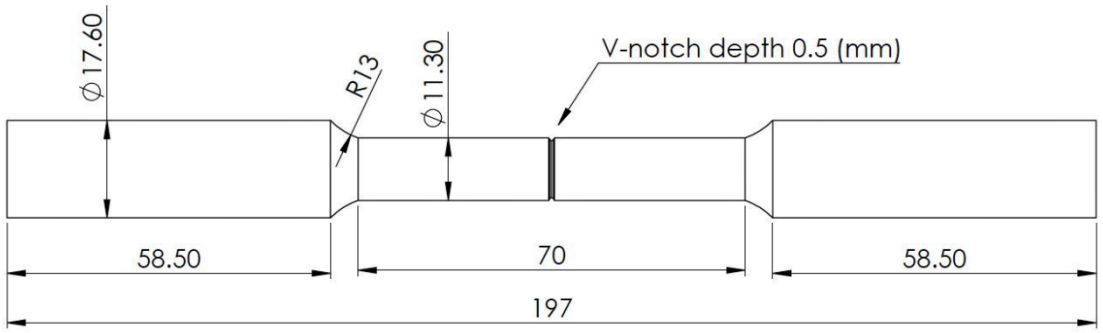
Ø17.60
R13
Ø11.30
V-notch depth 0.5 (mm)
58.50
70
58.50
197

(b)

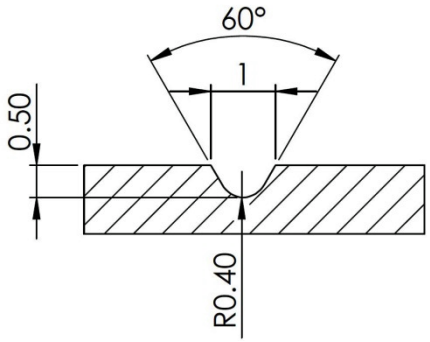
60°
1
0.50
R0.40

(c)

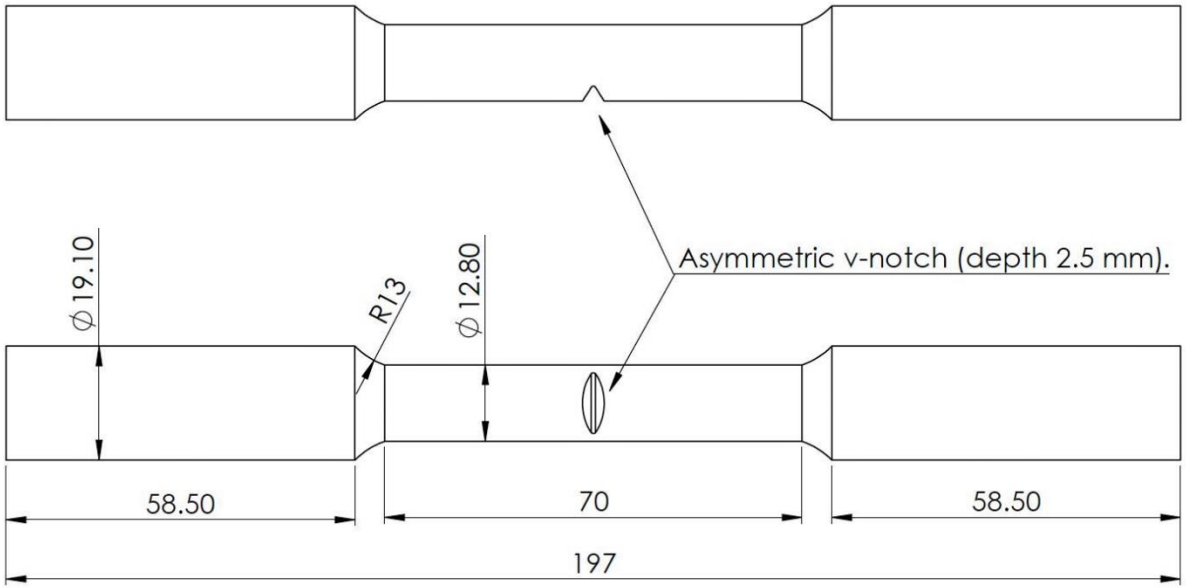
Asymmetric v-notch (depth 2.5 mm).
Ø19.10
R13
Ø12.80
58.50
70
58.50
197

(d)

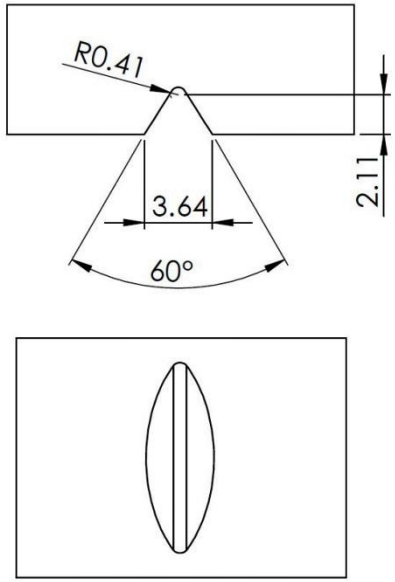
R0.41
2.11
3.64
60°

(e)

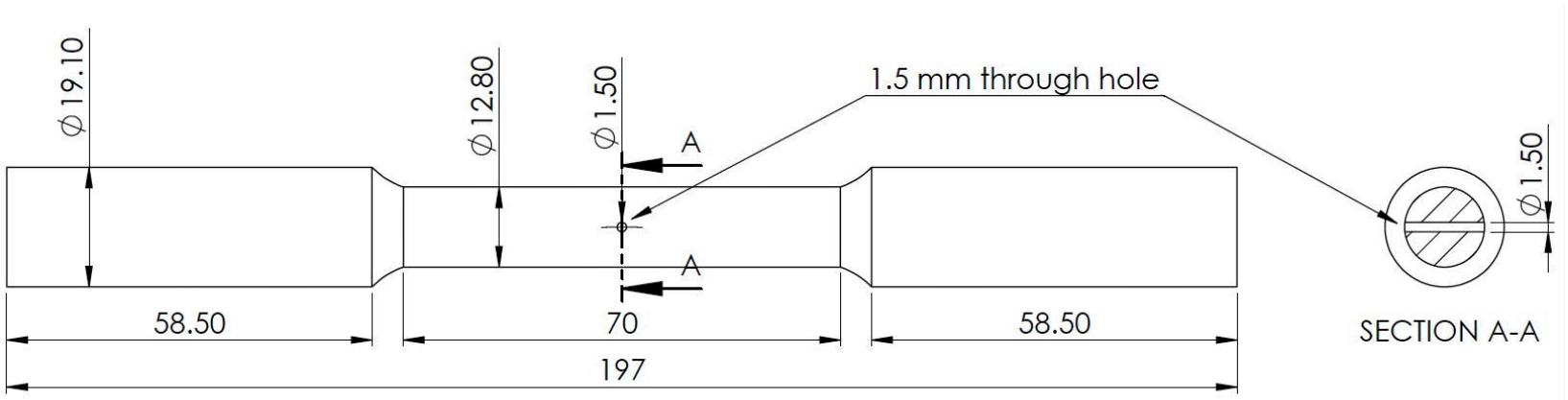

(f)

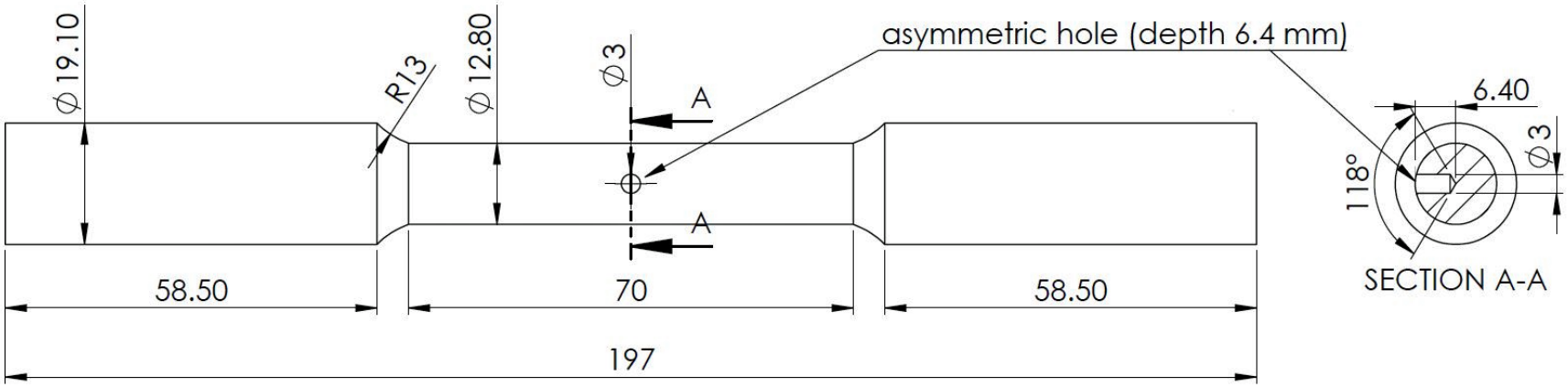

Figure 3.9 Schematic diagram showing details of notches machined in tensile test bars: (a) specimen with symmetric V-notch, (b) details of the symmetric V-notch, (c) specimen with asymmetric V-notch, (d) details of the asymmetric V-notch, (e) specimen and details of the symmetric hole, (f) specimen and details of the asymmetric hole.

3.6 MECHANICAL TESTING

3.6.1 AMBIENT TEMPERATURE TENSILE TESTING

Tensile testing at ambient temperature was carried out using an MTS Servo-hydraulic mechanical testing machine at a strain arte of 4 x 10^{-4} s^{-1}, as shown in Figure 3.10(a), for the as-cast and heat treated test bars. The attachable extensometer (strain gauge), shown in Figure 3.10(b), was used to measure the deformation that takes place in the samples during the test, and the data acquisition system attached to the machine converts it to an accurate measure of the percentage elongation. The data acquisition system provides the tensile properties in terms of ultimate tensile strength (UTS), yield strength (YS), and the percentage elongation to fracture (%El). Five test bars for each alloy/condition were tested and the average values of ultimate tensile strength (UTS), 0.2% offset yield strength (YS), and percentage elongation to fracture (%El) were reported as representing the tensile properties of the corresponding alloy/condition.

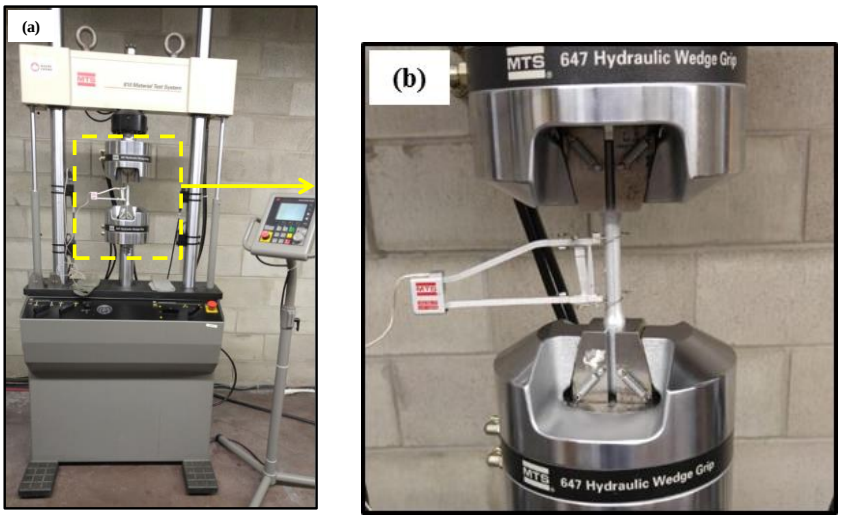

Figure 3.10 (a) MTS Mechanical Testing machine used for room temperature tensile testing, and (b) the attachable extensometer.

3.6.2 ELEVATED-TEMPERATURE TENSILE TESTING

An Instron Universal mechanical testing machine was used to carry out the tensile testing at elevated temperature (250°C), using the same strain rate as used in the room temperature tensile testing (4×10^{-4} s^{-1}); the testing machine is shown in Figure 3.11. The testing was carried out at 250°C after holding the test bar for half an hour at the testing temperature in order to homogenize the temperature of the sample to 250°C throughout. The test sample was kept unmounted from one side inside the heating chamber during the holding process to avoid compressive stresses that might arise from the expansion of the bar, and then it was mounted from the other side and kept at the testing temperature for another 30 min.

A data acquisition system attached to the machine provided the tensile data, namely, the ultimate tensile strength (UTS), the yield strength at 0.2% offset strain (YS), the modulus of elasticity (E), and the percent elongation to fracture (%El), calculated over the gauge length of the test bar. Five test bars were used for each alloy composition/condition studied. The average values of UTS, YS, and %El from each set of five bars were considered as representing the tensile properties of that alloy/condition.

3.6.3 HARDNESS TESTING

Hardness measurements were carried out on the prepared hardness test bar samples in the as-cast and heat-treated conditions (according to the procedures described in Table 3.2). A Rockwell hardness tester and F scale was employed using a 1/16-inch steel ball indenter and a load of 60 Kgf. Ten measurements were made per sample, and the

average value was reported as the Rockwell hardness value of that alloy sample/condition; the Rockwell hardness tester is shown in Figure 3.12.

Figure 3.11 Instron Universal mechanical testing machine with a chamber for high temperature testing.

Figure 3.12 Rockwell hardness tester.

3.6.4 IMPACT TESTING

Impact test bars were prepared from the star-like mold castings as described previously in section 3.3.1. The test bars have a cross-sectional area of 10 mm x 10 mm and a length of 55 mm, as shown in Figure 3.4(c).

A computer-aided instrumented SATEC SI-1 Universal Impact Testing Machine, SATEC Systems Inc., Model SI-1D3, was used to carry out the impact testing. The machine, shown in Figure 3.13, is capable pf providing four operating capacities based on the pendulum latching mode (high latch or low latch) and bolt-on weights; these capacities are described as follows: a capacity of 25 ft-lbs (33.9 J) on low latch pendulum and 60 ft-lbs (81.35 J) on high latch pendulum without the bolt-on weights attached, and a capacity of 50 ft-lbs (67.8 J) on low latch pendulum and 120 ft-lbs (162.7 J) on high latch pendulum with the additional weights attached. A data acquisition system is attached to the impact testing machine in order to monitor the dynamic behavior of the machine as well as to measure the load and energy values as a function of time.

The instrument and the attached data acquisition system provide the total absorbed energy (E_t) of the sample during the impact test. Five samples for each alloy/condition were tested and the average value of the total energy obtained over the five samples was taken as the impact energy representative of that particular alloy/condition.

Figure 3.13 A computer-aided instrumented SATEC SI-1 Universal impact testing machine, with a Dynatup IPM/PC impact testing system for data acquisition.

3.7 METALLOGRAPHY - MICROSTRUCTURAL CHARACTERIZATION

The main purpose of characterizing the microstructure of the alloys investigated is to correlate their tensile properties with their microstructural features. Multiple techniques were employed in characterizing the alloy microstructure in order to obtain a qualitative and quantitative analysis of microstructural features of interest such as the phases and intermetallic compounds formed, strengthening precipitates resulting from the heat treatments employed, as well as characteristics of the fracture surfaces of the tensile- and impact-tested samples of these alloys.

3.7.1 DSC ANALYSIS

Differential scanning calorimetry (DSC) may be used to characterize the sequence of reactions occurring during the heating and/or cooling cycles of an alloy sample during a DSC scan which continuously changes with the increasing or decreasing temperature cycle to produce peaks according to the two expected reactions:

- $Phase\ formation \rightarrow heat\ emission \rightarrow exothermic\ peak;$
- $phase\ dissolution \rightarrow heat\ absorption \rightarrow endothermic\ peak.$

For reliable results, the DSC curves must be accompanied by microstructural observations in order to assign a specific reaction to the corresponding DSC peak.

The DSC analysis was carried out using a computerized differential scanning calorimeter (Perkin Elmer DSC 8000) under a protective atmosphere of pure argon as shown in Figure 3.14. Samples used in this analysis were taken from the slowly cooled as-cast graphite mold castings. The DSC samples were punched out from 0.7 mm-thick cut slices as discs with a diameter of 4 mm; the mass of each disc was approximately 20 mg. Slight grinding of the punched discs was carried out using 320 and 600 grit size papers; washed thoroughly in an ultrasonic cleaner for about 15 minutes, and finally weighed using a precise balance. For each alloy condition, three DSC samples were tested and their results were found to be almost identical. The DSC heating and cooling curves were normalized to the specimen weight, i.e. the obtained heat data is divided by the weight of the DSC sample discs, in order to avoid any discrepancies that may occur due to possible variation in the sample weight.

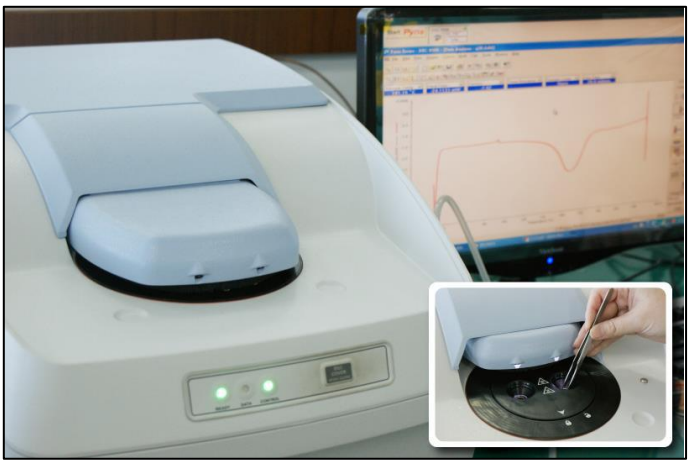

Figure 3.14 Perkin Elmer DSC 8000 apparatus.

The DSC curve is commonly obtained from corrective and sample run curves. The corrective curve is obtained when the cell is equilibrated, heated up at the desired heating rate within the anticipated temperature range, and cooled down using the same parameters, under an argon atmosphere; this step is executed while the reference and sample pans of the apparatus are empty. A sample corrective curve is shown in Figure 3.15(a). The sample run curve is obtained by applying the previous procedure but in the presence of the test sample in the sample pan, Figure 3.15 (b). The true DSC curve, shown in Figure 3.15(c), is obtained by subtracting the corrective curve from the sample run curve (Figure 3.15-b)). The heating and cooling rates employed in the DSC analysis were 10 °C/min, using a protective atmosphere of pure argon.

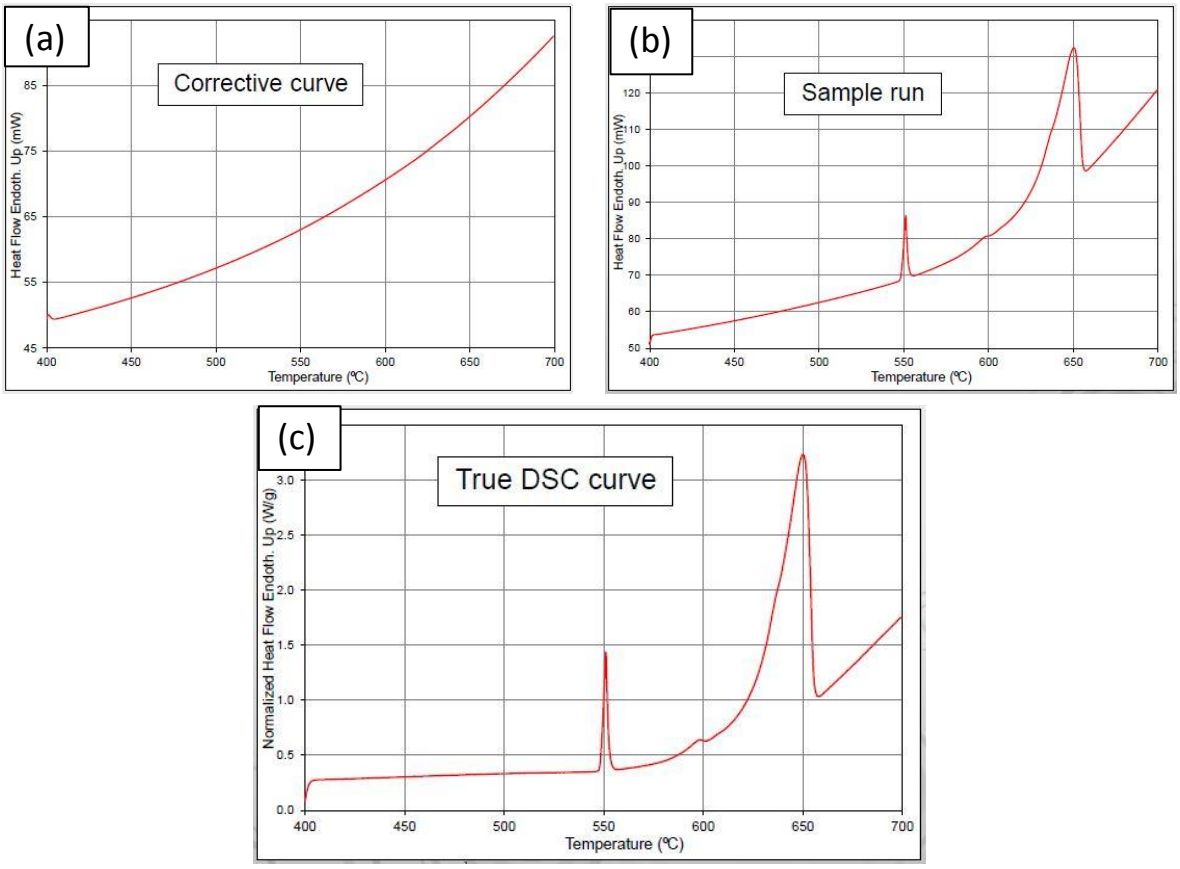

Figure 3.15 DSC curve: (a) Corrective curve, (b) Sample curve, and (c) true DSC curve.

3.7.2 OPTICAL METALLOGRAPHY

For selected alloys/conditions, samples were sectioned from fractured tensile test bars, 10 mm beneath the fracture surface as shown in Figure 3.16, for preparing metallographic samples. Each sample was mounted individually in bakelite, and then ground and polished to obtain a mirror-like surface. The samples were examined using an Olympus PMG3 optical microscope connected to a Clemex Vision PE image-analysis system.

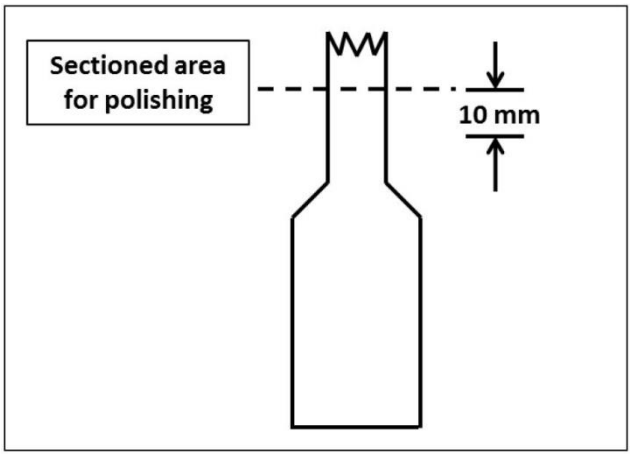

Figure 3.16 Schematic representation of the sectioned area of a tensile-tested bar prepared for metallographic analysis.

The Struers LaboPress-3 and TegraForce-5 machines shown in Figure 3.17 were used to respectively mount the samples in bakelite, and for grinding and polishing the mounted samples to a fine finish. The grinding process was accomplished by using a set of silicon carbide (SiC) grinding papers of successively increasing grit size i.e. from 120 grit size, through 240, 320, 400, 600, 800, to 1200 grit sizes, the fineness of the papers increasing with the increase in the grit size number. Water was used as the lubricant in the grinding process.

The polishing process was carried out using Struers diamond suspension which contains diamond particles 6μm in size, as the first step of the polishing process. Subsequent steps involved using the same suspension containing smaller diamond particles of sizes 3μm, and 1μm. The Struers DP-lubricant was used as the lubricant in these stages. The final polishing step was accomplished using a Mastermet colloidal silica suspension, SiO_2 having a particle size of 0.6μm; water was used as the lubricant in this final polishing stage, after which the samples displayed a mirror-like surface and were ready for

microstructural examination. The surfaces of the polished samples were examined using the optical microscope-image analysis set-up shown in Figure 3.18.

Figure 3.17 Struers LaboPress-3 (left), and TegraForce-5 (right) machines, for mounting and polishing samples for metallography.

Figure 3.18 Optical microscope and Clemex Vision PE image-analysis system used in the current study.

3.7.3 SILICON PARTICLE CHARACTERISTICS

For quantification purposes, the polished samples were examined using a Clemex Vision PE image-analysis system connected to an optical microscope. The eutectic silicon particle characteristics of as-cast and solution heat-treated samples were quantified by analyzing the 2D optical micrographs to determine the changes in the morphology of the silicon particles with solution treatment. The measurements were carried out over 20 fields per sample, by traversing the entire sample in a regular, systematic manner. Thresholding of each image (field) was achieved by outlining and coloring the eutectic silicon particles manually, as shown in Figure 3.19, followed by analysis of the colored particles using the image analysis software program. The characteristics measured included the average particle area (μm^2), the average roundness percent (%), the average sphericity percent (%), and the average aspect ratio.

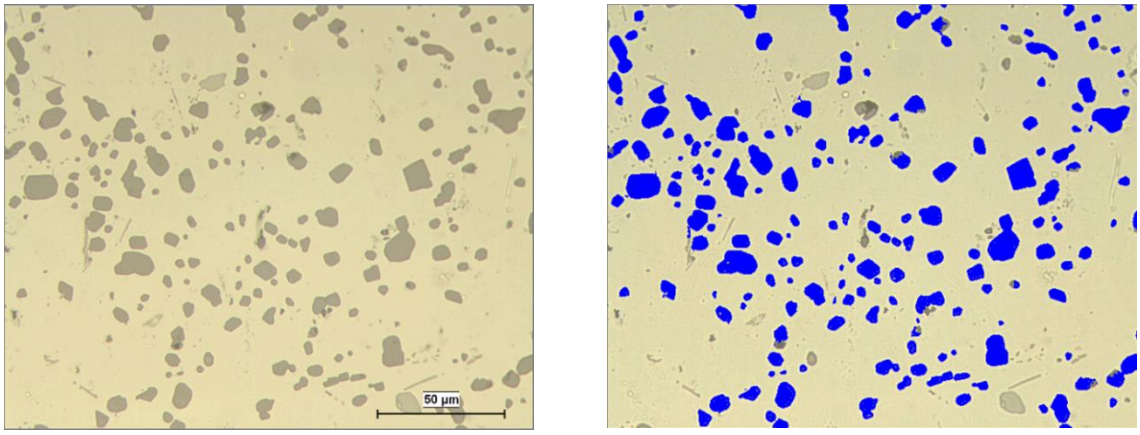

Figure 3.19 Preparing to quantify the characteristics of eutectic Si particles by thresholding (coloring) the Si particles.

It is worth mentioning here that the standard deviation values associated with these measurements do not reflect the actual coarsening and spheroidization trend of the silicon particles during solution treatment. Very small particles are obtained in the structure,

particularly in the case of extended solution treatments of up to 200 h, due to dissolution of smaller particles and, correspondingly, the coarsening of others. As these tiny Si particles are expected to be present in large numbers at the maximum solutionizing time (200 h), the large variation in the eutectic silicon particle size would result in an unrealistic calculation of the average particle size and high standard deviation values.

Based on the aforementioned, a criterion to be followed was established to decide whether the tiny particles would be included or omitted from the analysis, based on the area fraction of these very small particles. The smallest three intervals of particle area were taken into consideration where the area fraction was estimated for each solution treatment condition by calculating the area fraction of the tiny particles, in each particle size interval, to the total area of the silicon particles considered in the analysis of the specified sample. The quantitative analysis concentrated on three characteristics, namely, the equivalent circle diameter, the aspect ratio, the roundness, and the sphericity. These parameters are shown schematically in Figure 3.20, Figure 3.21, Figure 3.22, and are calculated using Equations 3.1 through 3.4. The roundness relates to the sharpness or smoothness of the particle's corners or edges; whereas the sphericity (or circularity) determines how the overall shape of the particles approaches that of a sphere (3D) or a circle (2D). In this study the term 'sphericity' will be used to describe the particle shape in 2D (instead of 'circularity').

The equivalent circular diameter is the diameter of a circle that has the same area (A) as the Si particle; and may be calculated using the following formula:

$$Equivalent\ circular\ diameter\ (d) = \sqrt{\frac{4 * particle\ area\ (A)}{\pi}} \quad \textbf{(3.1)}$$

The aspect ratio of the particle is calculated by drawing an imaginary best fit ellipse to the particle projection; by measuring the major and minor axes of the ellipse, the aspect ratio can be calculated according to the following relation:

$$Aspect\ ratio\ (A.R.) = \frac{Major\ axis\ length\ (L)}{Minor\ axis\ length\ (B)} \quad \textbf{(3.2)}$$

The sphericity or circularity of the Si particles is a function of the perimeter (P) and the particle area (A); its value lies between 0 and 1, where the maximum value of 1 refers to a perfect circle. The sphericity is quantified by:

$$Sphericity = \frac{4 * \pi * particle\ area\ (A)}{Perimeter\ (P)^2} \quad \textbf{(3.3)}$$

Finally, the roundness of the particle's edges is a function of the particle area (A) and the length of the best fit ellipse major axis (L):

$$Roundness = \frac{4 * particle\ area\ (A)}{\pi * major\ axis\ length\ (L)^2} \quad \textbf{(3.4)}$$

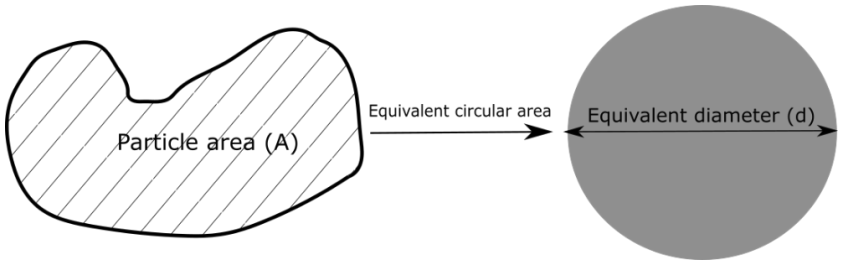

Figure 3.20 Schematic representation showing the projection of the Si particle at a plane, the equivalent circle with the same area (A), and the equivalent circular diameter (d)**.**

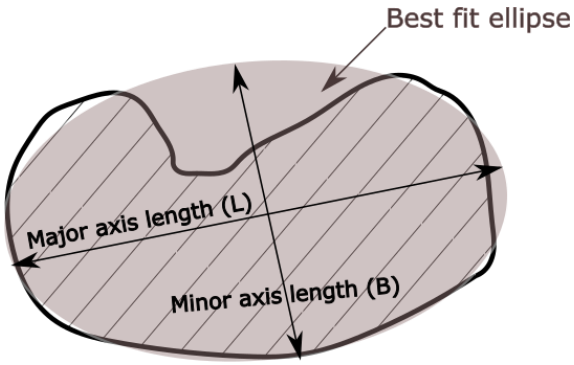

Figure 3.21 Schematic representation showing the best fit ellipse to the projection of the Si particle at a plane.

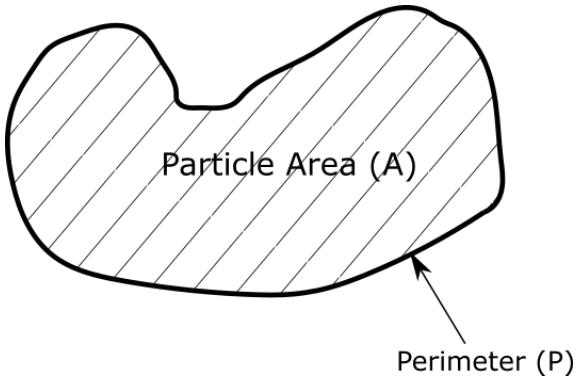

Figure 3.22 Schematic representation showing the projection of the Si particle at a plane and parameters to measure the sphericity.

In order to better understand and visualize the morphological changes occurring in the silicon particles during extended solution treatment, the samples were deep etched using Keller's etchant to dissolve the aluminum matrix and expose the eutectic silicon particles. These samples were then examined in a Hitachi-SU8000 field emission scanning electron microscope (FESEM) using the backscattered electron (BSE) mode, as will be described and shown later on in Figure 3.24.

3.7.4 SCANNING ELECTRON MICROSCOPY

A scanning electron microscope (SEM) equipped with an energy dispersive X-ray spectrometer (EDS) was used to identify intermetallic phases present in the alloys studied, whereas a field emission scanning electron microscope (FESEM) was used to characterize the strengthening precipitates associated with the various heat treatment conditions as well as to examine the deep-etched solutionized samples for characterizing the silicon particles.

The SEM used in the current study was a JEOL JSM.6480LV scanning electron microscope attached to an EDAX Phoenix system designed for image acquisition and energy dispersive X-ray (EDS) analysis, as shown in Figure 3.23. The SEM was operated at a voltage of 20 kV, with a maximum filament current of 3 amperes.

The fracture surfaces of tensile-tested samples were also examined using the same SEM, employing the backscattered electron (BSE) detector and EDS system. The fracture behavior was analyzed using the backscattered electron (BSE) images obtained, and analysis of the EDS spectra of phases observed on the fracture surface.

Figure 3.23 JEOL JSM.6480LV scanning electron microscope used in this study.

A Hitachi-SU8000 field-emission scanning electron microscope (FESEM), as was used in this study, can provide clear and less electrostatically distorted high resolution images even at low voltages, with an image resolution of 2.1 nm at 1 kV, and 1.5 nm at 15 kV. The FESEM instrument, shown in Figure 3.24, also comes equipped with a standard secondary electron detector (SE), a backscatter electron detector (BSE) and an energy dispersive X-ray spectrometer (EDS).

Figure 3.24 Hitachi-SU-8000 field emission scanning electron microscope used in the current study.

3.7.5 TRANSMISSION ELECTRON MICROSCOPY

Transmission electron microscopy was used in order to observe and identify the strengthening precipitates in heat-treated samples, and also to investigate the coherency of the precipitates with the matrix. Figure 3.25 shows the FEI Tecnai G^2 F20 electron microscope employed, equipped with an advanced control system which permits the integration of an EDAX™ chemical analysis system, scanning transmission electron

microscopy (STEM), and electron energy loss spectroscopy (EELS). The microscope was operated at an accelerating voltage of 200 kV.

Figure 3.25 FEI Tecnai G^2 F20 Electron Microscope.

The specimen preparation process for TEM investigations involves cutting a very thin slice, ~300µm thick, from the bulk samples solidified at a slow cooling rate of 0.35 °C s^{-1}. The slice was cut using a precise diamond disk cutter at a low speed to avoid any possibility of deformation in the slice. Afterwards, 3-mm diameter discs were punched out of these thin slices using a portable puncher. The discs were further ground to a thickness of about 50µm. The 50µm-thick discs were further dimpled down to 5-10µm with the EMS D500i dimpler provided by Electron Microscopy Science. The UniMill IV7 ion milling system shown in Figure 3.26 was then used to final thin the samples to electron transparency. This was achieved by using a high ion energy (8 kV) beam and final thinning

was conducted using 1.5 and 0.5 kV energy beams to reduce the amorphous layer thickness.

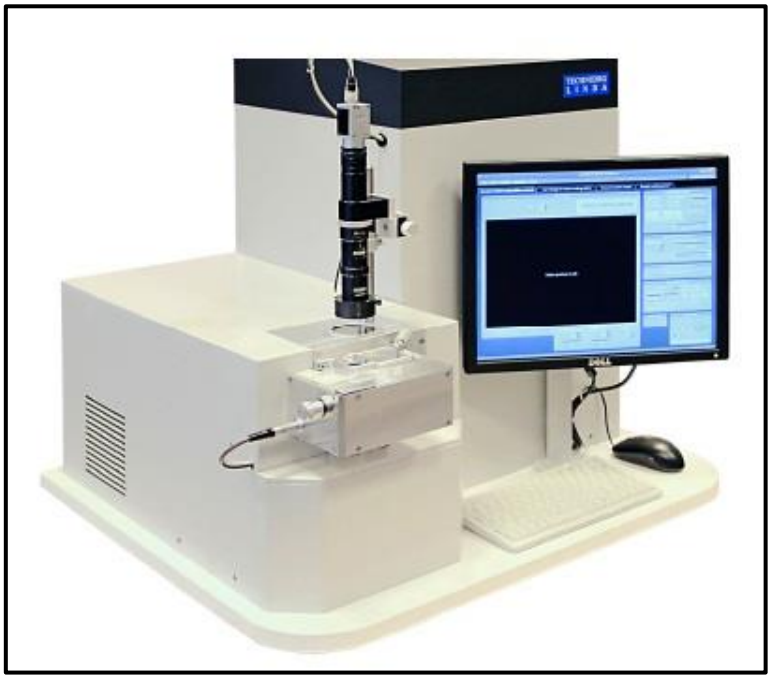

Figure 3.26 The UniMill IV7 fully automated ion beam thinning system.

CHAPTER 4

MICROSTRUCTURAL CHARACTERIZATION

CHAPTER 4

MICROSTRUCTURAL CHARACTERIZATION

4.1 INTRODUCTION

This chapter discusses the melting and solidification sequences, microstructural features, and identification of the strengthening precipitates for the 354-type alloys following the addition of three transition elements, namely, zirconium, nickel, and manganese, in different amounts and combinations. The differential scanning calorimetry (DSC) analysis was carried out for the slowly cooled samples obtained at a cooling rate of 0.35 $°Cs^{-1}$ (i.e. prepared from castings produced using the graphite mold). The purpose of the DSC analysis was to: (i) investigate the melting and solidification sequences in the alloys studied, (ii) decide on an optimum solutionizing temperature for these alloys to avoid the possibility of incipient melting, as well as (iii) study the effect of chemical additions on the active strengthening precipitates in these alloys. Microstructural examination using optical and scanning electron microscopy was carried out to reveal the phases formed in the alloys and to confirm their occurrence with the exothermic reactions (solidification sequence) observed on the DSC cooling curves of the respective alloys. TEM investigations were also carried out to observe and identify the active strengthening precipitates in the Al-Si-Cu-Mg 354-type alloys investigated in this study.

It is well established that the cooling rate has a significant effect on the microstructural constituents of alloys and hence on their mechanical properties. A low cooling rate deteriorates the mechanical properties of alloys owing to the difficulty of obtaining fine modified intermetallic structures, the attendant increase in porosity content, and a larger average pore size. On the positive side, slowly cooled castings allow for proper examination of the phases formed, as these have sufficient time to grow due to the slow solidification conditions which facilitates the detection and analysis of the existing phases in the microstructure.

Samples of all alloy compositions prepared were originally sectioned from the graphite mold cylindrical castings obtained at low cooling rate. These samples (20x15mm x 20mm thickness) were extracted from the centre of each casting at one third of its length from the bottom. These samples were then used for producing both the tiny discs (~ 20 mg) for the DSC analysis, as previously detailed in Chapter 3, and samples for qualitative microstructural analysis using optical and scanning electron microscopy. The DSC heating and cooling curves provide the main reactions which take place during the melting and solidification of the alloys studied, whereas the scanning electron microscopic examination in conjunction with energy dispersive spectroscopic (EDS) analysis gives the morphologies and the chemical composition of the intermetallic compounds detected.

The cooling curve of the DSC analysis provided information on the solidification sequence of the alloy examined, while the heating curves of as-cast and as-quenched samples respectively provided information on the dissolution of intermetallic compounds and the precipitation kinetics of the alloy sample in question.

For the as-cast samples, the DSC analysis was carried out at heating and cooling rates of 10 °C min^{-1} starting from room temperature, then heating up to 700°C and cooling down back to room temperature. For identifying the active strengthening precipitates and their characteristics, the DSC analysis was carried out on as-quenched (solutionized) samples for all compositions; in this case, the test involved only heating the samples from room temperature up to 600°C at a heating rate of 10 °C min^{-1} in order to simulate the artificial aging process.

4.2 MELTING AND SOLIDIFCATION CHARACTERISTICS

An exothermic reaction is defined as one which is accompanied by the release of energy (heat) to the surroundings in order to achieve a lower state of energy for the material. Solidification is considered as an exothermic reaction because heat is given off by the solidifying metal. An endothermic reaction, on the other hand, is defined as one that involves the absorption of energy (heat) from the surroundings, which is associated with the dissolution/melting of intermetallics. In this section, the DSC cooling and heating curves for the alloys studied and the detected exothermic and endothermic reactions associated with each will be addressed.

For purposes of recapitulation, Table 3.1 in Chapter 3 lists the actual chemical compositions of the alloys studied along with their corresponding codes.

The base alloy used in the present research work is a modified 354-type alloy with the addition of ~0.3 wt.% Zr. The chemistry of the alloys listed in Table 3.1 is mainly established based on the promising results reported in preceding research work done in the same research group on similar alloys systems.[11-13] It has been reported that the addition of

zirconium has a beneficial effect on the mechanical properties at both ambient and elevated temperatures compared to the properties obtained in case of the monolithic 354 alloy, i.e. without Zr.[11-13] The purpose of the present work, therefore, was to build on the previous knowledge in the context of alloy development as well as assess the mechanical performance of this set of alloys using different testing conditions. Tensile, hardness, and impact properties were determined at ambient and elevated temperatures, accordingly. It is crucial to characterize the corresponding microstructures of the tested alloys in order to interpret the mechanical testing data and correlate the alteration in mechanical properties observed to variations in the alloy structure.

It is a well-established fact that Al-Si-Cu-Mg alloys develop complex microstructures, as reported in several studies[11-14, 165, 194, 209]. The as-cast structure contains α-Al, eutectic silicon, copper aluminide (Al_2Cu) with different morphologies, Mg-rich phases such as magnesium silicide (Mg_2Si), Q-phase ($Al_5Cu_2Mg_8Si_6$), and Fe-based intermetallic phases including β-Al_5FeSi, α-$Al_{15}(Fe, Mn)_3Si_2$, and π-$Al_8FeMg_3Si_6$. New intermetallic phases are expected to form within the structure of the investigated alloys, however, because of the addition of the transition elements Zr, Ni, and Mn, in different amounts and combinations. To determine the extent of precipitation and dissolution of various intermetallic compounds formed in the alloys studied, DSC cooling and heating runs were carried out, followed by a thorough characterization and identification of the existing phases in the microstructure of the alloy samples using SEM and EDS analysis to verify the reactions observed on the DSC cooling curves.

Typical DSC cooling and heating curves for the five alloys studied are portrayed in Figure 4.1. The proposed peaks related to phase transformation reactions are numbered on these curves. Table 4.1 lists the average peak temperatures of the reaction peaks along with the suggested corresponding reactions with reference to literature.[12, 14, 24, 54, 69, 210, 211]

The cooling rate employed in the DSC analysis is 10 °C min^{-1} (≈ 0.167 °C s^{-1}); whereas, the solidification rates commonly used in the thermal analysis technique used in literature[11-14, 24, 54, 69, 210-212] are different. Consequently, the temperature variations observed in Table 4.1 in relation to the precipitation of phases during solidification using thermal and DSC analyses can then be attributed to the difference in the employed solidification rates in the two cases.

For the DSC heating and cooling curves, it should be noted that reporting the dissolution/precipitation temperatures using the peak temperature is easier and more accurate than reporting the onset temperature. Thus, the transformation temperatures reported in Table 4.1 are expressed as the peak temperatures of the corresponding reaction peaks. However, it should be kept in mind that the phase transformation reaction commences earlier, before reaching the peak temperature, i.e. at the onset temperature. According to K.S. Ghosh and N. Gao,[213] at the peak temperature of the precipitation reaction, the maximum precipitation rate is reached. The same concept may be also considered for those peaks representing the dissolution reactions.

From Figure 4.1, it is obvious that the Ni-free alloys (i.e. M1S and M3S) show peak patterns different to those observed for the Ni-containing alloys (i.e. M2S, M4S, and M5S). The dissimilarities in the peak patterns comprise new and disappearing peaks, difference in

peak heights which reflects the fraction of the precipitated phase, and shifting in the transformation temperature. According to the DSC cooling curves, the Ni-free M1S and M3S alloys, shown in Figure 4.1(a) and Figure 4.1 (c), start to solidify with the formation of the α-Al dendritic network, at ~590°C (Reaction 1), earlier than that observed in the Ni-containing M2S, M4S and M5S alloys, shown in Figure 4.1(b), Figure 4.1(d), and Figure 4.1(e), where the α-Al dendritic network precipitates at lower temperatures of ~580-584°C. The precipitation of the Al-Si eutectic structure and Fe-rich phases denoted by Reaction 2 takes place at ~556°C for the Ni-free alloys and at 548-552°C for the Ni-containing alloys. These observations may highlight the retarding effects of Ni addition on the kinetics of precipitation of the α-Al network, and the eutectic Al-Si structure.

Owing to the presence of Ni in M2S, M4S, and M5S alloys, the peaks denoted by Reactions 3, 4 and 7 are only observable on the DSC cooling and heating curves of these three alloys. The reactions 3 and 4 are believed to be associated with the formation/dissolution of Al_9FeNi and Al_3Ni phases, respectively, while Reaction 7 is thought to occur in relation to the formation of Al_3CuNi phase. It is also worth noting that the peak corresponding to the formation of Mg_2Si phase (Reaction 5) is more distinct on the DSC cooling and heating curves of the base alloy M1S, at 534 and 538°C, respectively, compared to the other alloys. Nevertheless, the Mg_2Si phase was detectable in the microstructures of these alloys, from the corresponding optical micrographs and SEM images, as will be discussed in the following section.

Due to the presence of Mg in the alloys studied, transformation of some of the β-Al_5FeSi needles into the π-$Al_8FeMg_3Si_6$ phase[214] during solidification is observed (Reaction 6), in the range of ~516-522°C. The precipitation of Al_3CuNi phase (Reaction 7) takes place in the range of ~514-519°C for the Ni-containing alloys, i.e. M2S, M4S, and M5S. The formation of Al_2Cu phase (Reactions 8) is clearly noted in the DSC cooling curves of M1S and M3S alloys, at ~495°C compared to the Ni-containing alloys. Finally, the last reaction (Reaction 9), which indicates the precipitation of the Q-phase at ~485°C, is barely detectable in all the DSC cooling curves.

The addition of Ni in alloys M2S, M4S, and M5S results in the consumption of a considerable amount of the strengthening copper in forming Al_3CuNi, as previously established by Mohamed and Samuel[165] and Hernandez-Sandoval *et al.*[194] This observation may also be understood from the DSC cooling and heating curves by observing the peaks corresponding to Reactions 7, 8, and 9. The peaks corresponding to Reaction 7 during formation and dissolution are clearly observed in the case of the Ni-containing M2S, M4S, and M5S alloys (Figure 4.1(b), Figure 4.1(d), and Figure 4.1(e)). On the other hand, the peaks corresponding to the formation and dissolution of Al_2Cu phase, Reaction 8, are distinctly higher in the curves of the Ni-free alloys, i.e. in M1S and M3S alloys (Figure 4.1(a) and Figure 4.1(c)), compared to the Ni-containing M2S, M4S, and M5S alloys. This observation implies that a relatively higher volume fraction of Al_2Cu phase presents in the Ni-free alloys compared to the Ni-containing alloys, which emphasises the consumption of a considerable amount of Cu in forming the Al_3CuNi phase in the presence of Ni.

For M4S alloy with 4 wt.% Ni, the superimposing of Reactions 2, 3, and 4 results in a distinctly high peak as may be observed in Figure 4.1(d). The precipitation of eutectic Al-Al_3Ni is expected to result from the addition of 4 wt.% Ni in alloy M4S as may be inferred from the Al-Ni phase diagram, Figure 2.26, where the eutectic point can be spotted at ~5 wt.% Ni and 640°C. This probable precipitation of Al-Al_3Ni might play an important role in increasing the height of the peak which is referring to the mutual formation of eutectic Al-Si and Al-Al_3Ni, and Al_9FeNi phase; the precipitation of this phase will be investigated in the microstructure observations section.

The data listed in Table 4.1 show some variations in the phase transformation temperatures between cooling and heating cycles for the same phase. For example, in the base alloy M1S, the formation temperature of the α-Al dendritic network is found to be 590 °C whereas the melting temperature of the same phase for the same alloy is found to occur at a somewhat higher temperature of 595°C. This temperature difference may be understood in light of the undercooling effect during the solidification which may arise because of the change from heating to cooling cycle. Similar observations are reported by Shaha[14] regarding this variation in formation and dissolution temperatures of the same phase within the same alloy. Evidently, the reported solidification and dissolution sequences in this study match to a large extent the sequences previously reported in investigations[11-14, 212] for similar alloy systems.

Table 4.1 Proposed main reactions occurring during solidification/melting of the investigated alloys (see Figure 4.1) compared to thermal analysis of other studies[12, 14, 24, 54, 69, 210, 211]

Reaction #	Peak temperature using thermal analysis (°C) [12, 14, 24, 54, 69, 210, 211]	Possible phase transformation during solidification and melting	Average peak temperature observed during solidification (°C)					Average peak temperature observed during melting (°C)				
			M1S	M2S	M3S	M4S	M5S	M1S	M2S	M3S	M4S	M5S
1	**600-597**	**- α-aluminum dendritic network**	590 ±0.8	584 ±0.7	590 ±0.6	581 ±1	580 ±1.1	595 ±0.5	585 ±1.3	595 ±0.7	588 ±1.3	587 ±0.6
2	**560-558**	**- Al-Si eutectic - post-eutectic β-Al_5FeSi phase - α-$Al_{15}(Fe, Mn)_3Si_2$ phase for Mn-containing alloys**	556 ±1.2	552 ±1	557 ±0.9	548 ±1.1	551 ±0.8	576 ±0.7	567 ±0.8	574 ±0.9	572 ±1.1	568 ±0.6
3	**555-556**	**- Al_9FeNi phase**	-	545 ±0.9	-	546 ±0.9	540 ±1.4	-	564 ±1.1	-0.5	570 ±0.9	565 ±1.4
4	**546-553**	**- Al_3Ni phase**	-	545 ±0.8	-	545 ±0.7	540 ±1.6	-	561 ±1.4	-	570 ±1.3	565 ±1.2
5	**540-538**	**- Mg_2Si phase**	534 ±0.9	535 ±1.2	540 ±1	534 ±1.2	538 ±1.2	538 ±1.1	560 ±0.7	558 ±1.2	559 ±0.7	561 ±0.8
6	**525-523**	**- Transformation of β-phase into π-$Al_8Mg_3FeSi_6$ phase**	516 ±1.1	517 ±0.7	516 ±0.7	522 ±1.3	516 ±0.8	520 ±0.7	535 ±1.3	538 ±0.5	542 ±1.1	535 ±1.3
7	**523-520**	**- Al_3CuNi phase**	-	514 ±0.8	-	519 ±1.5	516 ±1.3	-	535 ±0.4	-	541 ±1.1	535 ±1.4
8	**500-496**	**- eutectic Al-Al_2Cu phase**	496 ±0.7	497 ±0.8	494 ±0.8	502 ±1.1	496 ±0.8	507 ±1.4	507 ±1.2	507 ±1	512 ±0.8	507 ±0.7
9	**485-489**	**- Q-$Al_5Mg_8Cu_2Si_6$ phase**	485 ±0.9	486 ±1.4	485 ±0.7	486 ±0.9	486 ±1.3	-	-	-	-	-

(a) Alloy M1S

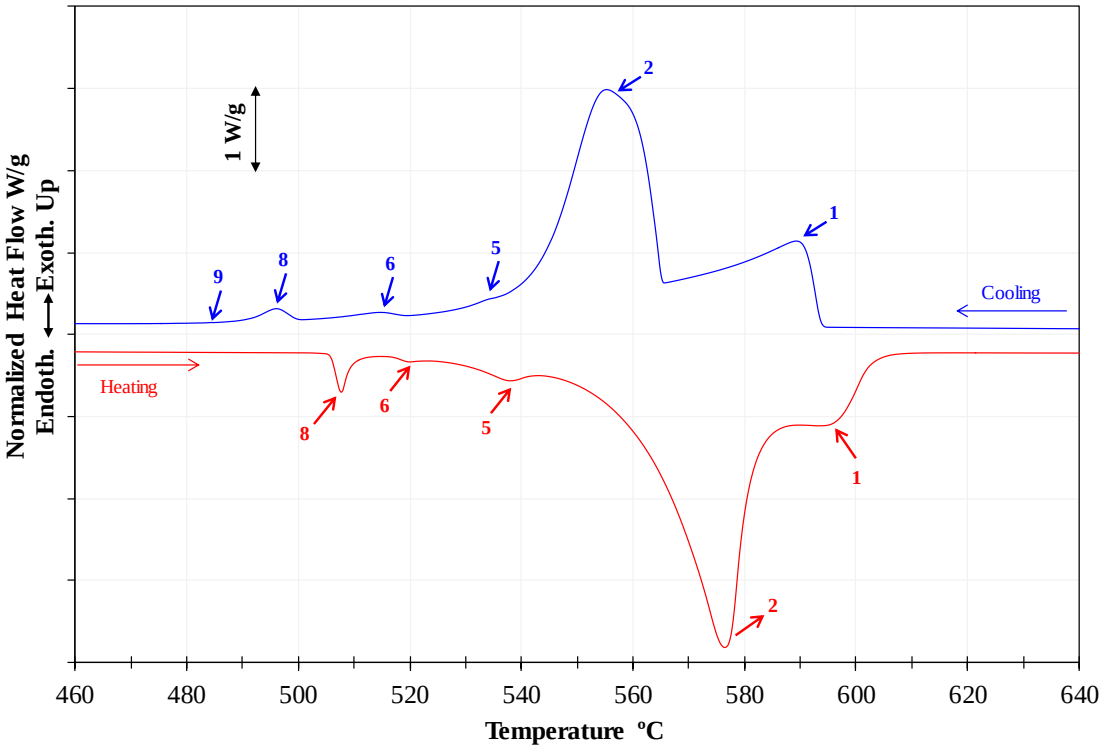

(b) Alloy M2S

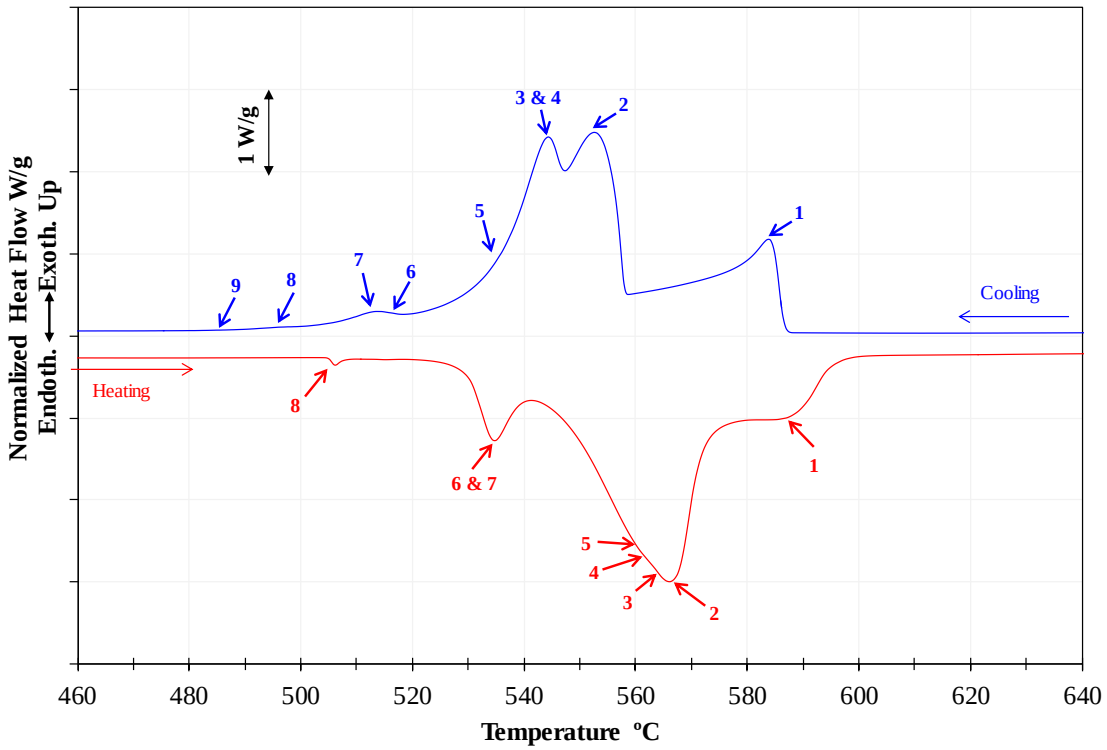

(c) Alloy M3S

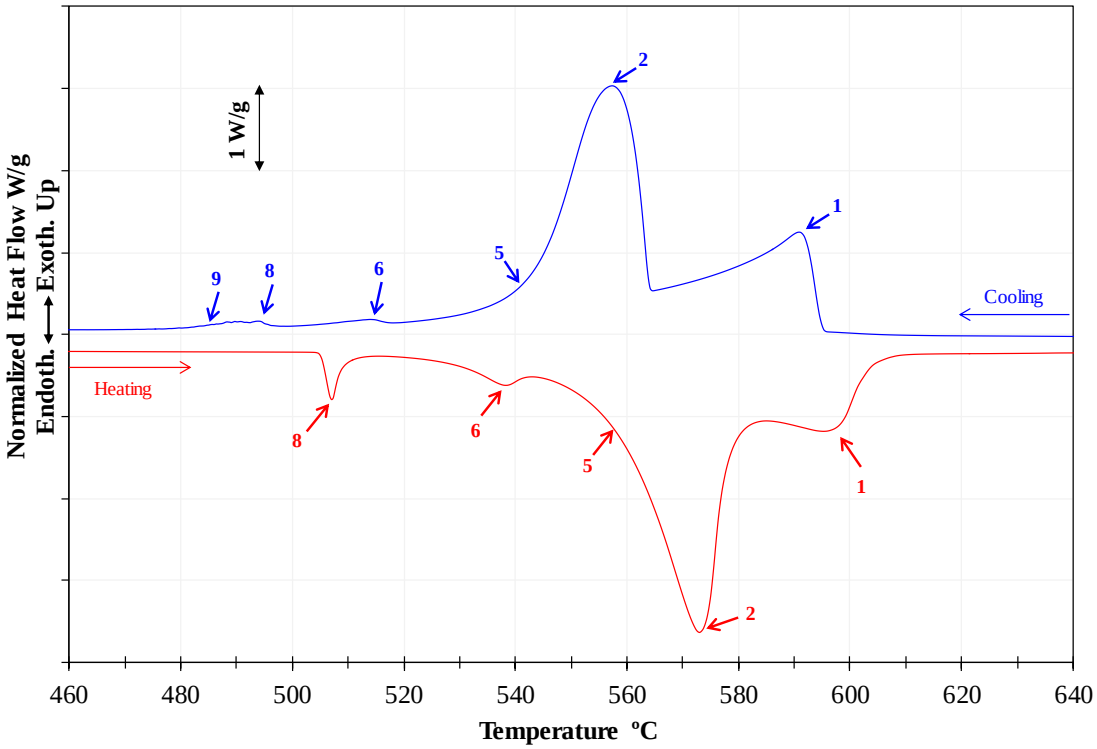

(d) Alloy M4S

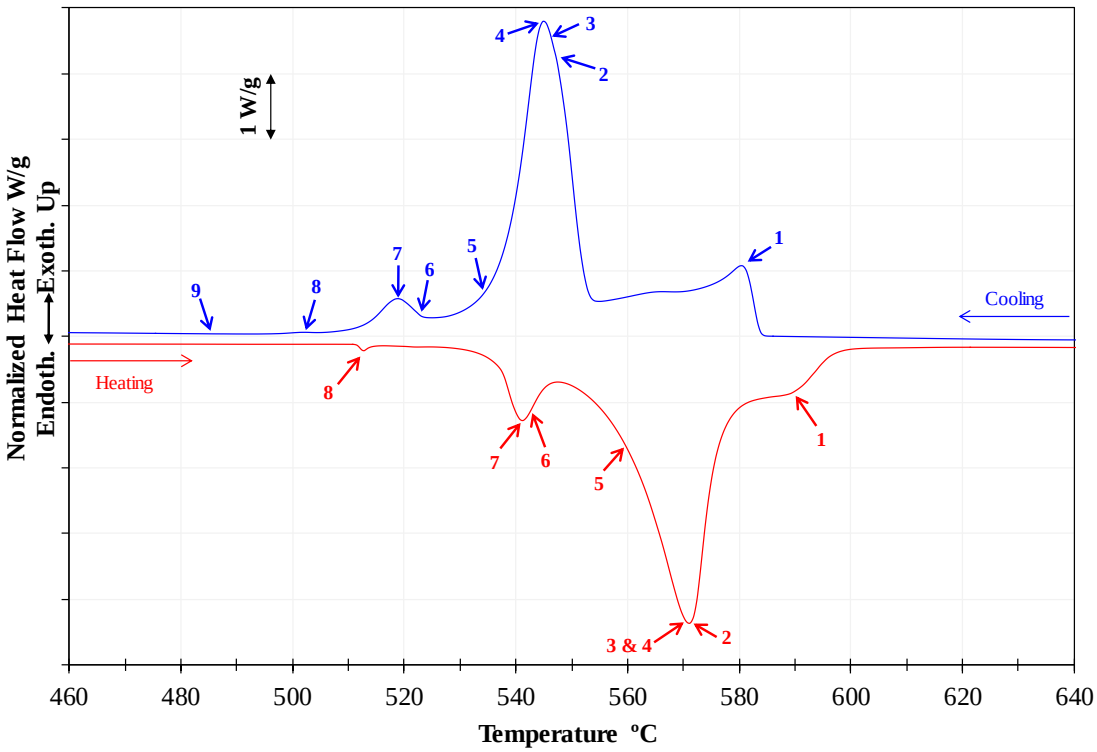

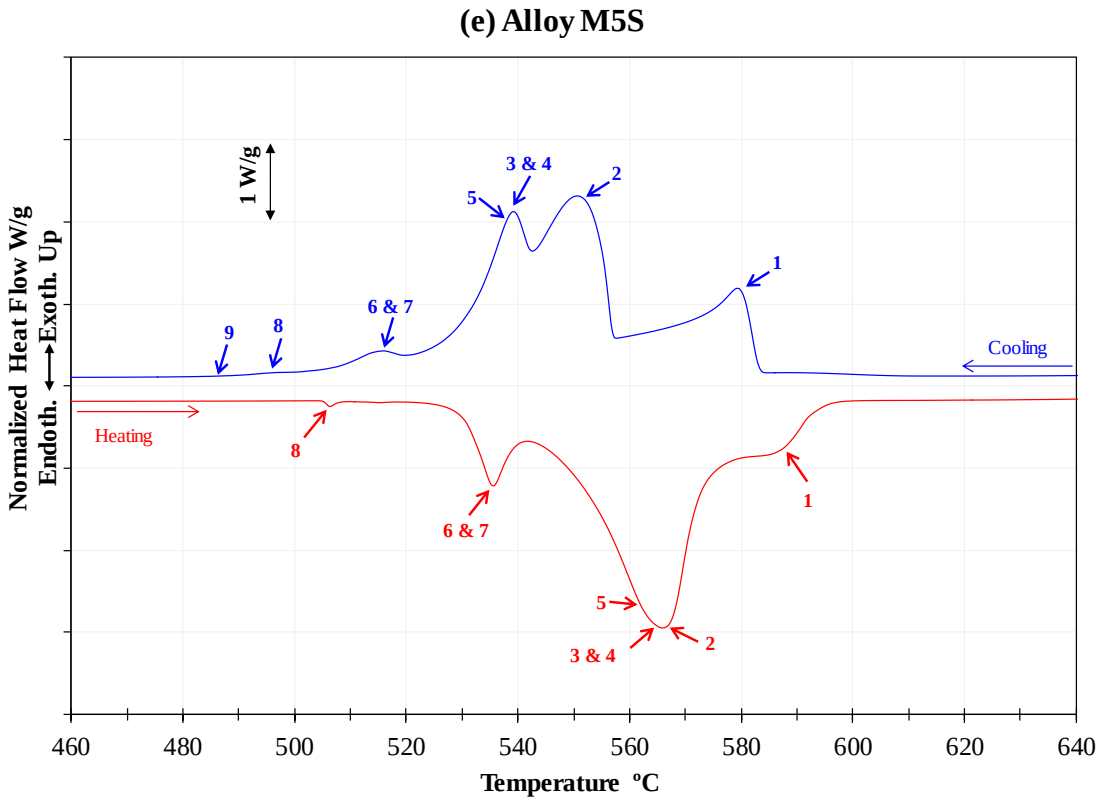

Figure 4.1 DSC heating and cooling (solidification) curves of: (a) M1S, (b) M2S, (c) M3S, (d) M4S, and (e) M5S alloys. The numbers on the curves refer to the phase transformation (Table 4.1).

The DSC heating curves for the alloys studied were also examined in order to identify the melting point of the Al_2Cu phase, to help in selecting an appropriate solutionizing temperature for the alloys, without the risk of incipient melting. The DSC heating curves portrayed in Figure 4.1along with Table 4.1 show that the melting point of the Al_2Cu phase for the studied alloys lies in the range 507-512°C. Accordingly, a conservative solutionizing temperature of 495°C was selected for the studied alloys. Following the selection of the solutionizing temperature (495°C), the effectiveness of the solutionizing parameters, *viz.* temperature and time, in dissolving the Al_2Cu phase in the α-

Al matrix was assessed, by investigating the DSC heating curves of the alloys in as-cast and as-quenched conditions.

Figure 4.2 shows the DSC heating curves of the alloys in the as-cast and as-quenched conditions, where three distinct peaks numbered 1 to 3 can be easily detected. Since the objective here is to determine the influence of solutionizing parameters on the dissolution of Al_2Cu in the α-Al matrix, only peak 1 will be assessed based on its height which could be adopted to represent the amount of the phase present. Thus, for each alloy, the difference between the heights of peak 1 in the as-cast and as-quenched conditions reveals the effectiveness of the solutionizing treatment on dissolving the Al_2Cu phase; the higher the height difference, the higher the dissolved phase amount and the effectiveness of the solutionizing treatment should prove to be.

From Figure 4.2, it is apparent that the height of peak 1 in the as-cast condition for the M1S and M3S alloys is considerably higher than that in the case of the Ni-containing M2S, M4S, and M5S alloys. As mentioned previously, this results from the consumption of a considerable amount of Cu in forming the Al_3CuNi phase in the presence of Ni. The height of peak 1 is substantially reduced in alloys M1S and M3S after applying solution treatment at 495°C for 5 hours, as may be discerned from Figure 4.2(a) and Figure 4.2(c), which emphasizes the high dissolution of the Al_2Cu phase in the alloy matrix following this solution treatment. A very limited amount of Al_2Cu phase remains undissolved in the alloy structure after solutionizing, as a result of which the presence of peak 1 in the DSC heating curves of the as-quenched M1S and M3S alloys is barely noticeable. In contrast, in the Ni-containing M2S, M4S, and M5S alloys (Figure 4.2 (b), Figure 4.2(d), and Figure 4.2(e)),

peak 1 almost completely disappears after solutionizing. This may be attributed to the fact that the Al_2Cu phase originally exists in these alloys in a little amount in the as-cast condition due to the formation of the Al_3CuNi phase instead.

It is important to highlight that the melting peaks shift towards higher temperatures after solutionizing. This observation may be ascribed to a possible alteration in the thermodynamic characteristics of the phases that would affect their melting points. This alteration could be due to the fragmentation and/or variations in the stoichiometric composition of the phases during solution treatment.[215]

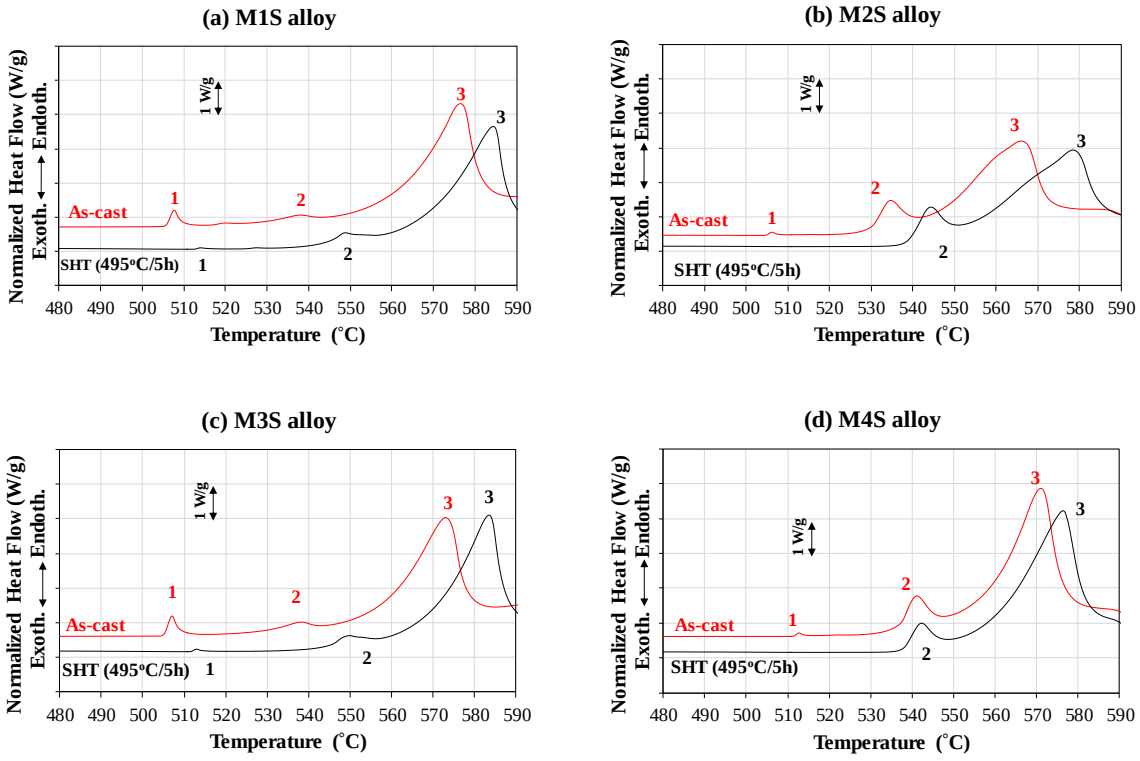

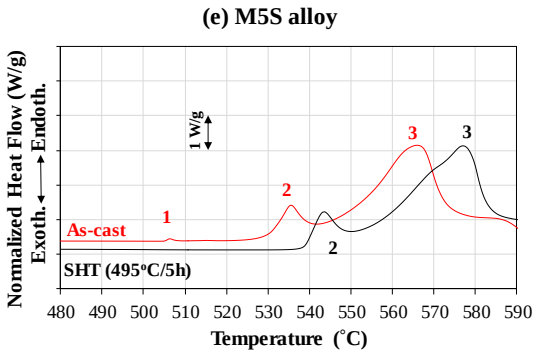

Figure 4.2 Portion of the DSC heating curves of as-cast and as-quenched samples of: (a) M1S, (b) M2S, (c) M3S, (d) M4S, and (e) M5S alloys.

In order to confirm the reaction peaks observed/defined on the DSC cooling curves, the following subsection will elaborate on the microstructural observations corresponding to these alloy samples/conditions.

4.2.1 EFFECT OF ALLOYING ELEMENTS ON ALLOY STRUCTURE

In this study, the melt was superheated up to 800°C in order to make sure that the Zr-rich compounds from the master alloy (i.e. Al-15 wt.% Zr) were dissolved. Garza-Elizondo[11] stated that the detrimental coarse Zr-rich phases observed in his study for similar alloys may have originated from the master alloy used because the Zr-containing alloys were located in the L-Al_3Zr region during the melting stage of the alloys, so that the Al_3Zr particles were not dissolved in the melt and provided favorable nucleation sites for the formation of Zr- and Ti- intermetallic phases from the melt during solidification.[148, 153] Therefore, further investigation of the existing phases in the present alloys was undertaken to reveal the effects of superheating and the slight increase in the Zr content, cf. 0.3 wt.% to 0.25 wt.% in Garza-Elizondo,[11] in relation to the phases formed. The phases detected in the

alloys studied (M1S through M5S), their suggested formulae as reported in the literature, [11, 12, 14, 194, 212] and their morphologies are listed in Table 4.2.

The following subsections will elaborately discuss these phase. For each alloy condition, optical microscopy was used to observe the dominant 354 alloy phases including α-Al and eutectic Si; whereas, backscattered imaging and EDS analysis were used to identify new phases resulting from the additives used.

Table 4.2 Summary of the existing phases in the alloys studied detected using SEM/EDS analysis

No.	Suggested phase	Phase morphology	Observed in Alloy/s
1	α-aluminum	Dendritic network	All the five alloys
2	Eutectic silicon particles	Both fibrous and acicular platelet-type	All the five alloys
3	Al_2Cu	Block-like	All the five alloys
4	$Al_5Cu_2Mg_8Si_6$	Chinese-script and block-like	All the five alloys
5	Mg_2Si	Chinese-script	All the five alloys
6	β-Al_5FeSi	Needle-like	All the five alloys
7	α-$Al_{15}(Fe,Mn)_3Si_2$	Block-like and Chinese-script	M3S, and M5S
8	$(Al,Si)_3Zr$	Needle-like	M1S
9	$(Al,Si)_3(Ti,Zr)$	Needle-like and platelet-like	M1S, and M3S
10	Al_9FeNi	Block-like	M2S, and M4S
11	Al_3Ni	Block-like, Chinese-script, eutectic form	M2S, and M5S
12	Al_3CuNi	Needle-like	M4S
13	$Al_9FeSi_3Ni_4Zr$	Platelet-like	M2S, M4S, and M5S

4.2.1.1 BASE ALLOY M1S (354 + 0.3% Zr)

The predominant phases that exist in alloy M1S are illustrated in the optical micrograph and BSE image shown in Figure 4.3(a) and Figure 4.3(b), respectively, whereas EDS spectra corresponding to intermetallic phases observed in the BSE image are displayed in Figure 4.3(c) through Figure 4.3(g). The optical micrograph (Figure 4.3(a)) reveals α-Al dendrites separated by modified and partially modified eutectic silicon colonies. The BSE image shows other existing phases in a better visualization owing to the varying degree of their gray color.

As can be seen from Figure 4.3(b), the Al_2Cu phase exists in the block-like form due to the presence of Mg which promotes copper segregation to localized areas so that the blocky Al_2Cu forms rather than the finer eutectic-like Al_2Cu particles.[36] The needles of the Fe-rich β-Al_5FeSi phase are easily observed, surrounded by the blocky Al_2Cu particles. It has been reported that the β-phase needles act as favorable nucleation sites for the Al_2Cu phase.[102] The Mg-rich Q-phase ($Al_5Cu_2Mg_8Si_6$) is also observed as small particles associated with the Al_2Cu phase.

The coarse Zr-rich phases (such as: $Al_3(Ti,Zr)$), which were regularly spotted and reported in Garza-Elizondo's work,[11] are hardly spotted in the alloy structure in the current study. This can be ascribed to the beneficial effect of the melt superheating before casting which allows for the efficient dissolution of Al_3Zr phase particles from the Al-15% Zr master alloy in the melt. The coarse Zr-containing phases are, therefore, rarely detected in the analysis because the undissolved Al_3Zr particles were reported to act as nuclei for theses coarse phases.[11] Therefore, the beneficial effect of melt superheating with respect to

the dissolution of the Al_3Zr particles, originated from the master alloy, in the melt could also make the precipitation of the desirable, fine Zr-containing phases much achievable during the solidification stage.

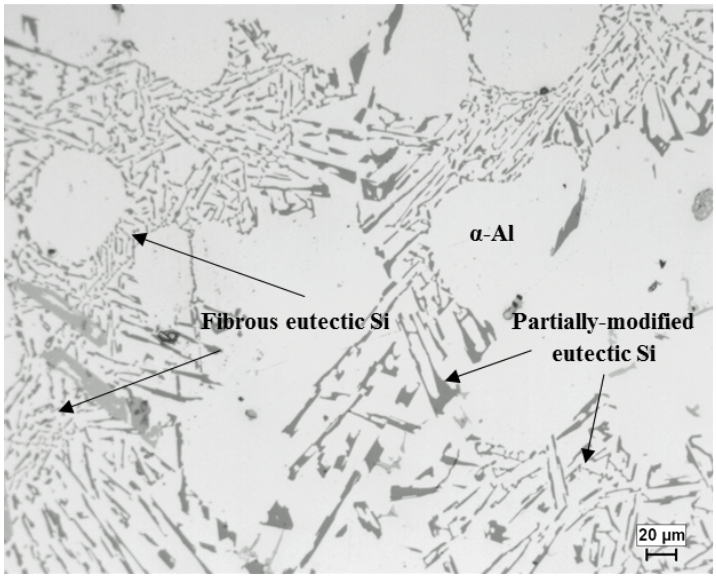

(a)

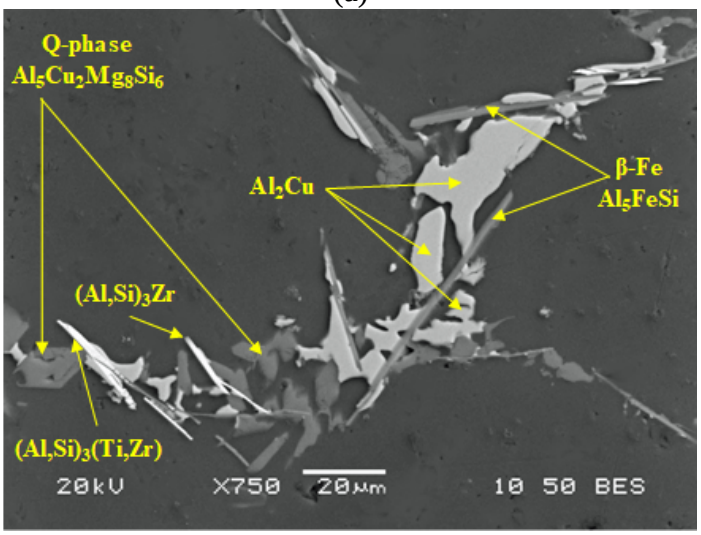

(b)

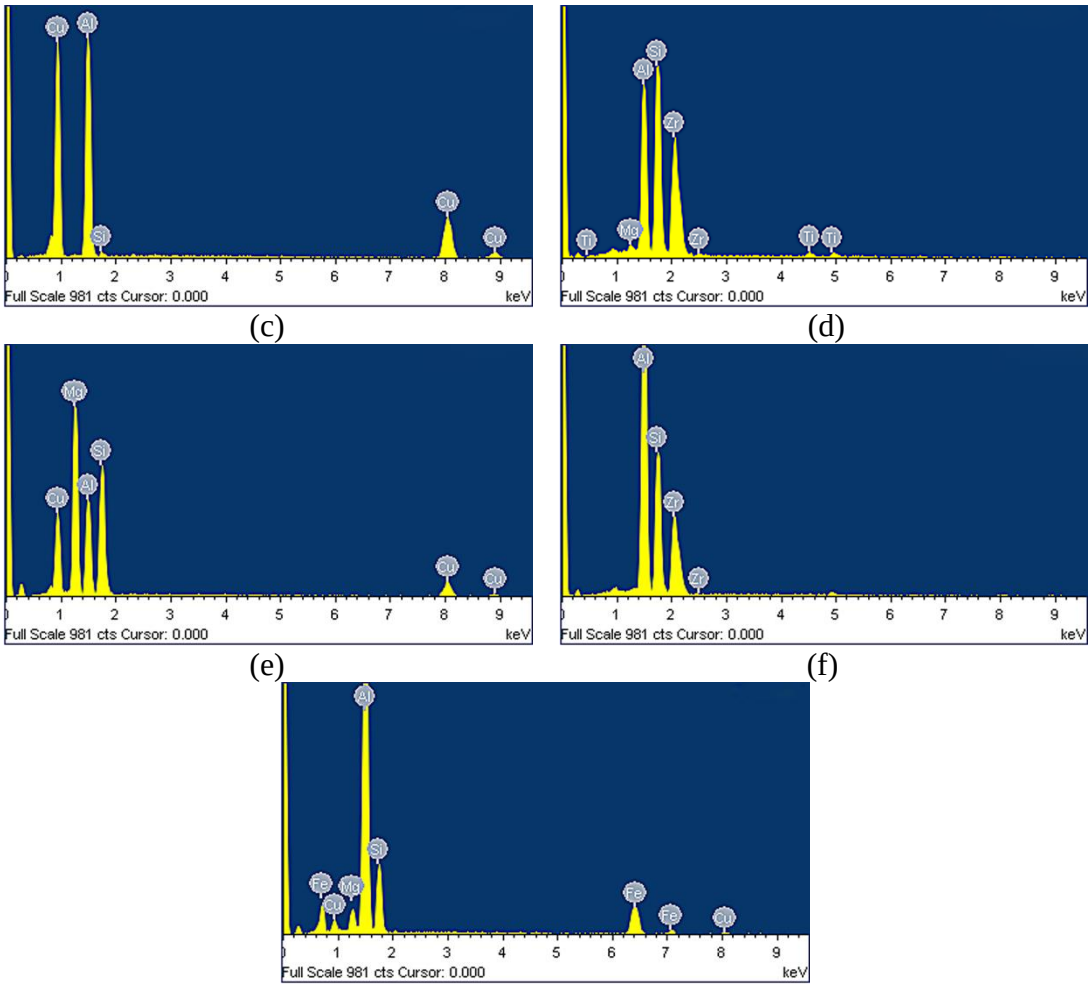

Figure 4.3 (a) Optical micrograph at 200X magnification, and (b) backscattered electron image of M1S (354+ 0.3wt.% Zr) alloy, obtained at low cooling rate of 0.35 °C/s, showing the different phases present in the alloy; (c-f) EDS spectra corresponding to Al_2Cu, $(Al,Si)_3(Ti,Zr)$, Q-$Al_5Mg_8Cu_2Si_6$, $(Al,Si)_3Zr$, and β-Al_5FeSi phases observed in (b).

4.2.1.2 ALLOY M2S (354 + 0.3% Zr + 2% Ni)

The optical micrograph of alloy M2S is shown in Figure 4.4(a), displaying main phases of the 354-type alloy, namely, the eutectic Si and the Mg_2Si, besides the primary α-Al. New intermetallic phases formed in alloy M2S due to the addition of Ni can be seen in the BSE image shown in Figure 4.4(b). These include the Al_9FeNi and Al_3Ni phases existing in both script and platelet forms, in addition to, Al_3CuNi and $Al_9FeSi_3Ni_4Zr$ phases.

The β-Fe and π-Fe phases were rarely detected in the alloy microstructure, which may suggest the possible consumption of their Fe content in forming the Al_9FeNi and $Al_9FeSi_3Ni_4Zr$ phases. As mentioned previously in section 4.2, the Mg_2Si particles were clearly detected, as evidenced from Figure 4.4(a) and Figure 4.4(b) despite the fact that the related formation peak was not distinctly displayed by the DSC cooling curve of alloy M2S (Figure 4.1(b)). EDS spectra corresponding to selected intermetallic phases shown in Figure 4.1(b) are illustrated in Figure 4.4(c) through Figure 4.4(g).

Coarse Zr-containing phases were also rarely detected in this alloy as was the case for the base M1S alloy. As stated previously, the complete dissolution of the Al_3Zr particles during the melt superheating and the consequent absence of the coarse Zr-containing phases could promote the precipitation of fine dispersoids of Al_3Zr during solidification. In order to investigate the existence of these dispersoids, higher magnification SEM imaging was used along with EDS X-ray mapping. Figure 4.5 shows a higher magnification BSE image taken from the M2S alloy and the corresponding X-ray maps. The BSE image clearly shows bright Al_3CuNi particles, whereas the X-ray color maps display the distribution of different alloying elements. The Zr distribution displayed in Figure 4.5(g) reveals that Zr is finely distributed and embedded in the matrix at the nano-scale, which emphasizes the possible formation of fine precipitates capable of resisting softening at elevated temperatures.

It can, therefore, be understood that the majority of Zr is consumed in forming these fine dispersoids instead of coarse phases, which act as crack initiators due to their needle-

like nature, and consequently the mechanical performance of these alloys could be improved.

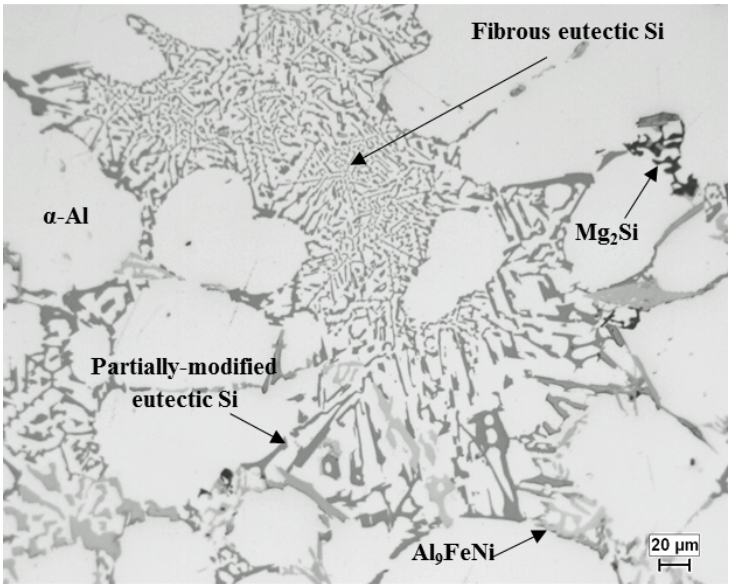

(a)

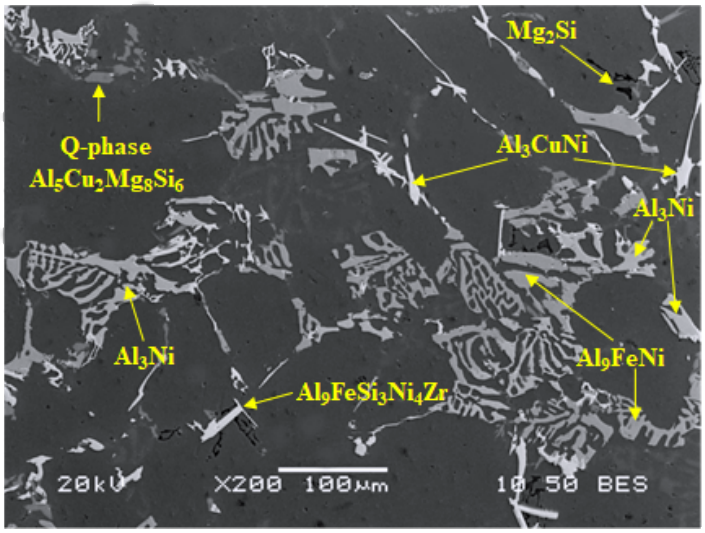

(b)

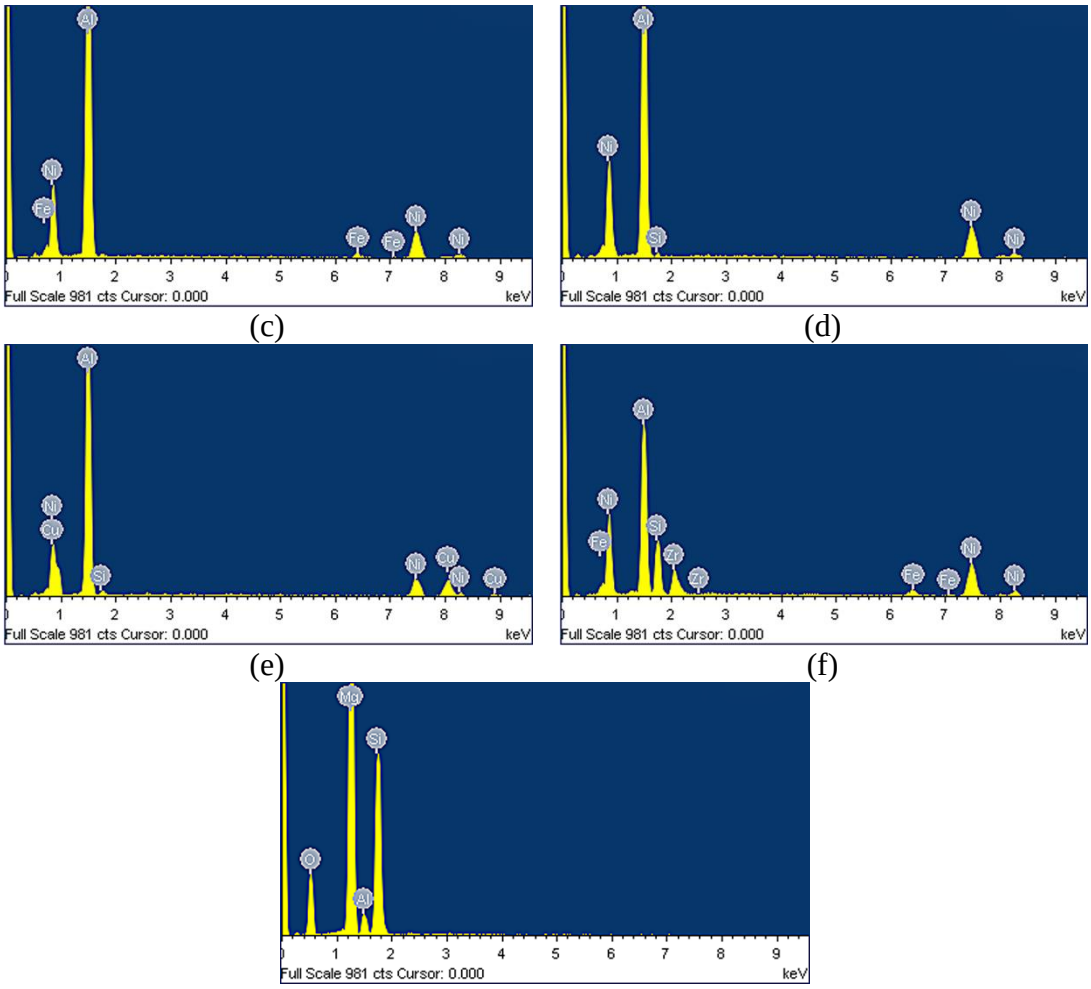

Figure 4.4 (a) Optical micrograph at 200X magnification, and (b) backscattered electron image of M2S (354+ 0.3 wt.% Zr+ 2 wt.% Ni) alloy, obtained at low cooling rate of 0.35 °C/s, showing the different phases present in the alloy; (c-g) EDS spectra corresponding to Al_9FeNi, Al_3Ni, Al_3CuNi,$Al_9FeSi_3Ni_4Zr$, and Mg_2Si phases observed in (b).

(a)

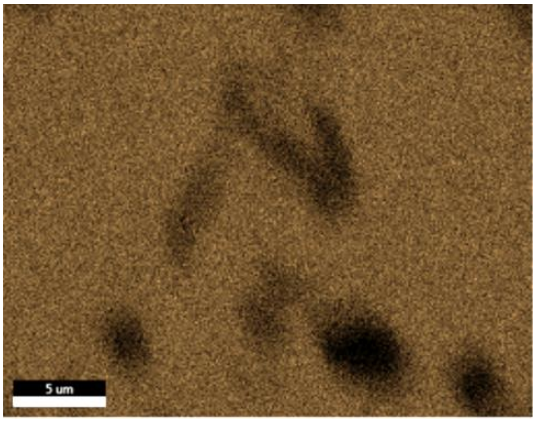

(b) Al

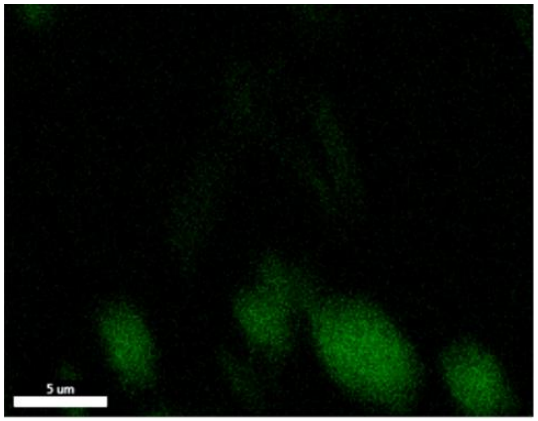

(c) Si

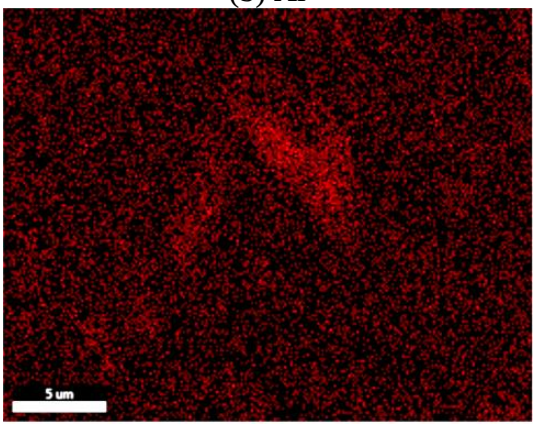

(d) Cu

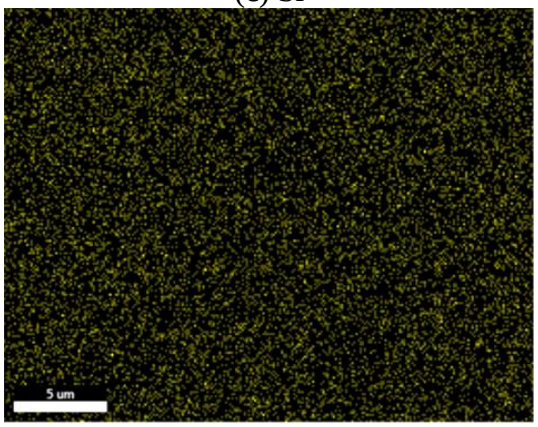

(e) Mg

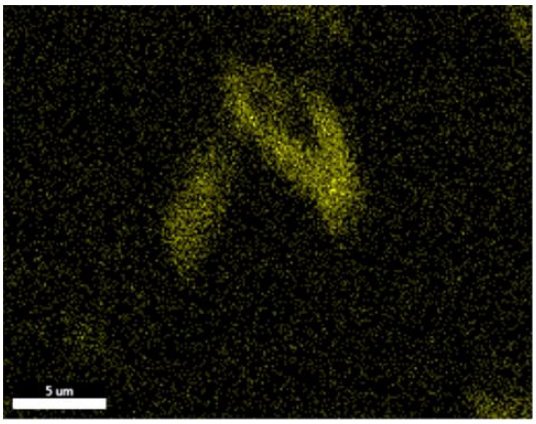

(f) Ni

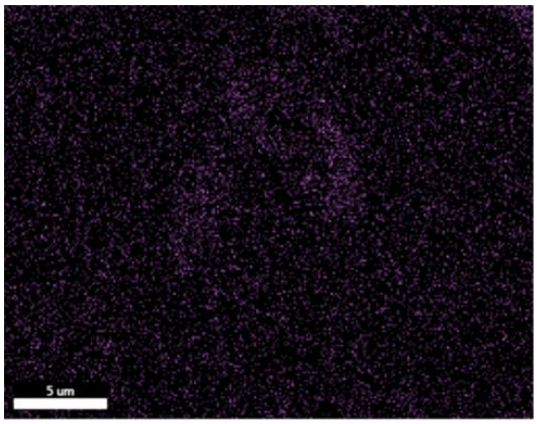

(g) Zr

Figure 4.5 (a) Backscattered electron image of alloy M2S (M1S+ 2 wt.% Ni) alloy, and (b) through (g) corresponding X-ray maps showing distribution of elements in (a).

4.2.1.3 ALLOY M3S (354 + 0.3% Zr + 0.75%Mn)

The addition of 0.75 wt.% Mn to the base alloy, i.e. alloy M3S, results in transforming some of the needles of the β-Al_5FeSi iron phase into the less detrimental α-$Al_{15}(Fe,Mn)_3Si_2$ phase. The α-$Al_{15}(Fe,Mn)_3Si_2$ iron phase appears as script-like and polygonal sludge particles, as can be seen in the optical micrograph and the BSE images shown in Figure 4.6(a) through Figure 4.6(c), respectively. It is well established that the sludge particles commonly form in Al-Si alloys in the presence of Mn, Fe, and Cr and/or at a high Mn/Fe ratio, with the composition of $Al_{15}(Fe,Mn,Cr)_3Si_2$ or α-$Al_{15}(Fe,Mn)_3Si_2$ in the absence of Cr.[76, 212] Due to the high level of Mn in M3S alloy, the sludge particles in the form of α-$Al_{15}(Fe,Mn)_3Si_2$ were frequently observed in the structure of this alloy. Figure 4.6(d) and Figure 4.6(e) show the EDS spectra obtained from the script-like and sludge particles of α-$Al_{15}(Fe,Mn)_3Si_2$ iron phase in Figure 4.6(b) and Figure 4.6(c), respectively.

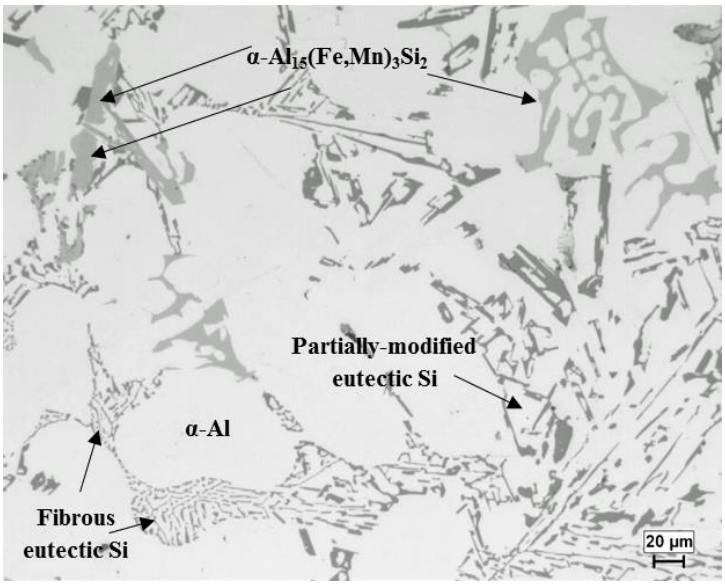
α-Al15(Fe,Mn)3Si2
Partially-modified
eutectic Si
α-Al
Fibrous
eutectic Si
20 μm

(a)

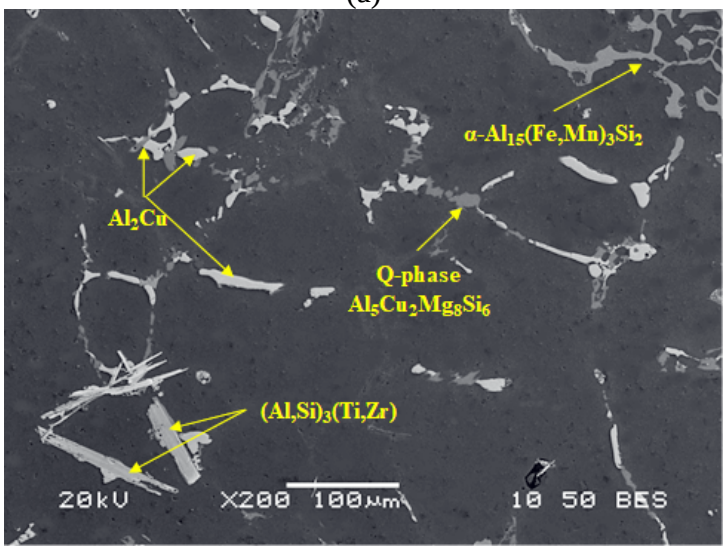
α-Al15(Fe,Mn)3Si2
Al2Cu
Q-phase
Al5Cu2Mg8Si6
(Al,Si)3(Ti,Zr)
20kV X200 100μm 10 50 BES

(b)

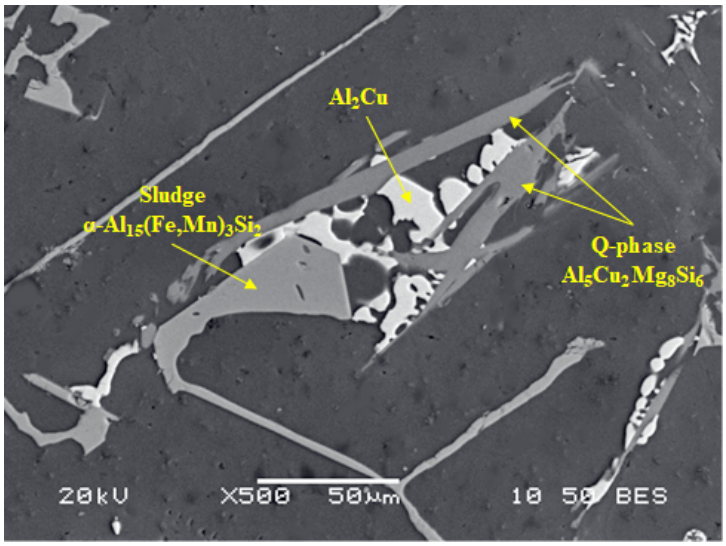

(c)

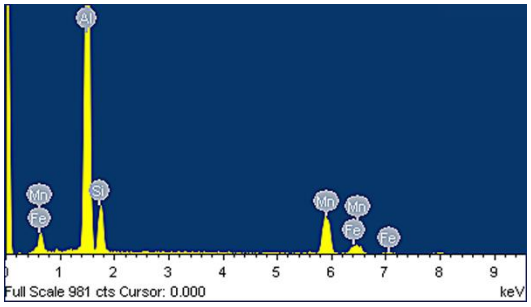

(d)

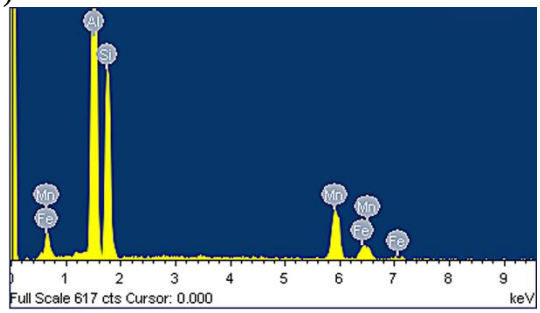

(e)

Figure 4.6 (a) Optical micrograph at 200X magnification, and (b and c) backscattered electron image of M3S (354+ 0.3 wt.% Zr+ 0.75 wt.% Mn) alloy, obtained at low cooling rate of 0.35 °C/s, showing the different phases present in the alloy; (d and e) EDS spectra corresponding to script-like and sludge forms, respectively, of α-$Al_{15}(Fe,Mn)_3Si_2$ phase observed in (b) and (c), respectively.

4.2.1.4 ALLOY M4S (354 + 0.3% Zr + 4% Ni)

The level of Ni is raised to 4 % in the M4S alloy compared to 2 % in the M2S alloy. Almost the same phases observed in the M2S alloy are also present in the M4S alloy, as can be seen in the optical micrograph and BSE image shown in Figure 4.7(a) and Figure 4.7(b), respectively. However, the Al_3Ni phase exists also in a eutectic form besides the blocky and script forms observed in the M2S alloy. The formation of this eutectic structure in the M4S alloy can be attributed to the increased Ni content of this alloy (4%)

which is close to its contents in near-eutectic Al-Ni alloys. As can be seen from the Al-Ni phase diagram shown in Figure 2.26,[31] the eutectic reaction occurs at about 5 wt.% Ni and 640°C. The Al_3Ni eutectic consumes a major part of the added Ni, and finely distributes in the interdendritic regions of α-Al which is believed to enhance the alloy strength at elevated temperature. Selected EDS spectra for certain phases are shown in Figure 4.7(c) through Figure 4.7(e).

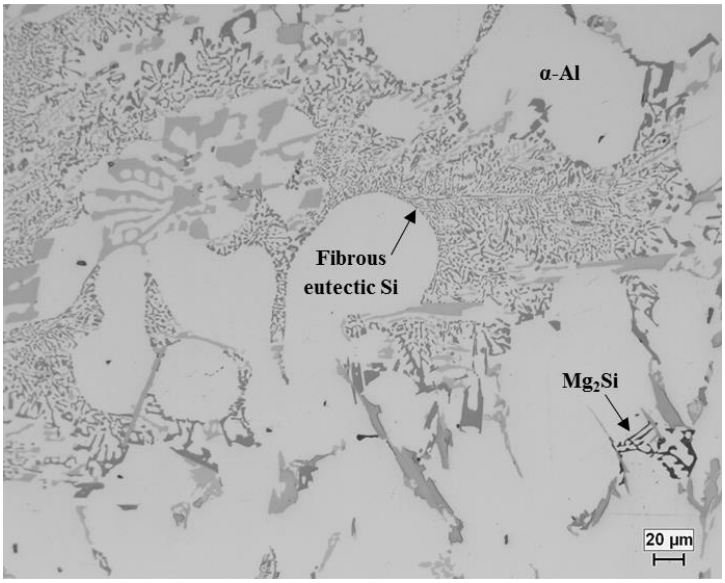

(a)

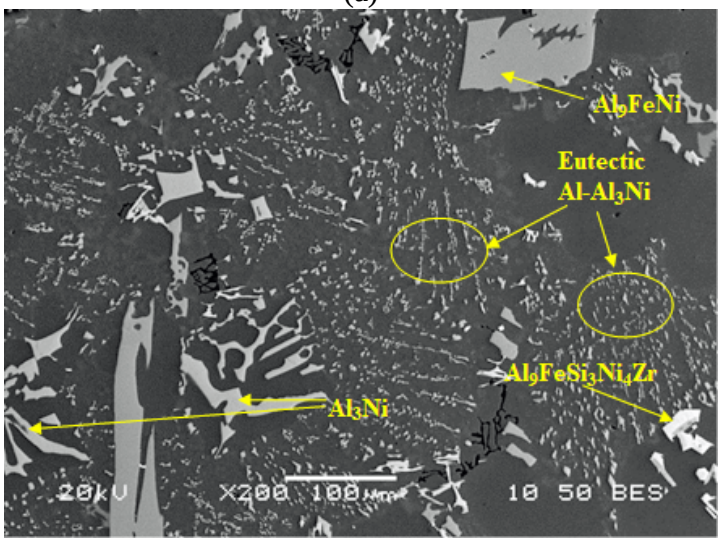

(b)

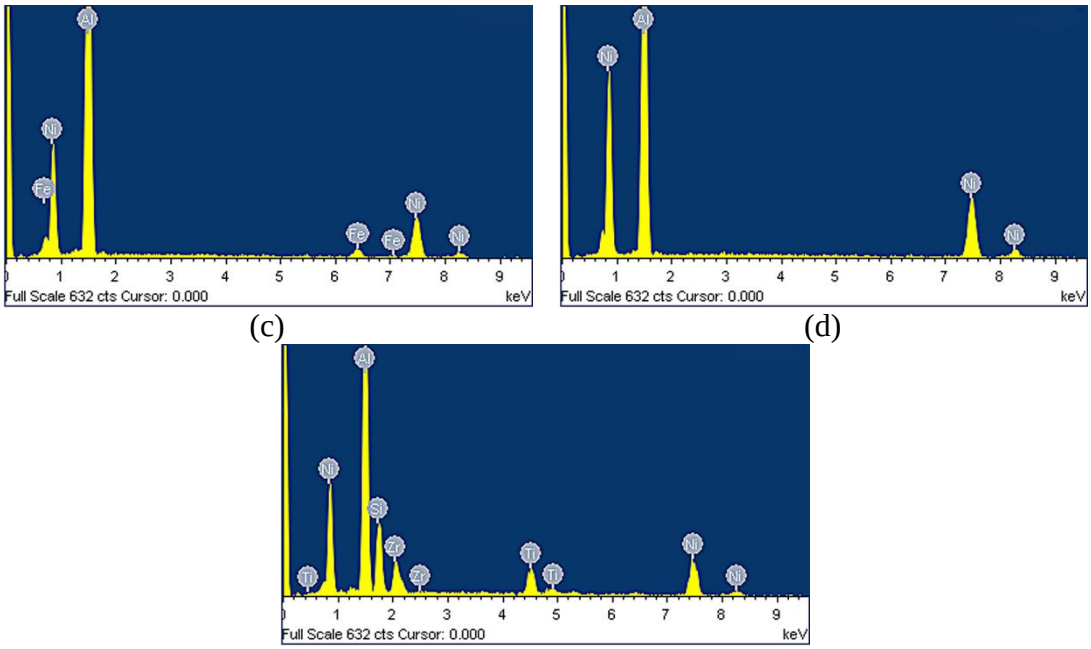

Figure 4.7 (a) Optical micrograph at 200X magnification, and (b) backscattered electron image of M4S (354+ 0.3 wt.% Zr+ 4 wt.% Ni) alloy, obtained at low cooling rate of 0.35 °C/s, showing the different phases present in the alloy; (c-e) EDS spectra corresponding to Al_9FeNi, Al_3Ni, and $Al_9FeSi_3Ni_4Zr$ phases observed in (b).

4.2.1.5 ALLOY M5S (354 + 0.3% Zr + 2% Ni + 0.75% Mn)

The optical micrograph and the BSE image of alloy M5S are shown in Figure 4.8(a) and Figure 4.8(b), respectively. Apart from the predominant phases (α-Al and eutectic Si particles) observed in the interdendritic regions, other phases may also be observed in the microstructure. As mentioned previously, in the context of alloy M3S, the addition of 0.75 wt.% Mn neutralizes the effect of Fe through the formation of the less harmful α-$Al_{15}(Fe,Mn)_3Si_2$, in the form of script-like particles and/or sludge particles at the expense of the harmful β-Al_5FeSi phase needles/platelets.

During the examination of the M5S alloy, the Al_9FeNi phase was hardly observed in the alloy microstructure in contrast to the case of alloy M2S, which contains the same Ni content (2 wt.%). This infrequent observation of the Al_9FeNi phase may be understood in view of the fact that the iron is consumed in forming the Fe-rich β-Al_5FeSi, α-$Al_{15}(Fe, Mn)_3Si_2$, and π-$Al_8FeMg_3Si_6$ phases. The EDS spectra for a number of the intermetallic phases detected in M5S alloy are shown in Figure 4.8(c) through Figure 4.8(e).

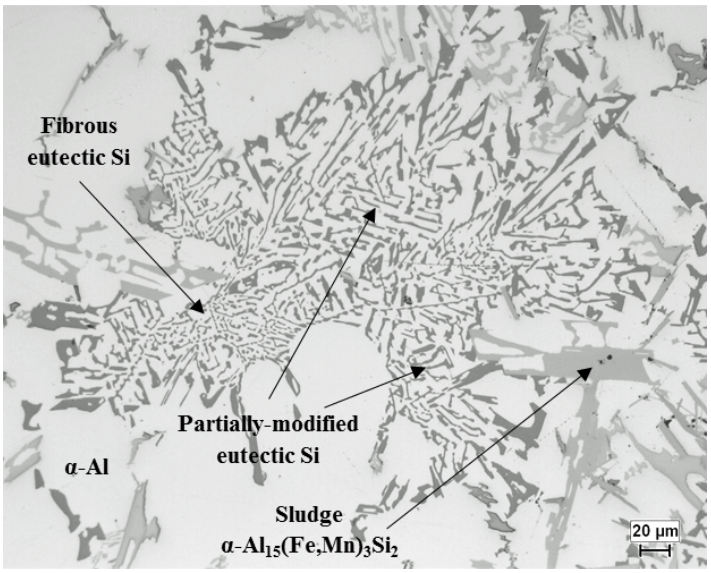

(a)

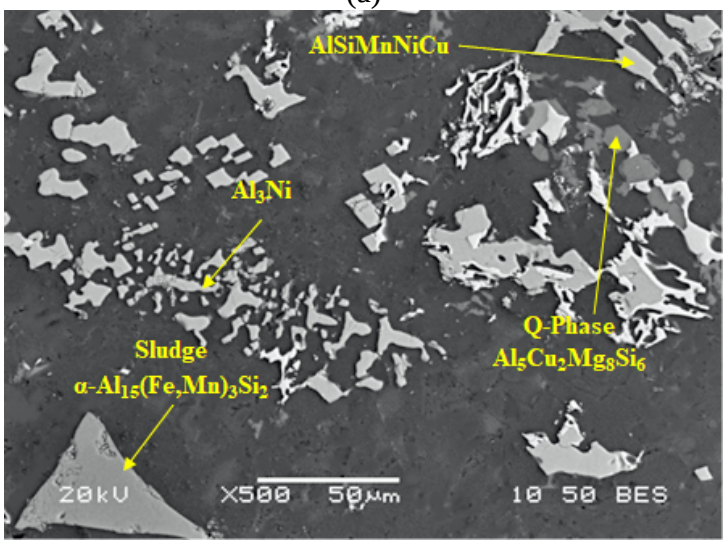

(b)

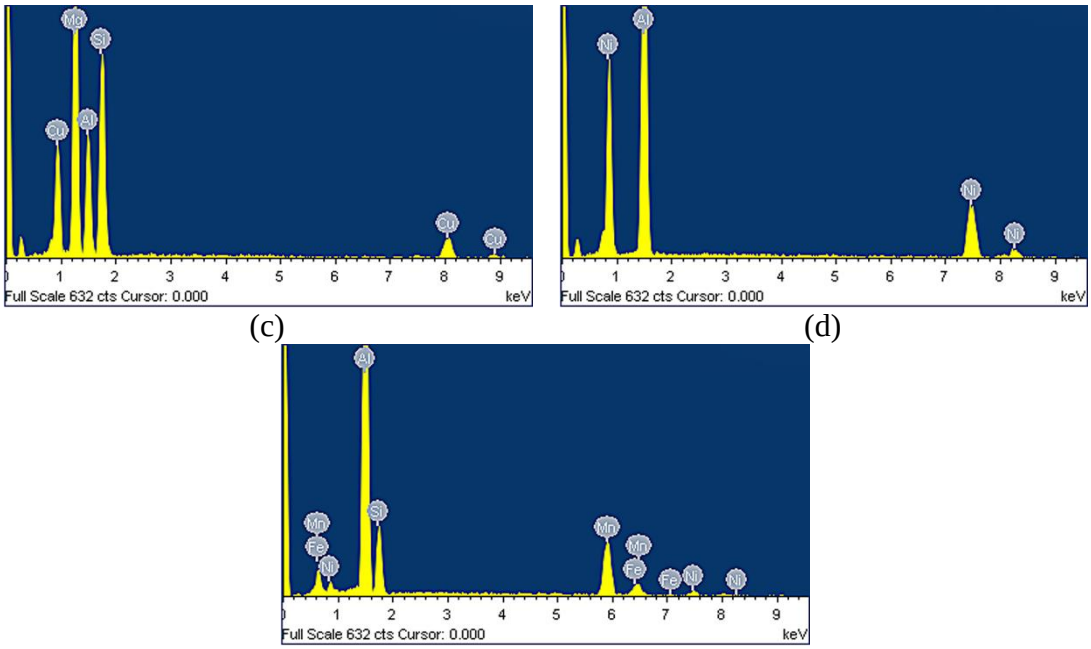

Figure 4.8 (a) Optical micrograph at 200X magnification, and (b) backscattered electron image of M5S (354+ 0.3 wt.% Zr+ 2 wt.% Ni+ 0.75 wt.% Mn) alloy, obtained at low cooling rate of 0.35 °C/s, showing the different phases present in the alloy; (c-e) EDS spectra corresponding to Q-$Al_5Mg_8Cu_2Si_6$, Al_3Ni, and sludge (α-$Al_{15}(Fe,Mn)_3Si_2$ phases observed in (b).

4.3 CHARACTERIZATION OF THE STRENGTHENING PRECIPITATES

It is a well-established fact that the mechanical performance of Al-Si-Cu-Mg cast-alloys enhances exceptionally after applying proper heat treatment procedures owing to the formation of coherent fine particles capable of hindering the dislocation gliding. The presence of both Cu and Mg in this category of alloys has an advantageous effect on improving the response to the applied heat treatment; however, their presence complicates the understanding of the precipitation-hardening process because of the probable formation of multiple types of precipitates.[108-111] With respect to the alloys under investigation, it is important to identify the active strengthening precipitates in the presence of various additions of Zr, Ni and Mn which may develop some secondary strengthening precipitates.

Combined strengthening effects of θ-Al_2Cu, and/or Q-$Al_5Mg_8Cu_2Si_6$, and/or S-Al_2CuMg, and/or β-Mg_2Si phases are thought to be responsible for making this category of Al-Si cast-alloys very responsive to heat treatments; however limited published data are describing this multi-strengthening effect.[216-218] This section in Chapter 4 of the present study addresses the characteristics of active strengthening precipitates which exist in the microstructure of the investigated alloys.

The solutionizing temperature used in this investigation is selected conservatively to be 495°C which is considerably low to dissolve the large particles of Mg_2Si phase in order to form the β-Mg_2Si fine dispersoids and their precursors.[38, 219, 220] Additionally, the dissolution peaks of Mg_2Si phase observed in Figure 4.2(a) through Figure 4.2(e) are more or less with the same characteristics showing no variations between as-cast and as-quenched conditions for each alloy. The latter observation indicates that the solutionizing treatment did not dissolve Mg_2Si particles partially or completely and hence the same amount exists in the as-cast and as-quenched conditions. Consequently, β-Mg_2Si fine precipitates and their precursors are not expected to be acting as strengthening dispersoids in the investigated alloys.

The formation of Q-$Al_5Mg_8Cu_2Si_6$ precipitates and their precursors were observed and reported by a number of authors[99, 221-226] for Al-Si-Cu-Mg wrought-alloys, as well as for cast-alloys.[227] However, the dissolution of this phase is not detectable in the DSC heating curves in Figure 4.2, because this phase is considered to be sluggish. Accordingly, the precipitation of the Q-$Al_5Mg_8Cu_2Si_6$ phase as fine particles is not expected in the microstructure of the investigated alloys, similar to β-Mg_2Si precipitates.

Based on the aforementioned, the combined strengthening effect, if exists, will be attributed to the presence of both θ-Al_2Cu and S-Al_2CuMg fine dispersoids. This hypothesis matches the knowledge from the ternary Al-Cu-Mg phase diagram shown in Figure 4.9. The red star shown in the ternary phase diagram (Figure 4.9) denotes the chemical composition of the alloys studied which is located on the boundary of α+θ+S phase field.

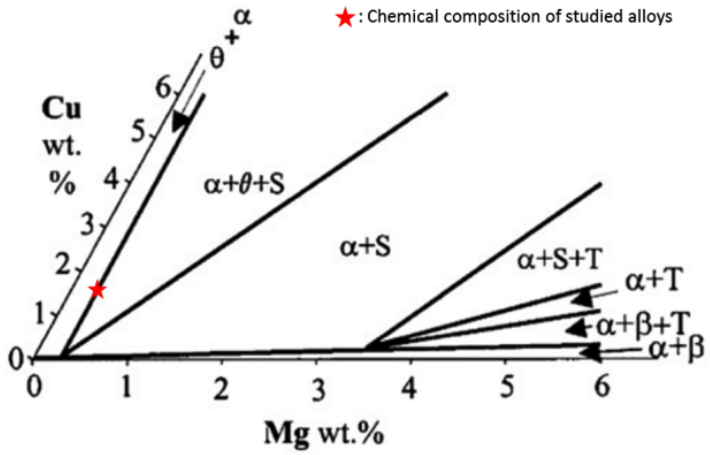

Figure 4.9 Isothermal section of the ternary Al-Cu-Mg phase diagram at 200°C.[228]

In the following subsections, the identification and characteristics of the active strengthening precipitates will be investigated using differential scanning calorimetry (DSC) and transmission electron microscopy (TEM).

4.3.1 DSC HEATING CURVES OF AS-QUENCHED SAMPLES

The strengthening precipitates are developed in the microstructure of age-hardenable alloys after applying artificial aging treatment. For investigation and research purposes, this aging treatment can be simulated using non-isothermal DSC heating runs for

as-quenched samples from age-hardenable alloys. This practice allows the detection of the precipitation (exothermic reactions) and dissolution (endothermic reactions) of the precipitates and their precursors by identifying the peaks on the DSC heating curves as well as their characteristics.

Figure 4.10 shows the average DSC heating curves obtained for as-quenched samples from the investigated alloys, M1S through M5S, at a heating rate of 10 °C min^{-1}. The DSC thermograms of the five alloys reveal more or less the same four exothermic reactions, A, B, C, and D, and the two endothermic reactions A', and D'; however, variations in the characteristics of those peaks per alloy can be observed. In the current subsection, the detectable reactions from DSC heating curves (Figure 4.10) will be identified in accordance to the previous published literature;[99, 114, 215, 229-233] then this identification will be verified using TEM investigations in the following subsection.

The exothermic peak A, shown in Figure 4.10, seems to be a broad peak (100-170°C) due to the overlapping of two exothermic peaks which possibly correspond to the formation of both GP and GPB zones. Whereas, the small endothermic peak A' taking place at ~200°C, probably, may be related to the dissolution of GP and GPB zones. Peak B can be attributed to the formation of S-Al_2CuMg phase. Upon further heating, the metastable θ', and equilibrium θ phases will precipitate producing exothermic peaks C and D, respectively. Finally, the progressively broad endothermic peak D' (360-470°C) is, possibly, associated to the dissolution of metastable θ' and equilibrium S-Al_2CuMg and θ-Al_2Cu phases.

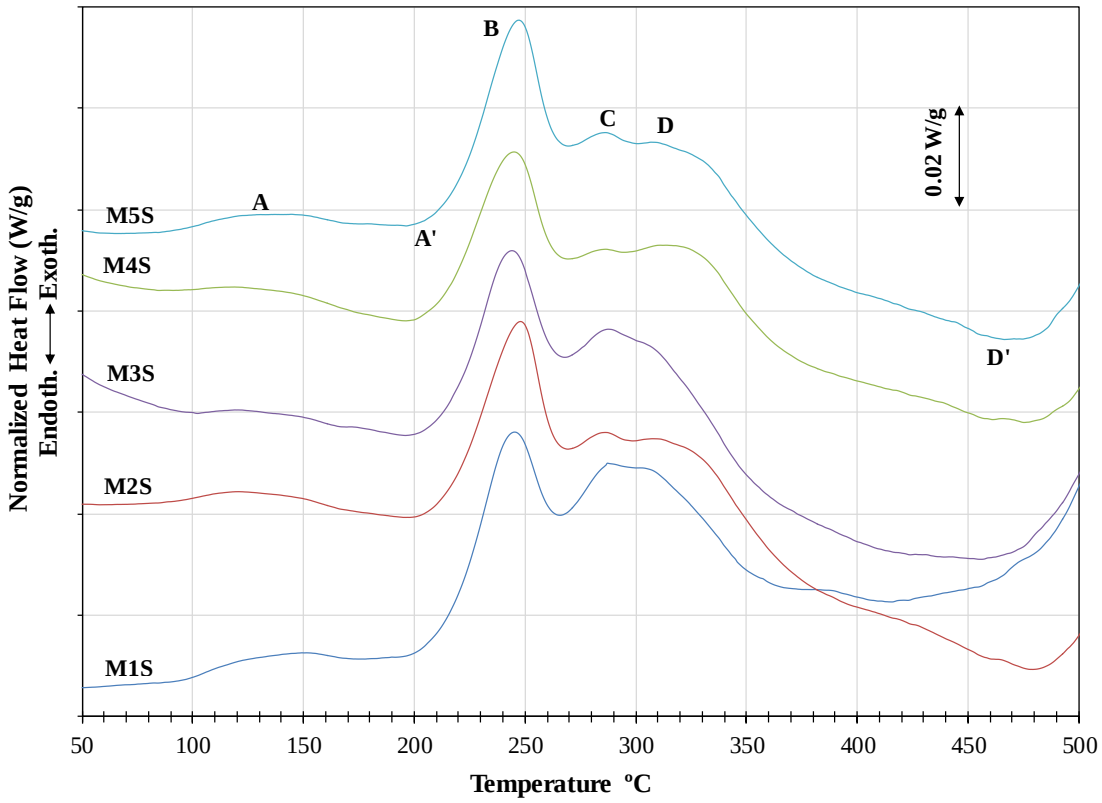

Figure 4.10 DSC heating curves of the as-quenched alloys M1S through M5S obtained at 10 °C/min.

For a better understanding of the reactions taking place during heating of as-quenched samples, it is necessary to separate the overlapped peaks in Figure 4.10, namely, A', B, C and D peaks. Peak A' seems to be overlapped with peak B but it will not be considered in the proposed peaks-separation analysis because preliminary trials of this analysis including peak A' showed negligible characteristics for this peak. Accordingly, the peaks-separation analysis considers only the overlapped peaks B, C, and D. Experimental data for these peaks can be manipulated as a superposition of three Gaussian peaks, whose centres for the base alloy M1S, as an example, are spotted at 240°, 290°, and 310°C (Figure 4.10). Origin Pro.8 software was used to carry out the peaks-separation analysis.

Figure 4.11 shows an estimation of the separated peaks, a new fitting for the overlapped peaks based on the estimated values, and the original experimental data. It is observable that the new fitted profiles are almost identical to the experimentally obtained ones as depicted in Figure 4.11 which reflects the accuracy of the peaks-separation procedure followed in this analysis.

It is known that the area under a reaction peak corresponds to the enthalpy associated with the reaction. The peak size (i.e. peak area, and height) is related to the amount –volume fraction– of the precipitated/dissolved phase during this specific reaction.[231] Table 4.3 lists the estimated area values for the three overlapped peaks, i.e. B, C, and D, per alloy. As represented in Table 4.3, the area of peak B for the five alloys shows insignificant variation. This means that the amount of the precipitated S-Al_2CuMg phase is almost constant regardless the investigated chemical composition. On the other hand, the area values of peak D show noticeable variations with respect to the alloy indicating that the equilibrium θ-Al_2Cu phase may exist in different amounts. Regarding the latter observation, this variation trend will not change if we consider the summation of the area values of peaks C and D for each alloy instead of considering peak D only. Accordingly, it is evident that the fraction of the θ-Al_2Cu phase and its precursors is dependent on the investigated chemical composition.

According to Table 4.3, alloys M1S and M3S, i.e. Ni-free alloys, contain the highest fractions of θ-Al_2Cu phase and its precursors; in contrast, amounts of metastable θ’ and equilibrium θ phases are lower in Ni-containing alloys, particularly alloy M4S. This finding emphasizes that the Ni addition consumes a considerable amount of Cu to form Al-Cu-Ni

phase and hence a lower volume fraction of the fine θ-Al_2Cu phase and its precursors precipitate which agrees with the findings of Hernandez-Sandoval *et al.*[194] and Mohamed *et al.*[165] Moreover, this observation was previously stated in section 4.2 with the evidence of DSC thermograms of the alloys studied in as-cast and as-quenched conditions (Figure 4.2).

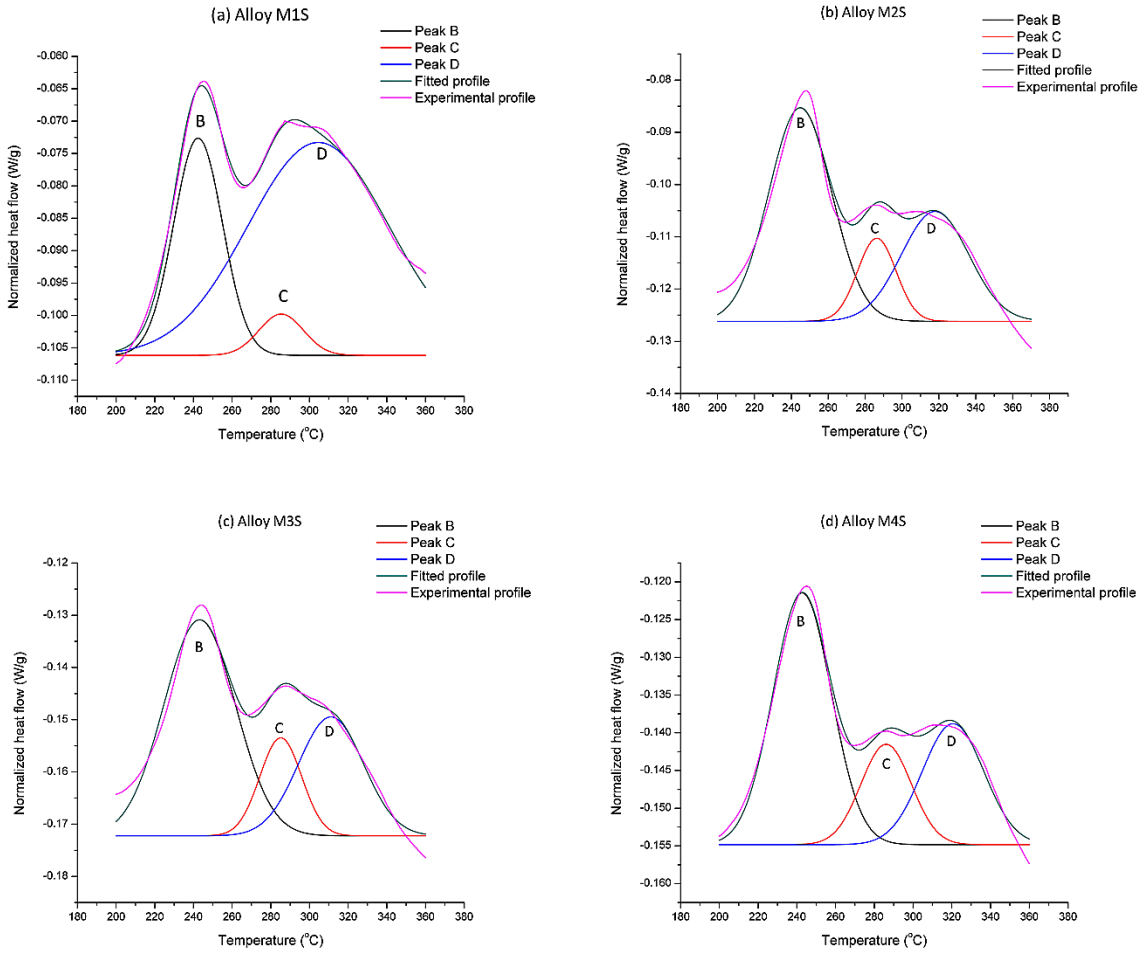

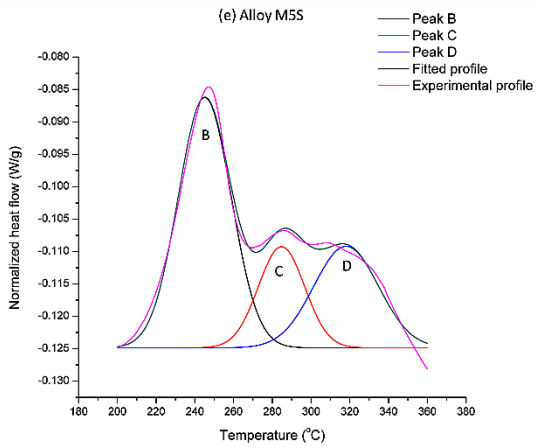

Figure 4.11 Separation of the overlapped peaks B, C, and D exist in Figure 4.10 into three Gaussian peaks for alloys: (a) M1S, (b) M2S, (c) M3S, (d) M4S, and (e) M5S.

Table 4.3 Area estimated values of the separated peaks B, C, and D shown in Figure 4.11

Peak identification	Alloys				
	M1S	**M2S**	**M3S**	**M4S**	**M5S**
B	1.30	1.60	1.70	1.25	1.30
C	0.25	0.50	0.70	0.43	0.55
D	2.20	0.96	1.20	0.64	0.70

As depicted in Figure 4.10, some of θ'-Al_2Cu phase transform into equilibrium θ-Al_2Cu phase before the end of its precipitation, in particular in alloy M1S; this explains the overlapping between peaks C and D which are believed to be correspondent to the precipitation of θ'-Al_2Cu and θ-Al_2Cu phase, respectively. For the base alloy M1S, the precipitation temperatures associated with peaks C and D are 285°C and 307°C, respectively. The various additions of Ni and Mn have insignificant effect on the precipitation temperature of the metastable θ'-Al_2Cu phase (peak C); whereas, the addition of Ni in alloys M2S, M4S, and M5S increased the precipitation temperature of the

equilibrium θ-Al_2Cu phase (peak D) to be 313°, 324°, and 316°C, respectively. Thus, it can be concluded that the Ni addition to the base alloy has a retarding effect on the formation of the strengthening precipitates in terms of the reduced amounts of available Cu for strengthening, which is considered detrimental to the mechanical properties, and increasing the precipitation temperature of the equilibrium θ-Al_2Cu phase which is believed to have a positive impact on the mechanical properties.

4.3.2 TRANSMISSION ELECTRON MICROSCOPY INVESTIGATIONS

It is apparent from the microstructural observations that the investigated alloys have complex microstructures with a wide variety of particles and precipitates exceeding those normally encountered in most cast Al-Si alloys. In addition to the observed large particles of intermetallic compounds, the presence of fine precipitates contributes in a positive way to the strength of these alloys. Transmission electron microscopy (TEM) was used to identify and investigate the characteristics of these fine precipitates; the existing precipitates may comprise primary strengthening particles, Cu- and/or Mg-containing dispersoids, and, also, to survey if secondary strengthening precipitates exist owing to the various additions made in this investigation. Furthermore, findings from TEM investigations are supposed to support the interpretation of the results obtained from DSC analysis of as-quenched samples. Samples used in TEM investigation were obtained by casting at a low cooling rate (0.35 °C s^{-1}) and they were extracted from deformation-free material.

Figure 4.12(a) shows a bright-field (BF) TEM image obtained from the base alloy M1S in T6-treated condition (SHT for 5h@495°C + quenching in warm water at 60°C + artificial aging for 8h@180°C) with electron beam parallel to the [001] zone axis. This figure shows a high density of uniformly distributed needle-like precipitates which are oriented along <110> family of directions and aligned along the {100} planes. The length of these precipitates ranges from 50 to 150 nm close to the reported size of θ'-Al_2Cu plates (50-100 nm long) reported for 319 aluminum alloys by Andrade-Gonzalez;[234] however, the observed precipitates are considered coarser than similar precipitates in the range of 12-50 nm obtained after aging for 8h at 190°C in the work of Elgallad *et al.*[215], and 35 nm long precipitates obtained after aging of alloy 319+Mg+Sr at 240°C for 8h in the investigation done by Tavitas-Medrano.[219] These precipitates are likely Al_2Cu since <110> family of directions is established to be their favorite orientation directions according to Tavitas-Medrano *et al.*[235] It is, also, evident that there are plate-like particles oriented at about 90° to the needle-like precipitates; these plate-like particles are the same phase as the needles; however, they are projected from a perpendicular direction to the one used to take this BF image.

Figure 4.12(b) represents the selected area electron diffraction (SAED) pattern obtained for BF image shown in Figure 4.12 (a). The observable discrete diffraction maxima for the precipitates in SAED pattern indicate the presence of θ'-Al_2Cu. The streaks result from the presence of fine S'-Al_2CuMg particles, most probably. Computer simulation studies[236-239] on the S'-phase reflections show that they are hidden within the streaks of θ'.

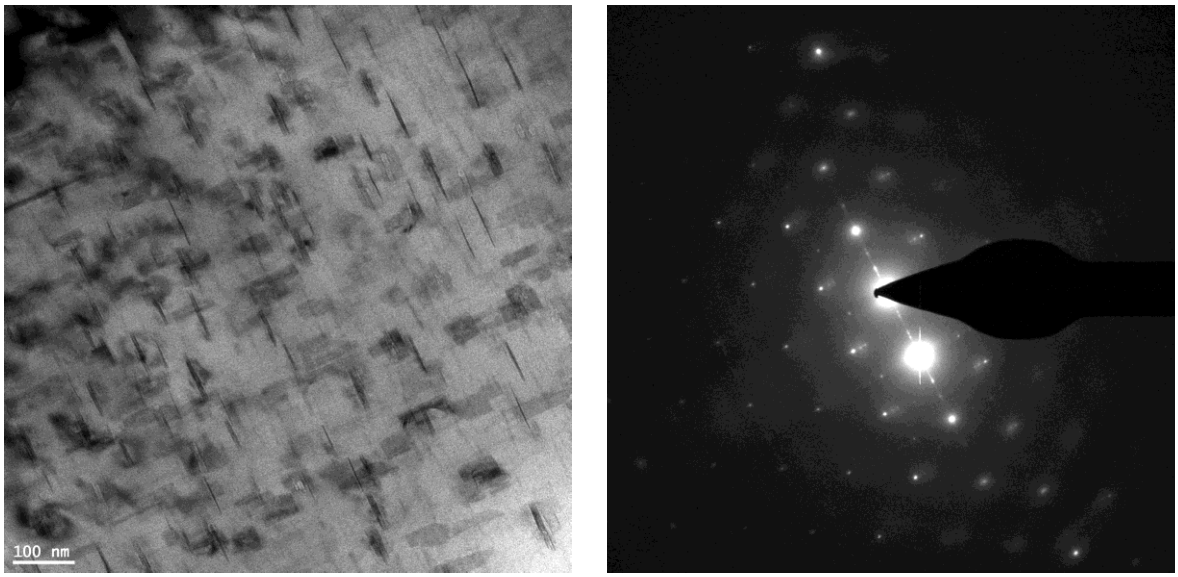

(a) (b)

Figure 4.12 (a) Bright-field TEM image of alloy M1S in T6-treated condition, and (b) the selected area electron diffraction (SAED) pattern.

Figure 4.13(a) shows a BF image for the same alloy and condition, i.e. T6-treated M1S; this image is obtained at a high magnification in order to investigate the chemical composition of the observed needle- and platelet-like particles. The corresponding EDS spectra obtained for the denoted points A through D (Figure 4.13(a)) reveal more or less the same chemical composition which means that the chemical composition of needle-like particles are the same as the platelet ones. Figure 4.13(b) displays the corresponding EDS spectrum obtained for point B shown in Figure 4.13(a) as a representative one for the other EDS spectra. By observing this spectrum, it is evident that these particles show strong reflections of Al and Cu and hence they are most likely Al_2Cu particles.

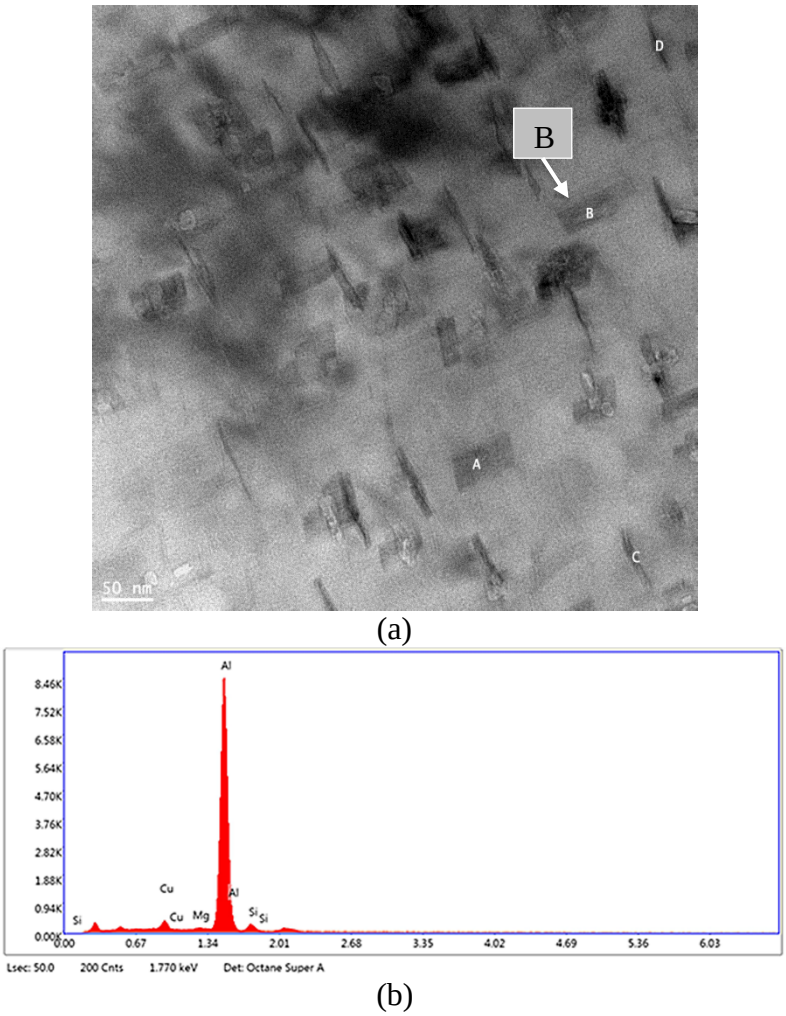

Figure 4.13 (a) Bright-field TEM image for alloy M1S in T6-treated condition, and (b) EDS spectrum corresponding to point B in (a).

The high angle annular dark field (HAADF) image, shown in Figure 4.14, portrays the morphology and distribution of the strengthening precipitates in the T6-treated base alloy (M1S). Since HAADF images are obtained in STEM mode, fine precipitates with a distinctive bright contrast are observed to be homogeneously distributed in the α-Al matrix; this contrast indicates that the constituent elements of these particles have higher atomic numbers than that of the α-Al matrix. The solid red and yellow arrows point to perpendicular needle-like precipitates. The broken yellow arrows refer to equiaxed particles which are possibly fine Si particles.

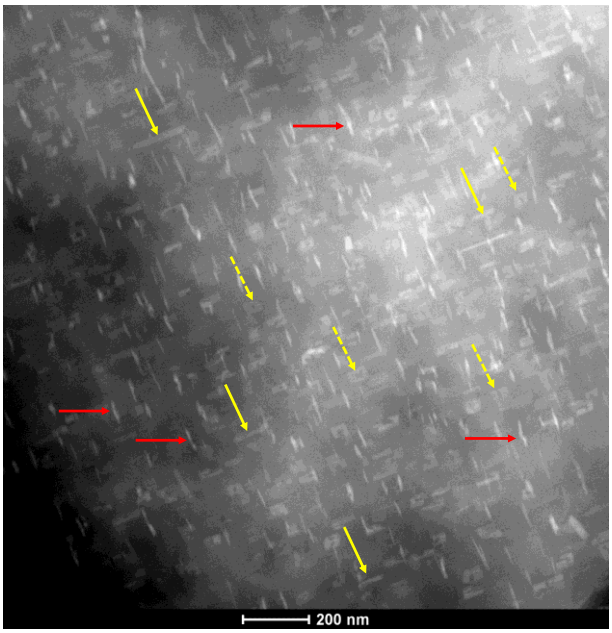

Figure 4.14 High angle annular dark field (HAADF) image obtained for the base alloy (M1S) in the T6-treated condition.

Figure 4.15(a) presents a high resolution bright-field TEM image obtained for the T6-treated base alloy M1S where the atomic planes of the α-Al matrix, Si-particle, and a needle-like particle can be clearly observed; the insert is the corresponding fast Fourier transition (FFT) pattern. This figure reveals a considerable coherency between the needle-like particle and the α-Al matrix, as indicated by the non-parallel red and blue lines, suggesting that this particle is possibly a metastable θ'-Al_2Cu. Figure 4.15(b) shows an inverse fast Fourier transition (IFFT) image for the area enclosed by the red square in Figure 4.15(a). This figure shows some of the misfit dislocations developed at the interface between the needle-like particle and the α-Al matrix due to the lattice distortion caused by the difference in the size of atoms of the particle and the Al-matrix. This distortion in the lattice structure produces coherency-strain fields, i.e. dislocations, leading to a strengthening effect. Figure 4.15(c) is a magnification for the area enclosed by the white rectangle in Figure 4.15(b) demonstrating more clearly the dislocation lines.

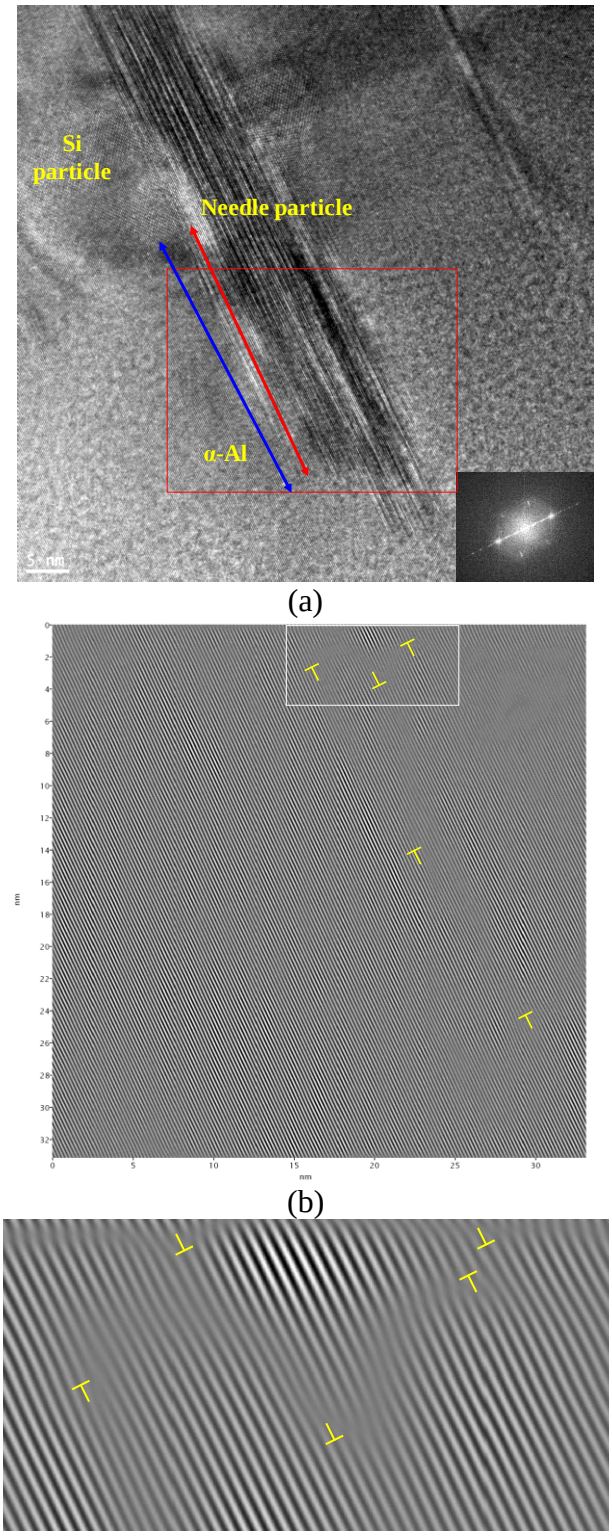

Figure 4.15 (a) High resolution bright field TEM image for the T6-treated base alloy M1S, (b) Inverse fast Fourier transition (IFFT) image for the area enclosed by the red square in (a), and (c) The enclosed area by the white rectangle in (b) at increased magnification.

Figure 4.16(a) is a bright-field TEM image showing the distribution of the precipitates in T6-treated alloy M4S (M1S+4 wt.% Ni); whereas, Figure 4.16(b) displays the SAED pattern obtained from this BF image. It is obvious that the density of the precipitates in alloy M4S is lower than that in the base alloy (Figure 4.12). This can be attributed to the considerable consumption of Cu in forming Al-Cu-Ni particles instead of θ-Al_2Cu strengthening dispersoids. Dislocation tangles appearing in Figure 4.16(a) can be ascribed to the development of dislocations due to the difference in coefficients of thermal expansion of the α-Al matrix and other microconstituents. During quenching from the high solutionizing temperature (495°C) into warm-water (60°C), the developed thermal stresses are released using these dislocations which tend to form tangles with the Si particles existing in the matrix.[122, 140, 240]

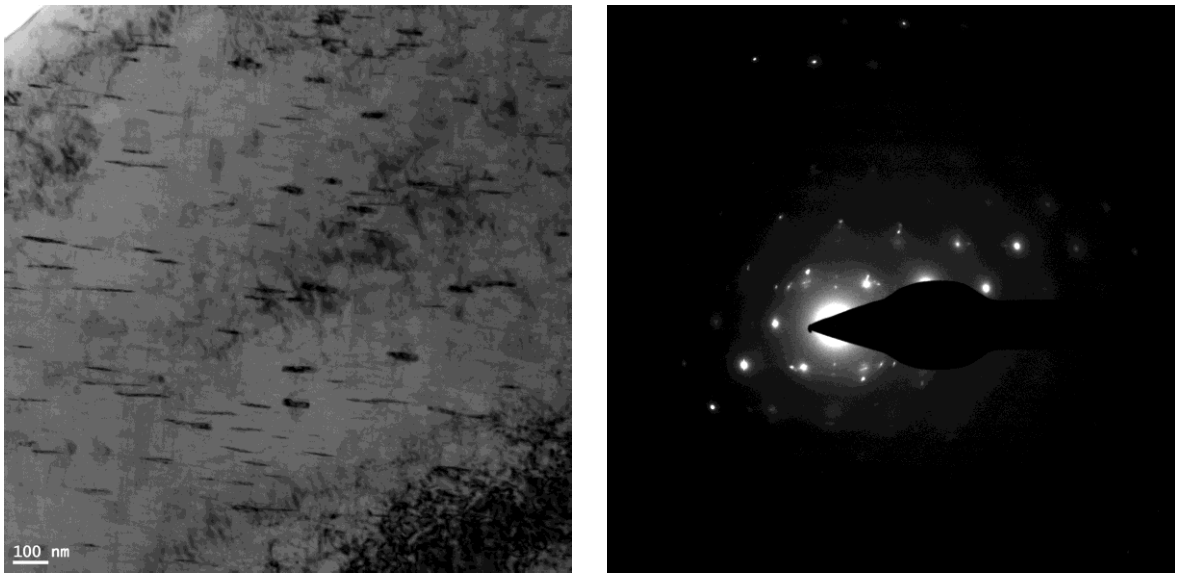

(a) (b)

Figure 4.16 Bright-field TEM image for alloy M4S in T6-treated condition, and (b) the selected area electron diffraction (SAED) pattern.

Figure 4.17(a) is a bright field TEM image shows a coarse Al-Cu-Ni particle surrounded by a precipitate free zone (PFZ) as a result to the depletion of Cu in this area due to its consumption in forming this large Al-Cu-Ni particle. Figure 4.17(b) and Figure 4.17(c) are the corresponding EDS spectra to points A and B, respectively, denoted in Figure 4.17(a).

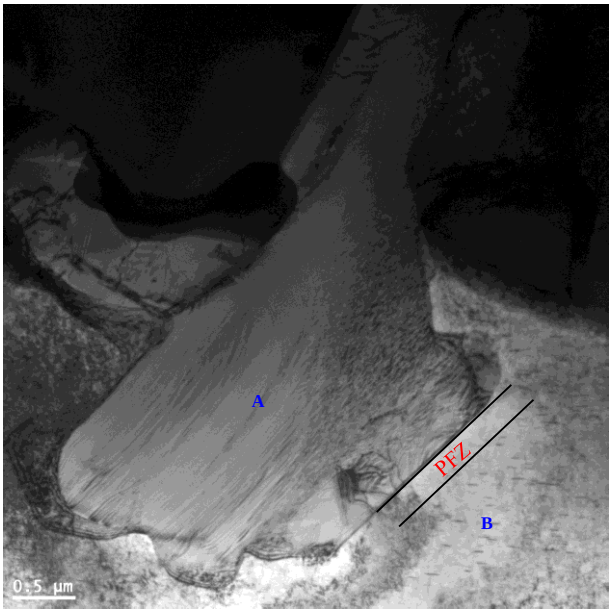

(a)

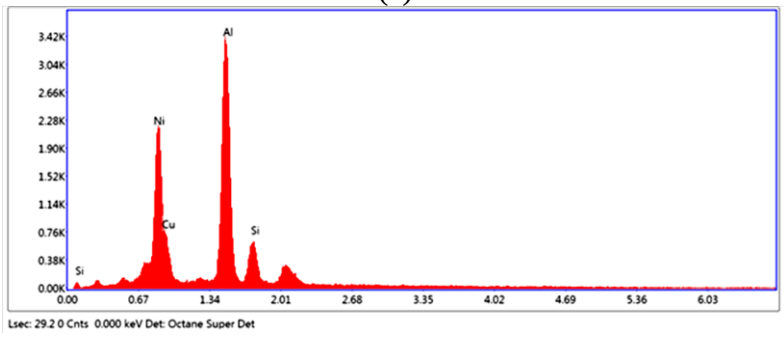

(b)

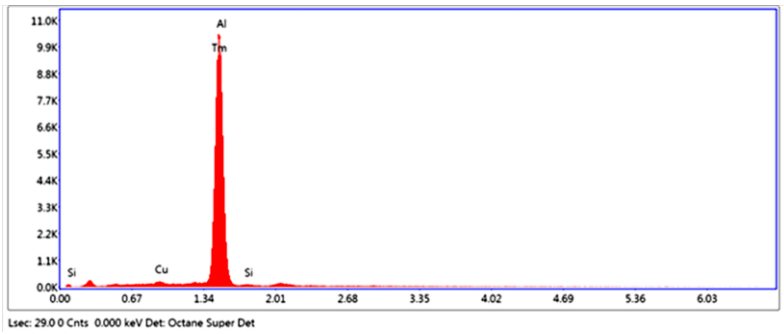

(c)

Figure 4.17 (a) Bright-field TEM image for alloy M4S in T6-treated condition, (b and c) EDS spectra corresponding to points A and B in (a), respectively.

In order to investigate the effect of prolonged thermal exposure on the characteristics of strengthening precipitates, samples from the base alloy (M1S) and the 4 wt.% Ni-containing alloy (M4S) were stabilized at 250°C for 200 hours after their treatment according to the T6-temper procedure followed in this study. The investigation of these stabilized conditions will ease the identification process of the active strengthening precipitates because of the expected coarsening behavior associated with the prolonged thermal exposure, as well as aid in examining the characteristics of those active precipitates.

The distribution of the strengthening precipitates in the stabilized T6-treated alloy M1S is portrayed in the bright-field TEM image shown in Figure 4.18(a); the selected area electron diffraction (SAED) pattern is displayed in Figure 4.18(b). The complete absence of streaks in this diffraction pattern indicates the absence of metastable phases and hence the equilibrium S-Al_2CuMg and θ-Al_2Cu phases exist rather the metastable phases. Interestingly, fine needle-like precipitates (yellow arrows) exist after this prolonged exposure of the T6-treated base alloy at 250°C for 200 hours along with the expected coarse precipitates. These fine precipitates are possibly transient ones due to the different

decomposition and precipitation processes taking place in sequence[234] or thermally-stable ones which coarsen at lower rates due to the addition of the transition elements.[14, 17]

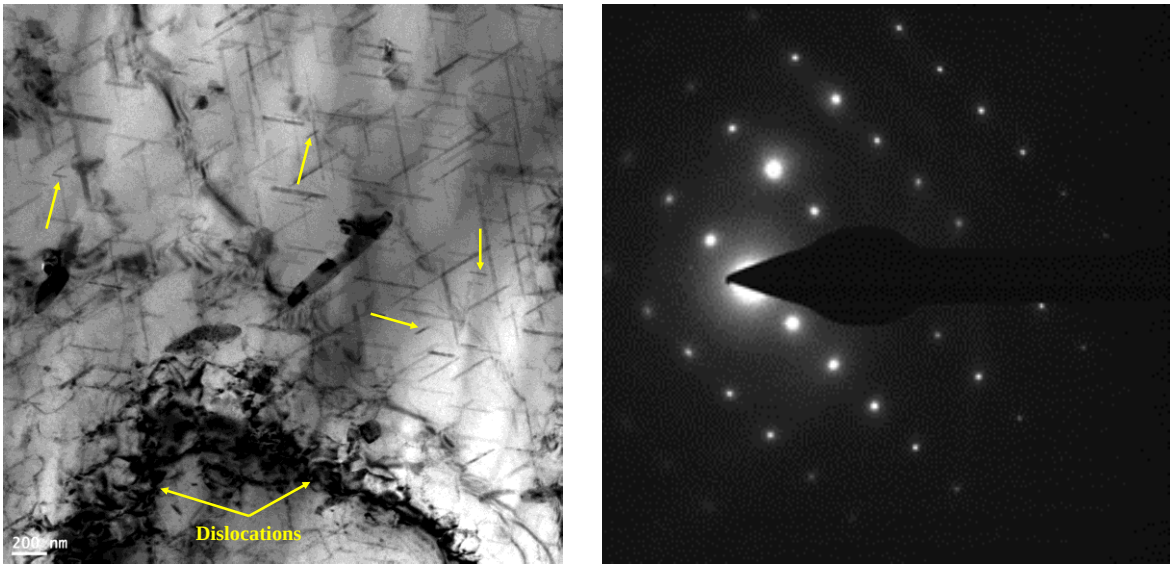

(a) (b)

Figure 4.18 Bright-field TEM image for the T6-treated alloy M1S after stabilization at 250°C for 200 hours, and (b) the selected area electron diffraction (SAED) pattern.

Figure 4.19(a) is a high angle annular dark field (HAADF) image showing different morphologies of existing precipitates in the structure of the same alloy and condition, i.e. T6-treated M1S alloy + 200h@250°C. Figure 4.19(b) through Figure 4.19(e) show the x-ray maps, obtained in the STEM mode, of the HAADF image shown in Figure 4.19(a). These x-ray maps reveal the presence of particles containing Al, Cu, and Mg; in addition to particles containing Al and Cu which are believed to be S-Al_2CuMg and θ-Al_2Cu phases, respectively. In addition, equiaxed Si particles exist in the structure of the alloy; and in some cases, these Si particles are located beneath the clearly identified S-Al_2CuMg phase. The distribution maps of Zr and Ti elements are not revealing distinct phases; however, they seem to be promising if the mapping process were to be continued for a higher number of scans since this mapping is obtained after only 50 scans.

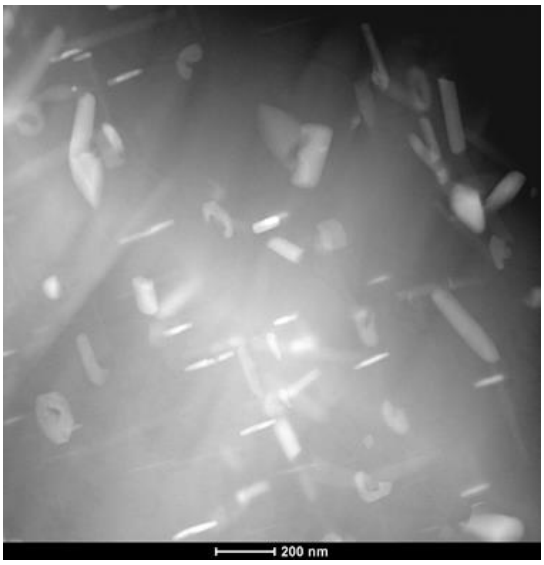

(a)

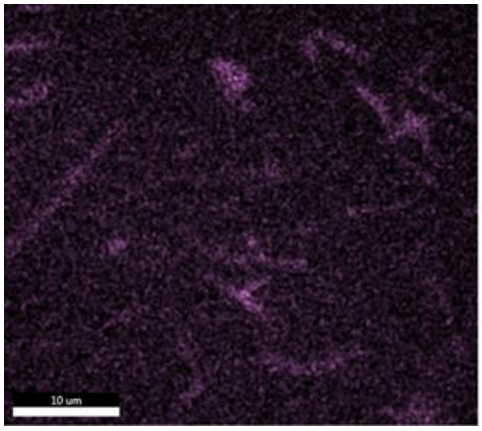

(b) Mg

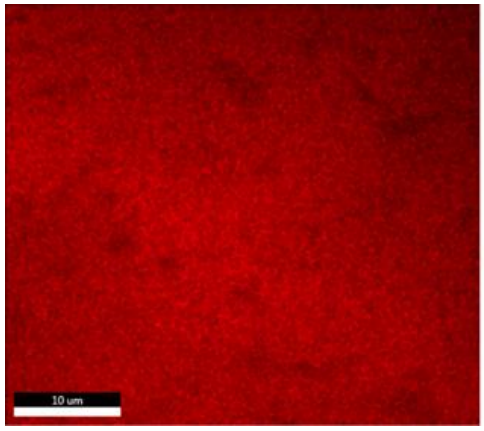

(c) Al

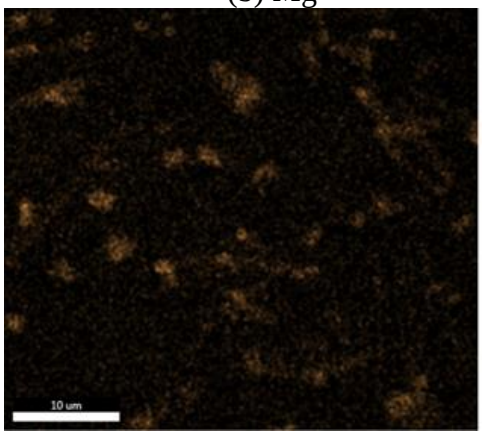

(d) Si

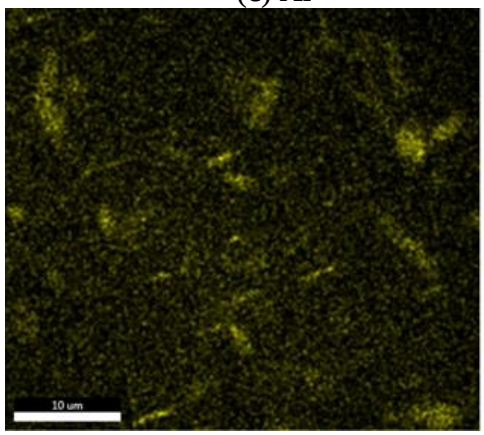

(e) Cu

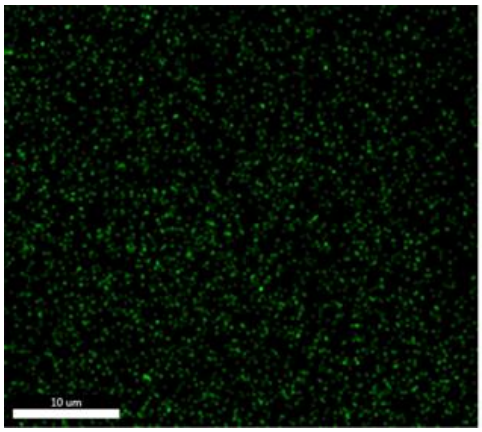

(f) Ti

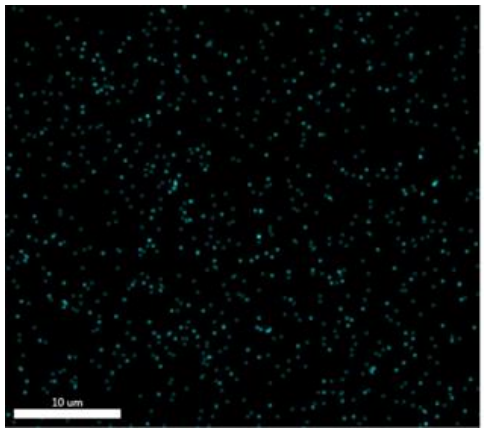

(g) Zr

Figure 4.19 (a) High angle annular dark field (HAADF) image for the T6-treated alloy M1S after stabilization at 250°C for 200 hours, and (b through g) corresponding X-ray maps showing distribution of elements in (a).

Figure 4.20 and Figure 4.21 show bright-field TEM images, the corresponding high angle annular dark field (HAADF) images, and x-ray maps showing the elemental distribution after 300 scans obtained at two different locations in the structure of the stabilized T6-treated base alloy (M1S). These maps support the conclusions made in the preceding subsection regarding the combined strengthening effect of θ-Al_2Cu and S-Al_2CuMg precipitates in the investigated alloys; this support comes in the form of detectable particles of θ-Al_2Cu and S-Al_2CuMg phases at various locations in the microstructure of the base alloy. S-Al_2CuMg particles are not clearly identified in the structures of T6-treated M1S and M4S alloys, though heating of the T6-treated alloy M1S for 200 hours at 250°C instigates coarsening of the fine precipitates and hence the primary strengthening precipitates, i.e. θ-Al_2Cu and S-Al_2CuMg, can be easily spotted as shown in Figure 4.20 and Figure 4.21.

Subsequent to the addition of 0.3 wt.% Zr, secondary strengthening precipitates in the form of fine elongated particle (~100*10 nm) can spotted in the high angle annular dark field (HAADF) image shown in Figure 4.20(b); this particle shows reflections of Al, Si, Zr, and Ti which possibly can be Al_x(Zr,Ti)Si phase. Similar observations can be noticed in the high angle annular dark field (HAADF) image shown in Figure 4.21(b) along with the corresponding elemental maps provided in Figure 4.21(c) through Figure 4.21(h). These particles cannot be detected in the structure of the T6-treated base alloy without stabilization, possibly, due to their ultra-fine size. However, after exposing to 250°C for 200 hours, detectable fine particles start to show in the alloy structure emphasizing their thermal stability and low coarsening rate in comparison to the main strengthening phases, i.e. θ-Al_2Cu and S-Al_2CuMg.

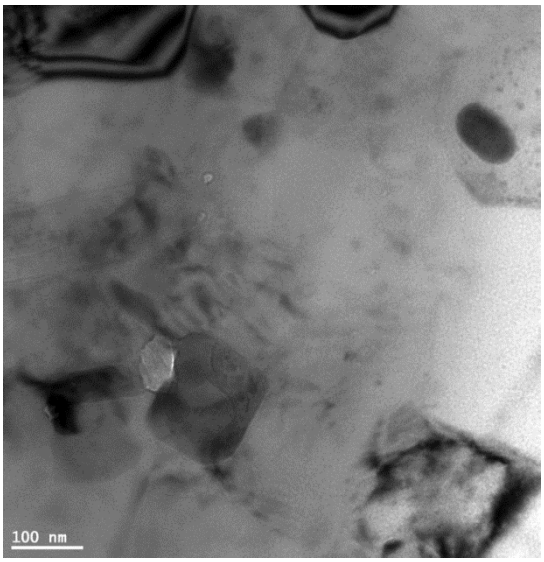

(a)

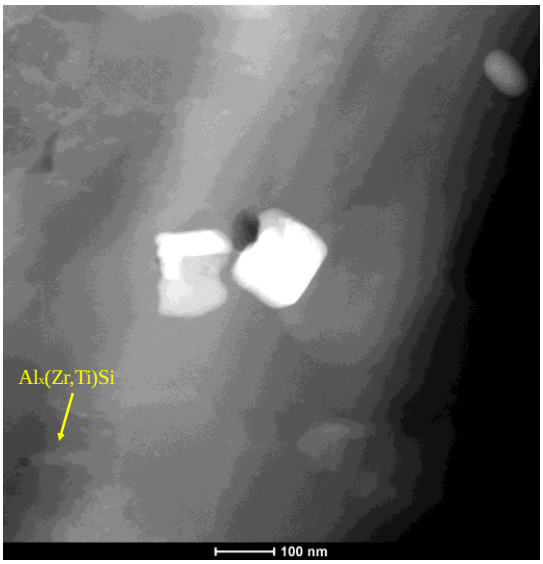

(b)

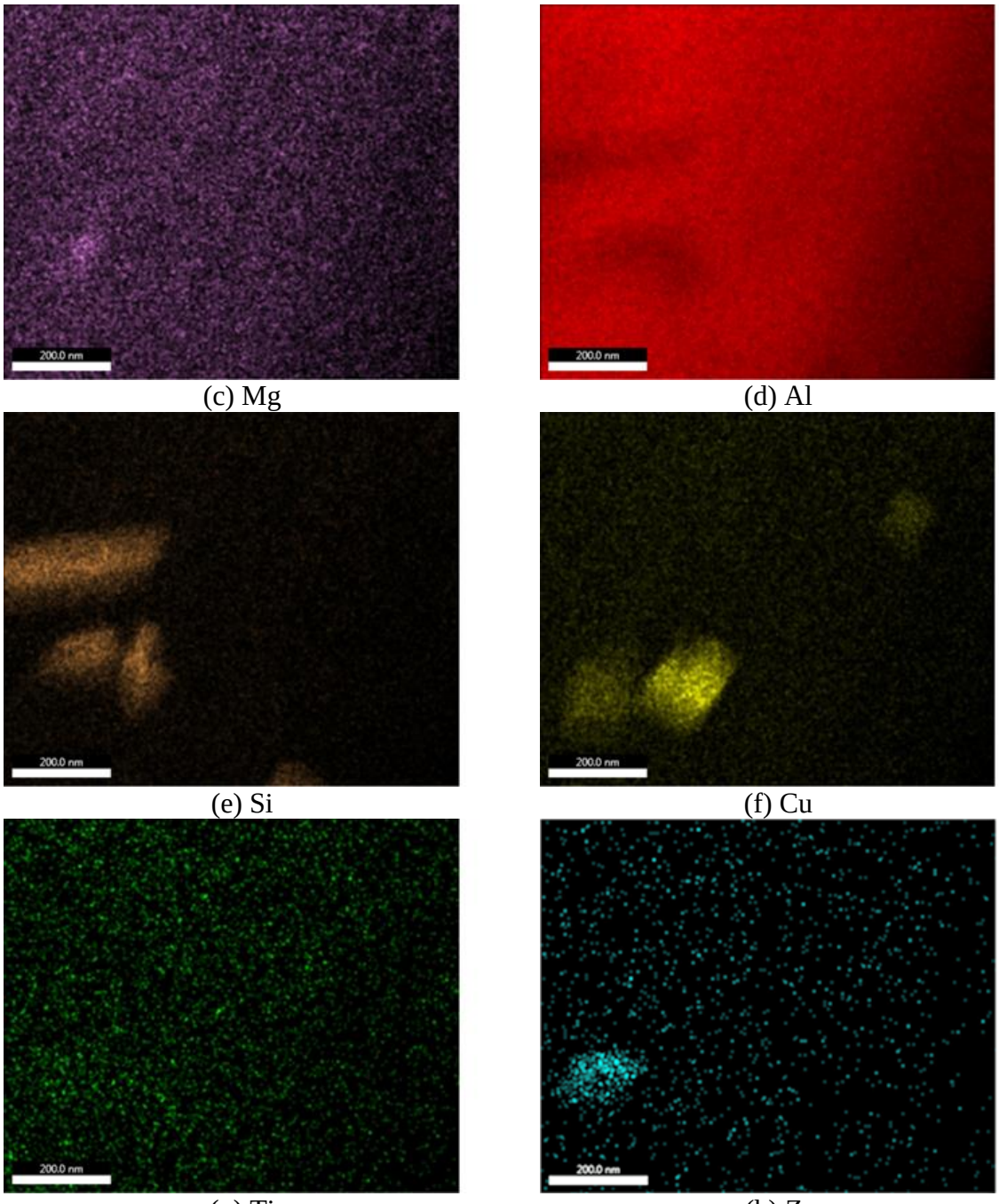

Figure 4.20 (a) Bright-field TEM image for the T6-treated alloy M1S after stabilization at 250°C for 200 hours, (b) Corresponding high angle annular dark field (HAADF) image for BF image in (a), and (c through h) corresponding X-ray maps showing distribution of elements in (b).

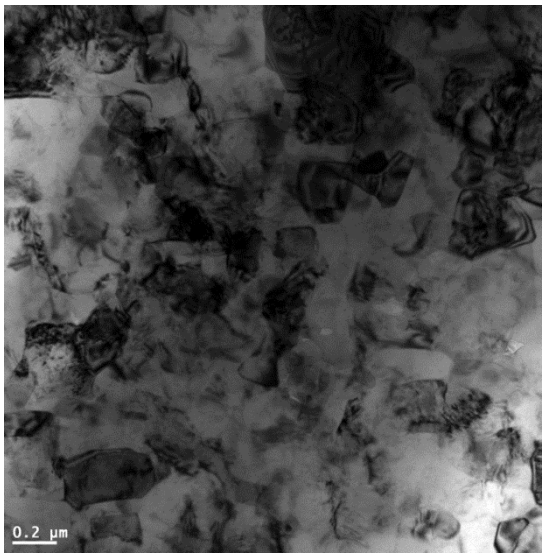

(a)

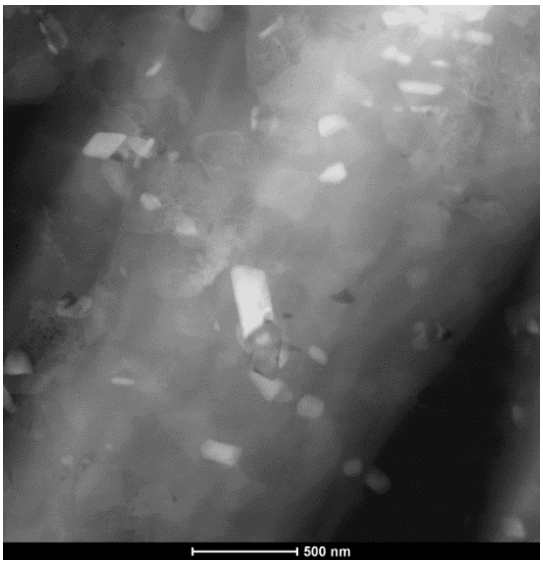

(b)

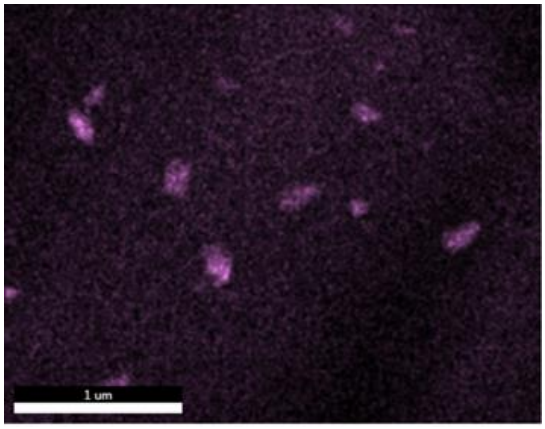

(c) Mg

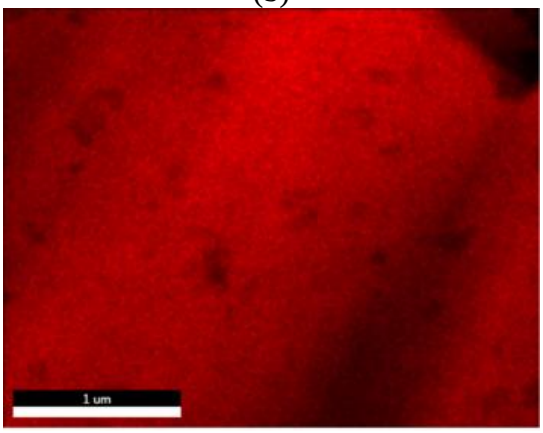

(d) Al

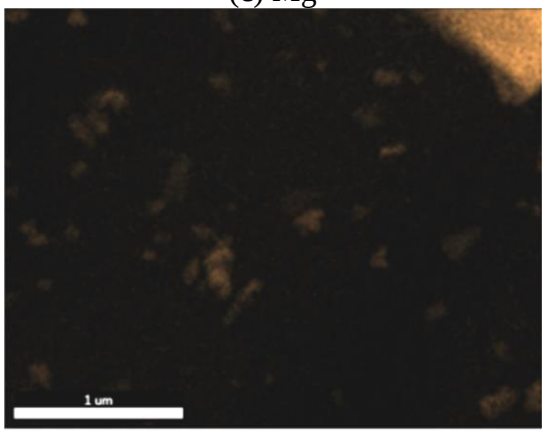

(e) Si

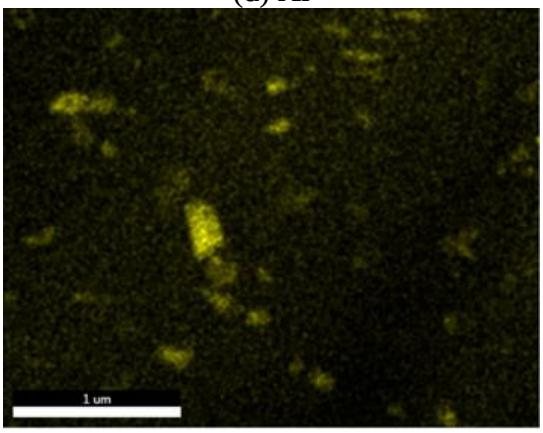

(f) Cu

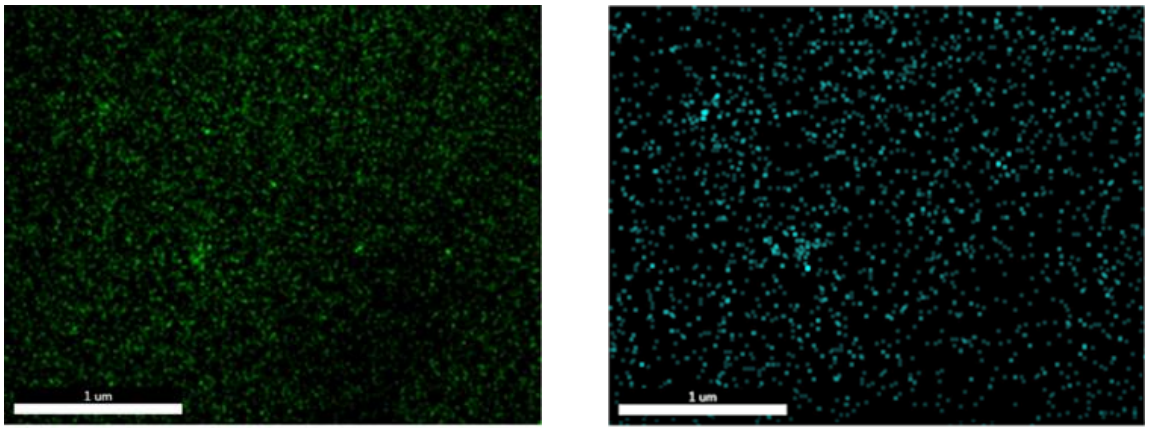

(g) Ti (h) Zr

Figure 4.21 (a) Bright-field TEM image for the T6-treated alloy M1S after stabilization at 250°C for 200 hours, (b) Corresponding high angle annular dark field (HAADF) image for BF image in (a), and (c through h) corresponding X-ray maps showing distribution of elements in (b).

A coarsened particle can be observed in the bright-field TEM image shown in Figure 4.22(a). This image shows interfaces between multiple agglomerated particles which are thought to be θ-Al_2Cu. It is interesting to observe that the coarsening of fine precipitates is achieved through two active mechanisms, namely, (i) diffusion, and (ii) agglomeration; however, these mechanisms are beyond the scope of the current investigation. By enlarging the circled area in Figure 4.22(a), the crystallographic planes can be viewed in the high resolution bright-field TEM image shown in Figure 4.22(b). For the two agglomerated particles, the measured interplanar spacing values between the observable atomic planes at this orientation are 2.35Å which confirms the similarity of their lattices and hence it is another evidence that this coarsened particle composes out of two smaller particles from the same composition; thus the mechanism of coarsening by agglomeration is proved to be active along with the well-defined diffusion one.

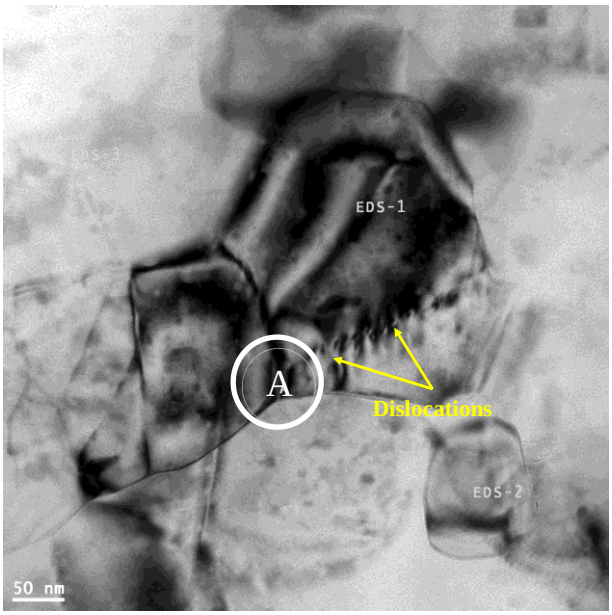

(a)

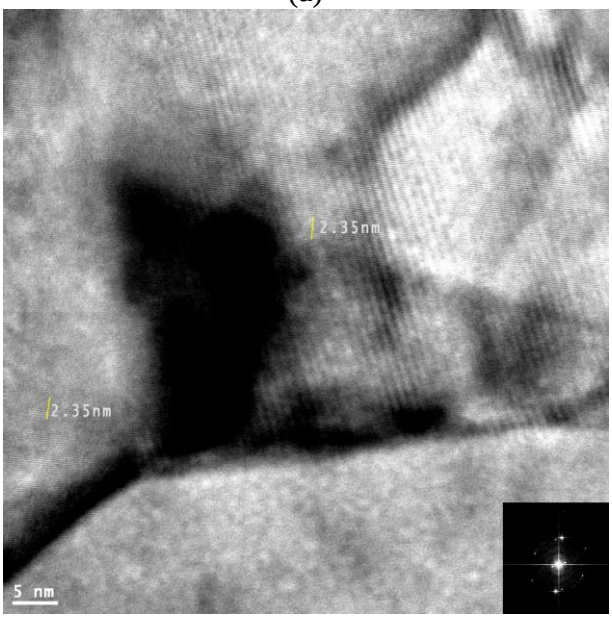

(b)

Figure 4.22 (a) Bright-field TEM image for the T6-treated base alloy M1S following stabilization at 250°C for 200 hours showing coarsened Al2Cu particle, and (b) High resolution bright field TEM image for the circled area A in (a), the insert is the fast Fourier transition (FFT) pattern obtained for this image.

Figure 4.23(a) represents a high resolution bright-field TEM image obtained for the T6-treated base alloy M1S after stabilization at 250°C for 200 hours; the atomic planes of the α-Al matrix and elongated particle can be clearly observed; the insert is the

corresponding fast Fourier transition (FFT) pattern obtained for this image. This figure reveals that the particle is totally incoherent with the α-Al matrix and hence the opposition to dislocation movements will be reduced leading to a reduction in the mechanical properties.[88, 106]

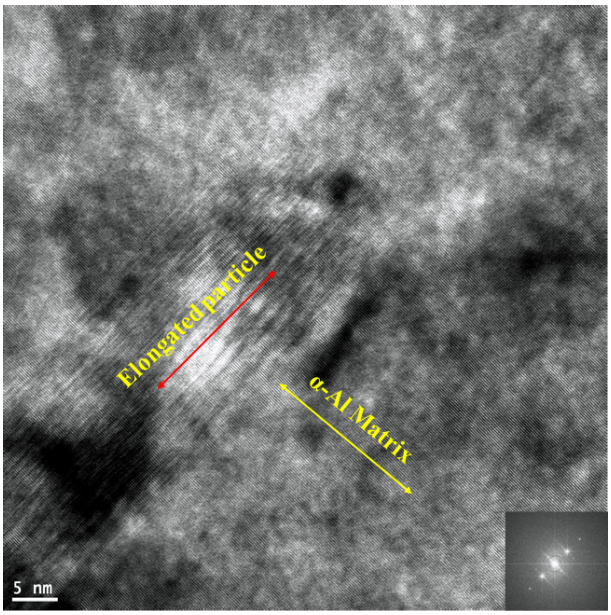

Figure 4.23 High resolution bright-field TEM image for the T6-treated base alloy M1S after stabilization at 250°C for 200 hours, the insert is the fast Fourier transition (FFT) pattern obtained for this image.

Figure 4.24(a) shows a bright-field TEM image obtained for T6-treated alloy M4S (containing 4 wt.% Ni) after exposing at 250°C for 200 hours, and Figure 4.24(b) is the SAED pattern obtained for this BF image. A mixture of two types of precipitates, dark and pale, can be noticed in the BF image. High angle annular dark field (HAADF) images along with x-ray maps are used to identify these particles, as shown in Figure 4.25 and Figure 4.26. The maps reveal the existing of acicular Al-Cu-Ni fine particles (<10 nm) besides $Al_x(Zr,Ti)Si$ particles. Most of the Cu in this alloy interacts with the added Ni to form Al-Cu-Ni particles and hence the paucity of θ-Al_2Cu can be easily noticed.

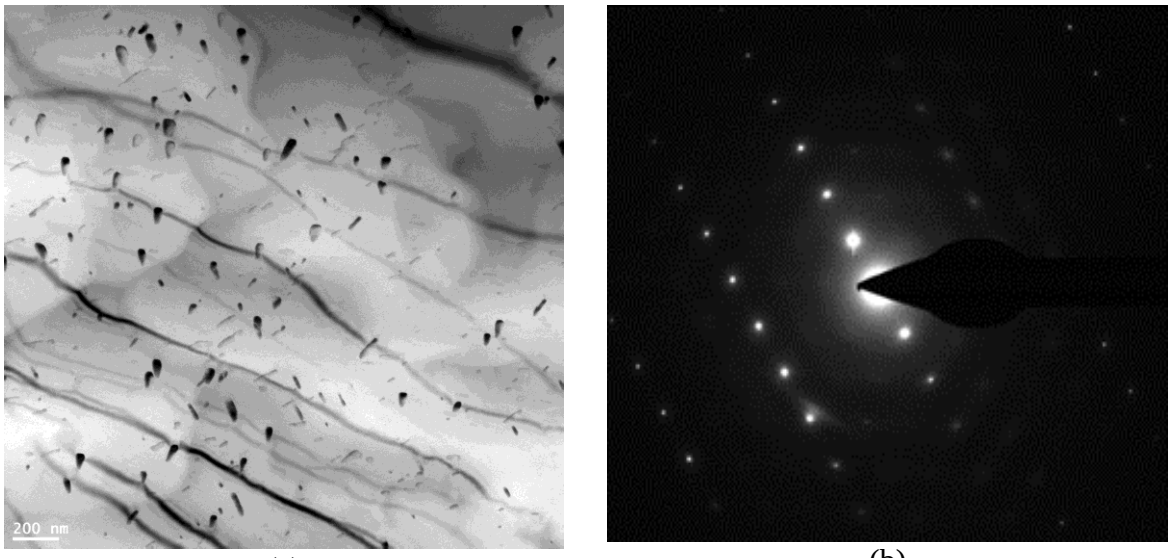

(a) (b)

Figure 4.24 Bright field TEM image for the T6-treated alloy M4S after stabilization at 250°C for 200 hours, and (b) the selected area electron diffraction (SAED) pattern.

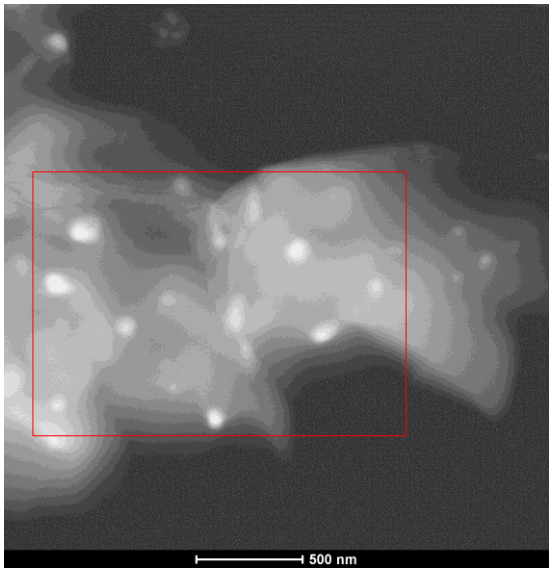

(a)

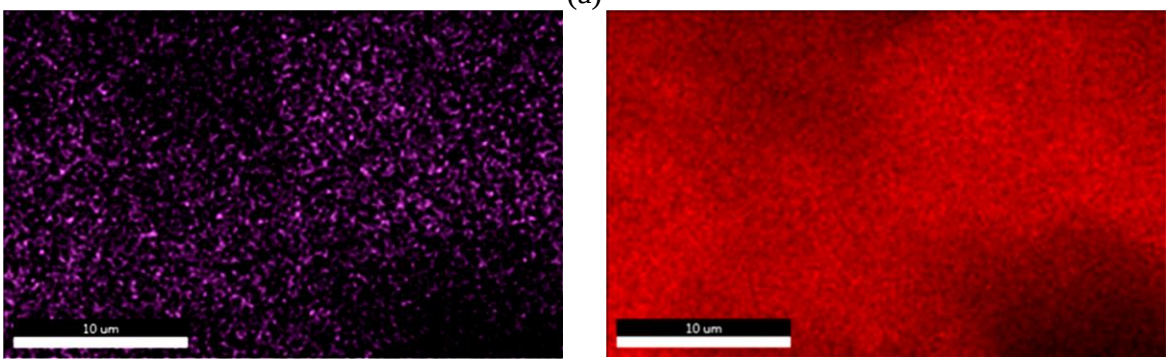

(b) Mg (c) Al

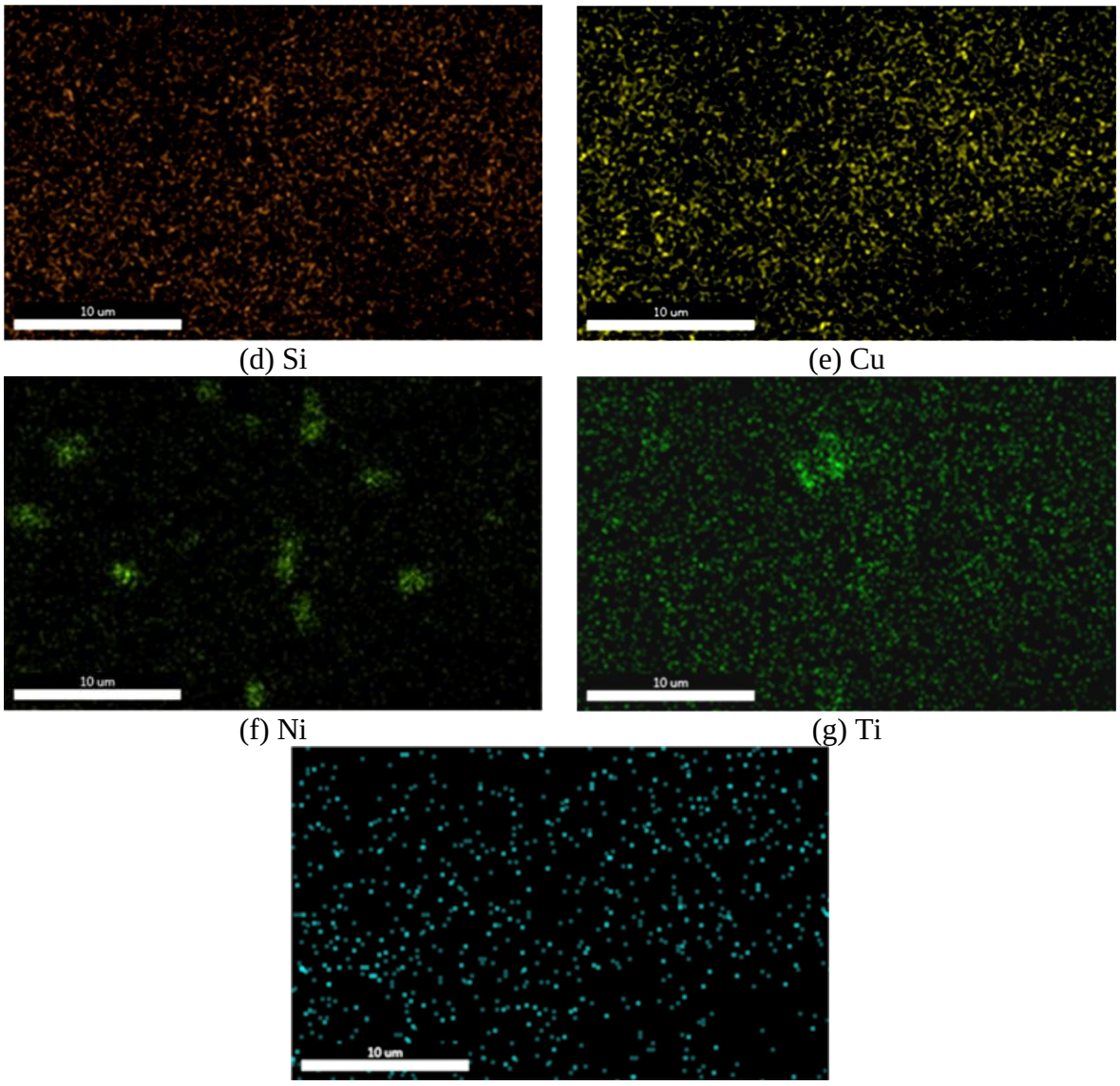

(d) Si (e) Cu

(f) Ni (g) Ti

(h) Zr

Figure 4.25 (a) High angle annular dark field (HAADF) image for the T6-treated alloy M4S after stabilization at 250°C for 200 hours, and (b through h) corresponding X-ray maps showing distribution of elements in the area enclosed by the red rectangle (a).

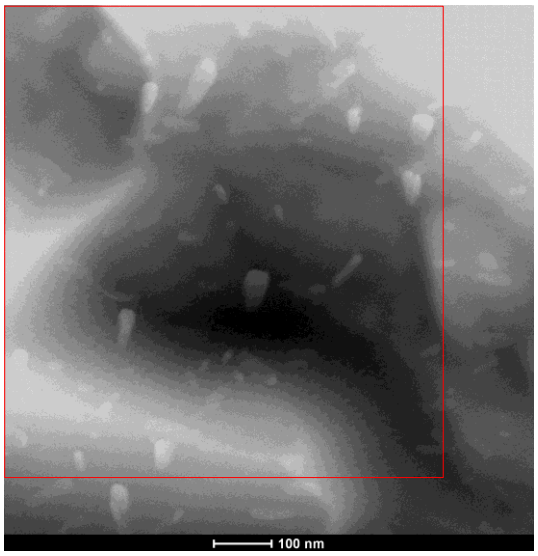

(a)

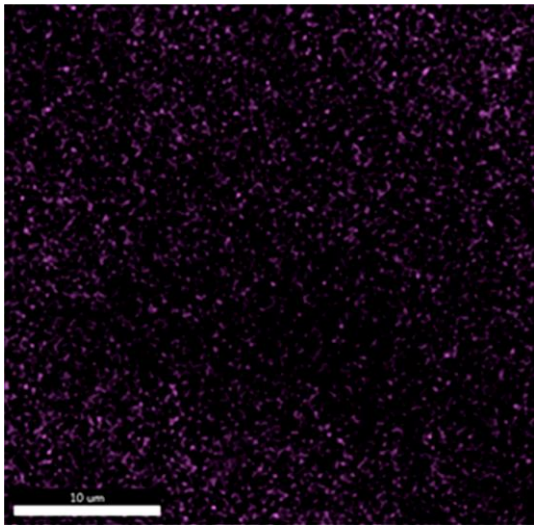

(b) Mg

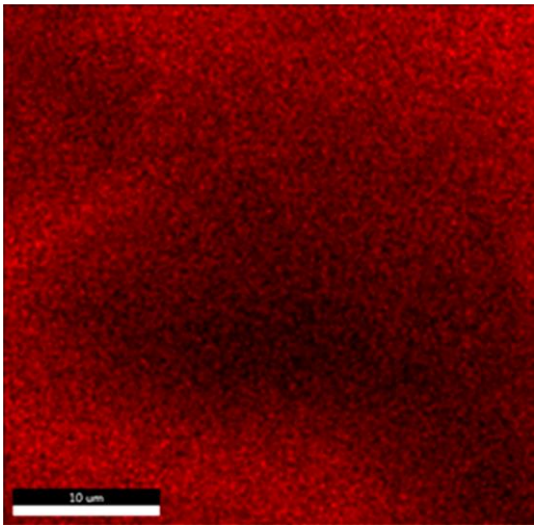

(c) Al

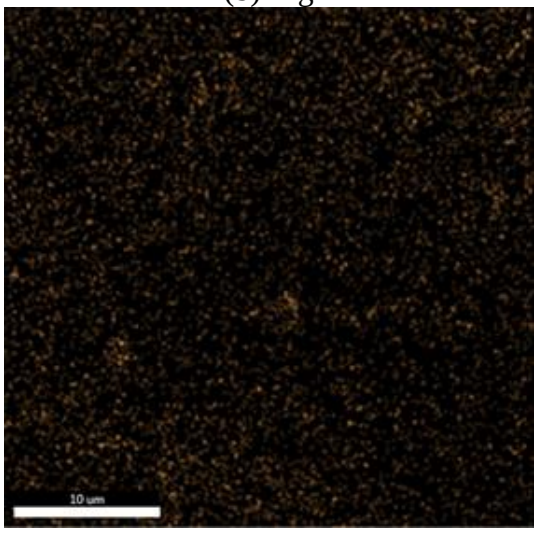

(d) Si

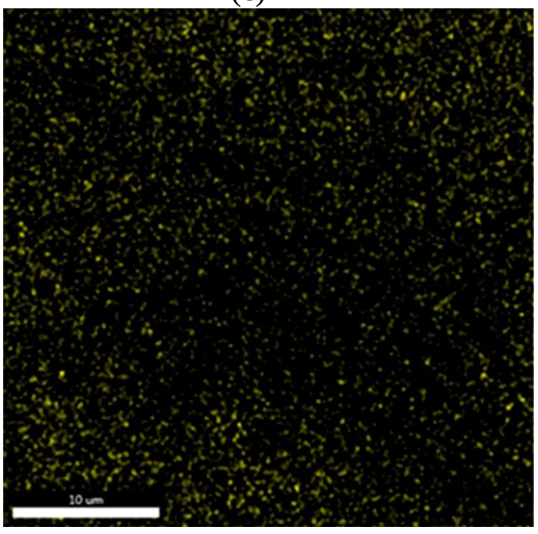

(e) Cu

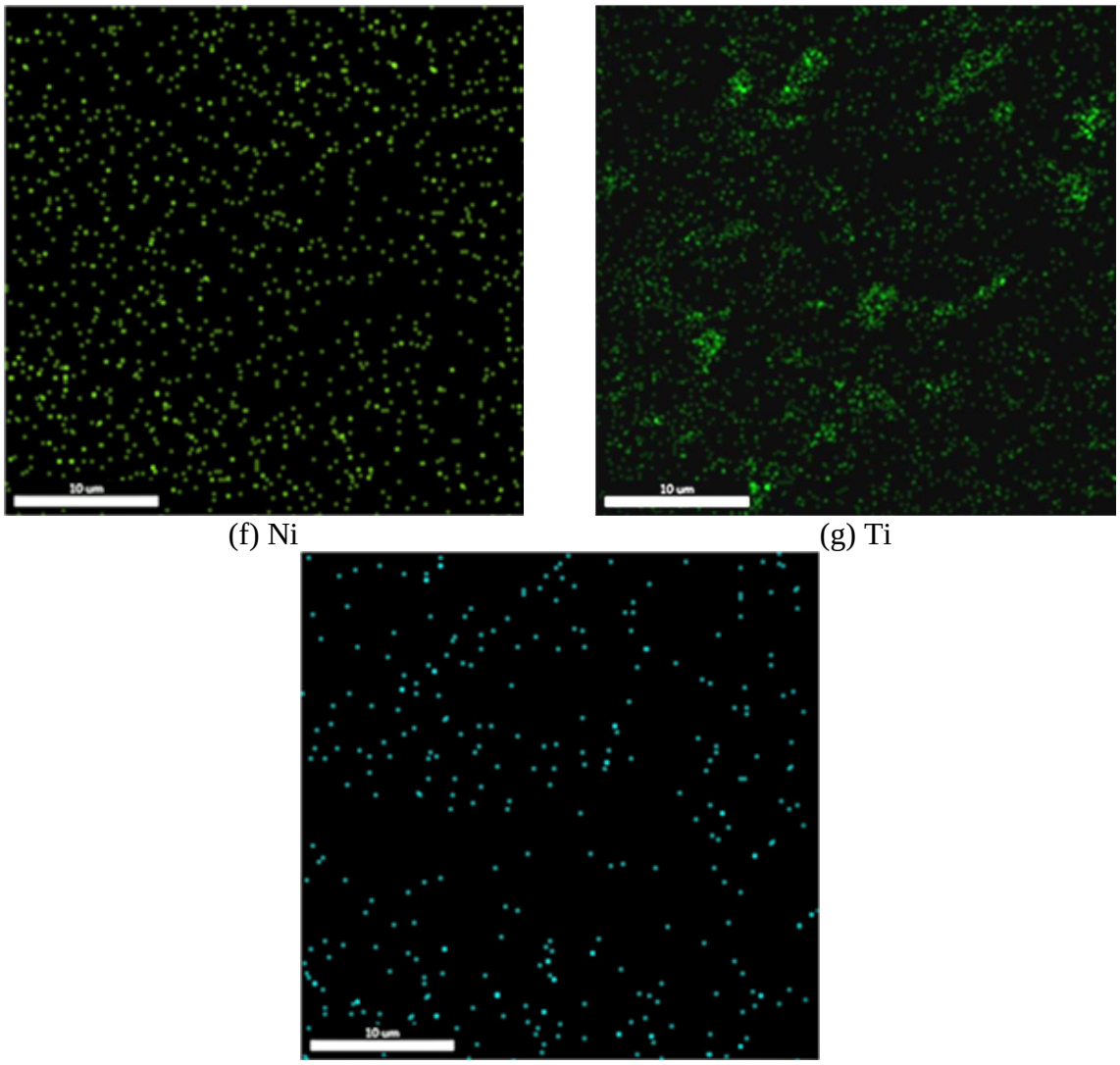

(f) Ni (g) Ti

(h) Zr

Figure 4.26 (a) High angle annular dark field (HAADF) image for the T6-treated alloy M4S after stabilization at 250°C for 200 hours, and (b through h) corresponding X-ray maps showing distribution of elements in the area enclosed by the red rectangle (a).

At the end of this subsection, it is important to explicitly state that TEM investigations support the interpretation of the results obtained for the DSC analysis of as-quenched samples in terms of the combined strengthening effect of θ-Al_2Cu and S-Al_2CuMg phases as well as the reduced amount of θ-Al_2Cu in Ni-containing alloys. Moreover, TEM investigations reveal the existence of the coarsening-resistant Al_x(Zr,Ti)Si and Al-Cu-Ni particles.

CHAPTER 5

ROLE OF ADDITIONS, HEAT TREATMENTS, AND GEOMETRICAL DISCONTINUITIES

CHAPTER FIVE

ROLE OF ADDITIONS, HEAT TREATMENTS, AND GEOMETRICAL DISCONTINUITIES

5.1 INTRODUCTION

This chapter comprises two parts, namely, characterization of the microstructure of test bars obtained at a high solidification rate of 7 °C s^{-1}, and characterization of the mechanical performance of the alloys studied. The first part discusses the effect of solution heat treatment on the microstructure of the alloys in terms of existing intermetallic compounds and their volume fractions before and after the solution treatment. The microstructural characterization section also includes qualitative and quantitative analyses of the average eutectic Si particle characteristics in the as-cast and as-quenched conditions of the test bars (i.e. high cooling rate). The data presented in Part I of this chapter are crucial to understand and correlate the mechanical performance of the alloys studied before and after heat treatments to the changes that may take place to the microstructural features.

Part II presents and compares the ambient- and elevated-temperature tensile properties for smooth (unnotched) and notched tensile bars subjected to various heat treatment conditions. The notched bars are introduced as a physical simulation of the geometry of the different parts in a real casting, representative of engine blocks. The last part of Chapter 5 will present the hardness and impact properties of the alloys investigated.

The base alloy in the present study contains a slightly higher Zr content, ~0.3 wt.% compared to ~0.25 wt.% used in the investigations of previous researchers in the same research group.[11, 13] This slight increase in Zr content renders the alloys studied from being hypo-peritectic to be near peritectic type alloys.[17] During melting, the melt was superheated to 800°C, exceeding the liquidus temperature of the Al_3Zr phase originating from the master alloy by ~50°C; this melt superheat is expected to melt the Zr present, allowing for better strengthening effects.[17]

The test bars used in the present study were produced using the same casting technique, i.e. the same cooling rate and SDAS values. The alloys were Sr-modified and grain refined to the same extent, i.e. 200 ppm Sr, and 0.2 wt.% Ti, respectively. The test bars were subjected to identical heat treatments, using the same temperature and time parameters. Accordingly, the variation in the mechanical performance may be understood solely in relation to the various transition element additions and the alloy response to the applied heat treatment.

PART I- MICROSTRUCTURE CHARACTERIZATION OF TEST BARS

In this part, the microstructural features in the test bars produced at the high cooling rate will be examined. As mentioned earlier, the variation in the cooling rate results in a variation in the size, distribution, and morphology of the microstructural constituents. This section will highlight the effect of solution treatment on the volume fractions of intermetallic compounds and the average eutectic silicon particle characteristics in the microstructure of test bars for all alloy compositions studied. The importance of studying these features lies in the fact that they determine the mechanical performance of the alloys studied. Backscattered electron images and optical micrographs were respectively

employed to examine the existing intermetallic compounds, and the Si particle characteristics in as-cast and as-quenched conditions in these alloys.

5.2 EFFECT OF SOLUTION TREATMENT ON INTERMETALLIC COMPOUNDS

It has been previously reported[241] that higher cooling rates result in supressing the formation of Fe-intermetallic phases as well as producing finer microconstituents in comparison to slower cooling rates. In Sr-modified 354-type alloys, the presence of both strontium and magnesium results in copper segregation in the eutectic silicon free-areas; which leads to the formation of the block-like Al_2Cu phase in higher amounts. Consequently, the dissolution of the block-like Al_2Cu phase will not be easy as in the case of the finer eutectic-like Al-Al_2Cu phase; this will be reflected in the mechanical properties of the heat-treated alloys since the solution treatment conditions used may not be that efficient.

Proper selection of solution treatment parameters, *viz.* temperature and time, can significantly alter the microstructural features of the alloys studied resulting in enhanced mechanical properties. The alloy response to heat treatment depends on various parameters such as silicon content, amount and combination of alloying elements, amount of intermetallic compounds formed, and the casting process. In the following paragraphs, the effect of solution treatment on the dissolution of various phases will be presented through a comparison of the as-cast and as-quenched microstructures of the alloys studied.

The volume fraction (%) of intermetallic compounds observed in as-cast and as-quenched tensile bars is presented in Table 5.1. The backscattered images shown to the right in Figure 5.1 demonstrate clearly the reduction in the volume fraction due to the dissolution of some of these intermetallics during solution treatment. For the as-cast condition, it is obvious that the addition of Ni and Mn in different amounts and combinations (i.e. alloys M2S through M5S) significantly increases the volume fraction of existing phases compared to the base alloy (cf. 2.5% for alloy M1S and 12.21% for alloy M4S). Alloy M4S, which contains 4 wt.% Ni, shows an excessive increase in volume fraction in comparison to alloys M2S, M3S, and M5S. This substantial increase may be attributed to the formation of Ni-containing phases such as Al_3CuNi, Al_9FeNi, and Al_3Ni in addition to the phases commonly observed in other alloys such as the Q-phase, Al_2Cu, Mg_2Si, and Fe-containing phases. Other Ni-containing alloys, i.e. M2S and M5S, contain almost the same phases; however, the structure of alloy M4S uniquely comprises the eutectic Al-Al_3Ni structure, as previously discussed in Chapter 4. This eutectic structure is believed to increase the overall volume fraction of intermetallic compounds in alloy M4S.

The addition of 0.75 wt.% Mn to the base alloy, i.e. alloy M3S, doubles the volume fraction in the as-cast condition, and may be ascribed to the formation of α-$Al_{15}(Fe,Mn)_3Si_2$ phase in script-like and sludge morphologies.[242] In addition, the presence of the α-$Al_{15}(Fe,Mn)_3Si_2$ phase which does not dissolve with solution heat treatment would explain the nearly three times higher volume fraction observed in the as-quenched condition for alloy M3S compared to the base alloy M1S, similar to the observations of Elgallad.[86]

Figure 5.1 compares backscattered electron (BSE) images of all alloys in the as-cast (left) and as-quenched (right) conditions. The backscattered images shown to the right in Figure 5.1 demonstrate clearly the reduction in the volume fraction of the intermetallic compounds in the as-quenched samples. As may be seen from Table 5.1 and Figure 5.1, applying solution treatment reduces the volume fraction (%) of intermetallic compounds owing to the dissolution of the Al_2Cu phase, as was previously confirmed using DSC heating curves for as-cast and as-quenched conditions reported in Chapter 4, section 4.2, and the partial dissolution of other phases such as Q-$Al_5Mg_8Cu_2Si_6$, Mg_2Si, Al_3CuNi, β-Al_5FeSi, π-$Al_8Mg_3FeSi_6$, and Al_9FeNi.[11]

Table 5.1 Volume fractions (%) of undissolved intermetallic compounds in the matrix of as-cast and as-quenched alloys

Volume Fraction (%)		**Alloy Code**				
		M1S	**M2S**	**M3S**	**M4S**	**M5S**
As-cast	**Average**	2.51	6.17	4.34	12.21	8.79
	SD	0.41	0.56	0.36	0.77	0.79
SHT	**Average**	1.11	5.54	3.64	9.60	7.68
	SD	0.28	0.61	0.16	0.65	0.52

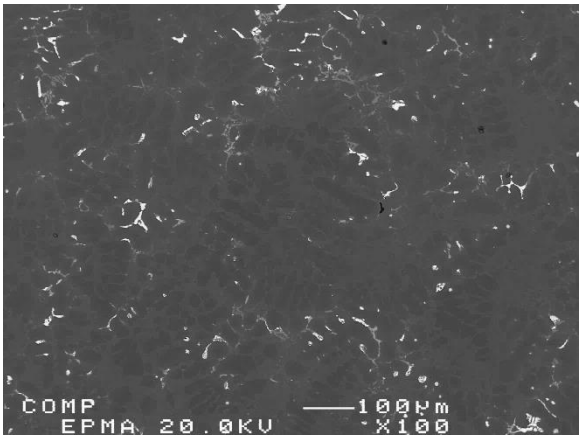

(a)

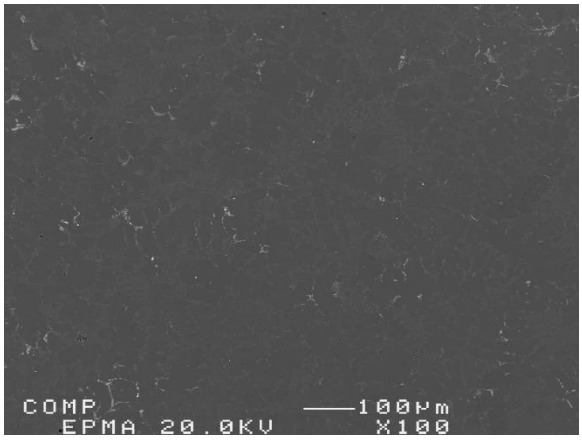

(b)

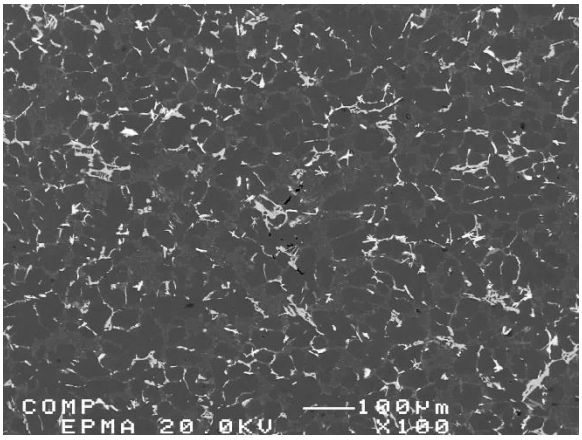
COMP
EPMA 20.0KV
100µm
X100

(c)

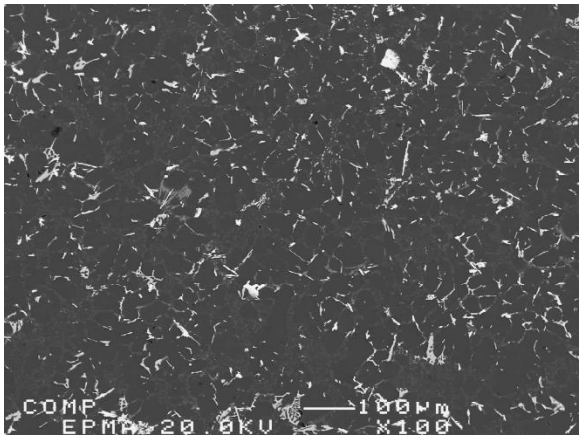
COMP
EPMA 20.0KV
100µm
X100

(d)

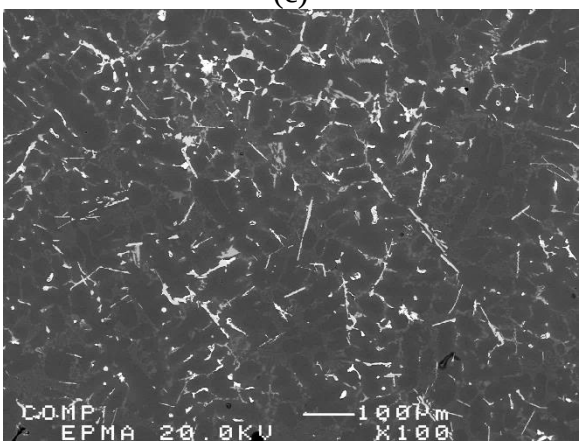
COMP
EPMA 20.0KV
100µm
X100

(e)

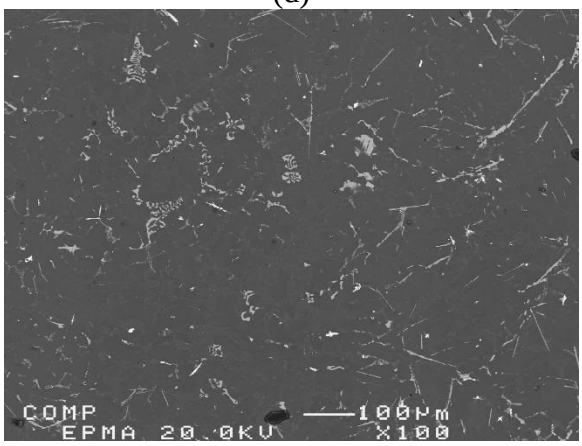
COMP
EPMA 20.0KV
100µm
X100

(f)

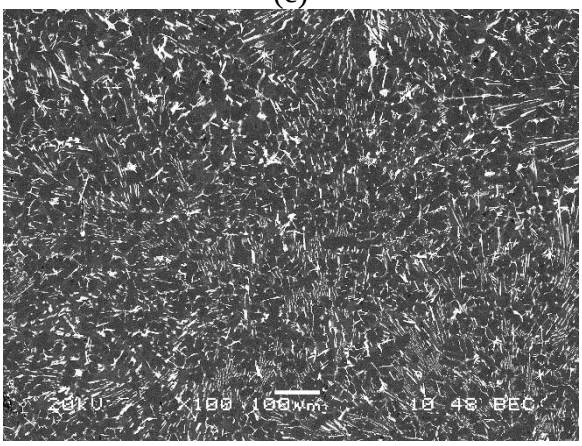
20kV
X100
100µm
10 48 BEC

(g)

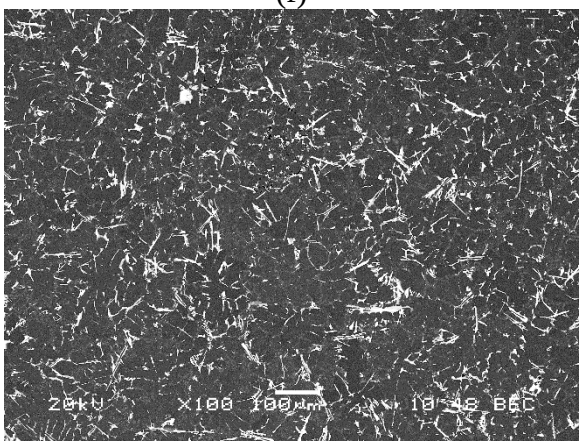
20kV
X100
100µm
10 48 BEC

(h)

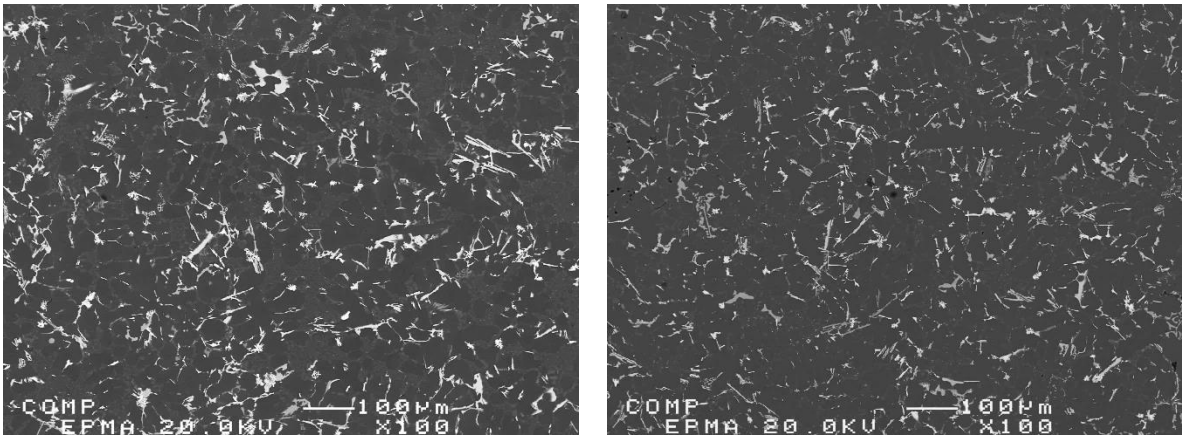

(i) (j)

Figure 5.1 Backscattered electron images for as-cast (left) and solution-heat treated (right) conditions of the alloys studied: (a, b) M1S (base alloy), (c, d) M2S (2 wt.% Ni), (e, f) M3S (0.75 wt.% Mn), (g, h) M4S (4 wt.% Ni), and (i, j) M5S (2 wt.% Ni + 0.75 wt.% Mn).

5.3 CHARACTERISTICS OF EUTECTIC SILICON PARTICLES

In the available literature,[120, 243, 244] it is well known that the morphology of eutectic silicon particles plays an important role in controlling the mechanical properties of Al-Si cast alloys; so that a quantitative analysis of the average eutectic silicon particle characteristics is important in order to have an idea of the morphological changes taking place in the eutectic silicon particles during solution heat treatment.

The alloys studied, M1S through M5S, were modified and grain refined by adding 200 ppm of strontium (Sr) and ~0.2 wt.% titanium (Ti), respectively. Therefore, it is expected that the eutectic silicon particles will be modified to a large extent in the as-cast condition in all alloys along with finer primary aluminum grains. Metallographic samples from the five compositions studied were sectioned from the centre of the gage length section of the corresponding as-cast and as-quenched tensile bars in the transverse direction. The solution heat treatment was carried out at 495°C for 5 hours, followed by quenching in warm water (60°C).

As described earlier in Chapter 3, an Olympus PMG3 optical microscope-Clemex Vision PE image-analysis system was used to measure the eutectic Si particle characteristics. The morphology of eutectic silicon particles in the as-cast and as-quenched alloy samples are displayed in the optical micrographs shown in Figure 5.2 through Figure 5.6, while the corresponding Si particle characteristics are listed in Table 5.2 and summarized in Figure 5.7 and Figure 5.8.

The optical micrographs shown in Figure 5.2(a), Figure 5.3(a), Figure 5.4(a), Figure 5.5(a), and Figure 5.6(a) for the as-cast alloy samples reveal that the majority of silicon particles are fully-modified; nevertheless partially-modified silicon particles may still be observed in these micrographs to a certain extent. The existence of these partially-modified silicon particles could be a result of the high Mg content, ~ 0.6 wt.%, of the alloys. It has been reported by Joenoes and Gruzleski[42] that the presence of about 1% Mg and copper can change the microstructure from a fully-modified structure into a partially-modified one due to the formation of Mg_2Sr(Si, Al) and Al-Cu-Sr phases which will result in reducing the amount of available strontium (Sr) to achieve the required degree of modification of the eutectic silicon particles. Dunn and Dickert[43] also studied the influence of Mg content on the mechanical properties of A380 and 383 cast alloys. They reported that Mg addition (up to 0.55%) was found to have a negative effect on Si modification using Sr, as it resulted in changing the Si morphology from a well-modified to a partially-modified one. This reduction in modification level was attributed to the formation of a complex $Mg_2SrAl_4Si_3$ intermetallic phase, which probably formed prior to the eutectic reaction.[42] In the present case, however, since the contents of Sr, Cu, and Mg are kept constant in the

alloys investigated, other explanations are mandatory to explain the variations in the modification level of the eutectic Si particles in these alloys.

As per the micrographs shown in Figure 5.4(a), Figure 5.5(a), alloys M3S (354 + 0.02 wt.% Sr + 0.3 wt.% Zr + 0.75 wt.% Mn) and M4S (354 + 0.02 wt.% Sr + 0.3 wt.% Zr + 4 wt.% Ni) appear to contain less amounts of partially modified eutectic silicon. This observation can be ascribed to the existing phases in the microstructure of the two alloys, which may contribute to variations in the free content of silicon and/or strontium. Such variations may lead to a more efficient modification in the case of a lower Si/Sr ratio and vice-versa.

On one hand, a high amount of the copper in alloy M4S (containing 4% Ni) is consumed in forming Al_3NiCu phase and thus the possibility of forming the Al-Cu-Sr phase reported by Joenoes and Gruzleski[42] will be reduced. Consequently, more Sr will not be consumed to form the Al-Cu-Sr phase and thus better modification would be expected for Ni-containing alloys, particularly those with higher Ni-content as in alloy M4S. On the other hand, the addition of 0.75 wt.% Mn in alloy M3S changes some of the β-Al_5FeSi iron phase into Chinese script-like α-$Al_{15}(Fe,Mn)_3Si_2$ phase and sludge particles. The mutual existence of the two Fe-based phases, i.e.β-Al_5FeSi and α-$Al_{15}(Fe,Mn)_3Si_2$, will lower the silicon content (i.e. reduce the Si phase) in alloy M3S to an extent which will allow a better modification level compared to that attained for the rest of the alloys studied, as depicted in Figure 5.4(a).

Thermal modification is yet another effective way to alter the morphology of eutectic silicon particles. It is evident from the micrographs shown in Figure 5.2(b), Figure 5.3(b), Figure 5.4(b), Figure 5.5(b), and Figure 5.6(b) that the solution treatment changes the fibrous interconnected eutectic silicon particles detected in the as-cast condition into globular particles with rounded edges. The evolution of the morphology of the eutectic silicon particles from fibrous to globular in these alloys is a direct result to the combined effect of solution-heat treatment and strontium modification, as previously stated by Chen *et al.*[192] and Yuying *et al.*[245] A detailed discussion on the effect of solution treatment on the morphology of non-modified and Sr-modified eutectic silicon particles will be presented in Chapter 7 of this study.

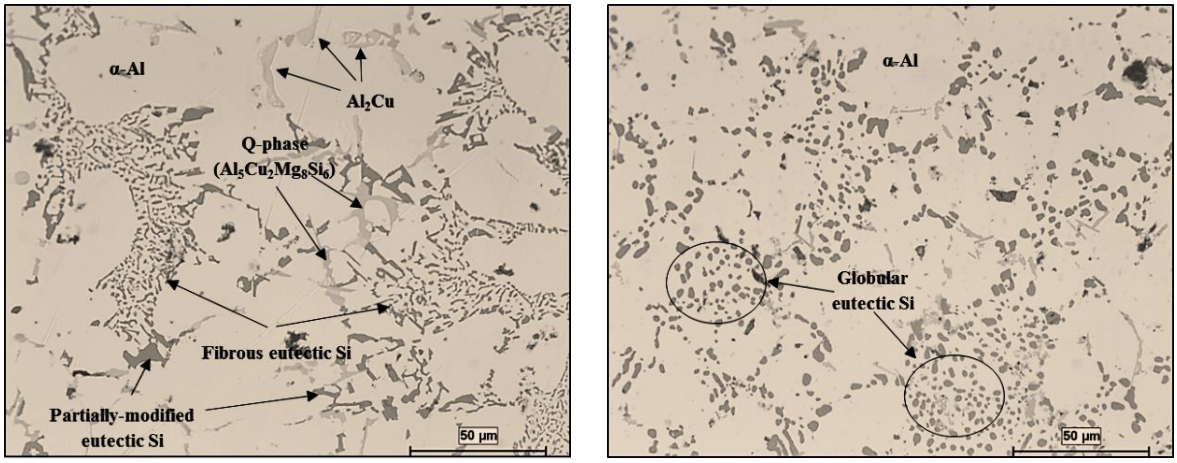

Figure 5.2 Optical micrographs at 500X showing the morphology of the eutectic silicon in alloy M1S (354+0.3wt%Zr): (a) As-cast and (b) after SHT @495°C/5h.

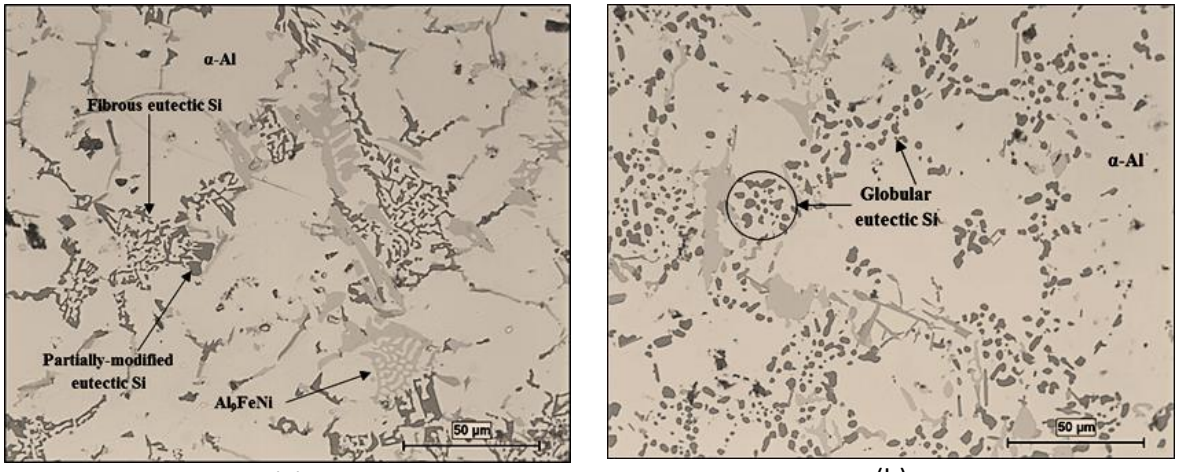

(a) (b)

Figure 5.3 Optical micrographs at 500X showing the morphology of the eutectic silicon in alloy M2S (M1S+ 2wt% Ni): (a) As-cast and (b) after SHT @495°C/5h.

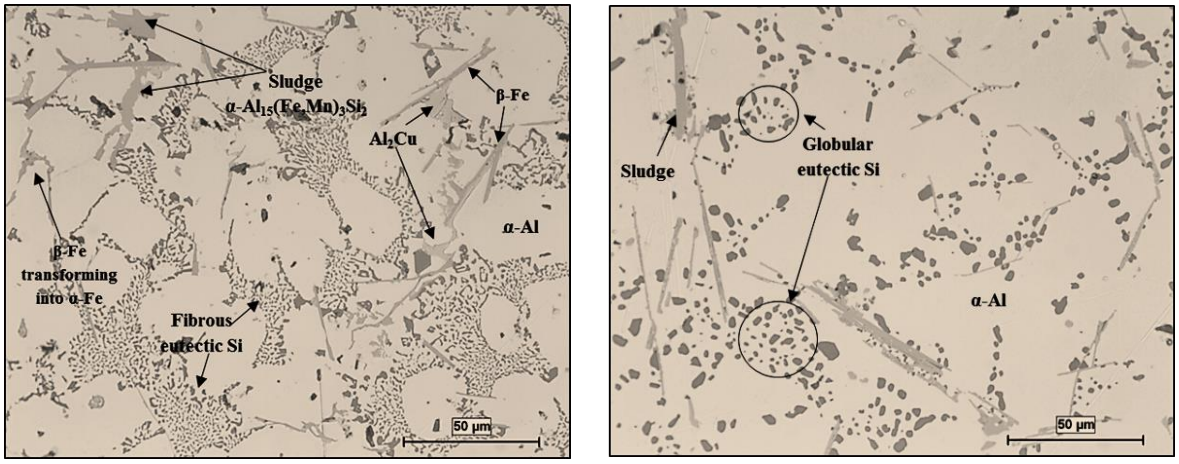

(a) (b)

Figure 5.4 Optical micrographs at 500X showing the morphology of the eutectic silicon in alloy M3S (M1S+ 0.75wt% Mn): (a) As-cast and (b) after SHT @495°C/5h.

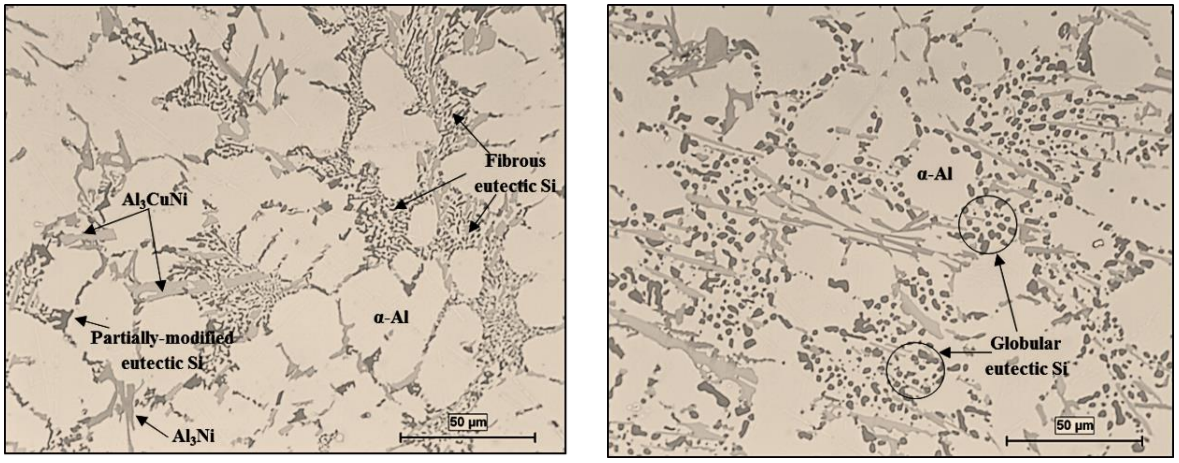

(a) (b)

Figure 5.5 Optical micrographs at 500X showing the morphology of the eutectic silicon in alloy M4S (M1S+ 4wt% Ni): (a) As-cast and (b) after SHT @495°C/5h.

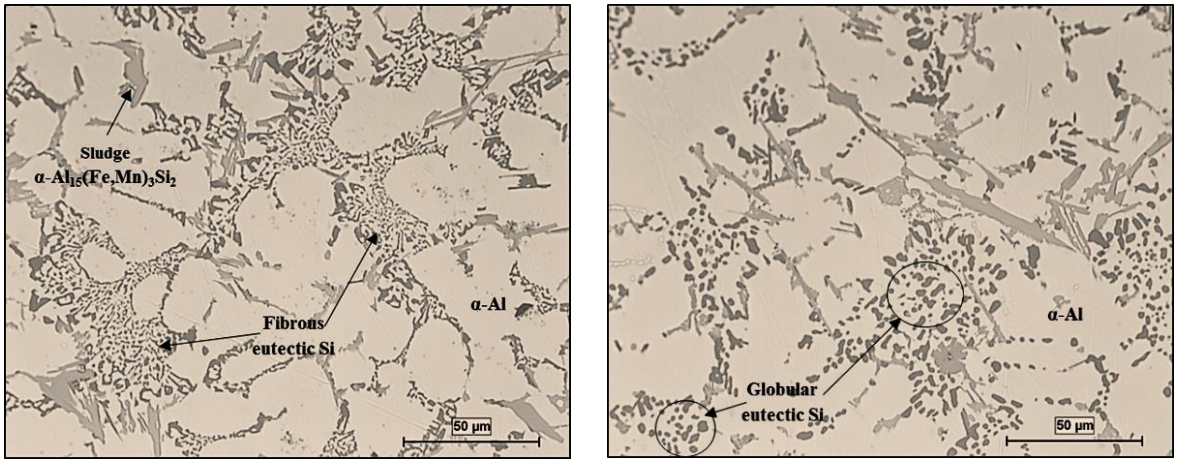

(a) (b)

Figure 5.6 Optical micrographs at 500X showing the morphology of the eutectic silicon in alloy M5S (M1+ 2wt% Ni + 0.75wt% Mn): (a) As-cast and (b) after SHT @495°C/5h.

The average eutectic silicon particle characteristics in as-cast and as-quenched conditions of the alloys studied are listed in Table 5.2, and plotted in Figure 5.7 and Figure 5.8. These values are the average values obtained from measurements of 20 fields per alloy sample/condition.

It is evident from the data presented in Table 5.2, Figure 5.7 and Figure 5.8 that the average Si particle area increases after solution treatment at 495°C for 5 hours for all the alloys. Additionally, the solutionizing treatment produces a noticeable improvement in the spheroidization of the Si particles concomitant with enhancements in the roundness values, as can be seen qualitatively from the micrographs shown in Figure 5.2 through Figure 5.6. The increase in sphericity and roundness values would produce a corresponding decrease in the aspect ratio as seen in Table 5.2.

The as-cast alloy M3S (354 + 0.3 wt.% Zr + 0.75 wt.% Mn) shows the lowest value of particle size which is also confirmed by the optical micrograph shown in Figure 5.4; moreover, this alloy also shows the highest rate of coarsening among all alloys. This

coarsening may be attributed to the small size of the Si particles in the as-cast structure which may facilitate the dissolution and diffusion processes which are considered as the mechanisms responsible for Si particle coarsening.[246] In contrast, the base alloy M1S (354 + 0.3 wt.% Zr) and alloy M4S (M1S +4%Ni) show the lowest tendency for coarsening of eutectic silicon following solution heat treatment. The roundness and sphericity values (in percentages) observed for the as-cast condition of the alloys studied remain almost unchanged whereas the solution treatment improves their roundness and sphericity values, as listed in Table 5.2.

Table 5.2 Characteristics of eutectic silicon particles in as-cast and solution-heat treated conditions of the alloys studied

Alloy Code and Condition	Particle Area (μm^2)		Particle Length (μm)		Aspect Ratio		Roundness (%)		Sphericity (%)	
	Av	SD	Av	SD	Av	SD	Av	SD	Av	SD
M1S-AC	2.85	4.39	2.67	2.48	1.96	1.33	0.49	0.21	0.75	0.28
M1S-SHT	3.71	4.71	2.60	2.10	1.71	1.49	0.58	0.19	0.85	0.21
M2S-AC	3.53	7.60	2.83	3.29	1.96	2.44	0.50	0.23	0.74	0.30
M2S- SHT	5.67	8.08	3.27	2.95	1.79	1.27	0.56	0.20	0.81	0.23
M3S-AC	1.92	3.10	2.14	2.22	1.92	2.43	0.51	0.22	0.77	0.28
M3S- SHT	5.35	6.04	3.12	2.32	1.69	2.92	0.61	0.17	0.86	0.19
M4S-AC	3.11	6.61	2.65	3.30	2.02	3.58	0.50	0.25	0.73	0.32
M4S- SHT	3.99	5.53	2.68	2.43	1.86	2.65	0.56	0.22	0.82	0.23
M5S-AC	3.87	6.88	3.12	3.43	2.12	6.27	0.48	0.22	0.70	0.30
M5S- SHT	5.70	7.44	3.52	3.20	1.95	3.60	0.54	0.20	0.78	0.25

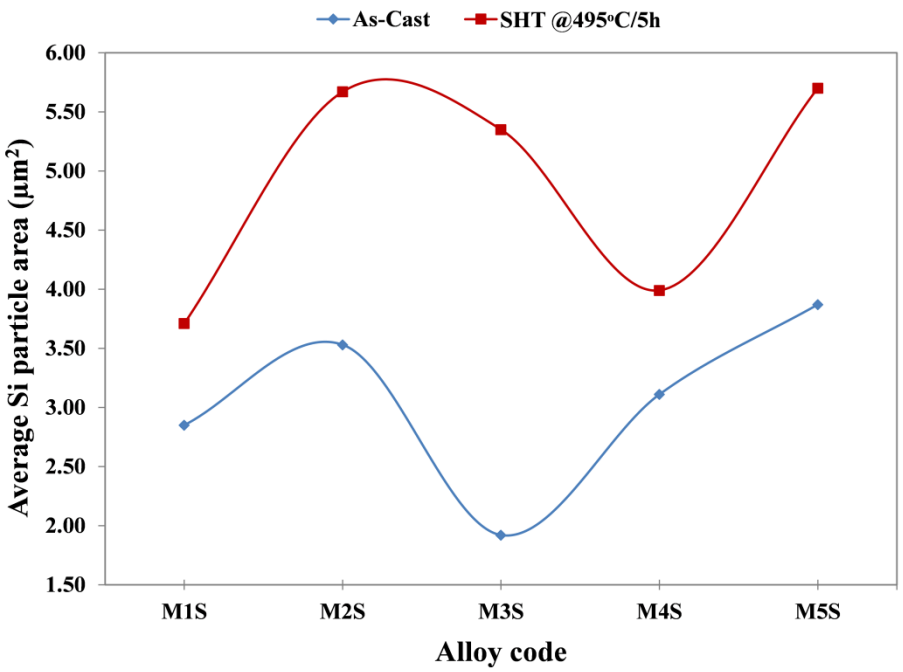

Figure 5.7 Average eutectic silicon particle areas in as-cast and SHT conditions of the alloys studied.

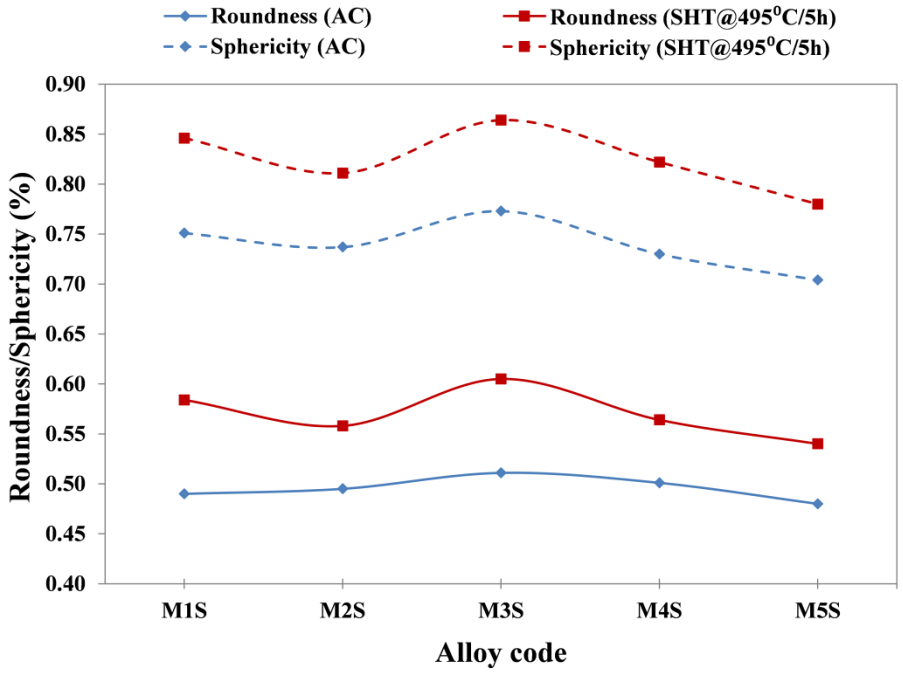

Figure 5.8 Average roundness and sphericity percentage values of eutectic silicon particles in as-cast and SHT conditions of the alloys studied.

PART II- CHARACTERIZATION OF THE MECHANICAL PERFORMANCE

Part II of Chapter 5 will investigate the mechanical performance, including, tensile, hardness, and impact properties of the alloys studied under different heat treatment conditions. With respect to the tensile properties, the effects of notches and their geometry on the ambient- and elevated-temperature tensile properties will also be discussed. The concept of quality index will be used for the sake of evaluating changes in the alloy quality which may stem from various chemical additions and/or applied heat treatments. This will help in deciding upon the optimum metallurgical parameters that would improve the alloy quality. The strengthening contribution of fine precipitates/dispersoids to the yield strength values will be assessed in the case of ambient-temperature tensile properties in the peak-aged (T6-treated) condition.

The reported tensile data are the ultimate tensile strength (UTS), the yield strength (YS), and the ductility value in terms of the percentage elongation to fracture (% El). The impact test data is represented in terms of the total absorbed energy to fracture. The tensile and impact data are the average values obtained by testing five bars per condition per alloy, while the hardness values are the average Rockwell hardness values obtained from ten measurements per condition per alloy.

5.4 TENSILE PROPERTIES

This section presents the tensile test data of smooth and notched bars obtained at room and 250°C temperatures. The results presented will be interpreted in relation to the various nickel and manganese additions made, and the heat treatments employed.

5.4.1 AMBIENT-TEMPERATURE TENSILE PROPERTIES OF SMOOTH BARS

The panel charts shown in Figure 5.9 provide full details of the tensile test data of the alloys obtained at ambient temperature, with respect to the additions and heat treatments used in each case. Figure 5.9(a) shows the strength (UTS and YS) values, while Figure 5.9(b) shows the ductility (%El) values. An immediately apparent observation is that all the tensile properties follow the same variation in relation to the applied heat treatment, regardless the chemical composition.

In the present study, the sole addition of ~0.3 wt.% Zr to the 354-type Al-Si-Cu-Mg cast alloy (i.e. the base alloy M1S) in the as-cast condition enhances the ambient-temperature strength values of the Zr-free 354 alloy (alloy A) used in previous investigations by Hernandez-Sandoval,[12] by ~26 MPa (UTS) and 40 MPa (YS), respectively. These enhancements in the strength values are accompanied by a very limited reduction in the alloy ductility (~0.054%). For the solution heat-treated condition, on the other hand, the UTS and ductility values of the base alloy M1S remain virtually constant at ~300 MPa and ~ 6.3 %, respectively, while the yield strength increases by ~33 MPa compared to alloy A in the work of Hernandez-Sandoval.[12] The improved strength values of Zr-containing Al-Si-Cu-Mg alloy emphasizes the role of Zr addition in enhancing the ambient-temperature tensile properties. As mentioned earlier, the strengthening role of Zr is

believed to be instigated through the formation of fine secondary strengthening precipitates (Al_3Zr) as reported by many authors.[14, 17, 156, 157]

For each alloy, one can easily observe from Figure 5.9(a) that the UTS and YS values in the T5 heat-treated condition are close to each other, and even more so for the T6-treated condition, in contrast to the widely separated UTS and YS values for the as-cast and as-quenched conditions. This behavior can be properly ascribed to the strengthening effect of the fine dispersoids, which precipitate during the artificial aging stage of the T5, and T6 treatments. The presence of these dispersoids considerably enhances the YS values and negatively affects the ductility values, as seen in Figure 5.9.

For the base alloy M1S, the immediate artificial aging of as-cast tensile bars at 180°C for 8 hours, or in other words the T5 treatment, increases the UTS of the base alloy M1S by ~30 MPa over its value in the as-cast condition (Figure 5.9(a)). Inversely, the UTS values of other alloys in the T5-treated condition, i.e. M2S through M5S, decrease compared to their as-cast values. The same trend is observed for the ductility values of the alloys M1S through M5S, which decrease following the application of the T5 heat treatment with reference to their as-cast values. Simultaneously, the yield strength values of the T5-treated alloys improve remarkably, by as much as 30-65 MPa, compared to the as-cast values. The highest improvement in YS, i.e. 65 MPa, is exhibited by alloy M2S which contains 2 wt.% Ni.

The strength values (UTS and YS) of alloys M1S, M2S (M1S + 2 wt.% Ni) , and M3S (M1S + 0.75 wt.% Mn) show distinct enhancements after applying the T6 treatment in comparison to the as-cast and as-solutionized conditions. In contrast, alloys M4S (M1S + 4

wt.% Ni) and M5S (M1S + 2 wt.% Ni + 0.75 wt.% Mn) exhibit a very limited enhancement in UTS (~15 MPa) after T6 heat treatment with reference to their strength in the as-cast and as-quenched conditions. Additionally, from Figure 5.9(b), it can be seen that the ductility values reduce considerably after T6 treatment when compared to the as-cast ductility values of the respective alloys.

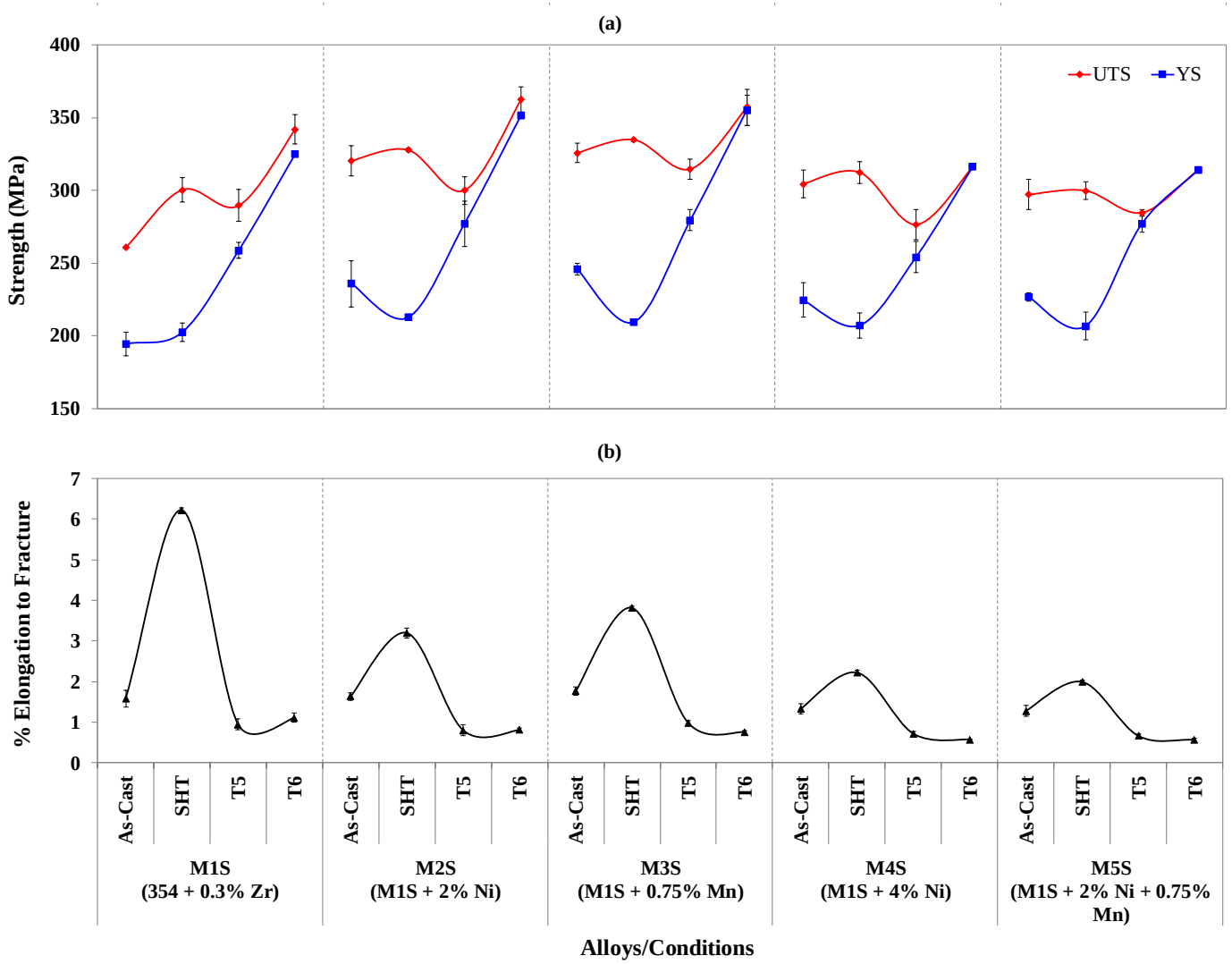

Figure 5.9 Variation in average (a) UTS, YS, and (b) %El values of the alloys studied in as-cast, solution heat-treated (SHT), T5- and T6-treated conditions obtained at ambient temperature for smooth bars.

5.4.1.1 TENSILE PROPERTIES OF AS-CAST AND AS-QUENCHED CONDITIONS

Strength and ductility values of the alloys in as-cast and solutionized conditions are presented in Figure 5.10. In the as-cast condition, the base alloy M1S (354 + 0.3 wt.% Zr) shows the lowest UTS and YS values. As-cast strength values of the other alloys, i.e. M2S through M5S, show enhancements of 14-25% and 16-26% in UTS and YS, respectively, compared to the base alloy (M1S). Anomalously, the ductility values of alloys M2S through M5S show inconsistent variations with respect to the ductility of the base alloy M1S; these variations comprise enhancements in case of alloy M3S, deteriorations in the case of alloys M4S and M5S, and almost unchanged ductility value in the case of alloy M2S. These evident alterations in the as-cast tensile properties can be ascribed uniquely to the possible changes in microstructural features resulting from the various additions of nickel and/or manganese to the base alloy.

The probable explanations for the enhanced strength values of alloy M3S are the formation of favourable phases, which are advantageous to the strength values, and the highly refined as-cast Si particles, Table 5.2, as a result to the addition of 0.75 wt.% Mn to the base alloy (M1S). It is well established that the addition of Mn neutralizes to some extent the deleterious effect of iron impurities by transforming the detrimental needle-like β-Al_5FeSi phase into the less harmful α-$Al_{15}(Fe, Mn)_3Si_2$ phase, which appears in either script-like form or as blocky sludge particles, or both, as described previously in Chapter 4, section 4.2.1, and in Part I of this chapter. While there is no doubt about the positive effect of the script-like α-phase on strength and ductility values, there is much debate, however, on the effect of the sludge particles on the tensile properties either they are harmful, as regularly believed,[76] or favourable to the tensile properties.[11, 80, 247]

Garza-Elizondo[11] has reported that the presence of these blocky sludge particles in the alloy microstructure does not necessarily affect the tensile properties in a negative manner. In fact, the presence of these hard particles in the soft α-Al matrix may contribute in enhancing the tensile properties of the respective alloys through the development of more uniformly distributed stresses within the matrix. Although this observation contradicts the well-established harmful effect of sludge formation as reported in the literature,[76, 242, 248] the difference in the morphology of the sludge phase particles in the present alloys may be the reason for these findings. The harmful effect of sludge particles is regularly reported in relation to the star-like morphology; whereas the beneficial effect is commonly observed with sludge particles which exhibit compact polyhedral and block-like morphologies.

For the Ni-containing alloys, enhancements in the strength values can be correlated to the formation of Ni-containing intermetallic compounds such as Al_9FeNi, Al_3CuNi, and Al_3Ni which can hinder the propagation of cracks; similar findings are reported in previous studies.[12, 165] Increasing the Ni content from 2 wt.% to 4 wt.% inversely affects the tensile properties at room temperature. It is believed that the precipitation of higher volume fractions of the acicular Al_3Ni phase in the as-cast alloy M4S (4 wt.% Ni) is responsible for the deterioration of the tensile properties at room temperature. Interestingly, the same phase can be advantageous to the tensile properties at both room and elevated temperatures if its morphology could be refined after solution treatment.

Apparently from Figure 5.10, the base alloy M1S proves to be very responsive to solution heat treatment because it shows an increase of 40 MPa and 8 MPa in the as-cast UTS and YS values, respectively, after solutionizing at 495°C for 5 hours. In addition, the ductility of the solutionized M1S alloy also shows an increase of ~5% over the ductility

value obtained for the as-cast condition. On the other hand, the other alloys, i.e. M2S through M5S, show small improvements, in the range of 2-10 MPa for UTS values, and a noticeable reduction in YS values (18-36 MPa) compared to their strength values in the as-cast condition. The ductility values of alloys M2S through M5S increase after solution treatment, with alloys M2S (base alloy + 2 wt.% Ni) and M3S (base alloy + 0.75 wt.% Mn) showing comparatively higher values compared to alloys M4S and M5S, as can be perceived from Figure 5.10(c).

The solutionizing treatment is intended to produce changes in the as-cast microstructure including dissolution of soluble intermetallic particles such as Mg_2Si and Al_2Cu that may exist in the as-cast structure, homogenizing segregation in the as-cast structure, and finally instigating morphological changes in the eutectic silicon particles. These factors will eventually enhance the ultimate tensile strength and ductility values of alloys through increased solid solution strengthening and the thermal-modification of the eutectic silicon particles from an acicular or fibrous interconnected morphology to well-separated spheroidal particles.

The enhanced ductility values after solution-heat treatment, in particular, related to the changes in the eutectic silicon morphology. Coarse acicular silicon particles serve as crack initiators, which is the case in the as-cast condition; whereas more spherical Si particles with rounded edges and decreased aspect ratios are obtained in the solution heat-treated case. Table 5.2 in Part I of this chapter elaborated upon the details of the Si particle characteristics.

Another interesting observation noted from Figure 5.10(b) is that the yield strength values for the solution-treated alloys are almost constant with the exception of minor discrepancies with respect to the various chemical compositions studied. In other words, Ni and Mn additions to the base alloy have only a feeble effect on the yield strength compared to what is observed in the as-cast condition. This behaviour may be understood in the light of the fact that the yield strength is mainly dependent on hardening effects caused by the strengthening elements Cu and Mg. By referring to the DSC heating curves of solution-treated alloy samples as described in Chapter 4 section 4.2, and the reported volume fractions of intermetallic compounds presented in Part I of this chapter, it is evident that Cu is almost completely dissolved in the α-Al matrix following solution treatment. Furthermore, since the Cu and Mg contents are the same in the five alloys studied, the yield strength values would be similar.

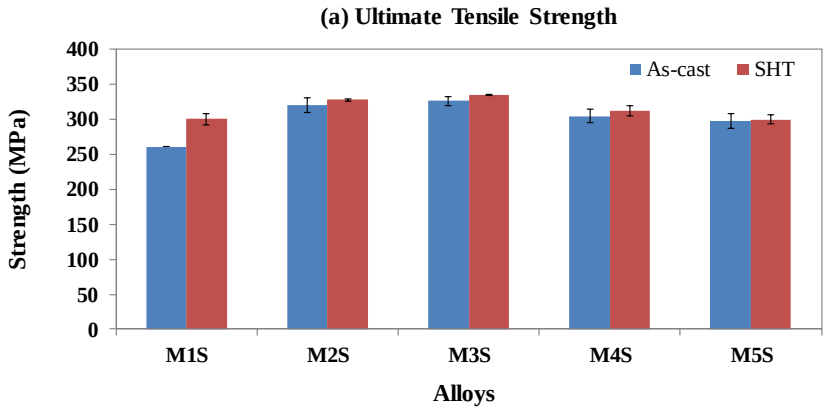

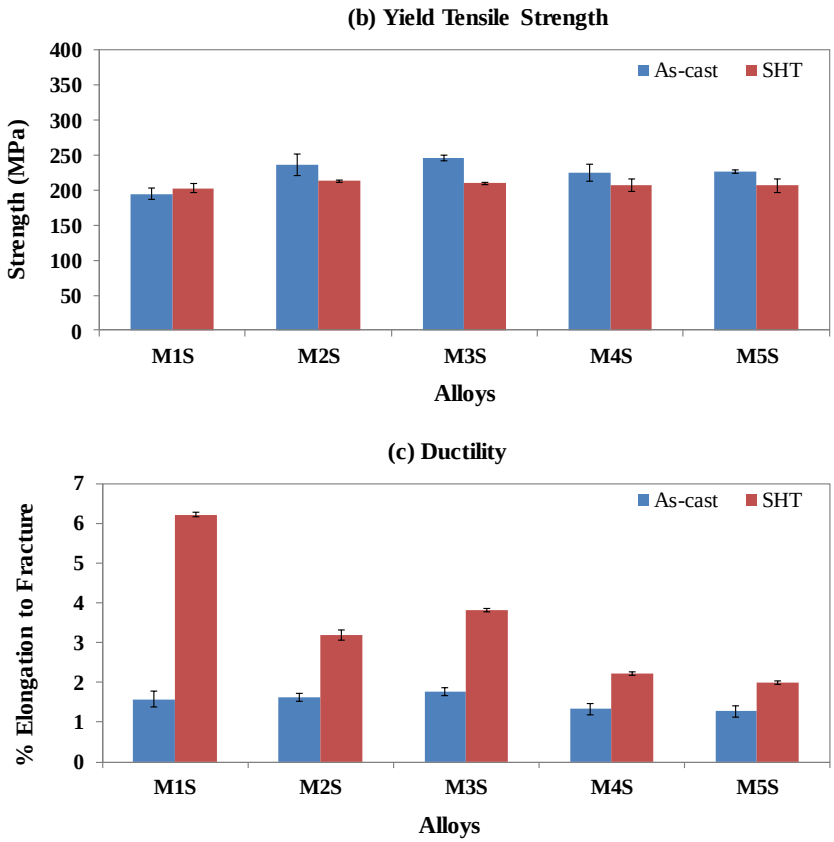

Figure 5.10 Tensile properties: (a) UTS, (b) YS, and (c) ductility, of the studied alloys in as-cast and SHT conditions tested at ambient temperature using smooth bars.

5.4.1.2 TENSILE PROPERTIES OF T5- AND T6-TREATED CONDITIONS

The as-cast microstructure of an alloy can be further improved by applying a suitable heat treatment and hence provide better mechanical properties. In order to investigate the effect of heat treatments on the tensile properties of the alloys studied, as-cast tensile bars of all alloy compositions were heat treated according to T5 and T6 tempers. The T5-treatment comprised artificial aging of the as-cast tensile bars at 180°C for 8 hours; whereas the T6-treatment consisted of solutionizing the as-cast tensile bars at 495°C for 5 hours followed by quenching in warm water at 60°C, and artificial aging at 180°C for 8 hours.

Figure 5.11(a) and Figure 5.11(b) show that the strength values of the base alloy M1S are 289 MPa (UTS)/259 MPa (YS) and 342 MPa (UTS)/ 325 MPa (YS) in the T5- and T6-treated conditions, respectively. Alloys M2S and M3S exhibit the highest strength among the alloys studied with values of 300 MPa (UTS)/277 MPa (YS), and 315 MPa (UTS)/279 MPa (YS), respectively, in the T5-treated condition; and 362 MPa (UTS)/352 MPa (YS) and 357 MPa (UTS)/355 MPa (YS) in the T6-treated condition respectively. In regard to the ductility values, Figure 5.11(c) shows that the base alloy M1S and the 0.75 wt.% Mn-containing alloy (M3S) exhibit the highest ductility values, 0.94% and 0.98%, respectively, in the T5-treated condition, while the 2 wt.% Ni-containing alloy (M2S) exhibits a lower value of 0.8% with the same T5 treatment.

With T6 heat treatment, the highest ductility value can be observed for the base alloy M1S with a value of ~1.1%; followed by alloy M2S with a value of 0.8% and alloy M3S with a ductility of 0.75%. Ductility values of the alloys studied are limited in general due to the high silicon content ~ 9wt.% and the presence Mg and Cu.[43]

The enhanced strength values of alloy M2S, particularly for the T6-treated condition, can be attributed to the presence of Ni-containing phases such as Al_3Ni, Al_9FeNi, and Al_3CuNi, in addition to the fine precipitates formed after applying T6 treatment.[249, 250]

With respect to alloy M3S, the improved strength values following T5- and T6-heat treatments can be ascribed to: (i) the presence of α-$Al_{15}(Fe, Mn)_3Si_2$ in the form of blocky hard particles, and (ii) the probable formation of Al_6Mn fine dispersoids in the presence of a high Mn content of 0.75 wt.%. These fine Mn-containing dispersoids have sizes in the

scale of 0.05-0.5μm, according to previous investigations.[78, 144] The presence of these Mn dispersoids significantly improves the yield and ultimate strength values without sacrificing the ductility[77-79] which is the case for alloy M3S, as shown in Figure 5.11.

Anomalously, the base alloy M1S in the T5- and T6-treated conditions exhibits tensile properties superior to those of the derived alloys M4S and M5S. Alloys M4S and M5S demonstrate almost similar ambient-temperature tensile properties in the T6-treated condition, with a very limited variation of ~5 MPa for both UTS and YS values, and unchanged ductility values. For the same two alloys, the T5 heat treatment results in more pronounced differences in tensile properties, where the UTS of alloy M5S is higher than that of M4S by ~9 MPa, the YS of alloy M5S is higher than that of alloy M4S by ~23 MPa, while the ductility value of alloy M4S is higher than that of alloy M5S by ~0.06%.

The presence of a high nickel content in alloy M4S (4 wt.%) results in deteriorating the tensile properties as can be inferred from Figure 5.11; similar observations have been noted by other authors.[11, 194, 251-254] This deterioration in the strength values is a direct result of the high content of Ni which, in turn, will consume the available copper in the alloy to form the detected Al_3CuNi phase. As a result, this will reduce the amount of copper available for strengthening through precipitation hardening during heat treatment.[194] Furthermore, the precipitation of Al_9FeNi and Al_3CuNi phases in high volume fractions (see Table 5.1) would facilitate cracking since they would act as stress raisers, causing instability in the flow strain, and hence the ductility of this alloy will reduce accordingly, as witnessed in Figure 5.11(c).

In general, the room-temperature tensile properties in the T6 heat-treated condition are better than those obtained with the T5 treatment for the alloys studied. Investigations by Crepeau *et al.*[255] Sepehrband *et al.*[150] and Gauthier *et al.*[256] acknowledge the effectiveness of the mutual strengthening of Al_2Cu and Mg_2Si in Al-Si-Cu-Mg alloys. Furthermore, the use of permanent mold casting, which is the technique used for producing the test bars, would preserve copper and magnesium in considerable amounts in solid solution due to the high solidification rate. Thus by applying artificial aging directly after solidification (i.e. T5 temper), large proportions of the dissolved Cu and Mg in the solid solution will form strengthening dispersoids, considered the main strengthening source in the case of T5 treatment. The T6 heat treatment, on the other hand, involves solutionizing the as-cast structure at a sufficiently high temperature in order to dissolve higher amounts of Cu and Mg in solid solution in order to form a supersaturated solid solution as well as to achieve further modification of the eutectic Si particles. Thus, the artificial aging in the case of T6 treatment will precipitate fine strengthening particles in a larger proportion than in the case of T5 treatment, which will enhance the alloy strength to a greater extent, however, at the expense of ductility. Consequently, higher strength and lower ductility values would be observed with T6 treatment compared to T5 treatment, as can be seen in Figure 5.11.

Depending on the industrial application of interest, it is crucial to have an acceptable compromise between the tensile properties, particularly the relative trade-off between strength and ductility values, because of the vast discrepancies in these properties with respect to alloy composition and applied heat treatments. This understanding was the motive to introduce the concept of the quality index, where the tensile properties of alloys are mathematically manipulated in order to calculate the quality index.

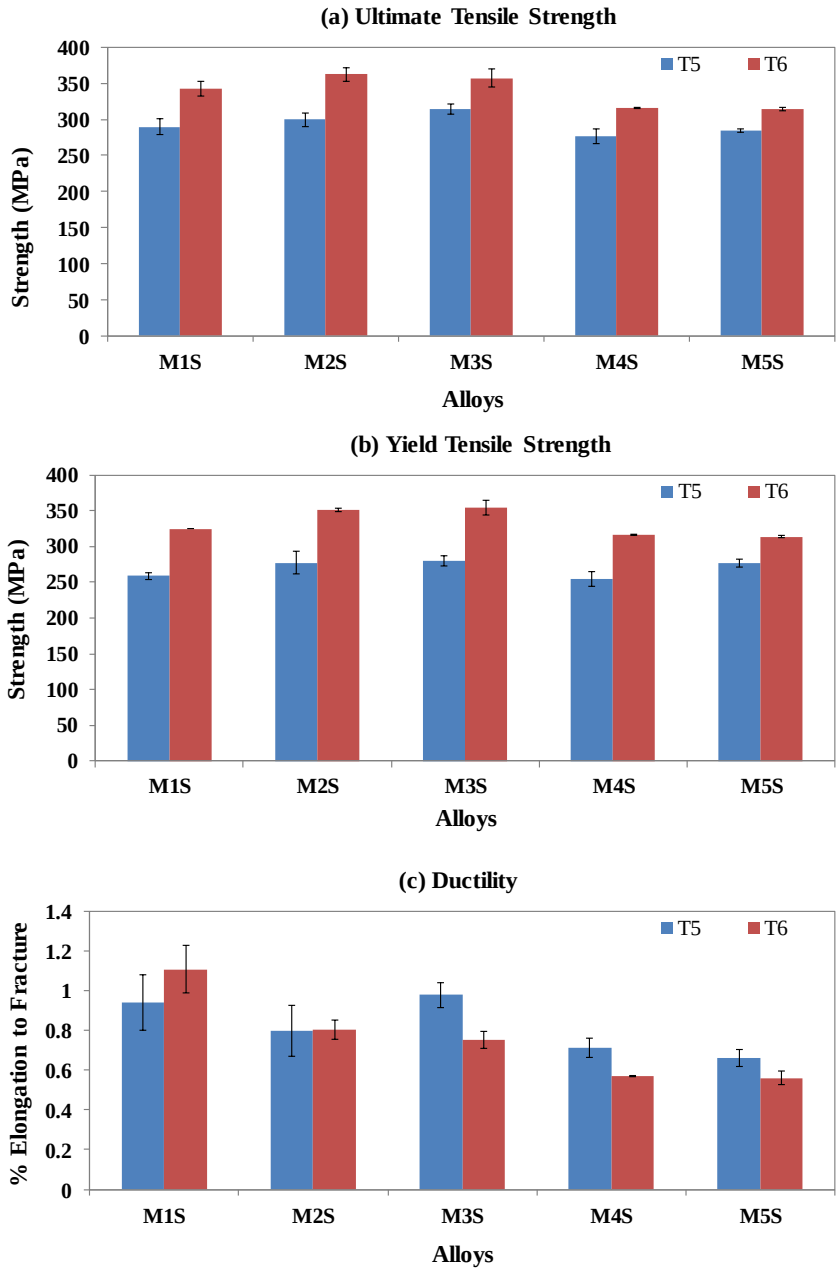

Figure 5.11 Tensile properties: (a) UTS, (b) YS, and (c) ductility, of the studied alloys in T5- and T6-treated conditions tested at ambient temperature using smooth bars.

For the ambient-temperature tensile data in the present study, the quality index values and chart according to the model developed by Cáceres[61] (Q_c) will be used because of the feasibility of calculating flow parameters of the alloys studied such as strain hardening exponent (n) and the strength coefficient (K). Additionally, for the ambient-temperature tensile properties, the quality index values will also be calculated using the empirical model of Drouzy *et al.*[60] (Q) for comparison with the quality index values obtained from tensile tests carried out at 250°C since, for the elevated-temperature tensile testing, the concept of quality index according to Drouzy *et al.*[60] was employed in the present study.

For the alloys studied, the ambient-temperature tensile testing data are listed in Table 5.3 along with the quality index values which were calculated using Equations 2.9 and 2.18 from Chapter 2 according to the models developed by Drouzy *et al.*[60] and Cáceres[61], respectively. Figure 5.12 shows the quality chart for the alloys studied based on the Cáceres[61] model, and depicts variations in the quality index values based on the chemical composition, and the applied heat treatment. Equations 2.15 and 2.16 from Chapter 2 were used to develop the *"iso-n"* and *"iso-q"* lines in the chart, with a constant "K" value of 680 MPa, for all conditions studied.

The quality index values Q and Q_c, listed in Table 5.3 show the same trend in variations, however, with different values. The difference between Q and Q_c increases in the T5- and T6-heat treated conditions which can be accredited to the fact that the alloy quality is affected by the net amount by which the increase in strength is balanced by the reduction in ductility. As can be seen from Table 5.3 and Figure 5.12, the best quality values for the alloys are obtained after solution heat treatment, attributed to the

microstructural changes that take place during the solution treatment including the dissolution of strengthening elements, the homogenization of the segregated as-cast structure, and the spheroidization of the eutectic silicon particles. These changes will significantly enhance the alloy ductility, in addition to a limited enhancement in UTS values. Consequently, the quality index values of the as-quenched (or solution heat-treated) alloys are remarkably higher than those in the as-cast condition, as seen in Figure 5.12.

While the T6-heat treatment improves the UTS values considerably, in comparison to the UTS values obtained after solution treatment, it does so at the expense of the ductility. This trade-off between UTS and ductility values will certainly affect the quality index values and not necessarily in a positive way. Likewise, a similar behavior is noted for the T5-treated alloys, as well, as can be inferred from Figure 5.12.

It is evident that the superior ductility of the base alloy M1S is the main reason for the improved quality indices of this alloy in the majority of the conditions studied. On the other hand, the mutual enhancement in the strength and ductility values of alloys M2S and M3S compared to those of alloys M4S and M5S is responsible for the higher quality indices of the former compared to those of the latter.

The addition of Mn in alloy M3S results in transforming the needles of the β-iron phase into the less detrimental α-iron phase; this favourable morphological change is believed to improve the ductility and strength values of alloy M3S. Whereas, the structure of alloy M2S contains Ni-bearing phases with acicular morphologies and β-iron needles which negatively affect the mechanical properties. Accordingly, the quality index values of alloy M3S are higher than those of the 2 wt.% Ni-containing alloy M2S in the as-cast, SHT,

and T5 conditions. In contrast, the quality index values of the T6-treated alloys M2S and M3S show a reversed behavior according to the marginal variations in their tensile properties and hence the quality index values.

From Table 5.3, it is observable that the quality index values calculated using Drouzy's approach are higher than those obtained by the model developed by Cáceres for all treatment conditions per each alloy, except for solution-treated conditions. This can be attributed to the improved ductility of as-quenched conditions which will allow more accurate determination of the material parameters (K and n). Thus it would be advisable to calculate the quality index values of solution-treated conditions using Cáceres' model, especially for materials with low ductility at room temperature.

Table 5.3 Variation in average UTS, YS, %El, Q_c, and Q values of the alloys studied in as-cast, SHT, T5-, and T6-treated conditions obtained at ambient temperature for smooth bars

Alloy	Condition	UTS (MPa)	YS (MPa)	Total strain (%)	Plastic Strain (%)	E (GPa)	n	K	q	Q_c (Eq. 2.18)	Q (Eq. 2.9)	Difference (Q-Q_c) (MPa)
M1S	**As-Cast**	260.86	194.39	1.58	1.16	62.66	0.18	580.56	0.07	277.88	290.50	12.62
	SHT	300.34	202.51	6.22	5.74	62.50	0.17	579.26	0.34	512.36	419.43	-92.93
	T5	289.50	258.75	0.94	0.48	63.06	0.13	591.69	0.04	217.06	285.43	68.38
	T6	341.95	324.99	1.1075	0.56	62.45	0.10	576.91	0.06	281.53	348.60	67.07
M2S	**As-Cast**	320.35	235.85	1.63	1.16	67.58	0.19	763.78	0.06	342.14	352.19	10.05
	SHT	327.74	212.61	3.20	2.70	66.23	0.17	759.32	0.16	531.09	403.43	-127.66
	T5	299.97	277.19	0.80	0.34	65.64	0.15	701.96	0.02	167.10	285.22	118.12
	T6	362.33	351.57	0.80	0.24	64.71	0.11	707.79	0.02	196.04	348.16	152.12
M3S	**As-Cast**	325.78	245.72	1.76	1.26	64.73	0.15	648.89	0.08	354.71	362.55	7.84
	SHT	334.75	209.43	3.81	3.30	64.47	0.12	646.47	0.27	549.26	421.97	-127.29
	T5	314.58	279.39	0.98	0.49	64.14	0.13	634.49	0.04	238.21	313.10	74.89
	T6	357.01	355.14	0.75	0.20	64.32	0.08	624.21	0.02	192.02	338.50	146.48
M4S	**As-Cast**	304.40	224.61	1.33	0.87	66.10	0.20	836.77	0.04	293.64	322.87	29.23
	SHT	312.32	207.09	2.22	1.75	66.56	0.18	821.35	0.10	469.59	364.27	-105.32
	T5	276.44	254.14	0.71	0.31	68.43	0.20	857.07	0.02	99.28	254.51	155.24
	T6	315.98	315.98	0.5705	0.11	67.10	0.10	634.74	0.01	77.52	279.41	201.89
M5S	**As-Cast**	297.07	226.59	1.27	0.83	66.91	0.20	792.01	0.04	273.91	312.80	38.89
	SHT	299.79	206.64	1.99	1.54	67.35	0.17	780.35	0.09	437.14	344.62	-92.52
	T5	284.61	277.00	0.66	0.22	64.74	0.15	722.11	0.01	97.20	257.45	160.25
	T6	314.04	314.04	0.56	0.11	67.89	0.11	677.64	0.01	45.43	276.32	230.89

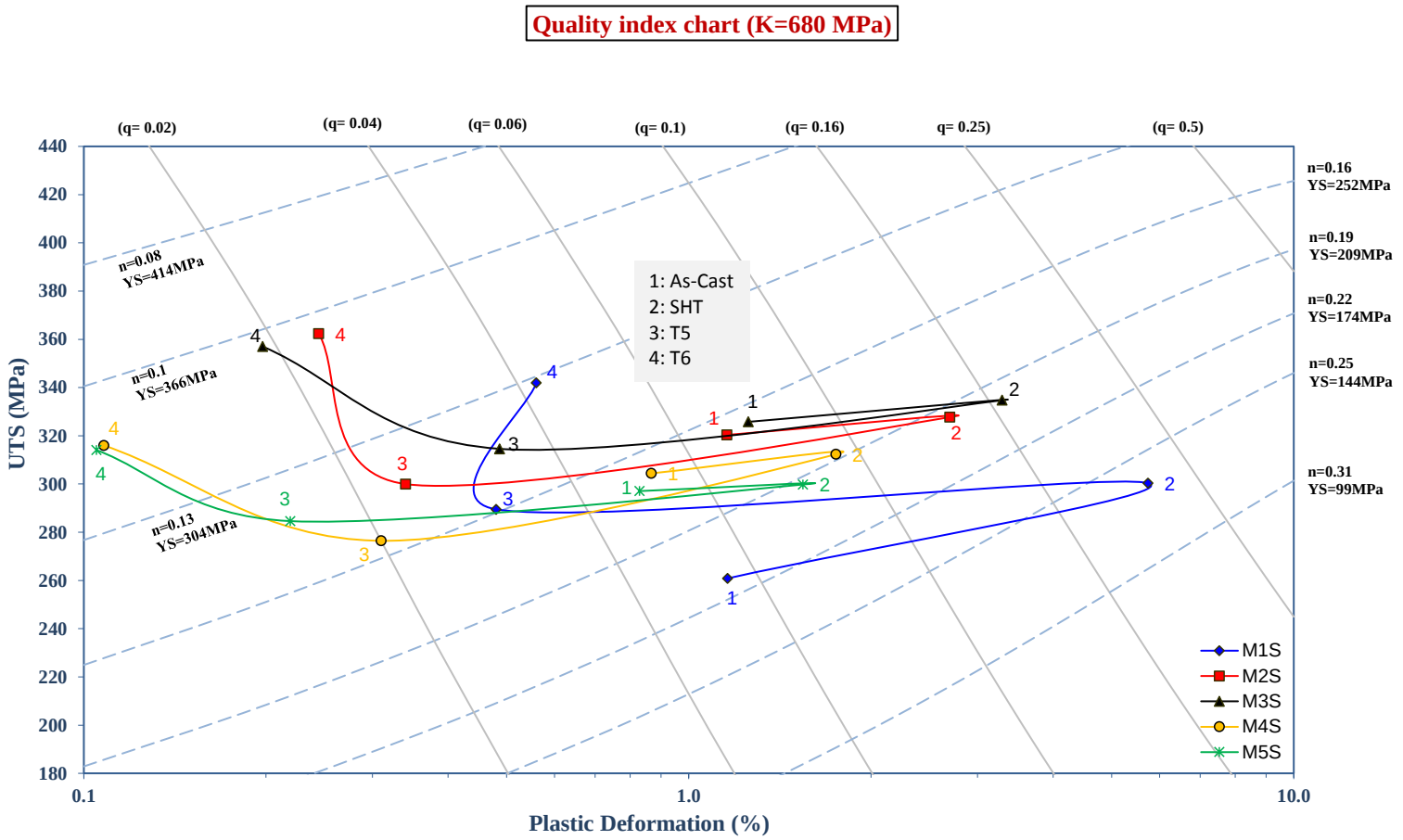

Figure 5.12 Cáceres quality chart representing the relation between the UTS and the percent plastic deformation values of the alloys studied in the as-cast, SHT, T5- and T6-treated conditions obtained at ambient temperature for smooth bars.

5.4.1.3 EFFECT OF HEAT TREATMENT ON YIELD STRENGTH VALUES

Owing to the significance of the yield strength of aluminum casting alloys from the applications point of view, this subsection will address the individual strengthening effects of the various microstructural features existing in the alloy structure on the evolution of the overall yield strength in the peak-aged conditions of the alloys studied. This objective will be accomplished by quantifying the individual strengthening effects of the microstructural components including the contribution of the α-aluminum matrix, eutectic silicon, solid solution, intermetallic compounds, and fine precipitates. The overall yield strength of the alloy may be expressed as the sum of individual strengthening factors, as proposed in Equation 5.1 by various authors[257-262] for peak-aged alloys:

$$\sigma_{peak} = \sigma_i + \sigma_{eutectic} + \sigma_{ss} + \sigma_p \quad \textbf{(5.1)}$$

where σ_{peak} is the overall yield strength in the peak-aged condition, σ_i is the intrinsic aluminum strength, $\sigma_{eutectic}$ is the strengthening contribution of eutectic silicon particles, σ_{ss} is the strengthening contribution of solid solution, and σ_p is the strengthening contribution of fine precipitates.

Referring to Table 5.1 in Part I of this chapter, it is evident that the microstructures of the tailored alloys M2S through M5S comprise high volume fractions of intermetallic compounds which will certainly affect the overall yield strength; however, the contribution of these compounds is not included in Equation 5.1. The effect of the very limited volume fraction of intermetallic compounds in the as-quenched base alloy may be neglected and hence Equation 5.1 is valid for the base alloy. On the other hand, for the tailored alloys,

Equation 5.1 would have to be modified slightly to include the effect of intermetallic compounds to be in the form:

$$\sigma_{peak} = \sigma_i + \sigma_{eutectic} + \sigma_{ss} + \sigma_{int} + \sigma_p \quad \textbf{(5.2)}$$

where σ_{int} is the strengthening contribution of intermetallic compounds in the tailored alloys M2S through M5S.

The intrinsic aluminum strength (σ_i) can be assumed to be 10 MPa at the ambient temperature with reference to Wang *et al.*[263] The strengthening contribution of the eutectic silicon phase (σ_{eutectic}) was calculated experimentally during the course of this study by tensile testing a binary Al-9% Si alloy. To obtain the sole strengthening effect of the eutectic silicon phase, the intrinsic aluminum strength (i.e. 10 MPa) was subtracted from the overall yield strength of the binary Al-9% Si alloy. Though the binary Al-9% Si alloy is not heat treatable, it was solutionized at 495°C for 5 hours, employing the same solutionizing parameters used for alloys M1S through M5S, in order to account for the thermal modification of the eutectic silicon particles. The alloy test samples were then pulled to fracture at room temperature in the as-quenched condition.

Obviously, Equation 5.1 can be slightly modified with respect to the condition studied. For example, the strengthening contribution of fine precipitates (σ_{p}) almost equals zero for the overall yield strength of the as-quenched condition (σ_{aq}), assuming that no precipitates are formed or are present during quenching. Thus for the base alloy, Equation 5.1 can be modified to be:

$$\sigma_{aq} = \sigma_i + \sigma_{eutectic} + \sigma_{ss} \quad \textbf{(5.3)}$$

while for as-quenched conditions of alloys M2S through M4S, Equation 5.2 can be modified as :

$$\sigma_{aq} = \sigma_i + \sigma_{eutectic} + \sigma_{ss} + \sigma_{int} \quad \textbf{(5.4)}$$

The σ_{aq} is obtained experimentally for each alloy by tensile testing the solution heat-treated samples, the intrinsic strength of the aluminum matrix is considered to be 10 MPa, and $\sigma_{eutectic}$ is experimentally evaluated by tensile testing the binary Al-9% Si alloy. Consequently, the yield strength of the solid solution σ_{ss} can be experimentally calculated using Equation 5.3 in the following form for the base alloy M1S only:

$$\sigma_{ss} = \sigma_{aq} - \sigma_i - \sigma_{eutectic} \quad \textbf{(5.5)}$$

However, it is not feasible to use Equation 5.4 to experimentally find the yield strength of solid solutions for alloys M2S through M5S because there is another unknown term, which is σ_{int}. Fortunately, the strengthening contribution of the solid solution can be calculated using the empirical Equation 5.6, which may then be modified by incorporating constants A and B in Equation 5.7. Thus, the strengthening contribution of the solid solution in the base alloy M1S will be used to determine constants A and B in Equation 5.7 which will allow us to calculate σ_{ss} for alloys M2S through M5S; and then substituting its value in Equation 5.4 to calculate the strengthening contribution of intermetallic compounds.

The solid solution strengthening (σ_{ss}) is mainly dependent on the solubility (C_{ss}) of alloying and strengthening elements (solutes) in the α-Al matrix (solvent). Equation 5.6 is used to calculate the value of σ_{ss} according to Deschamps *et al.*[264], while Equation 5.7 was introduced by Sharma *et al.*[261] to modify values obtained by Equation 5.6:

$$\sigma_{ss} = \sqrt{3} k_{ss} (C_{ss})^m \quad \textbf{(5.6)}$$

$$\sigma_{ss} = A(C_{ss})^m + B \quad \textbf{(5.7)}$$

where k_{ss} and m are material constants with approximate values of k_{ss}= 24 MPa per atomic percent and m= 2/3 for dilute solutions of Al-Cu and Al-Mg, according to Sharma *et al.*[261] For all the alloys studied, an assumption is made that Si, Cu, and Mg are dissolved partially in the α-Al matrix during the solutionizing treatment in amounts of 1.17%, 1%, and 0.5%, respectively, taking into consideration the phase diagrams of the Al-Si, Al-Cu, and Al-Mg systems, and the over-conservative solutionizing temperature (495°C) used. Based on these values of the dissolved Si, Cu and Mg, C_{ss} can be considered to be equal to 2.67 following similar assumptions as those made by Shaha[14] for 354-type Al-Si-Cu-Mg cast alloys.

For the base alloy M1S, the experimental σ_{aq} has a value of 202.50 MPa, σ_i is considered 10 MPa, and $\sigma_{eutectic}$ is found experimentally to be 100 MPa from testing the binary Al-9% Si alloy. Thus according to Equation 5.5, the experimental value of σ_{ss} is calculated to be 92.50 MPa; whereas the calculated value of σ_{ss} using Equation 5.6 is found to be ~80 MPa. These values are then used to calculate the constants of A and B in Equation 5.7. Since the difference between the experimental and calculated values of σ_{ss}

for the base alloy is ~12.5 MPa, we can assume the constant B in Equation 5.7 to be equal to this difference, i.e. 12.5 MPa, and thus constant A is calculated to be 41.57 MPa.

The addition of Ni in alloys M2S, M4S and M5S consumes a considerable amount of Cu to form the Al_3CuNi phase, so that it is reasonable to assume that the content of the dissolved Cu in the α-Al matrix is halved (i.e. 0.5%) in these alloys. Accordingly, the value of C_{ss} is considered to be ~2.15 according to Al-Cu, Al-Mg, and Al-Si phase diagrams with the assumption that 0.5% Cu, 0.5% Mg, and 1.17 % Si are dissolved in the α-Al matrix of alloys M2S, M4S, and M5S. By substituting the new value of C_{ss} in Equation 5.7 and knowing constants A and B, the calculated value of σ_{ss} for the Ni-containing alloys M2S, M4S, and M5S is found to be ~81.75 MPa. Since alloy M3S is a Ni-free alloy and hence the dissolved Cu is assumed to be similar to that of the base alloy, then the σ_{ss} value of 92.5 MPa for the base alloy is considered valid for alloy M3S.

The results of the calculations for the alloys studied in the as-quenched and peak-aged conditions are presented in Table 5.4. For the peak-aged condition, efficient precipitation is assumed during the aging treatment and hence the solid solution strengthening (σ_{ss}) will be equal to zero. Explanations for the data listed in Table 5.4 seem to be in large agreement with those provided previously for the ambient-temperature tensile properties of the alloys studied, particularly with respect to the formation of secondary fine precipitates of Al_6Mn in alloy M3S and the reduction of strengthening by precipitates in alloy M4S owing to the consumption of Cu.

Table 5.4 Summary of the yield strength contributions from various constituents in the alloys studied in the as-quenched and peak aged (T6) conditions (testing at ambient temperature using smooth bars)

Alloy	Condition	σ_i (MPa)	σ_{eu} (MPa)	σ_{ss} (MPa)	σ_{int} (MPa)	σ_p (MPa)	σ_{peak} (MPa)
Alloy M1S	**SHT**	10.00	100.00	92.51	0.00	0.00	202.51
	Peak-aged	10.00	100.00	0.00	0.00	214.99	324.99
Alloy M2S	**SHT**	10.00	100.00	81.75	20.86	0.00	212.61
	Peak-aged	10.00	100.00	0.00	20.86	220.71	351.57
Alloy M3S	**SHT**	10.00	100.00	92.51	6.92	0.00	209.43
	Peak-aged	10.00	100.00	0.00	6.92	238.22	355.14
Alloy M4S	**SHT**	10.00	100.00	81.75	15.34	0.00	207.09
	Peak-aged	10.00	100.00	0.00	15.34	190.64	315.98
Alloy M5S	**SHT**	10.00	100.00	81.75	14.89	0.00	206.64
	Peak-aged	10.00	100.00	0.00	14.89	189.15	314.04

5.4.2 AMBIENT-TEMPERATURE TENSILE PROPERTIES OF NOTCHED BARS

Notches are introduced to the tensile bars to physically simulate a part of the intricate geometry of the automotive engine block and to determine how these fine details may affect the overall mechanical performance of the materials employed in engine blocks. Materials can suffer unexpected and sudden cracking in the presence of notches, as a result of the localization of high stress near the notch root. For this reason, it is of a great importance for the design and material selection engineers and researchers to evaluate the tensile strength of alloys of interest in the presence of geometrical discontinuities, termed as notches. The notches used in the present study were made on standard cylindrical test bars in order to avoid varying the geometry of the test bars.

5.4.2.1 SYMMETRIC VERSUS ASYMMETRIC NOTCHES

The intricate geometry of automotive engine blocks comprises multiple details including geometrical discontinuities such as shoulders, keyways, oil holes, passages for cooling fluids, etc.; these geometrical discontinuities may be treated as notches. Some of those details are asymmetric in geometry. On the laboratory scale, however, symmetric notches have been widely investigated due to their relatively simple machining. With the objective of tackling most severe loading conditions, this subsection will discuss the effects of symmetric versus asymmetric notches in order to determine which category is the most severe, i.e. symmetric or asymmetric notches.

Four different notch geometries were used on standard cylindrical test bars, as previously described in Chapter 3. The four geometries were categorized in relation to the geometry of the notch, as holes or v-notches. The hole-notches comprise both symmetric and asymmetric holes; the same is the case for the v-notches. The cross-sectional area of the smooth bars is ~127 mm^2; notch dimensions were selected with the intention of having the same reduced area at a value of ~105 mm^2 for the four different notches of interest. The reduced area refers to the area of the tensile bar at the root of the notch.

The tensile testing was carried out at a strain rate of 4×10^{-4} s^{-1} for the notched bars of all alloy compositions in the T5- and T6-treated conditions. The ambient-temperature tensile data are portrayed in Figure 5.13 for symmetric holes and notches, alongside that for the asymmetric ones. The term notch tensile strength (NTS) is used instead of the tensile strength. NTS is calculated by dividing the maximum load achieved during pulling a notched test-bar by the reduced area, i.e. the cross-section area at the notch root. It is

important to highlight here that the scope of the analysis of notched tensile bars in the present study is not focused on solid mechanics but rather on the microstructural constituents.

It is apparent from Figure 5.13 that the presence of asymmetric notches is more deleterious to the tensile properties than symmetric ones, even if the reduced area is the same. This can be attributed to the complex states of stresses that may develop at the notch root so that premature fracture at lower NTS and ductility values is observed in relation to asymmetric notches. Furthermore, the effects of various chemical additions on ambient-temperature tensile properties of notched bars seem to be feeble compared to their obvious effects on the tensile properties of smooth bars (Figure 5.9). The focus in the rest of this work will be on holes and notches with asymmetric geometries, which are more detrimental to the mechanical performance of the investigated alloys.

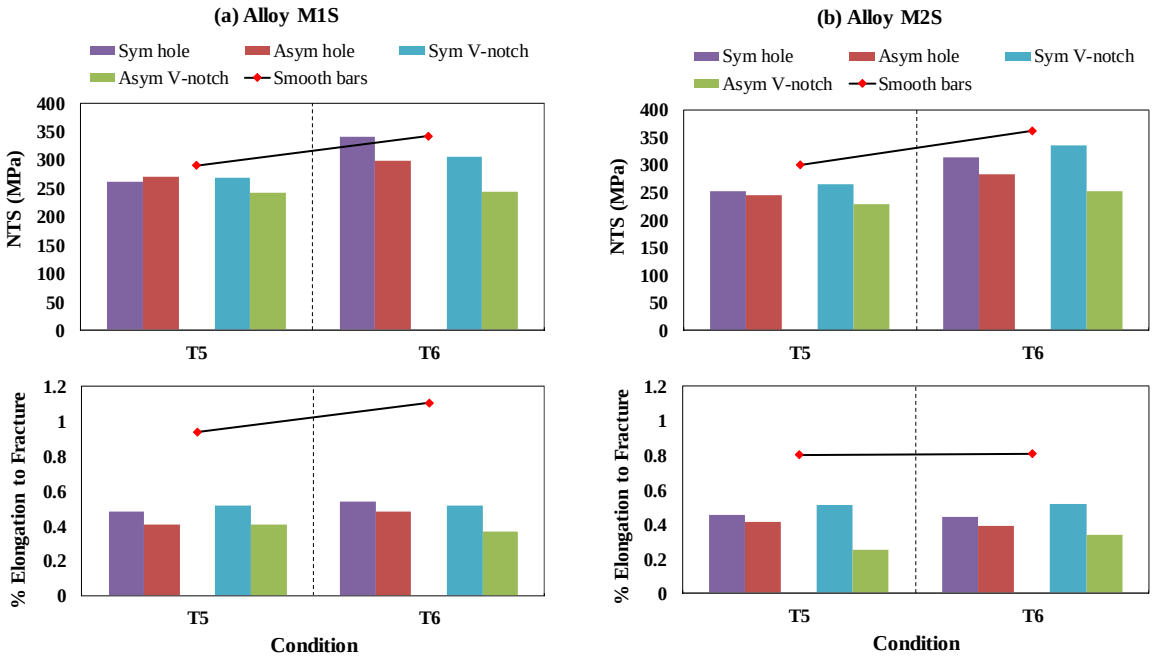

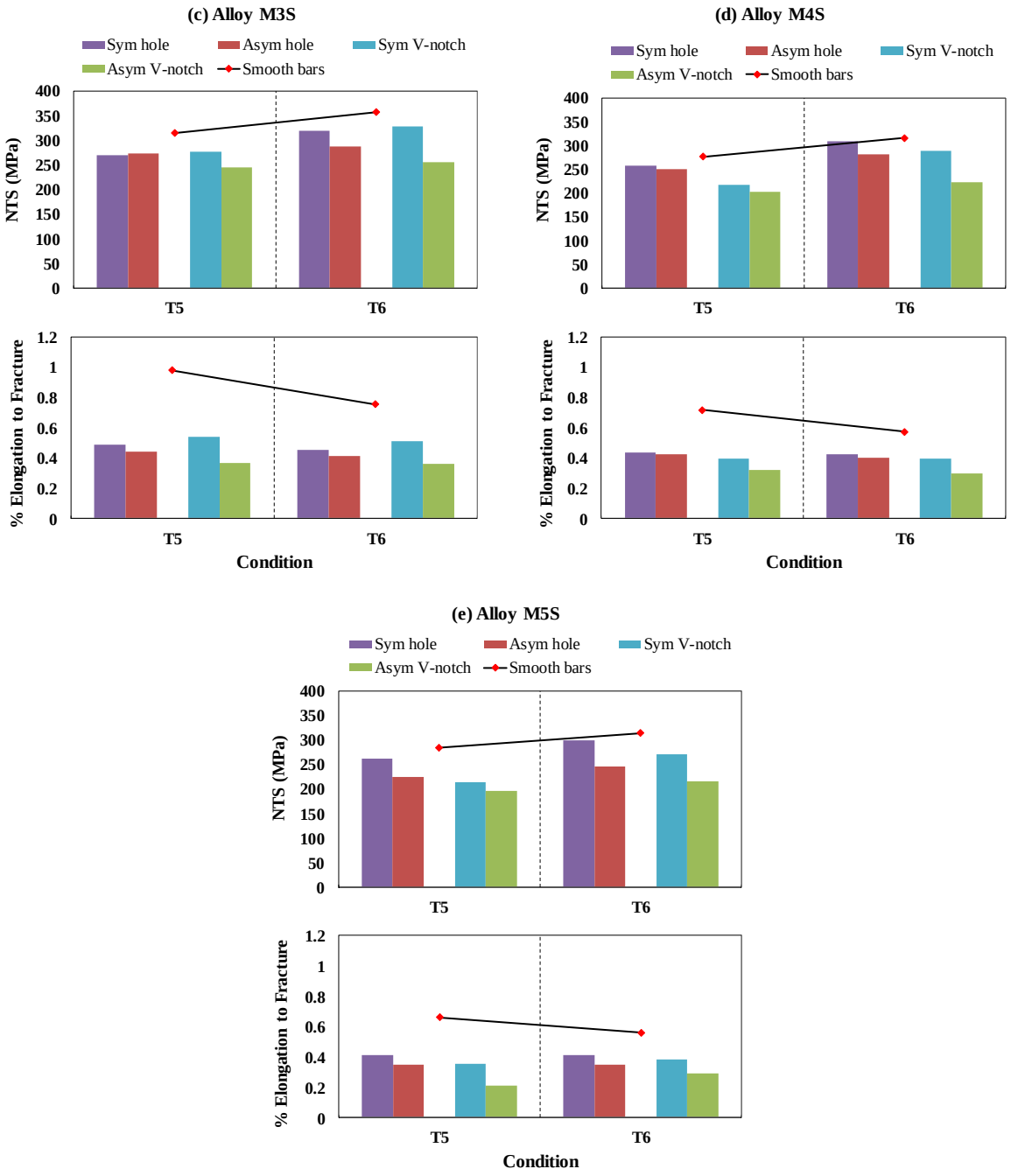

Figure 5.13 Notch tensile strength (NTS) and ductility values of the alloys studied: (a) M1S, (b) M2S, (c) M3S, (d) M4S, and (e) M5S, in T5- and T6-treated conditions obtained at ambient temperature for notched bars.

5.4.2.2 EFFECT OF ASYMMETRIC NOTCHES ON AMBIENT-TEMPERATURE TENSILE PROPERTIES

The tensile strength data of the notched bars versus treatment condition of the alloys studied is presented in Figure 5.14. For all the alloys, the NTS values are seen to follow the same trend in variation with respect to the condition studied. It is evident that the NTS values are lower than the tensile strength values obtained for the corresponding smooth (unnotched) bars. This behavior can be ascribed to the limited ductility of the Al-Si-Cu-Mg (354-type) cast alloys under study; according to Bayram *et al.*,[265] the notched samples of ductile materials exhibit NTS values higher than the tensile strength of the corresponding smooth samples, owing to the high constraint of the plastic flow in the vicinity of the notch in the case of ductile materials. Thus, the propagation of microcracks developed at the notch root during the tensile testing is easier in brittle materials, which will promote the premature fracture of the test bars. This would explain why alloy M5S exhibits the highest strength loss in all the studied conditions, i.e. as-cast, T5-, and T6-treated, because this alloy is reported to have one of the lowest ductility values in the case of smooth bars.

The high volume fraction of intermetallic compounds (Table 5.1) in the as-cast and solutionized structures of alloy M4S proves to be advantageous to NTS values of this alloy through its resistance to crack propagation during tensile testing of notched bars; hence, alloy M4S shows better resistance to premature cracking and fracture in the notched conditions (Figure 5.14). Alloys M2S and M3S show better NTS values in the as-cast condition with high ductility values, whereas the base alloy M1S shows lower NTS and improved ductility values in the as-cast condition. These three alloys M1S through M3S

demonstrate an increasing loss in the tensile strength in the less ductile T5- and T6-treated conditions.

NTS values of the notched bars are lower in the case of asymmetric V-notches than those obtained in the case of asymmetric holes. This can be ascribed to the increased acuity of the asymmetric V-notch compared to the asymmetric hole and hence increased localized stresses at the V-notch root, resulting in a higher embrittlement effect concomitant to the presence of asymmetric V-notch.

The notch sensitivity is commonly used to detect the notch brittleness of a material. The notch strength ratio (NSR) is a measure of the notch sensitivity of a material. According to Dieter,[185] the NSR is determined by calculating the ratio between the notch tensile strength (NTS) to the tensile strength of a corresponding unnotched material. If the calculated NSR value is less than unity (< 1), the material is said to be notch sensitive, i.e. the notch has an embrittlement effect on the material, and vice versa. The NSR values of the notches used in the present case against the alloy compositions studied are given in Figure 5.15. It is observed that the NSR values of the samples with asymmetric hole are higher than those obtained with the asymmetric V-notch, which emphasizes the reported higher embrittlement effect of the latter.

Based on the definition of the NSR, if the NSR value of a specific alloy is greater than unity, this means that this alloy poses a considerable amount of plasticity. Alloys M1S through M3S in the as-cast condition exhibit a good amount of plasticity in the unnotched condition, as shown in Figure 5.14(b), compared to T5- and T6-treated conditions. This explains the high NSR values of the as-cast alloys M1S through M3S shown in Figure 5.15.

The lowest NSR values in the as-cast condition are associated with alloys M4S and M5S for the two types of notches examined. The NSR values of alloys M4S and M5S in the as-cast, T5-, and T6-treated conditions are close in the case of the two studied geometries, as opposed to the distinctly separate NSR values observed for alloys M1S through M3S. This behavior of NSR values for alloys M4S and M5S can be attributed to the overall unchanged ductility values across the studied conditions and notch type per alloy (Figure 5.14(b)). The other alloys, however, exhibit greater variations in the ductility values of their notched samples.

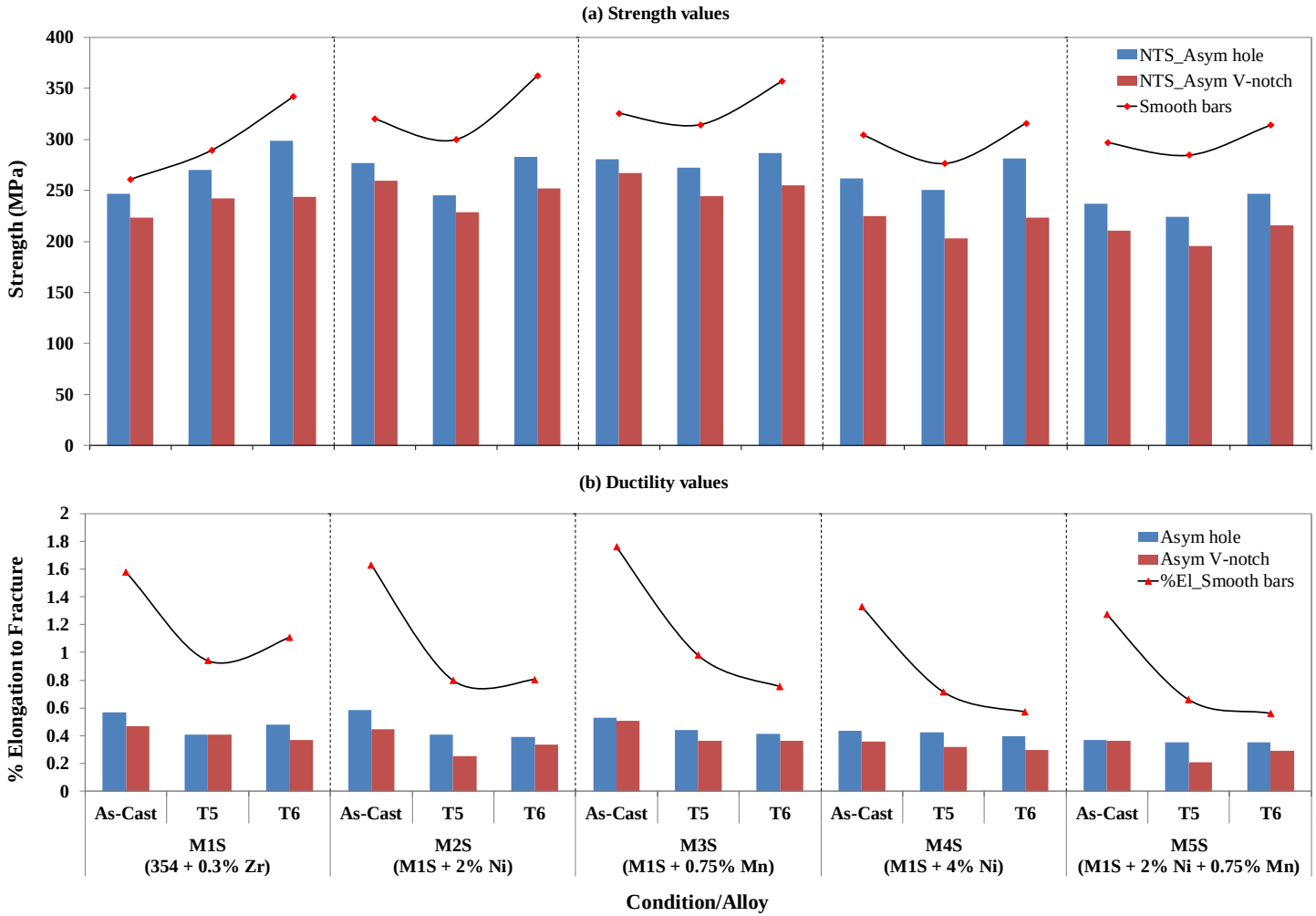

Figure 5.14 Variation in: (a) notch tensile strength (NTS) and (b) ductility values of the alloys studied in the as-cast, T5- and T6-treated conditions obtained at ambient temperature for notched bars.

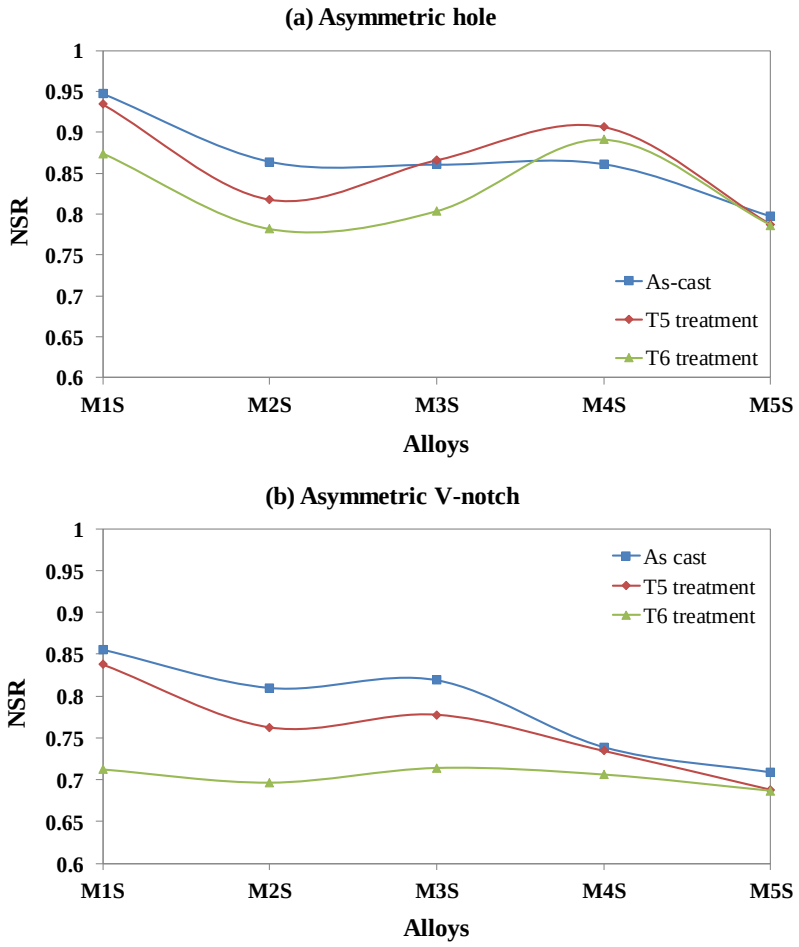

Figure 5.15 Notch strength ratio (NSR) values of the alloys studied in the as-cast, T5- and T6-treated conditions obtained at ambient temperature for notched bars: (a) Asymmetric hole, and (b) Asymmetric V-notch.

5.4.3 ELEVATED-TEMPERATURE TENSILE PROPERTIES OF SMOOTH BARS

It is essential to evaluate the tensile properties at elevated temperatures since the main objective of the present study is to enhance the elevated-temperature mechanical properties of the 354-type Al-Si-Cu-Mg alloy by introducing various amounts and combinations of selected transition elements and applying different heat treatments. The elevated-temperature tensile testing was carried out at 250°C, at a strain rate of 4×10^{-4} s^{-1}.

The tensile samples were held at the testing temperature for 1 hour before pulling in order to assure the uniformity of the temperature distribution in the sample.

The strengthening elements Cu and Mg are added to cast aluminum alloys in order to boost the ambient- and elevated-temperature strength values through the formation of various intermetallic compounds including θ-Al_2Cu, β-Mg_2Si, Q-$Al_5Cu_2Mg_8Si_6$, and S-Al_2CuMg. Alloys strength and ductility values are compromised due to the presence of these phases and others. In other words, the strength of the alloys improves owing to the presence of these phases; however, such phases poorly affect the ductility values. The iron-containing phases including β-Al_5FeSi and π-$Al_8Mg_3FeSi_6$ are considered to be very deleterious to the mechanical properties of Al-cast alloys; in order to neutralize the detrimental effect of Fe impurities, Mn is added at certain amounts in order to transform the harmful needles of β-Al_5FeSi phase into the less detrimental α-$Al_{15}(Mn, Fe)_3Si_2$ phase.[266, 267]

In the automotive industry, Al-Si-Cu-Mg 354-type alloys are widely used in engine components owing to their excellent strength and hardness values, though, at some sacrifice of ductility and corrosion resistance. These alloys are very responsive to heat treatment in light of the presence of both copper and magnesium. However during service, these alloys are subjected to elevated temperatures higher than 190°C; this high temperature instigates instability, coarsening and/or dissolution of the major strengthening phases such as θ'(Al_2Cu), β'(Mg_2Si), and S'(Al_2CuMg). Consequently, the resulting microstructures are not favourable for maintaining the mechanical performance at elevated temperatures.[165, 194]

Recently, additions of transition elements to Al-Si cast alloys have been investigated with the aim of improving the elevated-temperature mechanical properties through recovery of the alloy softening, which is initiated by the coarsening of the primary precipitates mentioned above. The idea is based on the formation of secondary fine heat-resistant Al_3M dispersoids, where "M" is a transition element such as Zr, Ni, and Mn.[17, 194] Based on the advantages of Cu, Mg and transition elements, minor additions of Zr, Ni, and Mn were made to the investigated Al-Si-Cu-Mg cast-alloys in the present study as a trial to achieve an appropriate chemistry of 354-type (Al-Si-Cu-Mg) alloys which could resist softening at elevated temperature during service.

Figure 5.16 reveals the elevated-temperature tensile properties obtained at 250°C for the alloys studied. By tensile testing at 250°C, all the investigated alloys, M1S through M5S, endure a significant softening owing to the possible coarsening of the strengthening precipitates which exist during tensile testing at room temperature (Figure 5.9). Figure 5.16(a) demonstrates that additions of Ni and Mn in different amounts and combinations to the base alloy, i.e. alloys M2S through M5S, slightly improve the strength values of the base alloy in the range of 5-15 MPa for both as-cast and T5-treated conditions. It is evident that the T5 heat treatment does not improve the elevated-temperature strength values of the as-cast alloys. This behavior can be ascribed to the limited differences in the microstructural features of as-cast and T5-treated conditions, as well as the low proportion of strengthening precipitates that exist in the structure of T5-treated alloys due to the absence of solution treatment.

In regard to the ductility values in the as-cast condition, Figure 5.16(b) reveals that the highest ductility value is observed to be associated with the base alloy M1S with a value of ~3.6%, followed by the ductility of the Mn-containing alloys M3S and M5S, and ending up with the lowest ductility values for alloys M2S and M4S, containing 2 and 4 wt.% Ni, respectively. The higher ductility values of the as-cast Mn-containing alloys M3S and M5S alloys can be attributed to the well refined Si particles, Table 5.2, and the transformation of a considerable amount of β-Al_5FeSi needles, which may act as crack initiators, into the less detrimental α-$Al_{15}(Mn,Fe)_3Si_2$ phase with script-like and/or sludge morphologies.

The addition of Ni, on the other hand, lowers the ductility values, even for alloy M5S which contains 0.75 wt.% Mn, when compared to alloy M3S which is Ni-free. The reduction in ductility values of the as-cast Ni-containing alloys can be directly correlated to the presence of acicular Ni-bearing phases with sharp edges, such as Al_3Ni, Al_9FeNi, and Al_3CuNi phases. These unrefined phases can act as crack initiators and hence poorly affect the tensile properties in the as-cast condition. Variation in chemical composition has a limited effect on the ductility values obtained at 250°C for the T5-treated alloys, since the maximum absolute difference in the ductility values of alloys M2S through M5S is found to be ~0.44%. Application of T5 and T6 heat treatments reduces the ductility observed in the as-cast condition as can be inferred from Figure 5.16(b). The ductility values in the T6-treated condition are generally lower than those obtained with T5 treatment conditions except for alloy M2S which exhibits higher ductility in the T6-treated condition.

The application of the T6-heat treatment enhances the strength values of as-cast conditions regardless the alloy composition, as shown in Figure 5.16(a). The enhanced strength values of alloy M4S after T6-heat treatment may be attributed to the formation of a high volume fraction of refined intermetallic compounds, mainly Ni-based compounds, which are insoluble in the α-Al matrix, as listed in Table 5.1. This high volume fraction of Ni-containing intermetallic compounds would obstruct the development of cracks and hence improve the strength values.[12, 165, 268] In elevated-temperature tensile testing, the formation of δ-Al_3CuNi proves to contribute effectively to the elevated-temperature strength of alloy M4S, in spite of a considerable amount of Cu that is consumed in forming this phase, which will certainly affect the amount of fine Al_2Cu dispersoids formed, which is consistent with the findings reported in references.[250, 269]

Interestingly, alloys M3S (354 + 0.75 wt.% Mn) and M4S (354 + 4 wt.% Ni) exhibit the highest and almost identical strength values at 250°C for the different conditions examined. Moreover, alloy M3S is considered to be more favourable between the two, since it exhibits higher ductility than that of the Ni-containing alloy M4S. These two alloys exhibit the best strength values (UTS and YS) in the T6-treated conditions among the investigated alloys; whereas, the strength values of the other three alloys, i.e. alloys M1S, M2S, and M5S, are close to each other and lower than the strength values obtained for alloys M3S and M4S by ~36 MPa. Generally, the closeness of the elevated-temperature strength values of the alloys studied can be credited to the presence of 0.3 wt.% Zr in each alloy, whereby the formation of the fine metastable $L1_2$-Al_3Zr particles is expected in the microstructures of all the alloys which, in its turn, will improve the alloy strength in a common manner.

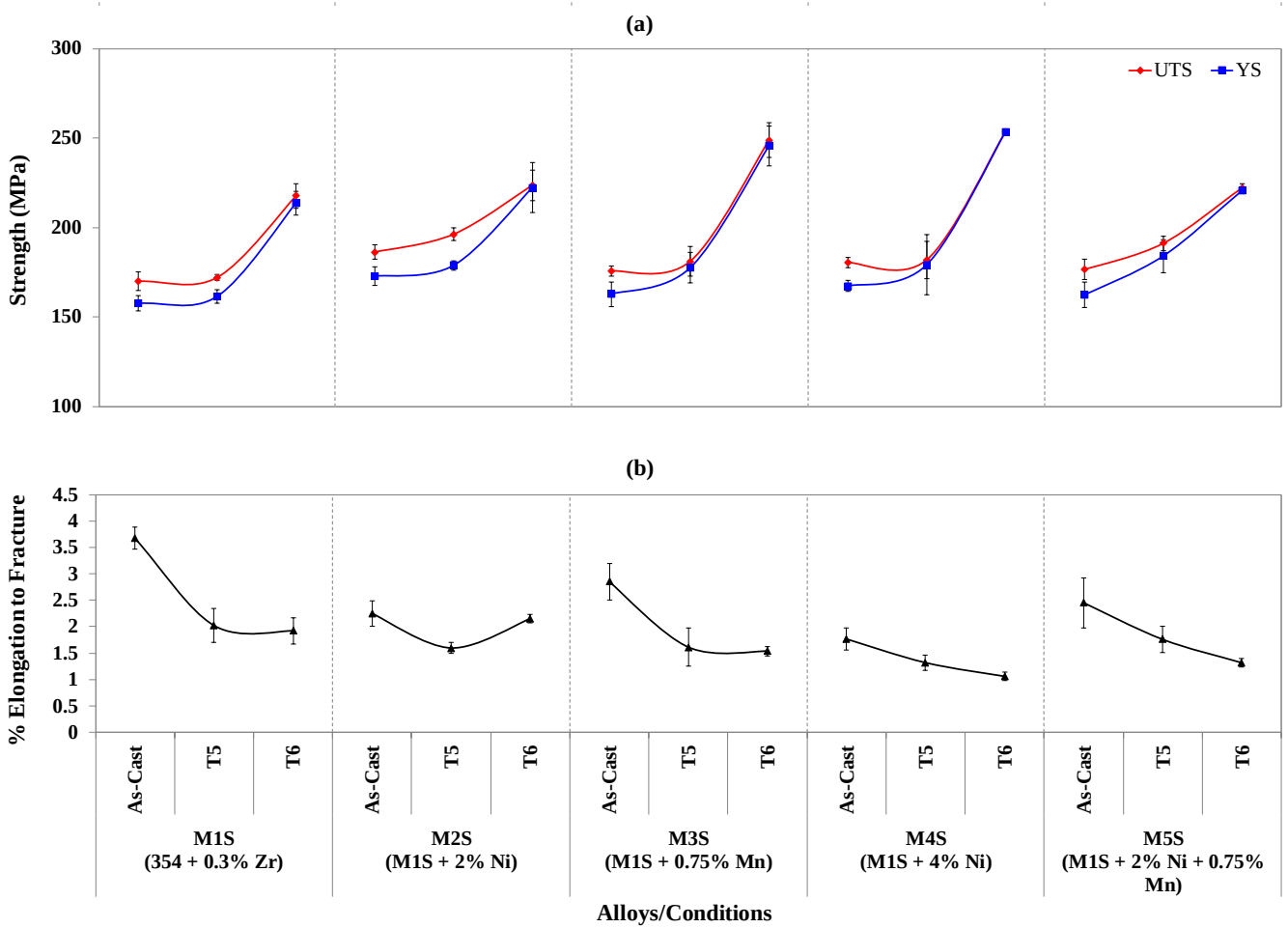

Figure 5.16 Variation in average (a) UTS, YS, and (b) %El values of the alloys studied in the as-cast, solution heat-treated (SHT), T5- and T6-treated conditions obtained at 250°C for smooth bars.

For elevated-temperature tensile properties, the concept of the quality index will be discussed according to the concept of Drouzy *et al.*[60] (Q). Table 5.5 demonstrates the elevated-temperature tensile data along with the quality index values (Q) of the alloys studied calculated using Equation 2.9 from Chapter 2. Figure 5.17 shows the quality chart obtained based on the calculations of Drouzy *et al.*[60]

As may be seen, the quality index values obtained at 250°C do not show wide variation in values, as was observed in the case of the ambient-temperature data. This limited variation can be understood in light of the balanced variation in UTS and ductility values obtained at the elevated temperature of 250°C. For example, the base alloy M1S in the as-cast condition exhibits the highest ductility value of 3.67% and a UTS value of 169.95 MPa while the lowest ductility is experienced by alloy M4S for the T6-treated condition with a value of 1.06% along with a UTS value of 253.58 MPa. By calculating the quality indices of these two conditions, they reveal Q values of 263.95 and 257.35 MPa for as-cast M1S and T6-treated M4S, respectively. Those two extreme conditions show that despite the considerable variation in the UTS values on the one hand, and ductility values on the other, for these two conditions, the quality indices in both cases remain almost unchanged due to the balanced trade-off between the UTS and ductility values. The relatively low UTS and ductility values obtained at elevated-temperature (250°C) for the T5-treated condition result in the T5-treated alloys exhibiting minimum Q values among the conditions studied, as shown in Figure 5.17.

Another interesting observation is that the quality index values for alloys M2S and M3S in the T6-treated condition are found to be the maximum for the alloys and conditions studied. This observation highlights the enhanced characteristics of alloy M3S which contains 0.75 wt.% Mn and emphasizes the positive influence of the high Mn-addition on the elevated-temperature tensile properties, which are found to be more or less comparable to those obtained with the addition of 2 and 4 wt.% Ni to the same base alloy.

Table 5.5 Variation in average UTS, YS, %El, and Q values of the alloys studied in as-cast, T5-, and T6-treated conditions obtained at 250°C for smooth bars

Alloy	Condition	UTS (MPa)	YS (MPa)	%El	Q (Eq.2.9)
M1S	**As-Cast**	169.95	157.56	3.67	254.65
	T5	172.07	161.51	2.02	217.91
	T6	217.65	213.65	1.92	260.14
M2S	**As-Cast**	186.32	172.84	2.25	239.15
	T5	196.25	178.85	1.60	226.71
	T6	223.72	222.33	2.15	273.65
M3S	**As-Cast**	175.76	162.84	2.85	243.99
	T5	181.07	177.45	1.61	212.16
	T6	248.74	245.62	1.54	276.68
M4S	**As-Cast**	180.53	167.35	1.77	217.57
	T5	181.86	179.13	1.32	199.85
	T6	253.58	253.32	1.06	257.35
M5S	**As-Cast**	176.48	162.32	2.45	234.92
	T5	191.10	184.02	1.76	227.86
	T6	222.09	220.55	1.32	239.96

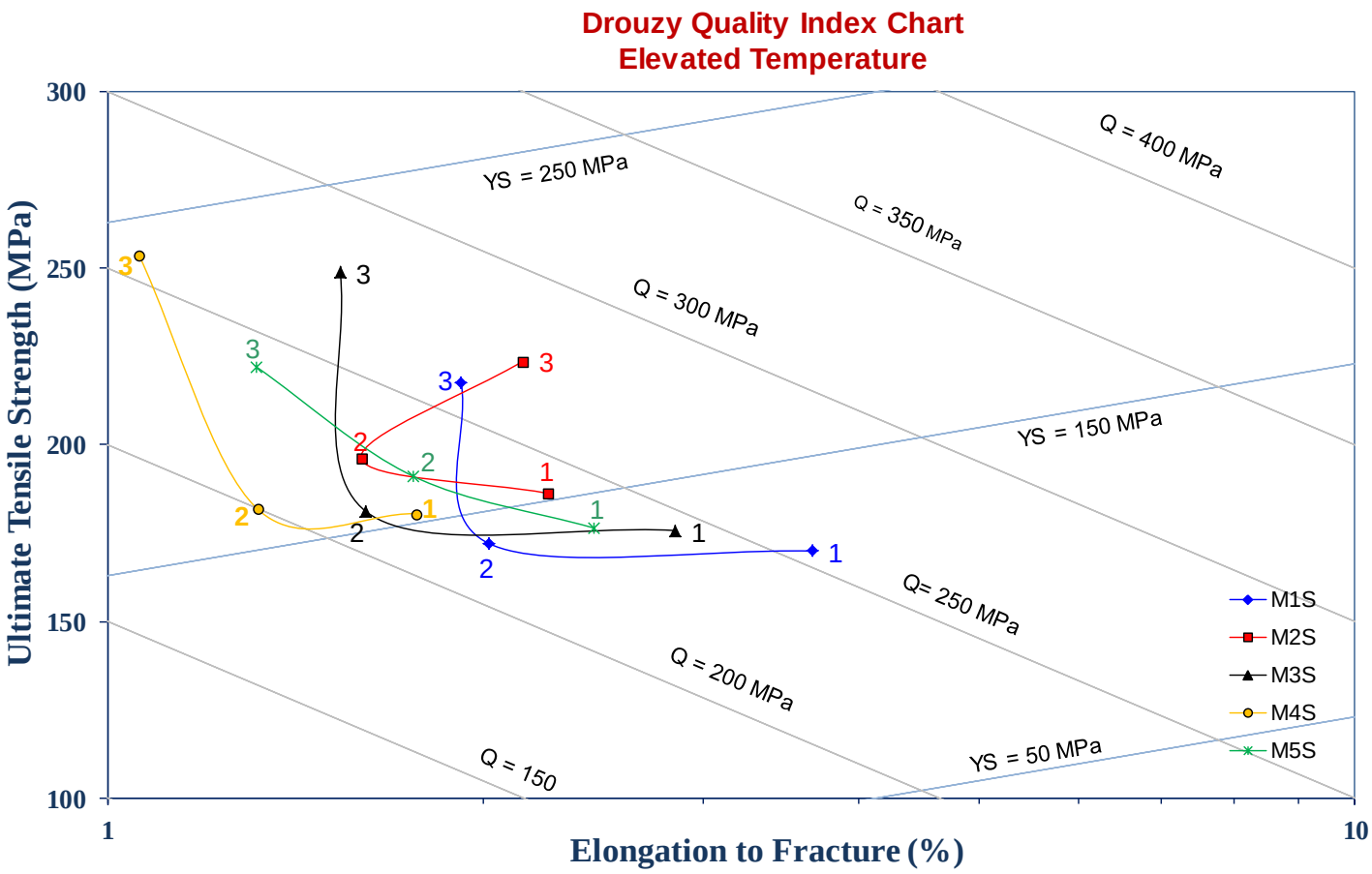

Figure 5.17 Drouzy quality chart representing the relation between the UTS and the percent elongation to fracture values of the alloys studied in the as-cast, T5- and T6-treated conditions obtained at 250°C for smooth bars.

5.4.4 ELEVATED-TEMPERATURE TENSILE PROPERTIES OF NOTCHED BARS

Figure 5.18 displays the tensile data obtained at 250°C for the notched bars. It is evident that the asymmetric V-notch is more deleterious to the tensile properties obtained at 250°C than the asymmetric hole, as previously reported for the ambient-temperature tensile properties of notched bars. The NTS values obtained at 250°C are generally close to the tensile strength of smooth (unnotched) bars and in some cases exceed the tensile strength values of smooth bars, particularly in bars with the asymmetric hole, as shown in Figure 5.18(a).

The softening that takes place during tensile testing at elevated temperatures renders the alloys some ductility, in particular alloys M1S through M3S. Consequently, the notched tensile bars with asymmetric holes of these alloys demonstrate high values of NTS compared to the tensile strength of unnotched bars subjected to similar treatment conditions, except for the T5-treated condition of alloy M2S. The enhanced ductility of alloys M1S through M3S at 250°C resists the plastic flow of the highly stressed material at the root of the notch and hence improved NTS values are obtained. However, the T5-treated condition of alloy M2S for bars with asymmetric hole shows a relatively lower NTS value owing to the original low ductility of smooth bars obtained with the same T5 treatment.

For alloy M4S in the T6-treated condition, bars with asymmetric hole also exhibit an NTS value higher than the tensile strength of their smooth counterparts, in spite of the apparent low ductility exhibited by the smooth bars of alloy M4S in the T6-treated condition. This behavior can be attributed to the presence of a high volume fraction of

intermetallic compounds in the microstructure of this alloy. These compounds will greatly hinder the propagation of cracks developed at the notch root, where high local stresses are generated during the tensile testing of notched bars. Additionally, for the T5-treated condition of alloy M4S, the difference between the NTS value of bars with an asymmetric hole and the tensile strength of unnotched bars is very limited which emphasizes the critical role of intermetallic phases in alloy M4S in resisting crack propagation.

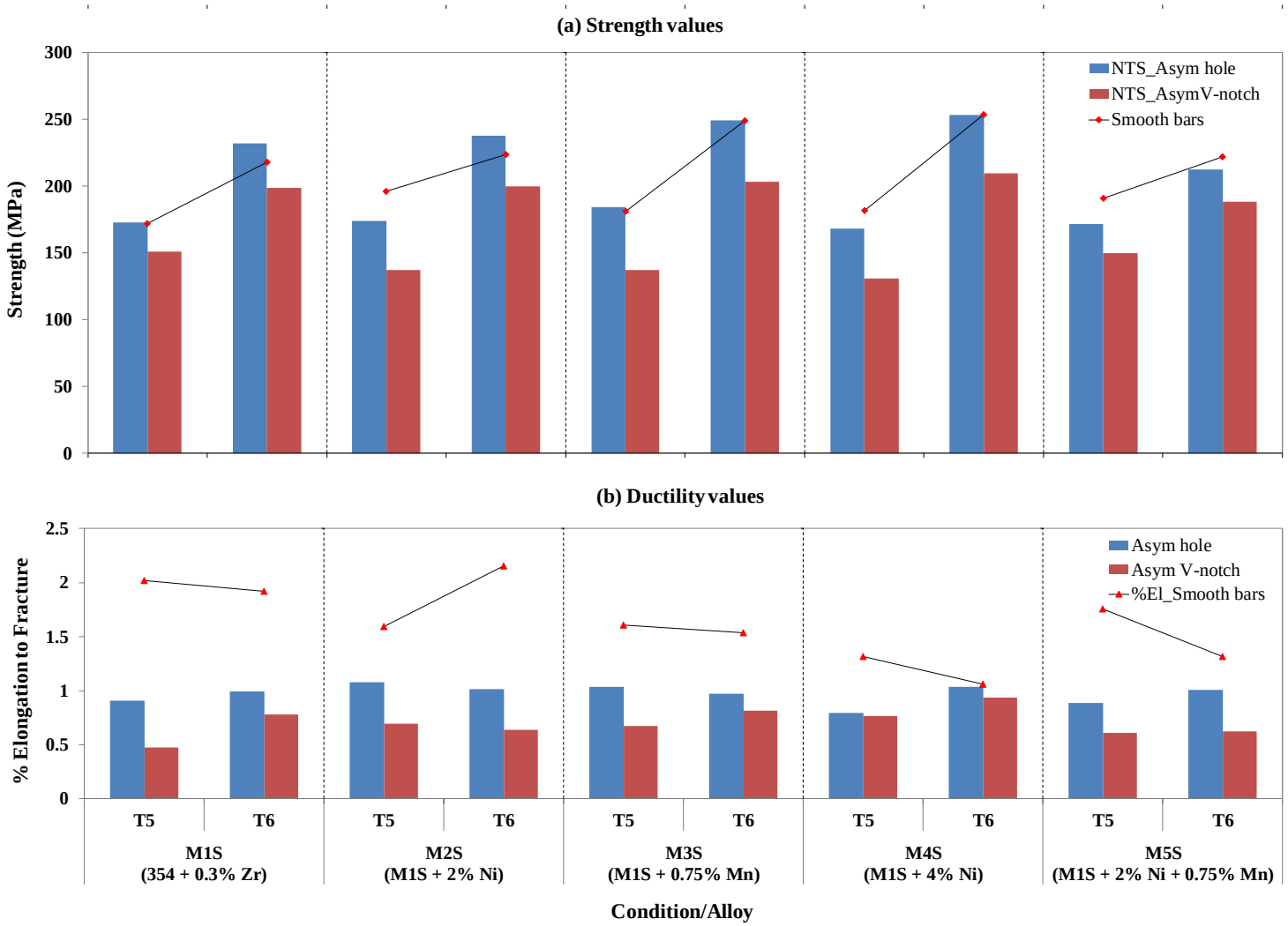

Figure 5.18 Variation in: (a) notch tensile strength (NTS) and (b) ductility values of the alloys studied in T5- and T6-treated conditions obtained at 250°C for notched bars.

The NSR values for asymmetric notches, i.e. hole and V-notch, of the alloys studied are shown in Figure 5.19. Similar to the data obtained at ambient temperature, the asymmetric V-notches produce an embrittlement effect higher than that of asymmetric holes. Thus, values of NSR are higher in the case of asymmetric holes rather than in asymmetric V-notches, as depicted in Figure 5.19. Interestingly, the T6-treated condition provides higher NSR values than the T5-treated condition, for all the alloys studied and for both types of asymmetric notches, i.e. holes and V-notches, in contrast to what was observed in the case of the ambient-temperature values, shown in Figure 5.15. This behavior can be accredited to the improved hot strength values of T6-treated conditions over those of T5-treated ones, in a similar manner to those obtained at ambient-temperature; but the slightly changed ductility values obtained at 250°C are much higher than those obtained from testing at 25°C for both T5- and T6-treated conditions and hence the higher strength values obtained at 250°C for the T6-treated conditions will play a vital role in improving NSR values of T6-treated conditions over those of T5-treated conditions at 250°C.

In the T5-treated condition, due to the direct aging of the as-cast structure without solution-heat treatment, a limited amount of the fine precipitates will form in the alloy microstructure and their amount will increase by further aging or exposure to an elevated temperature, which is the case in tensile testing at 250°C. This increased amount of hard fine particles will reduce the ductility of the alloys (Figure 5.18) and their NSR values (Figure 5.19) in the T5-treated condition. The opposite observation noted in the case of ambient-temperature testing can be understood as follows. The T6-treated alloys exhibit lower ductility values due to the presence of a large proportion of fine precipitates, whereas

the T5-treated alloys pose better ductility values in the light of limited amounts of the fine precipitates; thus, NSR values obtained at ambient temperature of the T5-treated alloys are higher than those of T6-treated ones, as shown in Figure 5.15.

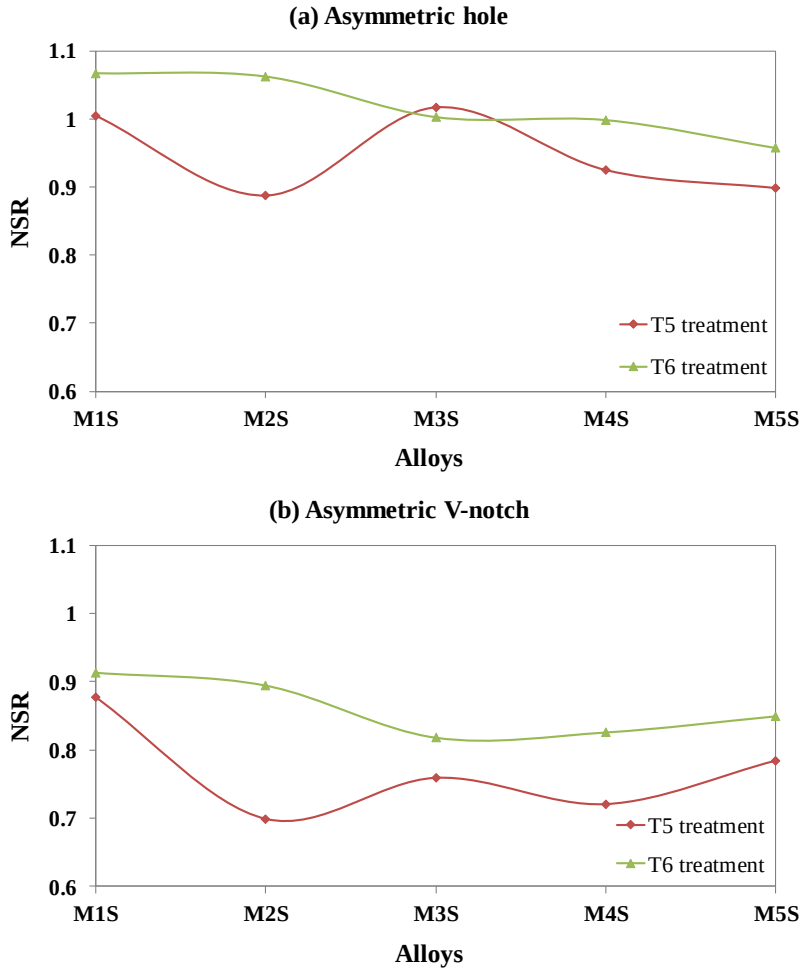

Figure 5.19 Notch strength ratio (NSR) values of the alloys studied in T5- and T6-treated conditions obtained at 250°C for notched bars: (a) Asymmetric hole, and (b) Asymmetric V-notch.

5.4.5 COMPARISON BETWEEN AMBIENT- AND ELEVATED-TEMPERATURE TENSILE PROPERTIES OF SMOOTH BARS

As discussed earlier, addition of Cu and Mg is intended to enhance the strength values at both ambient and elevated temperatures through the formation of a number of intermetallic phases such as θ-Al_2Cu, S-Al_2CuMg, and β-Mg_2S, which can resist coarsening up to a temperature of 190°C. The transition elements Zr, Ni, and Mn, on the other hand, are mainly added to the alloys studied in order to form coarsening resistant Al_3M compounds, which are capable of resisting the softening of the alloys when subjected to elevated temperatures. In view of these facts, it is important to compare the ambient-temperature and the elevated-temperature tensile properties in order to further elaborate on the effect of various additions in resisting alloy softening during tensile testing at the elevated temperature of 250°C.

For comparison purposes, the panel charts in Figure 5.20 illustrate variations in the tensile properties obtained at both ambient temperature and at 250°C. For each alloy, the changes observed in UTS, YS, and % El, according to the studied condition follow the same pattern at both ambient and elevated temperatures. Additionally, it is easily noticeable that the yield and ultimate tensile strength values obtained at 250°C are close to each other for the same treatment conditions.

From Figure 5.20(a), it is apparent that there is a reduction in the strength values (YS and UTS) in the case of tensile testing at 250°C, compared to the strength values obtained at ambient temperature, as opposed to the increased ductility values obtained at 250°C with respect to those obtained at room temperature, as shown in Figure 5.20(b). This behavior is attributed to the alloy softening associated with tensile testing at elevated

temperatures, resulting from the possible coarsening and the density reduction of the primary strengthening precipitates, such as Al_2Cu, Mg_2Si, and Al_2CuMg.

For the as-cast condition, it seems that additions of nickel and manganese in different amounts and combinations in alloys M2S through M5S produce an insignificant effect on the tensile properties at 250°C as opposed to their obvious effect on the room-temperature tensile properties. Quantitatively speaking, the enhancement in the elevated-temperature strength values (UTS and YS) following Ni and Mn additions is less than ~15% in the as-cast condition at 250°C, compared to ~25% at room temperature.

At ambient temperature, the strength values of the alloys increase by applying T5 and T6 heat treatments in comparison to the as-cast condition of the respective alloy; however the ductility values reduce slightly. Interestingly, alloy M3S (354 + 0.3 wt.% Zr + 0.75 wt.% Mn) behaves similar to alloy M2S (354 + 0.3 wt.% Zr + 2 wt.% Ni) in strength values in all the conditions studied. These two alloys exhibit the best strength values at room temperature. Additionally, the same Mn-containing alloy M3S behaves similar to alloy M4S (354 + 0.3 wt.% Zr + 4 wt.% Ni) in terms of elevated-temperature strength values, comprising also the best two compositions. Furthermore, as alloy M3S exhibits improved ductility values compared to those of alloys M2S and M4S at ambient temperature and 250°C, respectively, this gives it preference over the Ni-containing M2S and M4S alloys.

Regardless the absolute values, but in terms of softening resistance, alloys M4S and M5S exhibit the highest resistance to softening during testing at 250°C. In the T6-treated condition, in particular, the yield strength value of alloy M4S (containing 4 wt.% Ni) is

reduced from ~316 MPa at room temperature to 253 MPa, i.e. by 63 MPa. The yield strength of alloy M5S (2 wt.% Ni + 0.75 wt.% Mn) reduces by a value of 94 MPa, while the differences between the ambient- and elevated-temperature yield strength values of the other alloys M1S, M2S, and M3S are 111, 139, 109 MPa, respectively. In other words, the 2 wt.% Ni-containing alloy M2S shows the least softening resistance behavior (loss of 139 MPa) in terms of the yield strength values obtained at 250°C and room temperature; whereas, the 4 wt.% Ni-containing alloy M4S shows a high resistance to softening initiated by testing at 250°C. This behavior can be ascribed to the formation of fine Al_3Ni phase in the eutectic form (Al-Al_3Ni) with the increase in Ni-content from 2 to 4 wt.% Ni, as previously described in Chapter 4. This finely distributed Al_3Ni phase present in the microstructure of alloy M4S would enhance the elevated temperature properties considerably compared to its coarsened morphology observed in the microstructures of the 2 wt.% Ni-containing M2S and M5S alloys.

As mentioned above, the elevated-temperature tensile behavior of alloy M3S, which contains 0.75 wt.%, is almost typical to that of alloy M4S; which is the same as saying that the addition of 0.75 wt.% Mn is equivalent to the addition of 4 wt.% Ni to Al-Si-Cu-Mg-0.3%Zr alloy, and with the added advantage of higher ductility values. Thus the Mn-addition is considered better than the addition of 2 wt.% Ni in terms of elevated-temperature tensile strength values.

Additionally, it is found that ambient-temperature strength values of alloy M3S are similar to those of alloy M2S (2 wt.% Ni) and better than those of alloy M4S (4 wt.% Ni). Whereas, the addition of 0.75 wt.% Mn in the presence of 2 wt.% Ni, i.e. alloy M5S, has no

effect on the tensile strength values (UTS and YS). This finding will be of great economic benefits, if it is further proved and validated.

The quality charts according to the concept developed by Drouzy *et al.*[60] are shown in Figure 5.21; these charts represent differences in the quality index values (Q) of the different alloys/conditions tested at ambient temperature and at 250°C. The quality index values of the alloys are reduced by testing at 250°C because of the serious drop in the strength values in spite of the improved ductility values. Alloys M1S, M2S, and M3S have the best quality index values at both ambient and 250°C temperatures. The quality index values of alloy M4S are seen to be low, in general, with the exception of the quality value of the T6-treated condition tested at 250°C. This behavior can be ascribed to the noticeably increased strength value of the T6-treated condition of alloy M4S obtained at 250°C.

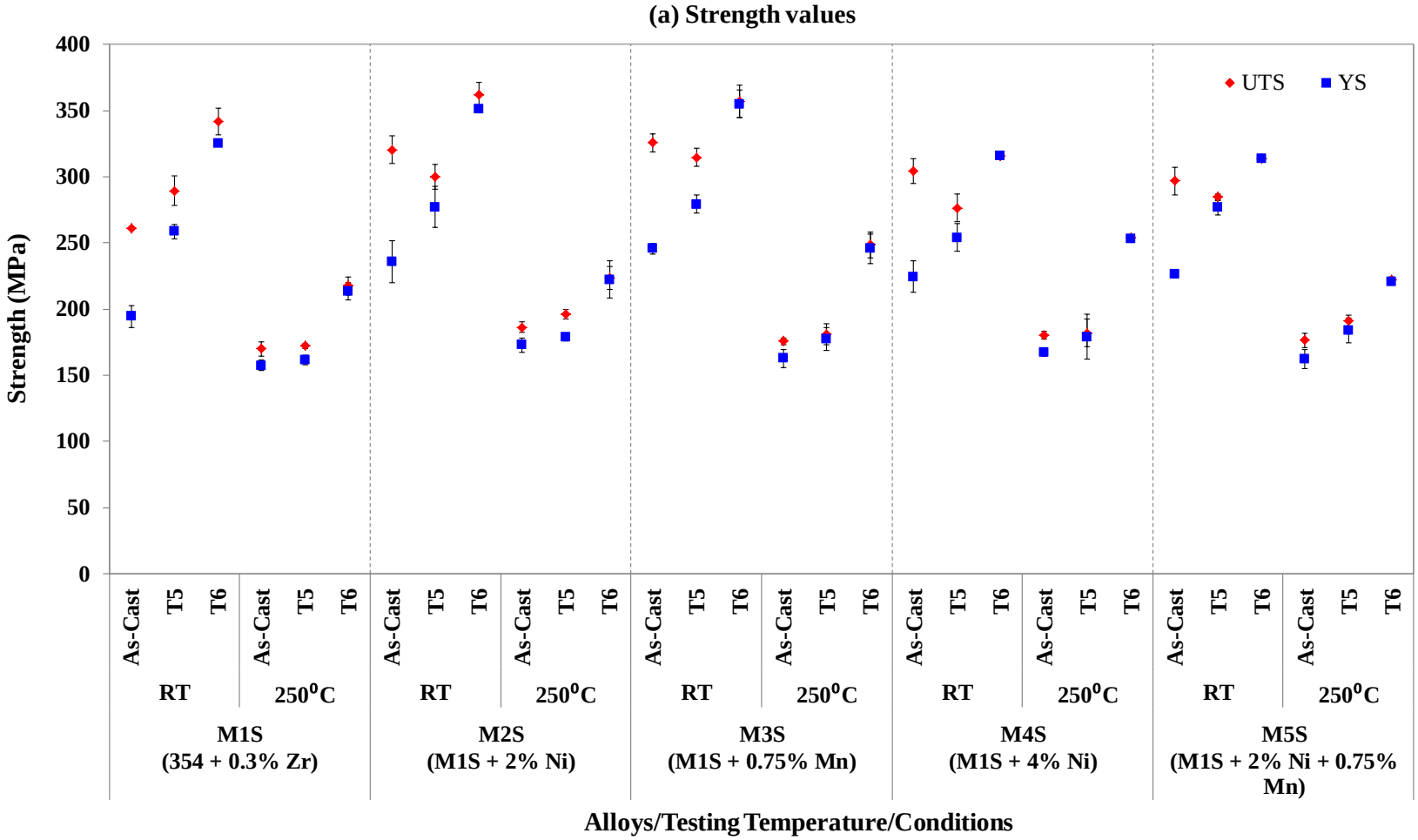
(a) Strength values
Strength (MPa)
400
350
300
250
200
150
100
50
0
UTS
YS
As-Cast
T5
T6
RT
250°C
M1S
(354 + 0.3% Zr)
M2S
(M1S + 2% Ni)
M3S
(M1S + 0.75% Mn)
M4S
(M1S + 4% Ni)
M5S
(M1S + 2% Ni + 0.75% Mn)
Alloys/Testing Temperature/Conditions

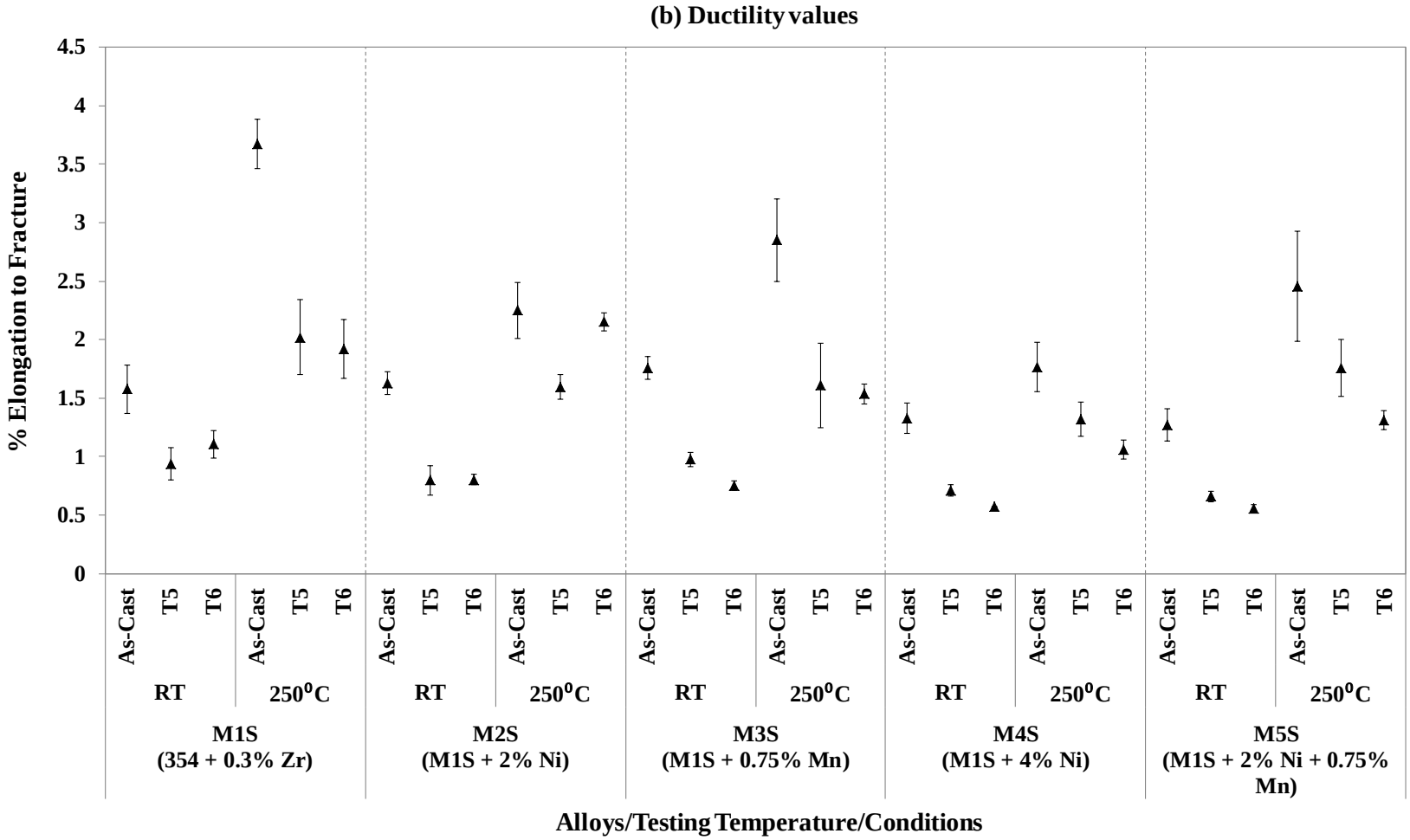

Figure 5.20 Variation in (a) strength values and (b) ductility values of the alloys studied in as-cast, T5-, and T6-treated conditions obtained at ambient temperature and 250°C for smooth bars.

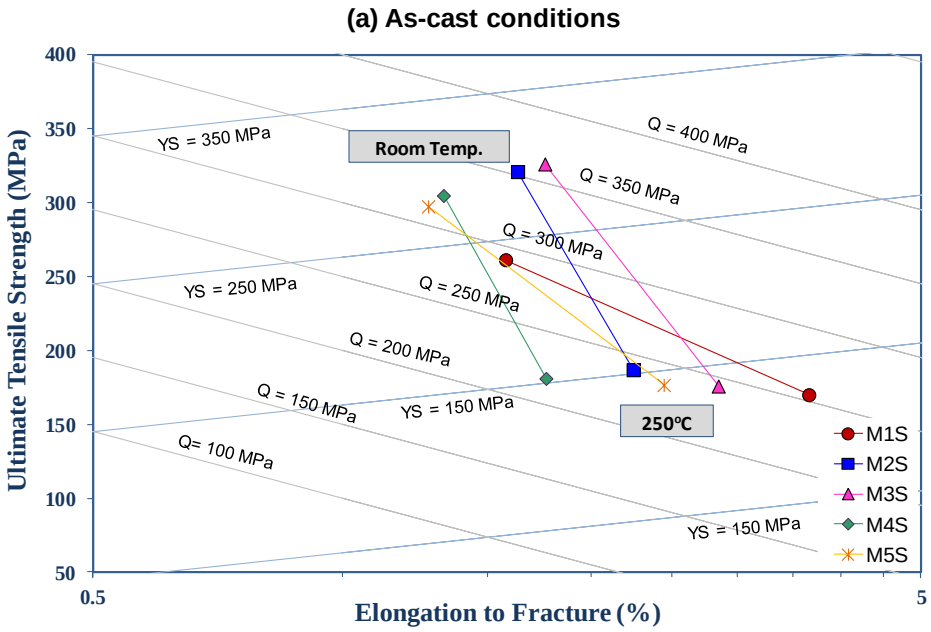
(a) As-cast conditions
Ultimate Tensile Strength (MPa)
Elongation to Fracture (%)
400
350
300
250
200
150
100
50
0.5
5
YS = 350 MPa
Q = 400 MPa
Room Temp.
Q = 350 MPa
Q = 300 MPa
YS = 250 MPa
Q = 250 MPa
Q = 200 MPa
Q = 150 MPa
YS = 150 MPa
250ºC
Q= 100 MPa
YS = 150 MPa
M1S
M2S
M3S
M4S
M5S

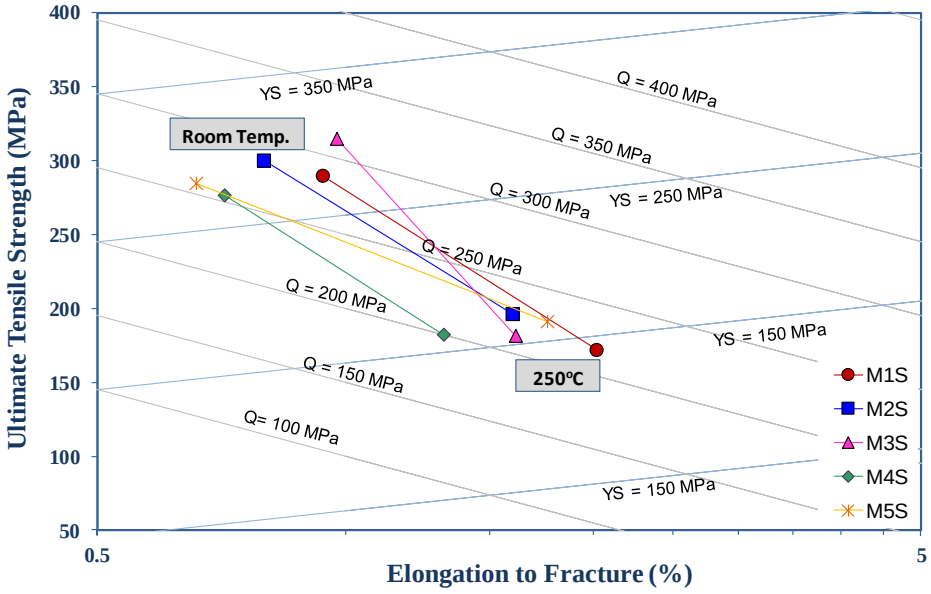
(b) T5-treated conditions
Ultimate Tensile Strength (MPa)
Elongation to Fracture (%)
400
350
300
250
200
150
100
50
0.5
5
YS = 350 MPa
Q = 400 MPa
Room Temp.
Q = 350 MPa
Q = 300 MPa
YS = 250 MPa
Q = 250 MPa
Q = 200 MPa
YS = 150 MPa
Q = 150 MPa
250ºC
Q= 100 MPa
YS = 150 MPa
M1S
M2S
M3S
M4S
M5S

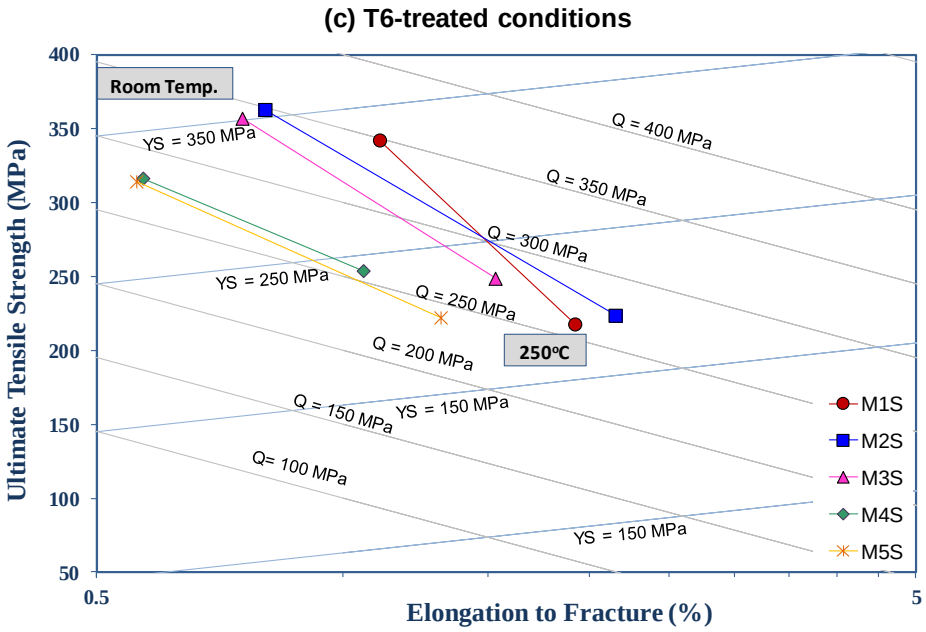

Figure 5.21 Drouzy quality charts representing the variation in the alloy quality of the alloys studied in: (a) as-cast, (b) T5-treated, and (c) T6-treated conditions obtained at ambient temperature and 250°C for smooth bars.

5.5 HARDNESS VALUES

Hardness measurements were carried out to assess the changes in the structure of alloys following various additions of transition elements and applied heat treatments. The measurements were carried out on polished surfaces of samples with in as-cast and heat-treated conditions. The average value of ten hardness measurements was reported as the hardness value of a specific alloy/condition. A Rockwell hardness tester with 1/16'' steel ball and scale F with a load of 60 Kgf was used to assess the hardness values of the alloys studied.

Figure 5.22 illustrates the variation in the hardness values of the alloys as a function of the applied heat treatment. At first glance, one can observe from Figure 5.22 that the hardness values of different alloys show insignificant variations for the same conditions.

For each alloy, the peak-aged condition exhibits the highest hardness value among all conditions. Also, the tailored alloys, i.e. M2S through M5S, show better hardness values than those obtained for the base alloy in all the conditions studied.

Variations in hardness values of the alloys in the as-cast condition can be attributed to the additions of Ni and/or Mn made to the base alloy M1S. It was seen that additions of Ni and/or Mn in various amounts increased the volume fractions of intermetallic compounds considerably, as listed in Table 5.1. The variations in hardness values follow the same trend as variations in the percentage volume fraction of intermetallic compounds. Thus the base alloy M1S exhibits the lowest hardness value in the as-cast condition, having the lowest volume fraction according to Table 5.1; and the highest hardness value of the same condition is associated with alloy M4S which has the highest volume fraction of intermetallic compounds. This observation highlights the effective role of intermetallic compounds in enhancing the hardness values, similar conclusions are reported by Mohamed[44], and Elgallad.[86]

It is clear that each step of the peak-aging treatment, i.e. solution treatment and/or artificial aging, affects the hardness values of the alloys studied, as depicted in Figure 5.22. The dissolution of the strengthening elements over the course of the solution treatment reduces the hardness values, in spite of the improved homogeneity in composition and evolution of the eutectic silicon morphology following solution treatment. This behavior emphasizes the crucial role of intermetallic phases in influencing the mechanical performance of alloys. It is established that the hardness value of a specific alloy corresponds to the combination of the tensile yield strength and work-hardening rate of the

alloy.[44, 270] The order of the alloys studied according to the hardness value in the as-quenched condition matches to a large extent the order of the alloys with respect to their yield strength in the same as-quenched condition which emphasize findings reported by Mohamed[44], and Barresi *et al.*[270]

Direct artificial aging following casting of test bars, i.e. T5-temper treatment, introduces slight improvements in the hardness values with respect to those obtained for the as-cast condition. This can be attributed to the limited changes in the microstructure of the as-cast alloys/bars following direct artificial aging without solution treatment. The slight increase in the hardness values in the T5-treated condition emphasizes the positive role of employing a high solidification rate in the casting process. This high solidification rate allows for partial solubility of Cu and Mg in the α-Al matrix, such that subsequent artificial aging will precipitate a limited amount of strengthening precipitates, to produce the marginal increase in hardness values observed.

With respect to the peak-aged condition, the hardness values of alloys M2S through M5S are almost identical approaching ~100 HRF, whereas the hardness value of the base alloy for the same T6-treated condition is ~96 HRF. This variation can be ascribed to the combined effect of the strengthening precipitates and intermetallic compounds in the four alloys. The improvement in hardness of the base alloy in the T6-treated condition compared to the as-cast case is mainly attributed to the effect of the strengthening precipitates formed after the T6 treatment; because of the low volume fraction of intermetallic phases observed in the microstructure of the base alloy as listed in Table 5.1 (namely, ~2.51% in the as-cast

condition, and 1.11% in the as-quenched condition), which is too low compared to the other alloys.

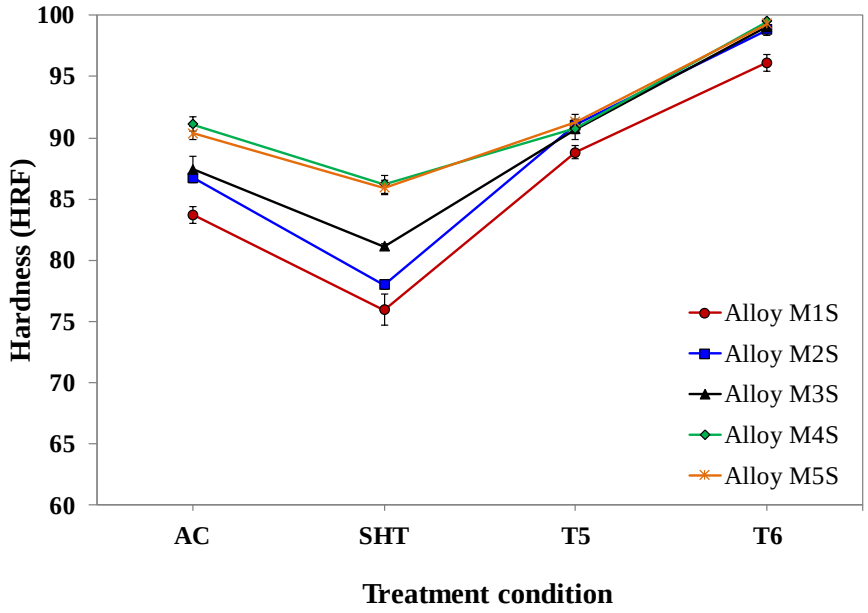

Figure 5.22 Variation in Rockwell hardness value (HRF) as a function of heat-treatment conditions for the alloys studied.

5.6 IMPACT PROPERTIES

Alloy toughness is defined as the total energy absorbed by the material before fracturing. Impact testing is commonly employed to assess the toughness of materials. It is important from the point of view of engineering applications to improve the ability of the material to absorb impact energy and hence withstand fracturing due to sudden shocks. From literature,[44, 86, 271, 272] it is known that the impact energy is influenced by the refinement of the microstructure and the morphology of the microstructural constituents.

In this section, impact properties of the alloys studied will be presented in order to assess the role of various additions of transition elements and applied heat treatments on the toughness values. The impact testing was carried out on unnotched samples with a square cross section area of 10x10 mm^2 and length of 55 mm. Five samples per condition per alloy were tested and the average value of the total energy obtained over the five samples was taken as the impact energy representative of that particular alloy/condition. The 354-type Al-Si-Cu-Mg cast-alloys are known for their low ductility and hence their low toughness values. Thus, contributions to increase the toughness values of this category of cast alloys, even slightly, will be highly valuable. The impact bars used in the present study were not notched based on three considerations: (i) the expected low toughness of 354-type alloys, (ii) increasing the measurement accuracy by excluding uncertainties associated with machining of notches, and (iii) emphasizing the effects of microstructural constituents.

The variation in the toughness values of the alloys studied as a function of the applied heat treatment is displayed in Figure 5.23. It is evident that values of the total absorbed energy for the alloys studied are relatively low in the as-cast, T5-treated, and T6-treated conditions compared to those obtained in the solution heat-treated conditions.

Kobayashi and Niinomi[273] have stated that the impact toughness, i.e. total absorbed energy, of Al-Si alloys in the as-cast condition is mainly dependent on: (i) the morphology of eutectic silicon particles, (ii) primary silicon particles, if they exist, (iii) the dendrite arm spacing of the aluminum matrix, and the presence of (iv) intermetallic phases, and (v) casting defects. Since parameters (ii), (iii), and (v) remain unchanged for the alloys studied, thus the morphology of the eutectic silicon particles and the volume fraction of

intermetallic compounds present will determine the impact properties of the as-cast alloys studied in the present investigation. It is worth mentioning that the sphericity and roundness parameters (in percentage) of the eutectic silicon particles in the as-cast condition did not vary substantially with respect to the alloy composition, as shown in Figure 5.8. Therefore, the only parameter affecting the impact properties of the as-cast alloys is the presence of intermetallic compounds. As can be inferred from Figure 5.23, the order of alloys according to the absorbed energy during impact testing matches that with respect to the volume fraction of intermetallic compounds shown in Table 5.1. Thus, it can be deduced that increasing the volume fraction of intermetallic compounds will increase the amount of absorbed energy and hence improve the impact properties.

The impact properties of the alloys studied in the as-cast condition substantially improved by applying solution heat treatment at 495°C for 5 hours. The increase in the total absorbed energy values for each alloy after solution treatment are as follows: (i) 15 J for the base alloy M1S, (ii) 11 J for alloy M2S, (iii) 12 J for alloy M3S, (iv) 9 J for alloy M4S, and (v) 8 J for alloy M5S. The probable explanations for the improved impact properties following solution heat treatment are discussed below.

Thermal-modification of eutectic silicon particles associated with solution heat treatment contributes to the improved impact properties in the as-quenched condition. As observed in the optical micrographs shown in Figure 5.2 through Figure 5.6, the eutectic silicon particles in the as-cast condition (micrographs on the left) consist of partially-modified particles in addition to the fibrous ones, with low average values of roundness and sphericity. The relatively sharp edges of these particles will contribute to an increase in

stress concentration at these locations, which will facilitate crack propagation, resulting in low toughness values. As seen from Figure 5.8, solution heat treatment of the Sr-modified alloys improves the sphericity and roundness of eutectic silicon particles. Moreover by recalling the optical micrographs shown in Figure 5.2 through Figure 5.6 for the as-quenched alloys (micrographs on the right), it is evident that the solution treatment produces well-separated silicon particles through the fragmentation of the interconnected fibrous silicon structure present in the Sr-modified as-cast structures. Such well-rounded small and separated silicon particles will make available greater areas of the ductile α-Al matrix and hence substantially improve the impact properties, as reported by Mohamed.[44]

The impact properties of an alloy are directly related to its ductility. Figure 5.24 illustrates the relationship between the impact properties and ductility values of the alloys studied. The relationship between these two properties shows a linear trend with a high goodness of fitting represented by the high value of R^2. The order of alloys with respect to their impact energy values (Figure 5.23) matches with the order of the alloys with respect to the ductility values (Figure 5.9) obtained from room temperature tensile testing.

The impact properties of the investigated alloys in T5- and T6-treated conditions are close in values and lower than the values obtained in the as-cast and as-quenched conditions, respectively. For the alloy studied, the T5-temper treatment aims at forming fine dispersoids of Al_2Cu, Al_2CuMg, and Mg_2Si during the direct aging of the as-cast structures, which may contain a considerable amount of dissolved Cu and Mg in the α-Al matrix following casting at high solidification rate. Higher proportions of these fine dispersoids are expected in the case of the T6-treated condition due to the solution

treatment stage, which produces a super saturated solid solution with high concentrations of Cu and Mg. These fine precipitates promote the initiation of fine cracks which will eventually reduce the impact properties.[274] This would explain the reduced impact properties observed in the T5- and T6-treated conditions of the alloys studied.

In their study of the impact properties of Al-Si foundry alloys, Paray *et al.*[274] suggested that the impact properties of Cu-containing alloys such as 319 and 332 are highly influenced by the Al_2Cu phase particles rather than by the eutectic silicon particles. This suggestion also appears to hold true for the alloys studied in the present investigation. The impact properties of the investigated alloys have no significant variations with respect to the condition studied, i.e. the total energies absorbed by the five alloys in the as-cast condition are close in their values, the same for the T5- and T6-treated conditions. This may be ascribed to the same copper content in the studied alloys and the existence of Al_2Cu-phase particles in their microstructures either in the form of fine dispersoids or coarser particles. On the other hand, the total absorbed energy values vary widely for the as-quenched alloys. This wide variation can be attributed to the dissolution of Al_2Cu-phase particles during the course of solution treatment, so that the impact properties are no longer dependent on the Al_2Cu particles but on other microstructural features reported to have noticeable differences.

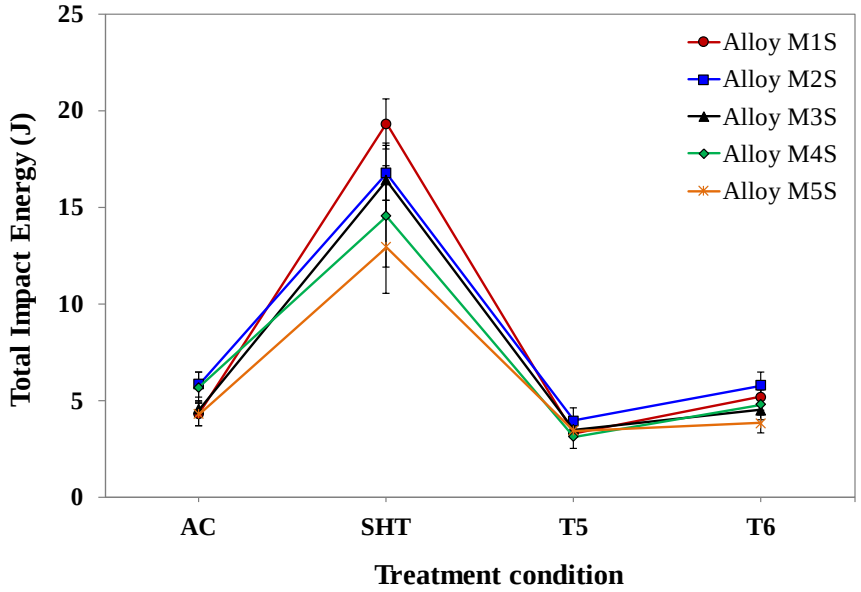

Figure 5.23 Variation in total impact energy value as a function of heat-treatment conditions for the alloys studied.

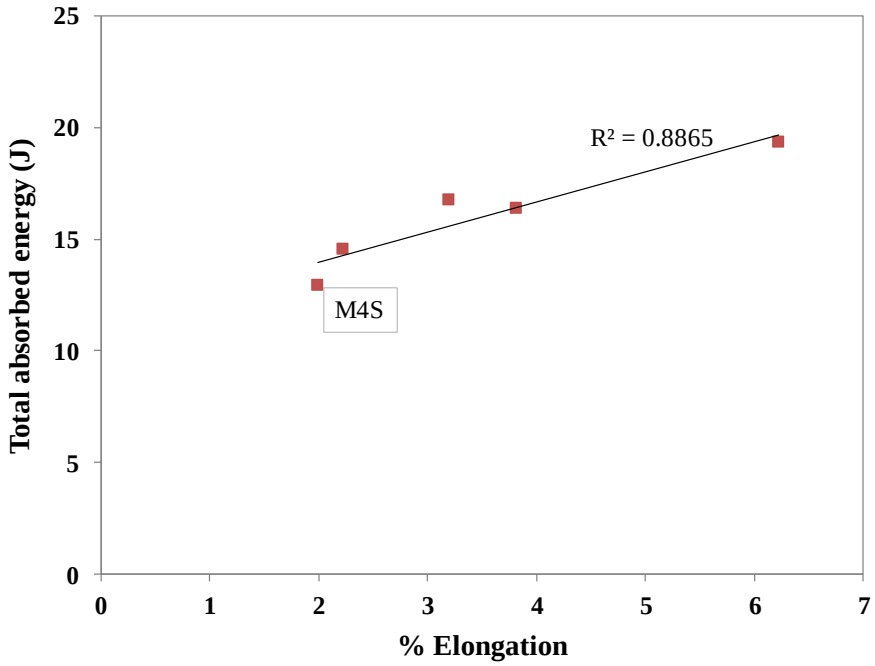

Figure 5.24 Correlation between impact energy and ductility values of the alloys studied in the solution-heat treated condition.

CHAPTER 6

PROLONGED THERMAL EXPOSURE

CHAPTER 6

PROLONGED THERMAL EXPOSURE

6.1 INTRODUCTION

The increased share of Al-Si cast alloys in the automotive industry, particularly in engine components, instigates major concerns regarding the deterioration in the mechanical properties of these alloys owing to the exposure to elevated temperatures for a long span of time during service life. This prolonged thermal exposure will definitely introduce changes in the microstructure of the alloys, which will certainly affect, and not in a positive way, their mechanical properties. The understanding and solution of this problem is receiving extensive research efforts nowadays. One of the promising solutions is to add transition and/or rare-earth elements to Al-Si cast alloys in order to preserve the mechanical properties at elevated temperatures.[11-15]

Alloys A356 and A357, which are widely used for engine components, when used in the peak aged (T6 heat-treated) condition, have been found to have some limitations when serviced for long times at high temperatures above 200°C. These limitations are ascribed to the rapid coarsening of the strengthening precipitates in this category of alloys. This coarsening is believed to be the primary factor responsible for the deterioration in the mechanical properties, in particular, the strength values.[166, 168, 169] Modern technological advances, such as downsizing, hybrid engines, and automatic start-stop engines, have been

introduced to automotive sector to minimize fuel consumption by reducing vehicle weight and thereby reduce harmful emissions. These technologies impose higher specific power, higher component temperatures, and increasing pressure on the alloys used in engine blocks.

Based on the above points, Al-Si-Cu-Mg cast-alloys are selected as a proper solution to overcome/minimize the limitations imposed on the use of A356/A357-type alloys in these new and harsh service conditions. The presence of Cu and Mg in Al-Si-Cu-Mg alloys enhances the ambient- and elevated-temperature mechanical properties. In recent years, extensive research efforts were focused in the direction of improving the high-temperature performance of Al-Si-Cu-Mg cast alloys through the addition of transition elements that would allow the formation of more stable precipitates that could resist coarsening over the course of prolonged thermal exposure.[14, 165, 169, 194, 268]

This chapter reports the effects of prolonged thermal exposure at 250°C on the mechanical properties of the alloys studied at ambient and elevated temperatures. The exposure temperature employed in the present investigation was selected to be 250°C, as the currently used aluminum alloys in automotive engines are limited to working temperatures of 230°C[7, 165, 194] and hence assessing the alloy performance at a higher temperature would be advantageous. The first section explores differences between the effect of static (single-step) versus dynamic (multi-step) thermal exposure techniques on the ambient-temperature mechanical properties. The static exposure (stabilization) is a feasible laboratory technique, i.e. it is easier to be carried out in laboratories, particularly when the stabilization treatment lasts for long times. Dynamic stabilization, on the other hand, is more representative of real working conditions. Subsequently, the influence of

thermal exposure at ambient- and elevated-temperature conditions will be investigated, in light of changes in the characteristics of the strengthening precipitates. At the end of the chapter, the fracture surface characteristics of tensile specimens tested at elevated temperature (250°C) will be presented and discussed, to elaborate on the nature of the fracture and the compounds involved in the development of cracks.

6.2 STATIC VERSUS DYNAMIC THERMAL EXPOSURE

The motive for undertaking this part of the study is to decide on the effectiveness of employing a continuous (static) thermal exposure for describing the behavior of a material during service in a real application, such as engine components. In other words, alloys used in engine components are subject to cyclic (dynamic) thermal exposure due to start-operate-stop cycles of an automotive engine. While the static thermal exposure technique is employed to describe material behavior in laboratories, as it is easier and more feasible, however, differences between the effects of these two techniques on the mechanical properties have never been explored. For the present study, the effects of static and dynamic thermal exposure will be explored by heating the material continuously - representing static exposure, and cyclically at 250°C - representing dynamic exposure, for the designated periods of time, in order to reveal if there will be significant discrepancies in the alloy behavior when subjected to static and dynamic exposure for the same times, between 5-200 hours and at the same elevated temperature, i.e. 250°C. The mechanical properties evaluated for this part of the study are the ambient-temperature tensile properties and Rockwell hardness values. The techniques of static and dynamic thermal exposure as well those for evaluating the ambient-temperature tensile properties and hardness values were described earlier on in Chapter 3.

6.2.1 AMBIENT-TEMPERATURE TENSILE PROPERTIES

This section deals with and interprets the room-temperature tensile data obtained for only three alloys, namely, the base alloy M1S (354 + 0.3 wt.% Zr), alloy M2S (M1S + 2 wt.% Ni), and alloy M3S (M1S + 0.75 wt.% Mn), after their exposure to a temperature of 250°C for different durations up to 200 hours. The three alloys were originally heat treated according to the T6 heat-treatment procedures described in Chapter 3 in Table 3.2, then the heat-treated bars were stabilized at 250°C for times of 5, 10, 25, 50, 100, and 200 hours. These stabilization periods were selected in order to provide a wide range of exposure times. The three alloys, M1S, M2S, and M3S, were selected for this investigation based on their improved performance as reported in Chapter 5. Apart from the present section, however, the rest of Chapter 6 will focus on the effect of thermal exposure on the mechanical performance of the five alloys used in this study, i.e. alloys M1S through M5S.

The majority of the reported data[11-13, 15, 171, 275-277] on the effect of thermal exposure on mechanical properties, i.e. tensile and hardness data, of Al-alloys are obtained after applying stabilization techniques similar to the so-called static stabilization used in the present study. The importance of assessing the effect of dynamic stabilization on the mechanical properties, and comparing it to the data obtained after static stabilization, arises from some concerns regarding the fatigue properties of alloys, in cases where heat effects are included in the testing procedures. For example, thermal fatigue testing is more or less uses similar approaches like static and dynamic stabilization however with applied cyclic mechanical loading. The tensile testing of statically stabilized materials can be considered analogous to isothermal fatigue testing, and the tensile testing of dynamically stabilized materials can be considered equivalent to thermomechanical fatigue testing (TMF), i.e.

cyclic thermal and mechanical loads. For many years, the isothermal fatigue data was used to describe TMF testing data because of the more feasible experimental set-up in case of isothermal fatigue. In recent years, and with advances in testing capabilities, TMF testing units are available to provide both cyclic mechanical and thermal loads. By comparing the TMF data of a specific alloy to the data obtained from isothermal fatigue testing, i.e. using only cyclic mechanical loading at a constant elevated temperature, noticeable discrepancies in results are observed, which put all the previously reported data in this context under criticism. That is why it is critical to check the variability in the tensile data with respect to the stabilization mode, either static or dynamic, before proceeding with the rest of this study on the effect of prolonged thermal exposure on the ambient- and elevated-temperature mechanical properties of the alloys investigated in the T5- and T6-treated conditions.

Figure 6.1 shows variations in the tensile properties (namely; UTS, YS, and %El) of alloys M1S, M2S, and M3S in the T6-treated condition, before and after stabilization at 250°C for different times. The tensile properties in the T6-treated conditions for each alloy, i.e. before stabilization, are considered as reference values. The X-axis represents the stabilization time in hours, where zero hour refers to the T6-treated condition without stabilization. The principal Y-axis represents the strength values (UTS and YS); while the percentage elongation to fracture is represented on the secondary Y-axis.

For purposes of recapitulation, static stabilization (thermal exposure) was achieved by holding the test bars at 250°C continuously for the times of interest; whereas the dynamic stabilization processes involved cyclic heating at 250°C for periods of time which will sum up the same stabilization times used in the static thermal exposure. In dynamic

stabilization, the test bars were removed from the furnace to cool down naturally to 25°C in 2 hours, then they were placed again in the furnace at 250°C; the first 30 minutes were not considered in the stabilization time, they were considered for heating the bars back to 250°C; after these 30 minutes of reheating the bars, the stabilization time was counted.

It is evident that prolonged exposure at 250°C has a deleterious effect on the tensile properties of the alloys studied; a noticeable reduction in the strength values, particularly the yield strength, and a remarkable increase in the ductility values can be observed in association with the increase in the exposure time. Interestingly, it can be noted that varying the stabilization technique has a subtle effect of the tensile data of a specific condition. For each alloy separately, the strength values obtained after applying static and dynamic stabilization show almost identical values with marginal variations for most of the conditions studied; whereas, the ductility values of statically stabilized conditions are higher than the values obtained after dynamic stabilization; this difference in ductility values increases with increase in the exposure time.

For the three alloys studied in this section, the reduction in ultimate tensile strength with increase in the exposure time up to 200 hours occurs at a lower rate than that of the yield strength. In contrast, ductility values show a continuous increasing trend with increase in exposure time; moreover, it is evident from Figure 6.1 that the base alloy (M1S) exhibits better ductility values than the other two alloys M2S and M3S alloys.

In general, the maximum rate of property change can be definitely reported at the start of the exposure treatment, i.e. in the first 5 hours of stabilization at 250°C. For ultimate and yield strength values, the rate of property change is witnessed to be high at the

beginning of stabilization, i.e. in the first 5 hours, for alloys M2S and M3S and a little bit slower for the base alloy M1S. The percentages of reduction in the strength values in the first 5 hours of stabilization for alloys M1S, M2S, and M3S are calculated to be 4% (UTS)/ 20% (YS), 20% (UTS)/ 31% (YS), and 14% (UTS)/ 33% (YS), respectively. Longer exposure times of more than 5 hours at 250°C lead to a noticeable reduction in the strength values of the base alloy M1S up to 100 hours, with values of 18% for UTS and 38% for YS, whereas the percentage of reduction in the strength values between the two stabilization times, i.e. 5 and 100 hours, are lower for alloys M2S and M3S with values of 2% (UTS)/ 23% (YS), and 11% (UTS)/ 30% (YS), respectively. Finally, the percentages of reduction in the strength values within the interval between 100 and 200 hours of stabilization are almost negligible for the three alloys.

The variation in the strength reduction rates experienced by the alloys at the start of the stabilization treatment can be understood by recalling Section 4.3 in Chapter 4, which discussed the characteristics of the strengthening precipitates. The first five hours of stabilization at 250°C, in the peak-aged condition, are possibly responsible for changing the structure of the metastable θ'-Al_2Cu phase to the equilibrium θ-Al_2Cu phase, which will certainly reduce the strength values, as depicted in Figure 6.1. The coarsening effect of the precipitates is not pronounced, and can be neglected in the first 5 hours of stabilization for the three alloys because of the expected low coarsening kinetics in this short time with respect to other conditions studied at longer times.

The ductility values of the base alloy M1S continuously increase with increasing exposure time up to 200 hours. However, the ductility values of alloys M2S and M3S increase with increasing exposure time up to 100 hours, followed by an insignificant

increase in the 100-200 hours range. This behavior can be attributed to the increased volume fractions of brittle intermetallic compounds, as well as the increased resistance to softening in alloys M2S and M3S compared to the base alloy M1S, due to additions of Ni and Mn, respectively.

The ambient-temperature tensile data is listed in Table 6.1, and reveals that the Mn-containing alloy M3S shows a slight enhancement in strength values compared to those of the Ni-containing alloy M2S, up to the stabilization time of 50 hours. However, for longer stabilization times, i.e. 100 and 200h, the Ni-containing alloy shows a slight enhancement in strength values, indicating that it offers a better resistance to softening in the presence of 2 wt.% Ni. This observation regarding resistance to alloy softening can be also verified from the obtained ductility values, with alloy M3S exhibiting better ductility values than alloy M2S at most of the stabilization times.

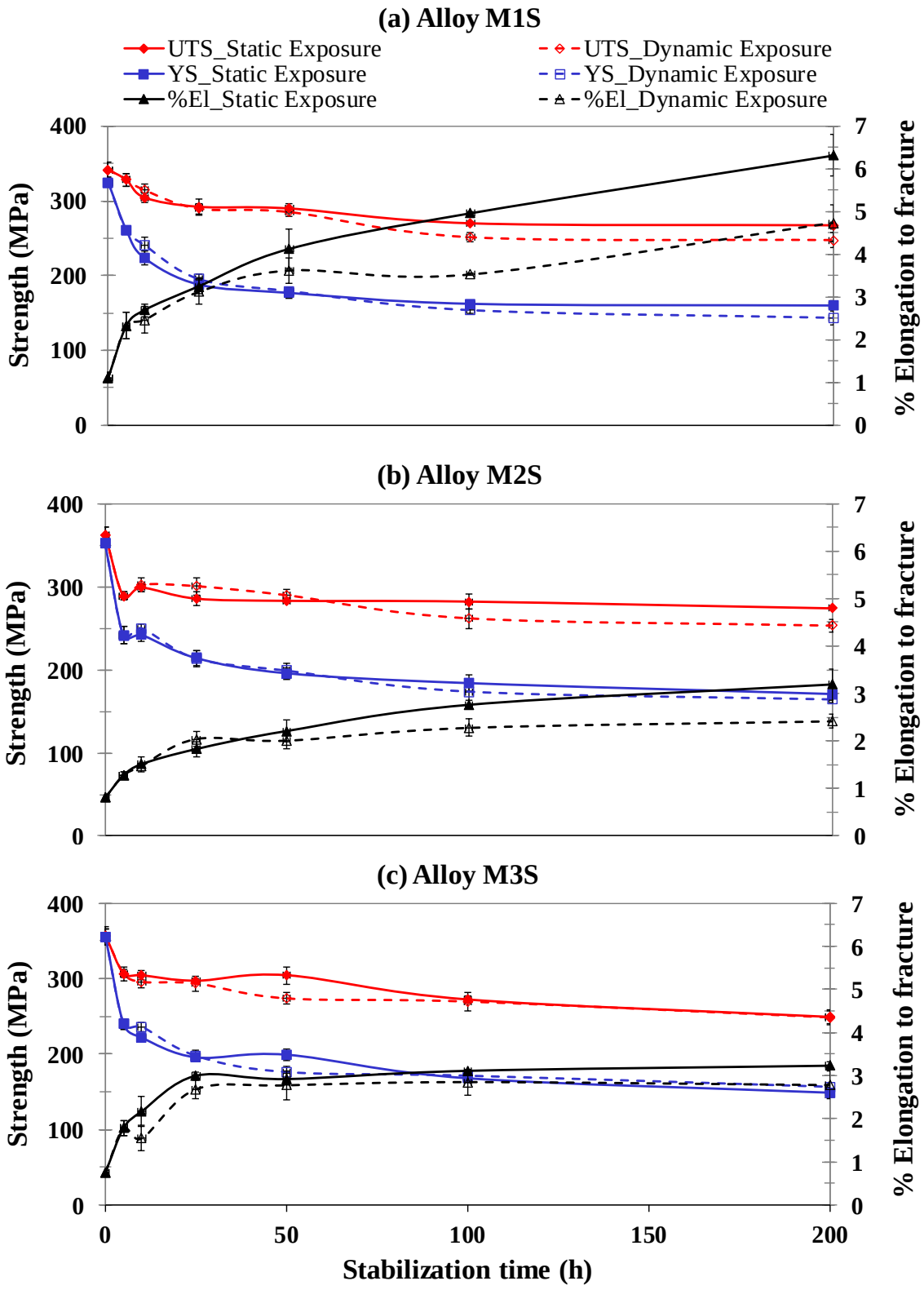

Figure 6.1 Variation in average UTS, YS, and %El values for alloys M1S through M3S in the T6-treated condition, and after static and dynamic stabilization at 250°C for 5h, 10h, 25h, 50h, 100h, and 200h (testing at ambient temperature).

Table 6.1 Variation in average UTS, YS, and %El values for alloys M1S through M3S in the T6-treated condition, and after static and dynamic stabilization at 250°C for 5h, 10h, 25h, 50h, 100h, and 200h (testing at ambient temperature)

Alloy Code	Stabilization time (h)	Static stabilization			Dynamic stabilization		
		UTS (MPa)	YS (MPa)	%El	UTS (MPa)	YS (MPa)	%El
M1S (354 + 0.3% Zr)	0	341.95	324.99	1.11	341.95	324.99	1.11
	5	328.20	260.90	2.33	328.20	260.90	2.33
	10	304.61	223.62	2.69	314.50	240.93	2.46
	25	292.25	188.12	3.25	289.66	195.50	3.12
	50	289.97	176.96	4.13	285.11	179.33	3.62
	100	270.14	162.35	4.96	251.46	153.85	3.53
	200	267.49	160.14	6.31	247.68	143.65	4.74
M2S (M1S + 2% Ni)	0	362.33	351.57	0.80	362.33	351.57	0.80
	5	288.78	241.32	1.27	288.78	241.32	1.27
	10	298.81	241.78	1.51	302.31	249.83	1.48
	25	285.53	214.08	1.83	300.54	213.44	2.04
	50	282.90	195.70	2.21	289.60	198.82	2.01
	100	282.00	183.89	2.76	261.84	173.66	2.27
	200	273.84	170.79	3.19	253.03	164.28	2.41
M3S (M1S + 0.75% Mn)	0	357.01	355.14	0.75	357.01	355.14	0.75
	5	306.60	239.56	1.78	306.60	239.56	1.78
	10	304.39	221.61	2.17	295.53	236.03	1.54
	25	297.09	195.40	2.99	293.44	197.46	2.68
	50	304.41	198.95	2.92	273.65	175.97	2.77
	100	272.25	167.74	3.11	269.41	171.17	2.85
	200	249.15	148.60	3.23	248.44	156.44	2.78

The tensile data obtained for the statically and dynamically stabilized alloys are replotted on quality chart of Cáceres[61] which is shown in Figure 6.2. Generally, the quality charts are used in order to better visualize the tensile data side by side to the alloy quality which is considered an important parameter to identify the alloy performance.

Since the quality indices obtained according to the Cáceres[61] model are functions of UTS and percentage of plastic deformation values, the discrepancies in quality index values obtained for the statically and dynamically stabilized conditions are more observable towards the very long stabilization times, i.e. 100 and 200 hours at 250°C. This can be ascribed to the noticeable variations in the ductility values at these prolonged exposure times. It is evident, also, that the quality index values of the base alloy M1S are higher than those of alloys M2S and M3S; and yet the quality index values of alloy M3S are higher than those of alloy M2S owing to variations in the ductility values of these alloys. Figure 6.2 shows that the strength values of the base alloy M1S are lower than those of alloys M2S and M3S, but the enhanced ductility values of the alloy highly promote its quality index values in the conditions studied.

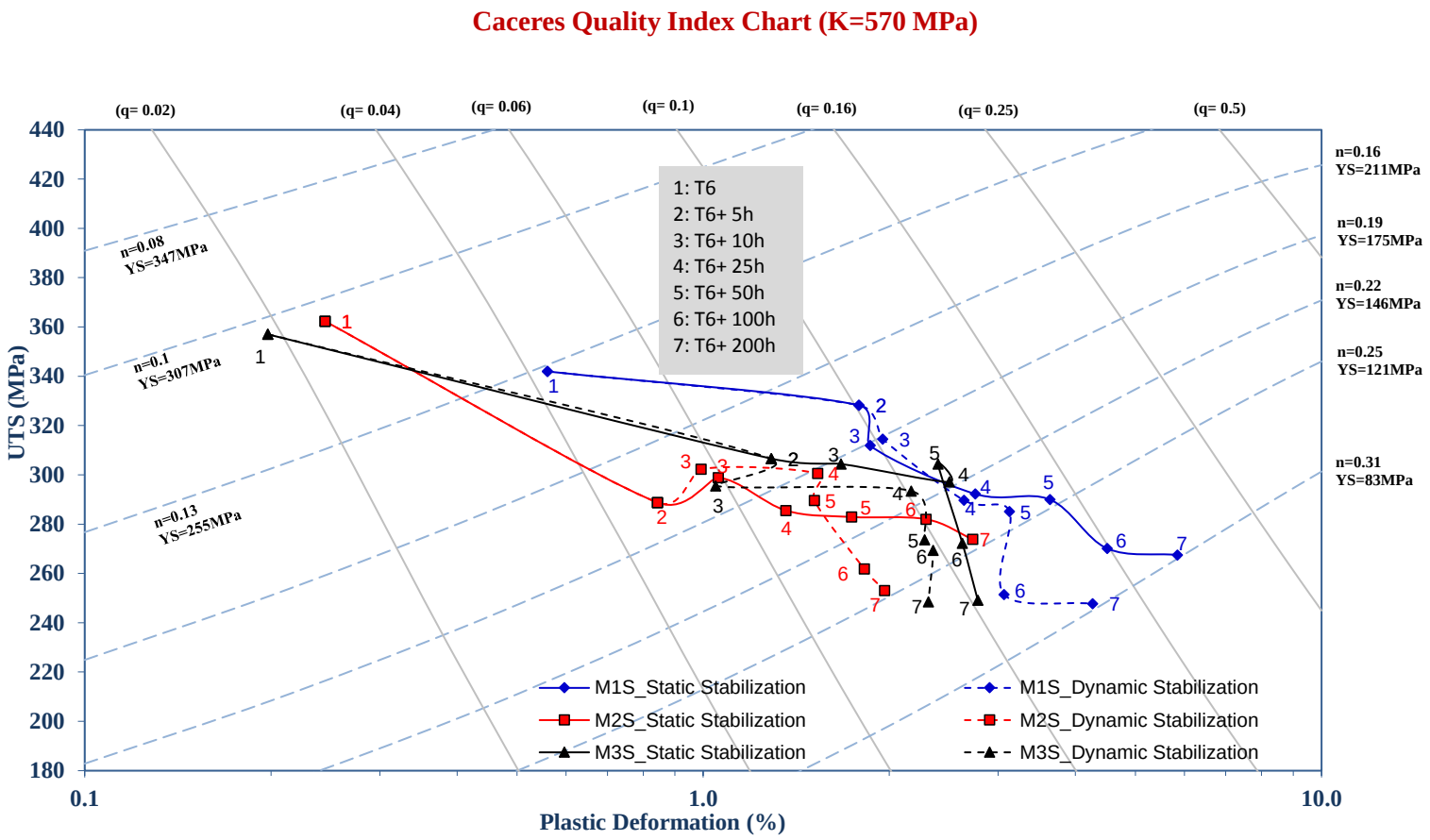

Figure 6.2 Cáceres quality chart representing the relation between the UTS and the percent plastic deformation of alloys M1S through M3S in the T6 condition, and after static and dynamic stabilization at 250°C for 5h, 10h, 25h, 50h, 100h, and 200h (testing at ambient temperature).

6.2.1.1 EFFECT OF STABILIZATION ON THE EVOLUTION OF YIELD STRENGTH VALUES

By recalling section 5.4.1.3 in Chapter 5, the overall yield strength (σ_{peak}) can be determined by adding up the individual strengthening factors of the microstructural features including the intrinsic aluminum strength(σ_i), the strengthening contribution of eutectic silicon (σ_{eu}), the strengthening contribution of solid solution (σ_{ss}), the strengthening contribution of intermetallic compounds (σ_{int}), and the strengthening contribution of fine precipitates (σ_p). The strengthening contribution of solid solution (σ_{ss}) is assumed as zero for the peak-aged conditions according to the assumption of efficient decomposition of the dissolved strengthening elements, i.e. Cu and Mg, to form fine dispersoids. Only the data obtained for the statically stabilized alloys will be considered in this analysis because of the close strength values obtained after static and dynamic stabilization (Figure 6.1).

Table 6.2 lists the results obtained for the peak-aged conditions of alloys M1S through M3S before and after stabilization at 250°C for the different exposure times. The variation in the strengthening effect of the precipitates with respect to variation in treatment conditions and alloys follow the same trend as that previously described in the context of the overall yield strength values of the alloys studied in this section (Figure 6.1).

In addition, it is evident that the strengthening values of the precipitates drop by ~50% for alloys M2S and M3S in the first 5 hours of stabilization compared to ~30% for the base alloy M1S. Since this analysis focuses solely on the strengthening effect of the precipitates, the interpretation in relation to the transformation of metastable θ' Al_2Cu precursors into the equilibrium θ-Al_2Cu phase mentioned previously is more acceptable in view of the results listed in Table 6.2.

Table 6.2 Summary of the yield strength contributions from various constituents in M1S, M2S, and M3S alloys in the T6 condition, and after static stabilization at 250°C for 5h, 10h, 25h, 50h, 100h, and 200h (testing at ambient temperature)

Alloy	Stabilization time (h)	σ_i (MPa)	$\sigma_{eutectic}$ (MPa)	σ_{ss} (MPa)	σ_{int} (MPa)	σ_p (MPa)	σ_{peak} (MPa)
M1S	0	10.00	100.00	0.00	0.00	214.99	324.99
	5					150.90	260.90
	10					113.62	223.62
	25					78.12	188.12
	50					66.96	176.96
	100					52.35	162.35
	200					50.14	160.14
M2S	0	10.00	100.00	0.00	20.86	220.71	351.57
	5					110.47	241.32
	10					110.93	241.78
	25					83.22	214.08
	50					64.85	195.70
	100					53.03	183.89
	200					39.94	170.79
M3S	0	10.00	100.00	0.00	6.92	238.22	355.14
	5					122.65	239.56
	10					104.69	221.61
	25					78.48	195.40
	50					82.04	198.95
	100					50.82	167.74
	200					31.68	148.60

Figure 6.3 through Figure 6.5 summarize the percentage contributions of microstructural constituents to the overall yield strength of alloys M1S, M2S, and M3S, respectively. The continuous reduction in the strengthening contribution of the precipitates with increase in the stabilization time is easily observed.

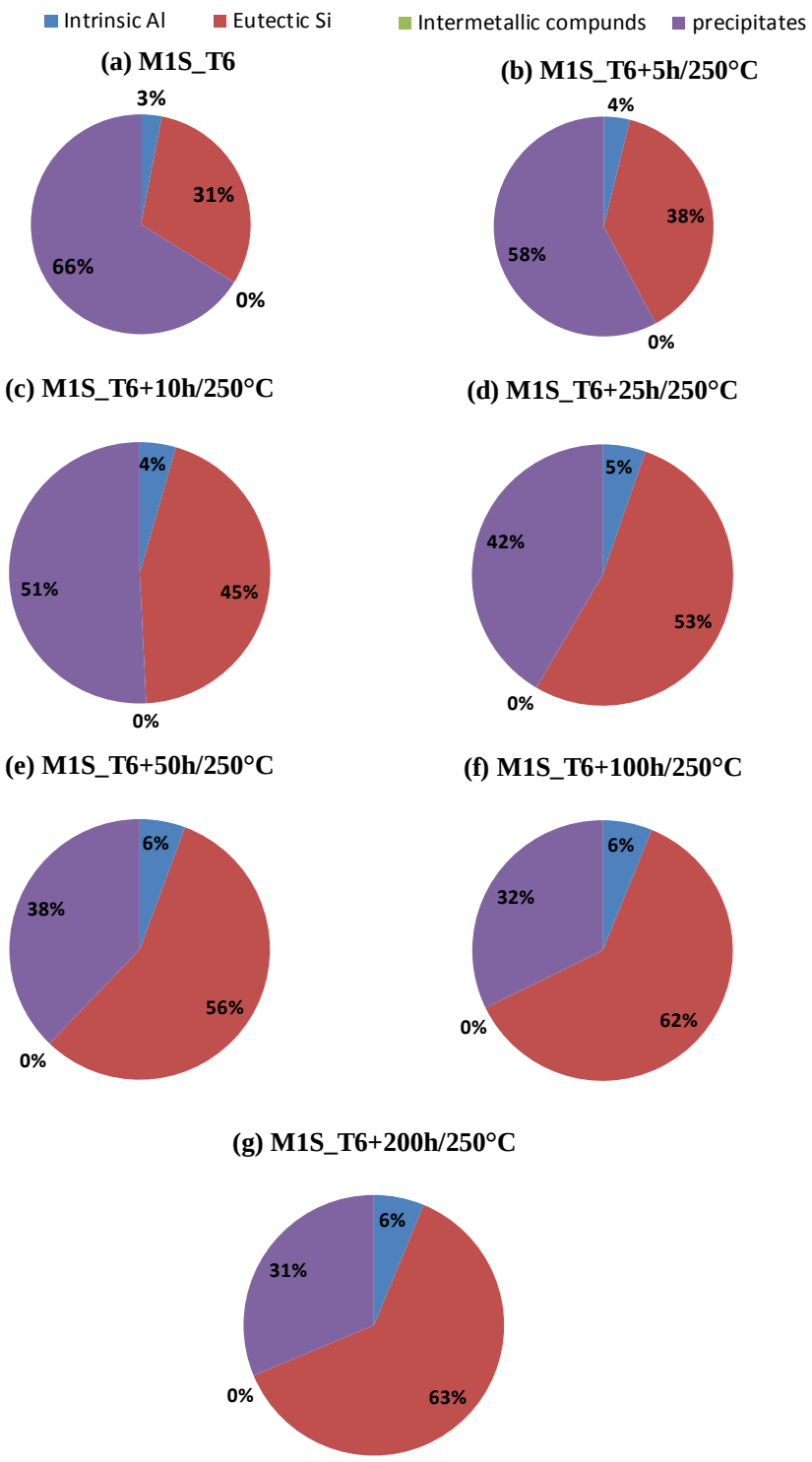

Figure 6.3 Percentage contributions of microstructural constituents to the overall yield strength of alloy M1S in (a) the T6 condition, and after static stabilization at 250°C for (b) 5h, (c) 10h, (d) 25h, (e) 50h, (f) 100h, and (g)200h (testing at ambient temperature).

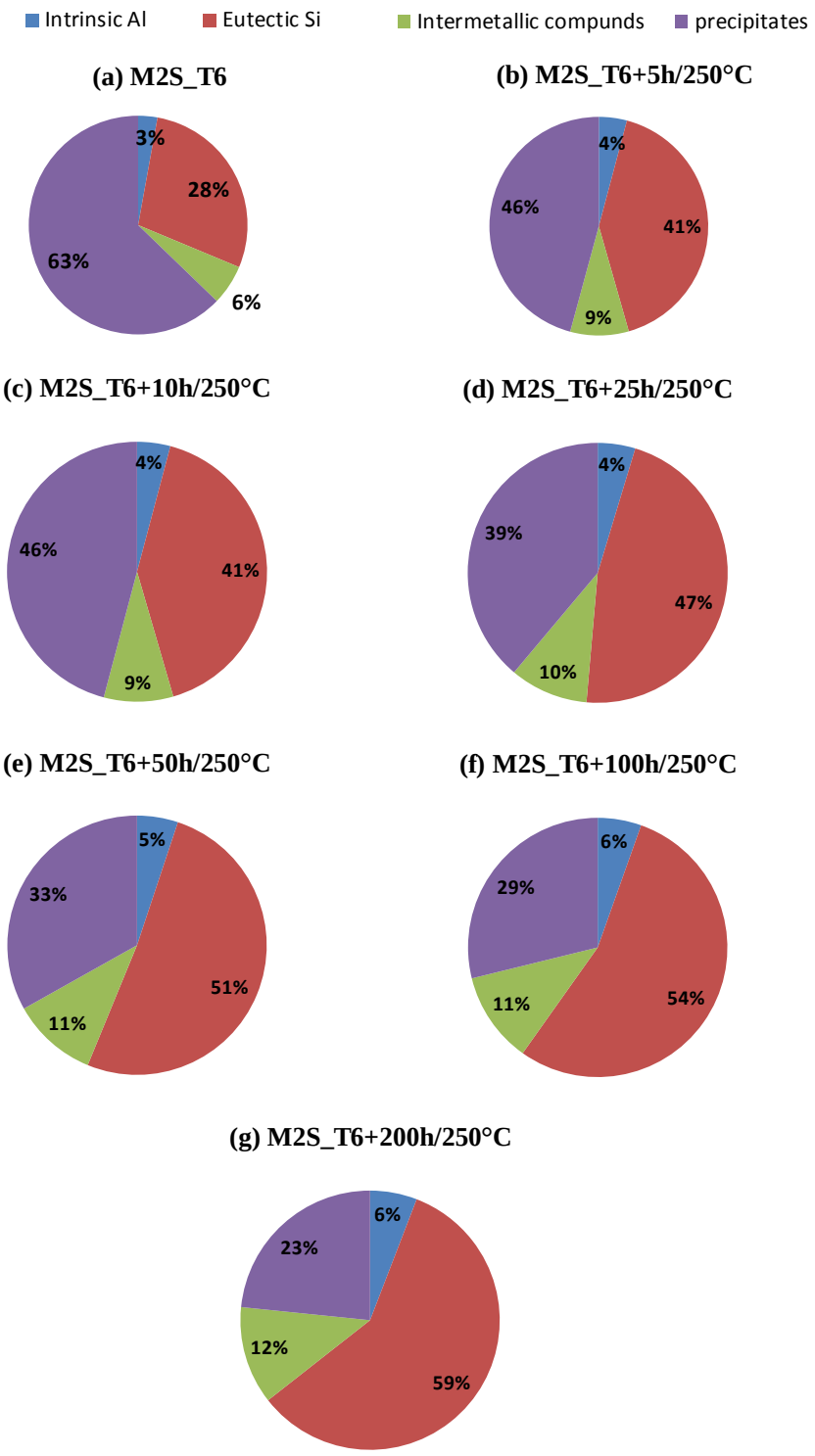

Figure 6.4 Percentage contributions of microstructural constituents to the overall yield strength of alloy M2S in (a) the T6 condition, and after static stabilization at 250°C for (b) 5h, (c) 10h, (d) 25h, (e) 50h, (f) 100h, and (g)200h (testing at ambient temperature).

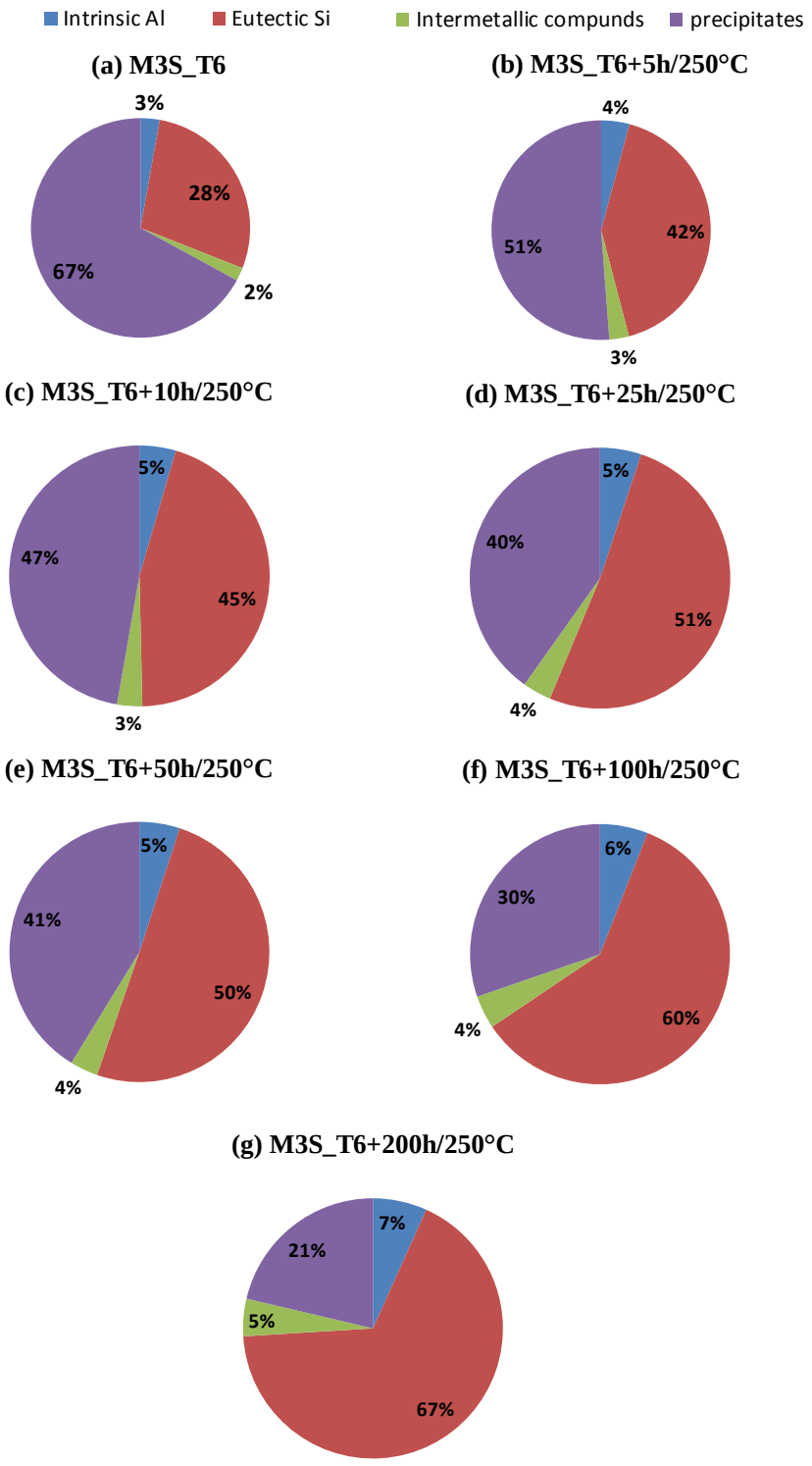

Figure 6.5 Percentage contributions of microstructural constituents to the overall yield strength of alloy M3S in (a) the T6 condition, and after static stabilization at 250°C for (b) 5h, (c) 10h, (d) 25h, (e) 50h, (f) 100h, and (g)200h (testing at ambient temperature).

Figure 6.6 compiles the experimental values of the precipitate strengthening contributions obtained for the three alloys studied versus the stabilization time. The relation between the strengthening contribution of the precipitates to overall yield strength of a peak-aged and stabilized condition and the stabilization time can be expressed as a second order exponential decay function with the constants given in the inset table shown in Figure 6.6. This equation is of importance to predict the deterioration in the strengthening provided by fine precipitates in Al-Si-Cu-Mg alloys due to the structural transformation and coarsening of the precipitates when the alloys are exposed to elevated temperatures following the peak aging treatment. This equation will be verified further on in a subsequent section.

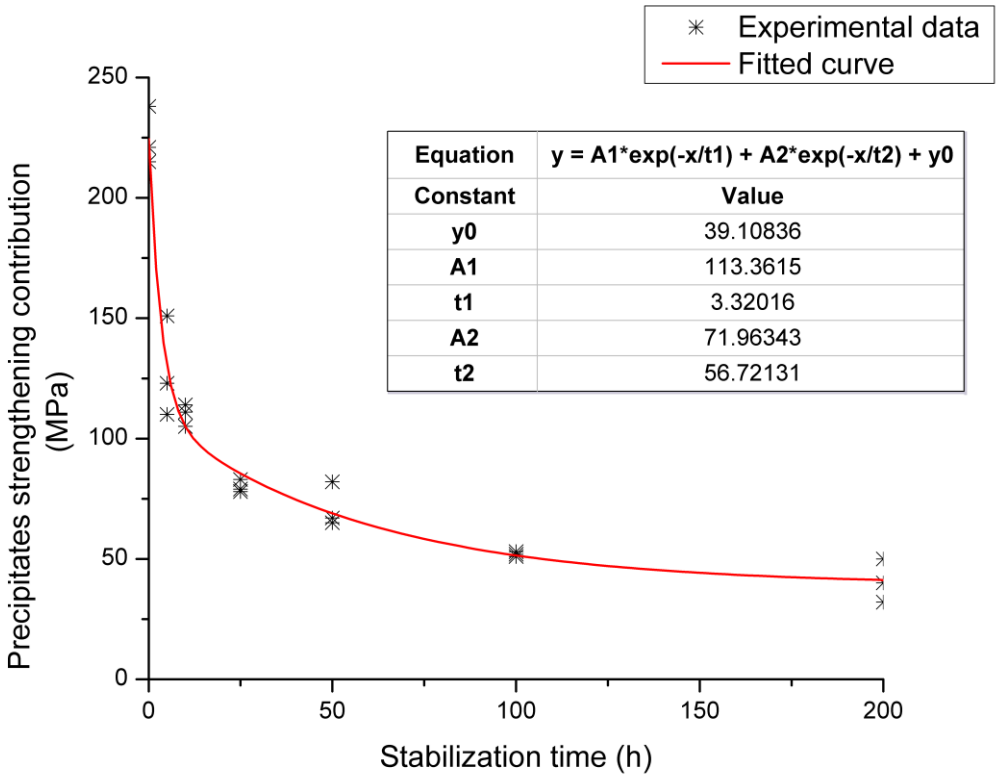

Figure 6.6 Precipitate strengthening contribution versus the stabilization time for alloys M1S through M3S**.**

In order to explore the evolution of strengthening precipitates as a result of applying the T6-heat treatment and further exposure to 250°C for times up to 200 hours, multiple samples from tensile-tested bars at room temperature were extracted and prepared for investigation using an Hitachi SU8000 field-emission scanning electron microscope.

It is well established for 319-type Al-Si-Cu-Mg alloys[234] that the precipitates are uniformly distributed and sized in the peak-aged, i.e. T6-treated condition. Prolonged elevated-temperature exposure, i.e. stabilization at elevated temperatures, of T6-treated alloys will result in coarsening of the fine precipitates developed during the T6 aging treatment. The fine precipitates coarsen by attracting atoms from the surrounding smaller precipitates to larger ones and hence the total number of precipitates in the α-Al matrix will reduce. This increase in precipitate size and reduction in their numbers seriously deteriorate the overall mechanical properties of the peak-aged materials depicted in Figure 6.1, by lowering the strengthening contribution of the precipitates as can be inferred from Figure 6.6 and Table 6.2.

The reduction in the precipitate strengthening effect is mainly instigated by lowering the total number of precipitates in the α-Al matrix and hence increasing the spacing between them. This increase in distance between precipitates allows for the easier movement of dislocations because the force required to cut through the precipitates is inversely proportional to the spacing or distance between neighboring precipitates. According to previous investigations,[24, 38, 122, 278, 279] in case of wide-spaced coarsened precipitates, the dislocations can bypass these precipitates readily by forming loops around them, i.e. by the Orowan mechanism, which will decrease the strengthening effect of the precipitates. The development of secondary coarsening-resistant precipitates following the

addition of Zr, Ni, and Mn is believed to reduce the deterioration rate in the mechanical properties of Al-alloys during their exposure to elevated temperatures.

Figure 6.7(a) and Figure 6.7(b) show the density and distribution of precipitates in alloys M1S and M2S, respectively, in T6-treated conditions. It is evident that the density of the main precipitates, i.e. Al_2Cu and Al_2CuMg, is much higher in the case of the base alloy M1S compared to alloy M2S, reflecting the effect of Ni addition in alloy M2S (Figure 6.7(b)) in reducing the amount of the available copper for strengthening by forming Al-Cu-Ni phases such as the Al_3CuNi-phase. On the positive side, the presence of such phases enhances the mechanical properties of the alloy, in particular, the elevated-temperature mechanical performance. Thus, the overall strengthening in Ni-containing alloys such as alloy M2S can be understood as a trade-off between minimizing the total number of the main strengthening precipitates θ-Al_2Cu and S-Al_2CuMg phases and their precursors, and the formation of the strengthening phases Al-Cu-Ni. This trade-off behavior can be verified by recalling the data listed in Table 6.2 where the strengthening contributions of the precipitates in the peak-aged condition of alloys M1S and M2S show a marginal variation, and hence there is no real strengthening loss in alloy M2S due to the consumption of Cu because of the formation of Al-Cu-Ni phases.

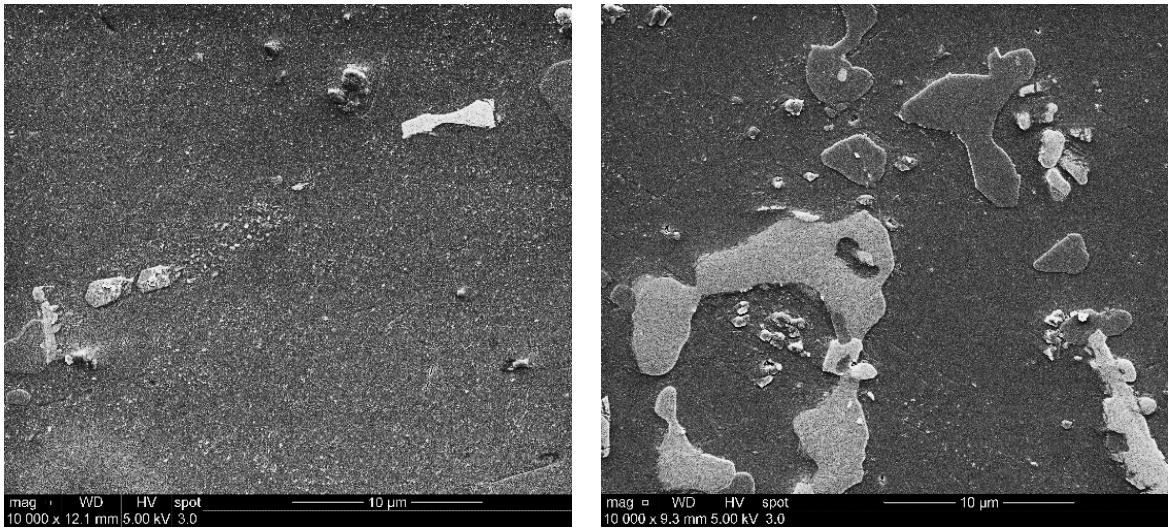

(a) (b)

Figure 6.7 Secondary electron images showing the distribution of fine dispersoids in T6-treated conditions of alloys: (a) M1S, and (b) M2S alloys in the T6-treated condition.

The fine precipitates which were spotted in the peak-aged T6 condition have coarsened after continuous heating for 50 hours at 250°C, as shown in the low magnification secondary electron images displayed in Figure 6.8(a) and Figure 6.8(b). These coarsened precipitates obtained after stabilization for 50 hours at 250°C are more visible than the fine precipitates which are shown in Figure 6.7 for the two alloys. Higher magnification images for the same condition, i.e. T6+50 hours at 250°C, of alloys M1S and M2S are shown in Figure 6.8(c) and Figure 6.8(d). These high magnification images show that the greyness of the precipitates in the base alloy M1S are almost the same; whereas, there is an obvious variation in the degree of greyness of the precipitates observed in the microstructure of alloy M2S. In Figure 6.8(d), the shiny particles in alloy M2S, delineated by broken arrows, are possibly fine Al-Cu-Ni particles; whereas other darker precipitates (solid arrows) are possibly the primary strengthening phases and their precursors. These findings emphasize the strengthening role of Al-Cu-Ni phases, which explains the

increased value of the precipitate strengthening contribution in spite of the low density of the primary strengthening precipitates.

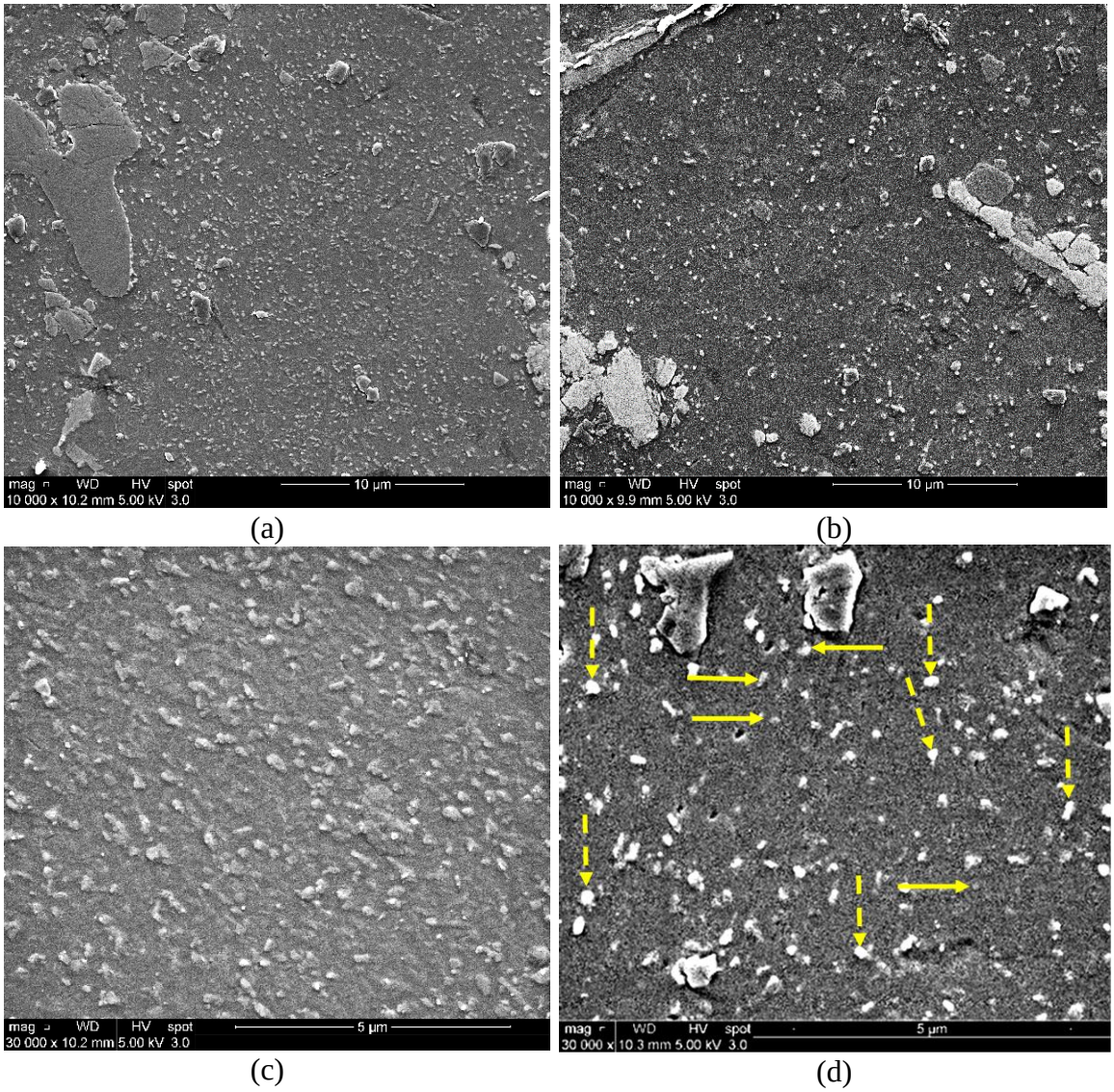

Figure 6.8 Secondary electron images showing the distribution of strengthening precipitates in T6-treated conditions after stabilization at 250°C for 50 hours for alloys: (a, and c) M1S, and (b, and d) M2S.

Figure 6.9 shows the strengthening precipitates in T6-treated M1S and M2S alloys after stabilization for 100 hours at 250°C. The low magnification secondary electron images shown in Figure 6.9(a) and Figure 6.9(b), reveal the decreased density of precipitates with respect to the finer precipitates seen in Figure 6.8(a) and Figure 6.8(b)

attained after 50 hours of stabilization at 250°C. This reduction in the total number of precipitates gives an indication of the continuing coarsening behavior of the precipitates with increasing exposure time at elevated temperatures. In terms of the mechanical properties, the coarsening behavior of the precipitates results in further reduction in the tensile strength values of the alloys. Obviously, the first 50 hours of stabilization results in a serious deterioration in the strength values, in the range of 65-70% of the peak-aged strength values, for the three alloys studied. On the other hand, the second 50 hours of stabilization at 250°C, i.e. 100 hours stabilization, results in 22%, 18%, and 39% deterioration in the strength values of alloys M1S, M2S, and M3S, respectively, as seen from Figure 6.1 and Table 6.1. These observations highlight that the coarsening kinetics decay with time, which may be attributed to the continuously increasing distance between the precipitates with increase in the stabilization time. The high magnification images of alloys M1S and M2S, shown in Figure 6.9(c) and Figure 6.9(d), respectively, demonstrate these observations clearly i.e., the density of precipitates and the increased distance between the precipitates because of their coarsening during the stabilization treatment.

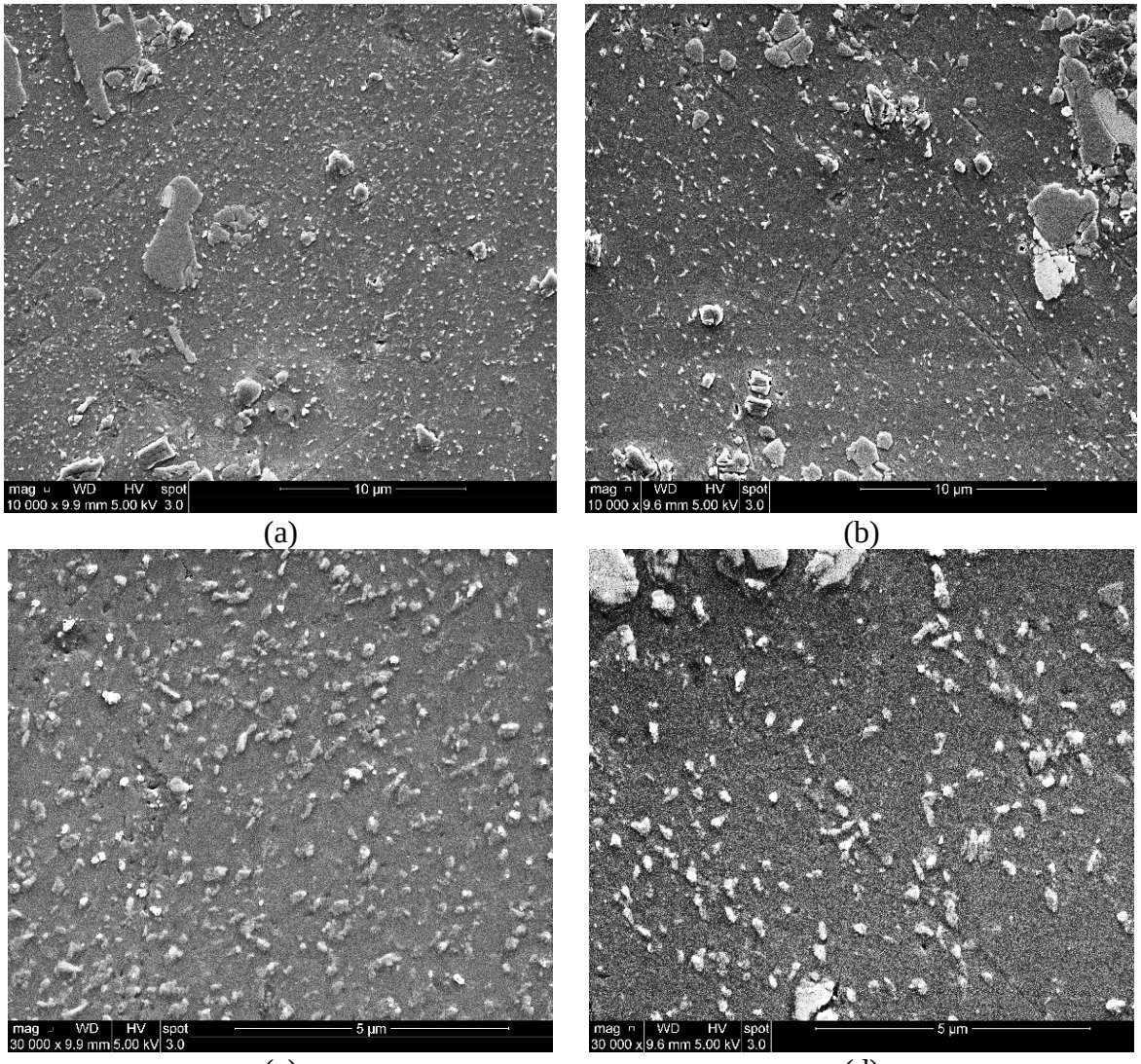

Figure 6.9 Secondary electron images showing the distribution of strengthening precipitates in T6-treated alloys after stabilization at 250°C for 100 hours for alloys: (a, and c) M1S alloy, and (b, and d) M2S alloy.

The characteristics of the strengthening precipitates observed in the T6-treated M1S and M2S alloys stabilized for 200 hours at 250°C, shown in Figure 6.10, do not reveal any noticeable variations with respect to those of the precipitates obtained after stabilization for 100 hours at 250°C, as shown in Figure 6.9. This observation emphasizes the reduced coarsening kinetics and explains, in addition, the limited reduction in the tensile strength values of the alloys stabilized for 100 hours and 200 hours at 250°C as shown in Figure 6.1.

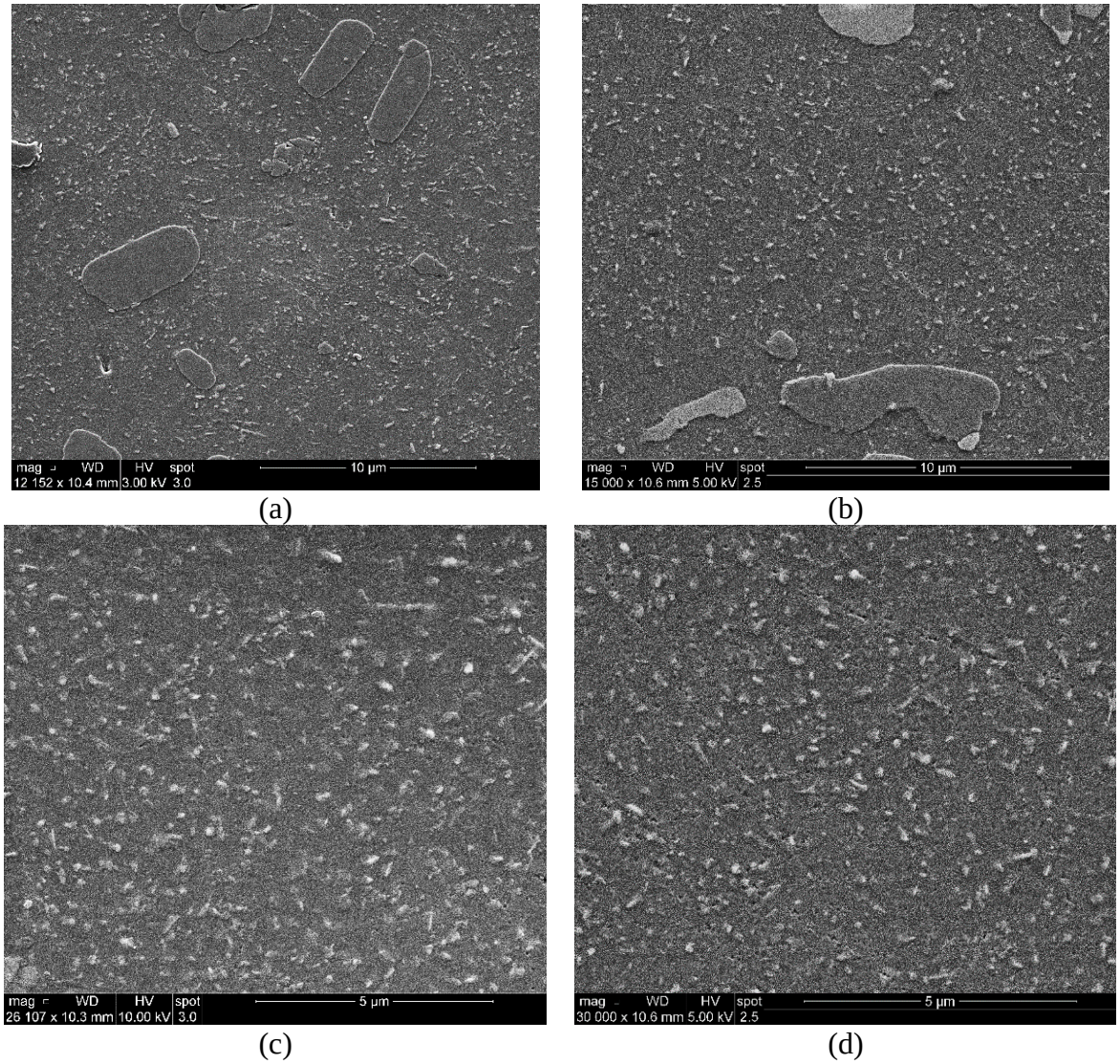

Figure 6.10 Secondary electron images showing the distribution of strengthening precipitates in T6-treated alloys after stabilization at 250°C for 200 hours for alloys: (a, and c) M1S alloy, and (b, and d) M2S alloy.

The presence of precipitate free zones (PFZ) in the alloy structure is not favourable for the sake of the distribution of the precipitates in the matrix and hence the corresponding mechanical performance.[15, 167] For the base alloy M1S, Figure 6.11(a) shows that the precipitates are evenly distributed in the interdendritic regions without noticeable PFZs; however, the density of the precipitates is reduced in the vicinity of the silicon particles. For alloy M2S, on the other hand, the addition of 2 wt.% Ni results in the presence of

clearly detected PFZs around existing phases, as shown in Figure 6.11(b). The addition of Ni promotes the formation of Al-Cu-Ni phases, as confirmed by the EDX spectrum shown in Figure 6.11(c) for the light grey branched phase particle detected in Figure 6.11(b), and hence the copper available for strengthening around these phases is depleted, due to the formation of Al-Cu-Ni phases, which affects the precipitate distribution around this phase.

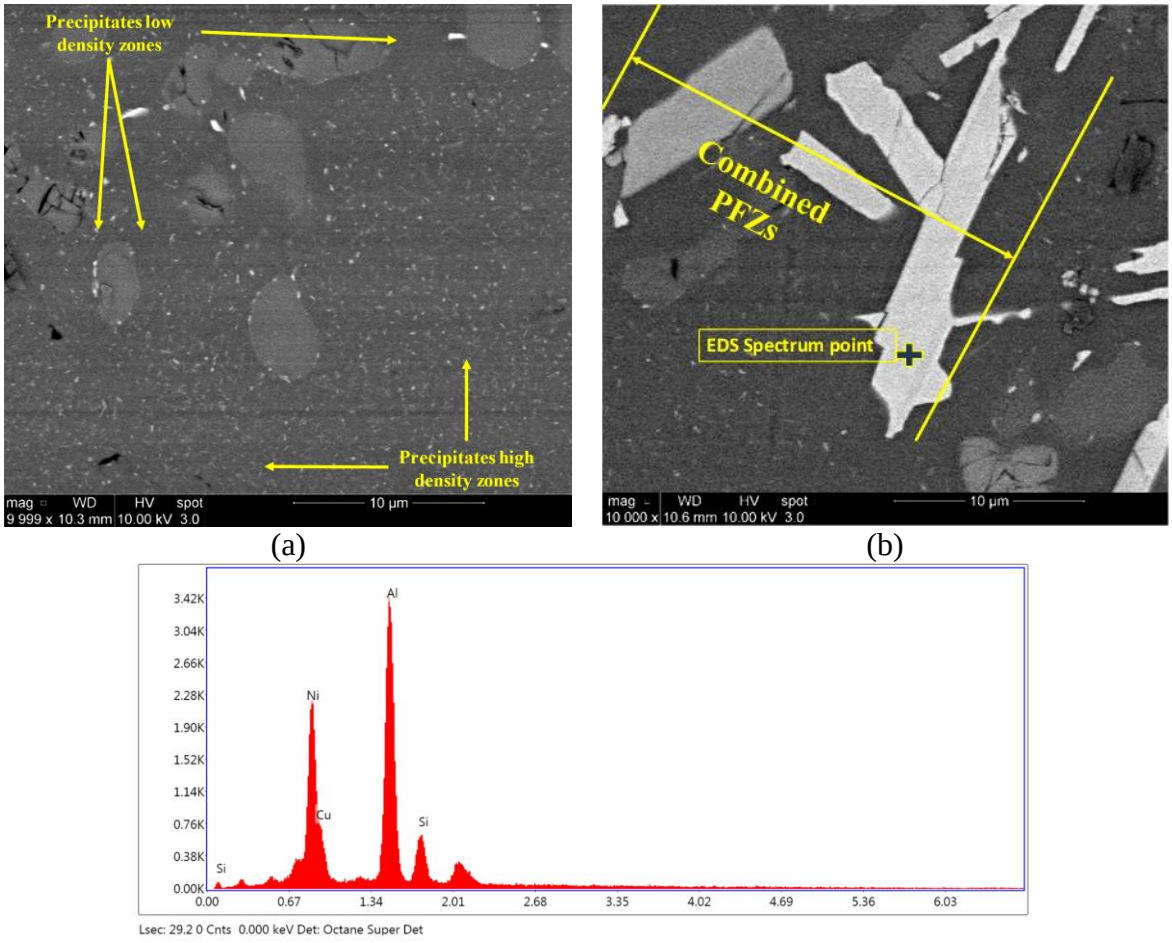

Figure 6.11 Backscattered electron images showing the density of precipitates in the T6-treated condition after stabilization at 250°C for 200 hours for alloys: (a) M1S and (b) M2S; (c) EDS spectrum corresponding to the location identified in (b) by the + sign.

The objective of adding Zr as a common addition in all the alloys studied was to form the stable $L1_2$-Al_3Zr precipitates, having a low misfit with the α-Al matrix; these precipitates are thermally stable, i.e. coarsening-resistant during exposure to elevated temperatures. The presence of these finely dispersed and coarsening-resistant small precipitates will hinder the movement of dislocations and enhance the strength of the alloys after exposure to elevated temperatures for a considerable amount of time.[11, 280] Figure 6.12 shows the distribution of elements in the vicinity of the Al-Cu-Ni phase in alloy M2S (with 2 wt.% Ni) after stabilization of the T6-treated alloy for 200 hours at 250°C. The distribution of Zr, shown in Figure 6.12(h), appears to be very promising in the context of achieving the objective of forming small and dispersed Al_3Zr particles. Although such particles were difficult to be spotted in the present study, they were observed, however, in the investigations of Shaha.[14]

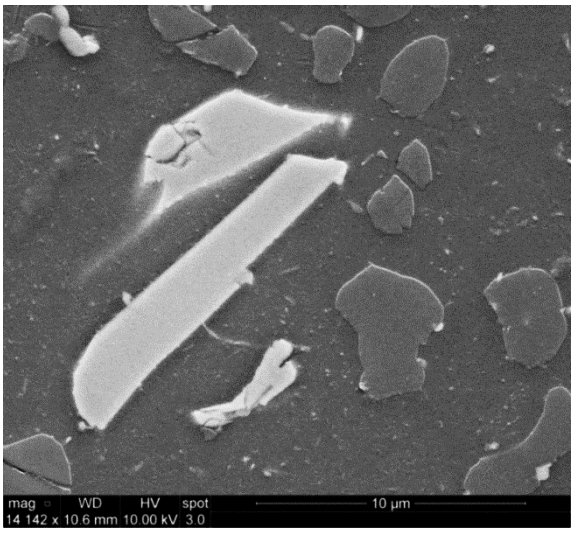

(a)

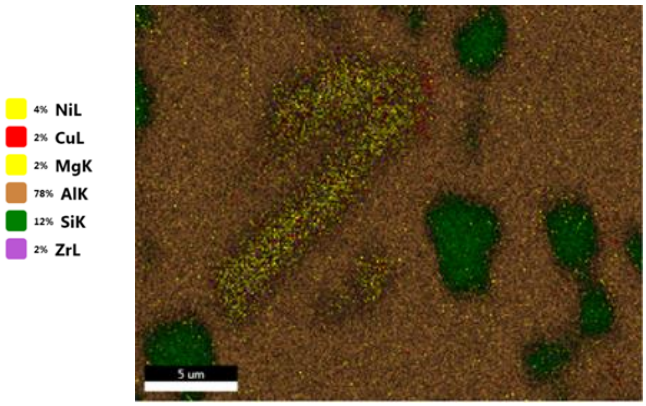

(b)

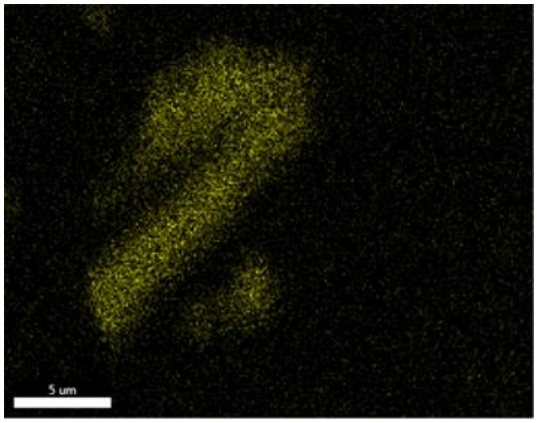

(c) Ni

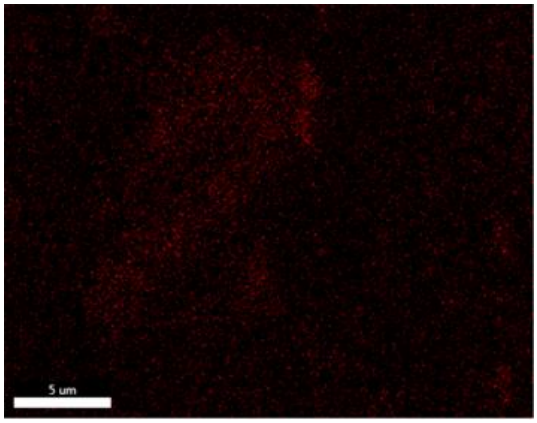

(d) Cu

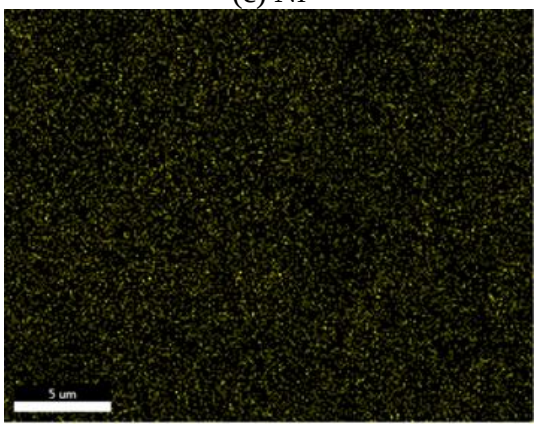

(e) Mg

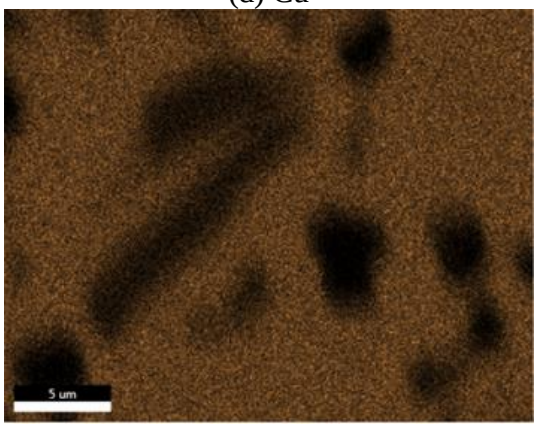

(f) Al

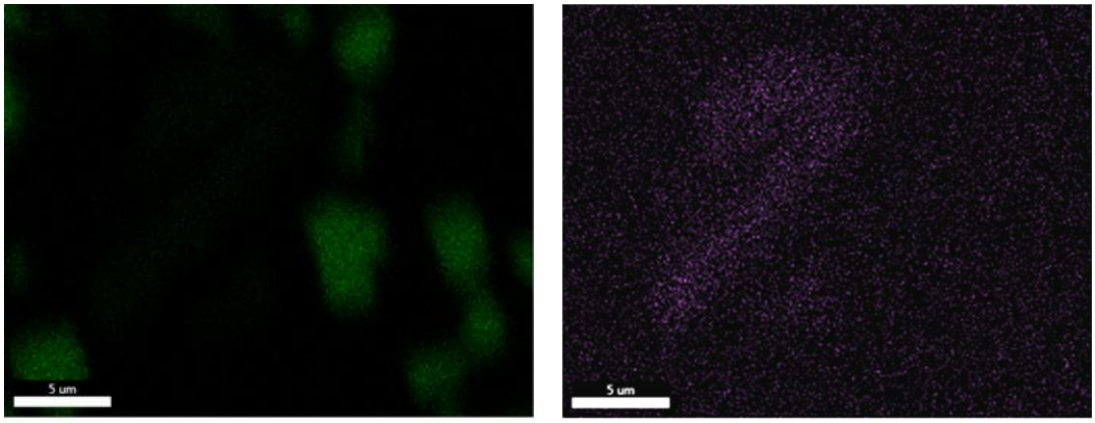

(g) Si (h) Zr

Figure 6.12 (a) Secondary electron image of T6-treated M2S alloy after stabilization at 250°C for 200 hours, (b) elements overlay, and (c) through (h) corresponding X-ray maps showing distribution of the different elements in the micrograph shown in (a).

Figure 6.13 exhibits the precipitation characteristics and distribution in the T6-treated M3S alloy containing 0.75 wt.% Mn after stabilization for 200 hours at 250°C. Figure 6.13(a) reveals a general view of the distribution and size of the precipitated particles after the stabilization treatment. It is interesting to observe that no clearly identified PFZs are found in the microstructure of the T6-treated alloy M3S after stabilization treatment. The higher magnification micrograph of Figure 6.13(b) shows that the coarsened particles have the morphology of more or less elongated platelets distributed in two perpendicular directions. Similar findings were also reported by Garza-Elizondo[11] and Tavitas-Medrano *et al.*[235] for 354-type Al-Si-Cu-Mg alloys and 319-type Al-Si-Cu-Mg alloys, respectively.

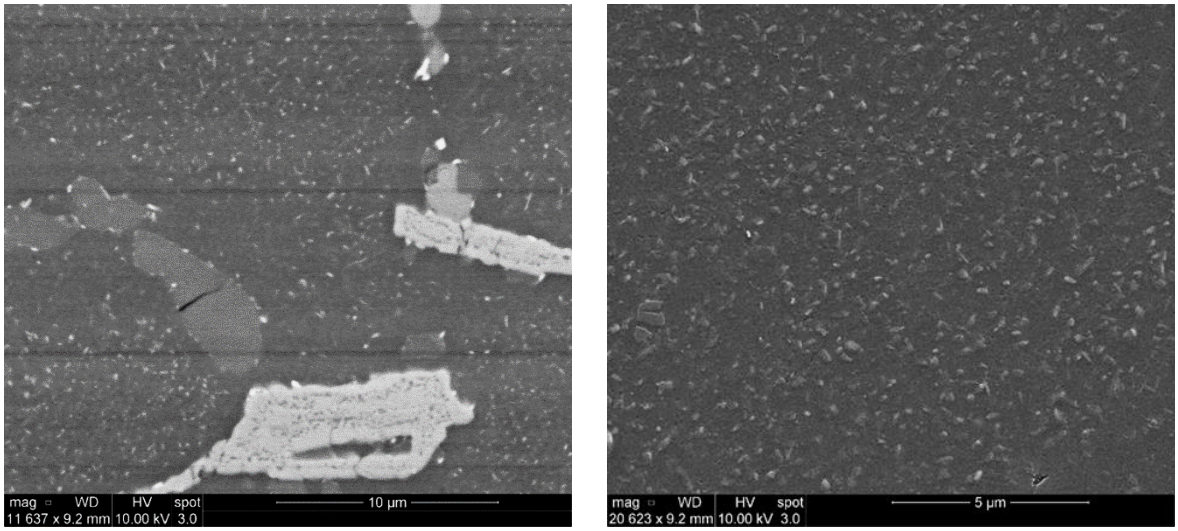

(a) (b)

Figure 6.13 Backscattered electron images showing the distribution of precipitates in the T6-treated M3S alloy after stabilization at 250°C for 200 hours: (a) low magnification image, and (b) high magnification image.

6.2.2 HARDNESS VALUES

Figure 6.14 illustrates variations in the hardness values of T6-treated alloys M1S, M2S, and M3S with respect to the stabilization time at 250°C. For each alloy studied, the hardness values obtained for dynamically- and statically-stabilized conditions show insignificant variations, in a manner similar to the reported tensile properties shown in Figure 6.1. For the three alloys studied, the hardness values decrease at a high rate in the first 100 hours of stabilization, following which the decrease in rate becomes almost negligible with further stabilization beyond the 100 hours at 250°C. In the first 5 hours of stabilization, the degradation rate is considered the highest experienced during the stabilization treatment. This behavior is similar to that reported for the tensile properties. The hardness values obtained for alloy M2S show slight enhancements over those obtained for alloys M1S and M3S.

In Chapter 4 of the present study, it was shown that the alloys studied are mainly strengthened by the formation of θ-Al_2Cu and S-Al_2MgCu and their precursors. Similar findings were previously reported by Reif *et al.*[236] The continuous reduction in hardness values with increase in the stabilization time is related primarily to the changes in the nature, size, shape, and distribution of the strengthening precipitates during prolonged exposure at 250°C. It is evident from the previous section that increasing the stabilization time at 250°C for the T6-treated alloys increases the size of the precipitates and hence reduces their total number in the alloy microstructure. As a result, the equilibrium phases of the primary strengthening precipitates (θ-Al_2Cu and S-Al_2MgCu) will be incoherent with the α-Al matrix and widely-spaced and will thus be responsible for the observed drop in hardness values, as seen in Figure 6.14.

In more detail, the hardness values represent a combination of the tensile yield strength and strain-hardening rate. In the stabilized T6-treated alloys, the tensile yield strength values were reduced due to the coarsened precipitates. The Orowan mechanism, i.e. forming loops around the precipitates, leads to higher strain-hardening rates compared to the obstacle shearing mechanism, i.e. the Friedel effect.[270] The coarsened precipitates change the favourable Orowan mechanism into the less advantageous Friedel effect from the strength point of view as well as strain-hardening rate. Subsequently, the combined reduction in the yield strength values and strain-hardening rates will lead to a serious reduction in the hardness values of the alloys studied.

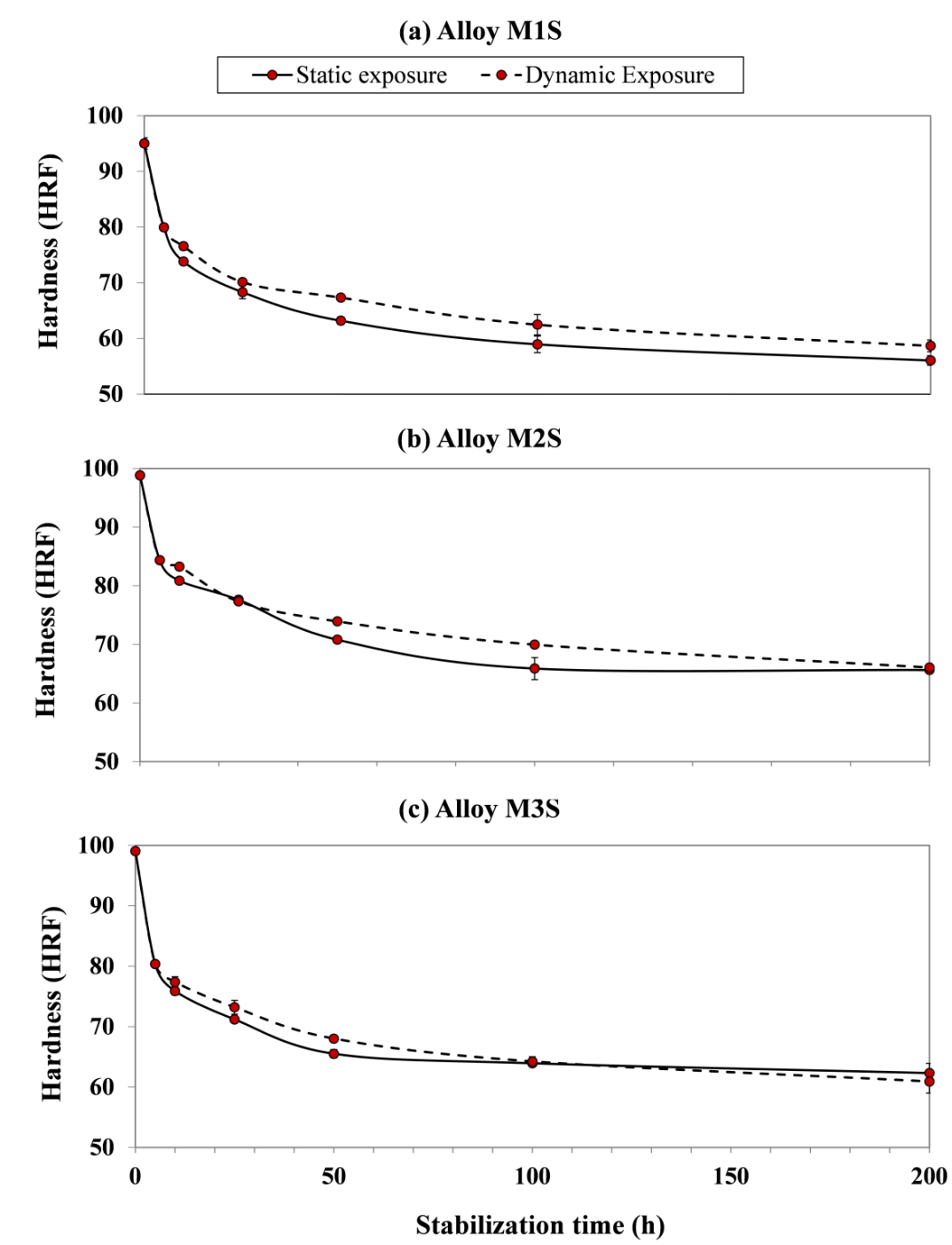

Figure 6.14 Variation in Rockwell hardness values of alloys M1S through M3S in the T6-treated condition, and after static and dynamic stabilization at 250°C for 5h, 10h, 25h, 50h, 100h, and 200h (testing at ambient temperature).

6.3 INFLUENCE OF THERMAL EXPOSURE ON AMBIENT-TEMPERATURE MECHANICAL PROPERTIES

This section reports on the effect of thermal exposure, i.e. stabilization at 250°C, on the mechanical properties of the alloys studied, taking all five alloys M1S through M5S into consideration, in the T5- and T6-treated conditions. The exposure times in this section are limited to two values only, namely, 100 and 200 hours at 250°C. The selection of these time spans are based on the results obtained in the previous section regarding the steep degradation in the strength values within the first 100 hours of exposure to 250°C and the subsequent limited degradation in the second 100 hours of exposure, i.e. up to 200 hours. The stabilization technique considered here is the static one because it is more feasible to use in laboratories and, as was shown earlier on, that no significant variations in the mechanical properties were obtained after applying the dynamic or the static stabilization techniques. The tensile properties along with hardness values obtained at ambient temperature are reported and interpreted in this section.

6.3.1 AMBIENT-TEMPERATURE TENSILE PROPERTIES

Figure 6.15 demonstrates ambient-temperature tensile properties obtained for the alloys M1S through M5S in the T5- and T6- treated conditions, before and after thermal exposure (stabilization) at 250°C for 100 and 200 hours. For each alloy studied, the tensile data obtained for the T5- and T6-treated conditions before stabilization are also displayed in Figure 6.15 as reference values. The codes for the stabilized conditions noted in columns across the X-axis comprise the applied heat treatment, followed by the number of hours of stabilization, i.e. T5+100h means the alloy was tested in the T5-treated condition, after stabilization at 250°C for 100 hours.

As previously mentioned in the preceding section, the thermal exposure has a serious deleterious effect on strength values of Al-Si-Cu-Mg alloys, in particular, the yield strength; on contrary to the ductility values which have markedly increased following exposing at 250°C for prolonged times up to 200 hours. On one hand, the variation trends in the strength values (UTS and YS) of stabilized T6-treated conditions are considered to be consistent for the alloys studied. Stabilized T5-treated conditions, on the other hand, show irregular variation trends in relation to the strength values of the alloys studied. However, with respect to the ductility values, stabilized T5- and T6-treated conditions demonstrate similar trends in relation to the improvement in the ductility values of the investigated alloys, as can be inferred from Figure 6.15.

Interestingly, Figure 6.15 reveals that the strength values (UTS and YS) obtained for the stabilized T5-treated conditions are comparable to, and in various alloys exceed, those obtained for the stabilized T6-treated conditions; whereas, the ductility values for stabilized T6-treated conditions are higher than those obtained with stabilized T5-treated conditions. If the observations regarding the strength values obtained after stabilization treatment are sufficiently verified, and acceptable high strength and ductility values of T5-treated conditions are attainable, this will be of great economic benefit in terms of heat treatment costs and higher production rates, because the solutionizing treatment, which is a time- and energy-consuming treatment, is not a step in the procedure of the T5-temper treatment.

The improved strength values of stabilized T5-treated conditions can be attributed to the limited amount of strengthening precipitates which exist in the structure of T5-treated alloys as a result of the direct artificial aging of as-cast structures without solutionizing. Alloy softening is mainly driven by coarsening of the strengthening precipitates. Thus, by increasing the volume fraction of the coarsened precipitates, the softening behavior will be noticeable, as in the case of stabilized T6-treated alloys, while the coarsening of a limited volume fraction of precipitates will not degrade the strength values much, as is the case for the stabilized T5-treated conditions. This interpretation may be rephrased in terms of microstructural stability: the more stable the microstructure is while being exposed at an elevated temperature, i.e. when microstructural changes are kept to a minimum, the less is the degradation in the mechanical properties. This concept is better understood in terms of the ductility values shown in (Figure 6.15(b)). The ductility values in the stabilized T5-treated conditions do not change considerably compared to the T5-treated condition, whereas the opposite is apparent for the T6-treated conditions before and after stabilization.

The highest resistance to softening is associated with alloys M4S and M5S in stabilized T5- and T6-treated conditions. The overall strength values of these alloys are the lowest in the T5- and T6-treated conditions compared to the other three alloys (M1S, M2S, and M3S). In terms of absolute strength values, however, the T6-treated M2S and M4S alloys, with 2 and 4 wt.% Ni, respectively, show the best strength values after 200 hours of stabilization at 250°C. This observation can be ascribed to the mutual existence of Al-Cu-Ni and Al_3Ni phases in all Ni-containing alloys M2S, M4S, and M5S. In particular, alloy M4S show the best resistance to softening and highest strength values after stabilization of the T6-treated alloy for 200 hours, owing likely to the uniformly distributed eutectic Al-

Al_3Ni structure shown in Figure 4.7 in Chapter 4, which is a stable structure and therefore advantageous to the mechanical properties.

Cáceres quality charts for the stabilized T5- and T6-treated conditions of the alloys studied are respectively shown in Figure 6.16 and Figure 6.17. These charts show variations in the quality of the alloys studied based on the tensile test data obtained in the stabilized T5- and T6-treated conditions at ambient temperature. The two figures reveal that the quality values of the alloys studied improve remarkably after the prolonged elevated-temperature exposure at 250°C owing to the highly improved plastic deformation values, despite the reduced strength values.

Regardless the differences in quality values of the alloys M1S through M3S, it is obvious that these three alloys display the best quality values rather than alloys M4S and M5S. For the base alloy M1S, stabilization of the T6-treated condition at 250°C for 100 and 200 hours, as shown in Figure 6.17, produces the best quality index because of its significantly improved ductility. The quality indices of alloys M2S and M3S in the stabilized T6-treated conditions, i.e. 100 and 200 hours, exhibit more or less the same values. However, for the stabilized T5-treated conditions of alloys M1S through M3S, the quality indices obtained for these conditions do not vary considerably except for the 200 hours stabilized T5-treated condition of the 0.75%Mn-containing M3S alloy.

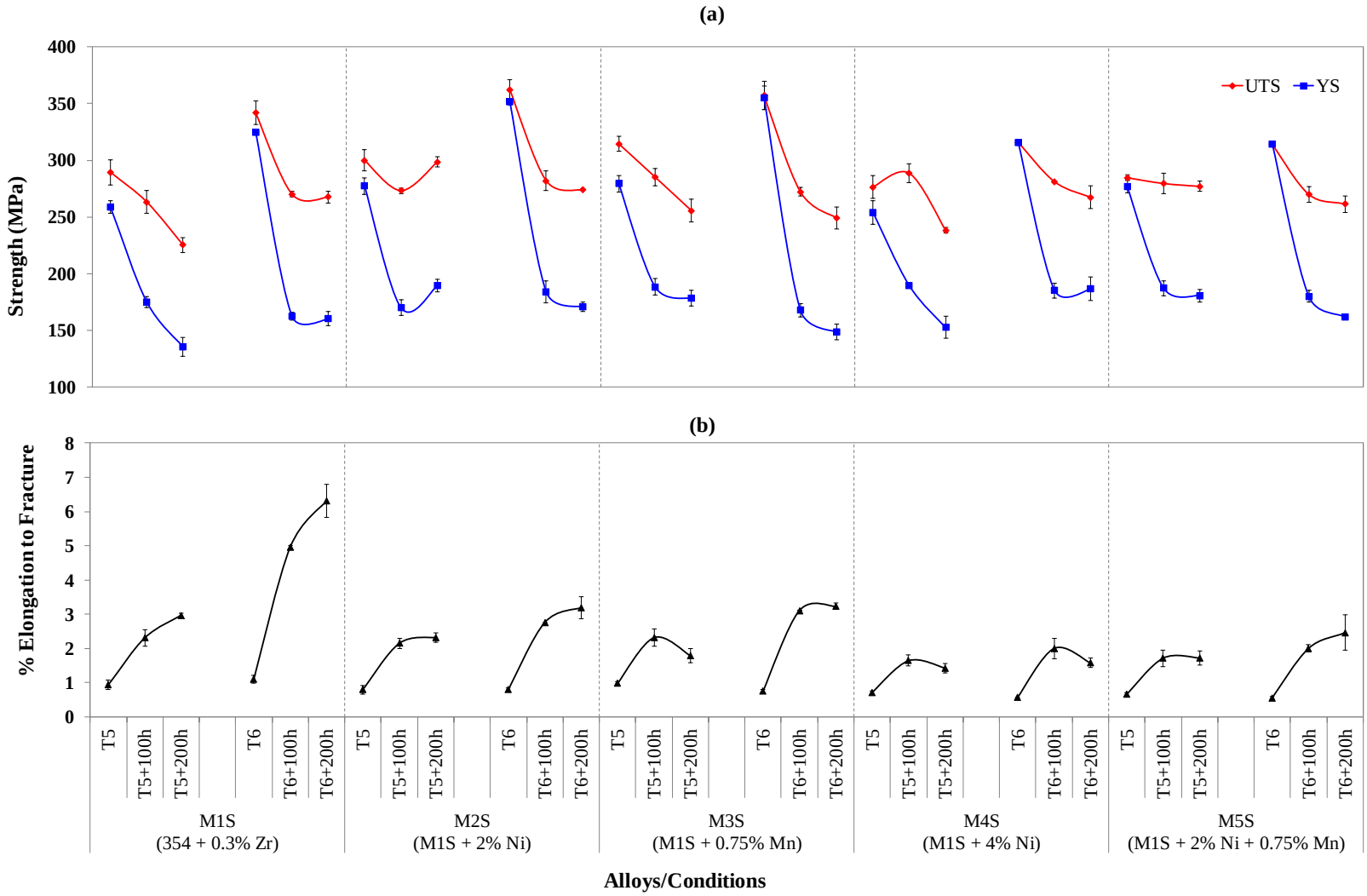

Figure 6.15 Variation in average UTS, YS, and %El values for alloys M1S through M5S in the T5, T6, and after static stabilization at 250°C for 100h, and 200h (testing at ambient temperature).

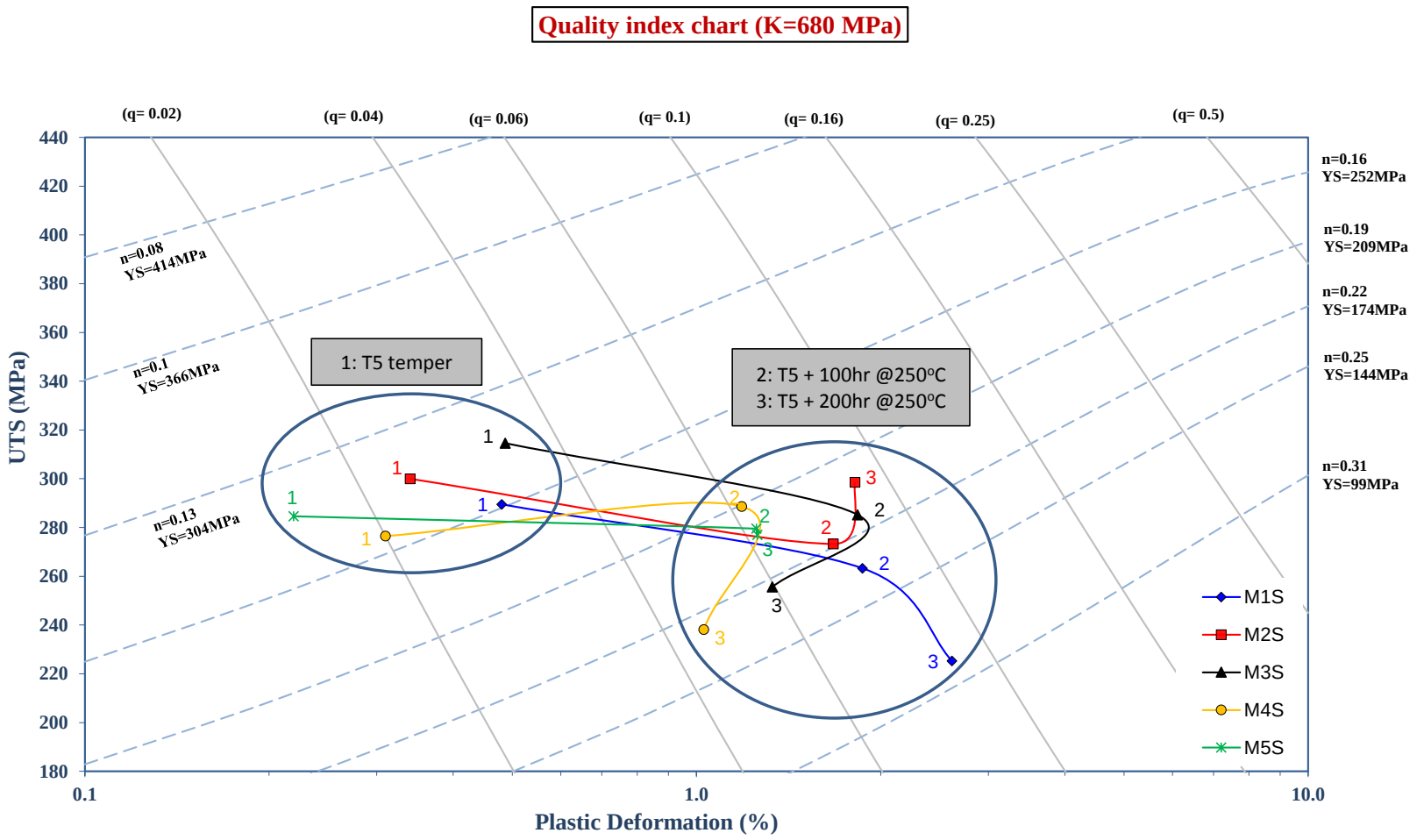

Figure 6.16 Cáceres quality chart representing the relation between UTS and percent plastic deformation of alloys M1S through M5S in the T5 condition before and after stabilization at 250°C for 100, and 200 hours (testing at ambient temperature).

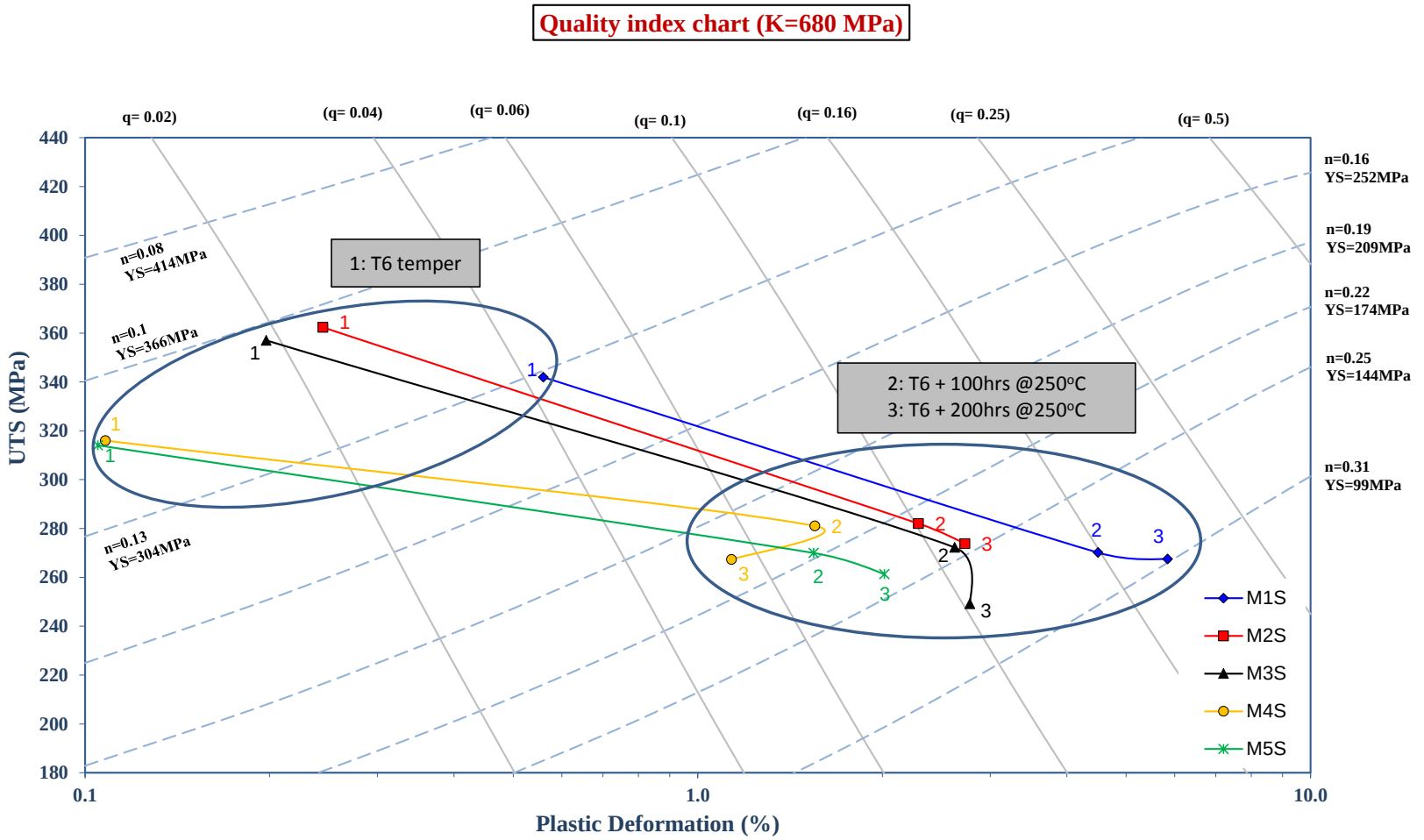

Figure 6.17 Cáceres quality chart representing the relation between UTS and percent plastic deformation of alloys M1S through M5S in the T6 condition before and after stabilization at 250°C for 100, and 200 hours (testing at ambient temperature).

Figure 6.18 compares the experimental values of the strengthening contribution of precipitates to the overall yield strength of alloys M4S and M5S with the calculated values obtained using the fitting equation developed in section 6.2.1.1. The calculated values show acceptable agreement with the experimental data for the stabilized conditions and hence this fitting equation can be used to predict the reduction in the strengthening contribution of the fine precipitates to the overall yield strength of the alloys when stabilized at 250°C for times of up to 200 hours. Nevertheless, there is a noticeable deviation between the calculated and experimental values obtained for the peak-aged condition (at stabilization time zero). This deviation is not crucial, however, because (a) it is more important to be able to predict strengthening contribution values after stabilization in order to avoid time-consuming treatments, and (b) because it is more reasonable to examine the properties in the peak-aged conditions experimentally.

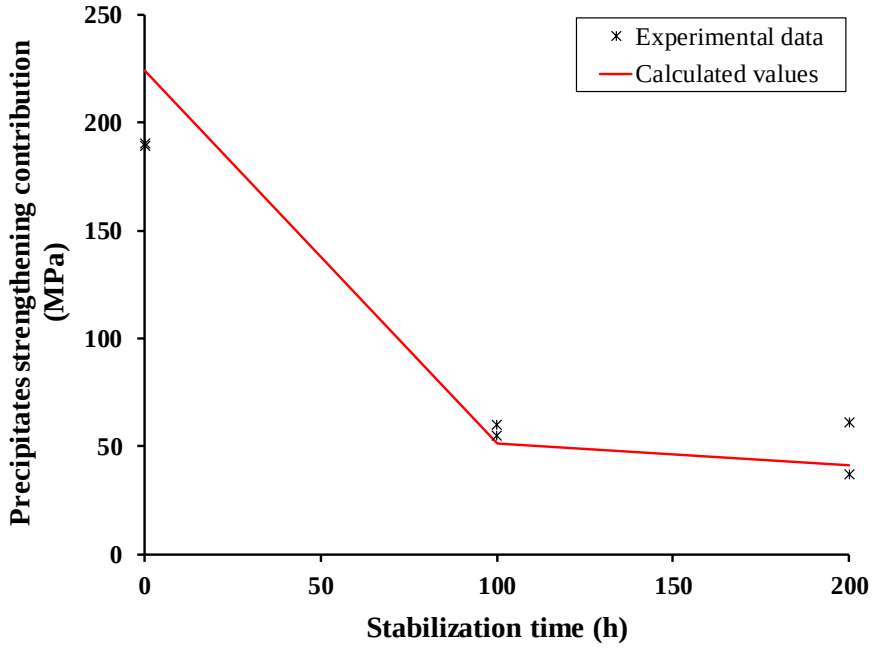

Figure 6.18 Experimental and calculated data for the precipitate contribution to the overall yield strength of alloys M4S and M5S as a function of the stabilization time.

6.3.2 HARDNESS VALUES

This subsection explores the effect of prolonged exposure at 250°C on the Rockwell hardness values of the alloys studied in the T5- and T6-treated conditions. Figure 6.19 displays the variations in hardness values with respect to alloy composition, applied heat treatment, and stabilization time. There is a serious drop in the hardness values following stabilization at 250°C for 100 hours of the T5- and T6-treated alloys. For example, for the T5-treated base alloy, the hardness drops from 88 HRF to 63.5 HRF and from 93.5 HRF to 61.7 HRF for the T6-treated alloy. However, further stabilization at 250°C reduces the hardness values at a much slower rate.

From Figure 6.19, it is obvious that the hardness values, before and after the stabilization treatment, are dependent on the volume fraction of intermetallic compounds present in the alloy. The base alloy M1S, with the lowest volume fraction of intermetallic phases, exhibits the lowest hardness values in all the conditions studied. Alloy M4S which contains 4 wt.% Ni and has the highest volume fraction of intermetallic compounds shows the highest hardness values for almost all of the conditions studied (cf. 93.5 with 99.5 HRF and 55.9 with 69.8 HRF for the two alloys in the T6 and T6+200h/250°C conditions, respectively).

Hardness values of T6-treated alloys are noticeably higher than those of T5-treated alloys before the stabilization treatment. In contrast, the stabilized T5-treated conditions of 100 and 200 hours at 250°C show improved hardness values compared to those obtained with stabilized T6-treated conditions per alloy. Similar observations regarding the enhanced tensile properties of stabilized T5-treated conditions over those of stabilized T6-treated

conditions were reported in the preceding subsection. This behavior can be ascribed to the fact that after stabilization, the T6-treated alloys will contain a considerable amount of coarsened precipitates, which will obviously deteriorate the hardness and strength values. Microstructures of alloys in the T6-treated (peak-aged) condition already comprise a high amount of fine precipitates following solutionizing, quenching, and artificial ageing treatments. Thus, further exposure to elevated temperatures will lead to the coarsening of these fine precipitates, and hence lower their numbers and reduce their strengthening effect. Microstructures of alloys in the T5-treated condition, on the other hand, contain lower fractions of the fine precipitates, because of the artificial aging of the as-cast microstructure, without solution treatment and quenching. This is because the precipitation process in the T5-temper depends on the already dissolved Cu and/or Mg in the α-Al matrix during solidification of the cast material at a high cooling rate. Accordingly, stabilization of T5-treated microstructures will not result in a rapid coarsening of the fine precipitates due to the fewer numbers of precipitates and hence the relatively large distances between these particles. In more detail, coarsening (Ostwald ripening) of the strengthening precipitates is mainly favoured at elevated temperatures, i.e. during the stabilization process, where the larger particles may grow further at the expense of smaller precipitate particles. This process occurs by the diffusion of atoms from the smaller particles towards the larger precipitate particles since the latter are preferred from the energy point of view. Consequently, coarsening is accompanied by a reduction in the total number of precipitates. As the coarsening phenomenon is a dissolution- and diffusion-controlled process, thus, if the particles are separated, due to their fewer numbers, by long distances as in the case of T5-treated alloys, the coarsening rate will be slower and hence the deterioration rate in hardness and strength values will be lower compared to that in the T6-treated alloys.

The same understanding can be applied to explain the low hardness values of alloys M1S and M3S, which contain higher fractions of the equilibrium θ-Al_2Cu precipitates, as previously discussed in Chapter 4, section 4.3. Consequently, the coarsening rates in alloys M1S and M3S are expected to be higher than in the Ni-containing M2S, M4S and M5S alloys, so that these two alloys will exhibit reduced hardness values in the stabilized T6-treated conditions. Moreover, low volume fractions of intermetallic compounds in the base alloy M1S and the Mn-containing alloy M3S would be another factor contributing to their low hardness values.

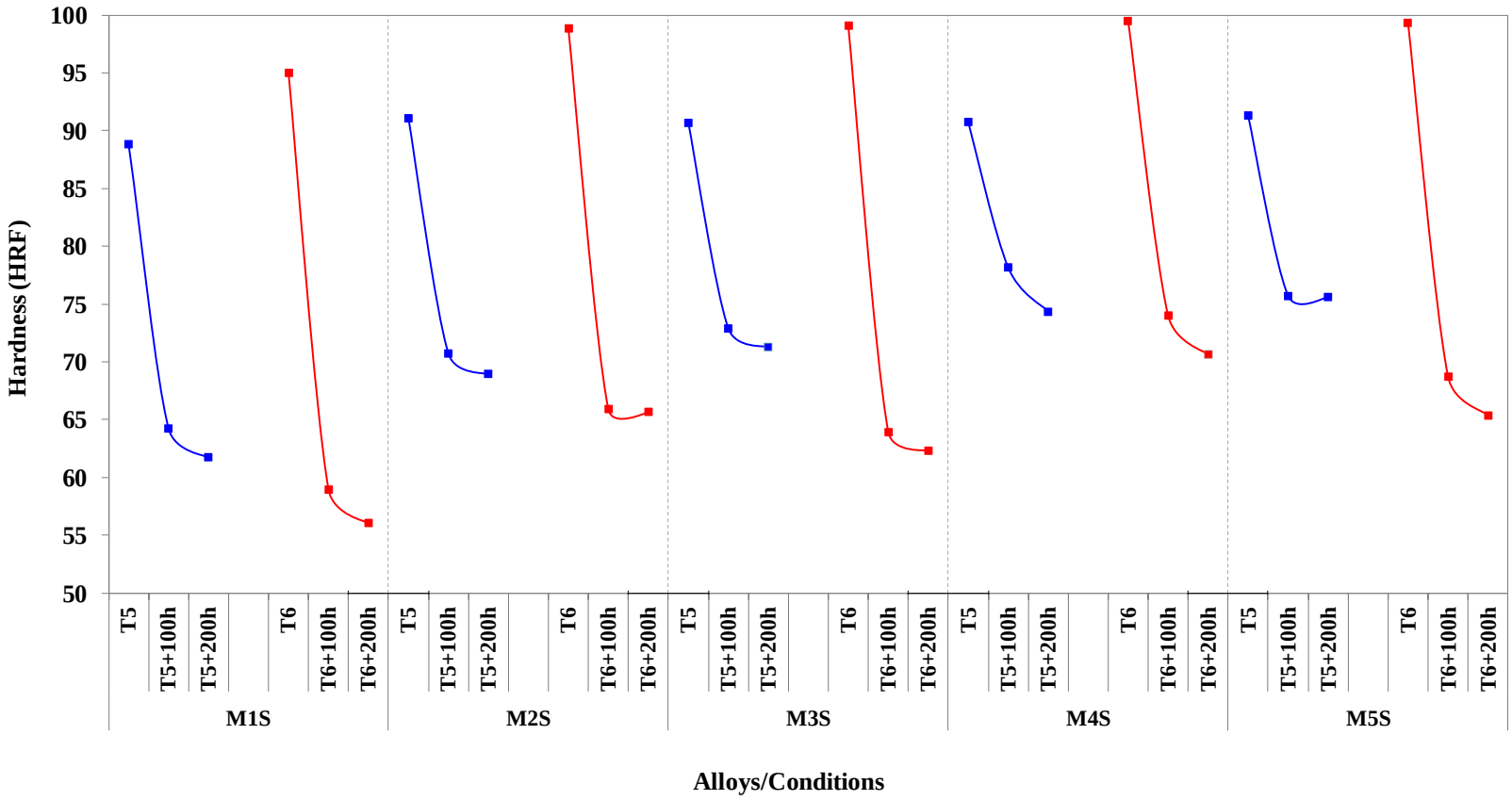

Figure 6.19 Variation in average Rockwell hardness values for alloys M1S through M5S in the T5 and T6 conditions, and after static stabilization at 250°C for 100h, and 200h (testing at ambient temperature).

6.4 INFLUENCE OF THERMAL EXPOSURE ON ELEVATED-TEMPERATURE TENSILE PROPERTIES

It is of importance to investigate the tensile behavior of the alloys studied after exposure to severe conditions, in particular, elevated temperatures. Accordingly, this section will address the effect of prolonged exposure at 250°C on the elevated-temperature tensile properties of the alloys studied. The thermal exposure and elevated-temperature tensile testing conditions used match the real service conditions of alloys employed in engine components. Thus, the results presented in this section are essential in properly defining the effect of transition element additions in retaining the mechanical properties of alloys employed in high-temperature applications. A study of the fracture surfaces of tensile bars tested at 250°C using T6-treated alloys M1S, M2S, and M3S after stabilization for one, and 200 hours at 250°C is also presented.

6.4.1 ELEVATED-TEMPERATURE TENSILE PROPERTIES

Figure 6.20 presents the tensile properties of the investigated alloys obtained at 250°C for the stabilized T5- and T6-treated conditions. An immediately noticeable observation in Figure 6.20 is that the stabilized T5-treated conditions exhibit better strength values (UTS and YS) than those obtained with stabilized T6-treated conditions for each alloy except for the 4 wt.% Ni-containing M4S alloy. In this alloy, the strength values remain more or less unchanged for the stabilized T5- and T6-treated conditions. The ductility values obtained after stabilization of T5-treated conditions are dramatically lower than those obtained after stabilization of T6-treated conditions (cf. 2.26% and 4.57%); without stabilization treatment, the ductility values in the two cases differ by about 0.3% in favor of the T6-treated condition. It is also seen that alloys M4S and M5S are the least

ductile alloys, when tested at 250°C after being exposed to 250°C for 100 and 200 hours. This behavior highlights the effective resistance to softening of these alloys, following the addition of 4 wt.% Ni in alloy M4S and the combined addition of 2 wt.% Ni and 0.75 wt.% Mn in alloy M5S. Moreover, these two alloys exhibit the highest ultimate tensile and yield strengths among the alloys studied in case of T6-treated conditions after the stabilization treatment at 250°C for 200 hours, as can be inferred from Figure 6.20(a), which emphasizes again the effective role of the additions to these alloys in resisting softening when exposed to elevated temperatures.

According to investigations by Rana *et al.*[281] and Hanafee,[282] the highest benefits from nickel addition are attained when the microstructure comprises a large volume fraction with an advantageous distribution of the Al_3Ni phase. This observation was noted for the microstructure of alloy M4S, as previously shown in Figure 4.7 in Chapter 4. Consequently, the addition of 4 wt.% Ni to the base alloy to form alloy M4S gives the best strength values at 250°C after holding at the testing temperature, i.e. stabilization, for 200 hours.

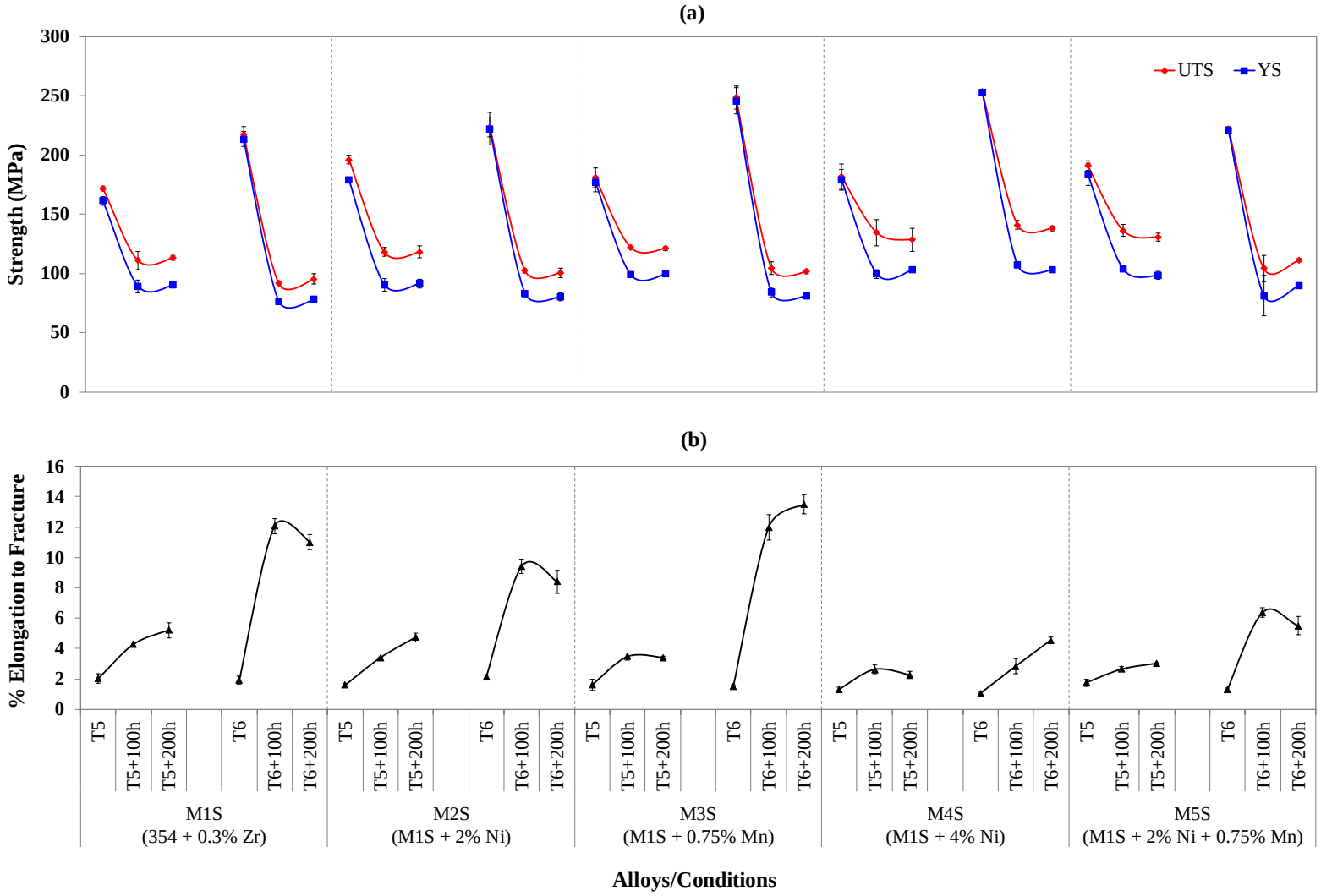

Figure 6.20 Variation in average UTS, YS, and %El values for alloys M1S through M5S in the T5 and T6, and after static stabilization at 250°C for 100h, and 200h (testing at 250°C).

In practice, the addition of Ni to Al-alloys is kept to a minimum because of its high price and its negative effect on ductility. While the author of this study is aware of the fact that the addition of 4 wt% Ni to cast Al-alloys is neither practical nor industrially feasible, however, the 4 wt.% Ni-containing alloy was considered in these investigations, for the sake of comparison with the other additions, i.e., 2 wt.% Ni, 0.75 wt.% Mn, and 2 wt.% Ni + 0.75 wt.% Mn. In terms of elevated-temperature tensile properties before and after the stabilization treatment, it was surprisingly found that the addition of 0.75 wt.% Mn in alloy M3S is competitive with the addition of 2 wt.% Ni in alloys M2S and M5S with respect to the strength values, and better, with respect to ductility values, as depicted in Figure 6.20. This observation has valuable benefits to industry due to its economic implications because the tonnage price of manganese is about 2000 USD in comparison to ~13000 USD for nickel.[283] Elaborating further, the similar effects of the two additions on the elevated-temperature strength is equivalent to reducing the cost of producing one tonne of the alloy of interest by ~245 USD since the 2 wt.% Ni addition costs ~260 USD compared to ~15 USD in case of 0.75 wt.% Mn addition instead.

The enhanced ductility values of alloy M3S can be attributed to the morphological transformation of the β-Al_5FeSi phase needles into the more compact, less detrimental α-$Al_{15}(Mn,Fe)_3Si_2$ phase owing to the addition of Mn.[241, 284, 285] Increasing the manganese content over 0.5 wt.%, which is the case in the present study, will not only transform the β-Al_5FeSi phase into α-$Al_{15}(Mn,Fe)_3Si_2$ phase, but may also produce fine dispersoids capable of enhancing the mechanical performance. These fine dispersoids, which appear in the form of Al_6Mn, are incoherent with the α-Al matrix, and hence increase the strength by hindering dislocation glide through their pinning action on dislocations. Whereas, the enhanced

ductility arises from the change in the slip system to cross-slip due to the hindered dislocations; this cross-slip allows maintaining good ductility of the alloy together with the increased strength values.[77, 79] Based on this discussion, the observed improvement in strength values of alloy M3S without loss in ductility in the present study can be attributed to the formation of such non-shearable incoherent Al_6Mn fine particles.

Quality index charts according to the model developed by Drouzy *et al.*[60] are shown respectively in Figure 6.21, and Figure 6.22 for stabilized T5- and T6-treated conditions of the alloys studied. Generally, the quality index values of stabilized T6-treated conditions are higher than those of stabilized T5-treated conditions, and may be attributed to the improved ductility values in case of stabilized T6-treated conditions owing to the high proportion of coarsened strengthening precipitates, even though the UTS values are higher in the case of stabilized T5-treated conditions.

The prolonged thermal exposure produces balanced variations in the ultimate tensile strength and ductility values of the alloys studied, i.e. increased strength values concomitant to reduced ductility values, and vice versa. This balanced variation in UTS and ductility values results in slight discrepancies in the quality index values of the various conditions studied. Another observation from Figure 6.21 regarding the stabilized T5-treated conditions is that the quality indices are so close for all the investigated alloys after applying the stabilization treatment. In contrast, Figure 6.22 shows a clear sorting of the high quality index values of alloys M1S, M2S, and M3S and the reduced quality index values of alloys M4S, and M5S. This observation may be understood in terms of the reported low ductility values of alloys M4S and M5S in spite of their improved elevated-temperature ultimate strength obtained after the stabilization treatment.

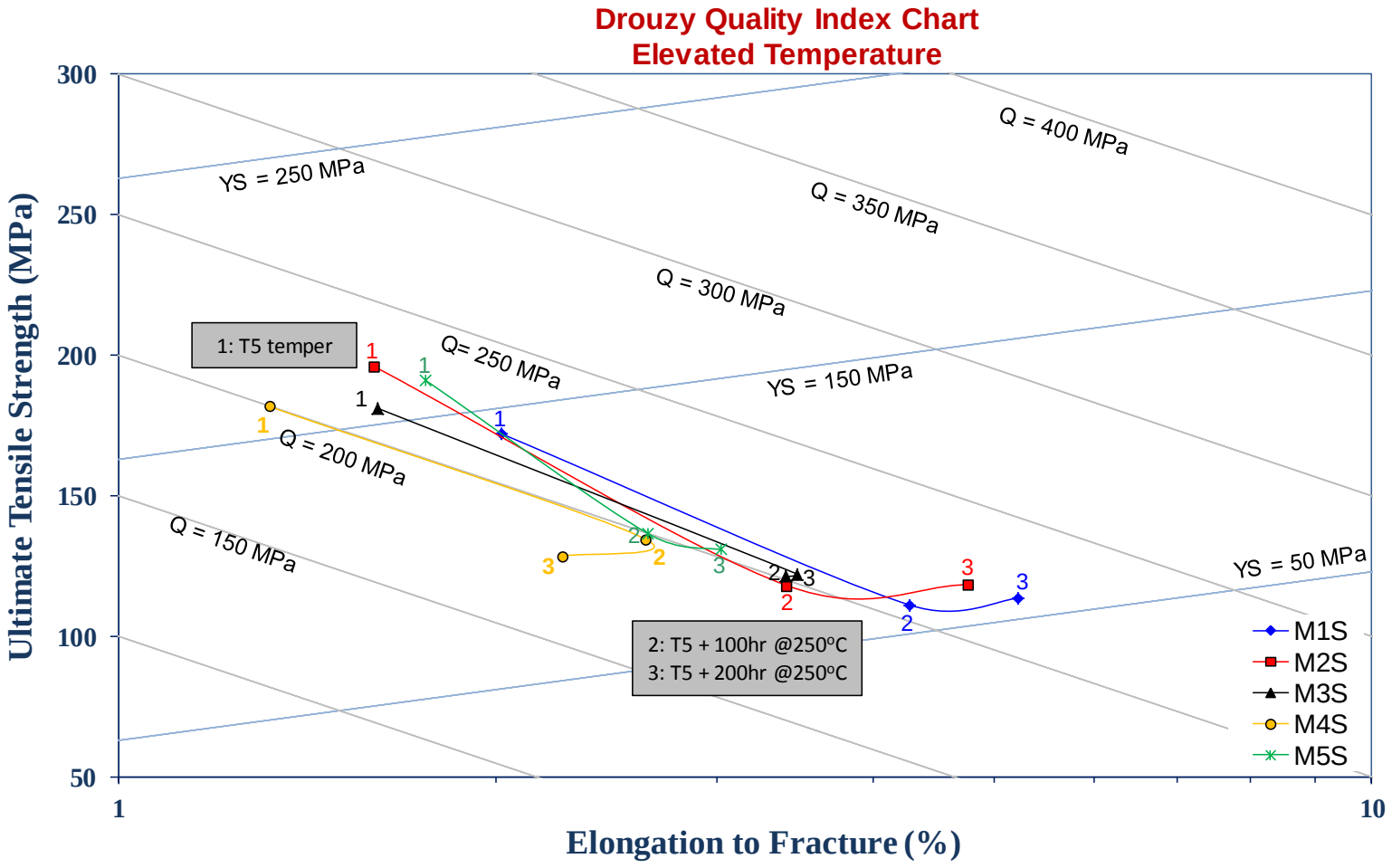

Figure 6.21 Drouzy quality chart representing the relation between the UTS and the percent elongation to fracture of alloys M1S through M5S in the T5-treated condition, before and after stabilization at 250°C for 100, and 200 hours (testing at 250°C).

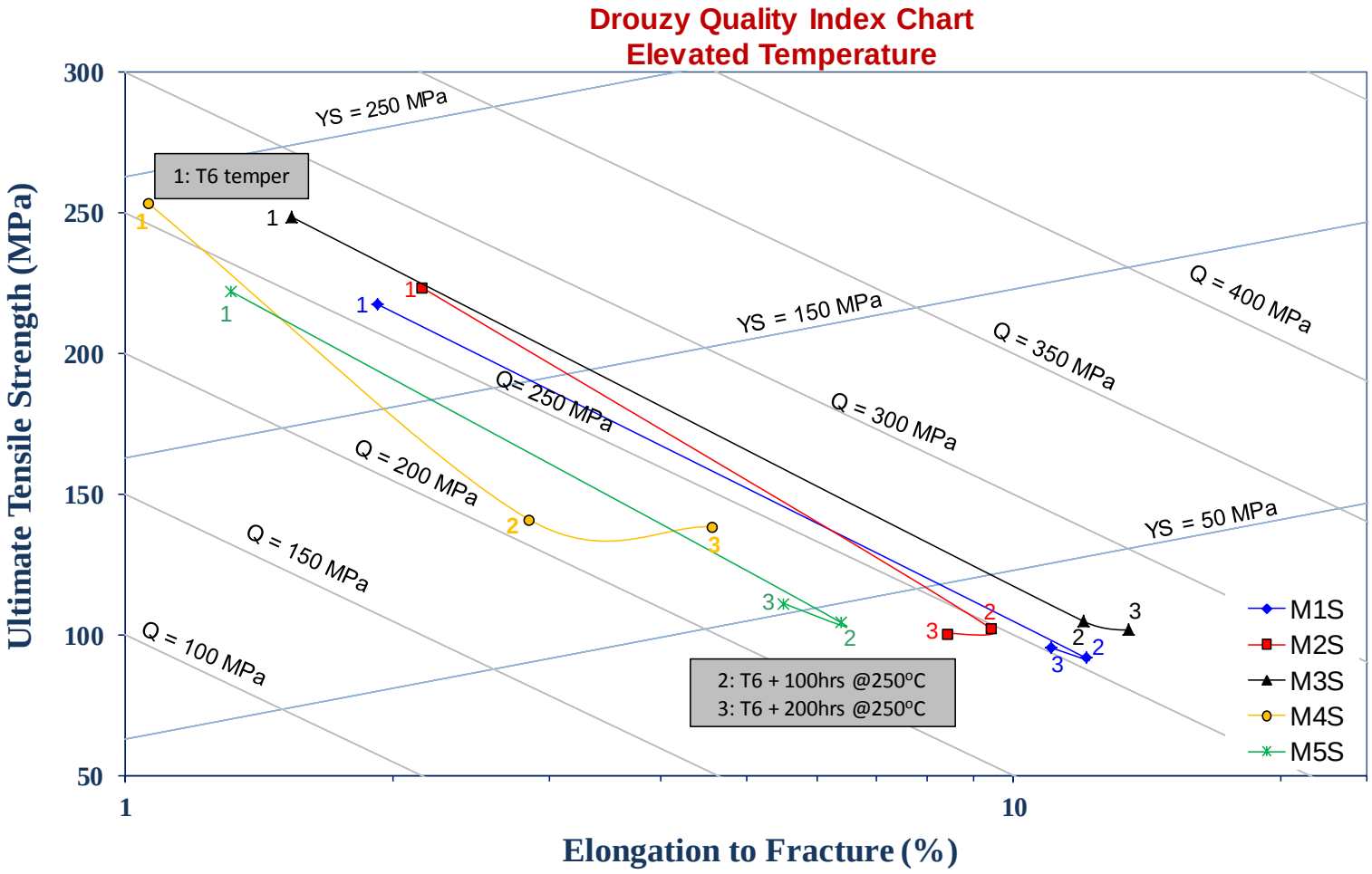

Figure 6.22 Drouzy quality chart representing the relation between the UTS and the percent elongation to fracture of alloys M1S through M5S in the T6-treated condition, before and after stabilization at 250°C for 100, and 200 hours (testing at 250°C).

The characteristics and distribution of the strengthening precipitates were examined for T6-treated alloys M1S, M2S, and M3S, stabilized at 250°C for 1 and 200 hours before testing at 250°C. The data of alloys held at 250°C for one hour before testing are reported as the elevated-temperature tensile properties obtained at that temperature. Samples for metallographic examination were obtained from the tensile-tested bars, 10 mm below the fracture surface.

Low precipitation densities are observed in Figure 6.23 for the T6-treated M1S, M2S, and M3S alloys following one hour of stabilization at 250°C. This may be attributed to the insufficient coarsening kinetics of the precipitates during this period. Since the coarsening behavior comprises dissolution-controlled and diffusion-controlled processes, this short time of stabilization may result only in dissolving some precipitates without completing the diffusion process.

The microstructure of alloy M3S reveals a higher number of precipitates under the same treatment/stabilization conditions in comparison to the microstructure of alloys M1S and M2S, as seen in Figure 6.23. This increased density of precipitates in the M3S alloy supports the possibility of the formation of the fine Al_6Mn precipitates together with the principal strengthening precipitates θ-Al_2Cu and S-Al_2CuMg phases and their precursors.

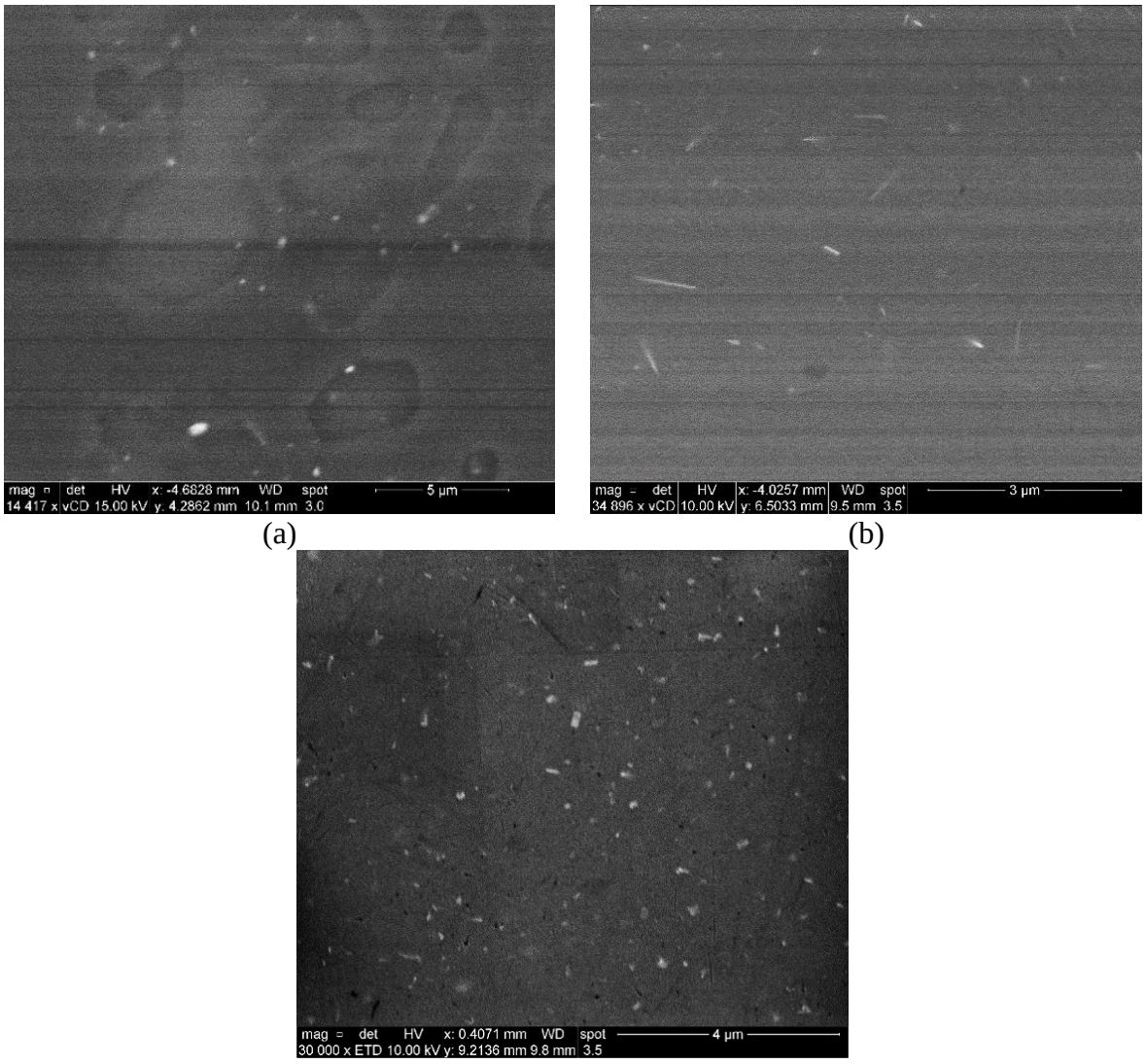

Figure 6.23 Backscattered electron images showing the size and distribution of precipitates in T6-treated alloys after stabilization at 250°C for 1 hour: (a) M1S, (b) M2S, (c) M3S alloys (testing at 250°C).

The BSE image of alloy M2S, shown in Figure 6.24(a), reveals the presence of a certain phase whose particles exhibit different morphologies and a wide range of sizes. The associated EDS spectrum of this phase, Figure 6.24(b), showed strong reflections of Al, Si, Zr, and Ti elements, indicating that the phase is possibly an $Al_x(Zr,Ti)Si$ compound. This complex compound exists in multiple morphologies including spherical particles, thin and thick elongated platelets, and irregular-shaped particles. The size of these particles varies

considerably, from large particles about 4 μm in length, to very fine particles in the nano-scale. Similar observations were previously reported by Garza-Elizondo[11] for 354-type Al-Si-Cu-Mg alloys with different percentages of Ni and Zr additions. The presence of these particles is considered to be very beneficial to the mechanical performance at elevated temperatures because they are known to be thermally stable particles which resist coarsening and hence maintain acceptable values of the mechanical properties at elevated temperatures.[17, 280]

The limited variation in the elevated-temperature strength values of the alloys before and after stabilization treatment, seen in Figure 6.20(a), can be understood in terms of some factors, including: the existence of the thermally stable Zr-containing dispersoids in the five alloys studied, as was previously confirmed in Chapter 4, owing to the same Zr content in all alloys, the similar casting procedures followed in producing all test bars, and the same parameters used in the applied heat treatments.

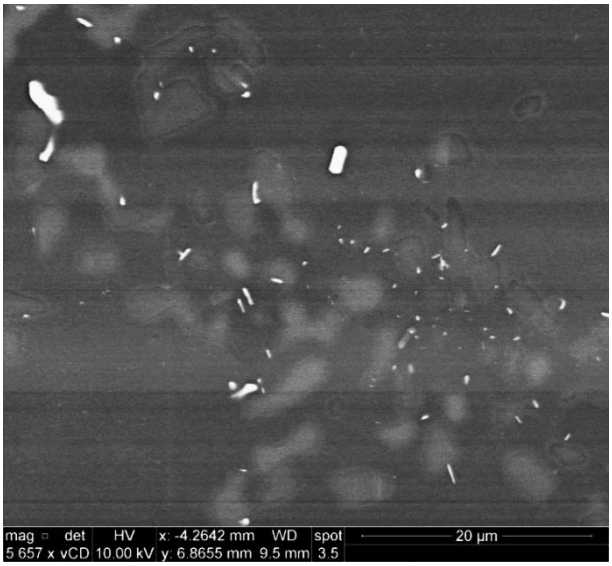

(a)

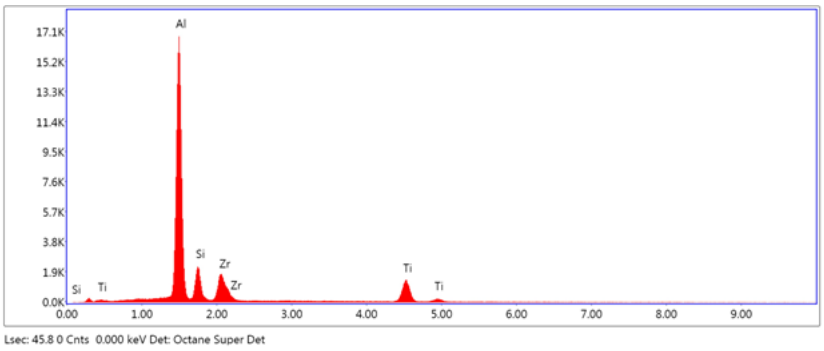

(b)

Figure 6.24 Backscattered electron images showing (a) shiny coarse and fine dispersoids in the T6-treated M2S alloy after stabilization at 250°C for 1 hour and testing at the same temperature, (b) EDS spectrum corresponding to the shiny particles in (a).

The backscattered electron (BSE) image shown in Figure 6.25(a) exhibits some interesting features obtained from the T6-treated M3S alloy after stabilization for one hour at 250°C. A high magnification image of the inset in (a) highlights the microstructural features observed more clearly in Figure 6.25(b). The elemental distribution maps corresponding to the different elements present are also shown in Figure 6.25. The point of interest in this figure is the distribution of Mn, Figure 6.25(g), which shows a faint reflection covering the whole field of the image. This indicates that Mn is distributed across the microstructure on a small scale that is possibly related to the formation of tiny Al_6Mn particles[77, 78] which are considered one of the main reasons for the improved mechanical performance of Mn-containing alloys.

Figure 6.26(a) is a BSE image showing a general view of the precipitates in the microstructure of the T6-treated base alloy M1S after stabilization for 200 hours at 250°C and testing at 250°C. Higher magnification BSE images for the same condition, shown in Figure 6.26(b) and Figure 6.26(c), reveal the distribution of the coarsened precipitates. The corresponding EDS spectrum, Figure 6.26(d), of these precipitates shows reflections of Al

and Cu, which is possibly due to the Al_2Cu phase. Generally, the orientation of the rod-like Al_2Cu particles is established to lie along the <110> family of directions.[235] Specifically for these coarsened particles of Al_2Cu in Figure 6.26, they appear to be originally oriented along two perpendicular directions; in these images, however, these particles are not showing a perfect perpendicularity, given that the samples examined were obtained from tensile-tested bars.

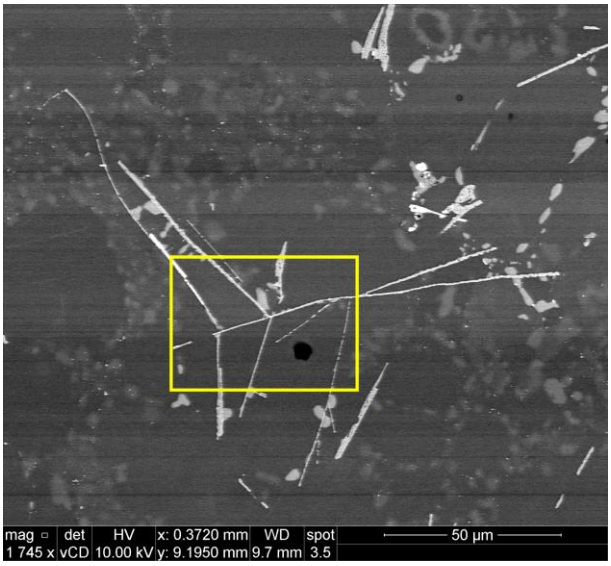

(a)

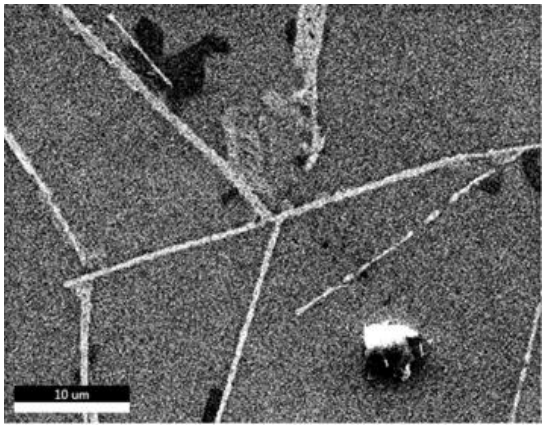

(b)

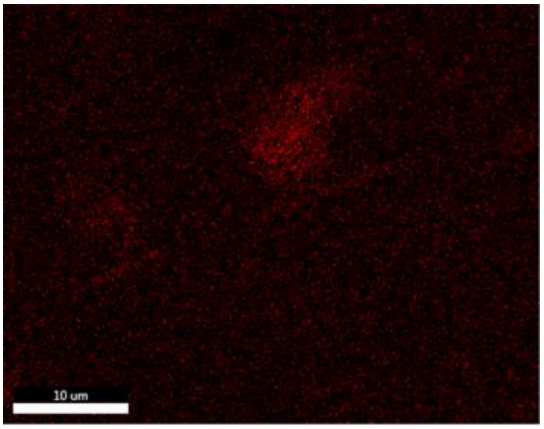

(c) Cu

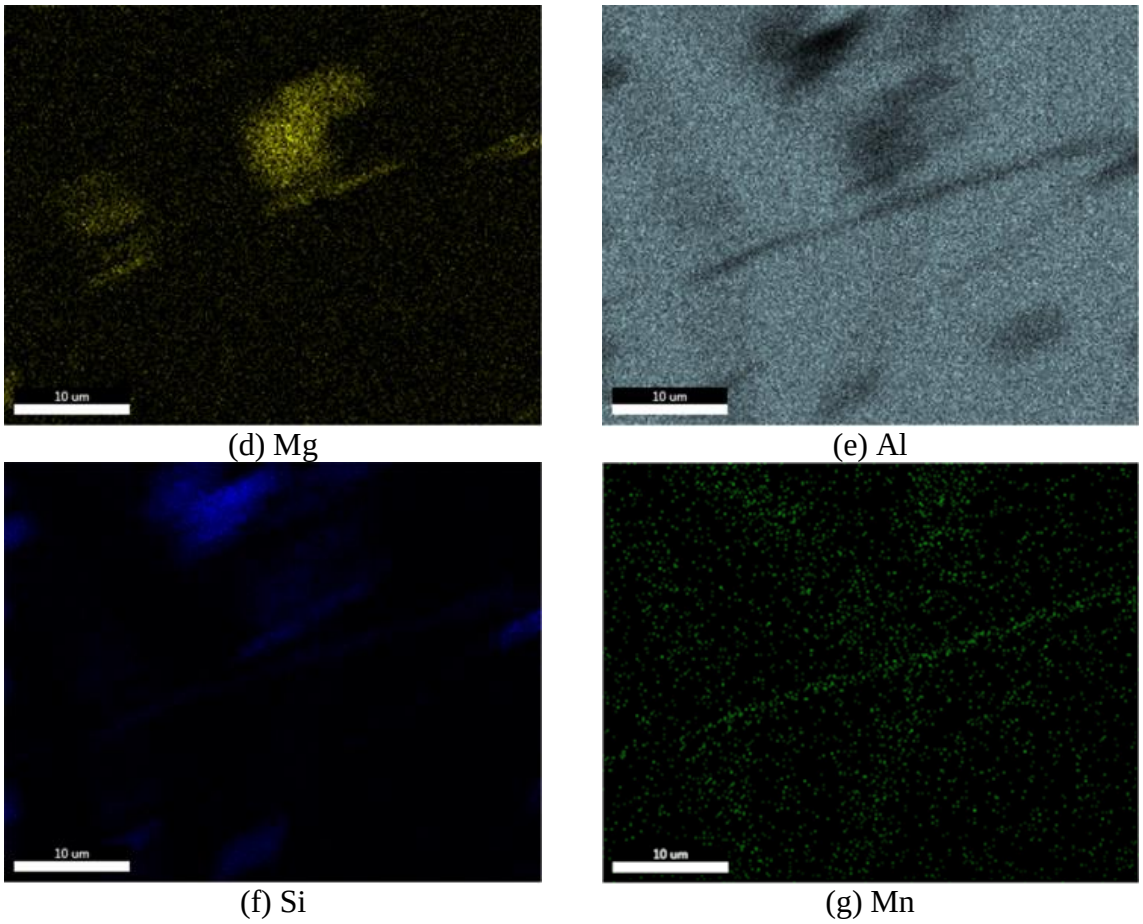

(d) Mg (e) Al

(f) Si (g) Mn

Figure 6.25 (a) Backscattered electron image of T6-treated M3S alloy after stabilization at 250°C for 1 hour, (b) higher magnification of the inset in (a), and (c) through (g) X-ray maps showing the distribution of elements in (b).

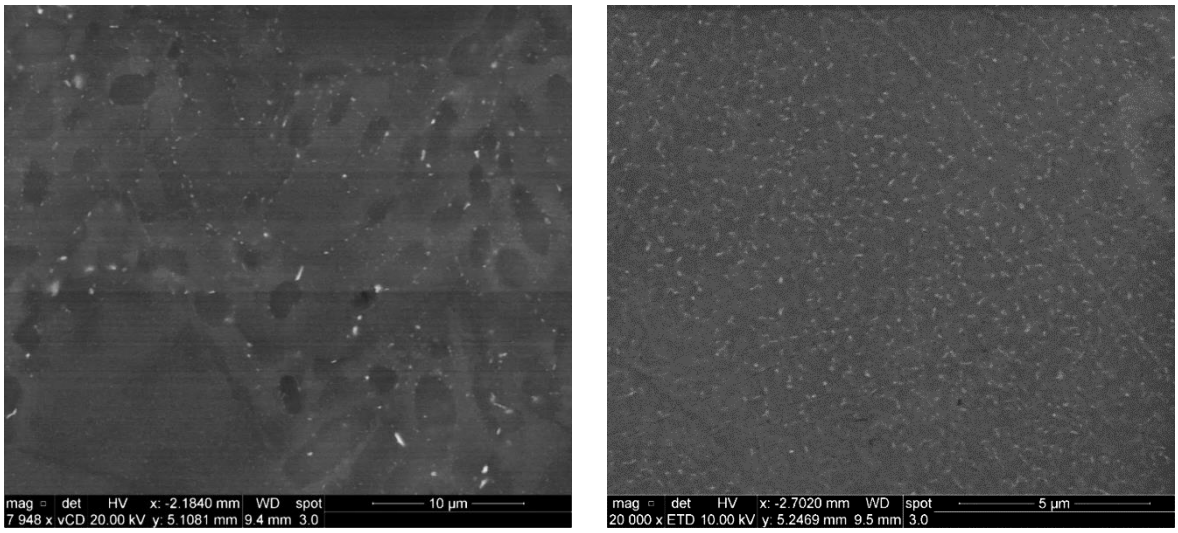

(a) (b)

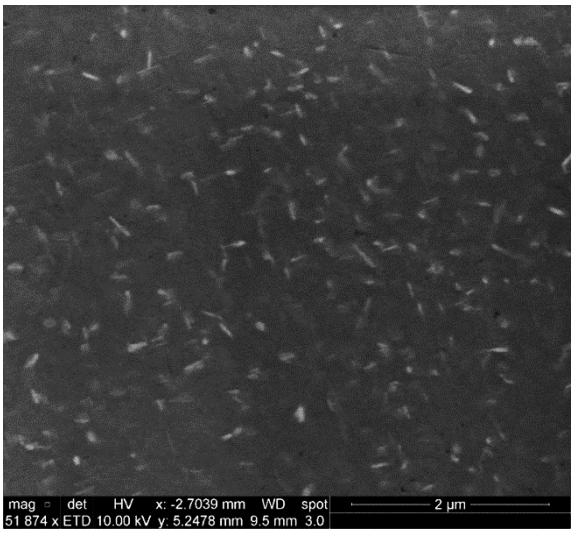

(c)

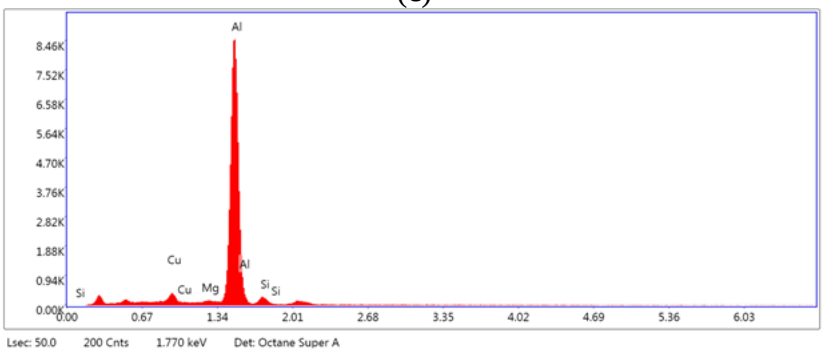

(d)

Figure 6.26 (a, b, and c) Backscattered electron images at different magnifications showing the size and distribution of precipitates in the T6-treated M1S alloy after stabilization at 250°C for 200 hours; (d) EDS spectrum corresponding to the rod-like particles in (c).

After the stabilization of T6-treated alloy M2S for 200 hours at 250°C, the microstructure still comprises a considerable amount of the very fine bright precipitates previously reported in section 6.2.1.1, as shown in Figure 6.27(a). The corresponding EDS spectrum in Figure 6.27(b) reveals that these tiny precipitates are most likely the coarsening-resistant Zr-containing compounds. By comparing the Zr-containing precipitates observed in Figure 6.8 after 1 hour of stabilization at 250°C to the particles shown in Figure 6.27(a), it can be easily observed that these dispersoids still exist, which

proves the thermal stability of such Zr-containing precipitates and hence their vital role in resisting alloy softening when employed in elevated-temperature applications.

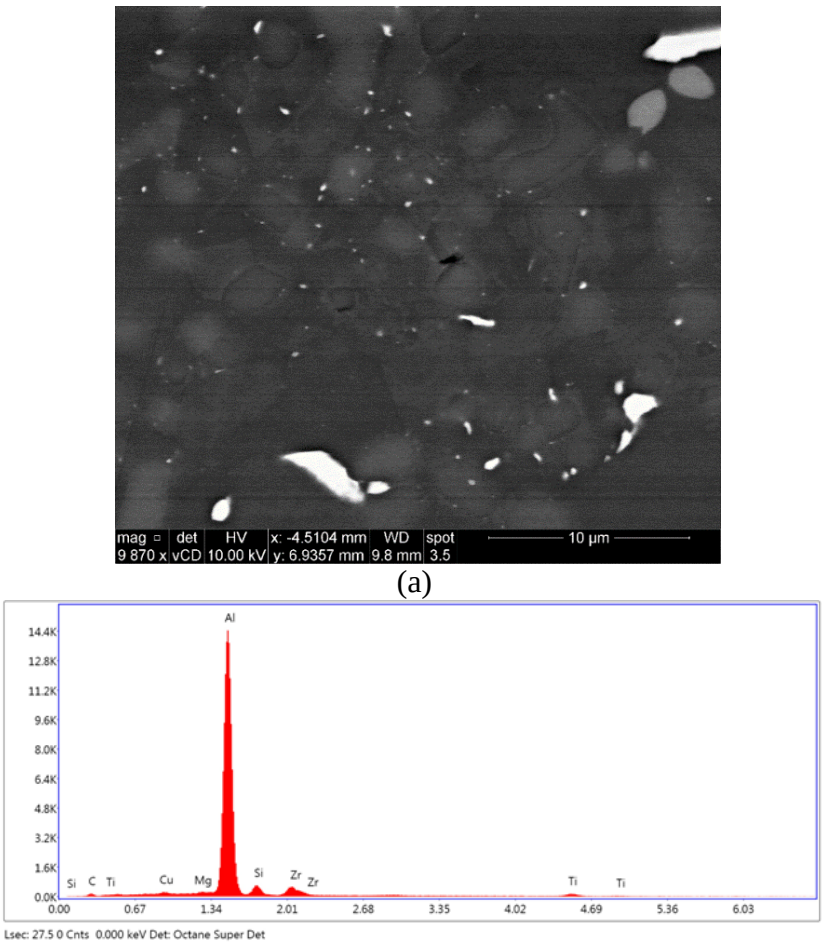

Figure 6.27 Backscattered electron image showing (a) shiny coarse and fine dispersoids in T6-treated M2S alloy after stabilization at 250°C for 200 hours and testing at the same temperature; (b) EDS spectrum of bright particles in (a).

The high magnification BSE image presented in Figure 6.28(a) shows the microstructure of the same T6-treated alloy M2S stabilized for 200 hours, highlighting the paucity of Al_2Cu precipitates, attributable to the consumption of the Cu available for strengthening in forming other phases such as Al-Cu-Ni. On the other hand, the BSE image shown in Figure 6.28(b) demonstrates the fine distribution of the coarsened Al_2Cu

precipitates in the interdendritic region in the microstructure of T6-treated M3S alloy under the same stabilization conditions (200 hours at 250°C).

The BSE image of Figure 6.29 shows that the size of the precipitate free zones (PFZs) in the microstructure of the T6-treated M3S alloy after stabilization for 200 hours at 250°C is relatively small, taking into account the reduced number of precipitates. This is in keeping with the coarsening behavior, which increases the distances between neighbouring precipitates, and contributes positively to the mechanical performance of the M3S alloy, as depicted in Figure 6.20(a).

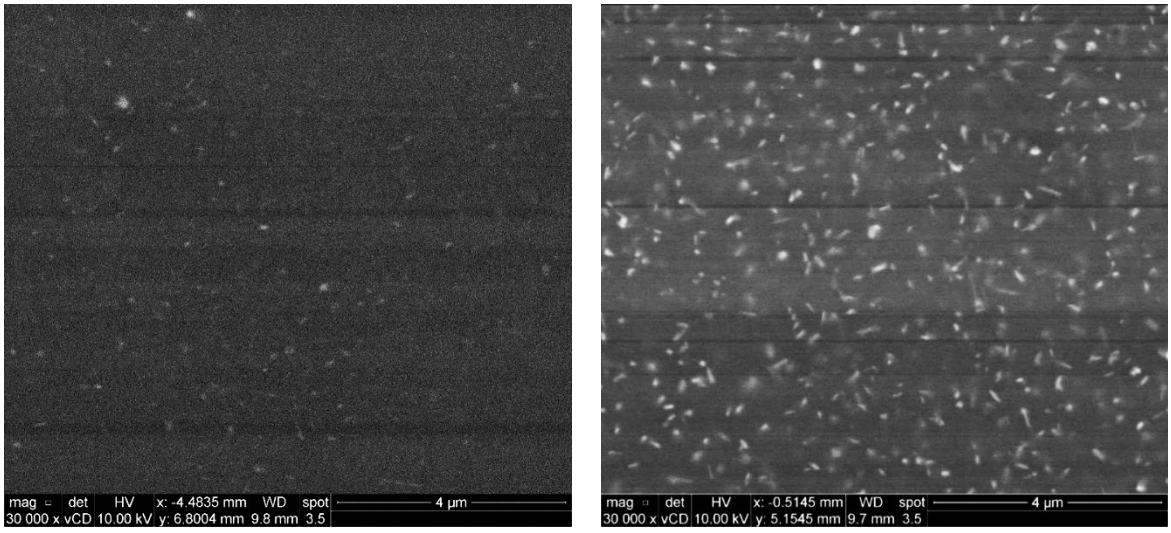

(a) (b)

Figure 6.28 Backscattered electron images showing the density and distribution of the strengthening precipitates in T6-treated alloys after stabilization at 250°C for 200 hours: (a) M2S, and (b) M3S alloy (tested at 250°C).

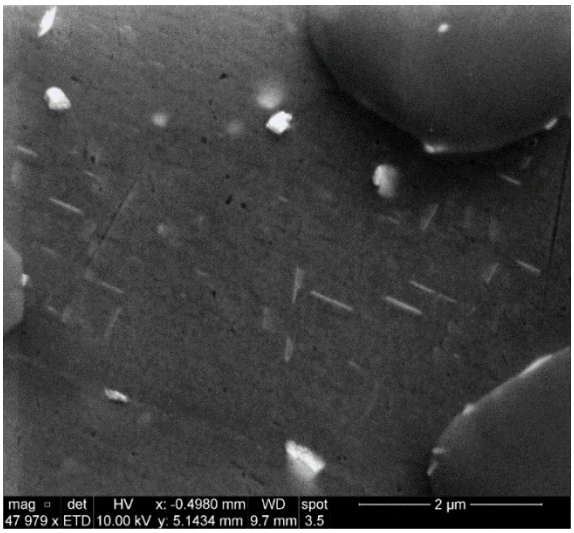

Figure 6.29 Backscattered electron images showing PFZs in T6-treated M2S alloy after stabilization at 250°C for 200 hours.

It is important to verify the formation of the fine Al_6Mn precipitates, since they were not detected during the course of this investigation, as a detailed TEM investigation was not in the scope of this study. The fine Al_6Mn precipitates are considered to be responsible for the increased strength and ductility values of the M3S alloy at room temperature and at 250°C, as well as before and after the stabilization treatment. Thus by investigating the distribution of elements in the microstructure of the stabilized T6-treated alloy M3S shown in Figure 6.30, the distribution of Mn noted in Figure 6.30(h) is promising in supporting the formation of these fine precipitates. Additionally, the distribution of Zr, shown in Figure 6.30(f) reveals that fine Zr-containing precipitates are likely to form as well; and hence improved mechanical performance at elevated temperatures is expected for alloy M3S.

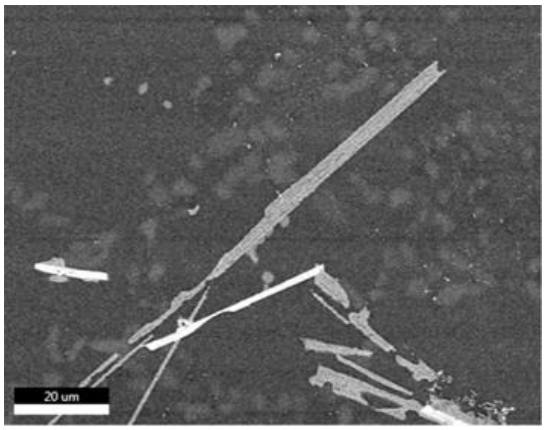

(a)

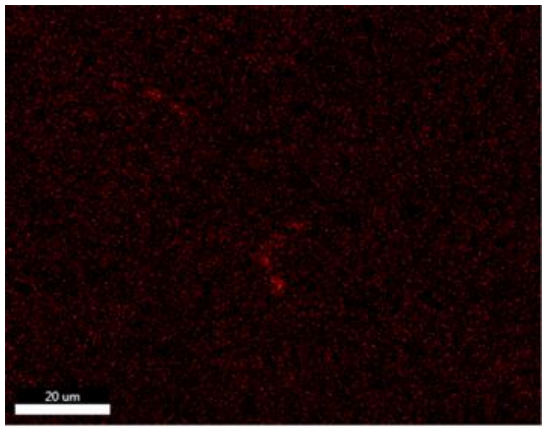

(b) Cu

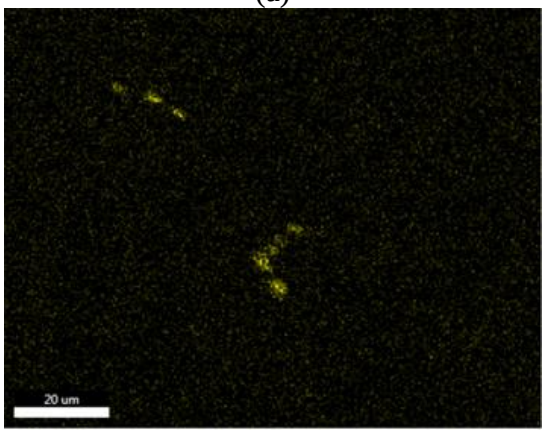

(c) Mg

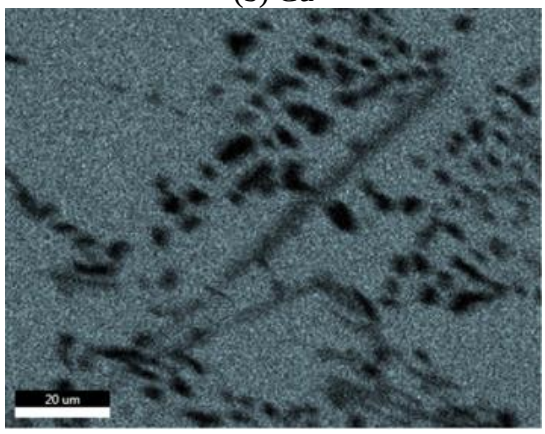

(d) Al

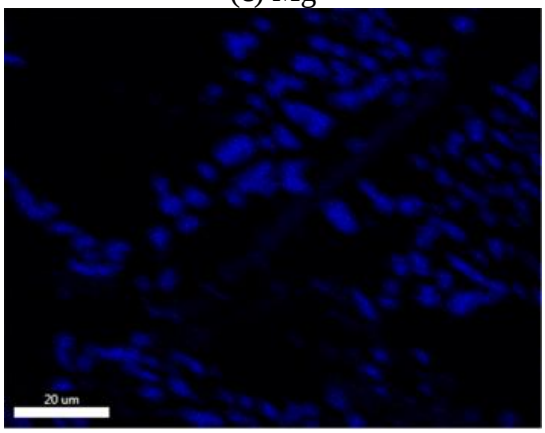

(e) Si

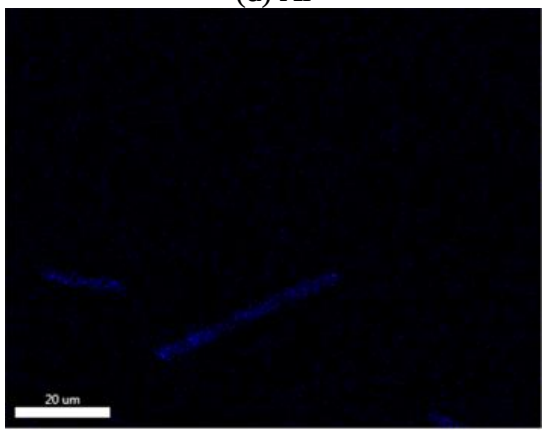

(f) Zr

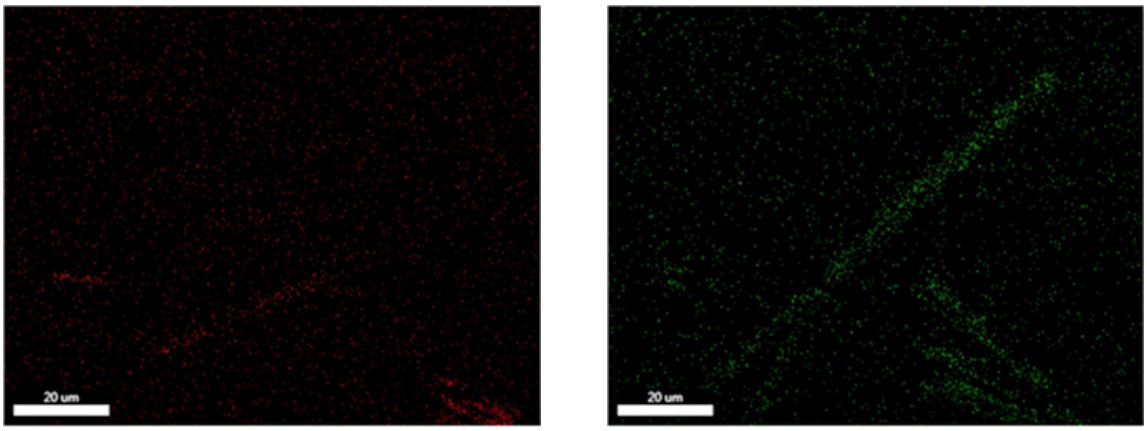

(g) Ti (h) Mn

Figure 6.30 (a) Backscattered electron image of T6-treated M3S alloy after stabilization at 250°C for 200 hours, and (c-h) corresponding X-ray maps showing distribution of elements in (a).

6.4.2 FRACTOGRAPHY

This section presents the results of a detailed investigation of the fracture surfaces of tensile bars of alloys M1S, M2S, and M3S tested at 250°C. For each alloy, the test bar samples were examined in the T6-treated conditions, following two stabilization treatment conditions, corresponding to (i) 1 hour at 250°C, and (ii) 200 hours at 250°C. It is important to recall that the T6-temper treatment comprises solution treatment at 495°C for 5 hours followed by quenching in warm water at 60°C, and then artificial aging at 180°C for 8 hours. The T6-temper treatment was focused upon, as it is widely used in industry and hence understanding the fracture behavior of the alloys in the T6-treated condition would be helpful from the point of view of potential applications. The fractographs depicted in this section are backscattered electron (BSE) images obtained using the JEOL JSM.6480LV scanning electron microscope (SEM), and are deemed suitable for identifying the microstructural features responsible for crack initiation employing the energy dispersive X-ray spectrometer (EDS) facilities accompanying the SEM.

The BSE image shown in Figure 6.31(a) reveals the fracture surface of the tensile-tested base alloy M1S in the T6-treated condition and after stabilization for one hour at 250°C. It is noticeable that the fracture surface has a dimpled-structure throughout, which indicates the ductile nature of the fracture mode. Additionally, the BSE image reveals the presence of $Al_x(Zr,Ti)Si$ complex compound, as was confirmed by the EDS spectrum in Figure 6.31(b), appearing in star-like and blocky morphologies; cracks can be spotted in various particles of this complex compound, as indicated by the arrows. The higher magnification BSE image shown in Figure 6.31(c) displays a cracked $Al_x(Zr,Ti)Si$ phase particle with a blocky morphology. This phase is considered to contribute mainly to the fracture behavior of this alloy by facilitating the crack initiation process.

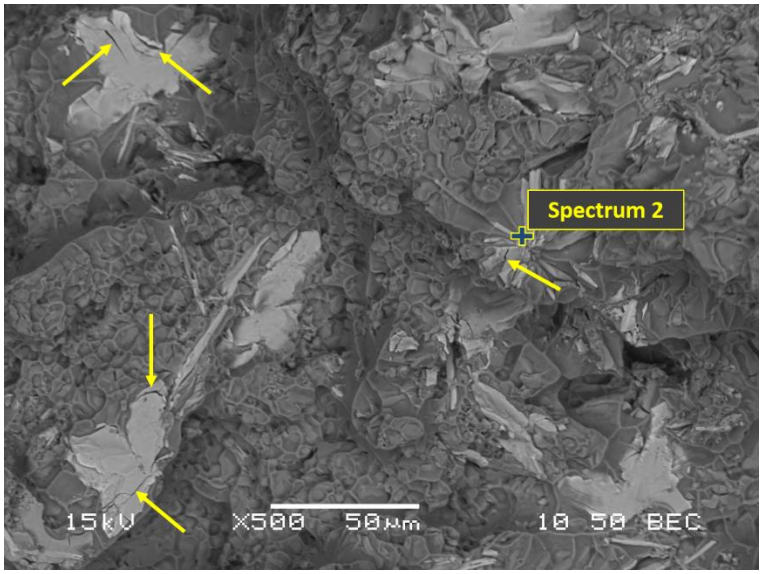

(a)

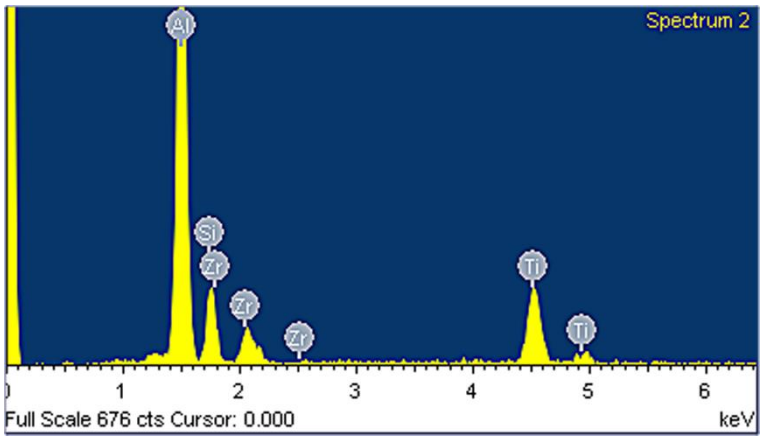

(b)

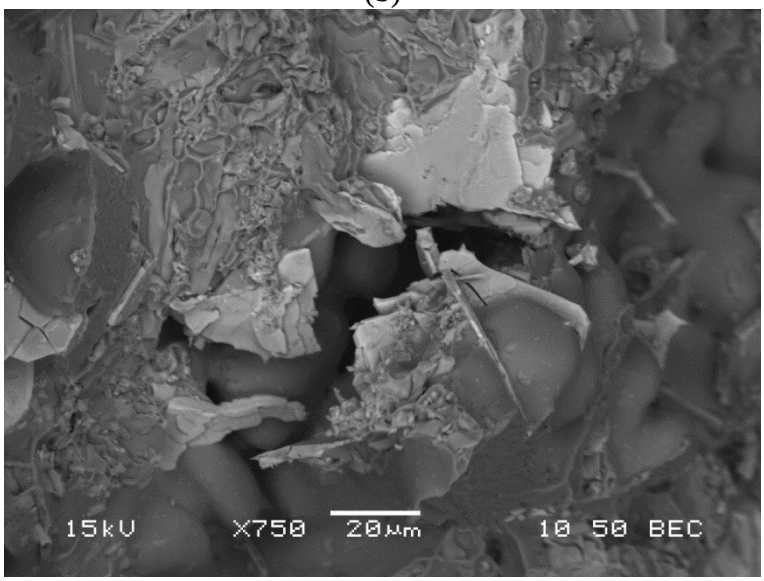

(c)

Figure 6.31 SEM images of T6-treated M1S alloy after stabilization at 250°C for 1 hour: (a) BSE image showing a uniform dimple structure and cracked particles (arrowed), (b) EDS spectrum corresponding to the point of interest in (a), and (c) high magnification BSE image shown a cracked Al-Si-Ti-Zr particle.

Additionally, Fe-bearing phases including the π-Al-Si-Mg-Fe and β-Al-Si-Fe phases were detected in the BSE image shown in Figure 6.32(a) and confirmed by the EDS spectra shown in Figure 6.32(b) and Figure 6.32(c), respectively. The arrows point to fine precipitates appearing near the observed intermetallic compounds and away from the dimpled regions on the fracture surface.

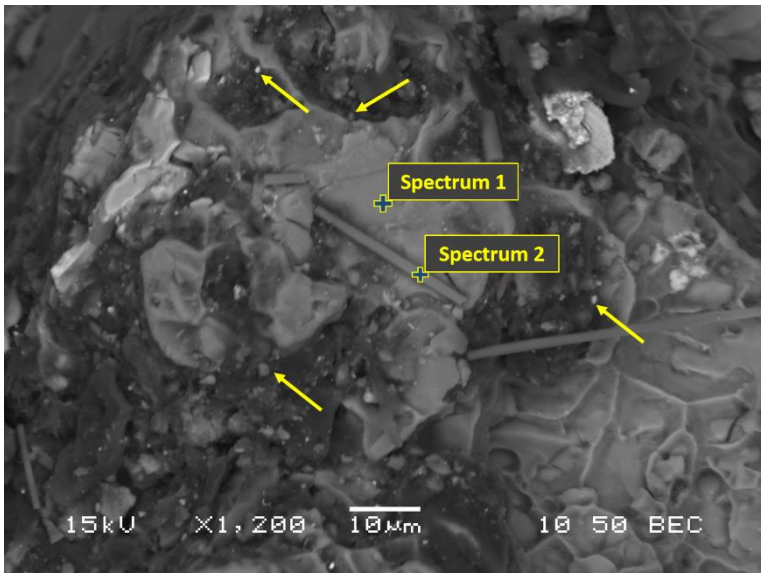

(a)

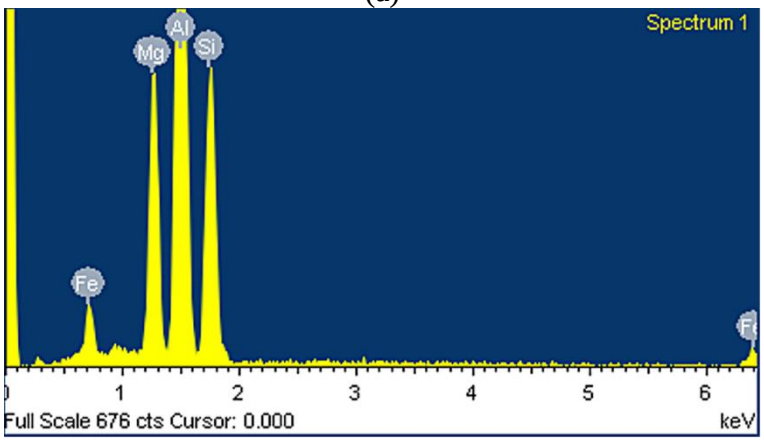

(b)

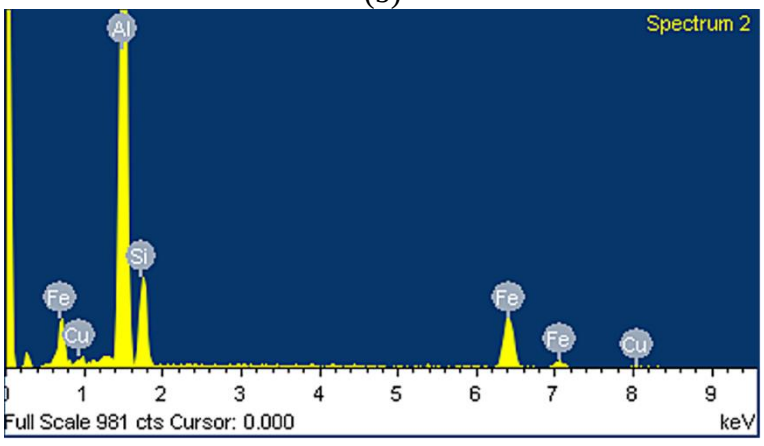

(c)

Figure 6.32 (a) BSE image of T6-treated M1S alloy after stabilization at 250°C for 1 hour showing Fe-bearing phases, and (b, c) EDS spectra corresponding to the points of interest in (a), confirming the presence of π-Al-Si-Mg-Fe, and β-Al-Si-Fe phases, respectively.

Figure 6.33(a) shows the fracture surface of the T6-treated base alloy M1S tested at 250°C after stabilization for 200 hours at the testing temperature. The dimples in this case are coarser compared to those observed after the one-hour stabilization at 250°C. This highlights the improved ductility of the alloy due to the softening behavior associated with the prolonged elevated-temperature exposure at 250°C. Coarsened precipitates appear in the interiors of the dimples, as indicated by the oval contours in Figure 6.33(a). The BSE image and the EDS spectrum shown in Figure 6.33(b) and Figure 6.33(c), respectively, confirm the presence of Alx(Zr,Ti)Si phase particles which possibly act as crack initiation sites.

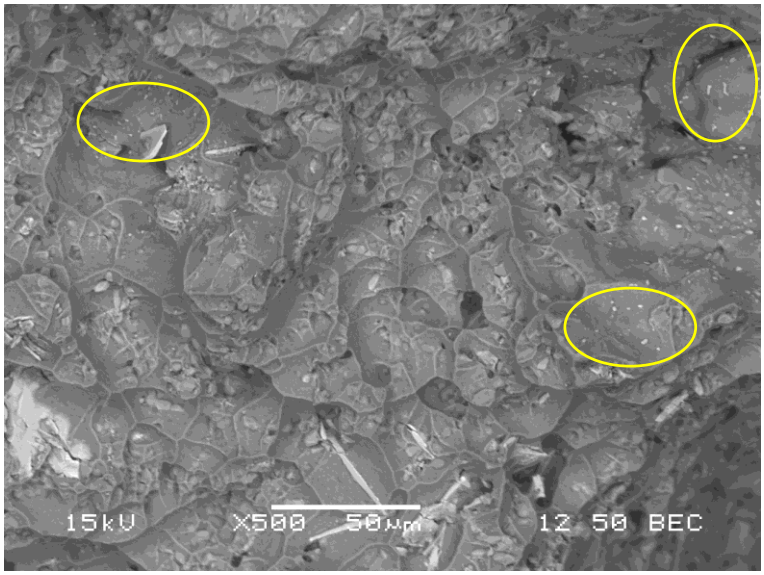

(a)

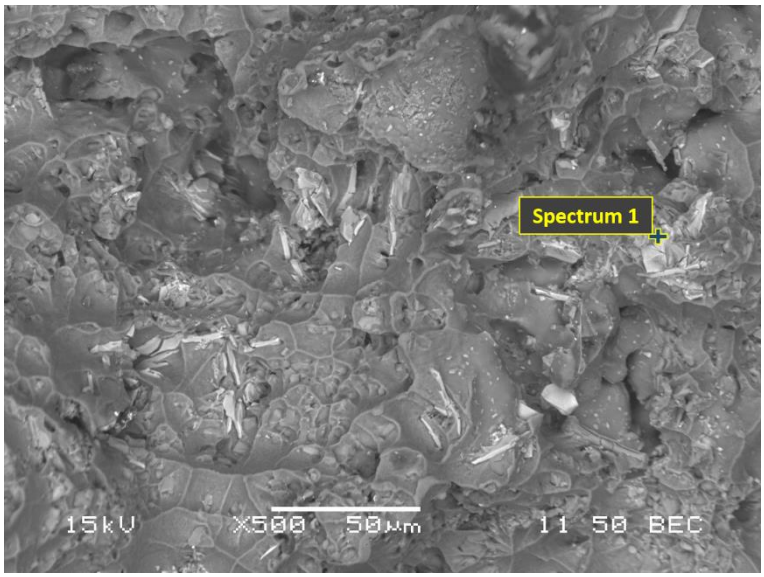

(b)

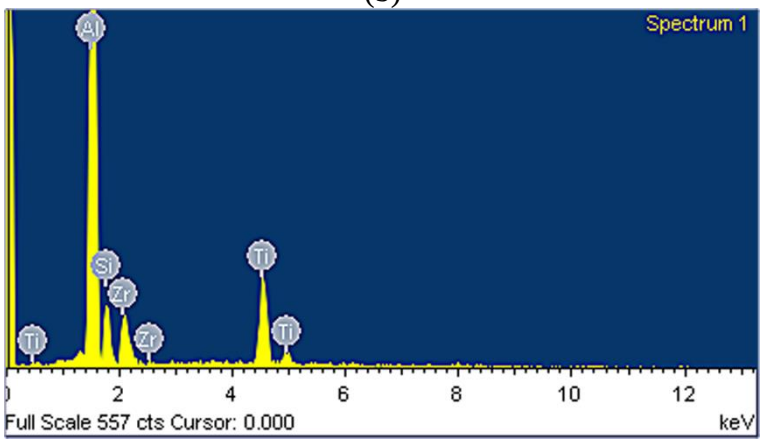

(c)

Figure 6.33 (a, b) BSE images of T6-treated M1S alloy after stabilization at 250°C for 200 hours showing a coarse dimpled structure, coarsened precipitates and $Al_x(Zr,Ti)Si$ particles involved in the crack initiation process, and (c) corresponding EDS spectrum of the phase of interest shown in (b).

The fracture surface of the T6-treated alloy M2S tested at 250°C after one hour of stabilization is shown in Figure 6.34(a). Micro-cracks can be observed associated with the Ni-rich phases (solid arrows). The fracture surface exhibits a lower density of dimples compared to that observed in the base alloy M1S after the same treatment/condition; this observation emphasizes the low ductility of the M2S alloy in comparison to alloy M1S. The enhanced ductility of the base alloy over that of alloy M2S can be attributed to the higher

volume fraction of intermetallic phases formed in the M2S alloy. The EDS spectrum in Figure 6.34(b) confirms the presence of Al-Cu-Ni-Fe phase. Figure 6.35(a) shows a high magnification BSE image of the cracked phase in the circled area in Figure 6.34(a). This BSE image, and the associated EDS spectra shown in Figure 6.35(b), Figure 6.35(c), and Figure 6.35(d), reveal the presence of multiple cracked Ni-rich phases which are believed to contribute to the crack initiation process.

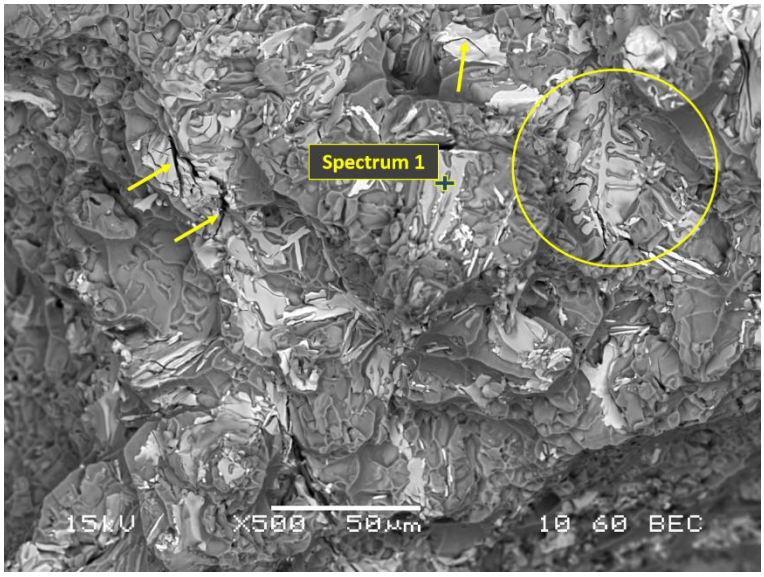

(a)

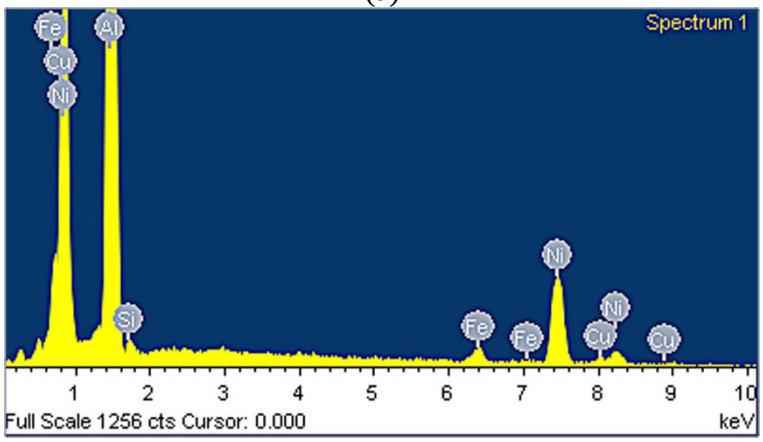

(b)

Figure 6.34 SEM images of T6-treated M2S alloy after stabilization at 250°C for 1 hour: (a) BSE image showing micro-cracks associated with Ni-rich phases, and (b) EDS spectrum corresponding to the point of interest in (a).

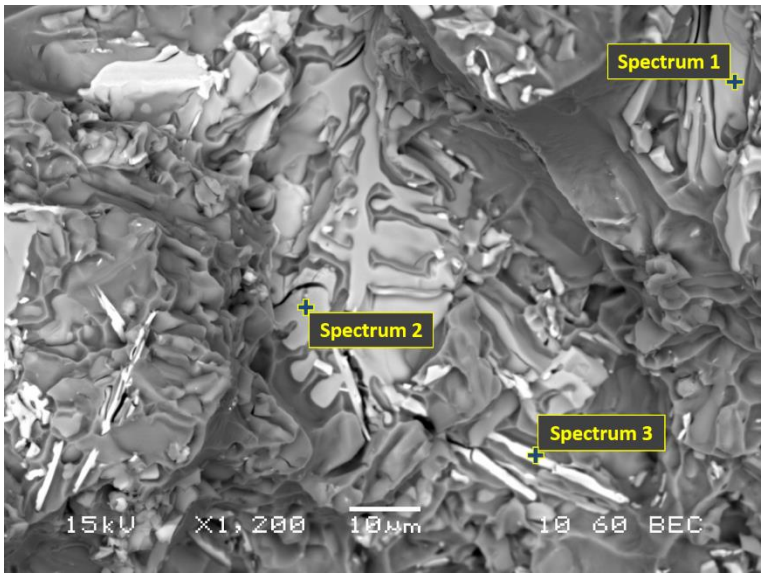
Spectrum 1
Spectrum 2
Spectrum 3
15kV X1,200 10µm 10 60 BEC

(a)

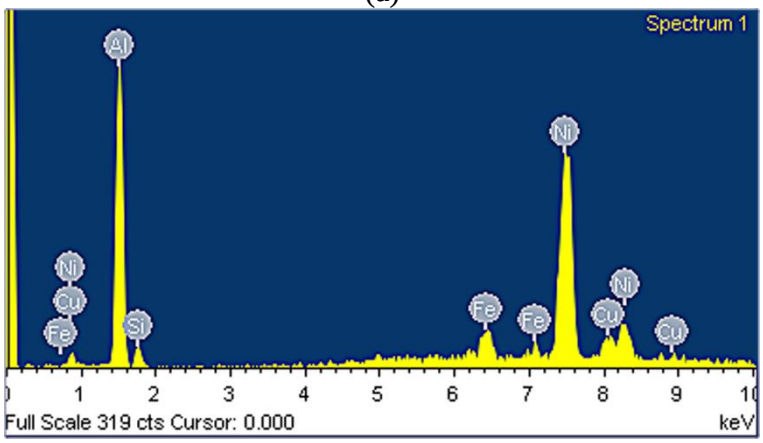
Spectrum 1
Al
Ni
Ni
Cu
Fe
Si
Fe
Fe
Ni
Cu
Cu
1 2 3 4 5 6 7 8 9 10
Full Scale 319 cts Cursor: 0.000
keV

(b)

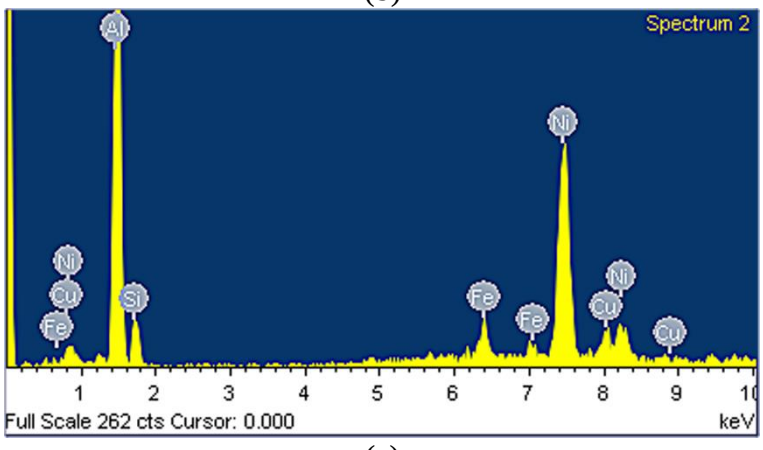
Spectrum 2
Al
Ni
Ni
Cu
Fe
Si
Fe
Fe
Ni
Cu
Cu
1 2 3 4 5 6 7 8 9 10
Full Scale 262 cts Cursor: 0.000
keV

(c)

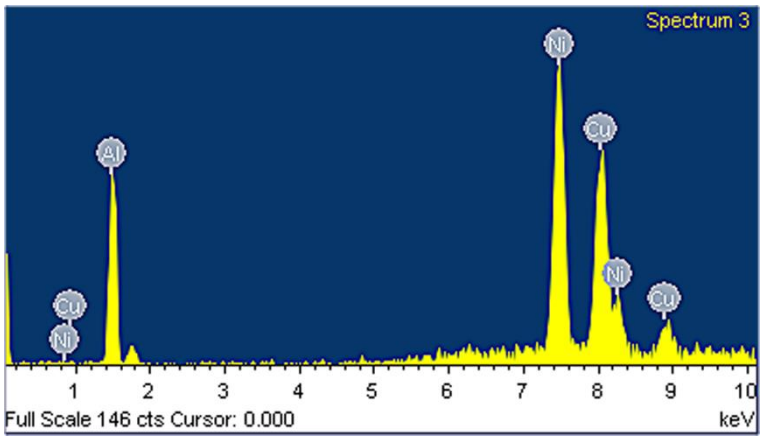

(d)

Figure 6.35 (a) High magnification of the circled area shown in Figure 6.34(a), (b, c, and d) EDS spectra showing the chemical composition of the cracked phases in (a).

By increasing the stabilization time at 250°C up to 200 hours for the T6-treated M2S alloy, the dimple nature of the fracture surface, depicted in Figure 6.36(a), is not very different from that observed after 1 hour of stabilization at 250°C. The fracture surface presents similar features with respect to the presence of Ni-rich phases as those observed in Figure 6.34(a). The arrows point at some of the shiny particles, which are possibly fine Ni-containing precipitates. The EDS spectra shown in Figure 6.36(b) and Figure 6.36(c) confirm the presence of Al-Ni-Fe and Al-Ni-Cu-Fe phases, which are key phases in controlling the fracture behavior of alloy M2S.

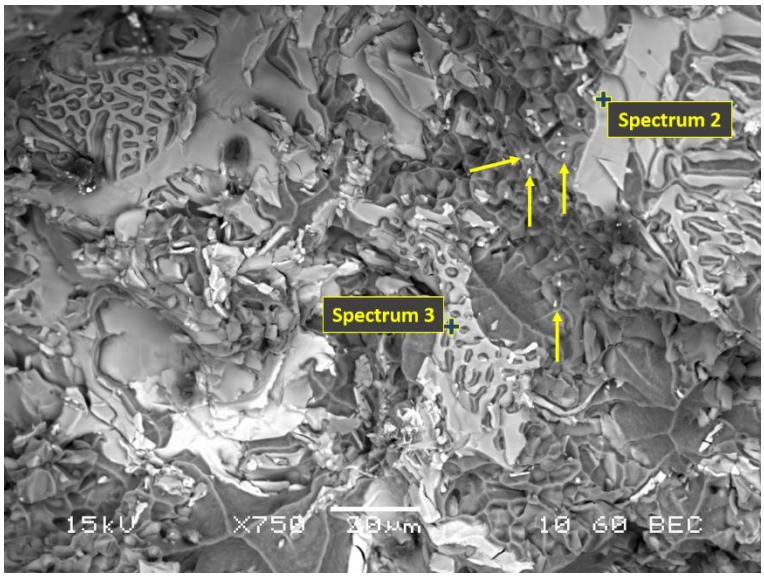

(a)

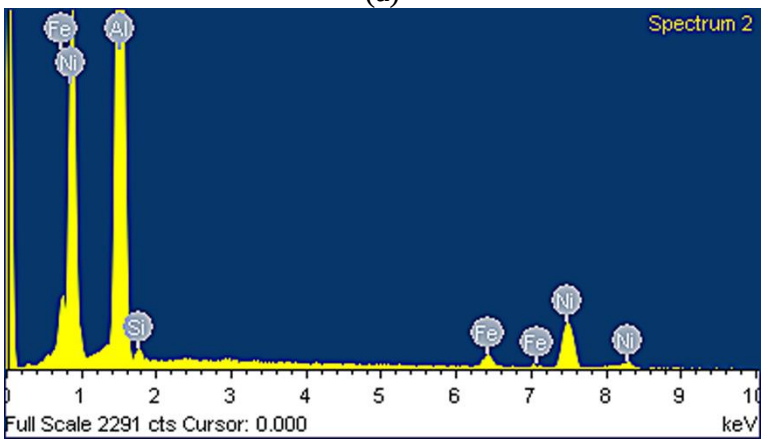

(b)

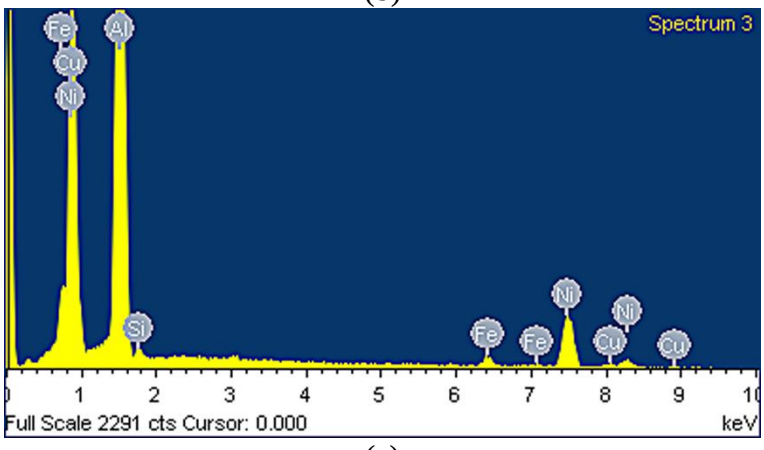

(c)

Figure 6.36 (a) BSE image of T6-treated M2S alloy after stabilization at 250°C for 200 hours showing the dimple structure, coarsened precipitates and phases involved in the crack initiation process, and (b, c) EDS spectra identifying the Ni-rich phases shown in (a).

The presence of sludge particles in the microstructure of alloy M3S plays a vital role in controlling the tensile properties and hence the fracture behavior of this alloy. The fracture surface of the T6-treated M3S alloy stabilization at 250°C for 1 hour before testing at 250°C is displayed in the BSE image shown in Figure 6.37(a). The propagation of the branched crack developed in the Q-phase, as confirmed by the corresponding EDS spectrum of Figure 6.37(b), appears to hindered by the presence of the blocky sludge particle, identified by the associated EDS spectrum shown in Figure 6.37(c). Similar action of the sludge particles in retarding crack propagation can be noted in Figure 6.37(d). Yet another interesting observation made from this figure is that, while many of the intermetallic phase particles appear cracked, as indicated by the solid arrows, the sludge particles, however, are crack-free. This observation emphasizes the favorable effect of the presence of sludge particles on the mechanical properties. Besides the sludge particles, the fracture surfaces show noticeable dimpled structure which reflects the good level of ductility experienced by this alloy during tensile testing at 250°C.

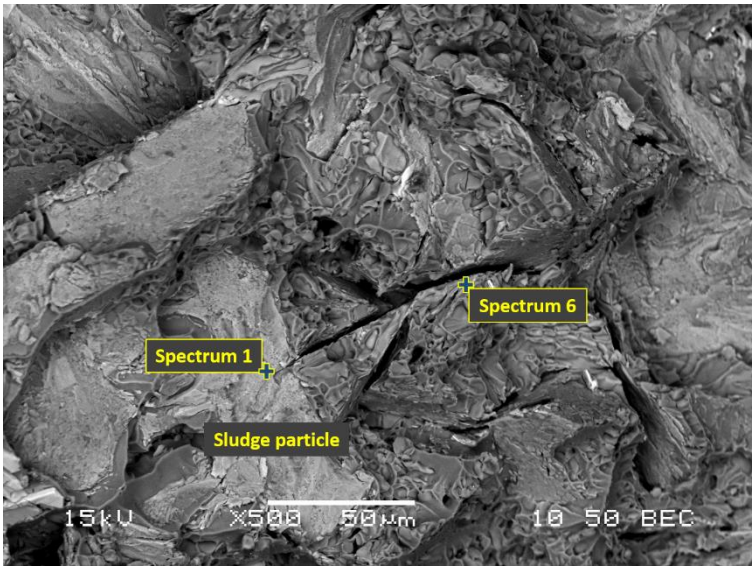

(a)

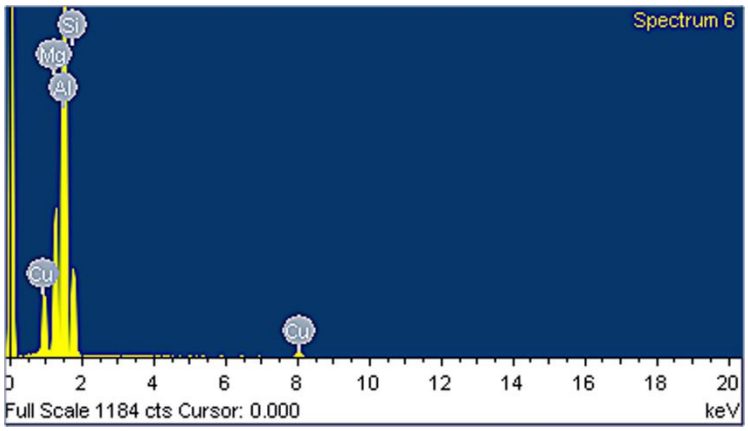

(b)

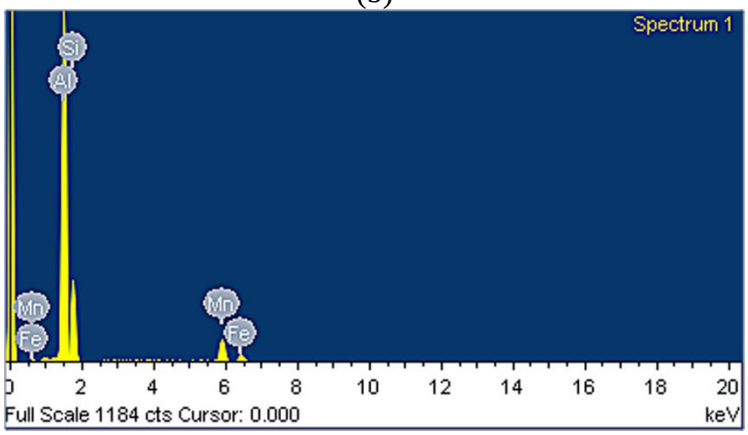

(c)

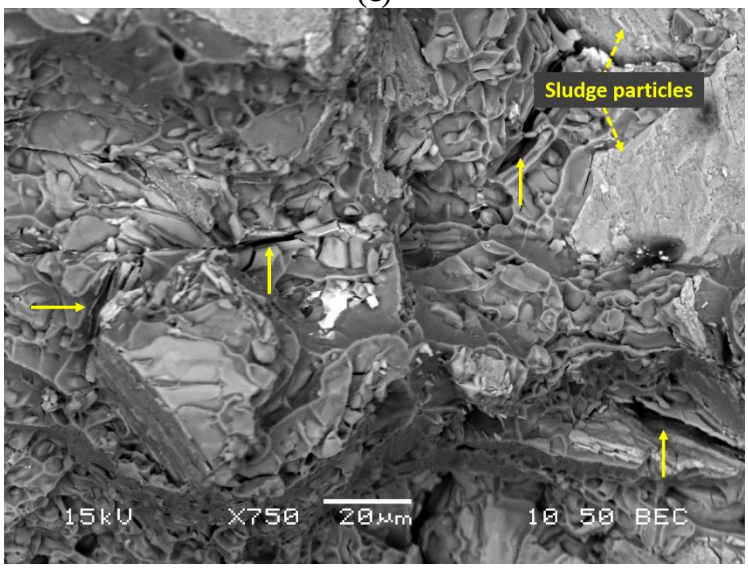

(d)

Figure 6.37 SEM images of T6-treated M3S alloy after stabilization at 250°C for 1 hour: (a) BSE image showing a branched crack in a Q-phase particle and sludge particles preventing crack propagation, (b, c) EDS spectra corresponding to the Q-phase and the sludge particle observed in (a), and (d) BSE image showing various cracked intermetallic phases and crack-free sludge particles.

Figure 6.38(a) shows the fracture surface of T6-treated M3S alloy after stabilization for 200 hours at 250°C and tested at the same temperature. The propagation of the crack detected in the star-like Alx(Zr,Ti)Si phase particle is hindered by the adjacent blocky sludge particle, as depicted in the BSE image shown in Figure 6.38(a). The corresponding EDS spectra shown in Figure 6.38(b) and Figure 6.38(c) confirmed the two phases. The fracture surface in Figure 6.38(a) exhibits coarse and deep dimples because of the improved elevated-temperature ductility of this alloy after applying the stabilization treatment.

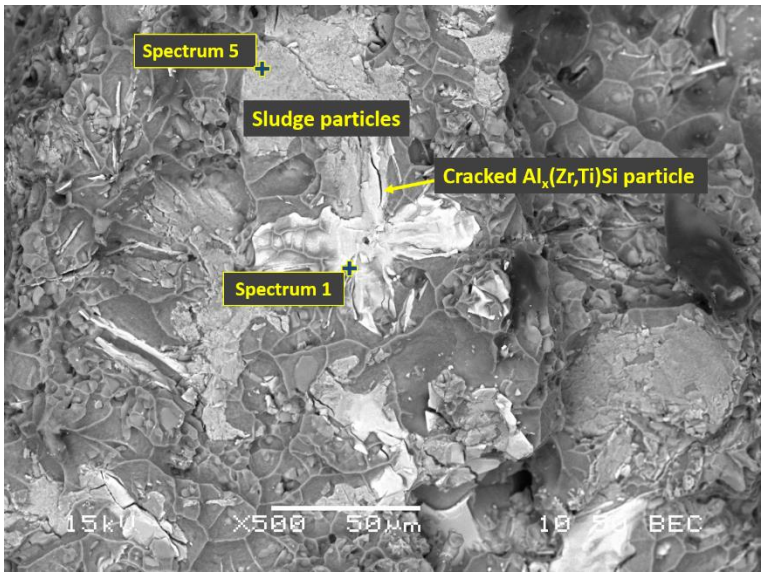

(a)

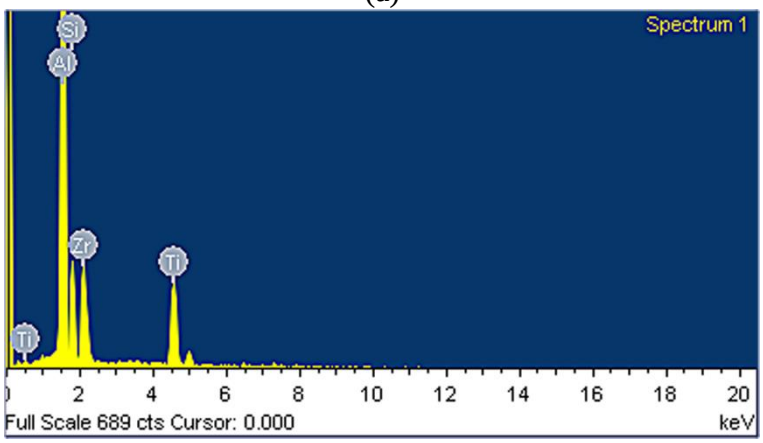

(b)

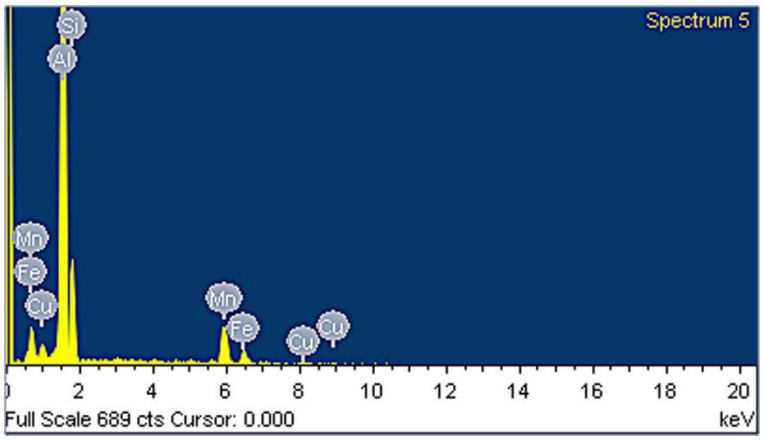

(c)

Figure 6.38 (a) BSE image of T6-treated M3S alloy after stabilization at 250°C for 200 hours showing the dimple structure (upper right corner), coarsened precipitates and a cracked star-like Al-Si-Ti-Zr and sludge particles; and (b, c) EDS spectra corresponding to the Al-Si-Ti-Zr and sludge particles shown in (a).

Figure 6.39(a) shows the coarsened precipitates distributed over the fracture surface of the T6-treated M3S alloy after stabilization at 250°C for 200 hours. Thin plates of Alx(Zr,Ti)Si phase with different orientations are also seen in the BSE image. The corresponding EDS spectrum displayed in Figure 6.39(b) confirmed these plates to be the Alx(Zr,Ti)Si phase.

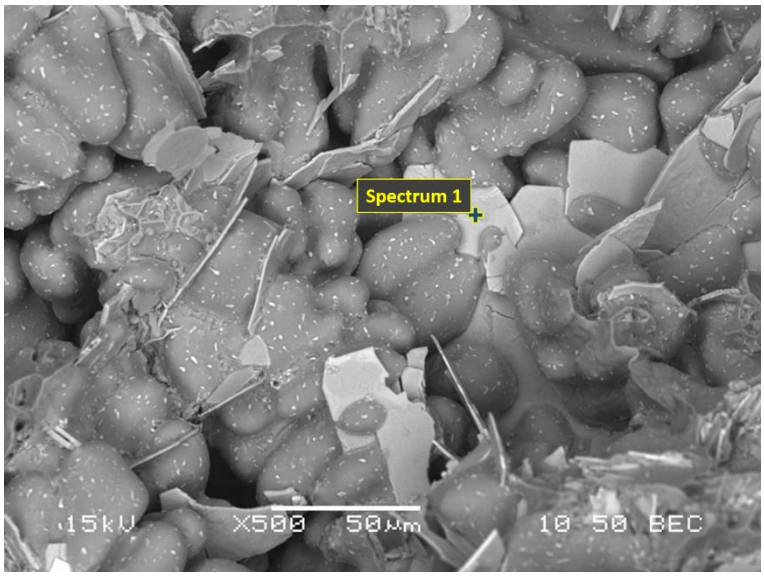

(a)

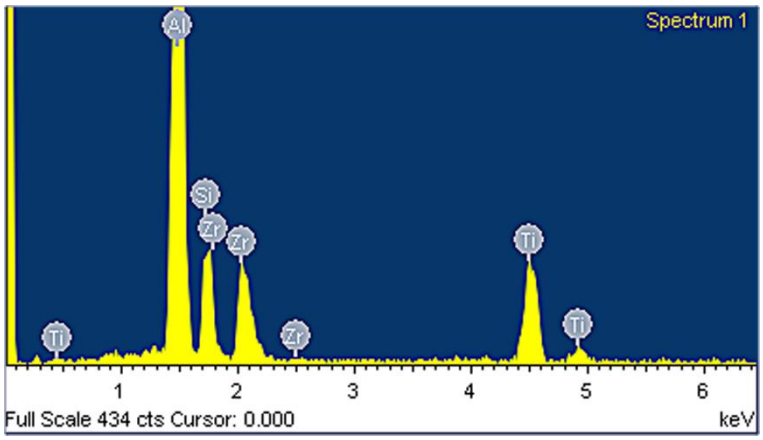

(b)

Figure 6.39 (a) BSE image of T6-treated M3S alloy after stabilization at 250°C for 200 hours showing the distribution of coarsened precipitates and Al-Si-Ti-Zr thin plates, and (b) EDS spectrum corresponding to the Al-Si-Ti-Zr plates observed in (a).

CHAPTER 7

EXTENDED SOLUTION TREATMENT

CHAPTER 7

EXTENDED SOLUTION TREATMENT

7.1 INTRODUCTION

Studying morphological changes of eutectic silicon particles during solution heat treatment and their effect on the mechanical properties have been extensively investigated for the past several decades. However, this topic still receives the attention of researchers worldwide because it is a broad research subject, which is extended further through the utilization of advanced characterization techniques and interesting novel approaches to analyze this phenomenon and its effects. It is considered a broad research area because of the ample variations in morphologies of the micro-constituents present in Al-Si alloys and consequently the mechanical properties according to the alloy composition, casting process, and heat treatment process used.

The structure of the 3xx-series Al-alloys consists mainly of a ductile α-Al matrix reinforced with hard silicon particles and various intermetallic compounds based on the alloying elements present. However, the size and morphology of silicon particles play an important role in determining the overall mechanical performance of this category of alloys; besides, the fracture of Al-Si alloys is known to be initiated by the fracture of silicon particles.

Based on the aforementioned, a detailed investigation was undertaken to study changes in the eutectic silicon morphology during solution treatment and the effect of these morphological changes on the ambient- and elevated-temperature mechanical performance. This chapter, consisting of two parts, will describe and interpret the experimental data obtained in the work phase III, concerning extended solution-heat treatments. The first part will focus on the morphological changes in the eutectic silicon particles that take place during the extended solution treatment; the second part will discuss the effect of these morphological changes on the tensile properties of the alloys studied.

PART I- EVOLUTION OF EUTECTIC SILICON PARTICLES DURING EXTENDED SOLUTION-HEAT TREATMENT

It is well established that the morphology of the eutectic silicon is mainly affected by (i) the solidification rate, (ii) modification using chemical additives, and (iii) the solution treatment stage of traditional T6 and T7 heat treatments. In the present study, the effect of strontium addition and extended solution treatment (i.e. varying the solution time up to 400 hours) on the morphology of the eutectic silicon particles will be investigated for the specific set of alloys which were described in Chapter 3 (Table 3.1). To study the effect of Sr-addition, the non-modified base alloy (M1) was compared with the same base alloy containing 200 ppm Sr, namely, Sr-modified base alloy (M1S). In addition, 356 alloys (non-modified and Sr-modified) were also investigated in this part of the experimental work. The intermetallic compounds in 356-type alloys are limited in comparison to the 354 alloys under study (i.e. alloys M1 and M1S). Thus it will be worthwhile to investigate the role of intermetallic compounds in affecting the evolution of eutectic silicon particles by comparing the evolution of the eutectic silicon particle morphology in 354-type alloys

(containing a high fraction of intermetallic compounds) to that of 356-type alloys (with a low fraction of intermetallic compounds).

For each category of the alloys (i.e. 354- and 356-type alloys), the maximum possible solutionizing temperature without incipient melting was chosen. The 356-type alloys allow the use higher solutionizing temperature due to the absence of copper; thus a temperature value of 550°C was selected. For the 354-type alloys, a lower solutionizing temperature of 510°C was used due to their relatively high copper content (1.8 wt.%). The applied solutionizing temperature (i.e. 510°C) to 354-type alloys in this phase of work is higher than the solutionizing temperature which was commonly used in the rest of the experimental work in this study, for the following reasons. With the constancy of the sample size, fragmentation, dissolution and coarsening kinetics of the eutectic silicon particles are mainly dependent on the solutionizing temperature and time; so that the maximum possible temperature as well as affordable long durations, up to 200 hours for the 354-type alloys and up to 400 hours for the 356-type alloys, were selected to produce the maximum possible changes in the morphology of Si particles. Durations of 8, 25, 50, 100, and 200 hours were selected for the 354-type alloys in order to be able to study the fragmentation as well as the spheroidization and coarsening behavior of the Si particles. Longer durations were used in the case of 356-type alloys, namely 8, 50, 100, and 200 hours in addition to the longest duration of 400 hours. Eutectic silicon characteristics were studied in the as-cast condition as a reference condition with zero hour of stabilization, and after solution treatment, at the temperatures and times previously mentioned; a summary of the studied conditions are listed in Table 7.1.

7.2 CHARACTERIZATION OF EUTECTIC SILICON PARTICLES

In this section, results of investigating the effect of extended solution treatment on eutectic silicon particles characteristics for both 354- and 356-type alloys will be presented. Metallographic specimens of the alloys investigated were prepared and examined to provide a qualitative and quantitative analysis. While the qualitative analysis will describe the general trend of the evolution of the eutectic silicon size and morphology during extended solution treatments, the quantitative analysis will address the progress of fragmentation, spheroidization, and coarsening taking place the during extended solution treatment through measurements of the eutectic Si particle characteristics. The morphological evolution of the eutectic Si particles will be further studied by examining deep etched samples using a field emission scanning electron microscope (FESEM). Deep etching results in exposing some of the silicon particles by dissolving the soft aluminum matrix around them; this enables examination of the silicon particle morphology in 3D, which is more realistic and representative.

Table 7.1 Summary of investigated alloys and conditions

Alloy type	Alloys	Condition code	Solution treatment temperature	Solution treatment time (hours)	Quenching
354	**M1, and M1S**	**As-cast**	NA	NA	NA
	M1, and M1S	**T4**	510°C	8, 25, 50, 100, 200	Warm water 60°C
356	**M6, and M6S**	**As-cast**	NA	NA	NA
	M6, and M6S	**T4**	550°C	8, 50, 100, 200, 400	Warm water 60°C

7.2.1 QUALITATIVE ANALYSIS

Figure 7.1 through Figure 7.4 show the optical micrographs of the non-modified base alloy (M1), Sr-modified base alloy (M1S), non-modified 356-type alloys (M6), and Sr-modified 356-type alloy (M6S), respectively, in the as-cast condition and after solution treatment at different temperatures (i.e. 510°C for 354-type alloys and 550°C for 356-type alloys) and durations as mentioned in Table 7.1. It is clear from these micrographs that the size of the as-cast eutectic silicon particles increased significantly during solutionizing. It can also be observed that the spheroidal particles appeared to be more dominant in the Sr-modified alloys (i.e. alloys M1S and M6S) compared to the respective non-modified alloys (i.e. alloys M1 and M6). Figure 7.1(f) and Figure 7.3(f) reveal the existence of a considerable amount of elongated silicon particles in the Sr-free alloys (i.e. M1 and M6). This observation demonstrates the difficulty of attaining a high fraction of spherical silicon particles by employing solution treatment solely, even though a considerably high temperature and a sufficiently long time were used (e.g. 550°C and 400 hours), and emphasizes the essential role of Sr addition to obtain spherical silicon particles in a relatively high fraction, as can be inferred from Figure 7.2 and Figure 7.4.

These observations may be attributed to the fact that spheroidization and coarsening processes generally occur due to interface instability between two phases (α-Al and Si particles) and are driven by reduction in the total interfacial energy. Thus the elongated Si particles observed in solution treated non-modified alloys may be explained in terms of lower states of interfacial instability in the case of plate-like non-modified Si particles which means there is resistance to spheroidization. In contrast, the high spheroidization rate

observed in Sr-modified alloys occurs because the fibrous particles are more susceptible to shape perturbations and so the resistance to spheroidization is reduced.[133, 243]

The evolution of silicon particles during extended solution treatment follows the same trends and sequences, as can be deducted from Figure 7.1 through Figure 7.4, for the non-modified, as well as the Sr-modified 354- and 356-type alloys; however different evolution rates can be easily spotted from the micrographs presented hereafter.

In the simple non-modified 356 alloy (M6), it can be noticed that solutionizing at 550°C for 8 hours, Figure 7.3(b), resulted in rapid fragmentation and coarsening of eutectic silicon particles in comparison to that observed after solutionizing of the non-modified 354 alloy (M1) for the same period of 8 hours at 510°C. While the difference in solutionizing temperatures certainly plays a major role in this regard, the chemical additives in the 354-type alloy M1 may also play an important role in retarding the fragmentation and coarsening of the Si particles in this alloy system. The retarding effect may be understood in the context of the microstructural evolution process during solution treatment, including the dissolution of the strengthening phases and homogenization of the as-cast structure. These processes are mainly diffusion-controlled processes, as is the coarsening of eutectic silicon particles, which is achieved through the dissolution of small Si particles in order to coarsen the already larger particles which have more energetic stability; this is commonly known as the Ostwald ripening mechanism. Interaction of the different diffusion fields may result in retarding these diffusion-controlled processes (i.e. Si coarsening, dissolution of strengthening phases, and homogenization of the as-cast structure). Thus the existence of more chemical additives and consequently phases in the 354-type alloys compared to the 356 alloys may contribute to the lower fragmentation and coarsening rates in the former

alloy system compared to the latter, in addition to the certain contribution of the solutionizing temperature.

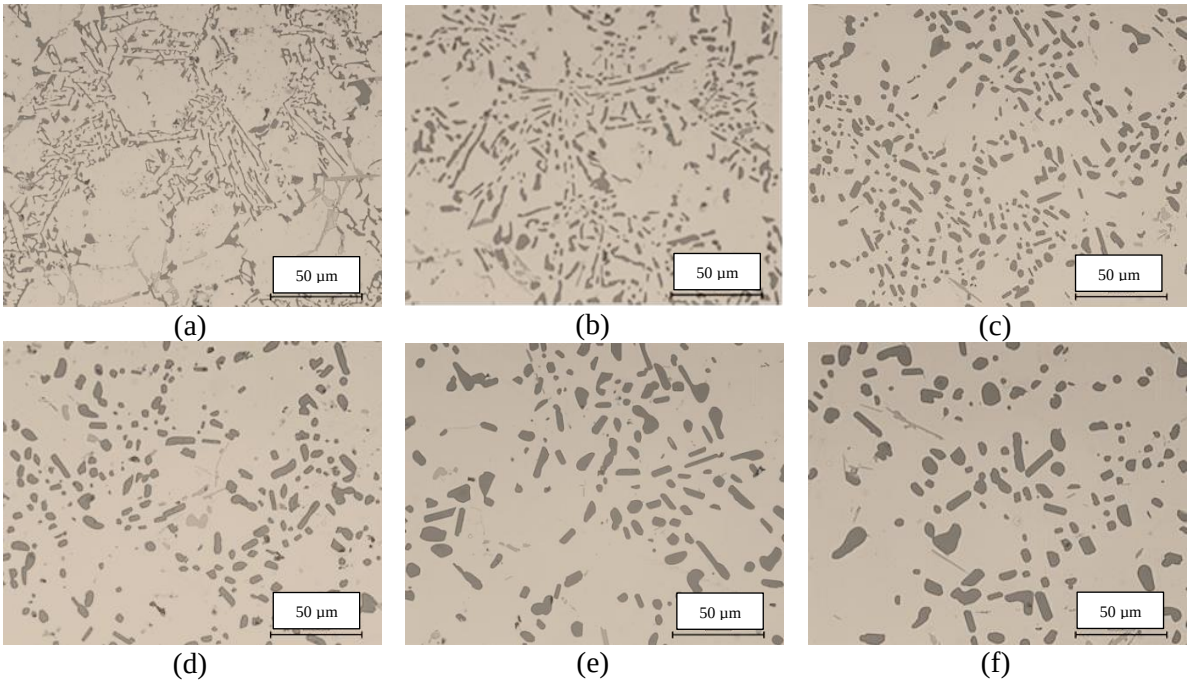

Figure 7.1 Optical micrographs (500X) of non-modified base alloy (M1) after solution treatment at 510°C for: (a) as-cast, (b) 8h, (c) 25h, (d) 50h, (e) 100h, and (f) 200h.

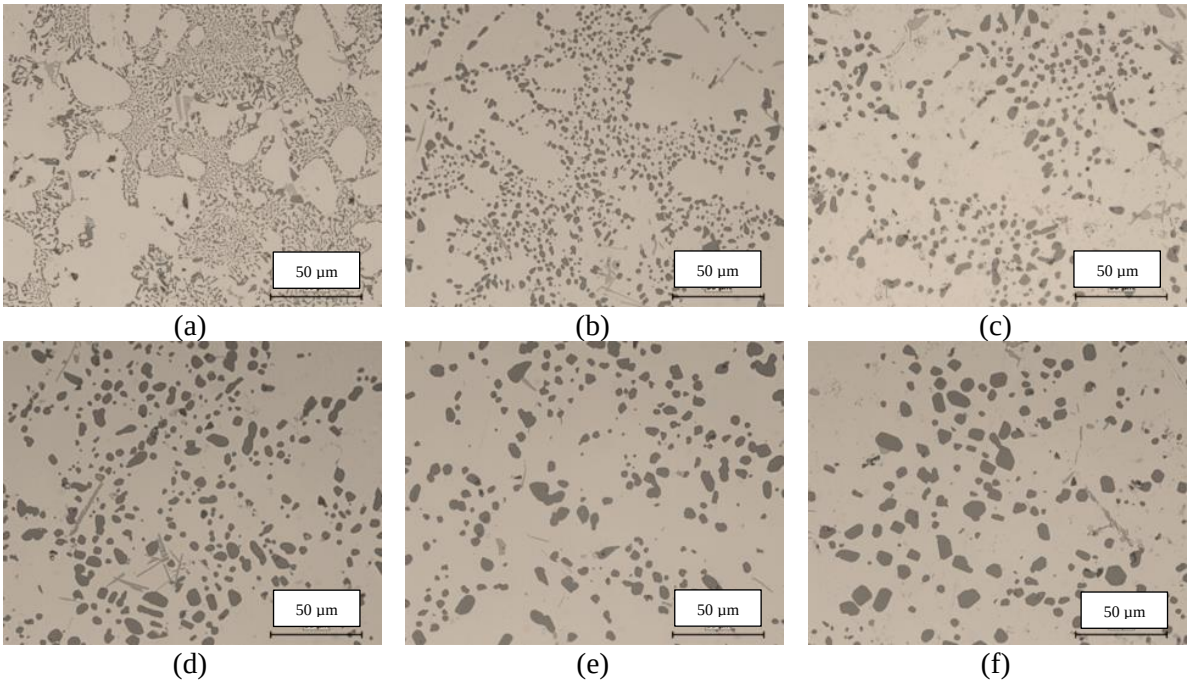

Figure 7.2 Optical micrographs (500X) of Sr-modified base alloy (M1S) after solution treatment at 510°C for: (a) as-cast, (b) 8h, (c) 25h, (d) 50h, (e) 100h, and (f) 200h.

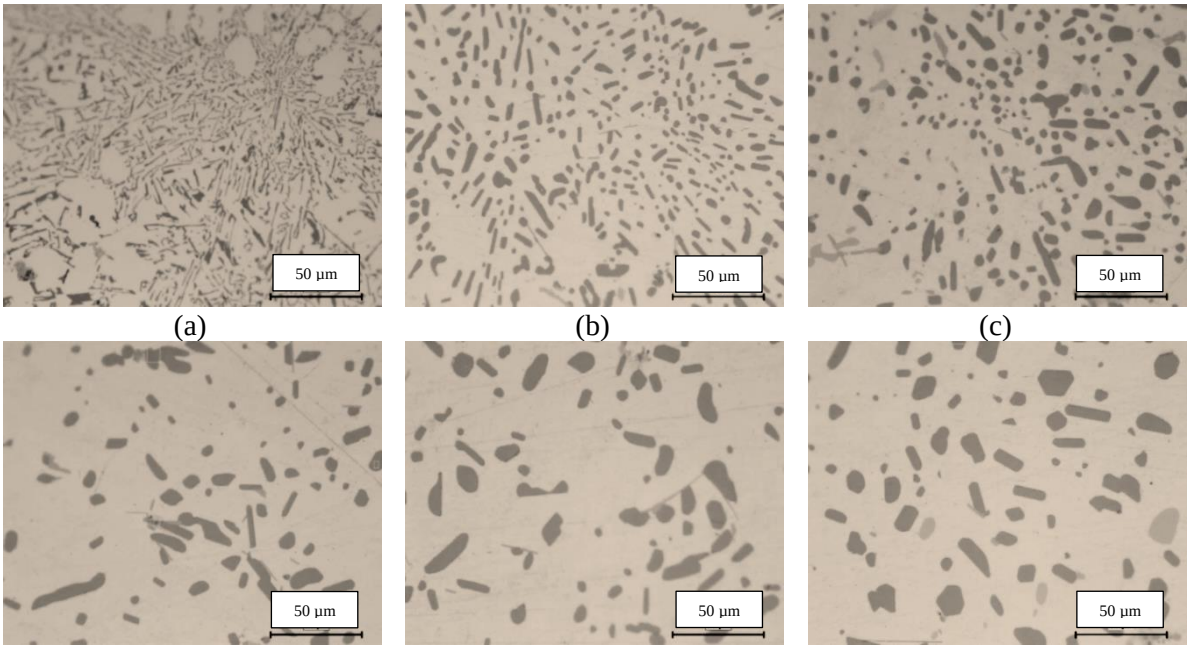

(a) (b) (c)

(d) (e) (f)

Figure 7.3 Optical micrographs (500X) of non-modified 356 alloy (M6) after solution treatment at 550°C for: (a) as-cast, (b) 8h, (c) 50h, (d) 100h, (e) 200h, and (f) 400h.

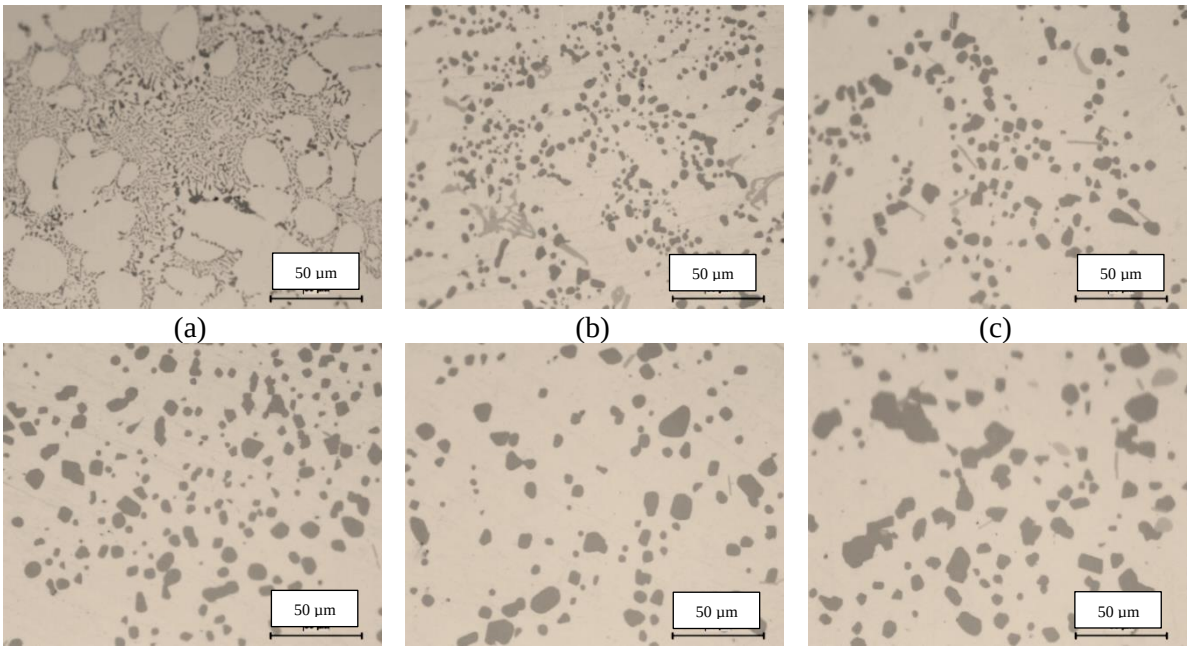

(a) (b) (c)

(d) (e) (f)

Figure 7.4 Optical micrographs (500X) of Sr-modified 356 alloy (M6S) after solution treatment at 550°C for: (a) as-cast, (b) 8h, (c) 50h, (d) 100h, (e) 200h, and (f) 400h.

7.2.2 DEEP ETCHED SAMPLES

In order to have a better understanding of the evolution of Si particles during extended solution treatment, deep-etched samples were prepared using Keller's etchant (5% HF) for a time sufficient to dissolve the soft aluminum matrix and expose the Si particles in a 3-dimensional form. These samples were examined using FESEM in order to have clearer images which would help in better understanding the evolution of the Si particle morphology, with an emphasis on the coarsening behavior. These 3-D images provide more information, and are preferable to the 2-D images obtained with optical microscopy.

By examining deep etched samples of the four alloys M1, M1S, M6, and M6S, it is clear that the coarsening behavior is almost the same in the non-modified alloys M1 and M6, and likewise for the Sr-modified alloys M1S and M6S. Thus the analysis of these samples will focus mainly on the 356-type alloys M6 and M6S, since the coarsening behavior of the Si particles in these alloys would be more obvious due to the higher solutionizing temperature as well as the simpler chemistry of these alloys compared to the 354-type alloys.

Figure 7.5 shows micrographs of eutectic silicon particles in non-modified and Sr-modified 354-type alloys (i.e. M1 and M1S) in the as-cast condition and after solution treatment at 510°C for 200 hours. These micrographs lead to conclusions similar to those derived from the optical micrographs in Figure 7.1 and Figure 7.2 regarding the morphology of eutectic Si particles under different conditions. On the one hand, plate-like silicon particles in the non-modified alloy M1 still exist in the alloy even after 200 hours at 510°C besides other spheroidal particles as shown in Figure 7.5(b). Yet, it is obvious that

with solution treatment, the edges of the coarsened plate-like particles become more rounded, compared to the sharp edges of the thin as-cast plate-like particles seen in Figure 7.5(a); this is indicated by the white arrows and dotted circles in Figure 7.5(a) and (b). On the other hand, the corals of interconnected fibrous silicon in the as-cast Sr-modified 354 alloy (M1S) were entirely fragmented, spheroidized, and coarsened after 200 hours at 510°C. Spherical particles with rounded edges exist predominantly in alloy M1S after 200 hours at 510°C however other faceted silicon particles also coexist with these spherical ones, as indicated by the white arrows in Figure 7.5(d). These observations are in good agreement with the findings reported in literature regarding the faster fragmentation (disintegration), spheroidization, and coarsening of eutectic silicon in Sr-modified alloys compared to non-modified alloys.[127, 134, 243]

Ogris *et al.*[286] reported that modified silicon corals in small parts of 356 alloy disintegrate promptly at 540°C and are completely spheroidized after one minute at this temperature; this observation was also reported by other authors,[243, 244, 287, 288] and seems to hold true for the Sr-modified 354 alloy (M1S) at the much lower solutionizing temperature of 510°C. Optical micrographs which were obtained for the M1S alloy after 5, 15, 30, and 60 minutes at 510°C are shown in Figure 7.6; these micrographs reveal that most of the fragmentation and spheroidization of the eutectic Si particles takes place in the first five minutes, which agrees well with the findings established from multiple studies.[120, 244, 286, 288] The optical micrograph of alloy M1S after solutionizing at 510°C for 5 minutes, shown in Figure 7.6(a), reveals the existence of globular silicon particles instead of the fibrous coral-like particles that appear in the as-cast microstructure of Figure 7.2(a).

Since the fragmentation and spheroidization processes are not within the scope of this study, no further details will be given for these short-time solution treatments. The main focus in this section will be on the coarsening behavior and active mechanisms during the extended solution treatments; in the following paragraphs more attention will be paid to the evolution of the eutectic Si in the non-modified and Sr-modified 356 alloys, which is similar to the coarsening behavior of Si particles in the 354 alloys, but with higher rates due to the higher solutionizing temperature and longer durations, and their simple chemistry.

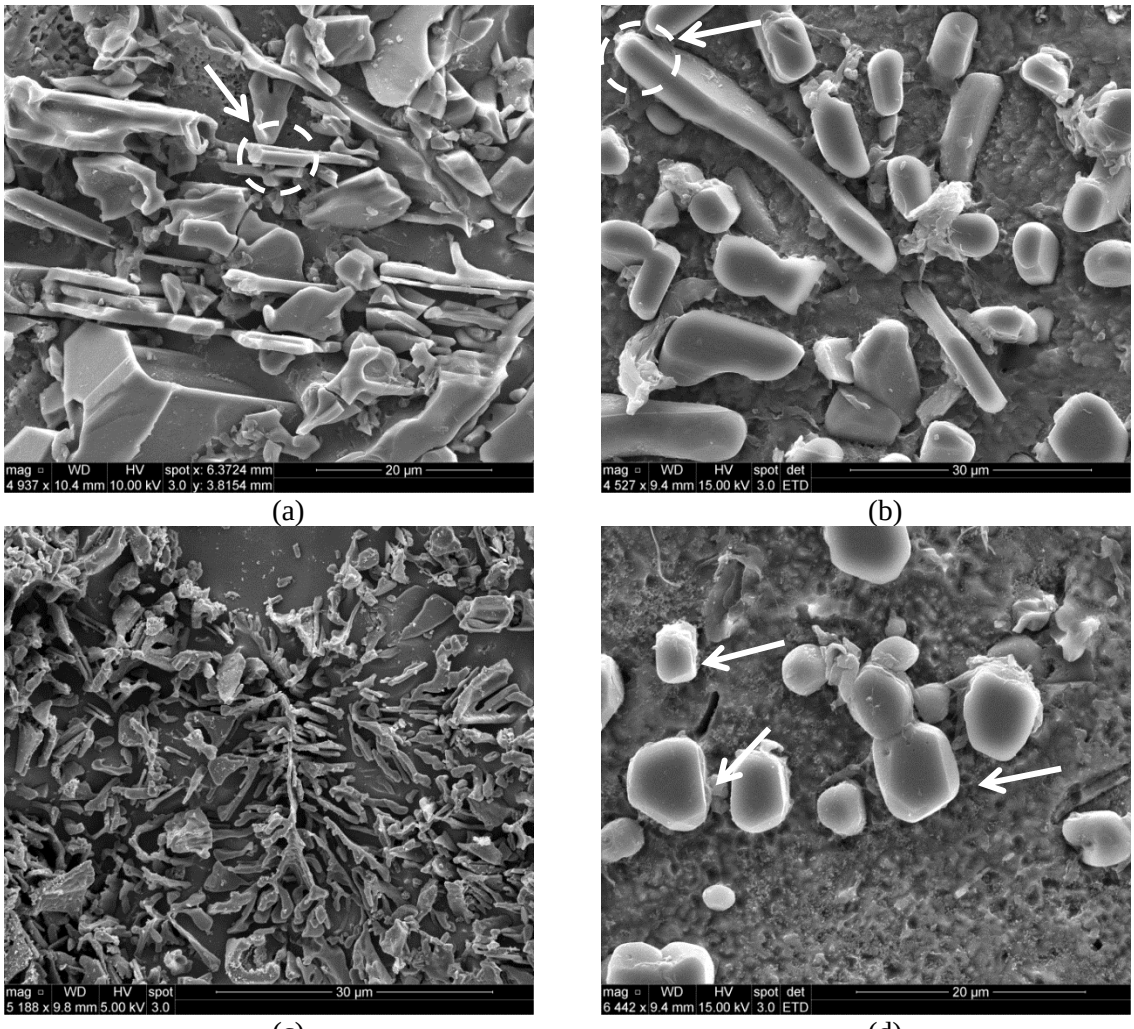

(a) (b)

(c) (d)

Figure 7.5 Morphological changes of eutectic silicon as a function of heat treatment: (a) and (b) non-modified 354 alloy (M1) in as-cast and after 200 h at 510°C, respectively; and (c) and (d) Sr-modified 354 alloy (M1S) in as-cast and after 200 h at 510°C, respectively.

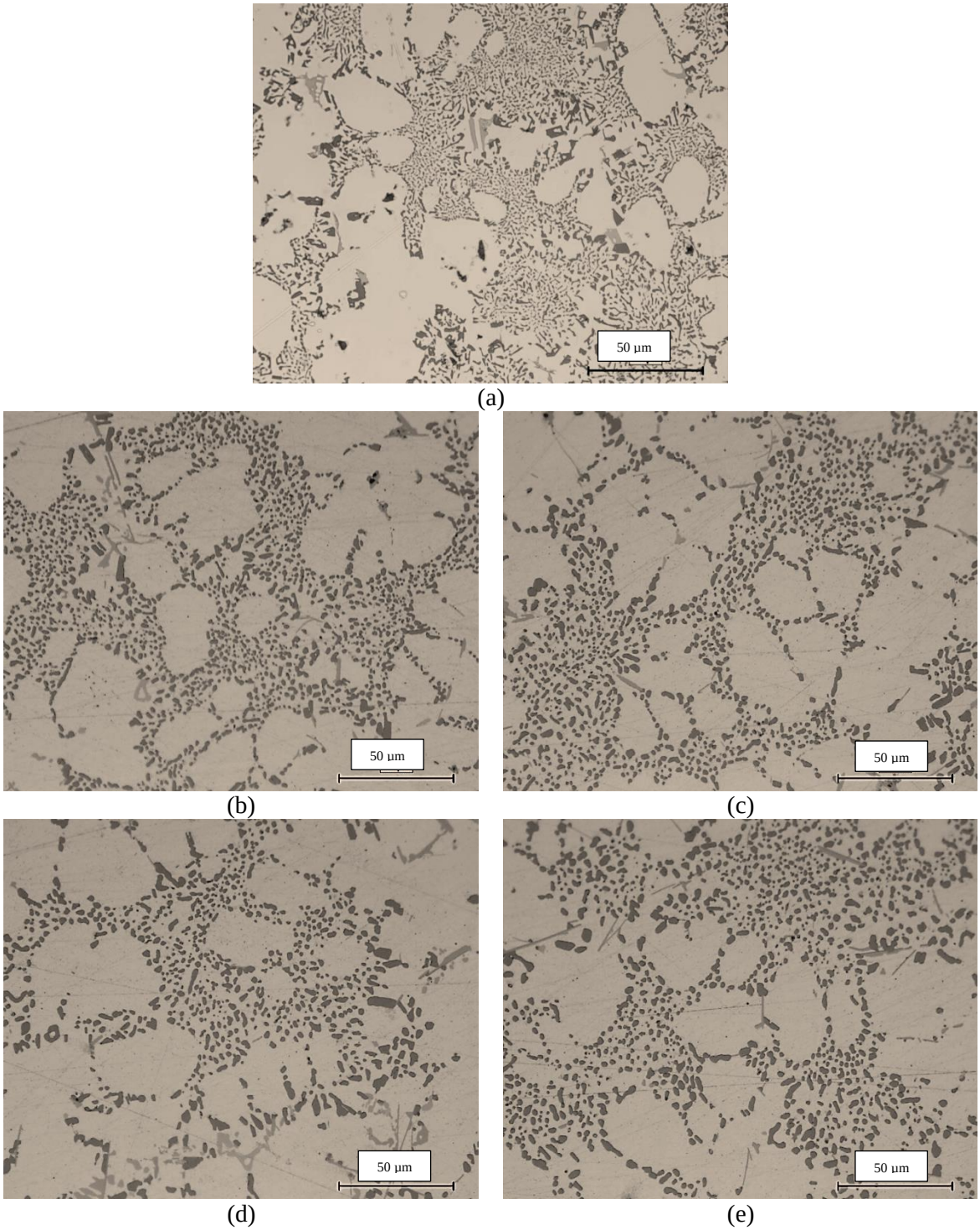

Figure 7.6 Optical micrographs (500X) of Sr-modified 354 alloys (M1S) after solution treatment at 510°C for: (a) as-cast, (b) 5 minutes, (c) 15 minutes, (d) 30 minutes, and (e) 60 minutes.

Figure 7.7 and Figure 7.8 show the size and morphology of eutectic Si particles in the non-modified (M6) and Sr-modified (M6S) 356-type alloys, deeply etched using Keller's etchant, in the as-cast condition and after solution treatment at 550°C for 8, 50, 200, and 400 hours. As can be seen from Figure 7.7(a), the eutectic Si particles precipitate as short platelets with sharp edges in the non-modified alloy. According to the model of the granulation of unmodified Si proposed by Zhu and Liu,[246] the spheroidization and the coarsening of eutectic Si particles is preceded by a fragmentation process. This fragmentation is a result of the mass transport of Si atoms from their original locations to more favourable ones with higher solubility of silicon in the matrix due to variations in the surface curvature of the particles and thus in the lattice deformation energy. The fragmentation process is thus completed by necking and then splitting of the branched eutectic Si platelets. The white arrow in Figure 7.7(b) points out a fractured Si particle at the necking point after solutionizing at 550°C for 8 hours; other fractured silicon particles were also spotted while examining this condition.

Apart from the fact that the Si particles no longer have the plate-like morphology, these observations indicate that solution treatment at 550°C for 8 hours is sufficient to complete most of the fragmentation process, so that the third stage of the granulation model i.e., spheroidization, becomes active, as may be seen in Figure 7.7(b). Longer durations of solutionizing at 550°C generally increase the spheroidization as well as coarsen the eutectic Si particles, as can be inferred from Figure 7.7(c), Figure 7.7(d), and Figure 7.7(e). The coarsening of eutectic Si particles appears to be achieved through particle coalescence and the Ostwald ripening mechanism. Thus it is assumed, based on observations of the deep etched samples, that both mechanisms are active at the same time; however, they operate

independently and additively. It is obvious from the micrographs in Figure 7.7 that some Si particles coarsen due to the coalescence (agglomeration) of nearby particles followed by their diffusion into one larger particle; this mode of coarsening is delineated by solid white arrows in Figure 7.7(c), Figure 7.7(d), and Figure 7.7(e); this particle coalescence mechanism was observed previously in a number of studies. [287, 289-291] Moreover, the broken arrows in Figure 7.7(c), and Figure 7.7(e) point out a possible dissolution of some small particles in the matrix that will cause coarsening of larger particles via the Ostwald ripening mechanism. Another observation made from Figure 7.7(e) is that some of the new fragments of the original Si platelets still maintain their platelet morphology, denoted by the solid circles, even after solutionizing for 400 hours at 550°C.

The addition of 200 ppm Sr changes the morphology of the as-cast silicon particles from platelets into fibrous coral-like morphology as shown in Figure 7.8(a). While the evolution mechanism of the eutectic Si particles in the Sr-modified alloys (M1S and M6S) is almost similar to that described previously for the non-modified alloys (M1 and M6), however, the fragmentation and spheroidization steps are accelerated in the Sr-modified alloys, as well stated by Apelian *et al.*[127], Ogris *et al.*[134], and Shivkumar *et al.*[243] The white solid arrows in Figure 7.8(d), Figure 7.8(f), and Figure 7.8(h) show small silicon particles that have already agglomerated with larger particle(s) and are in the final stages of diffusion to form one larger silicon particle. Thus the pinholes, referred to by the double-sided arrows in Figure 7.8(e) and Figure 7.8(f), that may exist in the silicon particles can be understood as the impress (impression or imprint) left behind of the agglomeration and diffusion of small particles with/into larger particles; this is in disagreement with the conclusion made by Mueller *et al.*[292] who stated that the formation of such pinholes is due

to the presence of alloy impurities such as Fe and Ti, which appears to be inaccurate, based on the observations made in this study.

(a)

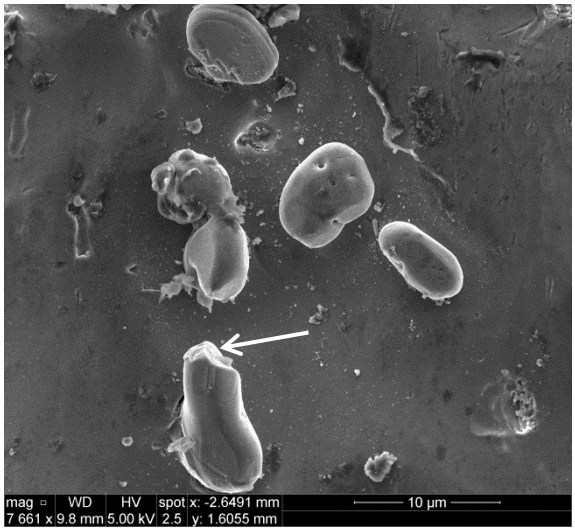

(b)

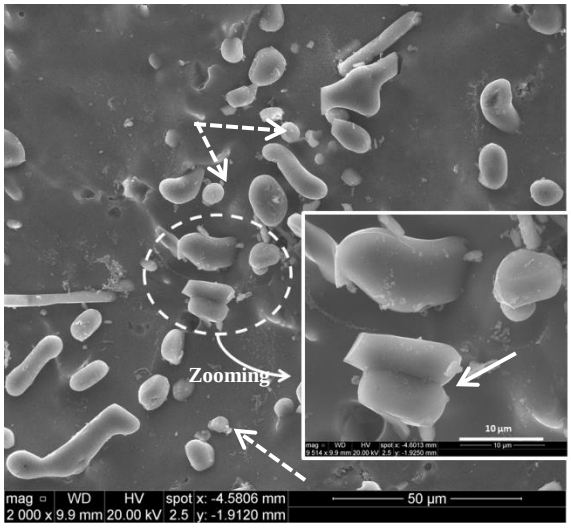

(c)

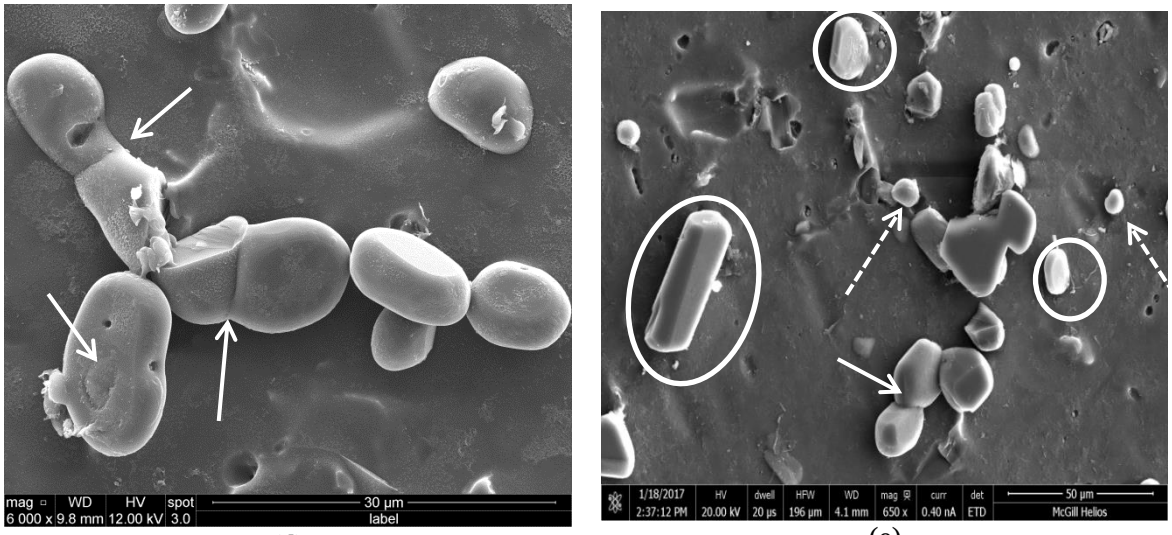

(d) (e)

Figure 7.7 Size and distribution of eutectic silicon particles in deep etched non-modified 356-type alloy (alloy M6) as a function of solution treatment: (a) As-cast, (b) 8h at 550°C, (c) 50h at 550°C, (d) 200h at 550°C, and (e) 400h at 550°C.

Furthermore, it is important to mention that the silicon particles modified with 200 ppm Sr are not spherical, as usually termed; rather, they are polyhedral or faceted, as denoted by the broken white arrows in Figure 7.8, even after 400 hours of solution treatment at 550°C. This observation of large portion of polyhedral Si particles negates the statement made by Paray and Gruzleski[132] and Shivkumar *et al.*[243] that long solution treatments can alter the morphology of Si particles from flake-like and polyhedral to spherical. Their conclusions are mainly based on 2D optical observations which seem to be right at this stage. However, by incorporating advanced electron microscopies, 3D observations reveals that the silicon particles still have more polyhedral morphologies rather than spherical ones after chemical and prolonged modification treatments. Thus, the previous knowledge regarding the term "spheroidization process" that instigated by thermal modification should be reconsidered and corrected.

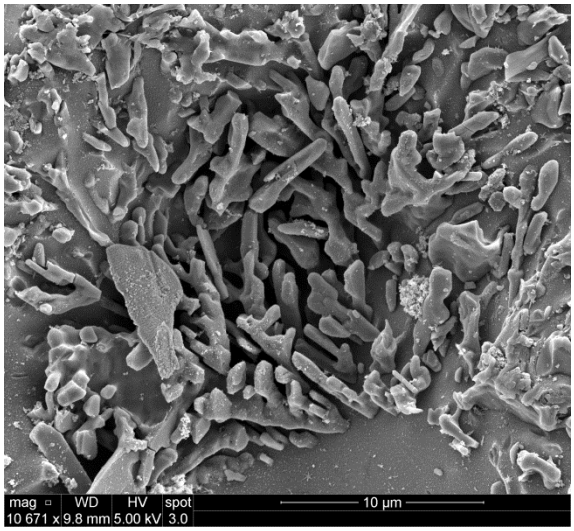
mag WD HV spot
10 671 x 9.8 mm 5.00 kV 3.0
10 µm

(a)

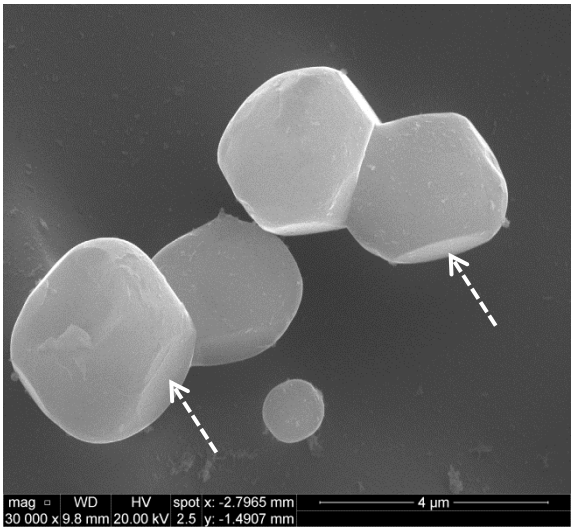
mag WD HV spot x: -2.7965 mm
30 000 x 9.8 mm 20.00 kV 2.5 y: -1.4907 mm
4 µm

(b)

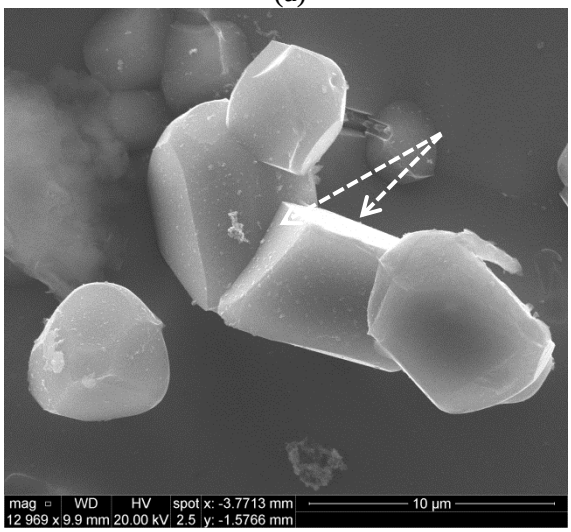
mag WD HV spot x: -3.7713 mm
12 969 x 9.9 mm 20.00 kV 2.5 y: -1.5766 mm
10 µm

(c)

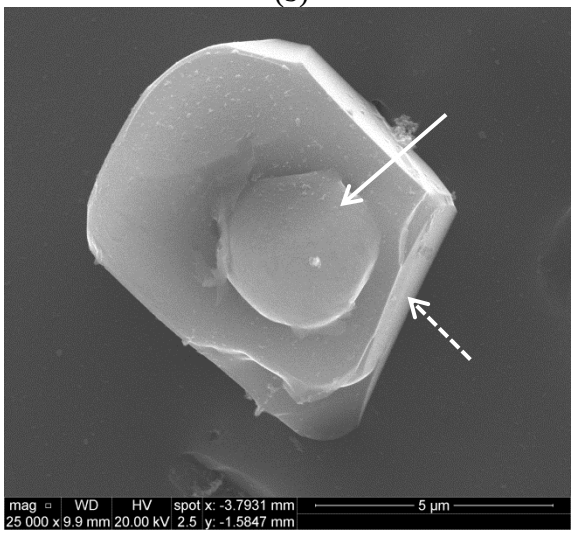
mag WD HV spot x: -3.7931 mm
25 000 x 9.9 mm 20.00 kV 2.5 y: -1.5847 mm
5 µm

(d)

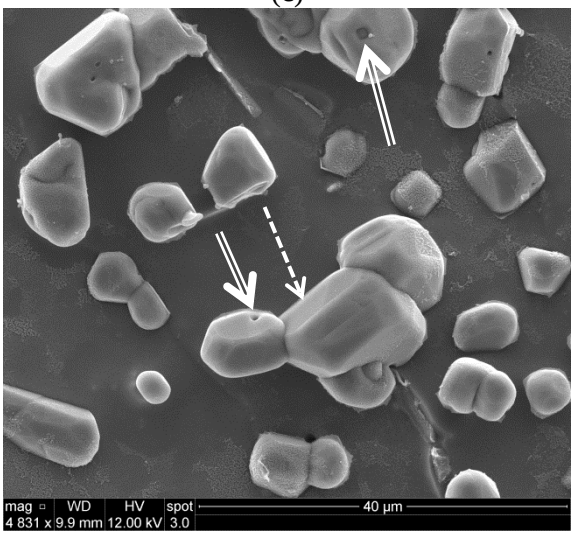
mag WD HV spot
4 831 x 9.9 mm 12.00 kV 3.0
40 µm

(e)

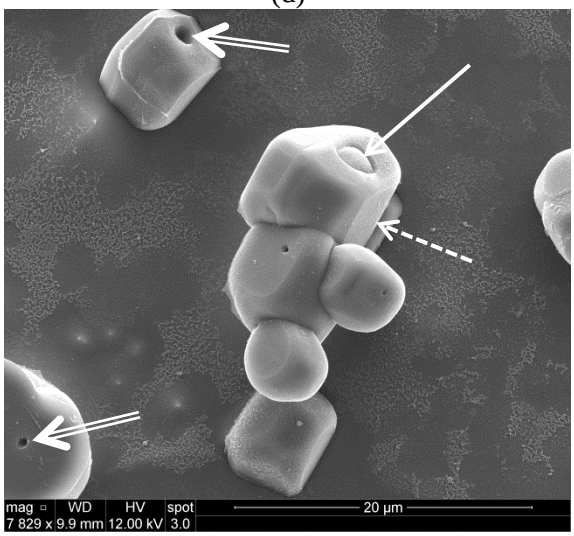
mag WD HV spot
7 829 x 9.9 mm 12.00 kV 3.0
20 µm

(f)

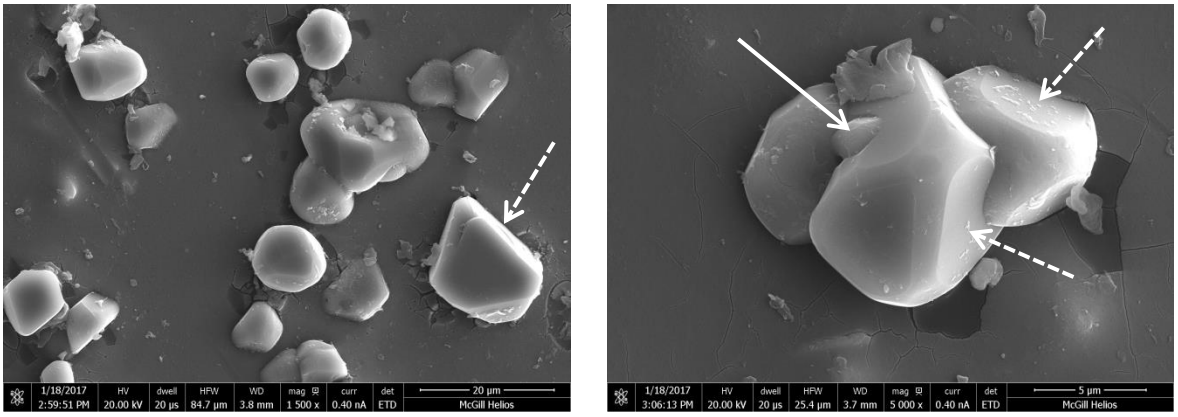

(g) (h)

Figure 7.8 Size and distribution of eutectic silicon particles in deep etched Sr-modified 356-type alloy (alloy M6S) as a function of solution treatment: (a) As-cast, (b) 8h at 550°C, (c) and (d) 50h at 550°C, (e) and (f) 200h at 550°C, and (g) and (h) 400h at 550°C.

7.2.3 ADJUSTING CRITERION FOR SILICON PARTICLE SIZE

In the subsequent analysis, a major concern that may arise while studying the coarsening behavior of silicon particles is that related to the realistic values of their particle size (area). During particle coarsening, and referring to the Ostwald ripening mechanism, smaller particles will dissolve and diffuse in order to coarsen larger particles; thus, for the purposes of analysis, there will be a large fraction of tiny particles being dissolved in the matrix. By taking such tiny particles and their high fraction into consideration, any quantitative analysis will definitely result in an inaccurate description of the real coarsening behavior. For example, after the maximum solutionizing time of 200 hours it is predictable that an analysis should reveal a considerable level of coarsening; however, if these very small particles, which exist in large numbers, are included in the analysis, this will give deceptive results and lead to unrealistic numerical conclusions regarding the coarsening behavior of the Si particles. The effect of these tiny particles on making unusual changes in producing unreliable conclusions has also been reported previously by other workers.[120, 287, 293]

Based on the aforementioned, a criterion was established to be followed, and to decide whether the tiny particles would be considered or omitted from the quantitative analysis of a specific condition defined by the solution treatment time. This criterion is essentially based on the area fraction of tiny particles with respect to the total area of the silicon particles in the sample corresponding to a specific solution treatment condition. The smallest four intervals of particles area up to 25 μm^2 will be considered in this criterion; namely particles area intervals of < 10, 10-15, 15-20, and 20-25 μm^2 will be included in this criterion. For a specific condition, the area fraction will be estimated by calculating the area fraction of the tiny particles in each of these four intervals, independently, to the total area of the silicon particles considered in the analysis for that solution treatment condition. A suitable limiting value of the area fraction will be set differently for each alloy studied, where this limiting value will decide whether the small particles will be considered in the analysis or not.

7.2.4 QUANTITATIVE ANALYSIS

A quantitative description of the morphological changes of eutectic silicon particles during solution heat treatment was carried out using Clemex Vision PE image-analysis system which is connected to the Olympus PMG3 optical microscope. This quantitative analysis was carried out on 20 different fields (micrographs) for each condition by thresholding the eutectic silicon particles in each image and performing the analysis on the selected particles. Thresholding was attained by outlining and coloring the eutectic silicon particles manually based on the degree of greyness. The data obtained for the alloys studied will be presented in the following pages.

Figure 7.9 shows the sensitivity analysis that was carried out to find proper limiting values of area fractions for each alloy as previously described in the proposed adjusting criterion. For each condition of solution treatment per alloy, the limiting value will decide whether a specific area interval of silicon particles will be included in the analysis or not, by comparing the area fraction of the tiny particles that exist in a certain area interval to the limiting value set for the respective alloy. If the limiting value is higher than the area fraction of the small particles in a specific area interval, the small particles will not be considered in this analysis and vice-versa.

As can be inferred from Figure 7.9, the area fraction limiting values for the alloys M1, M1S, M6, and M6S are 6, 10, 5, and 10 %, respectively. These values were selected because there is a definite separation between the data obtained after short and extended solution treatments especially at the smallest area interval (i.e. $< 10\ \mu m^2$). The limiting values for the Sr-modified alloys (i.e. M1S and M6S) are higher than the limiting values for the non-modified alloys. This can be understood in light of the existence of modified smaller silicon particles following the addition of 200ppm Sr. The modification effect will substantially increase the area fraction of the small particles and thus higher limiting values were set for the Sr-modified alloys. Since this study is concerned with the coarsening behavior (i.e. particle area), the average silicon particle area values will be presented with and without applying the adjusting criterion for the sake of comparison and judging this criterion. It should be noted that the values obtained after applying the adjusting criterion are referred to as “adjusted” values.

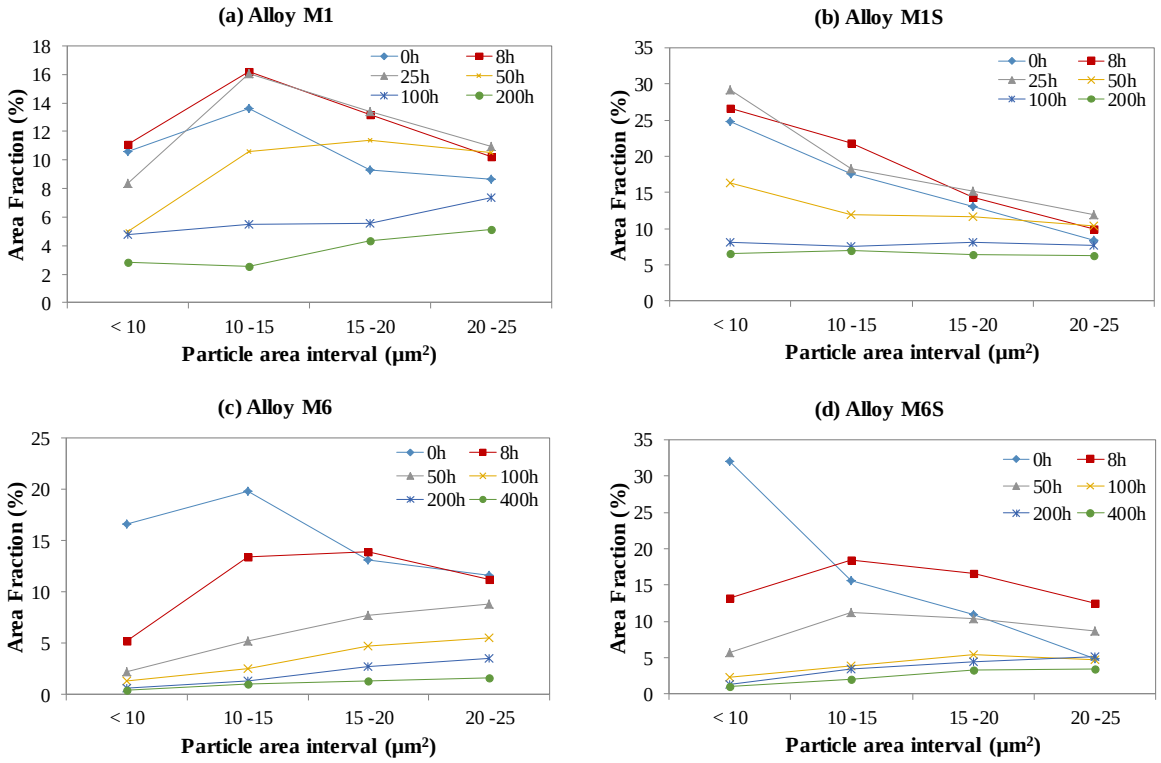

Figure 7.9 Results of sensitivity analyses performed to determine an appropriate area fraction limit as a criterion for omitting very small Si particles in the quantitative analysis of: (a) alloy M1, (b) alloy (M1S), (c) alloy M6, and (d) alloy M6S.

7.2.5 DISTRIBUTION ANALYSIS OF SI PARTICLES

Bar charts, showing results of the quantitative analysis, are presented in Figure 7.10 through Figure 7.15. These bar charts display the distribution of silicon particles for various characteristics in the as-cast condition, after solutionizing at 510°C for 8, 25, 50, 100, and 200 hours for alloys M1 and M1S (354-type base alloys), and after solutionizing at 550°C for 8, 50, 100, 200, and 400 hours for alloys M6 and M6S (356-type alloys). Interesting results regarding the morphological evolution of the eutectic Si particles may be witnessed from these bar charts.

For alloy M1, and referring to Figure 7.10(a), it is clear that the majority (~70%) of eutectic Si particles in the as-cast condition and after solution treatment at 510°C for 8 and 25 hours have equivalent circle diameters lower than 5μm. The addition of 200 ppm Sr increases this count fraction for the same conditions to be ~90%, as can be seen in Figure 7.10(b) for alloy M1S. Also, the count fraction of Si particles, which is lower than 5 μm after solution treatment for 50 hours at 510°C, has increased from ~45% in alloy M1 to around 75% in the Sr-modified M1S alloy. With respect to the equivalent circle diameter, the distribution of Si particles count fractions is largely similar after solution treatment for 100 hours at 510°C for both M1 and M1S alloys; though there is a slight increase of ~7% in the count fraction of Si particles within the range of 5-8 μm in alloy M1S compared to alloy M1. In contrast, for solution treatment at 510°C for 200 hours, the distribution of Si particle count fractions shows noticeable variations according to the state of modification. In the non-modified alloy M1, an increased number of silicon particles having equivalent circle diameters greater than 8 μm is observed, when compared to the Sr-modified M1S alloy. Figure 7.10(a) and Figure 7.10(b) show that almost all eutectic Si particles in the as-cast condition and after solution treatment for 8, 25, and 50 hours at 510°C were very small, with an equivalent circle diameter lower than 8μm; whereas silicon particles exist after 100 and 200 hours of solutionizing were finely distributed over larger intervals of the equivalent circular diameter. In the case of non- and Sr-modified 356-type alloys (M6 and M6S), similar trends were noted, as concluded from Figure 7.10(c), and Figure 7.10(d) regarding the distribution of Si particle count fractions along intervals of the equivalent circular diameter; however, the coarsening behavior was more obvious in these alloys than in the 354-type alloys, owing to their simple chemistry and higher solutionizing temperature and times.

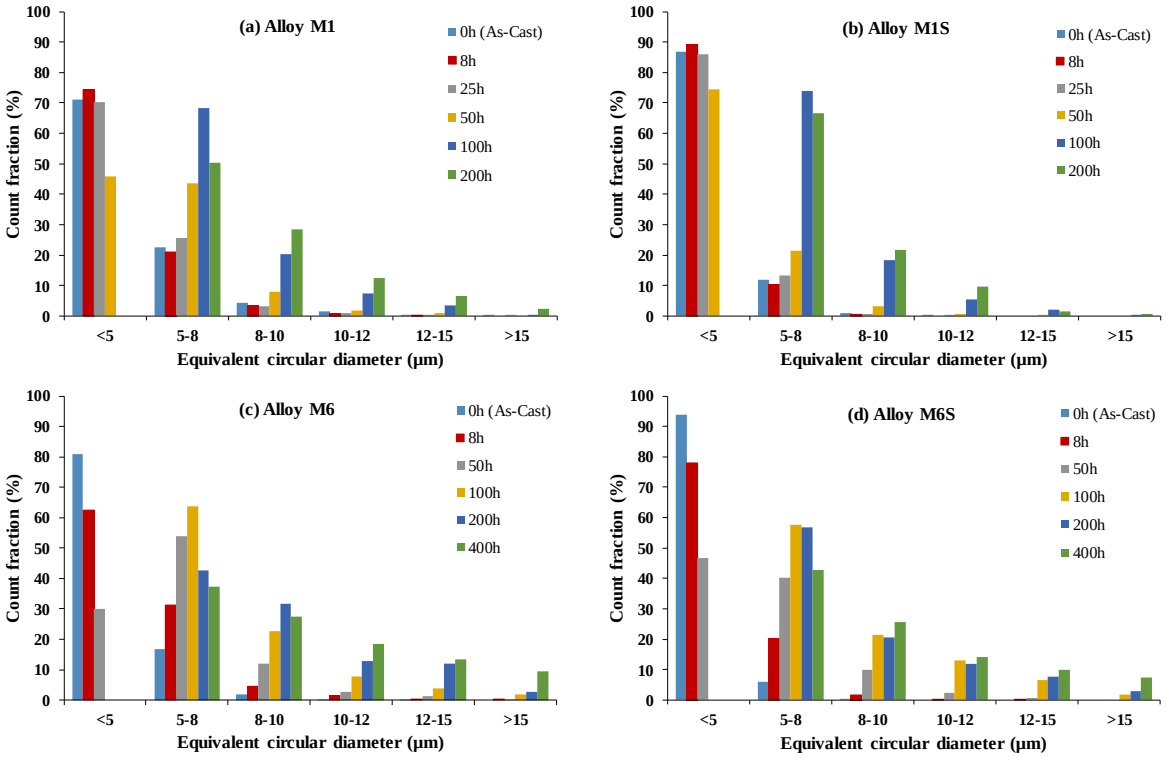

Figure 7.10 The distribution of eutectic Si particles according to the equivalent circular diameter after solution treatment of: (a) alloy M1 at 510°C, (b) alloy M1S at 510°C, (c) alloy M6 at 550°C, and (d) alloy M6S at 550°C.

Figure 7.11 shows the distribution of silicon particles with respect to values of the aspect ratio. The effect of Sr-addition can be clearly observed by comparing Figure 7.11(a) and Figure 7.11(c) with Figure 7.11(b) and Figure 7.11(d). Due to the rapid rate of spheroidization of the Si particles in the Sr-modified alloys, the majority of Si particles in alloys M1S and M6S in all solution treated conditions, and even in the as-cast condition, display aspect ratios in the range 1-2 which demonstrate the more spherical nature of the Si particles; whereas aspect ratio values for the non-modified alloys M1 and M6 show a wide distribution across the presented intervals of the aspect ratio. The aspect ratio in the as-cast conditions for both non-modified alloys M1 and M6 starts with values of three and more; which indicates the plate-like (elongated) nature of the Si particles in these conditions. However, after solutionizing for a considerable amount of time, these particles start to

spheroidize, at lower rates than those experienced by the Sr-modified alloys (M1S and M6S). In order to emphasize the spheroidization behavior of Si particles in the alloys studied, an elaborative analysis focusing on the sphericity and roundness percentages of silicon particles is provided hereafter.

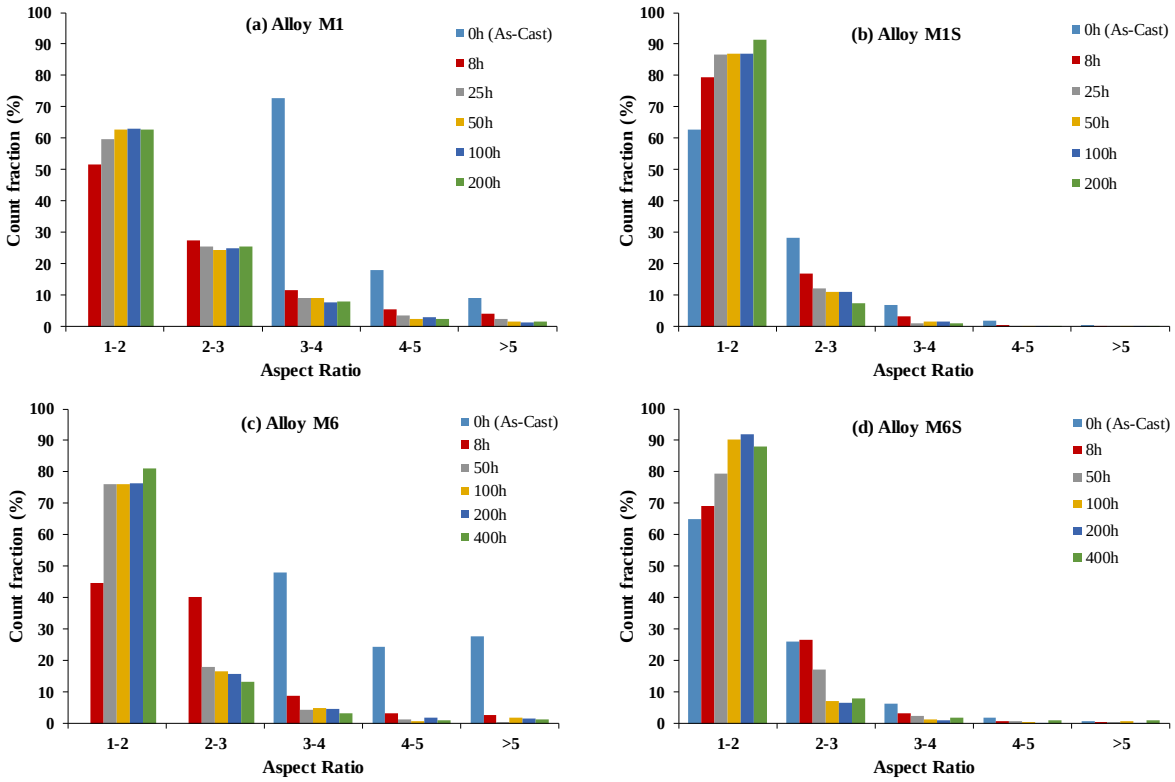

Figure 7.11 The distribution of eutectic Si particles according to the aspect ratio after solution treatment of: (a) alloy M1 at 510°C, (b) alloy M1S at 510°C, (c) alloy M6 at 550°C, and (d) alloy M6S at 550°C.

Figure 7.12 through Figure 7.15 present the distribution of the silicon particles as a function of their sphericity and roundness values. Figure 7.12 shows that Si particles with plate-like shape and very angular edges exist mainly within the as-cast structure of the non-modified 354-type alloy M1. Furthermore for the same alloy (M1), less than ~10% of Si particles exist with the same as-cast morphology after solutionizing at 510°C for 8 hours. Spherical eutectic particles started to appear after solutionizing of the same alloy (M1) for 8

hours and gradually increased to reach the maximum count fraction of spheroidal particles after 200 hours at 510°C. The microstructures corresponding to these two conditions of the non-modified alloy M1 (i.e. as-cast and solutionized for 8 hours), shown in Figure 7.1(a) and Figure 7.1(b), do not show any silicon particles which are spherical in shape. Moreover, the edges of the Si particles in the as-cast condition are not included in the well-rounded range, so that this interval of roundness percentage is free from non-modified as-cast silicon particles. As expected, increasing the solutionizing time improves the roundness and sphericity values of these non-modified Si particles.

Figure 7.13 emphasizes the increased rate of Si particle spheroidization and rounding of the particle edges in the Sr-modified alloy M1S compared to non-modified alloy M1. The majority of silicon particles in the M1S alloys exist in a spherical form with more rounded edges, as can be seen by comparing Figure 7.13 with Figure 7.12 for alloyM1. However, it should be noted that, a considerable fraction (~20%) of modified Si particles in the as-cast condition exhibit very low sphericity values (less than 30%) which may be attributed to the interconnected network of silicon particles in the form of coral-like morphology. The same observations and comments may be made with respect to the spheroidization and rounding of the Si particle edges in the non-modified and Sr-modified 356-type alloys (M6 and M6S) shown in Figure 7.14 and Figure 7.15, respectively.

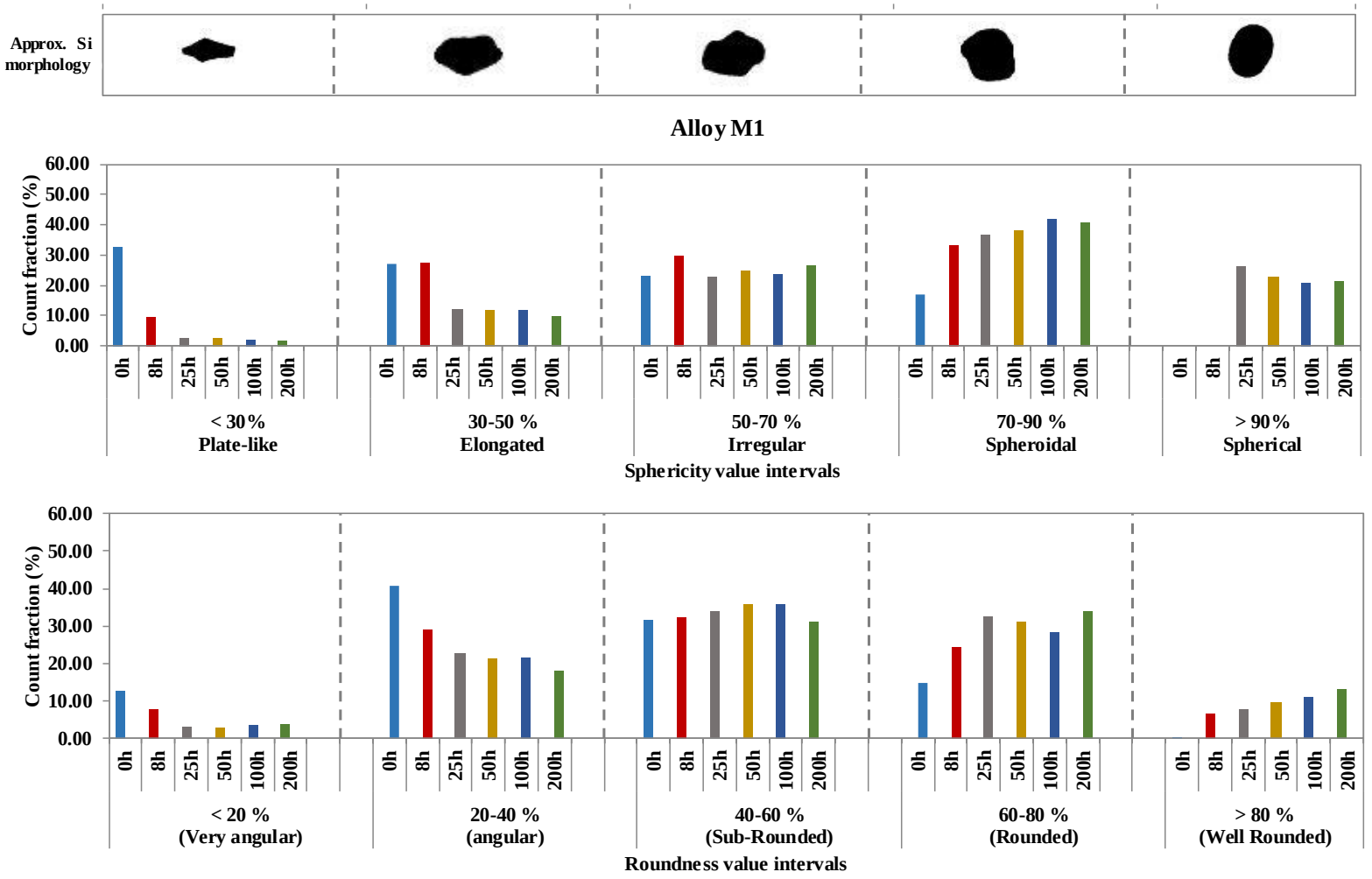

Figure 7.12 The distribution of eutectic Si particles according to shape characteristics after solution treatment of the non-modified base alloy (M1) at 510°C for 0(as-cast), 8, 25, 50, 100, and 200 hours.

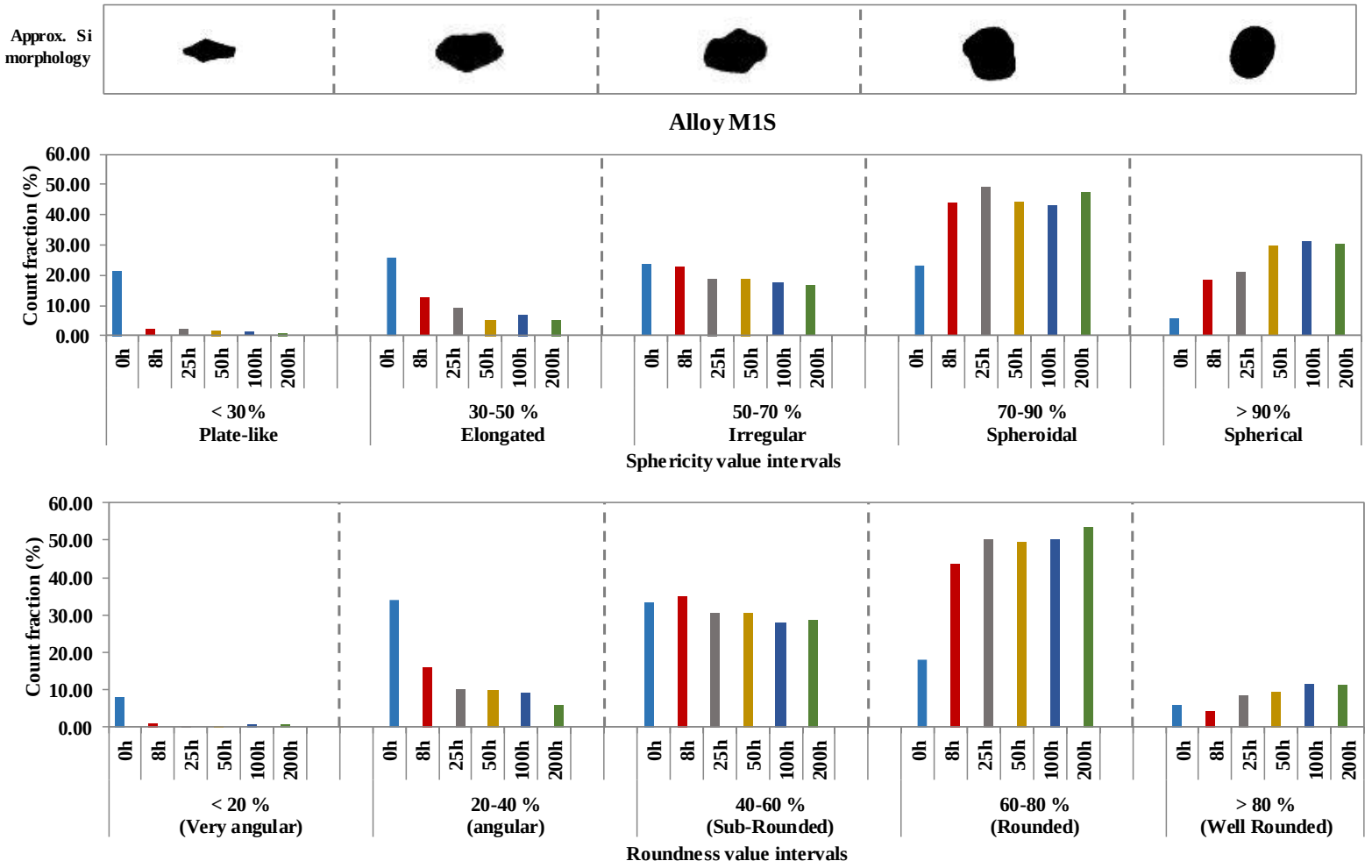

Figure 7.13 The distribution of eutectic Si particles according to shape characteristics after solution treatment of the Sr-modified base alloy (M1S) at 510°C for 0(as-cast), 8, 25, 50, 100, and 200 hours.

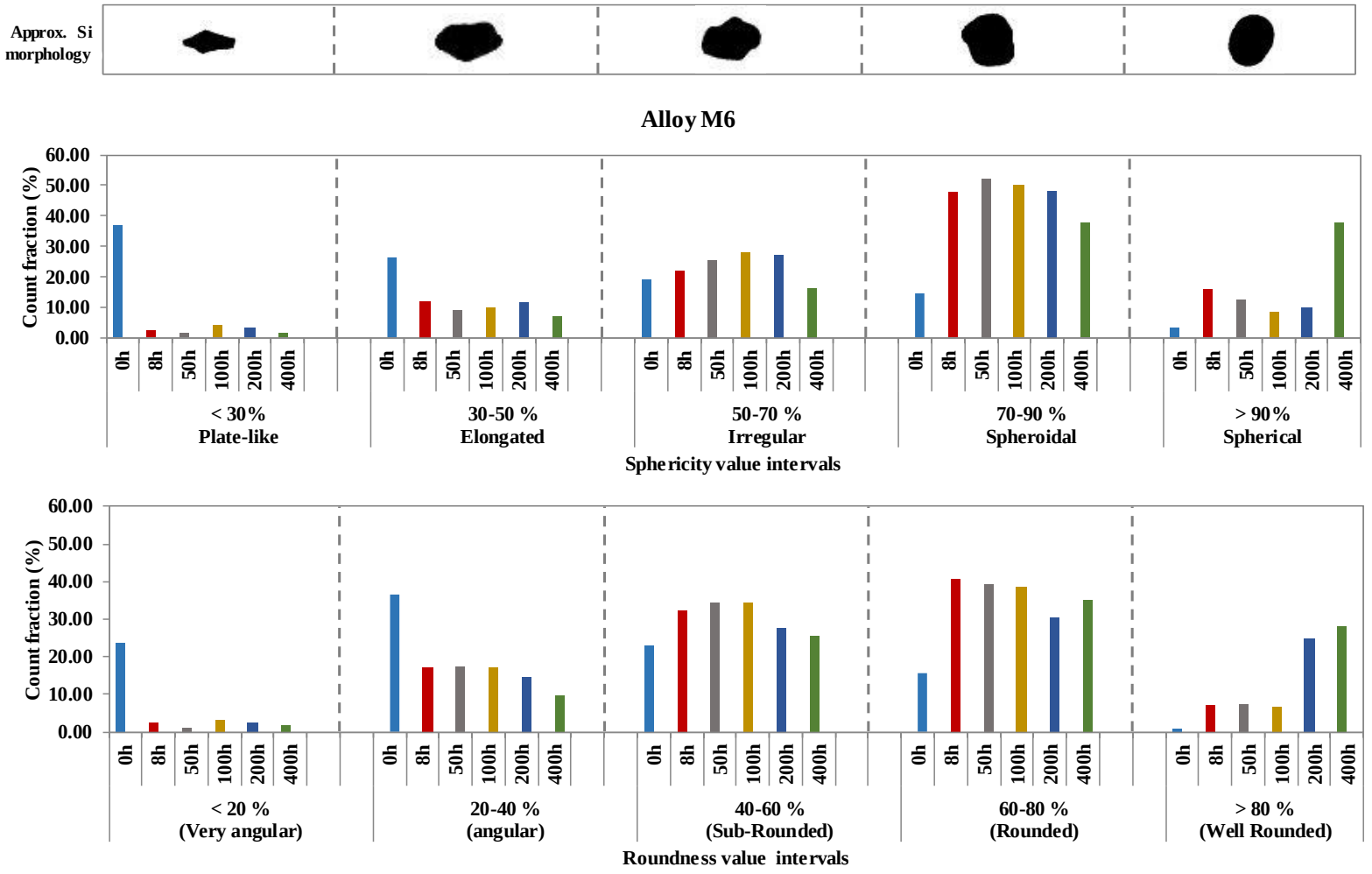

Figure 7.14 The distribution of eutectic Si particles according to shape characteristics after solution treatment of the non-modified 356-type alloy (M6) at 550°C for 0(as-cast), 8, 50, 100, 200, and 400 hours.

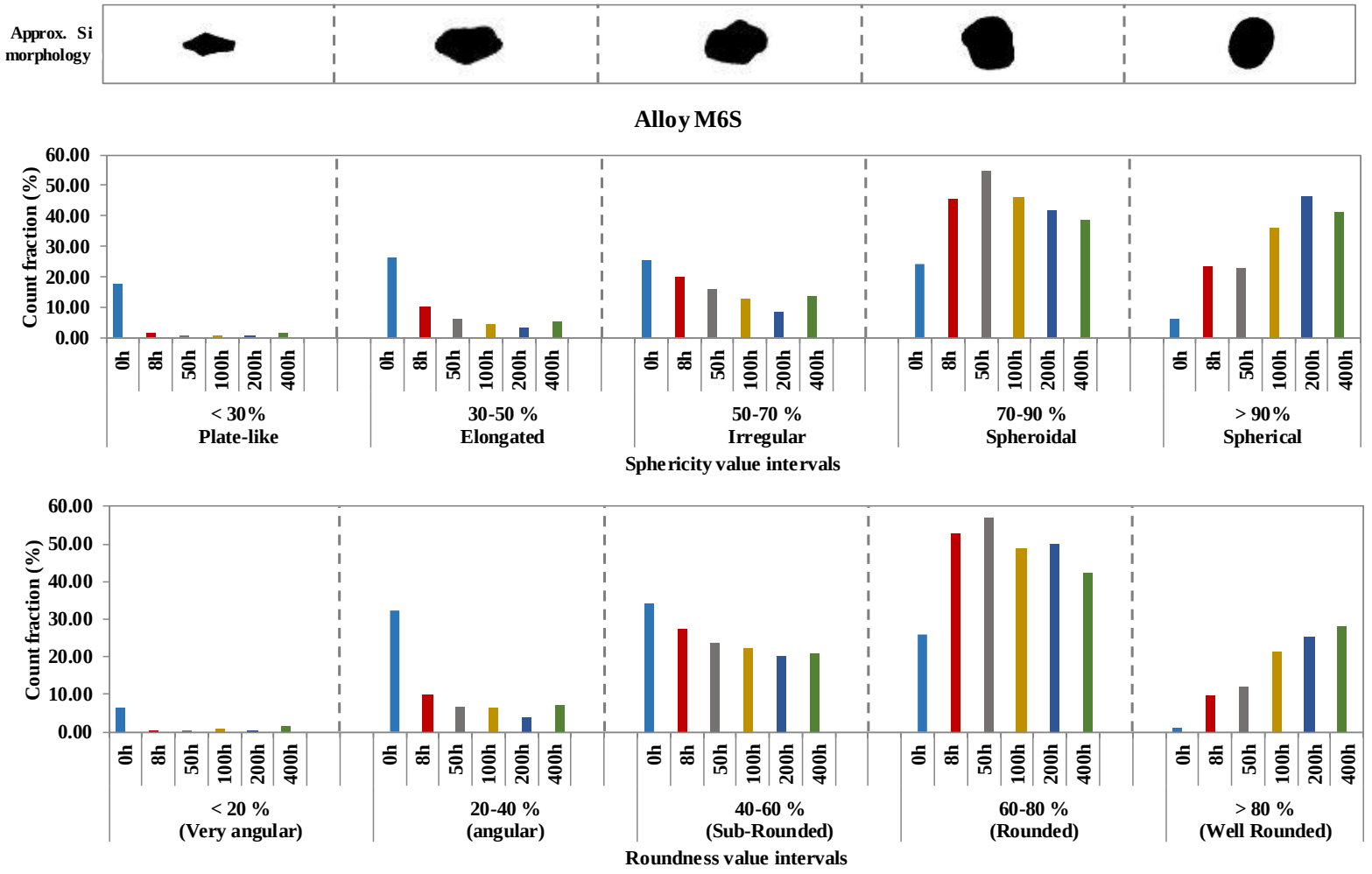

Figure 7.15 The distribution of eutectic Si particles according to shape characteristics after solution treatment of the Sr-modified 356-type alloy (M6S) at 550°C for 0(as-cast), 8, 50, 100, 200, and 400 hours.

7.2.6 AVERAGE SI PARTICLE CHARACTERISTICS

Table 7.2 and Figure 7.16 and Figure 7.17 show the average values of the eutectic silicon particle characteristics in alloys M1, M1S, M6, and M6S. These average values match the results and conclusion obtained from the distribution analysis regarding the coarsening, spheroidization, and values of the aspect ratio.

The density values of Si particles, listed in Table 7.2, show an inverse relation between the number of silicon particles and solution treatment time. This is a reflection of the increased size of the Si particles since the total volume of silicon remains constant and hence the distance between the silicon particles will increase due to the reduced number of Si particles. The increased distance between Si particles will make available larger continuous areas of the ductile α-Al matrix, which may lead to enhancement in ductility values for extended solution treatment conditions.

Figure 7.16(a) shows that for the non-modified alloy (M1), the average particle area reduces during the first 25 hours of solutionizing at 510°C. This reduction in the average particle area in the non-modified M1 alloy is probably due to the fragmentation process through which large plates of silicon are broken into smaller fragments. However by further solutionizing at the same temperature (i.e. 510°C), Si particles start to coarsen and the average particle area increases considerably, from ~ 14.9 μm after 25 hours of solutionizing to 37.8 μm with 200 hours of solutionizing. As stated previously in the qualitative analysis, the coarsening process takes place through both Ostwald ripening and particle agglomeration mechanisms, which are active at the same time. By applying the adjusting criterion for Si particle size, the same size evolution trend can be observed for the alloy M1,

however, higher average values of particle area may be attained due to omitting tiny particles from the data obtained after solutionizing for 50, 100, and 200 hours. Applying the criterion changed the average particle area as follows: (i) with 50 hours solutionizing, the value increased from 18.9 μm to 27.6 μm (46%), (ii) after 100 hours solutionizing, the value increased from 28.3 μm to 42 μm (48%), and (iii) after 200 hours, the value increased from 37.8 μm to 61.5 μm (63%). The adjusted values appear to be more representative of the coarsening behavior, as the micrographs in Figure 7.1 show dramatic changes in the size of the Si particles, as well as the fact that in studying the coarsening behavior, it is more reasonable to include growing particles and omit dissolving ones from the analysis.

The average Si particle area of the Sr-modified alloy M1S, shown in Figure 7.16(a), does not show any reduction in size after 8 hours of solution treatment. This is because the silicon particles in the as-cast modified alloy, with their fibrous and coral-like morphology, require only few minutes to be totally fragmented, as previously mentioned in the qualitative analysis section and shown in Figure 7.6. Thus, the Si particles start to coarsen earlier than the non-modified Si particles in alloy M1. The average particle area increases from 3.59 μm in the as-cast condition to 33.4 μm after solutionizing for 200 hours, almost linearly. By applying the adjusting criterion, the tiny particles are removed from the data obtained after 100 and 200 hours of solution treatment. The average particle area increases from 22.4 μm to 36.2 μm (61.6%) after 100 hours and from 33.4 μm to 47.3 μm (i.e. 42%) after 200 hours of solution treatment. Results of the average particle area obtained for non- and Sr-modified 354-type alloys emphasize the already established finding on the higher coarsening rate in the non-modified alloys compared to the Sr-modified alloys.[243] As the

non-modified silicon particles exist in a large range of sizes, this diversity in size may provide a larger driving force for their coarsening.[243]

In addition, it is a well-established fact that the spheroidization rate in the Sr-modified alloys is higher than the rate obtainable in the non-modified alloys. This finding is also valid for the alloys investigated in this study. The aspect ratio (equal to unity for a sphere), sphericity, and roundness are various parameters that may be availed of using an optical microscope-image analysis system, to provide a measure of the spheroidization of the particles of a phase being examined, in this case, the Si phase. Thus, any reduction in the aspect ratio associated with enhancement in the sphericity would indicate progress in the spheroidization of the Si particles. The aspect ratio drops significantly from ~4 in the as-cast Sr-free alloy (M1) to ~2.4 after solutionizing at 510°C for 8 hours, and continues to decrease at a slower rate with further solution treatment to reach ~2 after solutionizing up to 200 hours, as can be seen from Figure 7.16(b). On the other hand, the aspect ratio of the as-cast Sr-modified alloy (M1S) is ~2; this value is reduced after 8 hours of solutionizing at 510°C to ~1.65 which represents the maximum reduction achieved in this time; then the aspect ratio decreases slowly to reach 1.45 after 200 hours of solutionizing at the same temperature.

The values of the sphericity and roundness percentages of 354-type alloys are plotted in Figure 7.16(c) and Figure 7.16(d). The Sr-modified M1S alloy is always having higher roundness and sphericity values than those of the non-modified M1 alloy for all conditions studied. The sphericity percentage, Figure 7.16(c), increases rapidly in the first 25 hours of solution treatment for the non-modified M1 alloy because of the active

fragmentation process during this period of solutionizing; however, the values barely change with further increase in the solutionizing time. This means that the fragmentation process is completely attained in the first 25 hours of solutionizing. With respect to the Sr-modified M1S alloy, the sphericity percentage shows rapid increase after solutionizing the as-cast alloy, then continues to increase but at a lower rate, up to 50 hours of solution treatment, and remains almost unchanged thereafter, up to 200 hours.

Figure 7.16(d) shows that the curves of roundness percentage for M1 and M1S alloys are almost parallel, with an additional 10% increase exhibited by the Sr-modified M1S alloy. The values increase rapidly from the as-cast condition to the first solutionized condition after 8 hours, and then increase very slowly up to 200 hours of solutionizing at 510°C. By examining 356-type alloys (i.e. M6 and M6S), observations similar to those of the 345-type alloys can be made regarding the morphological evolution of the eutectic Si particles as displayed in Figure 7.17.

It is important to mention that values of the aspect ratio do not appear to approach unity, which represents completely spherical particles, so that 100% sphericity is not achievable even in the Sr-modified alloys (M1S and M6S), after 200 hours solution treatment for the 354-type alloy (M1S), and 400 hours for the 356-type alloy (M6S). This observation may be attributed to the active agglomeration mechanism of coarsening at prolonged durations of solution treatment; this mechanism produces an unidentifiable morphology, as shown in Figure 7.18, due to the agglomerated Si particles, and hence the sphericity and aspect ratio values never approach 100% or unity, respectively.

Table 7.2 Characteristics of eutectic Si particles in studied alloys (*Average value, ** standard deviation)

Alloy code	Solutionizing time (hr)	Particle area (μm^2)	Sphericity (%)	Roundness (%)	Aspect ratio	Density (particles/mm^2)
M1	0 (As-cast)	μ*= 19.00	μ= 44.00	μ= 36.60	μ= 3.87	μ= 18000
		σ**= 19.60	σ= 23.10	σ= 16.70	σ= 1.08	
	8	μ= 17.30	μ= 66.90	μ= 50.00	μ= 2.31	μ= 9800
		σ= 16.00	σ= 25.10	σ= 22.10	σ= 1.27	
	25	μ= 14.90	μ= 74.20	μ= 51.70	μ= 2.10	μ= 8200
		σ= 14.80	σ= 20.10	σ= 19.20	σ= 1.03	
	50	μ= 27.60	μ= 73.20	μ= 52.50	μ= 2.02	μ= 6300
		σ= 19.40	σ= 19.80	σ= 19.00	σ= 0.95	
	100	μ= 42.00	μ= 73.50	μ= 52.90	μ= 2.01	μ= 4400
		σ= 29.40	σ= 19.00	σ= 18.40	σ= 0.91	
	200	μ= 61.50	μ= 74.10	μ= 54.60	μ= 1.99	μ= 3400
		σ= 36.80	σ= 18.30	σ= 19.10	σ= 0.90	
M1S	0 (As-cast)	μ= 3.59	μ= 52.70	μ= 46.50	μ= 1.96	μ= 34000
		σ= 6.28	σ= 23.90	σ= 20.90	σ= 0.78	
	8	μ= 6.11	μ= 72.20	μ= 57.00	μ= 1.69	μ= 18000
		σ= 6.59	σ= 18.40	σ= 15.90	σ= 0.60	
	25	μ= 10.50	μ= 75.60	μ= 61.50	μ= 1.56	μ= 10000
		σ= 9.99	σ= 18.40	σ= 15.80	σ= 0.56	
	50	μ= 16.50	μ= 79.30	μ= 62.30	μ= 1.56	μ= 7500
		σ= 16.00	σ= 18.20	σ= 16.20	σ= 0.53	
	100	μ= 36.20	μ= 79.20	μ= 63.40	μ= 1.57	μ= 5400
		σ= 24.00	σ= 17.70	σ= 16.50	σ= 0.64	
	200	μ= 47.30	μ= 80.30	μ= 64.20	μ= 1.5	μ= 4400
		σ= 28.10	σ= 16.10	σ= 14.90	σ= 0.467	
M6	0 (As-cast)	μ= 14.30	μ= 41.60	μ= 36.30	μ= 2.44	μ= 27000
		σ= 11.70	σ= 22.70	σ= 19.00	σ= 1.53	
	8	μ= 21.50	μ= 72.50	μ= 56.30	μ= 1.83	μ= 1200
		σ= 17.30	σ= 18.00	σ= 17.70	σ= 1.53	
	50	μ= 33.70	μ= 72.90	μ= 56.40	μ= 1.73	μ= 7000
		σ= 22.80	σ= 16.30	σ= 16.90	σ= 0.81	
	100	μ= 48.00	μ= 78.20	μ= 64.90	μ= 1.78	μ= 3500
		σ= 48.70	σ= 18.10	σ= 24.20	σ= 0.98	
	200	μ= 69.10	μ= 79.20	μ= 63.80	μ= 1.79	μ= 2700
		σ= 44.10	σ= 18.30	σ= 24.10	σ= 1.12	
	400	μ= 85.60	μ= 81.00	μ= 66.80	μ= 1.71	μ= 3100
		σ= 63.70	σ= 18.80	σ= 22.70	σ= 1.15	
M6S	0 (As-cast)	μ= 6.82	μ= 54.90	μ= 46.30	μ= 1.88	μ= 44000
		σ= 6.05	σ= 23.20	σ= 17.50	σ= 0.81	
	8	μ= 15.30	μ= 75.50	μ= 62.20	μ= 1.53	μ= 17000
		σ= 11.60	σ= 17.40	σ= 15.20	σ= 0.56	
	50	μ= 28.40	μ= 78.30	μ= 64.80	μ= 1.54	μ= 7000
		σ= 20.90	σ= 15.2	σ= 14.70	σ= 0.90	
	100	μ= 42.60	μ= 82.70	μ= 67.50	μ= 1.53	μ= 5100
		σ= 40.30	σ= 15.60	σ= 17.80	σ= 0.74	

	200	μ= 60.00	μ= 85.80	μ= 69.90	μ= 1.45	μ= 3800
		σ= 43.70	σ= 14.40	σ= 17.10	σ= 0.58	
	400	μ= 77.90	μ= 82.60	μ= 69.00	μ= 1.56	μ= 4100
		σ= 65.00	σ= 18.00	σ= 21.00	σ= 0.93	

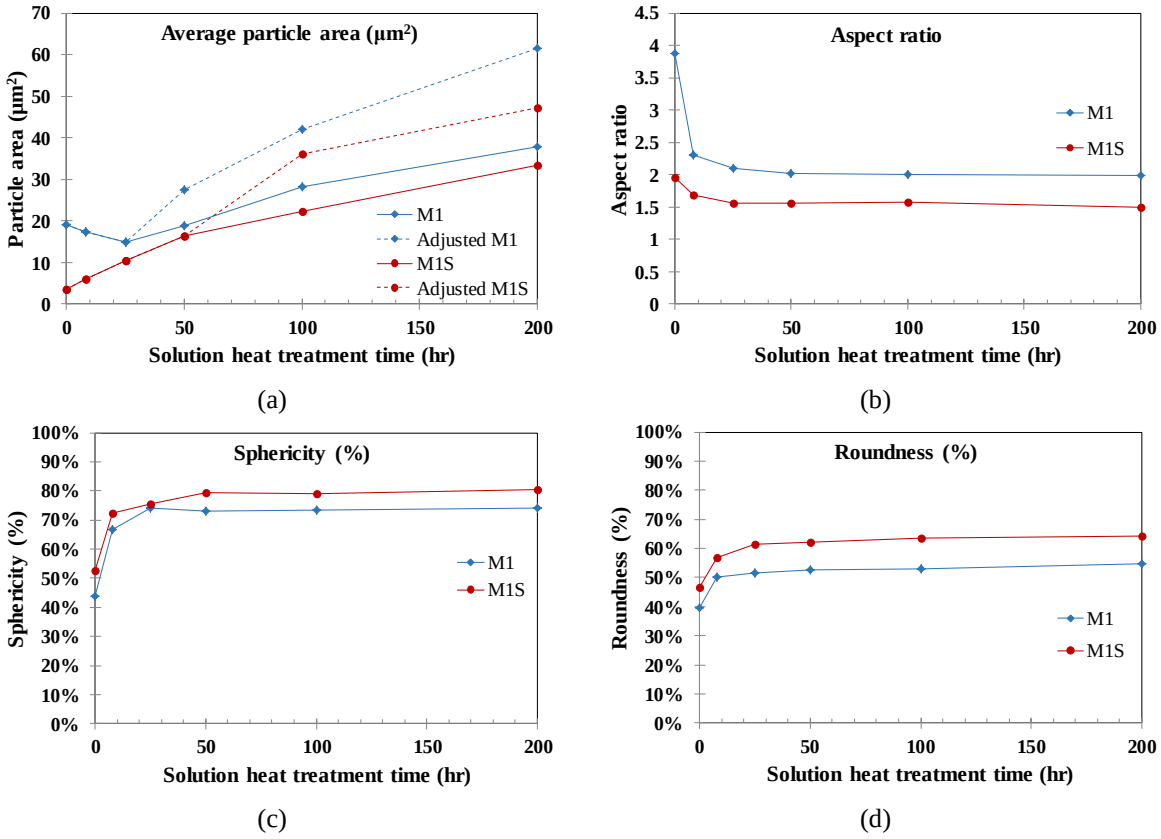

Figure 7.16 Average Si particle characteristics in M1 and M1S alloys after solution treatment at 510°C for 0(as-cast), 8, 25, 50, 100, and 200 hours: (a) particle area, (b) aspect ratio, (c) sphericity (%), and (d) roundness (%).

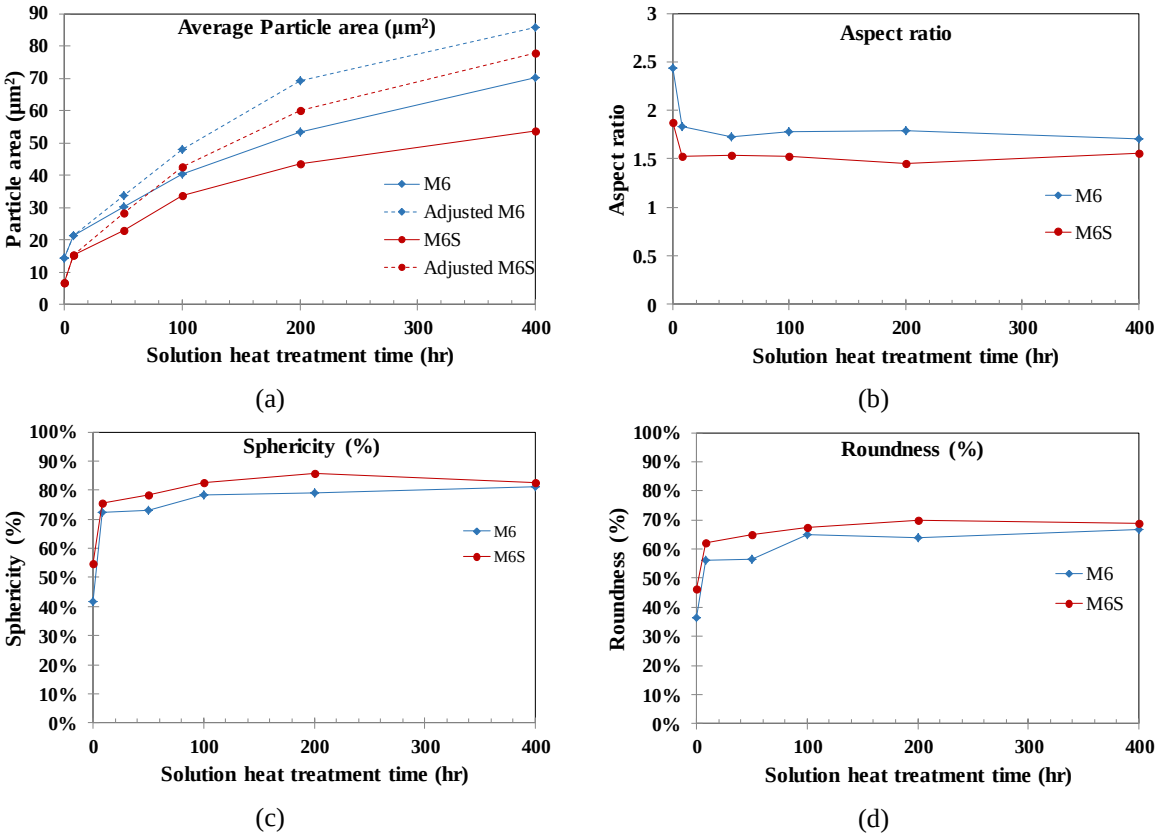

Figure 7.17 Average Si particle characteristics in M6 and M6S alloys after solution treatment at 550°C for 0 (as-cast), 8, 50, 100, 200, and 400 hours: (a) particle area, (b) aspect ratio, (c) sphericity (%), and (d) roundness (%).

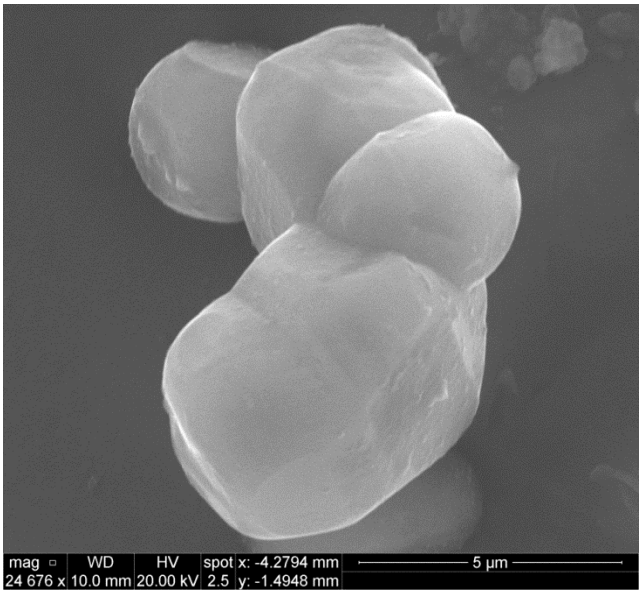

Figure 7.18 Coarsening of Si particles by agglomeration in M6S alloy after solution treatment at 550°C for 50 hours.

7.3 DISCUSSION ON THE COARSENING BEHAVIOR

It has been reported previously by Shivkumar et al.[243] that the coarsening rate of Si particles in non-modified (Sr-free) alloys is higher than that in Sr-modified alloys. This observation is evident for the alloys studied, as shown in Figure 7.16(a) and Figure 7.17(a), which plot the average values of the Si particle area as a function of solution time. Thus, an in-depth analysis of the coarsening behaviour will be of interest, particularly, for prolonged solutionizing times of up to 400 hours. Lifshitz, Slyozov, and Wanger developed a coarsening model also known as the LSW model, given by Equation 7.1.

$$\bar{r}^3 - \bar{r}_0^3 = K_{LSW} * t \qquad \textbf{(7.1)}$$

where $\bar{r}^3$ denotes the final average radius, $\bar{r}_0^3$ is the average radius at time (t)=0, and K_{LSW} is the coarsening rate constant.

The model is commonly used to describe the coarsening behavior in Sr-modified Al-Si alloys, in order to ensure that the coarsening process is in progress rather than fragmentation in non-modified alloys. For this reason, it is recommended to apply the model after solution treatment has been carried out for a considerable period, to make sure that the fragmentation process is ended and the coarsening process is active. Thus in the current study, the LSW model will be applied to both non- and Sr-modified alloys, starting with the 8 hours solution heat- treated condition, to investigate the validation of the model to describe the coarsening behavior in non-modified alloys.

By plotting the cube of the average equivalent radius of Si particles as a function of the solutionizing time (t), a linear relation can be fitted for the data obtained for both the Sr-modified and non-modified alloys before and after applying the adjusting criterion. These plots are shown in Figure 7.19 for the four alloys studied. The linear relation proves that the LSW model is valid for the alloys, even for the non-modified ones. The slope of each line in Figure 7.19 gives the coarsening rate constant (K) which is written in Equation 7.1 as K_{LSW}. Thus, the K-values are determined empirically in this study for all alloys under study. In Figure 7.19, each plot contains two sets of data for the same alloy, the first set is for the raw data obtained from the quantitative analysis of Si particles and the other set represents the adjustable data obtained after applying the adjusting criteria. The adjusted values as predicted give higher values of K because of higher values of the equivalent particle area obtained after applying the adjusting criterion. Once more, it is evident that the values of the coarsening rate constant (K) are generally higher in the case of non-modified alloys, Figure 7.19(a) and Figure 7.19(c), compared to the Sr-modified alloys, Figure 7.19(b) and Figure 7.19(d). Along with the K-values, the regression values "R^2" are also noted in the plots, to indicate the goodness of the linear fitting; all regression values are greater than ~0.95, which means accurate fitting.

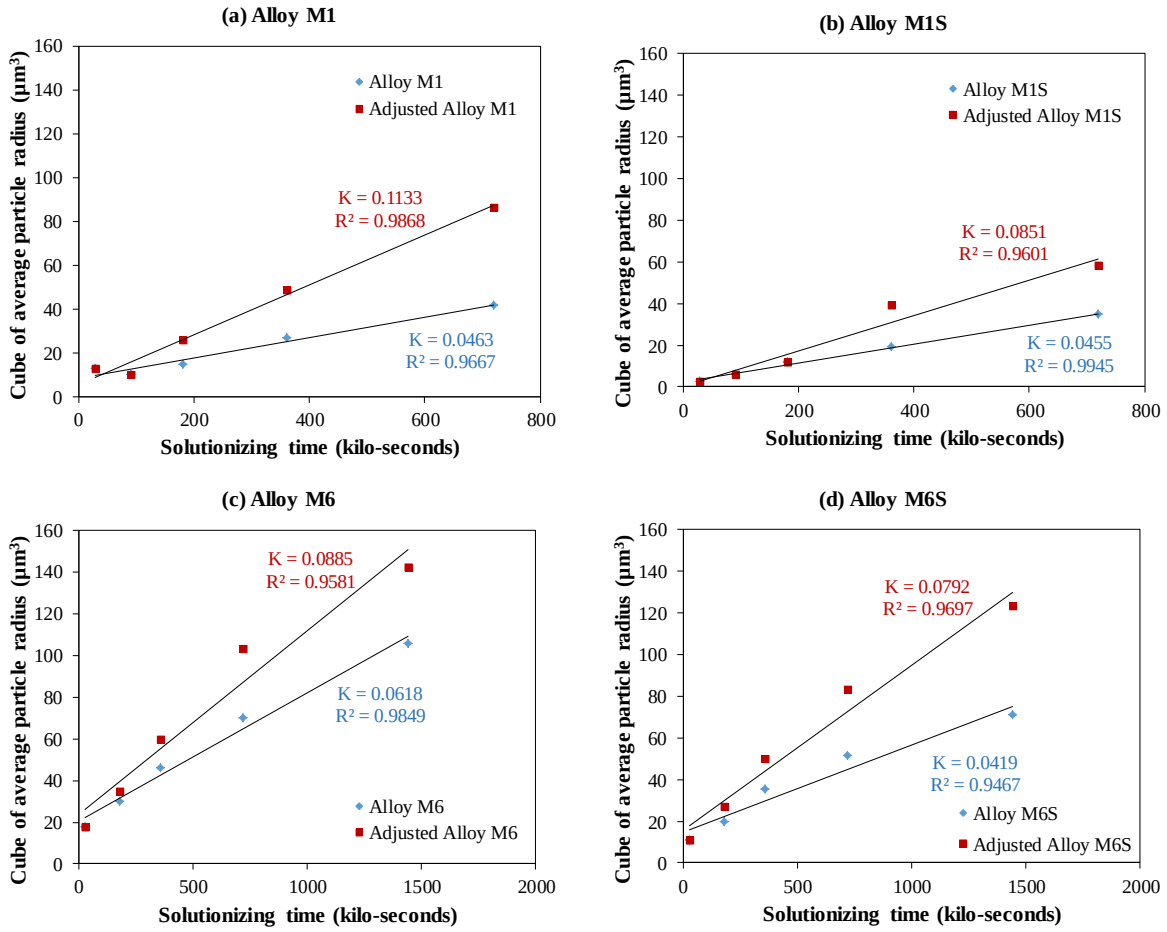

Figure 7.19 Plots of the cube average particle radius ($\bar{r}^3$) versus the solution treatment time for: (a) alloy M1, (b) alloy M1S, (c) alloy M6, and (d) alloy M6S.

The empirical values of the K constant can be used in the LSW model (i.e. Equation 7.1) in order to develop predicted values of the equivalent particle radius and hence to compare predicted values with the experimentally obtained ones in order to verify the assumption of linearity. Figure 7.20 shows predicted and experimental values of the average Si particle radius. The experimental data shows that it has a fairly uniform deviation from the predicted data and therefore the assumption of linearity is correct.

However for alloy M1, the experimental value of the equivalent radius in the 8 hours solutionized condition shows a large difference, of 15% and 24 % with the predicted values for the raw data and adjusted data (i.e. after applying the adjusting criterion), respectively. This disagreement mainly results from the fact that the coarsening process is not the active process in the non-modified M1 alloy after 25 hours of solutionizing, as the fragmentation process is still active. This was also shown to be the case previously, when discussing the average Si particle characteristics; it was stated that fragmentation in the non-modified M1 alloy was completed after solution treatment was carried out for more than 25 hours (i.e. 50 hours and above) at 510°C, as evidenced by the sphericity percentage plot presented in Figure 7.16(c); This conclusion is also supported by the fact that the average particle area in the non-modified alloy M1, Figure 7.16(a), shows a reduction in the first 25 hours of solutionizing due to the fragmentation process.

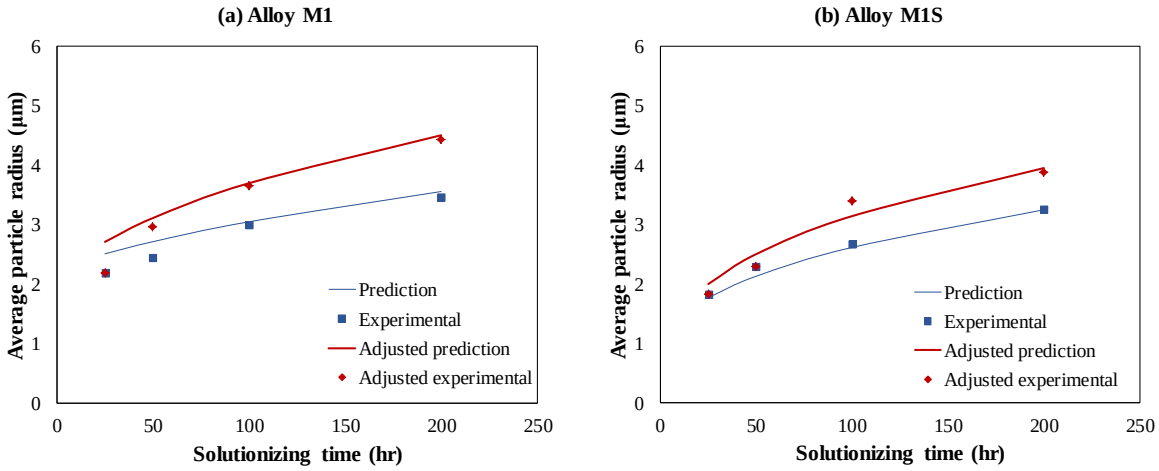

(a) (b)

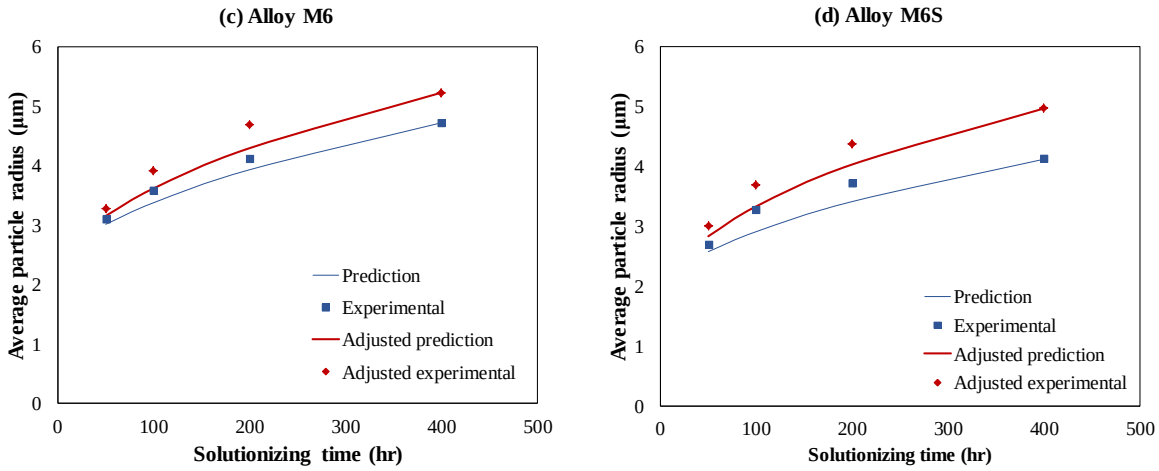

(c) (d)

Figure 7.20 LSW coarsening model predictions (lines) compared with experimental data (markers) for solution treated conditions of: (a) alloy M1, (b) alloy M1S, (c) alloy M6, and (d) alloy M6S.

Thus, in order to apply the LSW model to non-modified alloys, a higher initial time should be selected than the initial time in the Sr-modified alloys to be certain that the fragmentation process is over and coarsening behavior is active. On the other hand, the alloys M1S, M6, and M6S show good agreement between predicted and experimental data, even at the starting points of 25 h for the 354-type alloy and 50 h for the 356-type alloys, as well as at the ending points corresponding to 200 h for the 354-type alloy, and 400 h for the 356-type alloy.

PART II- EFFECT OF MORPHOLOGICAL CHANGES OF EUTECTIC SILICON PARTICLES ON THE TENSILE PROPERTIES

The tensile test data obtained at both ambient and elevated temperatures are presented in this part of the chapter, in order to investigate the effect of the changes in morphology of the eutectic silicon particles on the tensile properties. The elevated temperature tensile testing was carried out at 250°C. The soaking time of the tensile bars at the testing temperature, was kept to a minimum of 5 minutes in order to minimize the precipitation process during this soaking time before carrying out the tensile test. This was done in order to investigate the effect of Si particle morphology, solely, without the precipitation effect.

7.4 ROOM TEMPERATURE TENSILE PROPERTIES

The data describing the ambient-temperature tensile properties of 354-type alloys (M1 and M1S) in the as-cast and as-quenched (solutionized) conditions are presented in Table 7.3 and Figure 7.21(a) and Figure 7.21(b); whereas those of the 356-type alloys (M6 and M6S) for the same conditions are presented in Table 7.4 and Figure 7.21(c) and Figure 7.21(d). It is obvious from Figure 7.21 that the solution treatment resulted in several variations in the mechanical properties of these alloys.

Figure 7.21 presents the average UTS, YS, and elongation percent to fracture values as a function of the solution treatment time; the as-cast condition corresponds to the 0 hour solution time. For the 354-type alloys shown in Figure 7.21 (a) and Figure 7.21(b), the UTS shows a substantial increase after solution treatment for 8 hours at 510°C, compared to the as-cast condition for both the non-modified M1 and Sr-modified M1S alloys; whereas the

YS remains almost unchanged at a value of 206 MPa in alloy M1, and barely increases from 194.4 MPa in the as-cast condition to reach 198 MPa after 8 hours of solutionizing at 510°C in the Sr-modified M1S alloy. With further increase in the solution treatment time up to 200 hours, the UTS and YS of alloy M1 fluctuate around 325 MPa and 195 MPa, respectively; while the values of UTS and YS for alloy M1S fluctuate around slightly higher values of 335 and 206 MPa, respectively. The solution treatment of M1S alloy for 50 hours at 510°C results in a considerable increase in both UTS and YS, reaching values of 360.5 MPa and 231.2 MPa, respectively.

Regarding the effect of solution treatment time on ductility values, it is evident from Figure 7.21(a) and Figure 7.21(b) that ductility values of M1 and M1S alloys improve significantly by applying solution treatment to the as-cast structure; this enhancement continues after solutionizing for 8 hours at 510°C but at slower rates. The ductility of the non-modified M1 alloy shows a slight reduction after solutionizing for prolonged duration of 200 hours compared to the ductility of the same alloy solutionized only for 100 hours at the same temperature of 510°C (cf. 6.6% and 7.8% after 100 h).

The ambient-temperature tensile properties of 356-type M6 and M6S alloys are listed in Table 7.4 and plotted in Figure 7.21(c) and Figure 7.21(d). Both alloys show the same trend in strength variation for both UTS and YS. From Figure 7.21(c) and Figure 7.21(d), it can be observed that solution treatment for 8 hours for M6 and M6S alloys enhances UTS and YS. In the case of M6 alloy, the enhancement in strength (UTS and YS) halts with further solution treatment (longer than 8 hours), while a reduction in strength is observed for solution times longer than 50 hours. For the Sr-modified M6S

alloy, however, the improvement in strength values continues after solutionizing for 8 hours, reaching maximum values of UTS and YS after solution treatment for 50 hours at 550°C. The strength values begin to deteriorate thereafter for longer periods of solution treatment (i.e. 100, 200, and 400 hours).

The ductility behavior is also similar in the non-modified M6 and Sr-modified M6S alloys. Ductility values improve significantly after solution treatment for 8 hours at 550°C compared to the ductility values in the as-cast condition for both M6 and M6S alloys. The ductility of M6 alloy remains constant between 8 and 50 hours of solutionizing, followed by further enhancement to achieve a peak value of 9.7 % after 100 hours of solution treatment and remains almost constant up to 200 hours. On the other hand, ductility values of M6S alloy show a continuous enhancement up to 50 hours of solutionizing where the ductility reaches its peak value of 10.5%. The longest duration of solution treatment (i.e. 400 hours) results in reducing the ductility values of both M6 and M6S alloys to 7.6, and 8.3%, respectively.

Table 7.3 Ambient-temperature tensile properties (T4) of M1 and M1S alloys

Solution treatment time (hr)	Non-modified 354-type alloy (M1)			Sr-modified 354-type alloy (M1S)		
	UTS (MPa)	YS (MPa)	% El	UTS (MPa)	YS (MPa)	% El
As-cast	259.5 ± 10.3	206.9 ± 9.9	1.1 ± 0.3	260.9 ± 0.3	194.4 ± 8.0	1.6 ± 0.2
8	328.3 ± 10.4	206.0 ± 7.4	4.5 ± 0.5	325.7 ± 6.5	198.0 ± 10.8	5.6 ± 0.3
25	312.7 ± 9.9	192.2 ± 9.4	5.0 ± 0.3	318.9 ± 1.9	184.1 ± 6.1	6.7 ± 0.1
50	316.1 ± 6.8	186.0 ± 2.2	6.5 ± 0.4	360.5 ± 5.4	231.2 ± 9.7	6.5 ± 0.4
100	343.1 ± 5.1	198.5 ± 5.2	7.8 ± 0.5	331.4 ± 9.5	217.8 ± 8.9	6.9 ± 0.5
200	322.5 ± 6.5	191.3 ± 5.0	6.6 ± 0.4	328.7 ± 10	196.3 ± 9.4	7.1 ± 0.8

Table 7.4 Ambient-temperature tensile properties (T4) of M6 and M6S alloys

Solution treatment time (hr)	Non-modified 356-type alloy (M6)			Sr-modified 356-type alloy (M6S)		
	UTS (MPa)	YS (MPa)	% El	UTS (MPa)	YS (MPa)	% El
As-cast	278.5 ± 5.6	185.9 ± 1.2	2.4 ± 0.1	284.7 ± 1.8	192.1 ± 5.2	3.0 ± 0.7
8	352.3 ± 10.8	230.1 ± 10.5	6.5 ± 0.1	351.1 ± 10.5	228.2 ± 6.6	8.0 ± 0.3
50	340.9 ± 9.7	229.0 ± 6.6	6.4 ± 0.6	370.1 ± 0.5	246.4 ± 4.6	10.5 ± 0.1
100	339.2 ± 10.5	202.6 ± 5.2	9.7 ± 0.7	330.5 ± 7.1	237.1 ± 1.8	10.1 ± 0.5
200	323.2 ± 5.6	190.9 ± 2.6	9.5 ± 0.3	321.9 ± 5.9	210.1 ± 6.0	8.7 ± 0.4
400	330.9 ± 10.9	210.1 ± 3.1	7.6 ± 0.2	324.8 ± 6.1	215.8 ± 3.5	8.3 ± 0.7

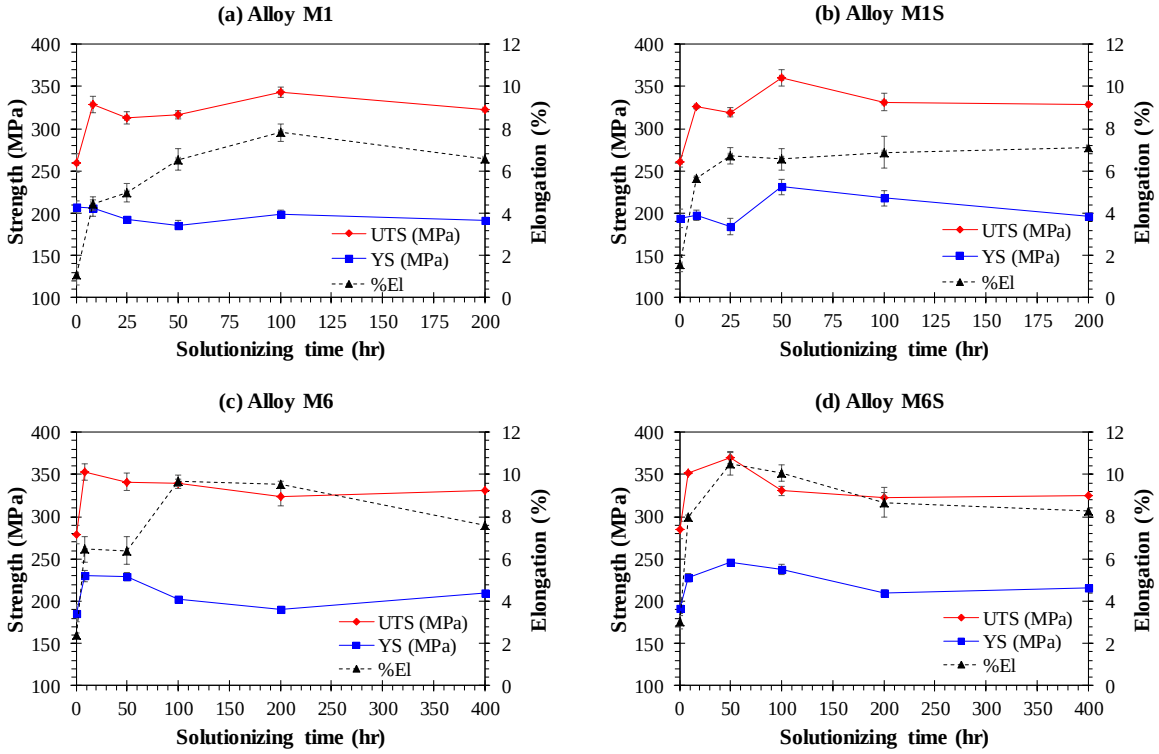

Figure 7.21 Plots of ambient-temperature tensile properties (T4) of: (a) alloy M1, (b) alloy M1S, (c) alloy M6, and (d) alloy M6S.

The purpose of solution treatment is to complete three important functions with regard to the microstructure of the alloy to be treated. As mentioned earlier in Chapter 2, the three intended functions are: (i) dissolution of soluble intermetallic compounds, (ii) homogenization of the as-cast structure, and (iii) changing the morphology of eutectic Si particles into spherical particles with rounded edges. The completion of the first two functions is important with respect to improving the yield strength after the aging treatment, which follows solution treatment in T6 and T7 tempers. The improvement in the yield strength arises from the improved precipitation hardening from the supersaturated solid solution achieved by efficiently increasing the solute contents to a maximum in the solid solution, and to homogenize their distribution during solution treatment. The third function, which is related to changing the morphology of the silicon particles into a spherical form through solution treatment, enhances the ductility in the solution-treated condition with respect to the ductility in the as-cast condition of the same alloy. The three functions are eventually independent of each other; however, applying solution treatment at a high enough temperature and for sufficient durations will lead to overall success in achieving the three functions simultaneously. The ultimate tensile strength commonly enhances by improving both the yield strength and the ductility value of a specific condition. This has been confirmed by Taylor *et al.* [294] who studied the trends of the mechanical properties through an empirical analysis of T6-treated Al-Si-Mg alloys.

It was reported by Han *et al.* [295] that 4 hours solution treatment at 490°C is sufficient to obtain a high and uniform concentration of copper in the matrix of Al-Si-Cu-Mg alloys. Thus the effect of the higher solution times used in this study (i.e. 8 hours and more) on the tensile properties will be mainly related to the morphology of the eutectic Si particles since

the dissolution and homogenization processes are completed within the first 4 hours.[295] Moreover, this understanding explains the limited variation in strength values of solution-treated conditions for almost all alloys studied due to the efficiency of the dissolution and homogenization functions common to all.

In contrast to the limited variations in strength values, high variations in ductility values are observed in the tensile test results. These variations in ductility values, which are concomitant with the increase in solution treatment times, can be understood in terms of the spheroidization and coarsening of the Si particles. The spheroidization (i.e. both sphericity and roundness) is attained by transforming the plate-like Si particles with sharp edges into spherical particles with rounded edges. The sharp edges would otherwise act as crack initiators, which would lead to rapid cracking and fracture at low ductility values. Thus, one seeks to improve the ductility values by transforming these plate-like particles into spherical ones, and their sharp edges into rounded ones, using solution heat treatment. The coarsening behavior results in reducing the number of Si particles in the matrix and forming a continuous Si structure capable of resisting crack propagation besides offering larger continuous regions of the ductile α-Al matrix. Consequently, the ductility of the alloy will increase accordingly.[243, 296]

The modified M1S alloy shows that the variation in ductility values of solution treated conditions is not significant, as the sphericity and roundness values of the Si particles in this alloy improved only slightly between 8 and up to 200 hours, as shown in Figure 7.16(c). This slight enhancement in sphericity is the reason for the observed limited increase in ductility values of the solution-treated conditions of the alloy, as can be inferred

from Figure 7.21(b). On the other hand, the non-modified M1 alloy shows enhanced ductility values with longer times of solution treatment except for the 200h solutionized condition. The gradual increase in ductility values from 4.5 % after 8 hours, to 5 % at 25 hours, to 6.5 % after 50 hours, and finally 7.8 % after 100 hours of solution treatment can be attributed to the continuous thermal modification of the Si particles that is more pronounced in the non-modified M1 alloy compared to the Sr-modified M1S alloy. Additionally, for both M1 and M1S alloys, the ductility values reduce after 200 hours of solutionizing. This reduction in ductility may be a direct result of the increased fraction of large silicon particle agglomerates composed of agglomerated Si particles. The agglomeration of Si particles as a mechanism of coarsening increases defects in these particles such as pinholes and fine notch-like edges, as shown in Figure 7.22, where the broken arrows refer to pinholes, and angles refer to the notch-like edges. These defects facilitate the fracture of silicon particles and hence reduce the overall alloy ductility. Thus, despite the fact that the silicon particles after such long solution treatment times are supposed to be spherical in shape and hence improve the alloy ductility, very long solution treatment times (more than 200 hours) turned out to be harmful to the alloy ductility, due to the increased number of coarsened Si particle agglomerates.

After applying solution treatments, ductility values of 356-type alloys in both non- and Sr-modified alloys show remarkable variations but, as usual, the strength values (UTS and YS) show little variations in the solution-treated conditions. When correlating the ductility values shown in Figure 7.21(c) and Figure 7.21(d) with the average Si particle characteristics of the same alloys and treatment conditions (Figure 7.17), one can say that the increase in sphericity percentages coupled with the improved roundness values lead to

the pronounced enhancement in ductility values observed for solutionized conditions up to 100 hours for alloy M6, and 50 hours for alloy M6S. Further solution treatment will reduce the ductility values owing to the above-mentioned defects, which may arise with the increased fraction of agglomerated particles during longer durations of solution treatment. It is important to highlight the difference in the solution treatment times at which the reduction in ductility values starts to take place: starting earlier in the modified alloy M6S after 50 hours vis-à-vis 100 hours in the non-modified M6 alloy. This difference can be attributed to the lower spheroidization kinetics in the non-modified alloys compared to Sr-modified alloys.[123, 124, 243]

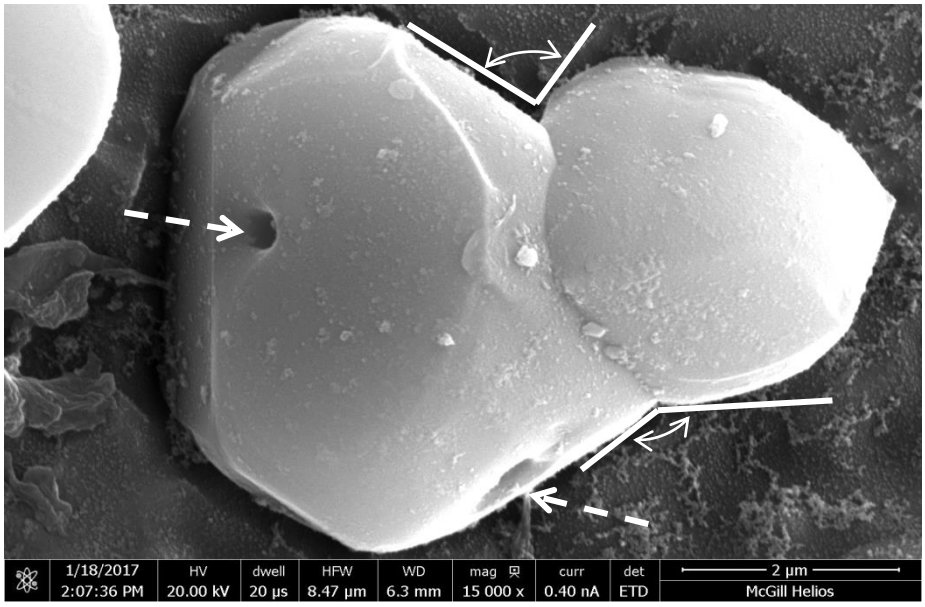

Figure 7.22 Coarsened Si particle in M1S alloy after solution treatment at 510°C for 200 hours showing pinholes (broken arrows) and notch-like edges (angles with solid lines).

7.5 ELEVATED TEMPERATURE TENSILE PROPERTIES

The tensile properties obtained at 250°C for alloys under study are listed in Table 7.5 and Table 7.6, and plotted in Figure 7.23. The testing of as-quenched (T4) conditions at elevated temperature (250°C) will result in the precipitation of strengthening dispersoids, which will eventually change the treatment condition to that of a T6 treatment. For this reason, the tensile bars were soaked at the testing temperature for only 5 minutes before starting the test, so that the objective of examining the sole role of morphological changes of silicon particles during solution treatment on the high-temperature tensile properties regardless the effect of precipitates would still be valid.

From Table 7.5 and Table 7.6 and Figure 7.23, , it is clear that strength values (UTS and YS) for each specific alloy are almost identical in the solutionized conditions with a maximum variation achieved among the four studied alloys of 15 MPa for the non-modified M6 alloy. The ductility values showed enhancements at shorter solution treatment times for all alloys, followed by reduction with solutionizing for longer periods. The ductility of M1 alloy increased from 1.7 % after 8 hours of solutionizing to 2.2 % after 50 hours; while the ductility of the modified alloy M1S increased slightly from 2.2 % after 8 hours to 2.4 % after 25 hours. On the other hand, the ductility of the non-modified 356-alloy M6 jumped from 1.6 % after solution treatment for 8 hours at 550°C to 2.5 % after 100 hours of solutionizing, while that of the Sr-modified 356-type alloy (M6S) also increased only slightly from 2.2 % after 8 hours of solutionizing to reach 2.5 % after 100 hours. The four studied alloys experienced reduction in ductility values with further

solution treatment after reaching the peak ductility values, similar to the observations reported for the ambient-temperature tensile behavior.

Table 7.5 High-temperature tensile properties (T4) of M1 and M1S alloys

Solution treatment time (hr)	Non-modified 354-type alloy (M1)			Sr-modified 354-type alloy (M1S)		
	UTS (MPa)	YS (MPa)	% El	UTS (MPa)	YS (MPa)	% El
8	264.6 ± 5.4	261.0 ± 1.1	1.7 ± 0.1	264.5 ± 5.7	258.1 ± 10.9	2.2 ± 0.2
25	265.1 ± 0.5	261.9 ± 1.9	1.9 ± 0.1	264.3 ± 3.9	261.1 ± 5.1	2.4 ± 0.3
50	266.7 ± 4.9	264.7 ± 4.6	2.2 ± 0.1	261.4 ± 4.5	260.0 ± 2.9	2.1 ± 0.4
100	264.9 ± 5.0	259.2 ± 2.3	2.0 ± 0.2	259.4 ± 2.0	254.5 ± 6.8	2.2 ± 0.3
200	254.5 ± 2.1	247.6 ± 4.3	1.9 ± 0.1	258.0 ± 10.1	254.4 ± 8.8	2.2 ± 0.1

Table 7.6 High-temperature tensile properties (T4) of M6 and M6S alloys

Solution treatment time (hr)	Non-modified 356-type alloy (M6)			Sr-modified 356-type alloy (M6S)		
	UTS (MPa)	YS (MPa)	% El	UTS (MPa)	YS (MPa)	% El
8	258.7 ± 9.8	258.5 ± 8.3	1.6 ± 0.3	238.3 ± 3.0	237.5 ± 3.3	2.2 ± 0.3
50	248.6 ± 6.2	243.0 ± 8.4	1.9 ± 0.1	238.4 ± 9.8	232.7 ± 6.3	2.3 ± 0.1
100	254.4 ± 9.7	253.1 ± 7.9	2.5 ± 0.3	237.9 ± 4.7	237.9 ± 4.7	2.5 ± 0.0
200	246.7 ± 4.0	246.0 ± 3.4	2.4 ± 0.3	240.7 ± 7.1	240.2 ± 7.6	2.4 ± 0.2
400	243.2 ± 7.3	238.4 ± 10.2	2.2 ± 0.1	248.3 ± 4.0	247.8 ± 3.5	2.2 ± 0.2

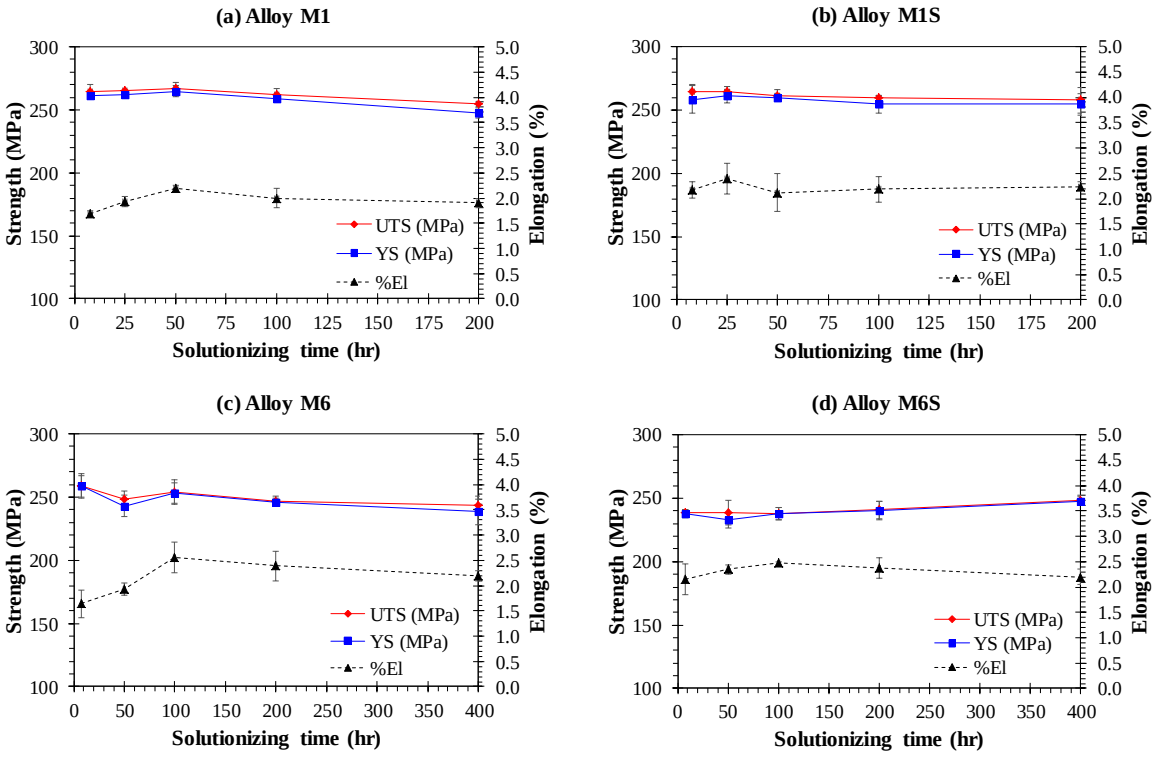

Figure 7.23 Plots of high-temperature tensile properties (T4) of: (a) alloy M1, (b) alloy M1S, (c) alloy M6, and (d) alloy M6S.

Morphological changes in the Si particles seem to have a very limited effect on the high-temperature tensile properties and, surprisingly, this limited effect is extended to the ductility values. The high values of both UTS and YS, which are almost identical for each specific alloy, reveal two important findings. The first is related to the fact that the morphological changes, which occur in the Si particles during the course of solution heat treatment, have no remarkable effect on the high-temperature strength values. The second finding is related to the improved yield strength, which is comparable to the UTS value and exceeds the ambient-temperature yield strength values of corresponding alloys and conditions. This indicates that a considerable amount of strengthening precipitates have been formed during the soaking and testing times at 250°C, and thus the effectiveness of the solution treatment in forming supersaturated solid solution may be considered.

CHAPTER 8

CONCLUSIONS

CHAPTER 8

CONCLUSIONS

8.1 INTRODUCTION

The main objective of pursuing this study was to understand and to determine how to enhance the mechanical performance of 354-type Al-Si-Cu-Mg cast alloys at both ambient and elevated temperatures through the addition of zirconium (Zr) as a base alloying element and subsequent additions of nickel (Ni) and manganese (Mn), to validate the use of such alloys in automotive engine applications. The full range of microstructural features, including: intermetallic compounds, eutectic silicon particles, and fine precipitates, have been investigated qualitatively and/or quantitatively using DSC analysis together with optical microscopy, SEM, FESEM, and TEM techniques. The effects of these microstructural features on the mechanical performance of the alloys studied, under various treatment conditions was investigated. The mechanical testing techniques comprised tensile testing at ambient and elevated temperatures, impact testing, and hardness measurements. Other important aspects such as examining the role of transition element additions, the effects of geometrical discontinuities, prolonged thermal exposure and extended solution treatment were also investigated, to simulate conditions close to those of actual components and working environments.

8.2 CONCLUSIONS

From the analysis and discussion of the experimental data presented in Chapters 4, 5, 6, and 7 of the current thesis, the following conclusions could be made. These conclusions are presented Chapter-wise, to highlight the salient findings corresponding to the different aspects investigated in this study. Recommendations for future work are provided at the end.

CHAPTER 4: MICROSTRUCTURAL CHARACTERIZATION

This chapter discussed the dissolution and solidification characteristics of existing phases using DSC analysis. Optical microscopy, SEM, and TEM techniques were employed to identify these phases and study the characteristics of the active strengthening precipitates. From the data presented in Chapter 4, the following conclusions may be drawn:

1. DSC analysis showed that the addition of Ni remarkably changed the solidification and melting characteristics of the 354 alloy.
2. The addition of transition elements Zr, Ni, and Mn in different amounts and combinations produces new phases, such as: (Al,Si)3(Ti,Zr), (Al,Si)3Zr, Al9FeNi, Al3Ni, Al3CuNi, Al9FeSi3Ni4Zr, and α-Al15(Fe,Mn)3Si2, in addition to the well-known phases of the structure of 354-type alloys, such as: α-Al, eutectic silicon, Al2Cu, Mg2Si, Q-Al5Cu2Mg8Si6, and Fe-based intermetallic phases.

3. Melt superheating at 800°C proved to be beneficial in terms of reducing the amount of the coarse Al3(Ti,Zr) phase observed in the alloy microstructure as a result of the efficient dissolution of the coarse Al3Zr particles originating from the master alloy.
4. The addition of Ni retards the kinetics of precipitation of the α-Al network, and the eutectic Al-Si structure. The presence of Ni consumes a considerable amount of Cu to form Al-Cu-Ni particles instead of Al2Cu particles.
5. Comparison between the DSC thermograms obtained for as-cast and as-quenched alloys reveals that the solution treatment at 495°C for 5 hours is sufficient to dissolve a large amount of Al2Cu particles in the α-Al matrix, which is mandatory for a successful aging treatment.
6. TEM investigations confirm that the investigated alloys are strengthened primarily by θ-Al2Cu and S-Al2CuMg precipitates and their precursors, in addition to a secondary strengthening effect by precipitates in the form of Alx(Zr,Ti)Si.
7. TEM investigations confirm that the base M1S alloy, which is a Ni-free alloy, contained a higher fraction of θ-Al2Cu precipitates than the 4 wt.% Ni-containing M4S alloy, owing to the consumption of Cu in forming Al-Cu-Ni particles.

CHAPTER 5: ROLES OF ADDITIONS, HEAT TREATMENTS, AND GEOMETRICAL DISCONTINUITIES

This chapter discussed the effects of the addition of transition elements and applied heat treatments on the microstructural characteristics of tensile bars including volume fractions of intermetallic compounds formed and the eutectic silicon particle characteristics followed by evaluating the ambient- and elevated-temperature tensile properties.

Symmetric and asymmetric geometrical discontinuities (notches) were made in the tensile test bars to examine their effects on the tensile behavior of the alloys. Hardness and impact properties were also examined and interpreted in terms of the various chemical additions as well as the heat treatments applied. The most important findings are as follows:

8. The proposed additions enhanced the overall mechanical performance of the alloys, namely, the ambient- and elevated-temperature tensile properties (cf. for as-cast conditions at 25°: UTS/YS values of the base alloy M1S are 260/194 MPa, whereas for alloy M4S are 305/225 MPa), and hardness (cf. for as-cast conditions at 25°: 91 HRF for M4S alloy compared to 84 HRF for the base alloy) and impact (cf. for as-cast conditions at 25°: 6 J for M4S alloy compared to 4 J for the base alloy) properties.
9. For the Mn-containing alloys, the improvement in properties results from the formation of polygonal sludge particles in the form of blocky α-Al15(Fe, Mn)3Si2 alongside the script-like α-iron phase which resist crack propagations. The precipitation of Ni-bearing phases in the Ni-containing alloys, such as Al9FeNi, Al3CuNi, and Al3Ni, hinders the propagation of cracks and thus improves the mechanical properties.
10. Alloys M3S (354 + 0.75 wt.% Mn) and M4S (354 + 4 wt.% Ni) exhibit the highest and almost identical strength values at 250°C for the different conditions examined; for example: UTS values are 175.76 MPa, and 180.53 MPa for as-cast conditions, 181.07 MPa and 181.86 MPa for T5-treated conditions, and 248.74 MPa and 253.58 MPa for T6-treated conditions.

11. Alloy M3S is considered more favorable than alloy M4S since it exhibits higher ductility values (cf. 1.54% in alloy M3S and 1.06% in M1S for T6-treated conditions tested at 250 °C).
12. The quality index values obtained at 250°C do not show wide variation in values (199.85- 276.68 MPa), as was observed in the case of the ambient-temperature data (254.51- 421.97 MPa), because of the balanced variation in UTS and ductility values obtained at the elevated temperature of 250°C.
13. The quality index values obtained at 250°C for alloys M2S and M3S in the T6-treated condition, 273.65 and 276.68 MPa, respectively, are found to be the highest for the alloys and conditions studied.
14. The presence of asymmetric notches is more deleterious to the tensile properties obtained at ambient temperature than symmetric notches (c.f. 340/298 MPa with holes and 305/244MPa with V-notches for T6-treated alloy M1S), even if the reduced area in the two cases is the same.
15. The effects of various chemical additions on the tensile properties obtained at ambient temperature and 250°C are feeble in the case of notched bars, compared to their obvious effects on the tensile properties of smooth (unnotched) bars.
16. Alloy M4S showed better resistance to premature cracking and fracture in notched bars at ambient temperature owing to the high volume fraction of intermetallic compounds in the as-cast and solutionized structures of this alloy which could resist the propagation of cracks during the tensile testing of the notched bars.
17. The softening that occurs during tensile testing at 250°C renders the alloys some ductility, in particular, the M1S, M2S and M3S alloys resulting in higher NTS

values (cf. 172.86 MPa/T5 and 232.22 MPa/T6 for alloy M1S) compared to the tensile strength values obtained at 250° C for unnotched bars (cf. 172.07 MPa/T5 and 217.65 MPa/T6 for alloy M1S) subjected to similar treatment conditions.

18. The variations in hardness values and impact properties followed the same trend as variations in the percentage volume fraction of intermetallic compounds.

19. The impact properties of the alloys are highly influenced by the Al2Cu phase particles rather than the eutectic silicon particles.

CHAPTER 6: PROLONGED THERMAL EXPOSURE

This chapter dealt with the concept of prolonged thermal exposure at 250°C, or stabilization, and its effect on the mechanical performance of the alloys studied. It covered investigating the effect of static versus dynamic stabilization modes for short and long durations (5 up to 200 hours) on the ambient-temperature tensile properties and the hardness values of T6-treated alloys. The effects of prolonged thermal exposure at 250°C for 100 and 200 hours on the mechanical performance of the T5- and T6-treated alloys were also studied, including: (i) ambient-temperature tensile properties, (ii) ambient-temperature hardness values, and (iii) elevated-temperature tensile properties. The fracture surfaces of tensile bars tested at 250°C after stabilization for 1, and 200 hours at the testing temperature were also presented. An analysis of the experimental data presented in this chapter led to the following conclusions.

20. Varying the thermal exposure technique from static to dynamic has minor effects on the room-temperature mechanical behavior. Thus, the static exposure (stabilization)

technique may be used to simulate the behavior of the material under dynamic thermal exposure conditions as in the case of actual engine components.

21. The prolonged exposure at 250°C has a deleterious effect on the mechanical performance due to coarsening of the strengthening precipitates; the kinetics of this coarsening behavior decay with time.

22. The values of quality indices obtained according to the Cáceres model show discrepancies for the statically and dynamically stabilized conditions towards the very long stabilization times, i.e. 100 and 200 hours at 250°C due to the noticeable variations in the ductility values at these prolonged exposure times; e.g. 428.2 MPa versus 371.75 MPa, respectively, for the statically and dynamically stabilized T6-treated alloy M1S for 200 hours compared to 390.09 MPa versus 383.91 MPa for the same alloy after only 25 hours of stabilization.

23. Coarsening of the strengthening precipitates following the prolonged exposure at 250°C has a deleterious effect on the tensile properties and hardness values. Noticeable reduction in the hardness (cf. 95 HRF for T6-treated condition without stabilization and 58.7 HRF after 200 hours of stabilization, in case of alloy M1S) and strength values, particularly the yield strength (cf. 324.99 MPa and 160.14 MPa, in case of alloy M1S), and a remarkable increase in the ductility values (cf. 1.1% and 6.3%, in case of alloy M1S) are observed.

24. The coarsening kinetics of the precipitates decay with time, due to the continuously increased distance between the precipitates with increasing the exposure time, causing the observed deterioration in the mechanical performance after thermal

exposure at 250°C up to 100 hours. Further thermal exposure up to 200 hours does not reduce the strength and hardness values thereafter.

25. The strength values (UTS and YS) obtained at room temperature for the stabilized T5-treated conditions (UTS/298.5 and YS/189.3 MPa in case of alloy M2S) are comparable to and in most alloys exceed those of the stabilized T6-treated conditions (UTS/273.8 and YS/170.8 MPa for alloy M2S), and always higher in the case of elevated-temperature tensile testing of the stabilized conditions (c.f. UTS/118.4 and YS/91.6 MPa for T5+200h and UTS/100.7 and YS/80.6 MPa for T6+200h conditions of alloy M2S).

26. Addition of 0.75 wt.% Mn is competitive with the addition of 2 and 4 wt.% Ni with respect to the elevated- and ambient-temperature strength values, respectively (cf. YS/99.63 MPa for alloy M3S compared to 91.65 MPa for alloy M2S obtained at 250°C after exposing T5-treated conditions at 250°C for 200h; and YS/178.10 MPa for alloy M3S compared to 152.46 MPa for alloy M4S obtained at 25°C after exposing T5-treated conditions at 250°C for 200h), with an advantage to the ductility values of Mn-containing alloy.

27. The equivalent effect of adding 0.75 wt.% Mn to 2 and 4 wt.% Ni is economically significant because of the lower price of manganese compared to that of nickel.

28. Cracked Alx(Zr,Ti)Si complex compound is observed with star-like and blocky morphologies on the fracture surface of T6-treated base alloy indicating that this phase may control the fracture behavior of the base alloy.

29. The appearance of micro-cracks in the Ni-rich phases observed on the fracture surface alloy M2S indicates that Ni-rich phases are affecting the fracture behavior of Ni-containing alloys.
30. The fracture surfaces of Mn-containing alloy (M3S) reveals that The presence of sludge particles is favourable in terms of hindering the propagation of the cracks developed in other phases.

CHAPTER 7: EXTENDED SOLUTION TREATMENT

This chapter discussed the effect of extended solution treatment on the morphological evolution of eutectic silicon particles in Sr-modified and non-modified 354 + 0.3 wt.% Zr, and 356 cast alloys. The solutionizing treatment parameters were 510°C up to 200 hours, and 550°C up to 400 hours for the two alloys, respectively. The effect of the morphological evolution of silicon particles on the ambient- and elevated-temperature tensile data was presented in this chapter, and the conclusions obtained are as follows.

31. Thermal modification of silicon particles is more effective in the Sr-modified alloys rather than in their Sr-free counterparts. The evolution of silicon particles during extended solution treatments follows the same trends and sequences for non-modified and Sr-modified 354- and 356-type alloys, at different evolution rates.
32. The coarsening of Si particles occurs through the particle agglomeration and Ostwald ripening mechanisms; however, although both mechanisms are active at the same time, they operate independently and additively.

33. The pinholes observed in the silicon particles derive from the impression or imprint left behind from the agglomeration of small particles with, and their diffusion into, larger particles.

34. Observation of polyhedral or faceted Si particles are noted frequently in the 200ppm Sr-modified M6S alloy after 400 hours of SHT at 550°C, and thus negates the statement made by previous researchers that long solution treatments can alter the morphology of Si particles from flake-like and polyhedral to spherical.

35. In order to apply the LSW model, which describes the coarsening of Si particles, to non-modified alloys, a higher value for the initial time should be used, than that used with Sr-modified alloys, to ensure that the fragmentation process is complete and that the coarsening step is active.

36. For the 354-type M1 and M1S alloys, the solution treatment for 8 hours at 510°C enhances the UTS values of as-cast conditions in both alloys (M1: from 259.5 to 328.3 MPa), whereas the YS remains almost unchanged at 206 MPa in alloy M1, and barely increases from 194.4 to 198 MPa in the M1S alloy.

37. Solution treatment at 510°C for 8 hours improves ductility values of as-cast M1 and M1S alloys (cf. 1.1% and 4.5% for alloy M1, and 1.6% and 5.6% for alloy M1S) after 8 hours; further solutionizing enhances ductility values at a lower rate.

38. Morphological changes in Si particles have a very limited effect on the high temperature tensile properties; this limited effect also extends to the ductility values.

8.3 RECOMMENDATIONS FOR FUTURE WORK

The promising results obtained in this study in regard to the improved mechanical performance of Al-Si-Cu-Mg 354-type alloys at ambient and high temperatures indicate that the addition of Zr, Ni, and Mn in different amounts and combinations to these alloys is advantageous from the point of view of their resistance to softening when subjected to elevated temperatures for prolonged durations. Consequently, these tailored alloys have the potential to be used in elevated-temperature applications, in particular automotive engine components. For a complete characterization of these newly developed alloys, it would be of interest to consider investigating the following aspects in future work.

1. Correlating the tensile properties of the notched bars to the microstructural constituents of the alloys studied by investigating the fractures surfaces.
2. Conducting detailed transmission electron microscopic (TEM) investigations on the strengthening precipitates including density of precipitates, precipitate free zones, and size and morphological characteristics of the precipitates before and after prolonged thermal exposure of the heat-treated alloys.
3. Exploring the fatigue characteristics under different combinations of mechanical and thermal loads including mechanical fatigue, isothermal mechanical fatigue, and thermomechanical fatigue.
4. Investigating the machinability characteristics of these alloys, associated with drilling, tapping, and milling processes.

REFERENCES

REFERENCES

1. G. Cole and A. Sherman, "Light Weight Materials for Automotive Applications". *Materials characterization*, 1995. 35(1): p. 3-9.
2. W. Miller, L. Zhuang, J. Bottema, A.J. Wittebrood, P. De Smet, A. Haszler and A. Vieregge, "Recent Development in Aluminium Alloys for the Automotive Industry". *Materials Science and Engineering: A*, 2000. 280(1): p. 37-49.
3. F. Palazzo, "Future of Aluminum in the Automotive Industry". *Alluminio*, 1977. 46(9).
4. I. Fridlyander, "Aluminum Alloys in Aircraft in the Periods of 1970–2000 and 2001–2015". *Metal science and heat treatment*, 2001. 43(1): p. 6-10.
5. I. Fridlyander, V. Sister, O. Grushko, V. Berstenev, L. Sheveleva and L. Ivanova, "Aluminum Alloys: Promising Materials in the Automotive Industry". *Metal Science and Heat Treatment*, 2002. 44(9): p. 365-370.
6. Schultz, D. "The past, present and future of aluminum in North American light vehicles." *Ducker Worldwide* (2012).
7. Lee, Jonathan A., and Po-Shou Chen. "High strength aluminum alloy for high temperature applications." U.S. Patent 6,918,970, issued July 19, 2005.
8. C. Kliemt. "Thermo-Mechanical Fatigue of Cast Aluminium Alloys for Engine Applications under Severe Conditions". PhD, Heriot-Watt University. (2012).
9. Lee, Jonathan A. "Cast aluminum alloy for high temperature applications." (2003).
10. R. Sampathi. *Die Casting Industry to Become a $76 Billion Market by 2020*. 2015 [cited; Available from: https://www.linkedin.com/pulse/vacuum-die-casting-overshadow-dominant-hpdc-market-76-sampathi.
11. Garza Elizondo, Guillermo Hernan. "Effect of Ni, Mn, Zr and Sc additions on the performance of Al-Si-Cu-Mg alloys." PhD diss., Université du Québec à Chicoutimi, 2016.
12. Hernandez Sandoval, Jacobo. "Improving the performance of 354 type alloy." PhD diss., Université du Québec à Chicoutimi, 2010.
13. Alyaldin, Loay. "Effects of alloying elements on room and high temperature tensile properties of Al-Si-Cu-Mg base alloys." MSc diss., Université du Québec à Chicoutimi, 2017.
14. S.K. Shaha. "Development and Characterization of Cast Modified Al-Si-Cu-Mg Alloys for Heat Resistant Power Train Applications". PhD, Ryerson University. (2015).
15. E. Zappi. "The Effect of Zr and V on the Structural and Mechanical Properties of the 2618 Al Alloy". NTNU. (2014).
16. Z. Asghar, G. Requena and F. Kubel, "The Role of Ni and Fe Aluminides on the Elevated Temperature Strength of an Alsi12 Alloy". *Materials Science and Engineering: A*, 2010. 527(21): p. 5691-5698.
17. K.E. Knipling. "Development of a Nanoscale Precipitation-Strengthened Creep-Resistant Aluminum Alloy Containing Trialuminide Precipitates", PhD diss., Northwestern University. (2006).

18. S. Shaha, F. Czerwinski, W. Kasprzak, J. Friedman and D. Chen, "Monotonic and Cyclic Deformation Behavior of the Al–Si–Cu–Mg Cast Alloy with Micro-Additions of Ti, V and Zr". *International Journal of Fatigue*, 2015. 70: p. 383-394.
19. A.F.S. Society and D.L. Zalensas, *Aluminum Casting Technology*. ed., ed. Vol. 1993: American Foundrymen's Society.
20. A.H. Volume, "2: Properties and Selection: Nonferrous Alloys and Special-Purpose Materials". *ASM international*, 1990. p. 889-896.
21. A.Y. Shash. "Effect of Processing Parameters on the Mechanical Characteristics of A356/(Al2o3)P Cast Metal Matrix Nano-Composites (Mmncs)". MSc, Cairo University. (2007).
22. Armstrong, G. Leslie. "Alloy selections for automotive aluminum castings.", No. 780249. SAE Technical Paper, 1978.
23. A.T. Spada, "In Search of Light-Weight Components: Automotive's Cast Aluminum Conversion". *Engineered Casting Solutions(USA)*, 2002. 4(2): p. 28-31.
24. Aluminum Association. *Aluminum: properties and physical metallurgy*. ASM International, 1984.
25. M. Angeloni. "Fatigue Life Evaluation of A356 Aluminum Alloy Used for Engine Cylinder Head". PhD, École normale supérieure de Cachan-ENS Cachan; Universidade de São Paulo. (2011).
26. R. Colás, A. Rodríguez, J. Talamantes and S. Valtierra, "Solidification Analysis of Aluminium Engine Block". *International Journal of Cast Metals Research*, 2004. 17(6): p. 332-338.
27. M. Abdelaziz. "Effect of Ceramic Nano-Particles on Wear and Corrosion Properties of Aluminium Silicon Hypereutectic Cast Alloy (A390)". MSc, Cairo University. (2012).
28. Y. Kurihara, "The Role of Aluminum in Automotive Weight Reduction—Part I". *JOM*, 1993. 45(11): p. 32-33.
29. H. Ye, "An Overview of the Development of Al-Si-Alloy Based Material for Engine Applications". *Journal of Materials Engineering and Performance*, 2003. 12(3): p. 288-297.
30. Ammar, Hany. "Effect of casting imperfections on the fatigue properties of aluminum-silicon casting alloys." MSc diss., Université du Québec à Chicoutimi; (2006).
31. Handbook, A. S. M. "Alloy phase diagrams." *ASM international* 3 (1992): 2-319.
32. Handbook, A. S. M. "Metallography and microstructures." *ASM international 9* (2004): 44073-0002.
33. Deshpande, Jayesh U. "The effect of mechanical mold vibration on the characteristics of Aluminum alloys." PhD diss., Worcester Polytechnic Institute, 2006.
34. M. Javidani and D. Larouche, "Application of Cast Al-Si Alloys in Internal Combustion Engine Components". *International Materials Reviews*, 2014. 59(3): p. 132-158.
35. Campbell, John. *Castings*. Elsevier, 2003.
36. Ammar H. "Influence of metallurgical parameters on the mechanical properties and quality indices of Al-Si-Cu-Mg and Al-Si-Mg casting alloys.", PhD diss., Université du Québec à Chicoutimi; 2010.

37. R. Lemon and C. Howle, "Premium Strength Aluminum Casting Alloys 354 and 359". *Trans. AFS*, 1963. 71: p. 465.
38. Kaufman, J. Gilbert, and Elwin L. Rooy. "Aluminum Alloy Castings." *Properties, Processes and Applications, ASM International* (2004).
39. J.R. Davis and J.R. Davis, *Aluminum and Aluminum Alloys*. ed., ed. Vol. 1993: ASM international.
40. Ma. Zheyuan, "Effect of Fe-Intermetallics and Porosity on Tensile and Impact Properties of Al-Si-Cu and Al-Si-Mg Cast Alloys.", PhD diss., Université du Québec à Chicoutimi. (2002).
41. F. Samuel and A. Samuel, "Effect of Heat Treatment on the Microstructure, Tensile Properties, and Fracture Behavior of Permanent Mold Al-10 Wt Pct Si-0.6 Wt Pct Mg/Sic/10 P Composite Castings". *Metallurgical and Materials Transactions A*, 1994. 25(10): p. 2247-2263.
42. A. Joenoes and J. Gruzleski, "Magnesium Effects on the Microstructure of Unmodified and Modified Al-Si Alloys". *Cast Metals*, 1991. 4(2): p. 62-71.
43. R. Dunn and W. Dickert, "Magnesium Effect on the Strength of A380. 0 and 383.0 Aluminum Die Casting Alloys". *Die Cast Eng*, 1975. 19: p. 2-20.
44. Mohamed A. "Effect of Additives on the Microstructure and Mechanical Properties of Aluminum-silicon Alloys.", PhD diss., Université du Québec à Chicoutimi; 2008.
45. A.L. Dons, G. Heiberg, J. Voje, J.S. Mæland, J.O. Løland and A. Prestmo, "On the Effect of Additions of Cu and Mg on the Ductility of Alsi Foundry Alloys Cast with a Cooling Rate of Approximately 3k/S". *Materials Science and Engineering: A*, 2005. 413: p. 561-566.
46. Y.H. Cho, Y.-R. Im, S.-W. Kwon and H.C. Lee. *The Effect of Alloying Elements on the Microstructure and Mechanical Properties of Al-12si Cast Alloys*. in *Materials Science Forum*. 2003. Trans Tech Publ.
47. M. Zeren, "Effect of Copper and Silicon Content on Mechanical Properties in Al–Cu–Si–Mg Alloys". *Journal of Materials Processing Technology*, 2005. 169(2): p. 292-298.
48. H. Doty, A. Samuel and F. Samuel. *Factors Controlling the Type and Morphology of Cu-Containing Phases in the 319 Aluminum Alloy*. in *100th AFS Casting Congress, Philadelphia, Pennsylvania, USA, April*. 1996.
49. G. Sigworth, "Aluminum Casting Alloys". *Special Communication*, 2008.
50. Z. Li, A. Samuel, F. Samuel, C. Ravindran and S. Valtierra, "Effect of Alloying Elements on the Segregation and Dissolution of Cual2 Phase in Al-Si-Cu 319 Alloys". *Journal of materials science*, 2003. 38(6): p. 1203-1218.
51. C. Meyers, K. Hinton and J.-S. Chou. *Towards the Optimization of Heat-Treatment in Aluminium Alloys*. in *Materials Science Forum*. 1992. Trans Tech Publ.
52. Mohamed, A. M. A., and F. H. Samuel. "A review on the heat treatment of Al-Si-Cu/Mg casting alloys." In *Heat Treatment-Conventional and Novel Applications*. InTech, 2012.
53. D. Apelian, "Aluminum Cast Alloys: Enabling Tools for Improved Performance". *North American Die Casting Association*, 2009.
54. Q. Wang, "Microstructural Effects on the Tensile and Fracture Behavior of Aluminum Casting Alloys A356/357". *Metallurgical and materials Transactions A*, 2003. 34(12): p. 2887-2899.

55. L.A. Narayanan, F. Samuel and J. Gruzleski, "Crystallization Behavior of Iron-Containing Intermetallic Compounds in 319 Aluminum Alloy". *Metallurgical and Materials Transactions A*, 1994. 25(8): p. 1761-1773.
56. Y. Awano and Y. Shimizu, "Non-Equilibrium Crystallization of Alfesi Compound in Melt-Superheated Al-Si Alloy Castings". *AFS Transactions*, 1990. 98: p. 889-895.
57. A. Samuel, F. Samuel and H. Doty, "Observations on the Formation of B-Al 5 Fesi Phase in 319 Type Al-Si Alloys". *Journal of Materials Science*, 1996. 31(20): p. 5529-5539.
58. C. Caceres, I.L. Svensson and J. Taylor, "Strength-Ductility Behaviour of Al-Si-Cu-Mg Casting Alloys in T6 Temper". *International Journal of Cast Metals Research*, 2003. 15(5): p. 531-543.
59. M. Tash, F. Samuel, F. Mucciardi and H. Doty, "Effect of Metallurgical Parameters on the Hardness and Microstructural Characterization of as-Cast and Heat-Treated 356 and 319 Aluminum Alloys". *Materials Science and Engineering: A*, 2007. 443(1): p. 185-201.
60. M. Drouzy, S. Jacob and M. Richard, "Interpretation of Tensile Results by Means of Quality Index and Probable Yield Strength-Application to Al-Si7 Mg Foundry Alloys-France". *International Cast Metals Journal*, 1980. 5(2): p. 43-50.
61. S. Jacob. *Quality Index in Prediction of Properties of Aluminum Castings- a Review*. in *Transactions of the American Foundry Society and the One Hundred Fourth Annual Castings Congress*. 2000.
62. C. Cáceres, "Microstructure Design and Heat Treatment Selection for Casting Alloys Using the Quality Index". *Journal of materials engineering and performance*, 2000. 9(2): p. 215-221.
63. C. Cáceres and J. Barresi, "Selection of Temper and Mg Content to Optimise the Quality Index of Al-7si-Mg Casting Alloys". *International Journal of Cast Metals Research*, 2000. 12(6): p. 377-384.
64. G. Sigworth, "Controlling Tensile Strength in Aluminum Castings". *Special Communication*, 2006.
65. G. Sigworth and C. Caceres. *Quality Issues in Aluminum Net-Shape Castings*. in *AFS Transactions: 108th Metalcasting Congress*. 2004. American Foundry Society.
66. A. Couture, "Iron in Aluminum Casting Alloys-a Literature Survey". *International cast metals journal*, 1981. 6(4): p. 9-17.
67. W. Bonsack, "Discussion on the Effect of Minor Alloying Elements on Aluminum Casting Alloys". *ASTM Bulletin*, 1942. 117: p. 45.
68. P. Crepeau, "Effect of Iron in Al-Si Casting Alloys: A Critical Review (95-110)". *Transactions of the American Foundrymen's Society*, 1995. 103: p. 361-366.
69. L. Backerud, G. Chai and J. Tamminen, "Solidification Characteristics of Aluminum Alloys. Vol. 2. Foundry Alloys". *American Foundrymen's Society, Inc., 1990*, 1990. p. 266.
70. G. Gustafsson, T. Thorvaldsson and G. Dunlop, "The Influence of Fe and Cr on the Microstructure of Cast Al-Si-Mg Alloys". *Metallurgical Transactions A*, 1986. 17(1): p. 45-52.
71. L.F. Mondolfo, "Manganese in Aluminum Alloys". *The Manganese Centre, 191 Ave. Charles de Gaulle, 92521 Neuilly sur Seine, France. 1978(Pamphlet)*. 1978.

72. J. Iglessis, C. Frantz and M. Gantois, "Conditions De Formation Des Phases De Fer Dans Les Alliages Al-Si De Pureté Commerciale". *Mémoires scientifiques de la revue de métallurgie*, 1977. 73(4): p. 237-242.
73. D. Colwell and R. Kissling, "Die and Permanent Mold Casting Aluminum Alloy Minor Elements". *AFS Transactions*, 1961. 69: p. 610-615.
74. Mascré, C. "Influence du fer et du manganèse sur les alliages du type de l'A-S13 (Alpax)." *Fonderie* 108 (1955): 4330-4336.
75. Y. Komiyama, K. Uchida and M. Gunshi, "Effects of Fe, Mn, Zn and Ti on Mechanical Properties and Micro-Structures of an Al-Si-Cu-Mg Casting Alloy". *Journal of Japan Institute of Light Metals*, 1976. 26(7): p. 311-319.
76. Gobrecht, J. "Ségrégation par Gravite du Fer, du Manganèse et du Chrome dans les Alliages Al-Si de Fonderie." (1977): 171-173.
77. S.W. Nam and D.H. Lee, "The Effect of Mn on the Mechanical Behavior of Al Alloys". *Metals and Materials International*, 2000. 6(1): p. 13-16.
78. D. Lee, J. Park and S. Nam, "Enhancement of Mechanical Properties of Al–Mg–Si Alloys by Means of Manganese Dispersoids". *Materials science and technology*, 1999. 15(4): p. 450-455.
79. D.S. Park and S.W. Nam, "Effects of Manganese Dispersoid on the Mechanical Properties in Al-Zn-Mg Alloys". *Journal of materials science*, 1995. 30(5): p. 1313-1320.
80. F. Samuel, A. Samuel and H. Liu, "Effect of Magnesium Content on the Ageing Behaviour of Water-Chilled Al-Si-Cu-Mg-Fe-Mn (380) Alloy Castings". *Journal of materials science*, 1995. 30(10): p. 2531-2540.
81. A. Dahle, K. Nogita, S. McDonald, C. Dinnis and L. Lu, "Eutectic Modification and Microstructure Development in Al–Si Alloys". *Materials Science and Engineering: A*, 2005. 413: p. 243-248.
82. J.E. Gruzleski and B.M. Closset, *The Treatment of Liquid Aluminum-Silicon Alloys*. ed., ed. Vol. 1990: Amer Foundry Society.
83. A. Hetke and R. Gundlach, "Aluminum Casting Quality in Alloy 356 Engine Components". *American Foundrymen's Society, Inc, Transactions of the American Foundrymen's Society*, 1994. 102: p. 367-380.
84. S. Shivkumar, D. Apelian and H. Brucher. *Melt Cleanliness in Die Cast Aluminum Alloys*. in *Transactions of the 16th International Die Casting Congress and Expositions, Detroit, Michigan, USA*. 1991.
85. D. Neff and P. Cooper, "Clean Metal for Aluminum Foundries: New Technology Using a Rotor Degasser and Filter Pump". *AFS Transactions*, 1990. 107: p. 579-584.
86. Elgallad, Emad Eldin. "Effect of additives on the mechanical properties and machinability of a new aluminum-copper base alloy.", PhD diss., Université du Québec à Chicoutimi, 2010.
87. Ragab, Khaled Ahmed. "The use of fluidized sand bed as an innovative technique for heat treating aluminum based castings.", PhD diss., Université du Québec à Chicoutimi, 2012.
88. F. Fracasso. "Influence of Quench Rate on the Hardness Obtained after Artificial Ageing of an Al-Si-Mg Alloy". Master Thesis, University of Padova, Padova, Italy. (2010).

89. Handbook A. S. M., "Heat Treating". *ASM International 4*, 1991. p. 72-74.
90. W.D. Callister, *Fundamentals of Materials Science and Engineering: An Interactive E. Text*. ed., ed. Vol. 5. 2001: Wiley New York.
91. W.D. Callister and D.G. Rethwisch, *Fundamentals of Materials Science and Engineering: An Integrated Approach*. ed., ed. Vol. 2012: John Wiley & Sons.
92. A. Mohamed and F. Samuel, "Influence of Mg and Solution Heat Treatment on the Occurrence of Incipient Melting in Al–Si–Cu–Mg Cast Alloys". *Materials Science and Engineering: A*, 2012. 543: p. 22-34.
93. M. Moustafa, F. Samuel and H. Doty, "Effect of Solution Heat Treatment and Additives on the Hardness, Tensile Properties and Fracture Behaviour of Al-Si (A413. 1) Automotive Alloys". *Journal of materials science*, 2003. 38(22): p. 4523-4534.
94. G. Sigworth, J. Howell, O. Rios and M. Kaufman, "Heat Treatment of Natural Aging Aluminum Casting Alloys". *International Journal of Cast Metals Research*, 2006. 19(2): p. 123-129.
95. A. Mohamed, A. Samuel, F. Samuel and H. Doty, "Influence of Additives on the Microstructure and Tensile Properties of near-Eutectic Al–10.8% Si Cast Alloy". *Materials & Design*, 2009. 30(10): p. 3943-3957.
96. A. Samuel, H. Doty, S. Valtierra and F. Samuel, "Defects Related to Incipient Melting in Al–Si–Cu–Mg Alloys". *Materials & Design*, 2013. 52: p. 947-956.
97. P. Ouellet and F. Samuel, "Effect of Mg on the Ageing Behaviour of Al-Si-Cu 319 Type Aluminium Casting Alloys". *Journal of Materials Science*, 1999. 34(19): p. 4671-4697.
98. P.-S. Wang, S.-L. Lee, J.-C. Lin and M.-T. Jahn, "Effects of Solution Temperature on Mechanical Properties of 319.0 Aluminum Casting Alloys Containing Trace Beryllium". *Journal of Materials Research*, 2000. 15(09): p. 2027-2035.
99. G. Wang, X. Bian, W. Wang and J. Zhang, "Influence of Cu and Minor Elements on Solution Treatment of Al–Si–Cu–Mg Cast Alloys". *Materials Letters*, 2003. 57(24): p. 4083-4087.
100. E. Sjölander and S. Seifeddine, "The Heat Treatment of Al–Si–Cu–Mg Casting Alloys". *Journal of Materials Processing Technology*, 2010. 210(10): p. 1249-1259.
101. E. Sjölander and S. Seifeddine, "Artificial Ageing of Al–Si–Cu–Mg Casting Alloys". *Materials Science and Engineering: A*, 2011. 528(24): p. 7402-7409.
102. F. Samuel, A. Samuel and H. Doty, "Factors Controlling the Type and Morphology of Cu-Containing Phases in 319 Al Alloy (96-30)". *Transactions of the American Foundrymen's Society*, 1996. 104: p. 893-902.
103. S. Shivkumar, S. Ricci, C. Keller and D. Apelian, "Effect of Solution Treatment Parameters on Tensile Properties of Cast Aluminum Alloys". *Journal of Heat Treating*, 1990. 8(1): p. 63-70.
104. D. Zhang and L. Zheng, "The Quench Sensitivity of Cast Al-7 Wt Pct Si-0.4 Wt Pct Mg Alloy". *Metallurgical and Materials Transactions A*, 1996. 27(12): p. 3983-3991.
105. A. Ardell, "Precipitation Hardening". *Metallurgical Transactions A*, 1985. 16(12): p. 2131-2165.
106. Polmear, Ian. *Light alloys: from traditional alloys to nanocrystals*. Elsevier, 2005.

107. D.A. Porter, K.E. Easterling and M. Sherif, *Phase Transformations in Metals and Alloys, (Revised Reprint)*. ed., ed. Vol. 2011: CRC press.
108. D. Eskin, "Decomposition of Supersaturated Solid Solutions in Al–Cu–Mg–Si Alloys". *Journal of materials science*, 2003. 38(2): p. 279-290.
109. D. Chakrabarti and D.E. Laughlin, "Phase Relations and Precipitation in Al–Mg–Si Alloys with Cu Additions". *Progress in Materials Science*, 2004. 49(3): p. 389-410.
110. C. Cayron and P. Buffat, "Transmission Electron Microscopy Study of the B′ Phase (Al–Mg–Si Alloys) and Qc Phase (Al–Cu–Mg–Si Alloys): Ordering Mechanism and Crystallographic Structure". *Acta Materialia*, 2000. 48(10): p. 2639-2653.
111. C. Wolverton, "Crystal Structure and Stability of Complex Precipitate Phases in Al–Cu–Mg–(Si) and Al–Zn–Mg Alloys". *Acta Materialia*, 2001. 49(16): p. 3129-3142.
112. K. Matsuda, D. Teguri, T. Sato and S. Ikeno. *Eftem Observation of Q'phase in Al-Mg-Si-Cu Alloy*. in *Materials Science Forum*. 2002. Trans Tech Publ.
113. J. Hwang, R. Banerjee, H. Doty and M. Kaufman, "The Effect of Mg on the Structure and Properties of Type 319 Aluminum Casting Alloys". *Acta Materialia*, 2009. 57(4): p. 1308-1317.
114. G. Wang, Q. Sun, L. Feng, L. Hui and C. Jing, "Influence of Cu Content on Ageing Behavior of Alsimgcu Cast Alloys". *Materials & design*, 2007. 28(3): p. 1001-1005.
115. J. Buha, R. Lumley and A. Crosky, "Microstructural Development and Mechanical Properties of Interrupted Aged Al-Mg-Si-Cu Alloy". *Metallurgical and Materials Transactions A*, 2006. 37(10): p. 3119-3130.
116. G. Edwards, K. Stiller, G. Dunlop and M. Couper, "The Precipitation Sequence in Al–Mg–Si Alloys". *Acta materialia*, 1998. 46(11): p. 3893-3904.
117. F. Vermolen, K. Vuik and S. van der Zwaag, "A Mathematical Model for the Dissolution Kinetics of Mg 2 Si-Phases in Al–Mg–Si Alloys During Homogenisation under Industrial Conditions". *Materials Science and Engineering: A*, 1998. 254(1): p. 13-32.
118. F. Vermolen and S. Van der Zwaag, "A Numerical Model for the Dissolution of Spherical Particles in Binary Alloys under Mixed Mode Control". *Materials Science and Engineering: A*, 1996. 220(1-2): p. 140-146.
119. P. Rometsch, L. Arnberg and D. Zhang, "Modelling Dissolution of Mg2si and Homogenisation in Al-Si-Mg Casting Alloys". *International Journal of Cast Metals Research*, 1999. 12(1): p. 1-8.
120. D. Zhang, L. Zheng and D. StJohn, "Effect of a Short Solution Treatment Time on Microstructure and Mechanical Properties of Modified Al–7wt.% Si–0.3 Wt.% Mg Alloy". *Journal of Light Metals*, 2002. 2(1): p. 27-36.
121. P. Rometsch, G. Schaffer and J. Taylor, "Mass Balance Characterisation of Al-7si-Mg Alloy Microstructures as a Function of Solution Treatment Time". *International Journal of Cast Metals Research*, 2001. 14(1): p. 59-69.
122. Martin, John Wilson. *Precipitation hardening: theory and applications*. Butterworth-Heinemann, 2012.
123. B. Parker. *Quantitative Evaluation of the Microstructure of a Strontium-Modified Al-Si-Mg Alloy Following Prolonged Solution Treatment*. in *METALS FORUM*. 1982.
124. F. Rhines and M. Aballe, "Growth of Silicon Particles in an Aluminum Matrix". *Metallurgical and Materials Transactions A*, 1986. 17(12): p. 2139-2152.

125. C. Meyers, "Solution Heat Treatment Effects on Ultimate Tensile Strength and Uniform Elongation in A357 Aluminum Alloys". *AFS Trans*, 1986. 91: p. 511-518.
126. S. Shivkumar, S. Ricci Jr, B. Steenhoff, D. Apelian and G. Sigworth, "An Experimental Study to Optimize the Heat Treatment of A356 Alloy". *AFS Transactions*, 1989. 97: p. 791-810.
127. D. Apelian, S. Shivkumar and G. Sigworth, "Fundamental Aspects of Heat Treatment of Cast Al-Si-Mg Alloys". *AFS transactions*, 1989. 97: p. 727-742.
128. F. Paray and J. Gruzleski, "Modification-a Parameter to Consider in the Heat Treatment of Al-Si Alloys". *Cast Metals*, 1993. 5: p. 187-187.
129. S. Hegde and K.N. Prabhu, "Modification of Eutectic Silicon in Al–Si Alloys". *Journal of materials science*, 2008. 43(9): p. 3009-3027.
130. H. Li, S. Shivkumar, X. Luo and D. Apelian, "Influence of Modification on the Solution Heat Treatment Response of Cast Al–Si–Mg Alloys". *Cast Metals*, 1989. 1(4): p. 227-234.
131. R-X. Li, R-D. Li, Y-H. Zhao and C.-X. Li, "Effect of Heat Treatment on Eutectic Silicon Morphology and Mechanical Property of Ai-Si-Cu-Mg Cast Alloys". *Transactions of Nonferrous Metals Society of China*, 2004. 14(3): p. 496-500.
132. F. Paray and J. Gruzleski, "Microstructure—Mechanical Property Relationships in a 356 Alloy. Part I: Microstructure". *Cast Metals*, 1994. 7(1): p. 29-40.
133. J.W. Martin, J.W. Martin, R.D. Doherty and B. Cantor, *Stability of Microstructure in Metallic Systems*. ed., ed. Vol. 1997: Cambridge University Press.
134. E. Ogris, A. Wahlen, H. Lüchinger and P. Uggowitzer, "On the Silicon Spheroidization in Al–Si Alloys". *Journal of Light Metals*, 2002. 2(4): p. 263-269.
135. I.M. Lifshitz and V.V. Slyozov, "The Kinetics of Precipitation from Supersaturated Solid Solutions". *Journal of physics and chemistry of solids*, 1961. 19(1-2): p. 35-50.
136. C. Wagner, "Theorie Der Alterung Von Niederschlägen Durch Umlösen (Ostwald-Reifung)". *Berichte der Bunsengesellschaft für physikalische Chemie*, 1961. 65(7-8): p. 581-591.
137. Clyne, T. W., and P. J. Withers. *An introduction to metal matrix composites*. Cambridge university press, 1995.
138. Hertzberg, Richard W. "Deformation and fracture mechanics of engineering materials.", Wiley, (1989).
139. Colley, Leo John. "Microstructure-property models for heat treatment of A356 aluminum alloy." PhD diss., University of British Columbia, 2011.
140. T. Gladman, "Precipitation Hardening in Metals". *Materials science and technology*, 1999. 15(1): p. 30-36.
141. Smallman, Raymond E., and A. H. W. Ngan. *Physical metallurgy and advanced materials*. Butterworth-Heinemann, 2011.
142. D. Srinivasan and K. Chattopadhyay, "Metastable Phase Evolution and Hardness of Nanocrystalline Al–Si–Zr Alloys". *Materials Science and Engineering: A*, 2001. 304: p. 534-539.
143. Z. Yin, Q. Pan, Y. Zhang and F. Jiang, "Effect of Minor Sc and Zr on the Microstructure and Mechanical Properties of Al–Mg Based Alloys". *Materials Science and Engineering: A*, 2000. 280(1): p. 151-155.

144. A. Farkoosh, X.G. Chen and M. Pekguleryuz, "Interaction between Molybdenum and Manganese to Form Effective Dispersoids in an Al–Si–Cu–Mg Alloy and Their Influence on Creep Resistance". *Materials Science and Engineering: A*, 2015. 627: p. 127-138.
145. Y. Chen, M. Fine, J. Weertman and R. Lewis, "Coarsening Behavior of Ll2 Structured Al3 (Zrx V1− X) Precipitates in Rapidly Solidified Al・ Zr・ V Alloy". *Scripta metallurgica*, 1987. 21(7): p. 1003-1008.
146. Y. Chen, M. Fine and J. Weertman, "Microstructural Evolution and Mechanical Properties of Rapidly Solidified Al・ Zr・ V Alloys at High Temperatures". *Acta Metallurgica et Materialia*, 1990. 38(5): p. 771-780.
147. K.E. Knipling, D.C. Dunand and D.N. Seidman, "Criteria for Developing Castable, Creep-Resistant Aluminum-Based Alloys–a Review". *Zeitschrift für Metallkunde*, 2006. 97(3): p. 246-265.
148. Nabawy, Ahmed. "Influence of zirconium and scandium on the microstructure, tensile properties, and hot-tearing susceptibility of Al-2wt% Cu-based alloys.", PhD diss., Université du Québec à Chicoutimi, 2010.
149. Totten, George E., and D. Scott MacKenzie, eds. *Handbook of Aluminum: Vol. 1: Physical Metallurgy and Processes*. Vol. 1. CRC Press, 2003.
150. P. Sepehrband, R. Mahmudi and F. Khomamizadeh, "Effect of Zr Addition on the Aging Behavior of A319 Aluminum Cast Alloy". *Scripta materialia*, 2005. 52(4): p. 253-257.
151. R. Mahmudi, P. Sepehrband and H. Ghasemi, "Improved Properties of A319 Aluminum Casting Alloy Modified with Zr". *Materials Letters*, 2006. 60(21): p. 2606-2610.
152. N. Belov, A. Alabin, D. Eskin and V. Istomin-Kastrovskii, "Optimization of Hardening of Al–Zr–Sc Cast Alloys". *Journal of materials science*, 2006. 41(18): p. 5890-5899.
153. D. Srinivasan and K. Chattopadhyay, "Non-Equilibrium Transformations Involving L1 2-Al 3 Zr in Ternary Al-X-Zr Alloys". *Metallurgical and Materials Transactions A*, 2005. 36(2): p. 311-320.
154. E. Nes, "Precipitation of the Metastable Cubic Al3zr-Phase in Subperitectic Al-Zr Alloys". *Acta Metallurgica*, 1972. 20(4): p. 499-506.
155. J. Robson and P. Prangnell, "Modelling Al 3 Zr Dispersoid Precipitation in Multicomponent Aluminium Alloys". *Materials Science and Engineering: A*, 2003. 352(1): p. 240-250.
156. K.E. Knipling, D.C. Dunand and D.N. Seidman, "Nucleation and Precipitation Strengthening in Dilute Al-Ti and Al-Zr Alloys". *Metallurgical and Materials Transactions A*, 2007. 38(10): p. 2552-2563.
157. K.E. Knipling, D.C. Dunand and D.N. Seidman, "Precipitation Evolution in Al–Zr and Al–Zr–Ti Alloys During Isothermal Aging at 375–425 C". *Acta Materialia*, 2008. 56(1): p. 114-127.
158. Z. Jia, G. Hu, B. Forbord and J.K. Solberg, "Effect of Homogenization and Alloying Elements on Recrystallization Resistance of Al–Zr–Mn Alloys". *Materials science and engineering: A*, 2007. 444(1): p. 284-290.

159. B. Forbord, H. Hallem and K. Marthinsen. *The Effect of Alloying Elements on Precipitation and Recrystallisation in Al-Zr Alloys*. in *Materials Forum*. 2004.
160. Kaufman, John Gilbert, ed. *Properties of aluminum alloys: tensile, creep, and fatigue data at high and low temperatures*. ASM international, 1999.
161. L. Sang-Yong, L. Jung-Hwan and L. Young-Seon, "Characterization of Al 7075 Alloys after Cold Working and Heating in the Semi-Solid Temperature Range". *Journal of materials processing technology*, 2001. 111(1): p. 42-47.
162. C.-L. Chen, A. Richter and R. Thomson, "Investigation of Mechanical Properties of Intermetallic Phases in Multi-Component Al–Si Alloys Using Hot-Stage Nanoindentation". *Intermetallics*, 2010. 18(4): p. 499-508.
163. Tillová, E., and M. Panušková. "Effect of solution treatment on intermetallic phases morphology in AlSi 9 Cu 3 cast alloy." *Metalurgija* 47, no. 3 (2008): 207-210.
164. D. Casari, T.H. Ludwig, M. Merlin, L. Arnberg and G.L. Garagnani, "The Effect of Ni and V Trace Elements on the Mechanical Properties of A356 Aluminium Foundry Alloy in as-Cast and T6 Heat Treated Conditions". *Materials Science and Engineering: A*, 2014. 610: p. 414-426.
165. A. Mohamed and F. Samuel, "Microstructure, Tensile Properties and Fracture Behavior of High Temperature Al–Si–Mg–Cu Cast Alloys". *Materials Science and Engineering: A*, 2013. 577: p. 64-72.
166. National Research Council. "Accelerated aging of materials and structures: the effects of long-term elevated-temperature exposure." (1996).
167. G. Weatherly and R. Nicholson, "An Electron Microscope Investigation of the Interfacial Structure of Semi-Coherent Precipitates". *Philosophical Magazine*, 1968. 17(148): p. 801-831.
168. B. Baradarani and R. Raiszadeh, "Precipitation Hardening of Cast Zr-Containing A356 Aluminium Alloy". *Materials & Design*, 2011. 32(2): p. 935-940.
169. L. Ceschini, A. Morri, A. Morri, F. Rotundo and S. Toschi, "Heat Treatment Response and Influence of Overaging on Mechanical Properties of C355 Cast Aluminum Alloy". *La Metallurgia Italiana*, 2014. 5: p. 11-17.
170. F. Xia, J.P. Li, Y.C. Guo and Z. Yang. *Microstructure Evolution and Mechanical Properties of an Al-Si-Cu-Mg-Ni Aluminium Alloy after Thermal Exposure*. in *Materials Science Forum*. 2013. Trans Tech Publ.
171. J. Jabra, M. Romios, J. Lai, E. Lee, M. Setiawan, J. Ogren, R. Clark, T. Oppenheim, O. Es-Said and E. Lee, "The Effect of Thermal Exposure on the Mechanical Properties of 2099-T6 Die Forgings, 2099-T83 Extrusions, 7075-T7651 Plate, 7085-T7452 Die Forgings, 7085-T7651 Plate, and 2397-T87 Plate Aluminum Alloys". *Journal of materials engineering and performance*, 2006. 15(5): p. 601-607.
172. S. Kai, J.-L. Chen and Z.-M. Yin, "Tem Study on Microstructures and Properties of 7050 Aluminum Alloy During Thermal Exposure". *Transactions of Nonferrous Metals Society of China*, 2009. 19(6): p. 1405-1409.
173. T. Din, A. Rashid and J. Campbell, "High Strength Aerospace Casting Alloys: Quality Factor Assessment". *Materials science and technology*, 1996. 12(3): p. 269-273.

174. N. Alexopoulos and S.G. Pantelakis, "Quality Evaluation of A357 Cast Aluminum Alloy Specimens Subjected to Different Artificial Aging Treatment". *Materials & design*, 2004. 25(5): p. 419-430.
175. N. Alexopoulos and S.G. Pantelakis, "Quality Assessment of Artificially Aged A357 Aluminum Alloy Cast Ingots by Introducing Approximate Expressions of the Quality Index Q D". *Metallurgical and Materials Transactions A*, 2004. 35(10): p. 3079-3089.
176. M. Tiryakioğlu, J.T. Staley and J. Campbell, "Evaluating Structural Integrity of Cast Al–7% Si–Mg Alloys Via Work Hardening Characteristics: Ii. A New Quality Index". *Materials Science and Engineering: A*, 2004. 368(1): p. 231-238.
177. S. Shivkumar, C. Keller and D. Apelian, "Aging Behavior in Cast Al-Si-Mg Alloys". *AFS Transactions*, 1990. 98: p. 905-911.
178. C. Cáceres, T. Din, A. Rashid and J. Campbell, "Effect of Aging on Quality Index of an Al–Cu Casting Alloy". *Materials science and technology*, 1999. 15(6): p. 711-716.
179. L. Ceschini, I. Boromei, A. Morri, S. Seifeddine and I.L. Svensson, "Microstructure, Tensile and Fatigue Properties of the Al–10% Si–2% Cu Alloy with Different Fe and Mn Content Cast under Controlled Conditions". *Journal of Materials Processing Technology*, 2009. 209(15): p. 5669-5679.
180. H. Ammar, C. Moreau, A. Samuel, F. Samuel and H. Doty, "Effects of Aging Parameters on the Quality of 413-Type Commercial Alloys". *Materials & Design*, 2009. 30(4): p. 1014-1025.
181. Westengen, Haakon, and Olav Holta. *Low Pressure Permanent Mold Casting of Magnesium-Recent Developments*. No. 880509. SAE Technical Paper, 1988.
182. M. Vogelsang, R. Arsenault and R. Fisher, "Anin Situ Hvem Study of Dislocation Generation at Al/Sic Interfaces in Metal Matrix Composites". *Metallurgical and Materials Transactions A*, 1986. 17(3): p. 379-389.
183. C. Cáceres, "A Rationale for the Quality Index of Al-Si-Mg Casting Alloys". *International Journal of Cast Metals Research*, 2000. 12(6): p. 385-391.
184. C. Cáceres, "A Phenomenological Approach to the Quality Index of Al-Si-Mg Casting Alloys". *International Journal of Cast Metals Research*, 2000. 12(6): p. 367-375.
185. G.E. Dieter and D.J. Bacon, *Mechanical Metallurgy*. Vol. 3. 1986: McGraw-Hill New York.
186. Davis, Joseph R., "Tensile testing". *ASM international*, 2004.
187. C. Caceres. *Particle Crack Damage and Quality Index of Al-Si-Mg Casting Alloys*. in *Transactions of the American Foundry Society and the One Hundred Fourth Annual Castings Congress*. 2000.
188. C. Cáceres, J. Sokolowski and P. Gallo, "Effect of Ageing and Mg Content on the Quality Index of Two Model Al・ Cu・ Si・ Mg Alloys". *Materials Science and Engineering: A*, 1999. 271(1): p. 53-61.
189. C. Caceres, M. Makhlouf, D. Apelian and L. Wang, "Quality Index Chart for Different Alloys and Temperatures: A Case Study on Aluminium Die-Casting Alloys". *Journal of Light Metals*, 2001. 1(1): p. 51-59.
190. C. Caceres, L. Wang, D. Apelian and M. Makhlouf, "Alloy Selection for Die Castings Using the Quality Index". *AFS Transactions*, 1999. 107: p. 239-247.

191. Cacers, C. H., Ingvar L. Svensson, and J. A. Taylor. "Microstructural Factors and the Mechanical Performance of Al-Si-Mg and Al-Si-Cu-Mg Casting Alloys." (2002): 49-57.
192. W. Chen, Y. Wang, J. Qiang and C. Dong, "Bulk Metallic Glasses in the Zr-Al-Ni-Cu System". *Acta Materialia*, 2003. 51(7): p. 1899-1907.
193. H. Ammar, A. Samuel, F. Samuel, E. Simielli, G. Sigworth and J. Lin, "Influence of Aging Parameters on the Tensile Properties and Quality Index of Al-9 Pct Si-1.8 Pct Cu-0.5 Pct Mg 354-Type Casting Alloys". *Metallurgical and Materials Transactions A*, 2012. 43(1): p. 61-73.
194. J. Hernandez-Sandoval, G. Garza-Elizondo, A. Samuel, S. Valtiierra and F. Samuel, "The Ambient and High Temperature Deformation Behavior of Al–Si–Cu–Mg Alloy with Minor Ti, Zr, Ni Additions". *Materials & Design*, 2014. 58: p. 89-101.
195. N. Alexopoulos, "Generation of Quality Maps to Support Material Selection by Exploiting the Quality Indices Concept of Cast Aluminum Alloys". *Materials & design*, 2007. 28(2): p. 534-543.
196. N. Alexopoulos, "Definition of Quality in Cast Aluminum Alloys and Its Characterization with Appropriate Indices". *Journal of materials engineering and performance*, 2006. 15(1): p. 59-66.
197. H. Ammar, C. Moreau, A. Samuel, F. Samuel and H. Doty, "Influences of Alloying Elements, Solution Treatment Time and Quenching Media on Quality Indices of 413-Type Al–Si Casting Alloys". *Materials Science and Engineering: A*, 2008. 489(1): p. 426-438.
198. Yen, C. S., and Thomas James Dolan. "A critical review of the criteria for notch-sensitivity in fatigue of metals." University of Illinois at Urbana Champaign, College of Engineering. Engineering Experiment Station., 1952.
199. Z. Zeng and A. Fatemi, "Elasto-Plastic Stress and Strain Behaviour at Notch Roots under Monotonic and Cyclic Loadings". *The Journal of Strain Analysis for Engineering Design*, 2001. 36(3): p. 287-300.
200. T. Hussain, M. Memon and Z. Mwmon, "Prediction of Elastic-Plastic Behavior of Structures at Notches". *Mehran University Research Journal of Engineering & Technology*, 2012. 31(3): p. 545-552.
201. H. Zhu, J. Xu and M. Feng, "Singular Fields near a Sharp V-Notch for Power Law Creep Material". *International journal of fracture*, 2011. 168(2): p. 159-166.
202. D. Tanner, W. Sun and T. Hyde, "Fe Analysis of a Notched Bar under Thermomechanical Fatigue Using a Unified Viscoplasticity Model". *Procedia Engineering*, 2011. 10: p. 1081-1086.
203. Neuber, Heinz. "Theory of notch stresses: Principles for exact stress calculation.", Vol. 74. JW Edwards, 1946.
204. Wahl, A. M., and R. Beeuwkes Jr. "Stress concentration produced by holes and notches." (2011).
205. G. Sachs, C.S. Smith, J.D. Lubahn, G.E. Davis and L.J. Ebert, "Nondestructive Measurement of Residual and Enforced Stresses by Means of X-Ray Diffraction I: Correlated Abstract of the Literature". 1945.
206. A.M. AGOG1NO, "Notch Effects, Stress State, Ail Ductility". 1978.
207. P. Ludwik and I. Scheu, "Notch Effects in Tests of Mild Steel Material". *Stahl und Eisen*, 1923. 43: p. 95.

208. A. Bayram, "The Influence of Manganese Addition on Mechanical Properties of Commercial Al-4mg Casting Alloys". *Materialwissenschaft und Werkstofftechnik*, 2004. 35(1): p. 29-35.
209. L. Lasa and J. Rodriguez-Ibabe, "Evolution of the Main Intermetallic Phases in Al-Si-Cu-Mg Casting Alloys During Solution Treatment". *Journal of materials science*, 2004. 39(4): p. 1343-1355.
210. S. Shabestari and S. Ghodrat, "Assessment of Modification and Formation of Intermetallic Compounds in Aluminum Alloy Using Thermal Analysis". *Materials Science and Engineering: A*, 2007. 467(1): p. 150-158.
211. S.G. Shabestari and R. Gholizadeh, "Assessment of Intermetallic Compound Formation During Solidification of Al–Si Piston Alloys through Thermal Analysis Technique". *Materials Science and Technology*, 2012. 28(2): p. 156-164.
212. G.H. Garza-Elizondo, A.M. Samuel, S. Valtierra and F.H. Samuel, "Phase Precipitation in Transition Metal-Containing 354-Type Alloys". *International Journal of Materials Research*, 2017. 108(2): p. 108-125.
213. K. Ghosh and N. Gao, "Determination of Kinetic Parameters from Calorimetric Study of Solid State Reactions in 7150 Al-Zn-Mg Alloy". *Transactions of Nonferrous Metals Society of China*, 2011. 21(6): p. 1199-1209.
214. E. Elsharkawi, E. Samuel, A. Samuel and F. Samuel, "Effects of Mg, Fe, Be Additions and Solution Heat Treatment on the Π-Almgfesi Iron Intermetallic Phase in Al–7si–Mg Alloys". *Journal of materials science*, 2010. 45(6): p. 1528-1539.
215. E. Elgallad, Z. Zhang and X.-G. Chen, "Effect of Two-Step Aging on the Mechanical Properties of Aa2219 Dc Cast Alloy". *Materials Science and Engineering: A*, 2015. 625: p. 213-220.
216. R. Li, R. Li, Y. Zhao, L. He, C. Li, H. Guan and Z. Hu, "Age-Hardening Behavior of Cast Al–Si Base Alloy". *Materials Letters*, 2004. 58(15): p. 2096-2101.
217. J.Y. Yao, G.A. Edwards and D.A. Graham. *Precipitation and Age-Hardening in Al-Si-Cu-Mg-Fe Casting Alloys*. in *Materials Science Forum*. 1996. Trans Tech Publ.
218. H. Kang, M. Kida, H. Miyahara and K. Ogi, "Hoyt Memorial Lecture-Age-Hardening Characteristics of Al-Si-Cu-Base Cast Alloys (99-27)". *Transactions of the American Foundrymen's Society*, 1999. 107: p. 507-516.
219. Tavitas-Medrano, Francisco Javier. "Artificial aging treatments of 319-type aluminum alloys", PhD diss., McGill University, 2007.
220. Kaufman, J. Gilbert. *Introduction to aluminum alloys and tempers*. ASM international, 2000.
221. E. Pan, J. Hu and C. Fan, "Solution-Treatment Conditions for Optimal Tensile Properties in A357 Alloy (96-152)". *Transactions of the American Foundrymen's Society*, 1996. 104: p. 1119-1132.
222. J. Gauthier and F. Samuel, "Tensile Properties and Fracture Behavior of Solution-Heat-Treated 319. 2 Al Automotive Alloy". *American Foundrymen's Society, Inc.(USA)*, 1996. p. 849-857.
223. J. Sokolowski, X. Sun, G. Byczynski, D. Northwood, D. Penord, R. Thomas and A. Esseltine, "A Metallurgical Study of the Heat Treatment of Aluminum Alloy 319 (Al-6si-3.5 Cu) Castings". *Journal of Materials Processing Technology*, 1995. 53: p. 1-2.

224. M. Moustafa, F. Samuel, H. Doty and S. Valtierra, "Effect of Mg and Cu Additions on the Microstructural Characteristics and Tensile Properties of Sr-Modified Al-Si Eutectic Alloys". *International Journal of Cast Metals Research*, 2002. 14(4): p. 235-253.
225. P.-S. Warng, Y.-J. Liauh, S.-L. Lee and J.-C. Lin, "Effects of Be Addition on Microstructures and Mechanical Properties of B319. 0 Alloys". *Materials chemistry and physics*, 1998. 53(3): p. 195-202.
226. S.-N. Yie, S.-L. Lee, Y.-H. Lin and J.-C. Lin, "Mechanical Properties of Al-11% Si Casting Alloys Containing Trace Be and Sr". *Materials Transactions, JIM*, 1999. 40(4): p. 294-300.
227. Tash, M. "Effect of metallurgical parameters on the machining behaviour of 356 and 319 alloys.", Ph. D. Dissertation. University of Quebec at Chicoutimi, 2006.
228. P. Villars, A. Prince and H. Okamoto, *Handbook of Ternary Alloy Phase Diagrams*. ed., ed. Vol. 1995: Asm Intl.
229. E. Elgallad, Z. Zhang and X.-G. Chen, "Effect of Quenching Rate on Precipitation Kinetics in Aa2219 Dc Cast Alloy". *Physica B: Condensed Matter*, 2017. 514: p. 70-77.
230. Shen, P., E. M. Elgallad, and X-G. Chen. "On the aging behavior of AA2618 DC cast alloy." In *Light Metals 2013*, pp. 373-377. Springer, Cham, 2016.
231. C.-J. Tseng, S.-L. Lee, T.-F. Wu and J.-C. Lin, "Effects of Fe Content on Microstructure and Mechanical Properties of A206 Alloy". *Materials Transactions, JIM*, 2000. 41(6): p. 708-713.
232. M.I. Daoudi, A. Triki and A. Redjaimia, "Dsc Study of the Kinetic Parameters of the Metastable Phases Formation During Non-Isothermal Annealing of an Al–Si–Mg Alloy". *Journal of thermal analysis and calorimetry*, 2010. 104(2): p. 627-633.
233. H. Lu, P. Kadolkar, K. Nakazawa, T. Ando and C. Blue, "Precipitation Behavior of Aa2618". *Metallurgical and Materials Transactions A*, 2007. 38(10): p. 2379-2388.
234. Andrade González, N. R."Aging Effects in 319-Type Alloys.", PhD diss., McGill University, 2006.
235. F. Tavitas-Medrano, J. Gruzleski, F. Samuel, S. Valtierra and H. Doty, "Effect of Mg and Sr-Modification on the Mechanical Properties of 319-Type Aluminum Cast Alloys Subjected to Artificial Aging". *Materials Science and Engineering: A*, 2008. 480(1): p. 356-364.
236. W. Reif, J. Dutkiewicz, R. Ciach, S. Yu and J. Krol, "Effect of Ageing on the Evolution of Precipitates in Alsicumg Alloys". *Materials Science and Engineering: A*, 1997. 234: p. 165-168.
237. M. Purtee, "Aging Effects of an Aluminum-Based 319 Alloy". *Foundry management & technology*, 1998. 126(10): p.
238. M. Takeda, F. Ohkubo, T. Shirai and K. Fukui. *Precipitation Behaviour of Ai-Mg-Si Ternary Alloys*. in *Materials Science Forum*. 1996. Trans Tech Publ.
239. A. Elwazri, R. Varano, F. Siciliano, D. Bai and S. Yue, "Characterisation of Precipitation of Niobium Carbide Using Carbon Extraction Replicas and Thin Foils by Fesem". *Materials science and technology*, 2006. 22(5): p. 537-541.
240. H. Kang, M. Kida, H. Miyahara and K. Ogi, "Age-Hardening Behavior of Al-Si-Cu Base Cast Alloys". *Journal of Japan Foundry Engineering Society*, 1997. 69(10): p. 828-834.

241. Elsharkawi, Ehab. "Effects of metallurgical parameters on the decomposition of π-AlFeMgSi phase in AL-SI-MG alloys and its influence on the mechanical properties.", PhD diss., Université du Québec à Chicoutimi, 2011.
242. S. Shabestari, "The Effect of Iron and Manganese on the Formation of Intermetallic Compounds in Aluminum–Silicon Alloys". *Materials Science and Engineering: A*, 2004. 383(2): p. 289-298.
243. S. Shivkumar, S. Ricci Jr and D. Apelian, "Influence of Solution Parameters and Simplified Supersaturation Treatments on Tensile Properties of A356 Alloy". *AFS Transactions*, 1990. 98: p. 913-922.
244. D. Zhang, L. Zheng and D. StJohn, "Effect of Solution Treatment Temperature on Tensile Properties of Ai-7si-O. 3mg (Wt-%) Alloy". *Materials science and technology*, 1998. 14(7): p. 619-625.
245. W. Yuying, L. Xiangfa, J. Binggang and H. Chuanzhen, "Modification Effect of Ni–38wt.% Si on Al–12wt.% Si Alloy". *Journal of Alloys and Compounds*, 2009. 477(1): p. 118-122.
246. P. Zhu and Q. Liu, "Kinetics of Granulation of Discontinuous Phase in Eutectic Structures". *Materials science and technology*, 1986. 2(5): p. 500-507.
247. A.M. Samuel, A. Pennors, C. Villeneuve, F.H. Samuel, H.W. Doty and S. Valtierra, "Effect of Cooling Rate and Sr-Modification on Porosity and Fe-Intermetallics Formation in Al-6.5% Si-3.5% Cu-Fe Alloys". *International Journal of Cast Metals Research*, 2000. 13(4): p. 231-253.
248. J. Jorstad, "Understanding" Sludge"". *Die Cast. Eng.*, 1986. 30(6): p. 30.
249. R. Molina, P. Amalberto and M. Rosso, "Mechanical Characterization of Aluminium Alloys for High Temperature Applications Part1: Al-Si-Cu Alloys". *Metallurgical Science and Technology*, 2011. 29(1): p. 5.
250. Y. Li, Y. Yang, Y. Wu, L. Wang and X. Liu, "Quantitative Comparison of Three Ni-Containing Phases to the Elevated-Temperature Properties of Al–Si Piston Alloys". *Materials Science and Engineering: A*, 2010. 527(26): p. 7132-7137.
251. J. Catherall and R. Smart, "The Effects of Nickel in Aluminium-Silicon Eutectic Alloys". *Metallurgia*, 1969. 79(476): p. 247-250.
252. T. Takahashi, A. Kamio and Y. Kojima, "Effects of Ni and Fe Addition on Various Properties in Heat Resisting Aluminum Casting Alloys". *J. Jap. Inst. Light Met.*, 1973. 23(1): p. 26-32.
253. N. Belov, D. Eskin and N. Avxentieva, "Constituent Phase Diagrams of the Al–Cu–Fe–Mg–Ni–Si System and Their Application to the Analysis of Aluminium Piston Alloys". *Acta Materialia*, 2005. 53(17): p. 4709-4722.
254. T. Savaşkan and Y. Alemdağ, "Effect of Nickel Additions on the Mechanical and Sliding Wear Properties of Al–40zn–3cu Alloy". *Wear*, 2010. 268(3): p. 565-570.
255. P. Crepeau, S. Antolovich and J. Warden, "Structure-Property Relationships in Aluminum Alloy 339-T5: Tensile Behavior at Room and Elevated Temperature". *AFS Trans*, 1990. 98: p. 813-822.
256. J. Gauthier, P. Louchez and F. Samuel, "Heat Treatment of 319.2 Aluminium Automotive Alloy Part 1, Solution Heat Treatment". *Cast Metals*, 1995. 8: p. 91-91.
257. H. Shercliff and M. Ashby, "A Process Model for Age Hardening of Aluminium Alloys—I. The Model". *Acta Metallurgica et Materialia*, 1990. 38(10): p. 1789-1802.

258. H. Shercliff and M. Ashby, "A Process Model for Age Hardening of Aluminium Alloys—Ii. Applications of the Model". *Acta Metallurgica et materialia*, 1990. 38(10): p. 1803-1812.
259. S. Esmaeili, D. Lloyd and W. Poole, "A Yield Strength Model for the Al-Mg-Si-Cu Alloy Aa6111". *Acta Materialia*, 2003. 51(8): p. 2243-2257.
260. S. Esmaeili, D. Lloyd and W. Poole, "Modeling of Precipitation Hardening for the Naturally Aged Al-Mg-Si-Cu Alloy Aa6111". *Acta Materialia*, 2003. 51(12): p. 3467-3481.
261. V. Sharma, K.S. Kumar, B.N. Rao and S. Pathak, "Studies on the Work-Hardening Behavior of Aa2219 under Different Aging Treatments". *Metallurgical and Materials Transactions A*, 2009. 40(13): p. 3186.
262. L. Cheng, W. Poole, J. Embury and D. Lloyd, "The Influence of Precipitation on the Work-Hardening Behavior of the Aluminum Alloys Aa6111 and Aa7030". *Metallurgical and Materials Transactions A*, 2003. 34(11): p. 2473-2481.
263. X. Wang, J. Embury, W. Poole, S. Esmaeili and D. Lloyd, "Precipitation Strengthening of the Aluminum Alloy Aa6111". *Metallurgical and Materials Transactions A*, 2003. 34(12): p. 2913-2924.
264. A. Deschamps, S. Esmaeili, W. Poole and M. Militzer, "Strain Hardening Rate in Relation to Microstructure in Precipitation Hardening Materials". *Le Journal de Physique IV*, 2000. 10(PR6): p. Pr6-151-Pr6-156.
265. A. Bayram, A. Uğuz and M. Ula, "Effects of Microstructure and Notches on the Mechanical Properties of Dual-Phase Steels". *Materials characterization*, 1999. 43(4): p. 259-269.
266. E. Rincon, H. Lopez, M. Cisneros, H. Mancha and M. Cisneros, "Effect of Temperature on the Tensile Properties of an as-Cast Aluminum Alloy A319". *Materials Science and Engineering: A*, 2007. 452: p. 682-687.
267. Z. Li, A. Samuel, F. Samuel, C. Ravindran, S. Valtierra and H. Doty, "Parameters Controlling the Performance of Aa319-Type Alloys: Part I. Tensile Properties". *Materials Science and Engineering: A*, 2004. 367(1): p. 96-110.
268. J. Rakhmonov, G. Timelli and F. Bonollo, "The Effect of Transition Elements on High-Temperature Mechanical Properties of Al–Si Foundry Alloys–a Review". *Advanced Engineering Materials*, 2016. 18(7): p. 1096-1105.
269. A. Farkoosh, M. Javidani, M. Hoseini, D. Larouche and M. Pekguleryuz, "Phase Formation in as-Solidified and Heat-Treated Al–Si–Cu–Mg–Ni Alloys: Thermodynamic Assessment and Experimental Investigation for Alloy Design". *Journal of Alloys and Compounds*, 2013. 551: p. 596-606.
270. J. Barresi, Z. Chen, C. Davidson, M. Murray, T. Nguyen, D. St John and W. Thorpe. *Casting of Aluminium Alloy Components*. in *MATERIALS FORUM-RUSHCUTTERS BAY-*. 1996.
271. Elsebaie, Ossama. "Effects of strontium-modification, iron-based intermetallics and aging conditions on the impact toughness of Al-(6-11)% Si alloys", PhD diss., Université du Québec à Chicoutimi, 2010.
272. A. Mohamed, F. Samuel, A. Samuel and H. Doty, "Influence of Additives on the Impact Toughness of Al–10.8% Si near-Eutectic Cast Alloys". *Materials & Design*, 2009. 30(10): p. 4218-4229.

273. T. Kobayashi and M. Niinomi, "Fracture Toughness and Fatigue Characteristics of Aluminum Casting Alloy". *J. Jpn. Inst. Met*, 1991. 41: p. 398-405.
274. F. Paray, B. Kulunk and J. Gruzleski, "Impact Properties of Al-Si Foundry Alloys". *International Journal of Cast Metals Research*, 2000. 13(1): p. 17-37.
275. Ibrahim, Ahmed. "On the effects of ambient temperature and high temperature on the performance of Al-Cu and Al-Si-Cu alloys." MSc diss., Université du Québec à Chicoutimi, 2017.
276. Q Liu, Q., P. Baburamani, and C. Loader. *Effect of High Temperature Exposure on the Mechanical Properties of Cold Expanded Open Holes in 7050-T7451 Aluminium Alloy*. No. DSTO-TN-0844. DEFENCE SCIENCE AND TECHNOLOGY ORGANISATION VICTORIA (AUSTRALIA) AIR VEHICLES DIV, 2008.
277. E. Rincon, H. Lopez, M. Cisneros and H. Mancha, "Temperature Effects on the Tensile Properties of Cast and Heat Treated Aluminum Alloy A319". *Materials Science and Engineering: A*, 2009. 519(1): p. 128-140.
278. J. Jorstad, W. Rasmussen and D. Zalensas, "Aluminum Casting Technology, American Foundrymen's Society". *Inc., Des Plaines, IL, USA*, 1993.
279. I. Polmear, "Light Alloys, Metallurgy of the Light Alloys". *Metallurgy and Materials Science, Arnold, Great Britain*, 1995. p. 168-95.
280. P. Prasad. "Characterization of New, Cast, High Temperature Aluminum Alloys for Diesel Engine Applications", PhD diss., University of Cincinnati. (2006).
281. R. Rana, R. Purohit and S. Das, "Reviews on the Influences of Alloying Elements on the Microstructure and Mechanical Properties of Aluminum Alloys and Aluminum Alloy Composites". 2012.
282. J. Hanafee, "Effect of Nickel on Hot Hardness of Aluminum-Silicon Alloys". *Modern Castings*, 1963. 44(4): p. 514-520.
283. InfoMine. *Commodity and Metal Prices*. 2017 [cited; Available from: http://www.infomine.com/investment/metal-prices/.
284. T. Mbuya, B. Odera and S. Ng'ang'a, "Influence of Iron on Castability and Properties of Aluminium Silicon Alloys: Literature Review". *International Journal of Cast Metals Research*, 2003. 16(5): p. 451-465.
285. L. Lu and A. Dahle, "Iron-Rich Intermetallic Phases and Their Role in Casting Defect Formation in Hypoeutectic Al− Si Alloys". *Metallurgical and Materials Transactions A*, 2005. 36(13): p. 819-835.
286. E. Ogris, H. Lüchinger and P.J. Uggowitzer. *Silicon Spheroidization Treatment of Thixoformed Al-Si-Mg Alloys*. in *Materials Science Forum*. 2002. Trans Tech Publ.
287. A. Samuel, H. Doty, S. Valtierra and F. Samuel, "Effect of Sr-P Interaction on the Microstructure and Tensile Properties of A413. 0 Type Alloys". *Advances in Materials Science and Engineering*, 2016.
288. H. Li, S. Shivkumar, X. Luo and D. Apelian, "Influence of Modification on the Solution Heat-Treatment Response of Cast Al-Si-Mg Alloys". *Cast Metals*, 1988. 1(4): p. 227-234.
289. R.M. Gomes, T. Sato and A. Kamio, "Microstructures and Coarsening Behavior of Silicon Particles in P/M Al–Si–Cu–Mg Alloys Containing Fe and Ni". *Journal of Japan Institute of Light Metals*, 1997. 47(2): p. 90-97.

290. R. MacKay and M. Nathal, "Γ′ Coarsening in High Volume Fraction Nickel-Base Alloys". *Acta Metallurgica et Materialia*, 1990. 38(6): p. 993-1005.
291. G. Wan and P. Sahm, "Particle Growth by Coalescence and Ostwald Ripening in Rheocasting of Pbsn". *Acta Metallurgica et Materialia*, 1990. 38(11): p. 2367-2372.
292. M.G. Mueller, M. Fornabaio and A. Mortensen, "Silicon Particle Pinhole Defects in Aluminium–Silicon Alloys". *Journal of Materials Science*, 2017. 52(2): p. 858-868.
293. M.F. Ibrahim, E.M. Elgallad, S. Valtierra, H.W. Doty and F.H. Samuel, "Metallurgical Parameters Controlling the Eutectic Silicon Charateristics in Be-Treated Al-Si-Mg Alloys". *Materials*, 2016. 9(2): p. 78.
294. J. Taylor, D. St John, J. Barresi and M. Couper, "An Empirical Analysis of Trends in Mechanical Properties of T6 Heat Treated Al-Si-Mg Casting Alloys". *International Journal of Cast Metals Research*, 2000. 12(6): p. 419-430.
295. Y. Han, A. Samuel, F. Samuel and H. Doty, "Dissolution of Al2cu Phase in Non-Modified and Sr Modified 319 Type Alloys". *International Journal of Cast Metals Research*, 2008. 21(5): p. 387-393.
296. D.M.S.a.J.A. Eady. *Metals in Mining* in 1981. Australian Inst. of Mining.